

Yn-Hwang Lin



Polymer

2nd
Edition

Viscoelasticity

Basics, Molecular Theories, Experiments
and Simulations

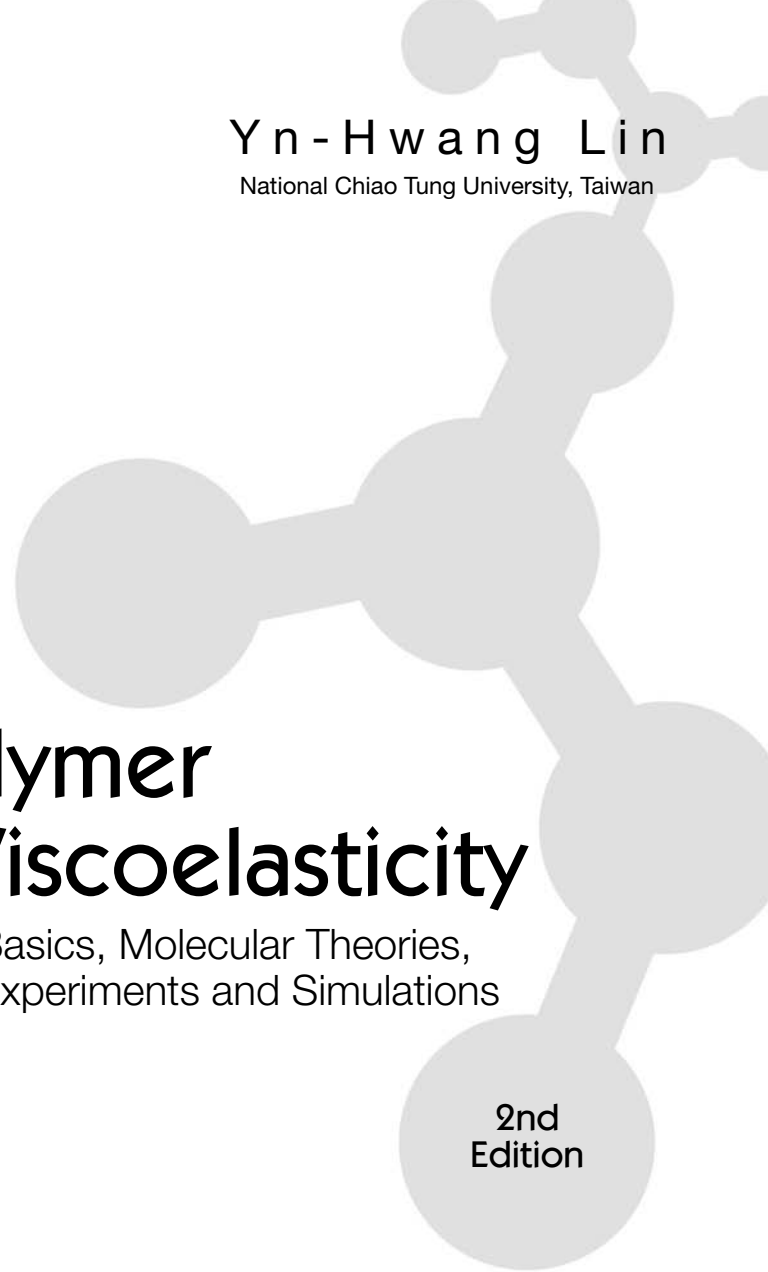


Polymer Viscoelasticity

Basics, Molecular Theories,
Experiments and Simulations

2nd
Edition

This page intentionally left blank



Yn-Hwang Lin

National Chiao Tung University, Taiwan

Polymer Viscoelasticity

Basics, Molecular Theories,
Experiments and Simulations

2nd
Edition

 World Scientific

NEW JERSEY • LONDON • SINGAPORE • BEIJING • SHANGHAI • HONG KONG • TAIPEI • CHENNAI

Published by

World Scientific Publishing Co. Pte. Ltd.

5 Toh Tuck Link, Singapore 596224

USA office: 27 Warren Street, Suite 401-402, Hackensack, NJ 07601

UK office: 57 Shelton Street, Covent Garden, London WC2H 9HE

Library of Congress Cataloging-in-Publication Data

Lin, Y.-H.

Polymer viscoelasticity : basics, molecular theories, experiments, and simulations / Yn-Hwang Lin. -- 2nd ed.

p. cm.

Includes bibliographical references and index.

ISBN-13: 978-981-4313-03-2 (hardcover : alk. paper)

ISBN-10: 981-4313-03-3 (hardcover : alk. paper)

1. Polymers--Viscosity. 2. Viscoelasticity. I. Title.

QD281.P6L56 2010

620.1'9204232--dc22

2010038333

British Library Cataloguing-in-Publication Data

A catalogue record for this book is available from the British Library.

Copyright © 2011 by World Scientific Publishing Co. Pte. Ltd.

All rights reserved. This book, or parts thereof, may not be reproduced in any form or by any means, electronic or mechanical, including photocopying, recording or any information storage and retrieval system now known or to be invented, without written permission from the Publisher.

For photocopying of material in this volume, please pay a copying fee through the Copyright Clearance Center, Inc., 222 Rosewood Drive, Danvers, MA 01923, USA. In this case permission to photocopy is not required from the publisher.

Typeset by Stallion Press

Email: enquiries@stallionpress.com

Printed in Singapore.

Contents

Preface	xiii
Preface to the Second Edition	xvii
1. Conformation of Polymer Chains	1
1.1 Introduction	1
1.2 Probability Distribution Functions, Moments and Characteristic Functions	2
1.3 A Central Limit Theorem	5
1.4 The Freely Jointed Chain Model	7
1.5 Distribution of the End-to-End Vector	10
1.6 The Gaussian Chain	11
Appendix 1.A — The Dirac Delta Function	13
References	15
2. Rubber Elasticity	16
2.1 Introduction	16
2.2 Entropy and Rubber Elasticity	17
2.3 Molecular Theory for Rubber Elasticity	18
References	25
3. Polymer Chain Dynamics	26
3.1 Introduction	26
3.2 The Smoluchowski Equation	28
3.3 The Langevin Equation	32
3.4 The Rouse Model	33

3.5	Diffusion Motion of the Rouse Chain	35
3.6	The Rouse Normal Modes of Motion	35
	Appendix 3.A — Eigenvalues and Eigenvectors of the Rouse Matrix	40
	Appendix 3.B — The Langevin Equation of a Particle in a Harmonic Potential	42
	Appendix 3.C — The Continuous Rouse Model	43
	Appendix 3.D — Binomial Random Walk	46
	References	49
4.	Linear Viscoelasticity	51
4.1	Introduction	51
4.2	Maxwell Equation	52
4.3	Boltzmann's Superposition Principle	57
4.4	Relaxation Modulus	58
4.5	Steady-State Shear Flow	60
4.6	Dynamic-Mechanical Spectroscopy	61
4.7	Steady-State Compliance	65
4.8	Creep Compliance	71
	Appendix 4.A — The Hopkins–Hamming Method for the Conversion of $G(t)$ into $J(t)$	75
	References	76
5.	Stress and Strain	78
5.1	Stress	78
5.2	Finite Strain	83
5.3	A neo-Hookean Material	90
5.4	A Newtonian Fluid	92
	Appendix 5.A — Tensor Operations	94
	References	97
6.	Molecular Theory of Polymer Viscoelasticity — Elastic Dumbbell Model	98
6.1	Introduction	98
6.2	The Smoluchowski Equation for an Elastic Dumbbell	99
6.3	Rheological Constitutive Equation of the Elastic Dumbbell Model	104
6.4	Applications of the Constitutive Equation	109

Appendix 6.A — Codeformational (Convected)	
Time Derivative	113
References	118
7. Molecular Theory of Polymer Viscoelasticity — The Rouse Model	119
7.1 The Smoluchowski Equation of the Rouse Model	119
7.2 Rheological Constitutive Equation of the Rouse Model	127
Appendix 7.A — Eigenvalues and the Inverse of the Rouse Matrix	130
References	132
8. Molecular Theory of Polymer Viscoelasticity — Entanglement and the Doi–Edwards (Reptation) Model	133
8.1 Introduction	133
8.2 The Primitive Chain	135
8.3 Diffusion Motion	138
8.4 Relaxation Modulus	141
8.5 Relaxation of Stress by Reptation	146
Appendix 8.A — Tension in a Gaussian Chain Between Two Fixed Points	150
Appendix 8.B — Equivalent Expressions for Rubber Elasticity	151
References	151
9. Molecular Theory of Polymer Viscoelasticity — The Extended Reptation Model	153
9.1 Intramolecular Processes	153
9.2 Contour Length Fluctuations of the Primitive Chain	156
9.3 Relaxation Processes before $t \approx T_{eq}$	161
9.4 Universality of the $G(t)$ Line Shape in Terms of the Extended Reptation Theory (ERT)	164
9.5 Zero-Shear Viscosity and Steady-State Compliance	165
9.6 Note: A Clarification of the Term “Transition Region”	167
Appendix 9.A — Contour Length Fluctuations of the Primitive Chain	168

Appendix 9.B — Rouse Motions in an Entanglement Strand: The Rouse–Mooney Normal Modes of Motion	171
Appendix 9.C — Eigenvalues and Eigenvectors of the Rouse–Mooney Matrix	176
Appendix 9.D — Hierarchy and Universality among the Inherent Characteristic Times in the (Extended) Slip-Link Model	177
References	180
10. Comparison of the Extended Reptation Theory (ERT) with Experiments	182
10.1 Effects of the Molecular-Weight Distribution of the Sample	183
10.2 Analysis of the $G(t)$ Line Shape	186
10.3 Zero-Shear Viscosity and Steady-State Compliance . . .	197
10.4 Viscoelasticity and Diffusion	205
10.5 Summary	209
Appendix 10.A — The Reason Why $G''(\omega)$ Should Be Excluded from the Line-Shape Analysis in Terms of the Rouse Theory or the ERT If Only the Entropic Region Is to Be Covered	211
References	213
11. ERT vs. Rouse Theory, Concentration Dependence and Onset of Entanglement, and Tube Dilation	215
11.1 Introduction	215
11.2 Entanglement Region	217
11.3 Entanglement-Free Region and Onset of Entanglement .	226
11.4 Tube Dilation	234
Appendix 11.A — Basic Form of the Blending Law in a Binary Blend	238
References	240
12. Molecular Theory of Polymer Viscoelasticity — Nonlinear Relaxation Modulus of Entangled Polymers	242
12.1 Chain-Tension Relaxation	243
12.2 Comparison of Theory and Experiment	249
References	256

13. Number of Entanglement Strands per Cubed Entanglement Distance, n_t	257
13.1 Introduction	257
13.2 Theoretical Basis and Experimental Support for n_t Being a Universal Constant	259
13.3 Concentration Dependence of n_t	263
13.4 Packing of Polymer Chains	263
13.5 Some Comments	264
Appendix 13.A — The Rouse Segment vs. the Kuhn Segment	266
References	268
14. Glass Transition-Related Thermorheological Complexity in Polystyrene Melts	269
14.1 Introduction	269
14.2 $G(t)$ Functional Forms	271
14.3 $J(t)$ Line-Shape Analyses of Entangled Systems	273
14.4 Analyses of $J(t)$, J_e^0 and η_0 in an Entanglement-Free System	286
14.5 Analyses of the $G^*(\omega)$ Spectra of Entanglement-Free Systems	294
14.6 Dynamic Anisotropy in Entangled Systems	298
14.7 Comparison of the A_G^f and β Values Extracted from the $J(t)$ and $G^*(\omega)$ Line Shapes	301
14.8 T_g Defined by the Structural Relaxation Time $\tau_S = 1,000$ sec.	303
14.9 Dependences of τ_S , s' and K' on $\Delta T = T - T_g$	305
14.10 Structure as Revealed in $G(t)$	312
14.11 Frictional Slowdown and Structural Growth	316
14.12 K Values in the Close Neighborhood of T_g	318
14.13 Internal Viscosity and Zero Shear Viscosity	321
Appendix 14.A — Calculations of the $G'(\omega)$ and $G''(\omega)$ Spectra from a $G(t)$ Functional Form	322
References	326
15. The Basic Mechanism for the Thermorheological Complexity in Polystyrene Melts	328
15.1 The Basic Mechanism of the Thermorheological Complexity (TRC)	329

15.2	Breakdown of the Stokes–Einstein Relation (BSE) Sharing the Same Basic Mechanism	331
15.3	Comparison of the TRC and BSE Results	332
15.4	A Discussion of the Glass Transition as Viewed from the Study of TRC	334
15.5	Specific Relations with Literature-Reported Studies of BSE	336
	Appendix 15.A — Comparison with the Two-State Model of BSE	337
	References	338
16.	Monte Carlo Simulations of Stress Relaxation of Rouse Chains	341
16.1	The Basic Monte Carlo Simulation Scheme as Applied to the Rouse Model	341
16.2	Simulation of the Rouse Relaxation Modulus — Following the Application of a Step Shear Strain	344
16.3	Simulation of the Rouse Relaxation Modulus — in an Equilibrium State	346
16.4	Comparison between Simulation and Theory of the Rouse Model	347
	Appendix 16.A — Molecular Expression for the Stress Tensor	350
	Appendix 16.B — Time-Correlation Functional Form for the Relaxation Modulus	350
	References	357
17.	Monte Carlo Simulations of Stress Relaxation of Fraenkel Chains — Linear Viscoelasticity of Entanglement-Free Polymers	358
17.1	The Fraenkel Chain Model	359
17.2	Equilibrium-Simulated Relaxation Modulus Curves . . .	360
17.3	Step Strain-Simulated Relaxation Modulus Curves . . .	368
17.4	Comparison between Simulation and Experiment	372
17.5	A Resolution of the Rouse–Kuhn Paradox	375
	Appendix 17.A — Application of the Virial Theorem to the Fraenkel Dumbbell	376

Appendix 17.B — Contribution of the Dynamic Couplings between Different Segments to the Relaxation Modulus	377
References	379
18. Monte Carlo Simulations of Stress Relaxation of Fraenkel Chains — Nonlinear Viscoelasticity of Entanglement-Free Polymers	381
18.1 Effects of the Nonlinearly Enhanced Tensile Force along the Fraenkel Segment	382
18.2 The Lodge–Meissner Relation for the Fraenkel Chain . .	388
18.3 Stress and Segmental Orientation	391
18.4 Similarities in Nonlinear Relaxation Modulus between Entangled Polymer and Entanglement-Free Fraenkel-Chain Systems	396
18.5 A Final Note	404
Appendix 18.A — Proof of The Lodge–Meissner Relation as Applied to the Fraenkel-Chain Model	404
Appendix 18.B — The Stress-Optical Rule in the Case of Simple Shear	406
References	408
Index	411

This page intentionally left blank

Preface

I became involved in the research of polymer viscoelasticity shortly after I began to work in the Exxon Chemical Company in 1980, two years after the landmark papers of Doi and Edwards were published. Even though there was a great deal of hope and excitement among polymer researchers regarding the Doi–Edwards theory, at the time I did not foresee that I would come to accept the theory so completely, as eventually the supporting evidence, a great deal of my own research over the years, convinced me. This book is an account of how the universal viscoelastic phenomena of nearly monodisperse polymers are explained quantitatively by the Doi–Edwards (reptation) theory and the extended reptation theory, developed on the framework of the Doi–Edwards theory. These include the transformation of the characteristic viscoelastic spectrum with molecular-weight change and/or dilution; the molecular-weight dependence of the zero-shear viscosity and of the steady-state compliance, and their respective transition points, M_c and M'_c ; the relation between viscoelasticity and diffusion; the damping function; and the slip-stick melt fracture phenomenon. The consistently quantitative agreements between theory and experiment led to the proposition that the number of entanglement strands per cubed tube diameter (or cubed entanglement distance) be a universal constant, which is now well supported by a large collection of data (Chapter 13). The ultimate significance of these results is that the basic mean-field assumption in the Doi–Edwards theory: $aL = \langle R^2 \rangle$ (a , the tube diameter; L , the primitive chain length; $\langle R^2 \rangle$, mean square end-to-end distance of the polymer chain) is valid for a (nearly) monodisperse system. Here the mean field is assumed rather than derived. The proposition of the characteristic length “ a ” for an entanglement system is as important as the conceiving of the Rouse segment twenty five years earlier. From the study of blend-solution

systems, it is shown in Chapter 11 that the extended reptation theory has bridged the gap between the Doi–Edwards theory and the Rouse theory. As shown in the same chapter, the tube dilation effect, which is found occurring in the long-time region of a binary-blend’s relaxation, indicates that the mean-field length $a = \langle R^2 \rangle / L$ has a dynamic aspect. It is hoped that the readers will recognize the far-reaching insight of Doi and Edwards’ assumption $aL = \langle R^2 \rangle$ in this book.

The first part of this book explains the basics of polymer conformation, rubber elasticity, viscoelasticity, and chain dynamics (Chapters 1–5). Knowledge of these basics is not only generally useful but is quite essential in understanding the molecular theories studied after Chapter 6. This book starts from a very fundamental level. Each chapter is built upon the contents of the previous chapters. The elastic-dumbbell model is introduced in Chapter 6 as a prerequisite for the Rouse model, studied in Chapter 7. Although the final theme of this book is about entanglement (Chapters 8–13), there are several essential reasons to include the Rouse model: Firstly, the Rouse theory is the foundation for modern theories of polymer dynamics and viscoelasticity. Without it this book would be quite incomplete. Secondly, in spite of its original intention for a dilute polymer solution, the Rouse theory has been generally accepted as valid for describing the viscoelastic behavior of an entanglement-free polymer melt system. A further in-depth experimental study supporting the validity of the Rouse theory is presented in Chapter 11. It is desirable to compare the Rouse theory with the Doi–Edwards theory and the extended reptation theory so that both the entanglement-free and entanglement regions can be studied in perspective. It is shown in Chapter 11 that the onset molecular weight of entanglement is equivalent to the entanglement molecular weight M_e determined from the plateau modulus ($G_N = 4\rho RT/5M_e$). Thirdly, the extended reptation theory is developed by incorporating the Rouse motions in the Doi–Edwards theory. Thus, for discussing this topic, it is quite essential to know the basic elements of the Rouse model.

This book includes a broad range of studies of polymer viscoelastic properties: basics, molecular theories, and experiments. It also covers both the entanglement and entanglement-free regions. Moving from one region to the other is made by either molecular-weight change or concentration change. The linear viscoelastic behavior is studied in Chapters 8–11; the nonlinear behavior is studied in Chapter 12. And a newly discovered law is discussed in Chapter 13. On the other hand, this book is limited mainly to the studies of polystyrene; viscoelastic-spectrum results of nearly

monodisperse polystyrene samples and their blends predominantly used in part of this book (Chapters 10–12) have been obtained and published by myself. Polystyrene is the most accessible system for study. In view of the universality existing among the flexible polymers as evidenced in several important cases, the ideas and theories presented in this book, which have been consistently and quantitatively tested by the experimental results of polystyrene, should be applicable to other kinds of polymers. To my knowledge, besides those studies of viscoelastic spectra reported by myself, there are few other studies of such a quantitative nature. It may strike the reader that the new theories and experimental spectrum results come mainly from my own work; this is due to the pioneering aspect of this field, to which I have devoted years of research, as well as the relative scarcity of parallel in-depth studies. Nevertheless, the agreement between theory and experiment has been further supported by experimental data obtained by Plazek and O'Rourke, Kramer *et al.*, Lodge *et al.*, Watanabe *et al.* and others at various key points.

In terms of the theories based on the tube assumption ($aL = \langle R^2 \rangle$), quantitative study is only possible for nearly monodisperse systems, due to the complexity caused by the tube dilation effect, which occurs in the system of broad molecular-weight distribution. As a result, the theories presented in the book may be limited from being directly applied to commercial polymers, whose molecular-weight distribution is broad in general. However, the theories and analyses presented in this book should be useful and valuable in many aspects of polymer research and development work. A unique problem in industry is the slip-stick melt fracture phenomenon that occurs in extrusion. The basic dynamic processes related to the phenomenon are discussed in Chapter 12. Because of the limited space of this book, the reader is referred to the original work for an explanation of the phenomenon in terms of the molecular dynamic processes. Since the viscoelastic properties of nearly monodisperse polymers can be analyzed quantitatively in terms of the molecular theories, dynamic mechanical measurement can be used very effectively to study the chain motions that correspond to various length-scales above the Rouse-segment size. Thus, very rich dynamic information can be obtained from the viscoelastic spectra for comparing studies with other spectroscopies, such as NMR, dielectric relaxation, dynamic light scattering, and neutron spin-echo spectroscopy, etc. Such interplay among different probing techniques should greatly enhance the studies and applications of chain dynamics.

Last but not least, I should mention that important concepts from early studies of polymer viscoelasticity have not been used and described according to their historical developments. Here, I should like to refer to the review by J. D. Ferry,^a which covers the key research works in the period from 1930 to 1970.

Y.-H. Lin
July 2002

^aFerry, J. D., *Macromolecules* **24**, 5237 (1991).

Preface to the Second Edition

The second edition has five additional chapters (Chapters 14–18), which further explore and extend the scope of the subjects that are covered in the first edition. These additional chapters incorporate new concepts and effects that have been developed or discovered in recent years, thanks to a large extent to the theories and experiments studied in the first edition. To more closely integrate the new and existing materials, modifications, insertions and additions have been made to the first 13 chapters at appropriate places.

There are two main themes in the newly added portion, which are complementary to each other: The first (Chapters 14 and 15) are the studies of viscoelastic response functions over the full dynamic range. The quantitative line-shape analyses of viscoelastic responses of polystyrene melts over the entropic region (modulus values below $\sim 4 \times 10^7$ dynes/cm²) covered in the first edition are extended to the energetic region (modulus values between $\sim 4 \times 10^7$ and $\sim 10^{10}$ dynes/cm²). The full-range analyses are carried out using the consistently successful description of the entropic region by the extended reptation theory (ERT; for entangled systems) or the Rouse theory (for entanglement-free systems) — extensively illustrated in Chapters 10 and 11 — as the frame of reference. The scheme allows the temperature dependence of dynamics in the energetic region being stronger than that in the entropic region of polystyrene samples to be analyzed consistently and systematically revealing universal aspects of the glass transition-related thermorheological complexity. The time and length scales of the glassy-relaxation process and the basic mechanism for the thermorheological complexity are evaluated or analyzed in terms of the molecular pictures as embodied in the ERT (Chapter 9) and the Rouse theory (Chapter 7). The second theme is the use of the Langevin

equation-based Monte Carlo simulations to study fundamental issues at the “Rouse”-segmental level. Firstly the simulation method is introduced and illustrated by applying it to the Rouse chain case (Chapter 16), where quantitative comparisons with the theoretical results (Chapters 3 and 7) can be made. The simulations of Fraenkel chains reveal previously unknown mechanisms — unlike the traditional explanations based on the Gaussian chain — for the occurrence of the entropic Rouse process and the holding of the (rubbery) stress-optical rule (Chapters 17 and 18). Concurrently, the Fraenkel chain model provides a theoretical basis for resolving the paradox that the experimentally determined sizes of the Rouse and Kuhn segments are nearly the same (Appendix 13.A) and gives a natural explanation for the coexistence of the energy-driven and entropy-driven modes.

I am grateful to Professors M. D. Ediger and T. Inoue for providing their data in digital form. The data from Professor Ediger are used in Fig. 15.1. The data from Professor Inoue allow the analyses of viscoelastic spectra to be a smooth process, as presented in Chapter 14.

I am thankful to my wife Ling-Hwa for her patience and support through my research career as well as writing of this book.

Y.-H. Lin
November 2009

Chapter 1

Conformation of Polymer Chains

1.1 Introduction

A polymer is formed by connecting many small molecules. For example, with the help of the catalyst, ethylene $\text{CH}_2=\text{CH}_2$ molecules can form long strings of polyethylene molecules $-\text{CH}_2-\text{CH}_2-\text{CH}_2\cdots\text{CH}_2-$. We refer to $\text{CH}_2=\text{CH}_2$ as the monomer, a structural unit CH_2- in the polymer chain as the chemical segment, and CH_2-CH_2- as the monomeric segment. A large number of different kinds of flexible polymers can be formed from different monomers. The chemical structure of the monomeric segment is generally referred to as the microstructure of the polymer. If all the monomers are the same, the formed polymer is called a homopolymer, such as polystyrene, poly(α -methyl styrene), etc. If more than two kinds of monomers are used, the formed polymer can be a random copolymer or a block copolymer. If a linking agent with multiple arms is added to the monomer in polymerization, a polymer with a “star shape” can be formed. The kind of polymer materials whose viscoelastic properties will be the main subject of study in this book are the linear flexible polymers, including homopolymers and random copolymers. As required for making quantitative comparisons with theories, the samples chosen for study are exclusively well-characterized nearly monodisperse polymers ($M_w/M_n < 1.1$), obtained mainly from anionic polymerization. When the word “polymer” is used in this book, it means this kind of polymer if no further specification is made. Although some of the derived conclusions and concepts from the study can be applied to star polymers and block copolymers, no discussion of them will be made in this book.

In a melt or solution, a polymer chain can take up an enormous number of configurations, as each chemical segment has the probability of pointing

in many different directions. In addition, because of the thermal fluctuation effect, the chain configuration is changing continuously. Thus, to describe the physical properties of the polymer chain, we can only consider the probability distribution function for the configuration and calculate the average value. The static properties of the polymer are studied if it is in the equilibrium state. The changing behavior of chain configuration with time is generally referred to as polymer chain dynamics. A large portion of this book is devoted to the study of chain dynamics and how the polymer viscoelastic properties are affected by them. In the first chapter, we shall study the polymer chain conformation in the equilibrium state. The basic theoretical assumptions used to treat the problem also play a fundamental role in the theories developed for describing various static and dynamic properties of the polymers. In this chapter, we will study two chain models: the freely jointed chain model and the Gaussian chain model. The importance of the latter model will become particularly apparent in the later chapters. In these models, the microstructural details are ignored. It is also understood that when a model chain of these two types is compared with a real chain, the length of each segment of the model is much longer than the microstructural length scale. These chain models are applicable mainly when the polymer chain is long, i.e. the molecular weight of the polymer is large. The physical properties that can be described by the models (such as low-frequency viscoelasticity of a polymer and the scattering structure factor in the small scattering vector region) exhibit universal behavior. That is, different kinds of polymers have the same kind of physical properties regardless of their different microstructure. Theoretically, this is a consequence of the central limit theorem.^{1,2} The freely jointed chain model and the Gaussian chain model have simplified the problem greatly and have allowed us to grasp the essential and universal aspects of the physical properties. Before studying these models in this chapter, we shall review several basic theories in statistics, which are not only needed here but also in studying the chain dynamic behavior in the later chapters.

1.2 Probability Distribution Functions, Moments and Characteristic Functions

Consider a stochastic variable X . If X has a countable set of realizations, $\{x_i\}$, where $i = 1, 2, \dots, n$ (n is either a finite integer or $n = \infty$),

a probability distribution function $P_X(x)$ can be defined as

$$P_X(x) = \sum_{i=1}^n p_i \delta(x - x_i) \quad (1.1)$$

where $\delta(x - x_i)$ is the Dirac delta function (see Appendix 1.A); and p_i is the probability for finding the variable X at x_i , which must satisfy the conditions $p_i \geq 0$ and $\sum_{i=1}^n p_i = 1$. If X can take on a continuous set of values, such as an interval on the real axis, we assume that there exists a piecewise continuous function, $P_X(x)$, such that the probability that X has a value in the interval $\{a \leq x \leq b\}$ is given by

$$\text{Prob}(a \leq x \leq b) = \int_a^b dx P_X(x). \quad (1.2)$$

Then $P_X(x)$ is the probability distribution for the stochastic variable, and $P_X(x) dx$ is the probability of finding the stochastic variable in the interval $x \rightarrow x + dx$. The probability distribution must satisfy the condition $P_X(x) \geq 0$ and $\int_{-\infty}^{\infty} P_X(x) dx = 1$.

Often we wish to find the probability distribution for another stochastic variable, $Y = H(X)$, where $H(X)$ is a known function of X . The probability distribution, $P_Y(y)$, for the stochastic variable Y , is given by

$$P_Y(y) = \int_{-\infty}^{\infty} dx \delta(y - H(x)) P_X(x). \quad (1.3)$$

If we can determine the probability distribution function $P_X(x)$ for the stochastic variable X , then we have all the information needed to characterize it. This sometimes cannot be obtained. However, in that case, we can often obtain the moments of X . The n th moment of X is defined by

$$\langle x^n \rangle = \int_{-\infty}^{\infty} dx x^n P_X(x). \quad (1.4)$$

The moment, $\langle x \rangle$, is also called the mean value of X ; the combination, $\langle x^2 \rangle - \langle x \rangle^2$, is referred to as the variance of X ; and the standard deviation of X , σ_X , is defined by

$$\sigma_X \equiv (\langle x^2 \rangle - \langle x \rangle^2)^{1/2}. \quad (1.5)$$

The moments give us information about the spread and shape of the probability distribution $P_X(x)$. The most important moments are the lower-order ones since they contain the information about the overall shape of the probability distribution.

The characteristic function $f_X(k)$, corresponding to the stochastic variable X , is defined by

$$\begin{aligned} f_X(k) &= \langle \exp(ikx) \rangle = \int_{-\infty}^{\infty} dx \exp(ikx) P_X(x) \\ &= \sum_{n=0}^{\infty} (ik)^n \frac{\langle x^n \rangle}{n!}. \end{aligned} \quad (1.6)$$

The series expansion in the equation above is meaningful only if the higher moments, $\langle x^n \rangle$, are small so that the series converges. From the series expansion, we see that it requires all the moments to completely determine the probability distribution, $P_X(x)$. The characteristic function is a continuous function of k and has the properties that $f_X(0) = 1$, $|f_X(k)| \leq 1$, and $f_X(-k) = f_X^*(k)$ (* denote complex conjugation). The product of two characteristic function is always a characteristic function. If the characteristic function is known, the probability distribution, $P_X(x)$, is given by the inverse Fourier transform

$$P_X(x) = \frac{1}{2\pi} \int_{-\infty}^{\infty} dk \exp(-ikx) f_X(k). \quad (1.7)$$

Furthermore, if we know the characteristic function, we can obtain moments by differentiating:

$$\langle x^n \rangle = \lim_{k \rightarrow 0} (-i)^n \left[\frac{d^n}{dk^n} f_X(k) \right] \quad (1.8)$$

The probability distribution function can be generalized for more than one stochastic variable. For simplicity, let us consider two stochastic variables, X and Y . The joint probability of finding X and Y in the interval $x \rightarrow x + dx$ and $y \rightarrow y + dy$, respectively, is denoted as $P_{X,Y}(x, y) dx dy$, which must satisfy the condition $P_{X,Y}(x, y) \geq 0$ and

$$\int_{-\infty}^{\infty} dx \int_{-\infty}^{\infty} dy P_{X,Y}(x, y) = 1. \quad (1.9)$$

The reduced probability distribution $P_X(x)$ for the stochastic variable X is defined by

$$P_X(x) = \int_{-\infty}^{\infty} dy P_{X,Y}(x, y). \quad (1.10)$$

The reduced probability distribution, $P_Y(y)$, is obtained in a similar manner.

If $Z = G(X, Y)$, where $G(X, Y)$ is a known function of X and Y , the probability distribution $P_Z(z)$ for the stochastic variable Z is given as

$$P_Z(z) = \int_{-\infty}^{\infty} dx \int_{-\infty}^{\infty} dy \delta(z - G(x, y)) P_{X,Y}(x, y). \quad (1.11)$$

Corresponding to the equation above, the characteristic function for the stochastic variable Z is then

$$\begin{aligned} f_Z(k) &= \int_{-\infty}^{\infty} dz \int_{-\infty}^{\infty} dx \int_{-\infty}^{\infty} dy \exp(izk) \delta(z - G(x, y)) P_{X,Y}(x, y) \\ &= \int_{-\infty}^{\infty} dx \int_{-\infty}^{\infty} dy \exp(ikG(x, y)) P_{X,Y}(x, y). \end{aligned} \quad (1.12)$$

If X and Y are two independent stochastic variables, then

$$P_{X,Y}(x, y) = P_X(x) P_Y(y). \quad (1.13)$$

1.3 A Central Limit Theorem^{1,2}

Let us consider a stochastic variable, Y_N , which is the deviation from the average of the arithmetic mean of N statistically *independent* measurements of a stochastic variable, X . Y_N may be written as

$$Y_N = \frac{(X_1 + X_2 + \cdots + X_N)}{N} - \langle x \rangle = Z_1 + Z_2 + \cdots + Z_N \quad (1.14)$$

where

$$Z_i = \frac{(X_i - \langle x \rangle)}{N}. \quad (1.15)$$

We want to obtain the probability distribution function of Y_N , $P_{Y_N}(y)$. First, the characteristic function, $f_Z(k; N)$, for the stochastic variable, $Z_{i,N}$, can be written as

$$\begin{aligned} f_Z(k; N) &= \int_{-\infty}^{\infty} dz \int_{-\infty}^{\infty} dx \exp(ikz) \delta\left(z - \frac{(x - \langle x \rangle)}{N}\right) P_X(x) \\ &= \int_{-\infty}^{\infty} dx \exp\left(ik \frac{(x - \langle x \rangle)}{N}\right) P_X(x) \\ &= 1 - \frac{k^2 \sigma_X^2}{2N^2} + \cdots \end{aligned} \quad (1.16)$$

where $\sigma_X^2 = \langle x^2 \rangle - \langle x \rangle^2$. Then the characteristic function of Y_N is

$$\begin{aligned}
 f_{Y,N}(k) &= \int_{-\infty}^{\infty} dy \int_{-\infty}^{\infty} dz_1 \cdots \int_{-\infty}^{\infty} dz_N \exp(iky) \delta\left(y - \sum_{i=1}^N z_i\right) \prod_{i=1}^N P_{Z_i}(z_i) \\
 &= (f_Z(k; N))^N \\
 &= \left(1 - \frac{k^2 \sigma_X^2}{2N^2} + \cdots\right)^N \\
 &\rightarrow \exp\left(-\frac{k^2 \sigma_X^2}{2N}\right) \quad \text{as } N \rightarrow \infty.
 \end{aligned} \tag{1.17}$$

Thus, as $N \rightarrow \infty$,

$$\begin{aligned}
 P_{Y,N}(y) &\rightarrow \frac{1}{2\pi} \int_{-\infty}^{\infty} dk \exp(-iky) \exp\left(-\frac{k^2 \sigma_X^2}{2N}\right) \\
 &= \left(\frac{N}{2\pi \sigma_X^2}\right)^{1/2} \exp\left(-\frac{Ny^2}{2\sigma_X^2}\right).
 \end{aligned} \tag{1.18}$$

Regardless of the form of $P_X(x)$, if it has finite moments, the average of a large number of statistically independent measurements of X will be a Gaussian function centered at $\langle x \rangle$, with a standard deviation which is smaller than the standard deviation of the probability distribution of a single measurement X , σ_X , by a factor of $N^{0.5}$.

If $\langle x \rangle = 0$, and $\langle x^2 \rangle = \sigma_X^2$ is finite, the stochastic variable

$$R_N = X_1 + X_2 + \cdots + X_N = NY_N \tag{1.19}$$

has the following Gaussian distribution

$$\begin{aligned}
 P_R(r) &= \int_{-\infty}^{\infty} dy \delta(r - Ny) P_Y(y) \\
 &= \left(\frac{1}{2\pi N \langle x^2 \rangle}\right)^{1/2} \exp\left(-\frac{r^2}{2N \langle x^2 \rangle}\right).
 \end{aligned} \tag{1.20}$$

Equation (1.20) has many applications in this book, such as the diffusion motion of a Brownian particle (Appendix 3.D) and the probability distribution of the end-to-end vector of a long polymer chain. The latter case will be studied in this chapter. Essentially, $\langle x^2 \rangle^{1/2}$ in Eq. (1.20) can be regarded as the mean projection of an independent segment (bond) vector in one of the three coordinate directions (i.e. x , y or z ; all three directions are equivalent). As long as the considered polymer chain is very long, we can always apply the central limit theorem, regardless of the local chemical structure.

Because the polymer chain is assumed to have an unlimited length, we can always divide the chain into sections of the same length which are sufficiently long so that each segment (section) is *independent of* each other, and at the same time, the number of segments is still very large. Then according to the central limit theorem, we do not need to fully know the probability distribution of a segment vector, as long as it has finite moments, to obtain the Gaussian distribution for the end-to-end vector of the polymer chain, with the mean square value being proportional to the number of the segments. However, as shown below, we shall study the special cases, the freely jointed chain model and the Gaussian chain model, where the distribution function for each independent segment is exactly known. A real chain, which is flexible, yet not infinitely extensible, is shown by simulations (Chapters 17 and 18) somewhere between these two models.³⁻⁶

1.4 The Freely Jointed Chain Model

In the simplest picture, the polymer molecule can be considered as a chain consisting of N segments with length b , each of which is free of any constraint to orient in an arbitrary direction. In other words, the orientation of a segment is totally independent of other segments in the chain and is random. Such a chain is referred to as the freely jointed chain model.

In this model, we have a set of $N + 1$ vectors to indicate the positions of the joints (including both ends of the chain) relative to the origin of a chosen coordinate system (see Fig. 1.1(a)):

$$\{\mathbf{R}_n\} \equiv (\mathbf{R}_1, \mathbf{R}_2, \dots, \mathbf{R}_{N+1}).$$

Corresponding to the set, we have a set of segment vectors:

$$\{\mathbf{b}_n\} \equiv (\mathbf{b}_1, \mathbf{b}_2, \dots, \mathbf{b}_N)$$

where

$$\mathbf{b}_n = \mathbf{R}_{n+1} - \mathbf{R}_n, \quad n = 1, 2, \dots, N. \quad (1.21)$$

Because all the segments are of fixed length b and are randomly oriented, the segmental distribution function for the x th segment is given by

$$\psi(\mathbf{b}_x) = \frac{1}{4\pi b^2} \delta(|\mathbf{b}_x| - b) \quad (1.22)$$

which means that finding the bond vector, \mathbf{b}_x , of the x th segment in the region $\mathbf{b}_x \rightarrow \mathbf{b}_x + d\mathbf{b}_x$ has the probability $\psi(\mathbf{b}_x) d\mathbf{b}_x$. The distribution

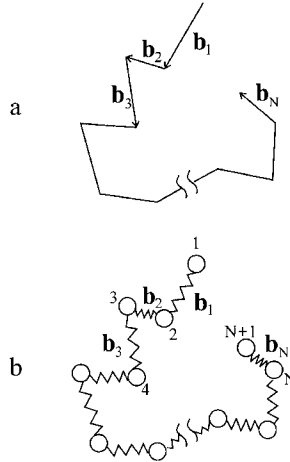


Fig. 1.1 (a) Freely jointed chain; (b) Gaussian chain.

function $\psi(\mathbf{b}_x)$ has been normalized, i.e.

$$\int \psi(\mathbf{b}_x) d\mathbf{b}_x = \frac{1}{4\pi b^2} \int_0^{2\pi} d\phi \int_0^\pi \sin\theta d\theta \int_0^\infty \delta(|\mathbf{b}_x| - b) |\mathbf{b}_x|^2 d|\mathbf{b}_x| = 1. \quad (1.23)$$

Since the orientations of all the segments in the chain are independent of each other, i.e. all the segmental vectors are independent stochastic variables, the configurational distribution function $\Psi(\{\mathbf{b}_n\})$ can be simply written as the product of the random distribution functions for the individual segments. That is

$$\Psi(\{\mathbf{b}_n\}) = \prod_{n=1}^N \psi(\mathbf{b}_n). \quad (1.24)$$

Then the average value of any physical quantity A associated with the molecular chain can be written as

$$\langle A \rangle = \int A(\{\mathbf{b}_n\}) \Psi(\{\mathbf{b}_n\}) d\mathbf{b}_1, d\mathbf{b}_2, \dots, d\mathbf{b}_N. \quad (1.25)$$

To describe the size of a chain coil, we consider the end-to-end vector \mathbf{R} of the chain.

$$\mathbf{R} = \mathbf{R}_{N+1} - \mathbf{R}_1 = \sum_{n=1}^N \mathbf{b}_n. \quad (1.26)$$

Then

$$\langle \mathbf{R} \rangle = \sum_{n=1}^N \langle \mathbf{b}_n \rangle = 0. \quad (1.27)$$

But $\langle \mathbf{R}^2 \rangle$ has a finite value.

$$\langle \mathbf{R}^2 \rangle = \sum_n \sum_m \langle \mathbf{b}_n \cdot \mathbf{b}_m \rangle = \sum_n \langle \mathbf{b}_n^2 \rangle + 2 \sum_{n>m} \langle \mathbf{b}_n \cdot \mathbf{b}_m \rangle. \quad (1.28)$$

Because \mathbf{b}_n and \mathbf{b}_m are independent of each other for $n \neq m$,

$$\langle \mathbf{b}_n \cdot \mathbf{b}_m \rangle = \langle \mathbf{b}_n \rangle \cdot \langle \mathbf{b}_m \rangle = 0 \quad (1.29)$$

and

$$\langle \mathbf{b}_n^2 \rangle = b^2. \quad (1.30)$$

Thus,

$$\langle \mathbf{R}^2 \rangle = Nb^2. \quad (1.31)$$

The square root of $\langle \mathbf{R}^2 \rangle$, $R = \langle \mathbf{R}^2 \rangle^{1/2} = N^{1/2}b$, is often used to characterize the size of the chain coil.

In the literature, the so-called Kuhn segment length b_k is often used to express the stiffness of a polymer chain.⁷⁻⁹ b_k is defined in terms of the fully stretched length of a polymer chain L and the mean square end-to-end distance as

$$b_k = \frac{\langle \mathbf{R}^2 \rangle}{L}. \quad (1.32)$$

The number of segments can be defined by

$$N = \frac{L}{b_k}. \quad (1.33)$$

Thus,

$$\langle \mathbf{R}^2 \rangle = Nb_k^2. \quad (1.34)$$

Obviously, the freely jointed chain model satisfies Eqs. (1.32)–(1.34).

1.5 Distribution of the End-to-End Vector

The end-to-end vector of a chain $\mathbf{R} = \sum_{n=1}^N \mathbf{b}_n$ changes as its configuration changes with time. Let $\Phi(\mathbf{R}, N) d\mathbf{R}$ denote the probability for finding the end-to-end vector in the region $\mathbf{R} \rightarrow \mathbf{R} + d\mathbf{R}$ for a chain with N segments. Using Eq. (1.11), $\Phi(\mathbf{R}, N)$ can be calculated from the configurational distribution function (Eq. (1.24)) as

$$\Phi(\mathbf{R}, N) = \int d\mathbf{b}_1 \int d\mathbf{b}_2 \cdots \int d\mathbf{b}_N \delta\left(\mathbf{R} - \sum_{n=1}^N \mathbf{b}_n\right) \Psi(\{\mathbf{b}_n\}). \quad (1.35)$$

The characteristic function $f_{\mathbf{R}, N}(\mathbf{k})$ for the stochastic variable \mathbf{R} is obtained from Eq. (1.35) as

$$\begin{aligned} f_{\mathbf{R}, N}(\mathbf{k}) &= \int d\mathbf{R} \exp(i\mathbf{k} \cdot \mathbf{R}) \Phi(\mathbf{R}, N) \\ &= \left[\int d\mathbf{b}_x \exp(i\mathbf{k} \cdot \mathbf{b}_x) \psi(\mathbf{b}_x) \right]^N. \end{aligned} \quad (1.36)$$

With the substitution of Eq. (1.22) and the use of the spherical coordinates, the term in brackets [] from Eq. (1.36) is rewritten as (with the direction of \mathbf{k} chosen as the z direction)

$$\begin{aligned} &\int d\mathbf{b}_x \exp(i\mathbf{k} \cdot \mathbf{b}_x) \psi(\mathbf{b}_x) \\ &= \frac{1}{4\pi b^2} \int_0^\infty db_x \int_0^{2\pi} d\phi \int_0^\pi d\theta b_x^2 \sin\theta \exp(ikb_x \cos\theta) \delta(b_x - b) \\ &= \frac{\sin(kb)}{kb}. \end{aligned} \quad (1.37)$$

Thus,

$$f_{\mathbf{R}}(\mathbf{k}) = \left[\frac{\sin(kb)}{kb} \right]^N. \quad (1.38)$$

From the inverse Fourier transformation of Eq. (1.38), we obtain the probability distribution function for the end-to-end vector \mathbf{R} .

$$\Phi(\mathbf{R}, N) = \left(\frac{1}{2\pi}\right)^3 \int d\mathbf{k} \exp(-i\mathbf{k} \cdot \mathbf{R}) \left[\frac{\sin(kb)}{kb} \right]^N. \quad (1.39)$$

When N is very large, the contribution of the integrand with $kb \gg 1$ to $\Phi(\mathbf{R}, N)$ is negligible; the main contribution comes from the integrand with $kb \ll 1$. The reciprocal of k represents a length λ . Physically, we are

interested in the size of the chain coil, as characterized by the end-to-end distance R . The magnitude of λ we need to consider is comparable to R and is much larger than b ; in other words, $k \ll 1/b$ is the range of k of interest. Thus, under the condition that N is very large, $[\sin(kb)/kb]^N$ can be approximated as

$$\begin{aligned} \left[\frac{\sin(kb)}{kb} \right]^N &\simeq \left[1 - \frac{k^2 b^2}{6} \dots \right]^N \\ &\simeq \exp\left(-\frac{Nk^2 b^2}{6} \right). \end{aligned} \quad (1.40)$$

Thus, $\Phi(\mathbf{R}, N)$ can be written as

$$\Phi(\mathbf{R}, N) = \left(\frac{1}{2\pi} \right)^3 \int d\mathbf{k} \exp\left(-i\mathbf{k} \cdot \mathbf{R} - \frac{Nk^2 b^2}{6} \right). \quad (1.41)$$

The integral of Eq. (1.41) is a standard Gaussian integral. Denoting the components of \mathbf{k} and \mathbf{R} as k_α and R_α ($\alpha = x, y, z$), Eq. (1.41) is expressed as

$$\begin{aligned} \Phi(\mathbf{R}, N) &= \left(\frac{1}{2\pi} \right)^3 \prod_{\alpha=x,y,z} \left[\int_{-\infty}^{\infty} dk_\alpha \exp\left(-ik_\alpha R_\alpha - \frac{Nk_\alpha^2 b^2}{6} \right) \right] \\ &= \left(\frac{1}{2\pi} \right)^3 \prod_{\alpha=x,y,z} \left(\frac{6\pi}{Nb^2} \right)^{1/2} \exp\left(-\frac{3R_\alpha^2}{2Nb^2} \right) \\ &= \left(\frac{3}{2\pi Nb^2} \right)^{3/2} \exp\left(-\frac{3\mathbf{R}^2}{2Nb^2} \right). \end{aligned} \quad (1.42)$$

Thus, as given by Eq. (1.42), the probability distribution function for the end-to-end vector \mathbf{R} is Gaussian. The distribution has the unrealistic feature that $|\mathbf{R}|$ can be greater than the maximum extended length Nb of the chain. Although Eq. (1.42) is derived on the freely jointed chain model, it is actually valid for a long chain, where the central limit theorem is applicable, except for the highly extended states.

1.6 The Gaussian Chain

Here, we consider a chain where the length of each segment has the Gaussian distribution, i.e.

$$\psi(\mathbf{b}_x) = \left(\frac{3}{2\pi b^2} \right)^{3/2} \exp\left(-\frac{3\mathbf{b}_x^2}{2b^2} \right) \quad (1.43)$$

and

$$\langle \mathbf{b}_x^2 \rangle = b^2. \quad (1.44)$$

Then the configurational distribution function of the chain is given by

$$\begin{aligned} \Psi(\{\mathbf{b}_n\}) &= \prod_{n=1}^N \left(\frac{3}{2\pi b^2} \right)^{3/2} \exp\left(-\frac{3\mathbf{b}_n^2}{2b^2}\right) \\ &= \left(\frac{3}{2\pi b^2} \right)^{3N/2} \exp\left[-\sum_{n=1}^N \frac{3}{2b^2}(\mathbf{R}_{n+1} - \mathbf{R}_n)^2\right]. \end{aligned} \quad (1.45)$$

A chain with the mathematical properties of Eq. (1.45) is called a Gaussian chain. As a freely jointed chain, the Gaussian chain does not contain microstructural details. Compared with a real chain, the distribution Eq. (1.45) of the Gaussian chain has unrealistic infinite extensibility. Thus, the Gaussian chain is not expected to be valid in the large deformation region. From comparison with experimental results, as detailed in the later chapters, the Gaussian chain model has been shown to accurately describe the physical properties associated with a sufficiently long chain section or whole chain in the small deformation region (not much higher than the linear region). Furthermore, one great advantage of using the Gaussian chain model is its mathematical simplicity. All the theories studied in this book are either based on or consistent with the Gaussian chain model. In a few cases, deviation from the theory will be discussed as related to the finite extensibility of the actual polymer chain. In particular, the Monte Carlo simulation studies on the Fraenkel chains^{4,5} detailed in Chapters 17 and 18 shed light on the merits and deficiencies of the Gaussian chain model. As shown in Fig. 1.1(b), the Gaussian chain with N segments is considered equivalent to a chain consisting of $N + 1$ beads connected by N Hookean springs. The potential energy of the n th Hookean spring is given by

$$V_o(\mathbf{R}_{n+1} - \mathbf{R}_n) = \frac{3kT}{2b^2}(\mathbf{R}_{n+1} - \mathbf{R}_n)^2. \quad (1.46)$$

Here, except for the spring potential, there is no interactional potential among the beads. The total potential of all the springs in the chain is expressed as

$$V(\{\mathbf{R}_n\}) = \frac{3kT}{2b^2} \sum_{n=1}^N (\mathbf{R}_{n+1} - \mathbf{R}_n)^2. \quad (1.47)$$

In equilibrium, the Boltzmann distribution of such a bead-spring model is exactly Eq. (1.45).

The Gaussian chain has an important property: the probability distribution of the vector $\mathbf{R}_n - \mathbf{R}_m$ between any two beads n and m is a Gaussian function, i.e.

$$\Phi(\mathbf{R}_n - \mathbf{R}_m, n - m) = \left(\frac{3}{2\pi b^2 |n - m|} \right)^{3/2} \exp \left[-\frac{3(\mathbf{R}_n - \mathbf{R}_m)^2}{2|n - m|b^2} \right]. \quad (1.48)$$

Equation (1.48) can be obtained from substituting Eq. (1.45) into an equation similar to Eq. (1.35) for the vector between any two beads. This result is simply a special case of the theorem that the sum of any number of Gaussian stochastic variables is also a Gaussian stochastic variable. As shown in the later chapters, this theorem finds applications in the study of chain dynamics as well.¹⁰

Equation (1.42), derived on the freely jointed chain model for a long chain (large N), is the same as Eq. (1.48) of the Gaussian chain model. In other words, the freely jointed chain model and the Gaussian chain model are basically the same in describing the physical properties associated with a long section of a polymer chain. While the distribution (Eq. (1.42)) based on the freely jointed chain model is Gaussian only when N is large, the Gaussian distribution of the Gaussian chain model (Eq. (1.48)) can be used between any two beads in the chain. Various calculations can be greatly simplified by the use of the Gaussian chain model, as will be shown in later chapters.

Appendix 1.A — The Dirac Delta Function^{11,12}

Consider a particle moving in one-dimensional space, x . A physical event associated with the particle can often be described in terms of the probability distribution of the particle in the real axis x . The probability of finding the particle in the region, $x \rightarrow x + dx$, is denoted by $p(x) dx$. Since a point does not have a width, it takes a special consideration to describe the state that the particle is surely at a certain point x' . From such a consideration, the Dirac delta function $\delta(x - x')$ is obtained. A simple way is to consider the probability function $p(x)$ given by

$$\begin{aligned} p(x - x') &= \frac{1}{\epsilon} & \text{for } |x - x'| \leq \frac{\epsilon}{2} \\ &= 0 & \text{otherwise.} \end{aligned} \quad (1.A.1)$$

It is clear that Eq. (1.A.1) is normalized, i.e.

$$\int_{-\infty}^{\infty} p(x - x') dx = 1. \quad (1.A.2)$$

The Dirac delta function is defined by

$$\delta(x - x') = \lim_{\epsilon \rightarrow 0} p(x - x'). \quad (1.A.3)$$

Then

$$\int_{-\infty}^{\infty} \delta(x - x') dx = \lim_{\epsilon \rightarrow 0} \int_{-\infty}^{\infty} p(x - x') dx = 1 \quad (1.A.4)$$

and

$$\begin{aligned} \delta(x - x') &= \infty && \text{for } x = x' \\ &= 0 && \text{for } x \neq x'. \end{aligned} \quad (1.A.5)$$

For any function $f(x)$

$$\begin{aligned} \int_{-\infty}^{\infty} f(x) \delta(x - x') dx &= \lim_{\epsilon \rightarrow 0} \int_{-\infty}^{\infty} f(x) p(x - x') dx \\ &= \lim_{\epsilon \rightarrow 0} \int_{x' - \epsilon/2}^{x' + \epsilon/2} \frac{f(x)}{\epsilon} dx \\ &= \lim_{\epsilon \rightarrow 0} [f(x') + O(\epsilon^2)] = f(x'). \end{aligned} \quad (1.A.6)$$

Equation (1.A.3) is not a well-defined mathematical function, which must have a definite value at every point x where it is defined. Dirac called it an “improper function,” which has the characteristic that “when it occurs as a factor in an integrand the integral has a well-defined value.”

Another useful representation of the Dirac delta function is given by

$$\delta(x - x') = \frac{1}{2\pi} \int_{-\infty}^{\infty} \exp[ik(x - x')] dk. \quad (1.A.7)$$

The properties of the Dirac delta function, namely, Eqs. (1.A.4)–(1.A.6), can be obtained by substituting the function $g(y)$ into the expression for

$f(x)$ of the following Fourier transform pair:

$$f(x) = \int_{-\infty}^{\infty} g(k) \exp(ikx) dk \quad (1.A.8)$$

$$g(k) = \frac{1}{2\pi} \int_{-\infty}^{\infty} f(x) \exp(-ikx) dx. \quad (1.A.9)$$

For a vector \mathbf{r} in the three-dimensional space with components x , y , and z , the Dirac delta function $\delta(\mathbf{r} - \mathbf{r}')$ is represented as

$$\begin{aligned} \delta(\mathbf{r} - \mathbf{r}') &= \delta(x - x')\delta(y - y')\delta(z - z') \\ &= \left(\frac{1}{2\pi}\right)^3 \int \exp[i(\mathbf{r} - \mathbf{r}') \cdot \mathbf{k}] d\mathbf{k} \end{aligned} \quad (1.A.10)$$

where $\int \cdots d\mathbf{k}$ is understood to mean $\int_{-\infty}^{\infty} \int_{-\infty}^{\infty} \int_{-\infty}^{\infty} \cdots dk_x dk_y dk_z$. It follows that

$$\int f(\mathbf{r})\delta(\mathbf{r} - \mathbf{r}') d\mathbf{r} = f(\mathbf{r}'). \quad (1.A.11)$$

References

1. Feller, W., *An Introduction to Probability Theory and Its Applications* (3rd edn), Wiley, New York, (1968).
2. Reichl, L. E., *A Modern Course in Statistical Physics* (2nd edn), Wiley, New York, (1998).
3. Lin, Y.-H., and Luo, Z.-H., *J. Chem. Phys.* **112**, 7219 (2000).
4. Lin, Y.-H., and Das, A. K., *J. Chem. Phys.* **126**, 074902 (2007).
5. Lin, Y.-H., and Das, A. K., *J. Chem. Phys.* **126**, 074903 (2007).
6. Inoue, T., and Osaki, K., *Macromolecules* **29**, 1595 (1996).
7. Kuhn, W., *Kolloid Z.* **76**, 258 (1936); *Kolloid Z.* **87**, 3 (1939).
8. Yamakawa, H., *Modern Theory of Polymer Solutions*, Harper & Row, New York, (1971).
9. Flory, P. J., *Statistical Mechanics of Chain Molecules*, Hanser Publisher, New York (1989). To express the stiffness of a chain, the worm-like chain is a useful model, which is characterized by two parameters: the persistence length l_p and the contour length L . In the limit of $L/l_p \rightarrow \infty$, the Kuhn segment length as defined by Eq. (1.32) is twice the persistence length.
10. Doi, M., and Edwards, S. F., *The Theory of Polymer Dynamics*, Oxford Univ. Press, Oxford, (1986).
11. Dirac, P., *The Principles of Quantum Mechanics* (4th edn), Clarendon Press, Oxford, (1958).
12. Wong, C. W., *Introduction to Mathematical Physics, Methods and Concepts*, Oxford Univ. Press, New York, (1991).

Chapter 2

Rubber Elasticity

2.1 Introduction

The only difference between a polymer melt and a rubber material is that the chains in the latter are cross-linked by chemical means. A rubber material can be regarded as a huge or macroscopic three-dimensional network formed of strands of polymer chain with both ends as cross-links. Such a material, maintaining the softness of a polymer above its melting temperature or glass transition temperature, will recover its original shape after being released from a deformation. Materials of this nature, such as tire, rubber, etc. are readily visible in our daily life. Because cross-links in a rubber keep the chain strands from moving away from their relative positions over a distance larger than the strand size itself, the chains do not flow with the deformation and are able to recover their conformations once the deformation is released. Thus, we only need to consider its elastic property. In contrast to this behavior, an un-cross-linked polymer exhibits the elastic response only under momentary deformations; however, under a prolonged deformation, it cannot recover its original shape because the chain molecules have flowed. For an un-cross-linked polymeric liquid, we need to consider both the elasticity and viscosity of the material — the main subject of interest in this book. In Chapter 4, we shall study the viscoelastic behavior of the polymer in linear region phenomenologically. In Chapters 6–12, we shall study the molecular theories that describe the viscoelastic properties of the polymers in the entangled and unentangled regions. The basic physical mechanism that gives rise to rubber elasticity is also responsible for the rubbery elastic aspect of the viscoelastic behavior of the polymer.¹ For our purpose of studying the viscoelastic behavior of a polymer fluid, we discuss the basic physics responsible for rubber elasticity here.

In Chapter 1, we have shown that the probability distribution of the end-to-end vector of a freely jointed chain with a sufficiently large number of segments is Gaussian. Here, we apply the Gaussian distribution to the vector between two cross-link ends of a strand of polymer chain. The conformation of such a chain strand in a piece of rubber changes as a deformation is applied to the rubber. To express an entropy change associated with the conformation change in terms of the Gaussian distribution function was the pioneering work of James and Guth.^{2,3} This entropy change is the origin of the restoring force of a rubber. Before discussing the molecular statistical model for describing such an effect, we show, by purely thermodynamic analysis of the experimental observations, that rubber elasticity arises from the entropy change caused by the applied deformation.

2.2 Entropy and Rubber Elasticity

The free energy of a strip of rubber can be written as

$$A = U - TS \quad (2.1)$$

where U is the internal energy and S the entropy.

If under a stretching force f , the rubber strip is elongated by a length dl , the change of the free energy is

$$dA = f dl - S dT. \quad (2.2)$$

Then the force can be expressed as

$$\begin{aligned} f &= \left(\frac{\partial A}{\partial l} \right)_T = \left(\frac{\partial U}{\partial l} \right)_T - T \left(\frac{\partial S}{\partial l} \right)_T \\ &= \left(\frac{\partial U}{\partial l} \right)_T + T \left(\frac{\partial f}{\partial T} \right)_l \end{aligned} \quad (2.3)$$

where the Maxwell relation $(\partial S/\partial l)_T = -(\partial f/\partial T)_l$ has been used. It is observed that in maintaining a constant length l the tensile force f increases with increasing temperature. (It is more correct experimentally to maintain a constant extension ratio l/l_o instead of simply constant length l , where l_o , denoting the length of the rubber piece in a strain-free state, changes with temperature. The constant extension ratio is used to correct for the so-called thermo-elastic inversion effect⁴⁻⁶ due to the change in volume of the rubber with temperature. To simplify our discussions here and below, we use constant length with the understanding that the correction

has been made.) That is, $(\partial f/\partial T)_l > 0$, which leads to $(\partial S/\partial l)_T < 0$. Thus, the entropy under constant temperature decreases with increasing elongation. According to Eq. (2.3), the $(\partial U/\partial l)_T$ value can be obtained from extrapolating the f values measured at different temperatures (above the glass transition temperature) to the absolute zero temperature. Experimental results indicate that this value is in general much smaller than $-T(\partial S/\partial l)_T$.⁴⁻⁶ In other words, the main contribution to the tensile force arises from the change in entropy with deformation. An ideal rubber is defined as having $(\partial U/\partial l)_T = 0$.

Rubber elasticity and gas pressure arise from the same thermodynamic principle. Corresponding to Eqs. (2.2) and (2.3), we have

$$dA = -P dV - S dT \quad (2.4)$$

and

$$P = - \left(\frac{\partial A}{\partial V} \right)_T = - \left(\frac{\partial U}{\partial V} \right)_T + T \left(\frac{\partial S}{\partial V} \right)_T \quad (2.5)$$

for a gas. For an ideal gas $(\partial U/\partial V)_T = 0$. Thus, the pressure of a gas arises from the entropy change caused by a change in volume.

2.3 Molecular Theory for Rubber Elasticity

Consider a strand of polymer chain between two cross-links. The vector \mathbf{R} between the positions of the two cross-links changes with deformation. Any molecular theory on rubber elasticity is based on the probability distribution function for \mathbf{R} . As seen in Chapter 1, if the number of segments N on the strand is large, the probability distribution $\Phi(\mathbf{R}, N)$ of the end-to-end vector \mathbf{R} is a Gaussian function

$$\begin{aligned} \Phi(\mathbf{R}, N) &= \left(\frac{3}{2\pi N b^2} \right)^{3/2} \exp \left(-\frac{3\mathbf{R}^2}{2N b^2} \right) \\ &= \left(\frac{3}{2\pi N b^2} \right)^{3/2} \exp \left[-\frac{3}{2N b^2} (X^2 + Y^2 + Z^2) \right] \\ &= W(X, Y, Z) \end{aligned} \quad (2.6)$$

where X , Y and Z are the three components of \mathbf{R} , and b is the length of the segment in the freely jointed chain model.

There are a large number of configurations, Ω , for the chain strand with a large N , which can all lead to the same end-to-end vector \mathbf{R} . For a freely

jointed chain, all these individual configurations have the same energy and the same probability of occurring. Thus, the number of configurations Ω at a certain \mathbf{R} is proportional to the probability distribution function $\Phi(\mathbf{R}, N)$. According to the Boltzmann equation, the entropy for the chain strand can be written as

$$s = k \ln(\Omega). \tag{2.7}$$

As

$$\Omega \propto W(X, Y, Z) \tag{2.8}$$

using Eq. (2.6), the entropy can be expressed as

$$s = -\frac{3k}{2Nb^2}(X^2 + Y^2 + Z^2) + C \tag{2.9}$$

where C is a constant. Since we are only interested in the change of entropy with deformation, the constant C plays no role, as it will be cancelled out when the difference is taken.

Consider the application of a uniaxial extension to a rectangular block of rubber, as shown in Fig. 2.1. The lengths of the three sides of the block are denoted by L_x^o , L_y^o and L_z^o before deformation, and by L_x , L_y and L_z after deformation. We may choose any chain strand in the piece of rubber and let its one cross-link end be fixed at the origin of the coordinate system and denote the position of the other end at $\mathbf{R}_o = (X_o, Y_o, Z_o)$ before deformation and at $\mathbf{R} = (X, Y, Z)$ after deformation (Fig. 2.2). If the

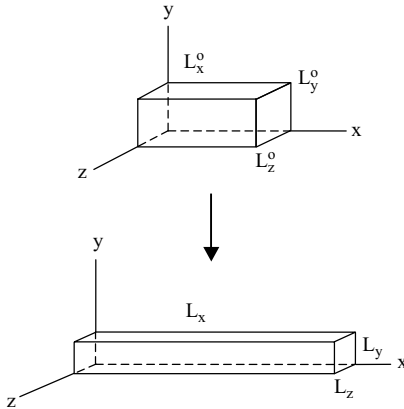


Fig. 2.1 Uniaxial extension of a rectangular block of rubber.

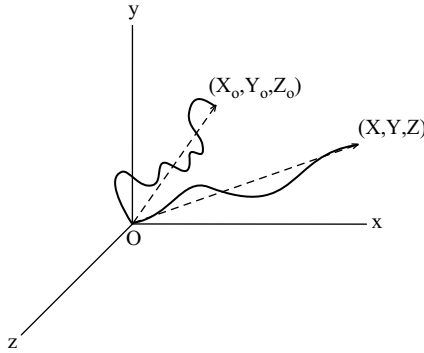


Fig. 2.2 Spatial configurations of a polymer strand in a piece of rubber before and after the application of a deformation as shown in Fig. 2.1.

displacement from \mathbf{R}_o to \mathbf{R} is linearly proportional to the deformation of the whole piece of rubber (such a deformation is referred to as the affine deformation),

$$\frac{X}{X_o} = \frac{L_x}{L_x^o} = \lambda_1 \quad (2.10)$$

$$\frac{Y}{Y_o} = \frac{L_y}{L_y^o} = \lambda_2 \quad (2.11)$$

$$\frac{Z}{Z_o} = \frac{L_z}{L_z^o} = \lambda_3. \quad (2.12)$$

Furthermore, we assume that the density of the rubber does not change with the deformation. Then we have the relation

$$\lambda_1 \lambda_2 \lambda_3 = 1. \quad (2.13)$$

Because of the symmetry of the deformation ($\lambda_2 = \lambda_3$), from Eq. (2.13), we obtain

$$\lambda_2 = \lambda_3 = \frac{1}{\sqrt{\lambda_1}}. \quad (2.14)$$

According to Eq. (2.9), the entropies before and after deformation, denoted by s_o and s respectively, are given by

$$s_o = -\frac{3k}{2Nb^2}(X_o^2 + Y_o^2 + Z_o^2) + C \quad (2.15)$$

$$s = -\frac{3k}{2Nb^2}(X^2 + Y^2 + Z^2) + C. \quad (2.16)$$

Using Eqs. (2.10)–(2.12) and (2.14), the entropy change associated with the single chain strand due to the deformation can be written as

$$\Delta s = s - s_o = -\frac{3k}{2Nb^2} \left[(\lambda_1^2 - 1)X_o^2 + \left(\frac{1}{\lambda_1} - 1 \right) Y_o^2 + \left(\frac{1}{\lambda_1} - 1 \right) Z_o^2 \right]. \quad (2.17)$$

If there are n chain strands in the total volume of the rubber piece $V = L_x^o L_y^o L_z^o = L_x L_y L_z$, and the rubber is isotropic in its equilibrium state before the deformation is applied, the total change in entropy ΔS can be obtained by multiplying Eq. (2.17) by n and replacing X_o^2 , Y_o^2 , and Z_o^2 by their equilibrium average value, namely,

$$\langle X_o^2 \rangle = \langle Y_o^2 \rangle = \langle Z_o^2 \rangle = \frac{\langle \mathbf{R}^2 \rangle}{3} = \frac{Nb^2}{3}. \quad (2.18)$$

Thus, with the energetic contribution neglected, the total change in free energy due to the deformation is given by

$$\Delta A = -T\Delta S = \frac{nkT}{2} \left(\lambda_1^2 + \frac{2}{\lambda_1} - 3 \right) \quad (2.19)$$

which, using the definition of λ_1 (Eq. (2.10)), can be rewritten as

$$\Delta A = \frac{nkT}{2} \left(\frac{L_x^2}{L_x^{o2}} + 2\frac{L_x^o}{L_x} - 3 \right). \quad (2.20)$$

Then the force f applied to the piece of rubber in the x direction is given by (Eq. (2.3))

$$f = \left[\frac{\partial(\Delta A)}{\partial L_x} \right]_{T,V} = nkT \left(\frac{L_x}{L_x^{o2}} - \frac{L_x^o}{L_x^2} \right). \quad (2.21)$$

The corresponding stress is defined by

$$\sigma = -\frac{f}{L_y L_z} = -\frac{nkT}{V} \left(\lambda_1^2 - \frac{1}{\lambda_1} \right). \quad (2.22)$$

In the literature, for practical purposes, the initial area of the cross section is sometimes used to express the “stress” (often referred to as the engineering

stress or the nominal stress)

$$\sigma' = -\frac{f}{L_y^o L_z^o} = -\frac{nkT}{V} \left(\lambda_1 - \frac{1}{\lambda_1^2} \right). \quad (2.23)$$

If the molecular weight of a chain strand between two cross-links is M_x ,

$$\frac{n}{V} = \frac{\rho N_A}{M_x} \quad (2.24)$$

where ρ is the density of the rubber material and N_A the Avogadro number. Using Eq. (2.24), Eq. (2.22) can be expressed as

$$\sigma = -G \left(\lambda_1^2 - \frac{1}{\lambda_1} \right) \quad (2.25)$$

where the modulus G is given by

$$G = \frac{\rho RT}{M_x} \quad (2.26)$$

with R being the gas constant.

From the measurement of the stress at a certain deformation λ_1 , the modulus G can be determined. Then, using Eq. (2.26), we can calculate the M_x value from the obtained G value. This is a useful way to estimate the degree of cross-linking in a rubber material.

Shown in Fig. 2.3 is the comparison between Eq. (2.23) and the experimental result.² Except at the high extension ratio, the agreement of Eq. (2.23) with experiment is good; the experimental “knee” is well reproduced by the theory. Deviation of the experimental result of the “stress”-strain relation from that given by Eq. (2.23) begins to occur at around $\lambda_1 = 3.5$. The main cause for the deviation can be attributed to two main effects:^{5,6}

(1) The use of the Gaussian function to describe the conformation of a chain strand allows it to be stretched infinitely. In reality, the maximum length of a polymer chain is limited by the rigid chemical bond lengths and angles of its microstructure. At a highly stretched state of the chain, the force, derived from the potential-energy changes which occur as the lengths and angles of the chemical bonds are affected by the applied deformation, will start to contribute to the total tensile stress.

(2) As $(\partial S/\partial l)_T < 0$, the entropy of a rubber material decreases with elongation. If the microstructure of the rubber has enough symmetry to

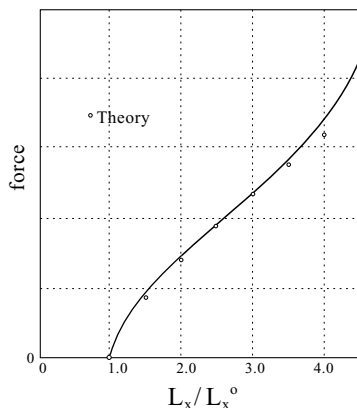


Fig. 2.3 Comparison of experimental and theoretical (Eq. (2.23)) length-force relations for rubber in a typical case. The vertical scale has been adjusted for the best fit. Reproduced, by permission, from Ref. 2.

allow crystallization to occur, the melting point T_m of a formed crystallite is determined by the enthalpy ΔH_f and entropy ΔS_f of fusion as

$$T_m = \frac{\Delta H_f}{\Delta S_f}. \quad (2.27)$$

Now, in a deformed state the entropy of the rubber is reduced; the entropy change ΔS_f involved in the first-order transition from the deformed rubber to the crystalline state is also reduced. With ΔH_f being basically unchanged, the reduction of ΔS_f leads to significant increase in the melting point T_m , when a large deformation is applied. In other words, crystallization in a rubber occurs much more easily when a large deformation is applied. The crystallites in the rubber, formed at large deformations, will act as additional “cross-links” and will greatly enhance the observed stress when additional deformation is applied. It is well known that natural rubber has such an effect.^{5,6}

Finally, it is interesting and helpful to make a comparison between rubber elasticity and gas pressure from the view point of statistical thermodynamics. A gas particle (atom or molecule) has more space to move about in a large container than in a small one. In other words, the total number of the states available for the gas particle to occupy, all having the same potential energy, is proportional to the volume V of the container. Thus, corresponding to Eq. (2.9), the entropy of the gas particle can be

expressed as

$$s = k \ln(V) + C \quad (2.28)$$

where C is just a constant. If there are n particles in the container and the interactions among the particles can be ignored because the gas is very dilute, the total entropy is

$$S = k \ln(V^n) + nC = nk \ln(V) + nC. \quad (2.29)$$

Then the pressure P is given by

$$P = - \left(\frac{\partial A}{\partial V} \right)_T = T \left(\frac{\partial S}{\partial V} \right)_T = \frac{nkT}{V} \quad (2.30)$$

which is the ideal gas law and is equivalent to Eq. (2.22) for the ideal rubber.

The basic physical effect responsible for rubber elasticity can be applied to any length of polymer chain which is sufficiently long. In a polymeric liquid, whose concentration is high and whose polymer chains are long, entanglements between polymer chains can occur. As we shall see in Chapters 8–12, an entanglement can be treated as an impermanent crosslink. Chain slippage through entanglement links will occur to equilibrate the uneven segmental distribution caused by the applied deformation. Before the chain slippage mechanism has a chance to take place after a step deformation is applied, the entanglement links can be regarded as fixed; the measured modulus (in the linear region) can be used to calculate the entanglement molecular weight M_e by using Eq. (2.26) (M_x is regarded as M_e). In a rubber, a chain strand can have an entanglement with another strand, which cannot become freed because of the cross-links; in other words, the measured modulus receives contributions from both cross-links and entanglements. Various models have been proposed to describe the additional effect from entanglement in a rubber.^{7,8} The application of Eq. (2.26) to a polymeric liquid to calculate M_e from the measured modulus as mentioned above is more exactly defined experimentally, as there is only the impermanent type of cross-link, namely, entanglement in the system.^a As it turns out, the obtained M_e value plays a pivotal role in the universal behavior of polymer viscoelasticity in the entanglement region; it is the basic structural size in terms of which the molecular weight of a polymer can be expressed

^aThe so-called plateau modulus is often used to calculate M_e . In doing so, the equation used is that of Eq. (2.26) multiplied by a factor of 4/5, which accounts for the effect of chain slippage through entanglement links. See Chapters 8–11 for the details.

or normalized. The important role of M_e will be extensively covered in Chapters 8–14.

References

1. Mark, H., and Tobolsky, A. V., *Physical Chemistry of High Polymeric Systems*, Interscience, New York (1950).
2. James, H. M., and Guth, E., *J. Chem. Phys.*, **11**, 455 (1943).
3. James, H. M., and Guth, E., *J. Polymer Sci.*, **IV**, 153 (1949).
4. Anthony, R. L., Caston, R. H., and Guth, E., *J. Phys. Chem.* **46**, 826 (1942).
5. Treloar, L. R. G., *Rep. Prog. Phys.* **36**, 755 (1973); Treloar, L. R. G., *The Physics of Rubber Elasticity* (3rd edn), Clarendon Press, Oxford (1975).
6. Flory, P. J., *Principles of Polymer Chemistry*, Cornell Univ. Press, Ithaca (1979).
7. Mark, J. E., and Erman, B., (eds.) *Elastomeric Polymer Networks*, Prentice Hall, New Jersey (1992).
8. Doi, M., and Edwards, S. F., *The Theory of Polymer Dynamics*, Oxford Univ. Press (1986).

Chapter 3

Polymer Chain Dynamics

3.1 Introduction

Consisting of a large number of atoms, a polymer chain molecule has a very large number of degrees of freedom. Corresponding to the large number of degrees of freedom, the polymer chain dynamics cover a very broad range of motional rates. The vibrational motions of the chemical bonds excluded, polymer chain dynamics range from the local segmental motions in the high-frequency region ($\sim 10^9 \text{ s}^{-1}$) to the slow movement of the whole chain over a distance of the whole-chain size scale (for instance, the characteristic rate can be easily as slow as 10^{-5} s^{-1} for a polymer of common molecular weight, say 5×10^5). A general rule is that the slower the mode of motion, the larger the involved domain of the chain. Almost all the physical properties of the polymer, such as viscoelasticity, diffusion, and the glass-rubber transition phenomenon, are in various degrees related to the chain dynamics in different frequency ranges.

To probe various modes of chain motions often requires using different kinds of measurement techniques. As shown in Fig. 3.1, starting from the high-frequency region, the commonly used measurement techniques are Rayleigh–Brillouin Scattering;^{1–3} NMR spin-lattice relaxation times in the laboratory frame and in the rotating frame;^{4,5} dielectric relaxation;⁶ dynamic depolarized Rayleigh scattering;^{7–11} quasi-elastic (spin-echo) neutron scattering;^{12–14} dynamic mechanical spectrum (or dynamic viscoelastic spectrum);^{15–21} and diffusion (including radiolabeling,²² forward recoil spectrometry,²³ marker displacement,²⁴ forced Rayleigh scattering,²⁵ pulsed field gradient spin echo NMR²⁶ etc.). It is of great research interest and importance to relate the different modes of chain motions as probed by these different techniques. In certain aspects, theoretical advances have

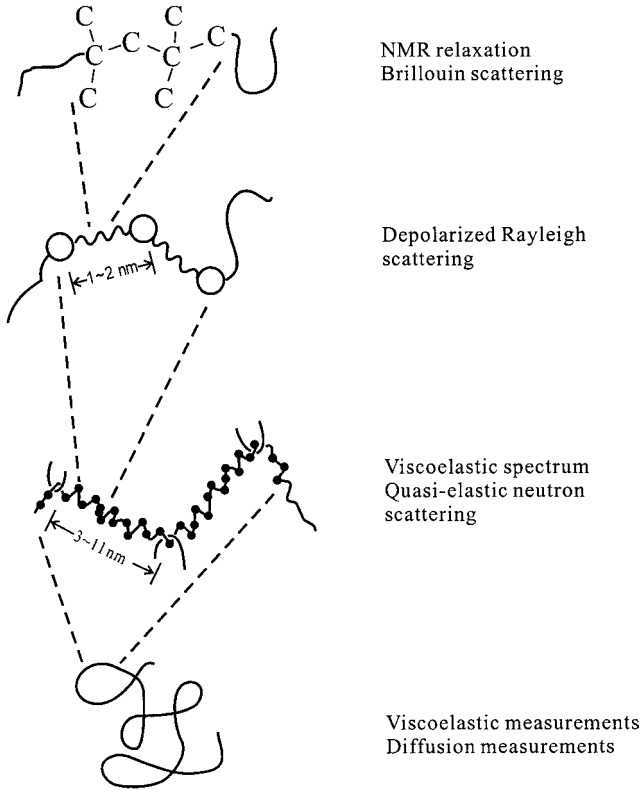


Fig. 3.1 Chain dynamics at different length scales: microstructure, Rouse segment, entanglement strand, and whole chain; and some of the usual techniques for probing them.

made the linkages. In particular, the quantitative relation between the polymer viscoelastic properties and the diffusion constant²⁷ will be discussed in detail in the later chapters of this book.

As shown in Chapter 1 for the static properties, universality occurs if the conformation and motions associated with a large chain section can be described in terms of the Gaussian chain model. Chain dynamics described in terms of the Gaussian chain picture in the free-draining limit are the well-known Rouse motions.²⁸ And each bead-spring segment is often referred to as a Rouse segment. In this chapter, we shall discuss the basic features in the Rouse model. Another structural size scale — the entanglement strand — is implied in Fig. 3.1. Each entanglement point is pictured as a slip-link. The constraint effect of the slip-links on the motions of a polymer

chain will be studied in detail in Chapters 8–12. The major part of this book deals with chain motions related to size scales equal to or greater than that of a single Rouse segment.

Rouse motions arise from subjecting each bead of the Gaussian chain to thermal fluctuation forces — Brownian motion. Thus, we first study the basic theory of Brownian motion. We treat the Brownian motion as a stochastic process and, on the basis of known macroscopic laws, to develop a phenomenological equation to describe the Brownian motion. This approach, originated by Einstein,^{29,30} is limited by several conditions, such as that a linear relation holds between fluxes and forces, and that the time-scale of the motion under consideration and its associated size scale (typically the Rouse segment size for a polymer) must be much greater than those characteristic of the small molecules in the fluid (including the microstructural segments in the case of the polymer). In terms of the motions illustrated in Fig. 3.1 for the polymer, the microstructural motions, as can be probed by Rayleigh–Brillouin scattering and NMR relaxations, are much faster than the motions associated with a Rouse segment or a larger chain section and, in the absence of solvent molecules, are the main source of the fluctuation forces experienced constantly by the Rouse bead.

There are two forms of phenomenological equations for describing Brownian motion: the Smoluchowski equation and the Langevin equation. These two equations, essentially the same, look very different in form. The Smoluchowski equation is derived from the generalization of the diffusion equation and has a clear relation to the thermodynamics of irreversible processes. In Chapters 6 and 7, its application to the elastic dumbbell model and the Rouse model to obtain the rheological constitutive equations will be discussed. In contrast, the Langevin equation, while having no direct relation to thermodynamics, can be applied to wider classes of stochastic processes.³¹ In this chapter, it will be used to obtain the time-correlation function of the end-to-end vector of a Rouse chain.

3.2 The Smoluchowski Equation

Consider the Brownian particles dissolved in a solution. The Brownian particles will diffuse from the higher concentration region to the lower concentration region. For simplicity, we consider one-dimensional diffusion. Let $C(x, t)$ be the concentration at position x and time t . The diffusion process is phenomenologically described by Fick's law, which says that the

flux, $j(x, t)$, is proportional to the spatial gradient of the concentration, i.e.

$$j(x, t) = -D \frac{\partial C}{\partial x} \quad (3.1)$$

where the constant D is called the diffusion constant.³²

Let us assume D is a constant; then Eq. (3.1), together with the continuity equation

$$\frac{\partial C}{\partial t} = -\frac{\partial j}{\partial x} \quad (3.2)$$

gives the diffusion equation,

$$\frac{\partial C}{\partial t} = D \frac{\partial^2 C}{\partial x^2}. \quad (3.3)$$

If an external potential field $V(x)$ is applied to the particle, Fick's law needs to be modified. As the potential $V(x)$ exerts a force

$$F = -\frac{\partial V}{\partial x} \quad (3.4)$$

on the particle, the average velocity of the particle v becomes non-zero. If F is not large, v is proportional to F , i.e.

$$\zeta v = F = -\frac{\partial V}{\partial x} \quad (3.5)$$

where ζ is called the friction constant. Then the total flux becomes

$$j = -D \frac{\partial C}{\partial x} + Cv = -D \frac{\partial C}{\partial x} - \frac{C}{\zeta} \frac{\partial V}{\partial x}. \quad (3.6)$$

From Eq. (3.6), an important relation can be obtained as in the following: In the equilibrium state, the concentration $C(x, t)$ follows the Boltzmann distribution

$$C_{eq}(x) \propto \exp\left(-\frac{V(x)}{kT}\right) \quad (3.7)$$

and the total flux must vanish:

$$-D \frac{\partial}{\partial x} C_{eq} - \frac{C_{eq}}{\zeta} \frac{\partial V}{\partial x} = 0. \quad (3.8)$$

From Eqs. (3.7) and (3.8), it follows that in equilibrium

$$D = \frac{kT}{\zeta}. \quad (3.9)$$

This equation is the well-known Einstein relation.

The Einstein relation states that, for particles (or a particle) undergoing thermal motion, the quantity D which characterizes the diffusion process is related to the quantity ζ which specifies the response to an external force. Substituting Eq. (3.9) into Eq. (3.6), one obtains

$$j = -\frac{1}{\zeta} \left(kT \frac{\partial C}{\partial x} + C \frac{\partial V}{\partial x} \right). \quad (3.10)$$

From Eqs. (3.2) and (3.10), it follows that

$$\frac{\partial C}{\partial t} = \frac{\partial}{\partial x} \frac{1}{\zeta} \left(kT \frac{\partial C}{\partial x} + C \frac{\partial V}{\partial x} \right). \quad (3.11)$$

This equation is called the Smoluchowski equation.

The Smoluchowski equation can be obtained more formally from the concept of chemical potential. Equation (3.10) can be rewritten as

$$j = -\frac{C}{\zeta} \frac{\partial}{\partial x} (kT \ln C + V) \quad (3.12)$$

which has a thermodynamic significance. The quantity $kT \ln C + V$ is the chemical potential of noninteracting particles of concentration C . Thus Eq. (3.12) indicates that the flux is proportional to the spatial gradient of the chemical potential and that when the external field is nonzero, what must be balanced in the equilibrium is not concentration but the chemical potential.

Defining the flux velocity by $v_f \equiv j/C$, we obtain from Eq. (3.12)

$$v_f = -\frac{1}{\zeta} \frac{\partial}{\partial x} (kT \ln C + V). \quad (3.13)$$

Then the Smoluchowski equation (Eq. (3.11)) is derived from the continuity equation

$$\frac{\partial C}{\partial t} = -\frac{\partial}{\partial x} (C v_f). \quad (3.14)$$

Consider a particle undergoing thermal motion. If we denote the probability for finding the particle at x and t as $\Psi(x, t)$, the above equations are equally valid with $C(x, t)$ replaced by $\Psi(x, t)$. For non-interacting particles,

the only difference between $C(x, t)$ and $\Psi(x, t)$ is that the latter is normalized while the former is not. Thus, the evolution equation for $\Psi(x, t)$ is

$$\frac{\partial \Psi}{\partial t} = \frac{\partial}{\partial x} \frac{1}{\zeta} \left(kT \frac{\partial \Psi}{\partial x} + \Psi \frac{\partial V}{\partial x} \right) \quad (3.15)$$

which is also called the Smoluchowski equation.

It is easy to generalize Eq. (3.15) for a system which has many degrees of freedom. Let $\{x_s\} \equiv (x_1, x_2, \dots, x_N)$ be the set of dynamical variables describing the state of Brownian particles. We need to know first the relation between the average velocity v_n and the force $F_m = -\partial V / \partial x_m$. Such a relation is generally expressed as

$$v_n = \sum_m L_{nm}(\{x_s\}) F_m \quad (3.16)$$

where the coefficients L_{mn} are called the mobility matrix and can be obtained using hydrodynamics. It can be proved that L_{mn} is a symmetric positive definite matrix,^{30,33} i.e.

$$L_{mn} = L_{nm}; \quad \sum_n \sum_m F_n F_m L_{nm} \geq 0 \quad \text{for all } F_n. \quad (3.17)$$

Corresponding to Eq. (3.13), we can write the flux velocity as

$$v_{fn} = - \sum_m L_{nm} \frac{\partial}{\partial x_m} (kT \ln \Psi + V). \quad (3.18)$$

Using the continuity equation

$$\frac{\partial \Psi}{\partial t} = - \sum_n \frac{\partial}{\partial x_n} (v_{fn} \Psi) \quad (3.19)$$

the Smoluchowski equation is obtained as

$$\frac{\partial \Psi}{\partial t} = \sum_n \sum_m \frac{\partial}{\partial x_n} L_{nm} \left[\frac{\partial}{\partial x_m} (kT \ln \Psi + V) \right] \Psi. \quad (3.20)$$

We will discuss Eq. (3.20) further in Chapters 6 and 7, where it will be used to obtain the rheological constitutive equations of the elastic dumbbell model and the Rouse chain model.

3.3 The Langevin Equation

An alternative way for describing Brownian motion is to study the equation of motion for the Brownian particle with the random force $f(t)$ written explicitly. This equation — the Langevin equation with the inertial term neglected (i.e. zero acceleration) — expresses the balance of the external, friction, and fluctuation forces:

$$\zeta \frac{dx}{dt} = -\frac{\partial V}{\partial x} + f(t) \quad (3.21)$$

or

$$\frac{dx}{dt} = -\frac{1}{\zeta} \frac{\partial V}{\partial x} + g(t).$$

Physically, the random force $f(t) = \zeta g(t)$ represents the sum of the forces arising from the ceaseless collisions with the fast moving small molecules (including microstructural segments) in the fluid. As we cannot know the precise time dependence of the random force, we regard it as a stochastic variable with an assumed plausible distribution $\Psi[f(t)]$. It can be shown that if the distribution of $f(t)$ is Gaussian characterized by the moments

$$\langle f(t) \rangle = 0 \quad (3.22)$$

or

$$\langle g(t) \rangle = 0$$

and

$$\langle f(t)f(t') \rangle = 2\zeta kT\delta(t-t') \quad (3.23)$$

or

$$\langle g(t)g(t') \rangle = 2D\delta(t-t')$$

the distribution of $x(t)$ determined by Eq. (3.21) satisfies the Smoluchowski equation (Eq. (3.11)).

The Langevin equation corresponding to the Smoluchowski equation of multiple stochastic variables — Eq. (3.20) — with the condition $\partial L_{nm}/\partial x_m = 0$, which is often true, is given by^{31,33}

$$\frac{dx_n}{dt} = \sum_m L_{nm} \left(-\frac{\partial V}{\partial x_m} \right) + g_n(t) \quad (3.24)$$

where the mean and variance–covariance of g_n are given, respectively, by

$$\langle g_n(t) \rangle = 0 \tag{3.25}$$

and

$$\langle g_n(t)g_m(t') \rangle = 2L_{nm}kT\delta(t - t'). \tag{3.26}$$

The Langevin equation and the Smoluchowski equation represent the same motion. Each of the equations has its advantages and disadvantages in solving the dynamic problems of interest. One would choose one over the other for its convenience in treating the problem of interest.

3.4 The Rouse Model

As discussed in Chapter 1, a Gaussian chain is physically equivalent to a string of beads connected by harmonic springs with the elastic constant $3kT/b^2$ (Eq. (1.47) with b^2 given by Eq. (1.44)). Here each bead is regarded as a Brownian particle in modeling the chain dynamics. Such a model was first proposed by Rouse and has been the basis of molecular theories for the dynamics of polymeric liquids.^{15,16,34}

Let $\{\mathbf{R}_n\} \equiv (\mathbf{R}_1, \mathbf{R}_2, \dots, \mathbf{R}_N)$ be the position vectors of the beads in a Gaussian chain (see Fig. 3.2). Then the motions of the beads are described

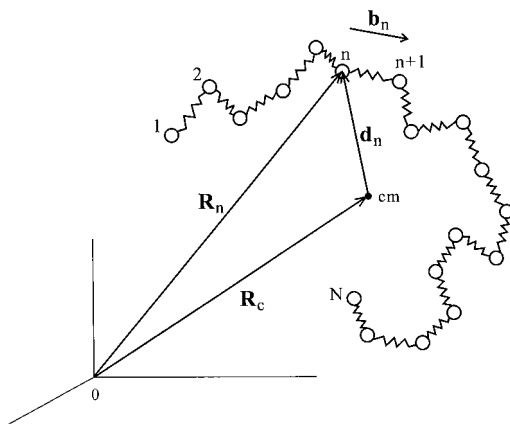


Fig. 3.2 Gaussian chain formed from $N - 1$ “springs” and N “beads” at positions: $\mathbf{R}_1, \mathbf{R}_2, \dots, \mathbf{R}_N$ relative to an arbitrary point in space. $\mathbf{b}_n = \mathbf{R}_{n+1} - \mathbf{R}_n$ is the bond vector, and \mathbf{R}_c is the position of the center of mass (cm) for $\mathbf{d}_n = \mathbf{R}_n - \mathbf{R}_c$ and $\sum_{n=1}^N \mathbf{d}_n = 0$.

by the following Smoluchowski equation

$$\frac{\partial \Psi}{\partial t} = \sum_{n=1}^N \sum_{m=1}^N \frac{\partial}{\partial \mathbf{R}_n} \cdot \mathbf{L}_{nm} \cdot \left[\frac{\partial}{\partial \mathbf{R}_m} (kT \ln \Psi) + \frac{\partial V}{\partial \mathbf{R}_m} \right] \Psi. \quad (3.28)$$

When Eq. (3.28) is expressed in the form of Eq. (3.20), the mobility matrix L for a chain of N beads will have the dimension $3N \times 3N$.

In the Rouse model, the hydrodynamic interaction^{35,36} and the excluded volume interaction³⁷⁻³⁹ among beads are disregarded and the mobility tensor and the interaction potential are given by

$$\mathbf{L}_{nm} = \frac{\delta}{\zeta} \delta_{nm} \quad (3.29)$$

$$V = \frac{3kT}{2b^2} \sum_{n=2}^N (\mathbf{R}_n - \mathbf{R}_{n-1})^2 \quad (3.30); (1.47)$$

where δ is the unit tensor (see Eq. (5.A.10)).

The Langevin equation corresponding to Eq. (3.28) is

$$\frac{d\mathbf{R}_n}{dt} = -\frac{3kT}{\zeta b^2} (2\mathbf{R}_n - \mathbf{R}_{n+1} - \mathbf{R}_{n-1}) + \mathbf{g}_n(t) \quad (3.31)$$

for the internal beads ($n = 2, 3, \dots, N-1$), and

$$\frac{d\mathbf{R}_1}{dt} = -\frac{3kT}{\zeta b^2} (\mathbf{R}_1 - \mathbf{R}_2) + \mathbf{g}_1(t) \quad (3.32)$$

$$\frac{d\mathbf{R}_N}{dt} = -\frac{3kT}{\zeta b^2} (\mathbf{R}_N - \mathbf{R}_{N-1}) + \mathbf{g}_N(t) \quad (3.33)$$

for the end beads ($n = 1$ and N). The random fluctuation \mathbf{g}_n is Gaussian, characterized by the moments which are given by substituting Eq. (3.29) into Eqs. (3.25) and (3.26),

$$\langle \mathbf{g}_n(t) \rangle = 0 \quad (3.34)$$

$$\langle g_{n\alpha}(t) g_{m\beta}(t') \rangle = \frac{2kT}{\zeta} \delta_{nm} \delta_{\alpha\beta} \delta(t-t') \quad (3.35)$$

where α and β represent the x , y and z coordinates.

3.5 Diffusion Motion of the Rouse Chain

The diffusion motion of a polymer chain is the translational behavior of its center of mass $\mathbf{R}_c(t)$ defined by

$$\mathbf{R}_c(t) = \frac{1}{N} \sum_{n=1}^N \mathbf{R}_n(t). \quad (3.36)$$

By summing the N equations as given by Eqs. (3.31)–(3.33), we obtain

$$\frac{d\mathbf{R}_c}{dt} = \frac{1}{N} \sum_{n=1}^N \mathbf{g}_n(t). \quad (3.37)$$

Thus

$$\langle (\mathbf{R}_c(t) - \mathbf{R}_c(0))^2 \rangle = \frac{1}{N^2} \sum_{n=1}^N \sum_{m=1}^N \int_0^t \int_0^t \langle \mathbf{g}_n(t') \cdot \mathbf{g}_m(t'') \rangle dt' dt''. \quad (3.38)$$

Using Eq. (3.35), one obtains from Eq. (3.38)

$$\langle (\mathbf{R}_c(t) - \mathbf{R}_c(0))^2 \rangle = \frac{6kTt}{\zeta N}. \quad (3.39)$$

The diffusion constant of the center of mass is defined by

$$D_G = \lim_{t \rightarrow \infty} \frac{\langle (\mathbf{R}_c(t) - \mathbf{R}_c(0))^2 \rangle}{6t}. \quad (3.40)$$

From Eqs. (3.39) and (3.40)

$$D_G = \frac{kT}{\zeta N}. \quad (3.41)$$

This result means that the diffusion constant for the whole Rouse chain is simply $1/N$ of the diffusion constant for the individual bead (kT/ζ).

3.6 The Rouse Normal Modes of Motion

Besides the diffusion motion, the dynamics of a polymer chain are also characterized by its internal motions, which can be expressed in terms of the normal modes.

With the bond vector \mathbf{b}_n defined by

$$\mathbf{b}_n = \mathbf{R}_{n+1} - \mathbf{R}_n. \quad (3.42)$$

Equations (3.31)–(3.33) can be rewritten as

$$\frac{d}{dt} \begin{pmatrix} \mathbf{b}_0 \\ \mathbf{b}_1 \\ \mathbf{b}_2 \\ \cdot \\ \cdot \\ \mathbf{b}_{N-2} \\ \mathbf{b}_{N-1} \end{pmatrix} = -\frac{3kT}{\zeta b^2} \begin{pmatrix} 2 & -1 & 0 & 0 & \cdot & \cdot & 0 \\ -1 & 2 & -1 & 0 & 0 & \cdot & 0 \\ 0 & -1 & 2 & -1 & 0 & \cdot & 0 \\ \cdot & \cdot & \cdot & \cdot & \cdot & \cdot & \cdot \\ \cdot & \cdot & \cdot & \cdot & \cdot & \cdot & \cdot \\ 0 & 0 & \cdot & \cdot & 0 & -1 & 2 & -1 \\ 0 & 0 & \cdot & \cdot & \cdot & 0 & -1 & 2 \end{pmatrix} \begin{pmatrix} \mathbf{b}_0 \\ \mathbf{b}_1 \\ \mathbf{b}_2 \\ \cdot \\ \cdot \\ \mathbf{b}_{N-2} \\ \mathbf{b}_{N-1} \end{pmatrix} + \begin{pmatrix} \mathbf{g}_2(t) - \mathbf{g}_1(t) \\ \mathbf{g}_3(t) - \mathbf{g}_2(t) \\ \mathbf{g}_4(t) - \mathbf{g}_3(t) \\ \cdot \\ \cdot \\ \mathbf{g}_{N-1}(t) - \mathbf{g}_{N-2}(t) \\ \mathbf{g}_N(t) - \mathbf{g}_{N-1}(t) \end{pmatrix} \quad (3.43)$$

which can also be expressed as

$$\frac{d\mathbf{b}_s}{dt} = -\frac{3kT}{\zeta b^2} \sum_{t=1}^{N-1} A_{st} \mathbf{b}_t + (\mathbf{g}_{s+1}(t) - \mathbf{g}_s(t)) \quad \text{for } s = 1, 2, \dots, N-1 \quad (3.44)$$

where (A_{st}) is often called the Rouse matrix given by

$$A_{st} = 2\delta_{st} - \delta_{s+1,t} - \delta_{s-1,t}. \quad (3.45)$$

Here the normal procedure is to do the transformation from the bond vectors $\{\mathbf{b}_s\}$ to the normal coordinates $\{\mathbf{q}_t\}$ which will diagonalize the Rouse matrix (A_{st}) . As shown in Appendix 3.A, the Rouse matrix has the eigenvalues:

$$a_p = 4 \sin^2 \left(\frac{p\pi}{2N} \right) \quad \text{for } p = 1, 2, \dots, N-1. \quad (3.46)$$

We can express the transformation as

$$\mathbf{b}_s = \sum_{t=1}^{N-1} U_{st} \mathbf{q}_t. \quad (3.47)$$

As shown in Appendix 3.A,

$$U_{st} = \sqrt{\frac{2}{N}} \sin\left(\frac{s\pi t}{N}\right) \quad (3.48)$$

(U_{st}) is an orthogonal matrix, whose transpose is the inverse matrix, i.e.

$$U_{st}^{-1} = U_{st}^T$$

or

$$\sum_{t=1}^{N-1} U_{ts} U_{tu} = \delta_{su}. \quad (3.49)$$

Using Eqs. (3.47) and (3.49), we can obtain from Eq. (3.44)

$$\begin{aligned} \frac{d\mathbf{q}_p}{dt} &= -\frac{3kT}{\zeta b^2} \sum_{s=1}^{N-1} \sum_{t=1}^{N-1} \sum_{u=1}^{N-1} U_{sp} A_{st} U_{tu} \mathbf{q}_u + \mathbf{h}_p(t) \\ &= -\frac{3kT}{\zeta b^2} a_p \mathbf{q}_p + \mathbf{h}_p(t) \end{aligned} \quad (3.50)$$

where

$$\mathbf{h}_p(t) = \sum_{s=1}^{N-1} U_{sp} (\mathbf{g}_{s+1}(t) - \mathbf{g}_s(t)). \quad (3.51)$$

Obviously from Eq. (3.34)

$$\langle \mathbf{h}_p(t) \rangle = 0. \quad (3.52)$$

By using Eq. (3.35), the substitution of Eq. (3.48) into Eq. (3.51) gives

$$\langle h_{p\alpha}(t) h_{q\beta}(t') \rangle = \frac{8kT}{\zeta} \sin^2(p\pi/2N) \delta_{\alpha\beta} \delta_{pq} \delta(t-t'). \quad (3.53)$$

Following the procedure shown in Appendix 3.B for solving the Langevin equation of a particle in a simple harmonic potential, we obtain from Eq. (3.50) in combination with Eqs. (3.52) and (3.53)

$$\langle \mathbf{q}_p(t) \cdot \mathbf{q}_p(0) \rangle = \delta_{pq} b^2 \exp\left(-\frac{t}{\tau_p}\right) \quad (3.54)$$

with

$$\tau_p = \frac{\zeta b^2}{3kT a_p} = \frac{\zeta b^2}{12kT \sin^2(p\pi/2N)}. \quad (3.55)$$

The normal coordinate \mathbf{q}_p with p being a positive integer represents the p th internal or intramolecular mode of motion of the polymer chain. Equation (3.54) indicates that if $p \neq q$, the p th mode of motion is not correlated with the q th mode. Equation (3.55) can be expressed as

$$\tau_p = K \frac{\pi^2 M^2}{12N^2 \sin^2(p\pi/2N)} \quad (3.56)$$

where K , which we refer to as the frictional factor, is independent of the molecular weight and is given by

$$K = \frac{\zeta b^2}{kT\pi^2 m^2} \quad (3.57)$$

with $m = M/N$ denoting the mass per Rouse segment.

The above results of the normal modes $\{\mathbf{q}_p(t)\}$ allow the numerous internal motions of the polymer chain to be classified into independent modes. Consider for example the end-to-end vector

$$\mathbf{R}(t) \equiv \mathbf{R}_N(t) - \mathbf{R}_1(t) = \sum_{s=1}^{N-1} \mathbf{b}_s(t). \quad (3.58)$$

Substituting Eqs. (3.47) and (3.48) into Eq. (3.58), the time correlation function of the end-to-end vector, after some algebraic derivation, can be expressed in terms of the normal modes as⁴⁰

$$\langle \mathbf{R}(t) \cdot \mathbf{R}(0) \rangle = \sum_{p=1,3,\dots}^{N-1} \frac{2b^2}{N} \cot^2 \left(\frac{p\pi}{2N} \right) \exp \left(-\frac{t}{\tau_p} \right) \quad (3.59)$$

where p 's are odd integers, the largest of which is $N-1$ for N being an even number and $N-2$ for N being an odd number. When $N \rightarrow \infty$, Eq. (3.59) can be reduced as

$$\begin{aligned} \langle \mathbf{R}(t) \cdot \mathbf{R}(0) \rangle &= \sum_{p=\text{odd}} \frac{2b^2}{N} \frac{4N^2}{\pi^2 p^2} \exp \left(-\frac{t}{\tau_p} \right) \\ &= Nb^2 \sum_{p=\text{odd}} \frac{8}{\pi^2 p^2} \exp \left(-\frac{t}{\tau_p} \right) \end{aligned} \quad (3.60)$$

with

$$\tau_p = \frac{\zeta N^2 b^2}{3kT\pi^2 p^2} = \frac{\tau_1}{p^2} \quad (3.61)$$

where

$$\tau_1 = \frac{\zeta N^2 b^2}{3kT\pi^2} = K \frac{M^2}{3} \quad (3.62)$$

which is in agreement with the result obtained from the continuous Rouse mode³³ (Appendix 3.C). Physically $\langle \mathbf{R}(t) \cdot \mathbf{R}(0) \rangle$ mainly represents the reorientation motion of the polymer molecule with the rotational relaxation time τ_r . Because of the strong $1/p^2$ dependence of the relaxation strengths of the odd modes in Eq. (3.60), τ_r is basically equivalent to τ_1 .

In summary, we have used the Rouse chain model to obtain the diffusion constant of the center of mass and the time-correlation function of the end-to-end vector, which reflects the rotational motion of the whole polymer molecule. Since N is proportional to the molecular weight M , and K is independent of molecular weight, Eqs. (3.41) and (3.62) indicate that D_G and τ_r depend on the molecular weight, respectively, as

$$D_G \propto \frac{1}{M} \quad (3.63)$$

and

$$\tau_r \approx \tau_1 \propto M^2. \quad (3.64)$$

These predictions do not agree with the experimental results of polymer chains in dilute θ solutions,^{41–45} which are summarized as

$$D_G \propto \frac{1}{\sqrt{M}} \quad (3.65)$$

and

$$\tau_r \propto M^{3/2}. \quad (3.66)$$

The disagreement arises from neglecting the hydrodynamic interaction in the dilute solution. Thus, in spite of its original intention, the Rouse model is now considered an inappropriate model for the polymer in a dilute solution. However, the model is very important conceptually in the theoretical developments of polymer chain dynamics. And the Rouse model has been found to describe very well the viscoelastic behavior of a melt¹⁸ or a blend solution⁴⁶ where polymer chains are sufficiently long for the Gaussian chain model to be applicable but not long enough to form entanglements (see Chapter 11).

As shown in Eq. (3.62), the relaxation time τ_1 is the product of the frictional factor K which is independent of molecular weight and a structural

factor, which is a certain function of molecular weight. All the temperature dependence of the relaxation time is contained in the frictional factor, which in a polymer melt or concentrated solution system is often described by the Vogel–Tammann–Fulcher (VTF) equation^{47–49} or equivalently the Williams–Landel–Ferry (WLF) equation.^{50,51} In Chapters 6–9, 12 and 14, we shall see more relaxation times expressed as a product of the frictional factor K and a structural factor for different modes of motion. We will also see that the relaxation modulus or viscoelastic spectrum of a polymer is expressed in terms of the normal modes.

As indicated by Eqs. (3.41) and (3.55), the molecular translational motion and the internal modes of motion of a Rouse chain ultimately depend on the diffusion constant of each individual Rouse bead, $D = kT/\zeta$. The diffusion of a Brownian particle (Eq. (3.3)) can be simulated by the random walk model as shown in Appendix 3.D, which in turn can be used to introduce the diffusion process into different discrete-time models of polymer dynamics (Chapters 8 and 16–18).

Appendix 3.A — Eigenvalues and Eigenvectors of the Rouse Matrix

Consider the Rouse matrix (A_{st}) of the dimension $z \times z$. The z eigenvalues $a_1, a_2, a_3, \dots, a_z$ of the matrix are the roots of the equation obtained by setting the determinant $D_z = |A_{st} - a\delta_{st}|$ equal to zero, i.e.

$$D_z = \begin{vmatrix} x & -1 & 0 & 0 & \cdot & \cdot & & 0 \\ -1 & x & -1 & 0 & \cdot & \cdot & & 0 \\ 0 & -1 & x & -1 & 0 & \cdot & & 0 \\ \cdot & \cdot & \cdot & \cdot & \cdot & \cdot & & \cdot \\ \cdot & \cdot & \cdot & \cdot & \cdot & \cdot & & \cdot \\ & & & & & & & \\ 0 & 0 & \cdot & & 0 & -1 & x & -1 \\ 0 & 0 & 0 & \cdot & & 0 & -1 & x \end{vmatrix} = 0 \quad (3.A.1)$$

where

$$x = 2 - a. \quad (3.A.2)$$

From Eq. (3.A.1), the recursion rule is found as follows:

$$D_z = xD_{z-1} - D_{z-2} \quad (3.A.3)$$

with

$$D_1 = x \tag{3.A.4}$$

and

$$D_2 = x^2 - 1. \tag{3.A.5}$$

We may express x as

$$x = 2 \cos \theta = \exp(i\theta) + \exp(-i\theta). \tag{3.A.6}$$

Then as a solution to Eq. (3.A.3), D_z can be expressed as

$$D_z = A_1 \exp(iz\theta) + A_2 \exp(-iz\theta) \tag{3.A.7}$$

where A_1 and A_2 are constants.

Using the expressions for D_1 and D_2 (Eqs. (3.A.4) and (3.A.5)), A_1 and A_2 are determined to be

$$A_1 = \frac{\exp(i\theta)}{\exp(i\theta) - \exp(-i\theta)} \tag{3.A.8}$$

$$A_2 = \frac{-\exp(-i\theta)}{\exp(i\theta) - \exp(-i\theta)}. \tag{3.A.9}$$

Using the result from substituting Eqs. (3.A.8) and (3.A.9) into Eq. (3.A.7), we have from Eq. (3.A.1)

$$D_z = \frac{\sin[(z+1)\theta]}{\sin \theta} = 0. \tag{3.A.10}$$

Then the z eigenvalues of the Rouse matrix A_{st} are produced when Eq. (3.A.10) is satisfied, i.e. when

$$\theta = \frac{p\pi}{z+1} \quad \text{for } p = 1, 2, \dots, z. \tag{3.A.11}$$

With x obtained from substituting Eq. (3.A.11) into Eq. (3.A.6), we obtain from Eq. (3.A.2) the eigenvalues

$$a_p = 2 - 2 \cos \left(\frac{p\pi}{z+1} \right) = 4 \sin^2 \left(\frac{p\pi}{2(z+1)} \right) \tag{3.A.12}$$

for $p = 1, 2, \dots, z$.

which is used in Eq. (3.46) for $z = N - 1$.

Let c_1, c_2, \dots, c_{N-1} be the components of the eigenvector of the Rouse matrix (for $z = N - 1$) which give rise to the p th eigenvalue, a_p . Then, using Eq. (3.45), we obtain the recursion relation,

$$c_{k+1} + c_{k-1} = (2 - a_p)c_k \quad (3.A.13)$$

with the boundary condition

$$c_2 = (2 - a_p)c_1; \quad c_{N-2} = (2 - a_p)c_{N-1}. \quad (3.A.14)$$

Substituting Eq. (3.46) or Eq. (3.A.12) with $z = N - 1$ into Eq. (3.A.13), we obtain

$$c_{k+1} + c_{k-1} = \left[\exp\left(\frac{ip\pi}{N}\right) + \exp\left(-\frac{ip\pi}{N}\right) \right] c_k. \quad (3.A.15)$$

The solution to Eq. (3.A.15) is given by

$$c_k = B_1 \exp\left(\frac{ikp\pi}{N}\right) + B_2 \exp\left(-\frac{ikp\pi}{N}\right) \quad (3.A.16)$$

where B_1 and B_2 are constants. The boundary condition, Eq. (3.A.14), requires

$$B_1 = -B_2. \quad (3.A.17)$$

By applying Eq. (3.A.17) and the normalization condition

$$\sum_{k=1}^{N-1} c_k^* c_k = 1 \quad (3.A.18)$$

to Eq. (3.A.16), we obtain

$$c_k = \sqrt{\frac{2}{N}} \sin\left(\frac{k\pi p}{N}\right). \quad (3.A.19)$$

Thus the transformation to the normal coordinates is given by Eqs. (3.47) and (3.48).

Appendix 3.B — The Langevin Equation of a Particle in a Harmonic Potential

The Langevin equation of a normal mode has the general form:

$$\frac{dx}{dt} = -\frac{h}{\zeta}x + g(t) \quad (3.B.1)$$

with

$$\langle g(t) \rangle = 0 \quad (3.B.2)$$

$$\langle g(t)g(t') \rangle = \frac{2kT}{\zeta} \delta(t - t'). \quad (3.B.3)$$

Physically, Eqs. (3.B.1)–(3.B.3) describe the one-dimensional Brownian motion of a particle in a harmonic potential:

$$V = \frac{h}{2} x^2. \quad (3.B.4)$$

To calculate the time correlation function $\langle x(t)x(0) \rangle$, $x(t)$ is first expressed in terms of $g(t)$ as

$$x(t) = \int_{-\infty}^t dt' \exp\left(-\frac{t-t'}{\tau}\right) g(t') \quad (3.B.5)$$

where

$$\tau = \frac{\zeta}{h}. \quad (3.B.6)$$

Then

$$\langle x(t)x(0) \rangle = \int_{-\infty}^t dt' \int_{-\infty}^0 dt'' \exp\left(-\frac{(t-t'-t'')}{\tau}\right) \langle g(t')g(t'') \rangle. \quad (3.B.7)$$

Using Eq. (3.B.3), from Eq. (3.B.7) we obtain

$$\langle x(t)x(0) \rangle = \frac{kT}{h} \exp\left(-\frac{t}{\tau}\right). \quad (3.B.8)$$

Appendix 3.C — The Continuous Rouse Model

If we are mainly interested in the motions involving a large section or the whole of a long chain, we can treat the suffix n labeling the bead as a continuous variable, and the Langevin equation can be written in the continuous form. In the transformation, we replace $\mathbf{R}_n - \mathbf{R}_{n-1}$ by $\partial\mathbf{R}_n/\partial n$; $\mathbf{R}_{n+1} + \mathbf{R}_{n-1} - 2\mathbf{R}_n$ by $\partial^2\mathbf{R}_n/\partial n^2$; δ_{nm} by $\delta(n - m)$; and Σ_n by $\int dn$. Then Eq. (3.31) is rewritten as

$$\frac{\partial\mathbf{R}_n}{\partial t} = \frac{3kT}{\zeta b^2} \frac{\partial^2\mathbf{R}_n}{\partial n^2} + \mathbf{g}_n(t). \quad (3.C.1)$$

In rewriting Eqs. (3.32) and (3.33) in the continuous form, we note that they are included in Eq. (3.C.1) if we define two hypothetical beads \mathbf{R}_0 and \mathbf{R}_{N+1} as

$$\mathbf{R}_0 = \mathbf{R}_1; \quad \mathbf{R}_{N+1} = \mathbf{R}_N \quad (3.C.2)$$

which mean, in the continuous limit:

$$\left. \frac{\partial \mathbf{R}_n}{\partial n} \right|_{n=0} = 0; \quad \left. \frac{\partial \mathbf{R}_n}{\partial n} \right|_{n=N} = 0. \quad (3.C.3)$$

Equation (3.C.2) or (3.C.3) serves as the boundary condition for the differential Eq. (3.C.1), while the moments of the random forces are given in the continuous limit by

$$\langle \mathbf{g}_n(t) \rangle = 0 \quad (3.C.4)$$

and

$$\langle g_{n\alpha}(t) g_{m\beta}(t') \rangle = \frac{2kT}{\zeta} \delta(n-m) \delta_{\alpha\beta} \delta(t-t'). \quad (3.C.5)$$

In summary, Eqs. (3.C.1) and (3.C.3)–(3.C.5) define the continuous Rouse model.

Equation (3.C.1) represents the Brownian motions of coupled oscillators. Similar to the discrete case (Eqs. (3.31)–(3.33)), the standard method to solve the differential equation of the continuous Rouse model is to find the normal coordinates, each with its own independent motion. Considering the boundary conditions given by Eq. (3.C.3), we may write the Fourier expansion for $\mathbf{R}_n(t)$ in terms of the normal coordinates $\{\mathbf{X}_q\}$ as

$$\mathbf{R}_n(t) = \mathbf{X}_0(t) + \left(\frac{2}{N}\right)^{1/2} \sum_{q=1}^{\infty} \mathbf{X}_q(t) \cos\left(\frac{q\pi n}{N}\right) \quad (3.C.6)$$

with $q = 1, 2, \dots$

Using the orthonormal property of the basis functions $\{(2/N)^{1/2} \cos(q\pi n/N)\}$, we can express the normal coordinates $\mathbf{X}_p(t)$ as

$$\mathbf{X}_p(t) = \left(\frac{2}{N}\right)^{1/2} \int_0^N \mathbf{R}_n(t) \cos\left(\frac{p\pi n}{N}\right) dn \quad (3.C.7)$$

and the coordinate $\mathbf{X}_0(t)$ represents the position of the center of mass $\mathbf{R}_c(t)$,

$$\mathbf{R}_c(t) = \frac{1}{N} \int_0^N \mathbf{R}_n(t) dn = \mathbf{X}_0(t). \quad (3.C.8)$$

Substituting Eq. (3.C.6) into Eq. (3.C.1), we obtain

$$\begin{aligned} \frac{\partial \mathbf{R}_c(t)}{\partial t} + \left(\frac{2}{N}\right)^{1/2} \sum_{q=1}^{\infty} \frac{\partial \mathbf{X}_q(t)}{\partial t} \cos\left(\frac{q\pi n}{N}\right) \\ = -\frac{3kT}{\zeta b^2} \left(\frac{2}{N}\right)^{1/2} \sum_{q=1}^{\infty} \left(\frac{q\pi}{N}\right)^2 \mathbf{X}_q(t) \cos\left(\frac{q\pi n}{N}\right) + \mathbf{g}_n(t). \end{aligned} \quad (3.C.9)$$

Performing the integration $\int_0^N dn$ on the both sides of Eq. (3.C.9) and following a procedure similar to the discrete case, the same diffusion constant (Eq. (3.41)) can be obtained.

Multiplying both sides of Eq. (3.C.9) by $(2/N)^{1/2} \cos(p\pi n/N)$ and then performing the integration $\int_0^N dn$, we obtain

$$\frac{\partial}{\partial t} \mathbf{X}_p(t) = -\frac{3kT}{\zeta b^2} \left(\frac{p\pi}{N}\right)^2 \mathbf{X}_p(t) + \mathbf{h}_p(t) \quad (3.C.10)$$

where

$$\mathbf{h}_p(t) = \left(\frac{2}{N}\right)^{1/2} \int_0^N \mathbf{g}_n(t) \cos\left(\frac{p\pi n}{N}\right) dn. \quad (3.C.11)$$

Using Eqs. (3.C.4) and (3.C.5), we obtain from Eq. (3.C.11)

$$\langle \mathbf{h}_p(t) \rangle = 0 \quad (3.C.12)$$

$$\langle h_{p\alpha}(t) h_{q\beta}(t') \rangle = \frac{2kT}{\zeta} \delta_{pq} \delta_{\alpha\beta} \delta(t-t'). \quad (3.C.13)$$

Equation (3.C.10) in combination with Eqs. (3.C.12) and (3.C.13), which describes the motion of the normal coordinate $\mathbf{X}_p(t)$, can be represented by the general form of the Langevin equation given by Eq. (3.B.1) in combination with Eqs. (3.B.2) and (3.B.3). Thus, the solution of Eq. (3.B.1) given in Appendix 3.B can be readily used here. Since the random forces of different modes are independent of each other (Eq. (3.C.13)), the motions of the \mathbf{X}_p 's are also independent of each other. Thus,

$$\langle X_{p\alpha}(t) X_{q\beta}(0) \rangle = \delta_{\alpha\beta} \delta_{pq} \frac{N^2 b^2}{3\pi^2 p^2} \exp\left(-\frac{t}{\tau_p}\right) \quad (3.C.14)$$

where

$$\tau_p = \frac{\zeta N^2 b^2}{3kT \pi^2 p^2} = \frac{\tau_1}{p^2} \quad \text{for } p = 1, 2, \dots \quad (3.C.15)$$

Using Eq. (3.C.6), the end-to-end vector

$$\mathbf{R}(t) \equiv \mathbf{R}_N(t) - \mathbf{R}_0(t) \quad (3.C.16)$$

can be expressed in terms of the normal coordinates $\{\mathbf{X}_p\}$ as

$$\mathbf{R}(t) = -2 \left(\frac{2}{N} \right)^{1/2} \sum_{p=\text{odd}} \mathbf{X}_p(t). \quad (3.C.17)$$

Using Eqs. (3.C.14) and (3.C.17), the time-correlation function $\langle \mathbf{R}(t) \cdot \mathbf{R}(0) \rangle$ is then derived as

$$\begin{aligned} \langle \mathbf{R}(t) \cdot \mathbf{R}(0) \rangle &= \frac{8}{N} \sum_{p=\text{odd}} \langle \mathbf{X}_p(t) \cdot \mathbf{X}_p(0) \rangle \\ &= Nb^2 \sum_{p=\text{odd}} \frac{8}{\pi^2 p^2} \exp\left(-\frac{tp^2}{\tau_1}\right) \end{aligned} \quad (3.C.18)$$

which is identical to Eq. (3.60). In general, \mathbf{X}_p represents the motion of a domain which contains N/p segments of the chain and corresponds to the motion with the length scale of the order $(Nb^2/p)^{1/2}$.³³

Appendix 3.D — Binomial Random Walk

Here we consider a particle constrained to move along the x -axis by random step of length s and study its probability of being at a certain point after a large number of steps. This is a special case of the central limit theorem as studied in Chapter 1. At any step, being independent of any previous steps, the probability of the particle taking a step to the right is the same as that to the left. For the n th step, define the stochastic variable X_n as having the realization $x_n = s$ for a step to the right and $x_n = -s$ for a step to the left. Then the probability density for the n th step is expressed by

$$P_{X_n}(x_n) = \frac{1}{2}\delta(x_n - s) + \frac{1}{2}\delta(x_n + s). \quad (3.D.1)$$

After N steps, the net displacement of the particle (along the x -axis) is given by

$$Y_N = X_1 + X_2 + \cdots + X_N. \quad (3.D.2)$$

The probability function of the stochastic variable Y_N is then expressed by

$$P_N(y) = \int \cdots \int \delta(y - x_1 - x_2 \cdots - x_N) \times P_{X_1}(x_1)P_{X_2}(x_2) \cdots P_{X_N}(x_N)dx_1dx_2 \cdots dx_N. \quad (3.D.3)$$

And the characteristic function (Sec. 1.2) for the stochastic variable Y_N is given by

$$\begin{aligned} f_{Y,N}(k) &= \int_{-\infty}^{\infty} \exp(iky)P_N(y)dy \\ &= \int \cdots \int \int_{-\infty}^{\infty} \exp(iky)\delta(y - x_1 - x_2 \cdots - x_N) \\ &\quad \times P_{X_1}(x_1)P_{X_2}(x_2) \cdots P_{X_N}(x_N)dx_1dx_2 \cdots dx_Ndy \\ &= \prod_{n=1}^N \int_{-\infty}^{\infty} \exp(ikx_n)P_{X_n}(x_n)dx_n = \prod_{n=1}^N f_{X_n}(k) \end{aligned} \quad (3.D.4)$$

where

$$\begin{aligned} f_{X_n}(k) &= \int \exp(ikx_n) \left[\frac{1}{2}\delta(x_n - s) + \frac{1}{2}\delta(x_n + s) \right] dx_n \\ &= \frac{1}{2} \exp(iks) + \frac{1}{2} \exp(-iks) = \cos(ks). \end{aligned} \quad (3.D.5)$$

Substituting Eq. (3.D.5) into Eq. (3.D.4), we obtain

$$f_{Y,N}(k) = [\cos(ks)]^N = \left[1 - \frac{(ks)^2}{2} + \cdots \right]^N \approx 1 - \frac{N(ks)^2}{2}. \quad (3.D.6)$$

We can find a differential equation for the characteristic function in the limit of both the step size s and the time between steps, Δt , becoming infinitely small. Let

$$f_{Y,N}(k) = f_Y(k, N\Delta t), \quad (3.D.7)$$

in which $N\Delta t$ may be denoted by t representing the time at which the N th step of movement has just taken place. As initially (at $t = 0$ or $N = 0$) $y = 0$, we may write

$$P_0(y) = \delta(y) \quad (3.D.8)$$

and

$$f_Y(k, 0) = 1. \quad (3.D.9)$$

From Eq. (3.D.6), we obtain

$$\begin{aligned} & f_Y(k, (N+1)\Delta t) - f_Y(k, N\Delta t) \\ &= [\cos(ks) - 1]f_Y(k, N\Delta t) = \left(-\frac{k^2 s^2}{2} + \dots\right) f_Y(k, N\Delta t) \end{aligned} \quad (3.D.10)$$

which in turn leads to the limiting form:

$$\begin{aligned} & \lim_{N \rightarrow \infty} \lim_{\Delta t \rightarrow 0} \frac{f_Y(k, (N+1)\Delta t) - f_Y(k, N\Delta t)}{\Delta t} \\ &= \lim_{N \rightarrow \infty} \lim_{\Delta t \rightarrow 0} \lim_{s \rightarrow 0} \left(-\frac{k^2 s^2}{2\Delta t}\right) f_Y(k, N\Delta t) \end{aligned} \quad (3.D.11)$$

or

$$\frac{\partial f_Y(k, t)}{\partial t} = -k^2 D f_Y(k, t) \quad (3.D.12)$$

with

$$D = \lim_{N \rightarrow \infty} \lim_{\Delta t \rightarrow 0} \lim_{s \rightarrow 0} \frac{s^2}{2\Delta t}. \quad (3.D.13)$$

The solution of Eq. (3.D.12) with Eq. (3.D.9) as the initial condition is given by

$$f_Y(k, t) = \exp(-k^2 D t). \quad (3.D.14)$$

Application of the inverse Fourier transformation to Eq. (3.D.14) gives the probability distribution function for the particle to accumulate a net displacement y :

$$\begin{aligned} P(y, t) \left(= \lim_{N \rightarrow \infty} P_N(y) \right) &= \frac{1}{2\pi} \int_{-\infty}^{\infty} \exp(-iky) \exp(-k^2 D t) dk \\ &= \sqrt{\frac{1}{4\pi D t}} \exp\left(-\frac{y^2}{4 D t}\right) \end{aligned} \quad (3.D.15)$$

which being a Gaussian illustrates the central limit theorem studied in Chapter 1. Note that $P(y, t)$ is the solution of the diffusion equation (with

y replaced by x):

$$\frac{\partial P(x, t)}{\partial t} = D \frac{\partial^2 P(x, t)}{\partial x^2} \quad (3.D.16)$$

with $P(x, t = 0) = \delta(x)$ as the initial condition. Thus, Eq. (3.D.13) may be used to define the diffusion constant of a Brownian particle when both s and Δt are sufficiently small and N is large. In three-dimensional space, the diffusion constant may also be defined by Eq. (3.D.13) as the one-dimensional random movement discussed above takes place in the same way along each of the three axes of the Cartesian coordinate system.

References

1. Lin, Y.-H., and Wang, C. H., *J. Chem. Phys.* **70**, 681 (1979).
2. Fytas, G., Lin, Y.-H., and Chu, B., *J. Chem. Phys.* **74**, 3131 (1981).
3. Meier, G., and Fischer, E. W., in *Polymer Motion in Dense Systems* (eds. D. Richter and T. Springer), Springer-Verlag, Berlin (1987).
4. Slichter, C. P., *Principles of Magnetic Resonance*, Springer-Verlag, Berlin (1990).
5. Froix, M. F., Williams, D. J., and Goedde, A. O., *Macromolecules* **9**, 354 (1976).
6. Kremer, F. and Schönhals, A. (eds.), *Broadband Dielectric Spectroscopy*, Springer-Verlag, Berlin (2003).
7. Berne, B. J., and Pecora, R., *Dynamic Light Scattering*, Wiley, New York (1976).
8. Lin, Y.-H., and Wang, C. H., *J. Chem. Phys.* **66**, 5578 (1977).
9. Wang, C. H., and Lin, Y.-H., *J. Colloid Interface Sci.* **63**, 270 (1978).
10. Lin, Y.-H., Fyta, G., and Chu, B., *J. Chem. Phys.* **75**, 2091 (1981).
11. Lin, Y.-H., and Lai, C. S., *Macromolecules* **29**, 5200 (1996).
12. Ewen, B., and Richter, D., Neutron Spin Echo Investigations on the Segmental Dynamics of Polymers in Melts, Networks and Solutions, in *Adv. Polym. Sci.* **134**, 1 (1997).
13. Richter, D., Monkenbusch, M., Arbe, A., and J. Colmenero, Neutron Spin Echo in Polymer Systems, in *Adv. Polym. Sci.* **174**, 1 (2005).
14. Lin, Y.-H., and Huang, C.-F., *J. Chem. Phys.* **128**, 224903 (2008).
15. Doi, M., *J. Polym. Sci., Polym. Phys. Ed.* **18**, 1005 (1980).
16. Lin, Y.-H. *Macromolecules* **17**, 2846 (1984).
17. Lin, Y.-H. *Macromolecules* **19**, 159 (1986).
18. Lin, Y.-H. *Macromolecules* **19**, 168 (1986).
19. Lin, Y.-H. *Macromolecules* **20**, 885 (1987).
20. Lin, Y.-H., *J. Rheology* **29**, 605 (1985).
21. Lin, Y.-H., *J. Non-Newtonian Fluid Mech.* **23**, 163 (1987).
22. Bueche, F., *J. Chem. Phys.* **48**, 1410 (1968).

23. Mills, P. J., Green, P. F., Palmstrom, C. J., Mayer, J. W., and Kramer, E. J., *Appl. Phys. Lett.* **45**, 958 (1984).
24. Green, P. F., Palmstrom, C. J., Mayer, J. W., and Kramer, E. J., *Macromolecules* **18**, 501 (1985).
25. Antonietti, M., Coutandin, J., Grutter, R., and Sillescu, H., *Macromolecules*, **17**, 798 (1984).
26. Callaghan, P. T., *Principles of Nuclear Magnetic Resonance Microscopy*, Oxford Univ. Press (1991); Tirrel, M., *Rubber Chem. Technol.* **57**, 523 (1984); Lodge, T. P., Rotstein, N. A., and Prager, S., *Advances in Chemical Physics LXXIX* (eds. I. Prigogine and S. A. Rice), Wiley, New York (1990), and references therein.
27. Lin, Y.-H., *Macromolecules* **18**, 2779 (1985); **24**, 5346 (1991).
28. Rouse, P. E., Jr., *J. Chem. Phys.* **21**, 1272 (1953).
29. Einstein, A., *Ann. Phys.* **17**, 549 (1905); **19**, 371 (1906).
30. van Kampen, N. G., *Stochastic Processes in Physics and Chemistry*, North-Holland, Amsterdam (1981).
31. Lax, M., *Rev. Mod. Phys.*, **38**, 541 (1966); Zwanzig, R., *Adv. Chem. Phys.*, **15**, 325 (1969); Ermak, D. L., and McCammon, J. A., *J. Chem. Phys.* **69**, 1352 (1978); Yang, D.-J. and Lin, Y.-H., *Polymer* **44**, 2807 (2003).
32. Crank, J., *The Mathematics of Diffusion*, Oxford Univ. Press (1975).
33. Doi, M., and Edwards, S. F., *The Theory of Polymer Dynamics*. Oxford Univ. Press (1987).
34. Zimm, B. H., *J. Chem. Phys.* **24**, 269 (1956).
35. Batchelor, G. K., *An Introduction to Fluid Dynamics*, Cambridge Univ. Press (1970).
36. Bird, R. B., Curtiss, C. F., Armstrong, R. C., and Hassager, O., *Dynamics of Polymeric Liquids*, Vol. 2, (2nd edn) Wiley, New York (1987).
37. Flory, P. J., *J. Chem. Phys.* **17**, 303 (1949).
38. Flory, P. J., *Principles of Polymer Chemistry*, Cornell Univ. Press, Ithaca (1953).
39. de Gennes, P. G., *Scaling Concepts in Polymer Physics*, Cornell Univ. Press, Ithaca (1979).
40. Lin, Y.-H., and Luo, Z.-H., *J. Chem. Phys.* **112**, 7219 (2000).
41. King, T. A., Knox, A., and McAdam, J. D. G., *J. Polym. Sci. Polym. Symp.* **44**, 195 (1974).
42. Han, C. C., and Crackin, F. L., *Polymer* **20**, 427 (1979).
43. Nose, T., and Chu, B., *Macromolecules* **12**, 590 (1979).
44. Schmidt, M., and Burchard, W., *Macromolecules* **14**, 210 (1981).
45. Adachi, K., and Kotaka, T., *Macromolecules* **20**, 2018 (1987).
46. Lin, Y.-H., and Juang, J.-H., *Macromolecules* **32**, 181 (1999).
47. Vogel, H., *Phys. Z.* **22**, 645 (1921).
48. Fulcher, G. S., *J. Am. Soc.* **8**, 339 (1925); *J. Am. Chem. Soc.* **8**, 789 (1925).
49. Tammann, G., and Hesse, G., *Z. Anorg. Allg. Chem.* **156**, 245 (1926).
50. Williams, M. L., Landel, R. F., and Ferry, J. D., *J. Am. Chem. Soc.* **77**, 3701 (1955).
51. Ferry, J. D., *Viscoelastic Properties of Polymers* (3rd edn), Wiley, New York (1980).

Chapter 4

Linear Viscoelasticity

4.1 Introduction

In Chapter 2 we studied the theory of rubber elasticity, which explains the snap-back phenomenon of a rubber piece after being released from stretching. A polymeric liquid, which has not been cross-linked to form a macroscopic network, will eventually flow under a slow deformation. The slow flow property of the polymer is characterized by its viscosity. If a deformation is applied to a polymeric liquid for a time period that is too short for the molecular chain to reach a new equilibrium state, the polymer material will regain at least part of its shape or conformation upon the release of the deformation. Thus, the polymeric liquid possesses both the properties of viscosity and elasticity; in other words, the polymeric liquid is viscoelastic. Polymer viscoelastic behavior can be studied in terms of chain dynamics, of which the Rouse theory¹ discussed in Chapter 3 is a very important model. We shall study the molecular relaxation mechanisms in Chapters 6–9 and 12 under the title: Molecular Theory of Polymer Viscoelasticity. In Chapters 17 and 18, the viscoelastic behavior of the Fraenkel-chain model which does not have an analytical solution will be studied by means of Monte Carlo simulations. Here, we shall limit the study of polymer viscoelastic properties to the linear region and to the phenomenological description, namely, the generalized Maxwell equation² or Boltzmann’s superposition principle.³ The term “linear region” means that the applied strain (or instead the applied rate-of-strain) is in the small magnitude region where the linear relation between the stress and the strain (or rate-of-strain) holds.⁴ This chapter also shows that the generalized Maxwell equation and Boltzmann’s superposition principle are equivalent. In the linear region, the phenomenological theory is a well-tested basic principle for the kind of polymeric liquid considered in this book. In this chapter, the viscoelastic responses to several

often-used types of strain or rate-of-strain will be derived from the basic principle.

Stress and strain expressed in the tensorial forms, which are essential to the molecular rheological theories and simulations as studied in the later chapters, will be discussed in Chapter 5. For the phenomenological description in the linear region, it is sufficient to discuss the stress–strain relation in terms of scalar quantities.

4.2 Maxwell Equation

We begin by giving a simple explanation for the physical meaning of viscosity and elasticity. In Fig. 4.1, it is shown that a layer of simple liquid is sandwiched between two parallel plates of area A , and of distance d apart. If the upper plate under the application of a constant force f is moving at a constant speed v relative to the lower plate in the direction parallel to the plate surface, we can define the shear deformation rate by

$$\dot{\lambda} = \frac{v}{d} \quad (4.1)$$

and the stress by

$$\sigma = -\frac{f}{A}. \quad (4.2)$$

Then the viscosity of the liquid is defined by

$$\eta = -\frac{\sigma}{\dot{\lambda}}. \quad (4.3)$$

Here, the sign is chosen by defining σ as the stress exerted by the system to the external. If the viscosity value is independent of the shear rate, the liquid is called a Newtonian fluid. Liquids of small molecules in general belong to this category.

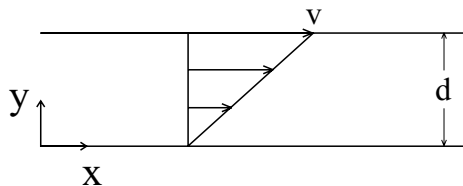


Fig. 4.1 Shear of a simple fluid sandwiched between two parallel plates, with a distance d apart; and the upper plate moving at a velocity v relative to the lower plate.

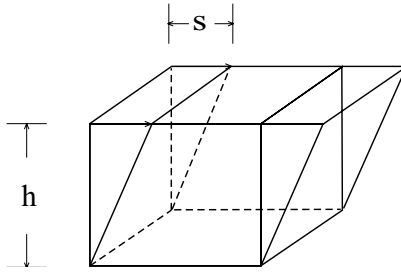


Fig. 4.2 Shear of a rectangular material block, with a height h ; and a displacement s of the upper surface relative to the lower one.

For elasticity, we consider a piece of solid material with top and bottom areas A and height h as shown in Fig. 4.2. If a constant shear force, f , is applied to the top and bottom surfaces, the relative position of the two surfaces can be displaced by a certain distance, s . Then the shear strain is defined by

$$\lambda = \frac{s}{h} \tag{4.4}$$

and the stress by

$$\sigma = -\frac{f}{A}. \tag{4.5}$$

According to the definition for a Hookean solid, the stress is linearly proportional to the strain

$$G = -\frac{\sigma}{\lambda} \tag{4.6}$$

where the proportional constant G is the modulus of the solid. Most metals and ceramics behave as Hookean solids under small deformations.

Mechanically, we may use a dashpot to represent the viscous property and a harmonic spring to represent the elastic property. In the Maxwell model, the dashpot and the spring are connected in series as shown in Fig. 4.3 to represent the viscoelastic nature of the system. When such a combination is shortened or elongated under a pushing or pulling force, the dashpot dissipates the energy while the spring stores the energy. We divide the total length of the system D into two parts: D_1 for the spring portion and D_2 for the dashport portion. Corresponding to Eq. (4.6), we write

$$G = -\frac{F}{(D_1 - D_o)} \tag{4.7}$$

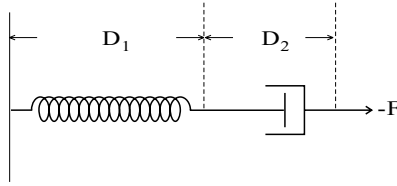


Fig. 4.3 Maxwell model as represented by a dashpot and a spring in series.

and corresponding to Eq. (4.3)

$$\eta = -\frac{F}{dD_2/dt} \quad (4.8)$$

where F is the tensile force on the system to counteract the force applied to elongate or to shorten the total length D of the system, and D_o is the length of D_1 at which the spring potential is at its minimum. Then from Eqs. (4.7) and (4.8), it follows that

$$\frac{dD}{dt} = \frac{d}{dt}(D_1 + D_2) = -\left[\frac{1}{G} \frac{dF}{dt} + \frac{F}{\eta}\right] \quad (4.9)$$

which can be rewritten as

$$F + \frac{\eta}{G} \frac{dF}{dt} = -\eta \frac{dD}{dt}. \quad (4.10)$$

For describing the viscoelastic behavior of a polymer material, we replace F by the stress σ and dD/dt by the rate-of-strain $\dot{\lambda}$; and corresponding to Eq. (4.10), we write

$$\frac{d\sigma}{dt} + \frac{\sigma}{\tau} = -\frac{\eta}{\tau} \dot{\lambda} \quad (4.11)$$

with

$$\tau = \frac{\eta}{G}. \quad (4.12)$$

Equation (4.11) is called the Maxwell equation; and τ , as given by Eq. (4.12), is the relaxation time of the viscoelastic system. The relaxation time plays an important role in determining whether the system behaves more as a Newtonian fluid or as a Hookean solid. If τ is very large and

$\tau(d\sigma/dt) \gg \sigma$, Eq. (4.11) can be approximated by

$$\tau \frac{d\sigma}{dt} = -\eta \dot{\lambda} \quad (4.13)$$

which, using Eq. (4.12), becomes the Hookean Eq. (4.6). On the other hand, if τ is small, and $\tau(d\sigma/dt) \ll \sigma$, Eq. (4.11) is approximated by the Newtonian fluid Eq. (4.3). Thus, the Maxwell Eq. (4.11) is expected to be capable of describing the viscoelastic behavior of a system which is between the two limits: the Newtonian fluid and the Hookean solid.

Equation (4.11) is an inhomogeneous first-order linear differential equation of $\sigma(t)$. By multiplying both sides of Eq. (4.11) by an integration factor $\exp(t/\tau)$, the Maxwell equation can be easily transformed into the integration form

$$\sigma(t) = - \int_{-\infty}^t G \exp\left(-\frac{(t-t')}{\tau}\right) \dot{\lambda}(t') dt' \quad (4.14)$$

which, using integration by parts, can be further transformed to

$$\sigma(t) = \int_{-\infty}^t \frac{G}{\tau} \exp\left(-\frac{(t-t')}{\tau}\right) \lambda(t, t') dt' \quad (4.15)$$

where

$$\lambda(t, t') = \int_t^{t'} \dot{\lambda}(t'') dt'' = \lambda(t') - \lambda(t). \quad (4.16)$$

In the above equation, the strain $\lambda(t, t')$ uses the time $t' = t$ as the reference point, i.e. $\lambda(t, t) = 0$; and $\lambda(t)$ may be defined with respect to any reference time.

Because of the large number of intramolecular degrees of freedom in a long-chain molecule, the polymer often contains many modes of motions with different relaxation times. We have seen the expression in terms of the normal modes for the time correlation function of the end-to-end vector, $\langle \mathbf{R}(t) \cdot \mathbf{R}(0) \rangle$, in Chapter 3. As a result, it is often necessary to take many relaxation times to adequately describe the viscoelastic behavior of a polymer system phenomenologically. The Maxwell equation may be generalized to contain a distribution of relaxation times. Mechanically, the generalization is equivalent to arranging many of the dashpot-spring combinations with different values of η and G together in parallel, as shown in Fig. 4.4. Corresponding to the arrangement of dashpots and springs in

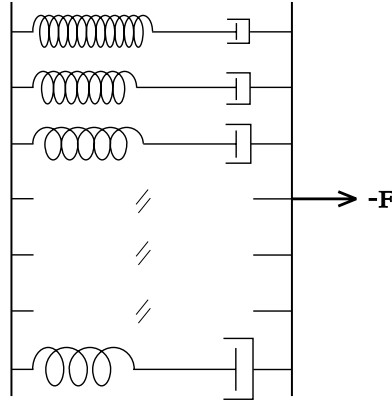


Fig. 4.4 Generalized Maxwell model as represented by multiple dashpot-spring combinations (Fig. 4.3) in parallel.

Fig. 4.4, the generalized Maxwell equation is given as

$$\sigma(t) = \sum_i \sigma_i(t) \quad (4.17)$$

with

$$\frac{d}{dt}\sigma_i(t) + \frac{1}{\tau_i}\sigma_i(t) = -\frac{\eta_i}{\tau_i}\dot{\lambda} \quad (4.18)$$

and

$$\tau_i = \frac{\eta_i}{G_i}. \quad (4.19)$$

Just as Eqs. (4.14) and (4.15) were obtained, Eqs. (4.17)–(4.19) can be written in the integration forms:

$$\sigma(t) = - \int_{-\infty}^t \sum_i G_i \exp\left[-\frac{(t-t')}{\tau_i}\right] \dot{\lambda}(t') dt' \quad (4.20)$$

and

$$\sigma(t) = \int_{-\infty}^t \sum_i \frac{G_i}{\tau_i} \exp\left[-\frac{(t-t')}{\tau_i}\right] \lambda(t, t') dt'. \quad (4.21)$$

The arrangement of dashpots-springs shown in Fig. 4.4 represents a phenomenological model. We may write Eqs. (4.20) and (4.21) in the

general forms:

$$\sigma(t) = - \int_{-\infty}^t G(t-t') \dot{\lambda}(t') dt' \quad (4.22)$$

and

$$\sigma(t) = \int_{-\infty}^t M(t-t') \lambda(t, t') dt' . \quad (4.23)$$

$G(t)$ is often referred to as the relaxation modulus and $M(t)$ as the memory function; they are related as

$$M(t) = - \frac{d}{dt} G(t) . \quad (4.24)$$

To build molecular models for obtaining the functional form of $G(t)$ and its relaxation times as a function of chain structure: molecular weight and chain branching is a very challenging research field, and has been actively pursued since the mid-1900s. Nevertheless, successful models for the linear polymer have been developed. In the later chapters, the Rouse theory for the entanglement-free region, the Doi–Edwards theory⁵ for the entanglement region and the extended reptation theory⁶ developed on the framework of the Doi–Edwards theory will be studied.

4.3 Boltzmann's Superposition Principle

Instead of using the generalized Maxwell picture, Eq. (4.22) can be obtained from a more formal argument, namely Boltzmann's superposition principle. It assumes that if the stress at the present time t is caused by a step strain at an earlier time t' , the stress is linearly proportional to the strain, and the proportionality (the modulus) decreases with the separation of the time, $t - t'$. The modulus, a decaying function of $t - t'$, is denoted by $G(t - t')$. Consider a system which has been inflicted by small step strains at different times, t_1, t_2, \dots before the present time t . According to Boltzmann's superposition principle, all the stresses as individually caused by these small step strains are *independent* of each other. As a result, the total stress at t is simply the sum of these stresses.

$$\sigma(t) = - \sum_i G(t - t_i) \Delta \lambda(t_i) \quad (4.25)$$

where $\Delta\lambda(t_i)$ represents the small step strain applied at $t_i < t$. We can regard any strain history before t as a sum of small strain changes, each of which has occurred within very short intervals. Thus, Eq. (4.25) can be rewritten as

$$\sigma(t) = - \sum_{t'} G(t-t') \frac{\Delta\lambda(t')}{\Delta t'} \Delta t'. \quad (4.26)$$

In the limit of $\Delta t' \rightarrow 0$, Eq. (4.26) can be written in the integration form identical to Eq. (4.22).

We have used the generalized phenomenological Maxwell model or Boltzmann's superposition principle to obtain the basic equation (Eq. (4.22) or (4.23)) for describing linear viscoelastic behavior. For the kind of polymeric liquid studied in this book, this basic equation has been well tested by experimental measurements of viscoelastic responses to different rate-of-strain histories in the linear region. There are several types of rate-of-strain functions $\dot{\lambda}(t)$ which have often been used to evaluate the viscoelastic properties of the polymer. These different viscoelastic quantities, obtained from different kinds of measurements, are related through the relaxation modulus $G(t)$. In the following sections, we shall show how these different viscoelastic quantities are expressed in terms of $G(t)$ by using Eq. (4.22).

4.4 Relaxation Modulus

The simplest viscoelastic response is the direct measurement of $G(t)$ itself. This measurement is done by monitoring the relaxation of the stress induced by the application of a step strain at some initial time, $t = 0$. As shown in Fig. 4.5, we let the applied strain reach a constant value λ_0 in a very short period of time ϵ . A perfect step strain is made when $\epsilon \rightarrow 0$. We further assume that the strain being applied within the period ϵ changes with time linearly. That is, the rate-of-strain is the constant, $\dot{\lambda} = \lambda_0/\epsilon$, from $t = -\epsilon$ to $t = 0$, and is zero before $t = -\epsilon$ and after $t = 0$. Then Eq. (4.22) can be written as

$$\sigma(t) = \lim_{\epsilon \rightarrow 0} \left[-\frac{\lambda_0}{\epsilon} \int_{-\epsilon}^0 G(t-t') dt' \right]. \quad (4.27)$$

By applying the L'hospital rule or the property of the Dirac delta function (see Appendix 1.A) to Eq. (4.27)

$$\sigma(t) = -\lambda_0 G(t). \quad (4.28)$$

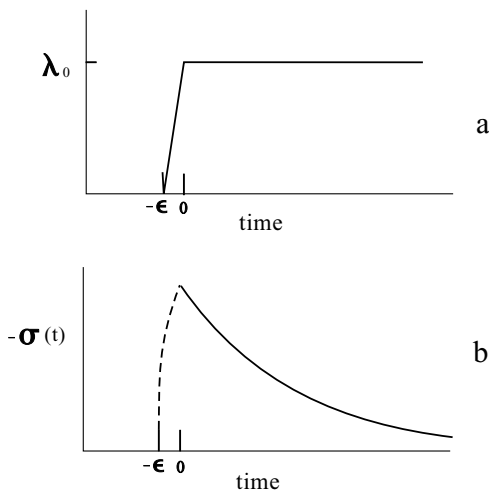


Fig. 4.5 Step-strain stress relaxation experiment: (a) a constant strain λ_0 is applied at time $t = 0$ ($\epsilon \rightarrow 0$) and maintained for all times $t > 0$; (b) the stress relaxation $\sigma(t)$ responding to the applied step strain.

Thus, $G(t) = -\sigma(t)/\lambda_0$. This result is expected from the definition of $G(t)$ as used in Boltzmann's superposition principle. The way in which $G(t)$ is obtained from Eq. (4.27) also illustrates an experimental problem encountered in the measurement of $G(t)$. Experimentally the application of a strain involves the movement of a mechanical device, often a motor, which has a rate limit. Thus, ϵ cannot be infinitely small experimentally. At $\lambda_0 \sim 0.1$, the order of 0.05 s for ϵ is basically the state of the art. How an experiment is affected by a finite ϵ is a relative matter. If the relaxation times of $G(t)$, which are the interest of study, are sufficiently larger than ϵ , errors caused by the finite ϵ are negligible.

Shown in Fig. 4.6 are the curves of relaxation modulus, $G(t)$, of a series of nearly monodisperse polystyrene samples of different molecular weights. The higher the molecular weight, the slower the relaxation rate. In these measurements, the step deformation rise time is 0.04 s, which is much shorter than the relaxation times of interest in these curves. The most noteworthy is the appearance of a modulus plateau when the molecular weight is sufficiently large. As will be discussed in the later chapters, the entanglement molecular weight M_e can be calculated from the plateau modulus G_N . The analyses of these relaxation modulus curves in terms of the extended reptation theory developed in Chapter 9 will be detailed

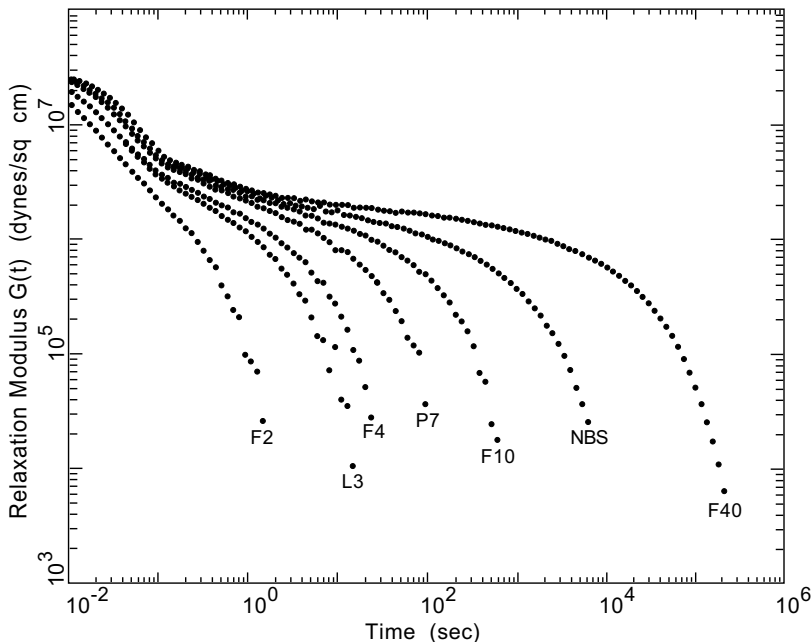


Fig. 4.6 Relaxation modulus for nearly monodisperse polystyrene melts. Molecular weight ranges from $M_w = 1.67 \times 10^4$ (F2) to $M_w = 4.22 \times 10^5$ (F40). Reproduced from Ref. 6(b).

in Chapter 10. With $\varepsilon \approx 0.04$ sec, the $G(t)$ curves shown in Fig. 4.6 are quantitatively accurate in the region $t > 0.2$ s, as indicated by comparing results obtained using transducers with different stiffness (see Fig. 1 of Ref. 6(b)); and confirmed by comparisons with the measured viscoelastic spectra of the same samples (see Chapter 10 for details).

4.5 Steady-State Shear Flow

The stress as defined by Eq. (4.3) corresponds to the stress arising from a shear rate which has been maintained at a constant value $\dot{\lambda}_0$ for a long time. Thus, from Eq. (4.22) we obtain the steady-state shear stress as

$$\begin{aligned} \sigma(t) &= -\dot{\lambda}_0 \int_{-\infty}^t G(t-t') dt' \\ &= -\dot{\lambda}_0 \int_0^{\infty} G(s) ds. \end{aligned} \quad (4.29)$$

From the comparison of Eqs. (4.3) and (4.29), the viscosity is related to $G(t)$ as

$$\eta = \eta_0 = \int_0^{\infty} G(t) dt. \quad (4.30)$$

In the linear region, the viscosity is independent of the rate-of-strain and has a constant value, and is often referred to as the zero-shear-rate viscosity or zero-shear viscosity and denoted by η_0 .

Shown in Fig. 4.7 are the zero-shear viscosities of various nearly monodisperse polymers as a function of molecular weight.⁷ They all show two regions with distinct molecular-weight dependences, separated by a rather sharp point, the critical molecular weight M_c . Above M_c the molecular-weight dependence follows the well-known 3.4 power law; below M_c the relation of $\log(\eta_0)$ to $\log(M_w)$ (corrected for the molecular-weight dependence of the glass transition temperature) has a slope of one. The explanation of this universal phenomenon by the extended reptation theory will be given in Chapter 10.

Since the viscosity is the integration of $G(t)$ (Eq. (4.30)), the relaxation modulus $G(t)$ should contain more detailed information than the single viscosity value η_0 . A wrong conclusion can be made if the conclusion is simply based on the viscosity result. On the basis of the viscosity data (Fig. 4.7), the onset of entanglement was traditionally believed to occur at $M_c \approx 2.4M_e$.⁷⁻⁹ Shown in Chapters 10 and 11, detailed studies of the viscoelastic spectra in terms of the extended reptation theory as well as the Rouse theory have indicated that the onset occurs at M_e .

4.6 Dynamic-Mechanical Spectroscopy

Rich and reliable viscoelastic data can be obtained from measuring the dynamic mechanical response of the polymeric liquid to a rate-of-strain $\dot{\lambda}(t)$ which is harmonically oscillatory:

$$\dot{\lambda}(t) = \dot{\lambda}^0 \cos(\omega t). \quad (4.31)$$

The result expressed as a function of the oscillatory frequency ω is often referred to as the viscoelastic spectrum. Because the polymeric liquid has both the viscous and elastic properties, the time dependence of the induced stress will not be totally either in phase or out of phase with the oscillatory rate-of-strain. Substituting Eq. (4.31) into Eq. (4.22), we obtain the stress

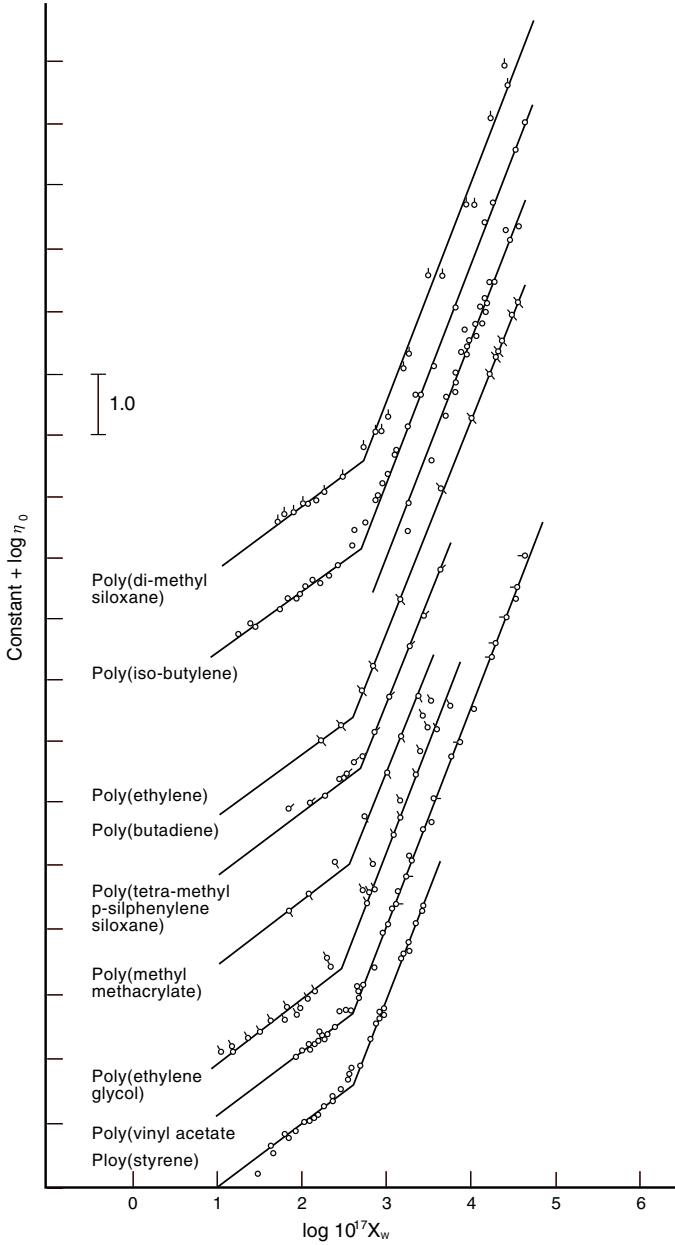


Fig. 4.7 Steady-state viscosity of various polymers in melt, where X_w is a parameter proportional to M_w . The curves are shifted vertically so as not to overlap each other. Reproduced, with permission, from Ref. 7.

response as

$$\sigma(t) = -\dot{\lambda}^0 \int_{-\infty}^t G(t-t') \cos(\omega t') dt'. \quad (4.32)$$

With the substitution of $s = t - t'$, Eq. (4.32) is rewritten as

$$\begin{aligned} \sigma(t) &= -\dot{\lambda}^0 \int_0^\infty G(s) \cos[\omega(t-s)] ds \\ &= -\eta'(\omega) \dot{\lambda}^0 \cos(\omega t) - \eta''(\omega) \dot{\lambda}^0 \sin(\omega t) \end{aligned} \quad (4.33)$$

where

$$\eta'(\omega) = \int_0^\infty G(s) \cos(\omega s) ds \quad (4.34)$$

and

$$\eta''(\omega) = \int_0^\infty G(s) \sin(\omega s) ds. \quad (4.35)$$

When ω approaches zero, Eq. (4.34) reduces to Eq. (4.30), i.e.

$$\eta'(\omega \rightarrow 0) = \int_0^\infty G(s) ds = \eta_0. \quad (4.36)$$

Using Eqs. (4.34) and (4.35), we define the complex viscosity $\eta^*(\omega)$ as

$$\eta^*(\omega) = \eta'(\omega) - i\eta''(\omega) = \int_0^\infty G(s) \exp(-i\omega s) ds. \quad (4.37)$$

As shown in Fig. 4.8, $\dot{\lambda}(t)$ (Eq. (4.31)) and $\sigma(t)$ (Eq. (4.33)), both being sinusoidal, have a phase-angle difference. We can express these two quantities, respectively, as

$$\dot{\lambda}(t) = \text{Re}[\dot{\lambda}^0 \exp(i\omega t)] \quad (4.38)$$

$$\sigma(t) = \text{Re}[\sigma^0 \exp(i\omega t)] \quad (4.39)$$

where Re indicates taking the real part of the complex variable in [...]. With Eq. (4.31) as the form for $\dot{\lambda}(t)$, $\dot{\lambda}^0$ in Eq. (4.38) is a real number. In contrast to $\dot{\lambda}^0$ being real, σ^0 in Eq. (4.39) is a complex number for a viscoelastic material. The relation between σ^0 and $\dot{\lambda}^0$ can be obtained by the following:

Given the definition of Eq. (4.37) for $\eta^*(\omega)$, Eq. (4.33) is equivalent to

$$\sigma(t) = -\text{Re}[\eta^*(\omega) \dot{\lambda}^0 \exp(i\omega t)]. \quad (4.40)$$

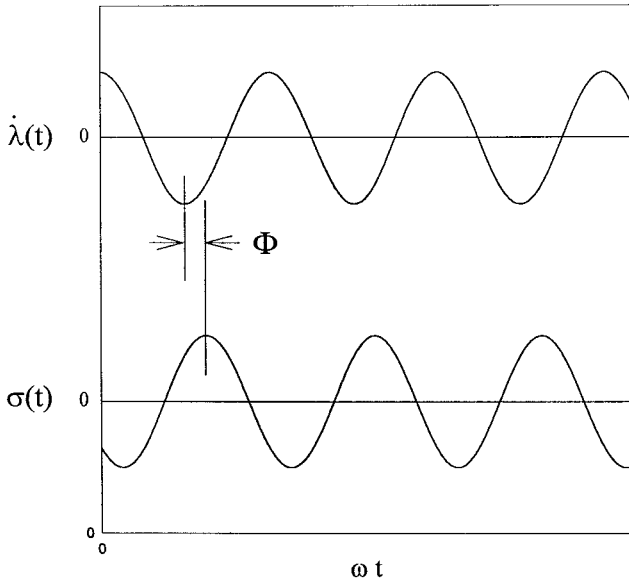


Fig. 4.8 The oscillatory rate-of-strain $\dot{\lambda}(t)$ and stress $\sigma(t)$ with a phase difference Φ for a viscoelastic fluid.

Comparison of Eqs. (4.39) and (4.40) gives

$$\sigma^0 = -\eta^*(\omega)\dot{\lambda}^0. \quad (4.41)$$

In terms of the complex viscosity η^* , the phase difference between the stress and the rate-of-strain can be expressed. Generally the stress induced by the rate-of-strain given by Eq. (4.31) can be written as

$$\sigma(t) = -A \cos(\omega t - \Phi) \quad (4.42)$$

where A is the amplitude of the stress and Φ is the phase angle. Equation (4.42) may be rewritten as

$$\sigma(t) = -A \cos \Phi \cos(\omega t) - A \sin \Phi \sin(\omega t). \quad (4.43)$$

From the comparison of Eqs. (4.33) and (4.43),

$$A \cos \Phi = \eta' \dot{\lambda}^0 \quad (4.44)$$

$$A \sin \Phi = \eta'' \dot{\lambda}^0. \quad (4.45)$$

Thus, η' represents the viscous contribution to the stress, i.e. the component in phase ($\Phi = 0$) with the rate-of-strain, and is related to the

dissipation of energy. And, η'' represents the elastic contribution to the stress, i.e. the component out of phase ($\Phi = \pi/2$) with the rate-of-strain, and is related to the storage of energy. The combination of Eqs. (4.44) and (4.45) can be expressed as

$$A = \sqrt{\eta'^2 + \eta''^2} \dot{\lambda}^0 \quad (4.46)$$

$$\Phi = \tan^{-1} \left[\frac{\eta''}{\eta'} \right]. \quad (4.47)$$

Thus, it is clear that $\eta'(\omega)$ and $\eta''(\omega)$ contain the same information as the oscillation amplitude A of the stress and the phase shift Φ at the frequency ω .

Another often-used viscoelastic response function, the complex modulus, is defined by

$$G^*(\omega) = i\omega\eta^*(\omega) = G'(\omega) + iG''(\omega) \quad (4.48)$$

where $G'(\omega)$ is called the storage modulus

$$G'(\omega) = \omega\eta'(\omega) = \omega \int_0^\infty G(s) \sin(\omega s) ds \quad (4.49)$$

and $G''(\omega)$ the loss modulus

$$G''(\omega) = \omega\eta''(\omega) = \omega \int_0^\infty G(s) \cos(\omega s) ds. \quad (4.50)$$

The ratio of G'' to G' is often referred to as the loss tangent

$$\tan \delta = \frac{G''}{G'} = \frac{\eta''}{\eta'}. \quad (4.51)$$

The measured G' and G'' (or equivalently η' and η'') values, as a function of the frequency ω , can be displayed as a spectrum — the viscoelastic spectrum. Figures 4.9 and 4.10 show the storage modulus spectra $G'(\omega)$ and the loss modulus spectra $G''(\omega)$, respectively, of a series of nearly monodisperse polystyrene samples.¹⁰

4.7 Steady-State Compliance

The scheme for carrying out the measurement of the steady-state compliance is shown in Fig. 4.11. Before $t = 0$, the polymeric liquid is in the equilibrium state. At $t = 0$, a constant shear stress σ_0 is abruptly applied to the fluid (Fig. 4.11(a)). In response, a strain change $\lambda(t)$ on the fluid

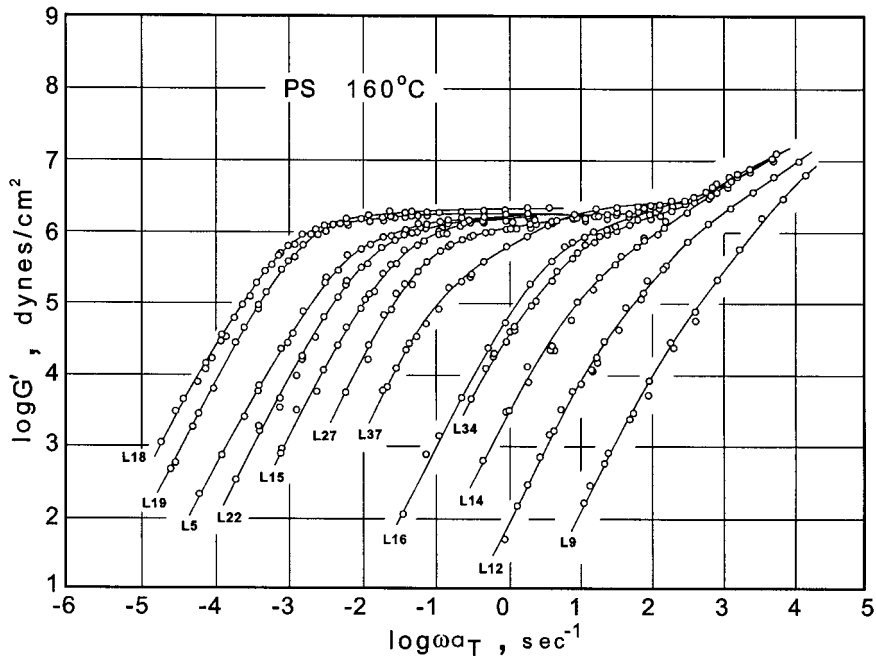


Fig. 4.9 Storage modulus vs. frequency for nearly monodisperse polystyrene melts. Molecular weight ranges from $M_w = 8.9 \times 10^3$ (L9) to $M_w = 5.8 \times 10^5$ (L18). Reproduced, with permission, from Ref. 10.

(Fig. 4.11(b)) is produced, which is in general measured with respect to $t = 0_-$ as the reference time — i.e. $\lambda(0_-) = 0$. After a sufficiently long time, the deformation of the fluid reaches a steady state; namely, the deformation proceeds with a constant rate-of-strain, $\dot{\lambda}_\infty$. The strain value λ_0 , obtained by extrapolating the strain in the steady-state region to the time $t = 0$, is a viscoelastic quantity of special meaning. We define the steady-state compliance J_e^0 as the ratio of λ_0 to the applied constant stress σ_0 :

$$J_e^0 = -\frac{\lambda_0}{\sigma_0}. \quad (4.52)$$

Such an experiment to obtain J_e^0 is often called the creep measurement. The relation of the steady-state compliance to the relaxation modulus $G(t)$ will be obtained as follows.

In the steady-state region, the total strain at time t can be written as

$$\lambda(t) = \lambda_0 + \dot{\lambda}_\infty t \quad (4.53)$$

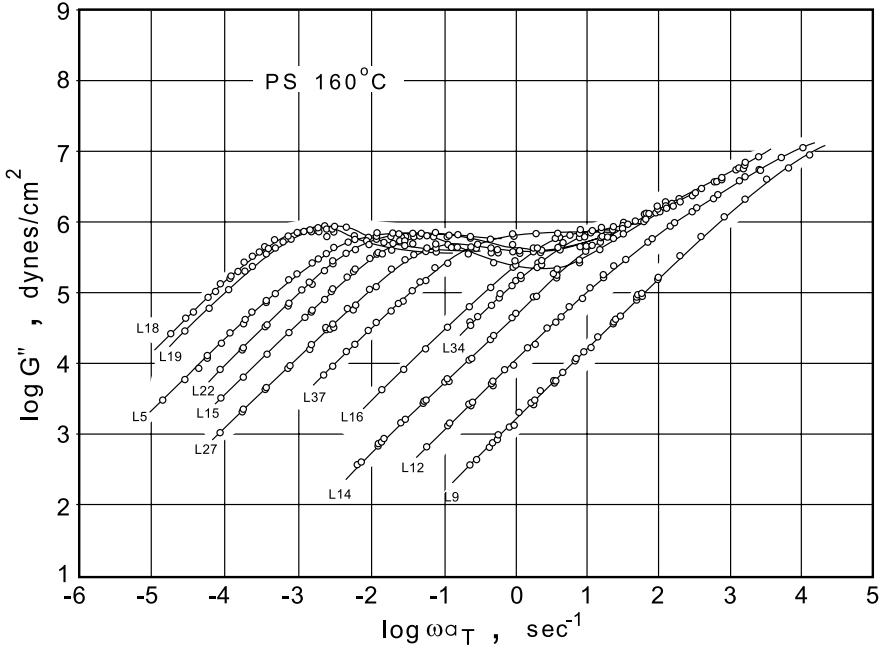


Fig. 4.10 Same as Fig. 4.9 for loss modulus.

Thus

$$\lambda_0 = \int_0^\infty (\dot{\lambda}(t') - \dot{\lambda}_\infty) dt' \tag{4.54}$$

where $\dot{\lambda}(t')$ is the actual rate-of-strain at any moment in time after $t = 0$. We can relate the stress in the steady-state region to the rate-of-strain by using Eq. (4.22) in two different ways. One is based on the viewpoint of a creep measurement:

$$\sigma_0 = - \int_0^t G(t-t') \dot{\lambda}(t') dt'. \tag{4.55}$$

The other is based on the viewpoint of the steady-shear flow:

$$\sigma_0 = - \int_{-\infty}^t G(t-t') \dot{\lambda}_\infty dt' \tag{4.56}$$

where the lower limit of the integration is $-\infty$, because reaching the steady-state region requires time that lasts longer than the longest relaxation time

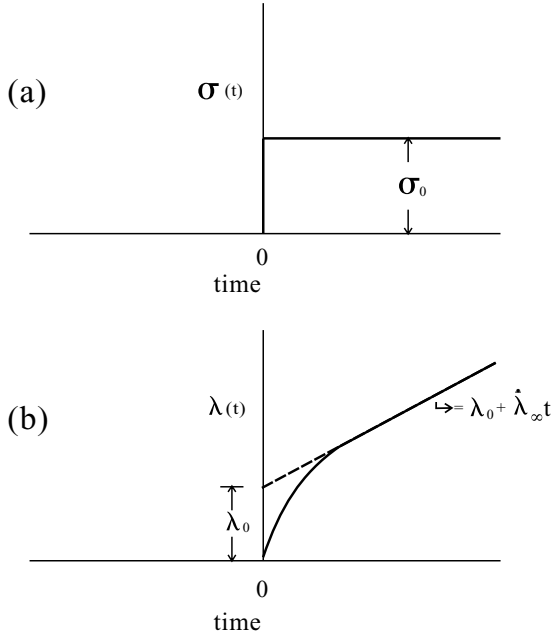


Fig. 4.11 Creep experiment: (a) a constant stress σ_0 is applied at time $t = 0$ and maintained for all times $t > 0$; (b) the strain measured relative to $t = 0$ increases with time. The dashed line is extrapolated from the strain in the steady-state region, whose intersection with the vertical axis at $t = 0$ gives λ_0 .

of the polymeric liquid, and waiting for such a long time is, in effect, equivalent to regarding the shear history as infinitely long.

Combining Eqs. (4.55) and (4.56), we have

$$\dot{\lambda}_\infty \int_{-\infty}^t G(t-t') dt' = \int_0^t G(t-t') \dot{\lambda}(t') dt'. \quad (4.57)$$

With the substitution of $s = t - t'$, Eq. (4.57) becomes

$$\dot{\lambda}_\infty \int_0^\infty G(s) ds = \int_0^t G(s) \dot{\lambda}(t-s) ds \quad (4.58)$$

which can be further rewritten as

$$\dot{\lambda}_\infty \int_t^\infty G(s) ds = \int_0^t G(s) [\dot{\lambda}(t-s) - \dot{\lambda}_\infty] ds. \quad (4.59)$$

By applying the integration over t , $\int_0^\infty \dots dt$, to both sides of Eq. (4.59) and exchanging the order of the double integrations, we obtain

$$\dot{\lambda}_\infty \int_0^\infty \left(\int_0^s dt \right) G(s) ds = \int_0^\infty G(s) \left(\int_s^\infty [\dot{\lambda}(t-s) - \dot{\lambda}_\infty] dt \right) ds. \quad (4.60)$$

By substituting $z = t - s$ and Eq. (4.54) into the right side of Eq. (4.60), we obtain

$$\begin{aligned} \dot{\lambda}_\infty \int_0^\infty s G(s) ds &= \int_0^\infty G(s) \int_0^\infty [\dot{\lambda}(z) - \dot{\lambda}_\infty] dz ds \\ &= \lambda_0 \int_0^\infty G(s) ds \\ &= \lambda_0 \eta_0. \end{aligned} \quad (4.61)$$

In the steady-state region

$$\sigma_0 = -\eta_0 \dot{\lambda}_\infty. \quad (4.62)$$

Using Eqs. (4.61) and (4.62), the steady-state recoverable compliance (Eq. (4.52)) becomes

$$J_e^0 = \frac{\int_0^\infty t G(t) dt}{\eta_0^2} = \frac{\int_0^\infty t G(t) dt}{\left(\int_0^\infty G(t) dt \right)^2}. \quad (4.63)$$

The factor t in the integrand of the numerator in Eq. (4.63) makes the steady-state compliance value very sensitive to the long-time region of the relaxation modulus, $G(t)$. As a result, the steady-state recoverable compliance of a polymeric liquid can be increased greatly by modifying its molecular-weight distribution with the addition of small amounts of high-molecular-weight polymers.

Shown in Fig. 4.12 are the data of steady-state compliance J_e^0 of nearly monodisperse polystyrene samples obtained by different laboratories.¹¹ Similar to the case with zero-shear viscosity, J_e^0 shows two regions with drastically different molecular-weight dependences, separated by a transition point M'_c . Above M'_c , J_e^0 is basically independent of molecular weight, and the data points fluctuate mainly because J_e^0 is very sensitive to the small variations among the molecular-weight distributions, even though all nearly monodisperse, of the studied samples. Below M'_c , the relation of $\log(J_e^0)$ to $\log(M_w)$ has an apparent slope of one. The explanation for the

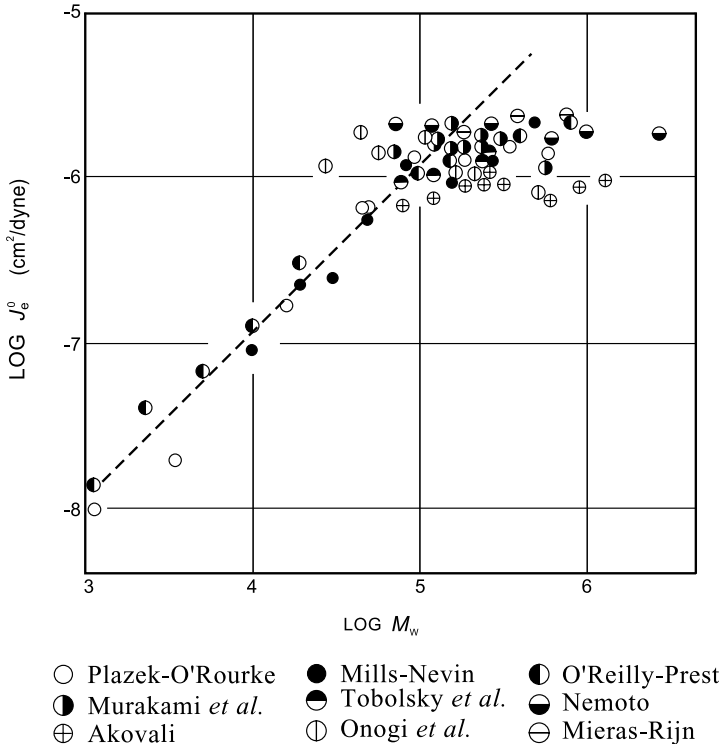


Fig. 4.12 Steady-state compliance J_e^0 of nearly monodisperse polystyrene melts at 160°C. The dashed line represents the result of the Rouse model. Reproduced, with permission, from Ref. 11.

molecular dependence of J_e^0 by the extended reptation theory will be given in Chapter 10; the apparent agreement with the Rouse model shown in Fig. 4.12 is a coincidence.

If we assume that the relaxation modulus has a certain distribution $\{A_i\}$ of relaxation times $\{\tau_i\}$, i.e.

$$\frac{G(t)}{G(0)} = \sum_i A_i \exp\left(-\frac{t}{\tau_i}\right) \quad (4.64)$$

it is easy to show from Eqs. (4.30) and (4.63) that

$$\eta_0 = G(0) \sum_i A_i \tau_i = G(0) \langle \tau \rangle \quad (4.65)$$

and

$$J_e^0 = \frac{G(0) \sum_i A_i \tau_i^2}{(G(0) \sum_i A_i \tau_i)^2} = \frac{1}{G(0)} \frac{\langle \tau^2 \rangle}{\langle \tau \rangle^2}. \quad (4.66)$$

Because zero-shear viscosity is related to the first moment of the relaxation-time distribution $\langle \tau \rangle$, while steady-state compliance is related to the second moment of the distribution $\langle \tau^2 \rangle$, the latter is much more sensitive to the molecular-weight distribution of the polymer sample than the former.

4.8 Creep Compliance

Following the application of a step stress σ_0 at $t = 0$ as shown in Fig. 4.11, the total strain $\lambda(t)$ can be measured to yield the creep compliance $J(t)$ defined as

$$J(t) = -\frac{\int_0^t \dot{\lambda}(t') dt'}{\sigma_0} = -\frac{\lambda(t)}{\sigma_0}. \quad (4.67)$$

The two viscoelastic response functions $J(t)$ and $G(t)$ are related to each other as shown in the following:

Using integration by parts, from Eq. (4.55) we obtain

$$\sigma_0 = -G(0)\lambda(t) + \int_0^t \left[\frac{\partial}{\partial t'} G(t-t') \right] \lambda(t') dt'. \quad (4.68)$$

Setting $t = 0$ in the equation obtained by substituting Eq. (4.67) into Eq. (4.68), we obtained the relation between the initial relaxation modulus and creep compliance:

$$G(0)J(0) = 1. \quad (4.69)$$

Applying the integration $\int_0^{t_f} dt$ on both sides of Eq. (4.68), we obtain

$$\sigma_0 t_f = -G(0) \int_0^{t_f} \lambda(t) dt + A \quad (4.70)$$

with

$$\begin{aligned} A &= \int_0^{t_f} \int_0^t \left[\frac{\partial}{\partial t'} G(t-t') \right] \lambda(t') dt' dt \\ &= \int_0^{t_f} \int_{t'}^{t_f} \left[\frac{\partial}{\partial t'} G(t-t') \right] \lambda(t') dt dt' \end{aligned} \quad (4.71)$$

as the order of integration is reversed. With $\tau = t - t'$, Eq. (4.71) is further expressed as

$$\begin{aligned} A &= - \int_0^{t_f} \int_0^{t_f-t'} \left[\frac{\partial}{\partial \tau} G(\tau) \right] \lambda(t') d\tau dt' \\ &= - \int_0^{t_f} G(t_f - t') \lambda(t') dt' + G(0) \int_0^{t_f} \lambda(t') dt'. \end{aligned} \quad (4.72)$$

Substituting Eq. (4.72) into Eq. (4.70) and using Eq. (4.67), we obtain

$$\int_0^t G(t-t') J(t') dt' = t. \quad (4.73)$$

It can be shown by applying the Laplace transformation that Eq. (4.73) is equivalent to:

$$\int_0^t J(t-t') G(t') dt' = t. \quad (4.74)$$

The convolution integral Eq. (4.73) may be solved numerically by the method of Hopkins and Hamming.¹²⁻¹⁵ The method is discussed in Appendix 4.A. Shown in Fig. 4.13 is the comparison of the $G(t)$ and $J(t)^{-1}$ curves of a nearly monodisperse polystyrene melt with $M_w = 4.69 \times 10^4$ obtained at 114.5°C (detailed in Chapter 14). The $G(t)$ line shape has more features — meaning different processes are better separated or resolved — than the $J(t)^{-1}$ curve, which are smeared by the conversion of $G(t)$ into $J(t)$ through Eq. (4.73) (see Sec. 14.3.c for details). The corresponding $G'(\omega)$ and $G''(\omega)$ spectra are shown in Fig. 4.14 (see Appendix 14.A for details).¹⁶ Also shown in Fig. 4.13 is the storage modulus spectrum $G'(\omega)$ plotted as a function of inverted frequency multiplied by 0.7 — namely $(0.7/\omega) \rightarrow t$. Because of the shown agreement between $G(t)$ and the so-inverted $G'(\omega)$ in line shape, $G'(\omega)$ is in general regarded as a near mirror image of $G(t)$. Over the short-time region (Fig. 4.13), the large-modulus values in $G(t)$ correspond to the small-compliance values in $J(t)$; the initial reciprocal relation between the two is indicated by Eq. (4.69). The dynamics in $G(t)$ over the high-modulus region ($> \sim 5 \times 10^7$ dynes/cm²) is often referred to as the glassy relaxation. The glassy-relaxation region, included in the ranges of these curves (or spectra), is absent from those shown in Figs. 4.6, 4.9 and 4.10, which cover only the entropic region. The molecular viscoelastic theories which are developed using the Rouse segment as the most basic structural unit

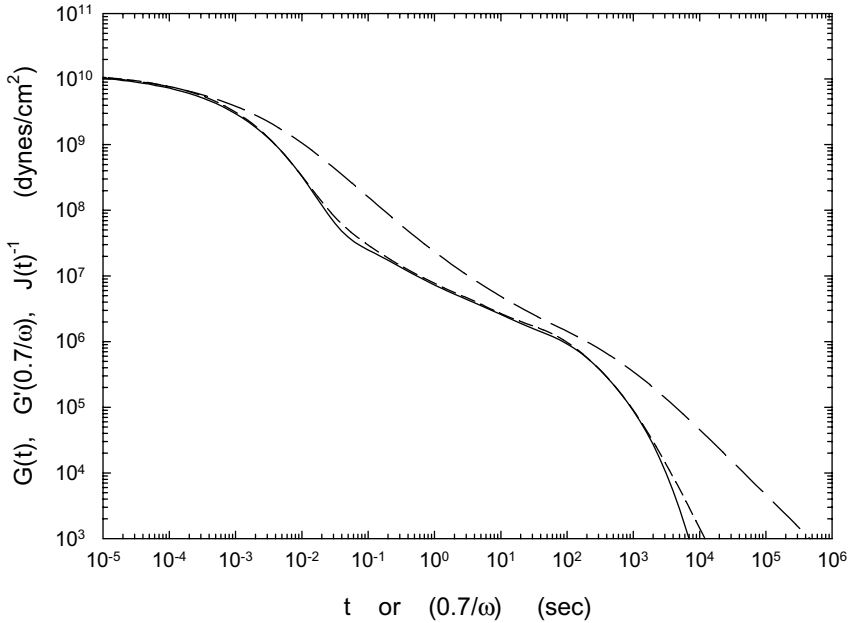


Fig. 4.13 Comparison of $G(t)$ (solid line), $J(t)^{-1}$ (long-dash line) and $G'(0.7/\omega)$ (short-dash line) of a nearly monodisperse polystyrene sample ($M_w = 4.69 \times 10^4$; at 114.5°C).

as studied in Chapters 6–9 are only applicable to the entropic region ($< \sim 5 \times 10^7$ dynes/cm²), which is also the range covered by most experimental studies. Measurements of $G(t)$ over the very high-modulus region or $J(t)$ over the very small-compliance region impose special technical requirements on the instrument. As shown in detail in Chapter 14, the dynamic and structural information contained in the high-modulus or small-compliance region is important to the understanding of the glass transition in polymer melts.

In summary, if $G(t)$, which is contained in Eqs. (4.30), (4.34)–(4.37), (4.49)–(4.51), (4.63) and (4.73), is known, all the linear viscoelastic quantities can be calculated. In other words, all the various viscoelastic properties of the polymer are related to each other through the relaxation modulus $G(t)$. This result is of course the consequence of the generalized Maxwell equation or equivalently Boltzmann’s superposition principle. The experimental results of linear viscoelastic properties of various polymers support the phenomenological principle.^{6,8} Some viscoelastic properties play more important roles than the others in certain rheological processes related to

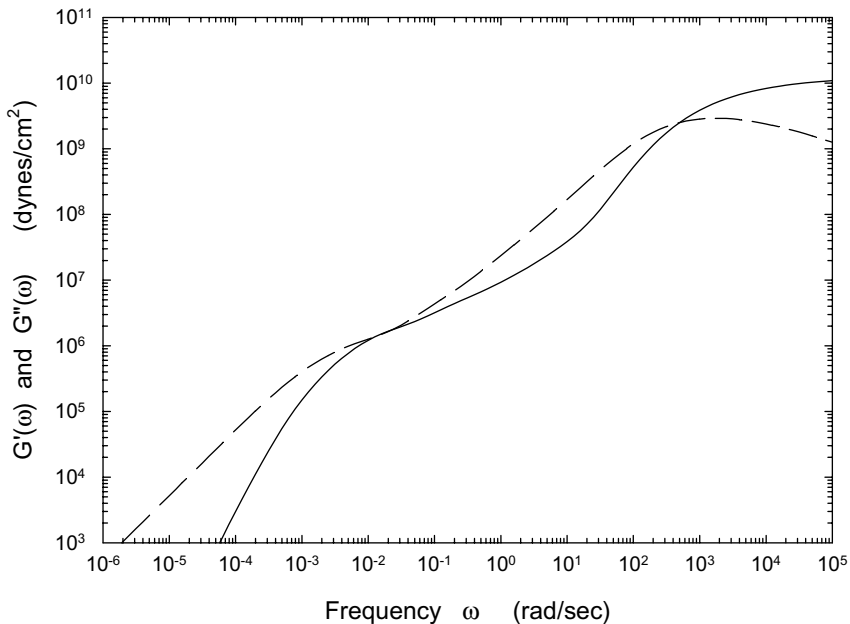


Fig. 4.14 The storage and loss modulus spectra, $G'(\omega)$ (solid line) and $G''(\omega)$ (dashed line), corresponding to the $G(t)$ and $J(t)$ curves shown in Fig. 4.13.

polymer processing. Thus, in practical applications, it is more convenient to measure them directly. In a nonlinear rheological process, the linear viscoelastic relations as discussed in this chapter are no longer applicable.

An important aspect of linear viscoelastic properties, particularly the response functions $G(t)$, $G^*(\omega)$ and $J(t)$, is their close relations to the molecular structure of the polymer, such as molecular weight, molecular-weight distribution, and chain branching. For linear polymers, the molecular theories developed so far have been very successful in explaining the relations, as studied in Chapters 7–11 and 14. Linear viscoelastic behavior is also much affected by the rigidity on the segments of which the polymer chain consists as studied in Chapters 16 and 17 by Monte Carlo simulations. On the other hand, linear viscoelastic behavior must gradually merge into nonlinear behavior as the strain or rate-of-strain increases. Thus, the understanding of linear viscoelastic behavior enlightens the study of the more complicated nonlinear viscoelastic behavior. The major chain dynamic processes that affect nonlinear viscoelastic behavior, and their relations with

the dynamic processes responsible for linear viscoelastic behavior, will be studied in Chapters 12 and 18.

Appendix 4.A — The Hopkins–Hamming Method for the Conversion of $G(t)$ into $J(t)$

$J(t)$ can be calculated numerically from $G(t)$ through Eq. (4.73). In doing so, the integration interval is divided into many subintervals which are small enough so that the $J(t)$ function can be replaced by a mean value over the subinterval and taken outside of the integral. Then, a recursion relation can be set up from which $J(t)$ as a function of time is obtained as a discrete set of values. Usually, the subintervals chosen are equally spaced along the t -axis or the $\log t$ -axis. That is, Eq. (4.73) is expressed as

$$t_n = \sum_{i=1}^{i=n} J(t_{i-1/2}) \int_{t_{i-1}}^{t_i} G(t_n - s) ds \quad (4.A.1)$$

where $J(t_{i-1/2})$ is a suitably determined mean value of $J(t)$ at t between t_{i-1} and t_i . Because the chosen magnitude of the spacing $t_i - t_{i-1}$ is very small, one may set

$$t_{i-1/2} = (t_i + t_{i-1})/2. \quad (4.A.2)$$

Using the definition:

$$d\eta(t_n - s) = -G(t_n - s)ds, \quad (4.A.3)$$

Eq. (4.A.1) is expressed as

$$t_n = - \sum_{i=1}^{i=n} J(t_{i-1/2}) [\eta(t_n - t_i) - \eta(t_n - t_{i-1})]. \quad (4.A.4)$$

Separating the last ($i = n$) term from the sum and using the condition $\eta(0) = 0$, Eq. (4.A.4) is rewritten as

$$t_n = J(t_{n-1/2})\eta(t_n - t_{n-1}) - \sum_{i=1}^{i=n-1} J(t_{i-1/2}) [\eta(t_n - t_i) - \eta(t_n - t_{i-1})]. \quad (4.A.5)$$

From the above equation, the recursion relation is obtained:

$$J(t_{n-1/2}) = \frac{t_n + \sum_{i=1}^{i=n-1} J(t_{i-1/2})[\eta(t_n - t_i) - \eta(t_n - t_{i-1})]}{\eta(t_n - t_{n-1})} \quad \text{for } n > 1 \quad (4.A.6)$$

with

$$J(t_{1/2}) = \frac{t_1}{\eta(t_1)} = \frac{2}{G(t_1) + G(0)} \quad (4.A.7)$$

as the starting value at $n = 1$.

Applying the trapezoidal rule, $\eta(t_k)$ is expressed as

$$\eta(t_k) = \sum_{i=1}^{i=k} \int_{t_{i-1}}^{t_i} G(s) ds = \frac{1}{2} \sum_{i=1}^{i=k} [G(t_i) + G(t_{i-1})](t_i - t_{i-1}). \quad (4.A.8)$$

If the subintervals are equally spaced along the t -axis, it is straightforward to calculate the $\{J(t_{i-1/2})\}$ values from Eqs. (4.A.6) and (4.A.8) using the starting value $J(t_{1/2})$ given by Eq. (4.A.7). However, the relaxation $G(t)$ usually spans many decades of time-scale; as a result, its values are measured or calculated equally spaced along the $\log t$ -axis. In this case, the $\eta(t_n - t_x)$ quantities ($x = i, i - 1$ or $n - 1$) as contained in Eq. (4.A.6) need first to be determined by interpolation using the set of $\eta(t_k)$ values calculated beforehand using Eq. (4.A.8).

References

1. Rouse, P. E. Jr., *J. Chem. Phys.* **21**, 1272 (1953).
2. Maxwell, J. C., *Phil. Trans. Roy. Soc.* **A157**, 49 (1867).
3. Boltzmann, L., *Pogg. Ann. Phys.* **7**, 624 (1876).
4. Bird, R. B., Armstrong, R. C., and Hassager, O., *Dynamics of Polymeric Liquids*, Vol. 1 (2nd edn), Chapter 5. Wiley, New York (1987).
5. Doi, M., and Edwards, S. F., *J. Chem. Soc., Faraday Trans. 2*, **74**, 1789 (1978); **74**, 1802 (1978).
6. Lin, Y.-H., *Macromolecules* (a) **17**, 2846 (1984); (b) **19**, 159 (1986); (c) **19**, 168 (1986); (d) **20**, 885 (1987).
7. Berry, G. C., and Fox, T. G., *Adv. Polym. Sci.* **5**, 261 (1968).
8. Ferry, J. D., *Viscoelastic Properties of Polymers* (3rd edn). Wiley, New York (1980).
9. Graessley, W. W., *J. Polym. Sci., Polym. Phys. Ed.* **18**, 27 (1980).
10. Onogi, S., Masuda, T., and Kitagawa, K., *Macromolecules* **3**, 109 (1970).

11. Odani, H., Nemoto, N., and Kurata, M., *Bull. Inst. Chem. Res. Kyoto Univ.* **50**, 117 (1972).
12. Hopkins, I. L., and Hamming, R. W., *J. Appl. Phys.* **28**, 906 (1957); *J. Appl. Phys.* **29**, 742 (1958).
13. Tschoegl, N. W., *The Phenomenological Theory of Linear Viscoelastic Behavior*, Springer-Verlag, Berlin (1989).
14. Lin, Y.-H., *J. Phys. Chem. B* **109**, 17654 (2005).
15. Lin, Y.-H., *J. Phys.: Condens. Matter* **19**, 466101 (2007).
16. Lin, Y.-H., *J. Phys. Chem. B* **109**, 17670 (2005).

Chapter 5

Stress and Strain

In the last chapter we discussed the relation between stress and strain (or instead rate-of-strain) in one dimension by treating the viscoelastic quantities as scalars. When the applied strain or rate-of-strain is large, the nonlinear response of the polymeric liquid involves more than one dimension. In addition, a rheological process always involves a three-dimensional deformation. In this chapter, we discuss how to express stress and strain in three-dimensional space. This is not only important in the study of polymer rheological properties in terms of continuum mechanics¹⁻³ but is also essential in the polymer viscoelastic theories and simulations studied in the later chapters, into which the chain dynamic models are incorporated.

5.1 Stress

Consider a fluid material body enclosing an infinitesimal volume element dV at the point p , as shown in Fig. 5.1. Choose any plane cutting through the volume element and let the cross section be denoted by dS . The direction perpendicular to the plane is regarded as the direction of the plane, indicated by the unit vector \mathbf{n} . If there are forces applied to the body, a surface force \mathbf{f}_n will be exerted on the plane of the volume element at the point p . In general, the directions of \mathbf{f}_n and \mathbf{n} are different. By dividing \mathbf{f}_n by dS , we obtain the stress $\mathbf{t}_n (= \mathbf{f}_n/dS)$ exerted on the plane at the point p . The stress can be separated into the component perpendicular to the plane (the normal stress) and those parallel to the plane (the shear stresses). At the point p , we choose a Cartesian coordinate system with \mathbf{n} as one direction and \mathbf{m} and \mathbf{l} in the plane as the other two. Then \mathbf{t}_n may be expressed as

$$\mathbf{t}_n = \mathbf{n}T_{nn} + \mathbf{m}T_{nm} + \mathbf{l}T_{nl} \quad (5.1)$$

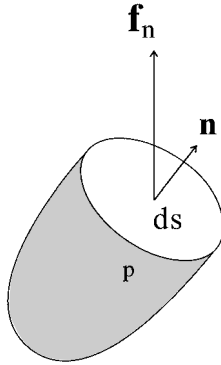


Fig. 5.1 A plane cutting through a volume element dV at the point p . The direction of the plane is represented by the unit vector \mathbf{n} ; and a surface force \mathbf{f}_n is exerted on the plane.

where the stress components are expressed in terms of the symbol T with two subscripts. The first subscript represents the direction of the plane onto which the stress is applied and the second subscript represents the direction of the stress component. If another plane with the direction \mathbf{c} cutting through the point p is chosen, a stress \mathbf{t}_c with the components T_{cc} , T_{cb} and T_{ca} exerting on the new chosen plane can in the same way be defined.

To any chosen plane, we can express the normal and shear stress components in terms of the symbol system given above. For any two chosen planes at the point p , the stresses exerted on them are related. The stress on any chosen plane at the point p can be obtained from a physical quantity called the stress tensor. The stress tensor is also a special device for mathematical derivation which allows the stress state at any point in the fluid body to be described.⁴

The meaning and use of the stress tensor are discussed in the following: In the close vicinity of the point p , three planes perpendicular to each other can be erected as shown in Fig. 5.2. Let the directions of the three planes be \mathbf{x} , \mathbf{y} , and \mathbf{z} . The stresses on these three planes are denoted by \mathbf{t}_x , \mathbf{t}_y and \mathbf{t}_z , respectively. Each of these three stresses has three components. For instance, \mathbf{t}_x has T_{xx} , T_{xy} and T_{xz} . Now we consider a plane which cuts across the three planes and forms a tetrahedron with the three planes enclosing the point p , as shown in Fig. 5.2. We denote the direction of the plane as \mathbf{n} . The total force experienced by the tetrahedron has to be zero; otherwise, the body will accelerate.

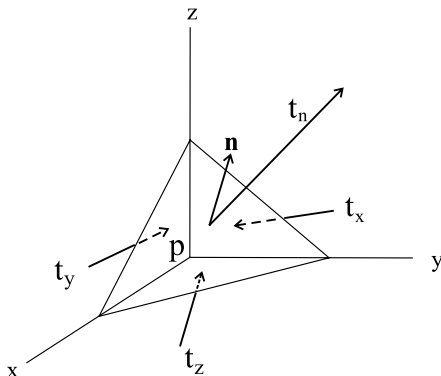


Fig. 5.2 Tetrahedron at the point p with three surfaces of directions \mathbf{x} , \mathbf{y} , \mathbf{z} perpendicular to one another. The stresses on the four surfaces are denoted by \mathbf{t}_x , \mathbf{t}_y , \mathbf{t}_z and \mathbf{t}_n , respectively.

Let the areas of the four surfaces of the tetrahedron be S_n , S_x , S_y and S_z respectively. From the balance of the forces from the four surfaces,

$$\mathbf{t}_n S_n = \mathbf{t}_x S_x + \mathbf{t}_y S_y + \mathbf{t}_z S_z. \quad (5.2)$$

As S_x is the projection of S_n on the \mathbf{x} plane,

$$S_x = \mathbf{n} \cdot \mathbf{x} S_n. \quad (5.3a)$$

Similarly,

$$S_y = \mathbf{n} \cdot \mathbf{y} S_n \quad (5.3b)$$

$$S_z = \mathbf{n} \cdot \mathbf{z} S_n. \quad (5.3c)$$

Substituting Eq. (5.3) into Eq. (5.2), we obtain

$$\mathbf{t}_n S_n = \mathbf{t}_x \mathbf{n} \cdot \mathbf{x} S_n + \mathbf{t}_y \mathbf{n} \cdot \mathbf{y} S_n + \mathbf{t}_z \mathbf{n} \cdot \mathbf{z} S_n. \quad (5.4)$$

By shrinking the size of the tetrahedron to zero at the point p , the stresses contained in Eq. (5.4) become the fixed values at p . When both sides are divided by S_n , Eq. (5.4) becomes

$$\mathbf{t}_n = \mathbf{n} \cdot (\mathbf{x} \mathbf{t}_x + \mathbf{y} \mathbf{t}_y + \mathbf{z} \mathbf{t}_z) \quad (5.5)$$

With \mathbf{t}_x , \mathbf{t}_y , and \mathbf{t}_z expressed in terms of their components (Eq. (5.1)), Eq. (5.5) is rewritten as

$$\begin{aligned} \mathbf{t}_n = \mathbf{n} \cdot (\mathbf{xx}T_{xx} + \mathbf{xy}T_{xy} + \mathbf{xz}T_{xz} + \mathbf{yx}T_{yx} + \mathbf{yy}T_{yy} + \mathbf{yz}T_{yz} \\ + \mathbf{zx}T_{zx} + \mathbf{zy}T_{zy} + \mathbf{zz}T_{zz}). \end{aligned} \quad (5.6)$$

In general, Eq. (5.6) is expressed in the abbreviated form

$$\mathbf{t}_n = \mathbf{n} \cdot \mathbf{T} \quad (5.7)$$

where \mathbf{T} is called the stress tensor. As shown in Eq. (5.6), a tensor is composed of terms with unit dyads, which contain two unit vectors, such as \mathbf{xx} , \mathbf{xy} , \dots , etc. In contrast to the tensor, a vector is composed of terms containing a single unit vector. The operations involving the tensor are illustrated in Appendix 5.A.

A fluid body cannot support a shear stress without flowing. Thus, a stationary fluid body has only normal stresses that balance each other. This means $T_{xx} = T_{yy} = T_{zz}$ (or $T_{11} = T_{22} = T_{33}$. We may use 1, 2, and 3 to replace x , y , and z ; and the symbols δ_1 , δ_2 , and δ_3 to replace the three orthogonal unit vectors \mathbf{x} , \mathbf{y} , and \mathbf{z} below). These normal stresses are the hydrostatic pressure P . And the stress tensor for a stationary fluid body may be written as

$$\mathbf{T} = P\delta = \begin{pmatrix} P & 0 & 0 \\ 0 & P & 0 \\ 0 & 0 & P \end{pmatrix} \quad (5.8)$$

where δ is the unit tensor (see Eq. (5.A.10)) defined by

$$\delta = \sum_i \sum_j \delta_i \delta_j \delta_{ij} = \begin{pmatrix} 1 & 0 & 0 \\ 0 & 1 & 0 \\ 0 & 0 & 1 \end{pmatrix}. \quad (5.9)$$

Thus, the total stress tensor of a fluid body is written as

$$\mathbf{T} = P\delta + \boldsymbol{\tau} \quad (5.10)$$

where $\boldsymbol{\tau}$ is the extra stress tensor.

Because the deviation from the simple Hookean or Newtonian behavior in response to a large deformation is often much greater than the compressibility effect of the fluid material, the material is often assumed to be incompressible in a rheological study. For an incompressible material, we may eliminate the hydrostatic pressure term and only consider the extra

stress tensor $\boldsymbol{\tau}$. Because $T_{ij} = \tau_{ij}$ ($i \neq j$), such a practice has no effect on the shear stresses. With the hydrostatic pressure eliminated, only the differences between the normal stresses:

$$T_{11} - T_{22} = \tau_{11} - \tau_{22} \quad (5.11)$$

and

$$T_{22} - T_{33} = \tau_{22} - \tau_{33} \quad (5.12)$$

need be considered. As the third difference value ($T_{11} - T_{33}$ or $\tau_{11} - \tau_{33}$) can be obtained from Eqs. (5.11) and (5.12), there are only two independent difference values.

The stress tensor is expected to be symmetrical; i.e. $T_{ij} = T_{ji}$ for $i \neq j$. This can be shown by considering the two shear-stress components, T_{13} and T_{31} , applied on a cube, as shown in Fig. 5.3. The two shear-stress components must balance out, i.e. $T_{13} = T_{31}$; otherwise the cube will start accelerating around the δ_2 direction. Similarly, $T_{12} = T_{21}$; and $T_{23} = T_{32}$. Thus, the stress tensor is symmetrical and has only six independent components. For expressing the symmetry of the stress tensor, we write

$$\mathbf{T} = \mathbf{T}^T \quad (5.13)$$

where \mathbf{T}^T is called the transpose of \mathbf{T} (see Appendix 5.A).

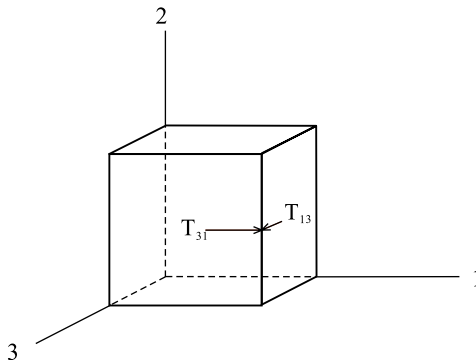


Fig. 5.3 If the two shear-stress components T_{13} and T_{31} are not equal, the cube will rotate about the δ_2 direction.

5.2 Finite Strain

In rheology, we study the mathematical expression for the relation between stress and deformation. Such an equation is usually referred to as the constitutive equation or the rheological equation of state. For expressing the constitutive equation in three dimensions, we need to find the proper way to express the deformation in the tensorial form as well.

Consider a piece of material, as shown in Fig. 5.4. p is a certain point in the material body, and q is a point in the neighborhood of p . The separation between the two points is expressed by the vector $d\mathbf{X}'$. Then the length of the vector is given by its absolute value $|d\mathbf{X}'|$ defined by

$$|d\mathbf{X}'| = (d\mathbf{X}' \cdot d\mathbf{X}')^{1/2} \quad (5.14)$$

and its direction is indicated by the unit vector:

$$\mathbf{u}' = \frac{d\mathbf{X}'}{|d\mathbf{X}'|}. \quad (5.15)$$

Here, we use the apostrophe mark “'” to indicate the state of the material body at a certain time t' in the past. Let the material body be changed to the shape shown in the right of Fig. 5.4. Both the p and q points change their positions as a result of rotation and/or deformation of the material body. The vector $d\mathbf{X}'$ between p and q is deformed to become $d\mathbf{X}$. The change in $d\mathbf{X}$ with respect to $d\mathbf{X}'$ is called the deformation gradient which is expressed by the dyad $(\nabla' \mathbf{X})^T$ (see Appendix 5.A), and is often represented

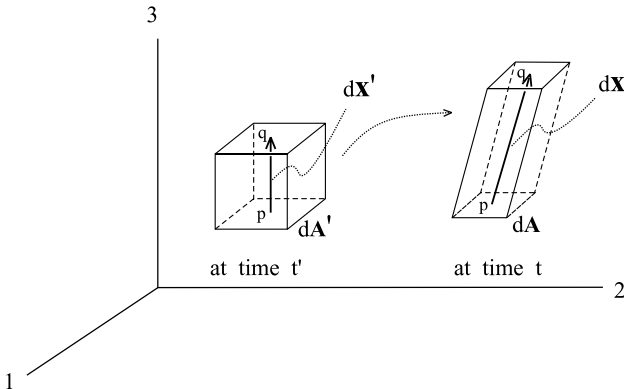


Fig. 5.4 The deformation between two neighboring points, p and q , in a piece of material under deformation.

by a tensor symbol \mathbf{E} :

$$\mathbf{E} = (\nabla' \mathbf{X})^T = \left[\sum_i \sum_j \delta_i \delta_j \frac{\partial X_j}{\partial X'_i} \right]^T = \sum_i \sum_j \delta_i \delta_j \frac{\partial X_i}{\partial X'_j} \quad (5.16)$$

or

$$E_{ij} = \frac{\partial X_i}{\partial X'_j}.$$

In defining \mathbf{E} this way, we have assumed that \mathbf{X} is a continuous function of \mathbf{X}' , i.e.

$$\mathbf{X} = \mathbf{X}(\mathbf{X}', t). \quad (5.17)$$

Then

$$d\mathbf{X} = \mathbf{E} \cdot d\mathbf{X}'$$

or

$$d\mathbf{X} = d\mathbf{X}' \cdot \mathbf{E}^T. \quad (5.18)$$

Three examples are given below to illustrate the operations of the deformation gradient tensor. Consider a rectangular block of material with dimensions $\Delta x'_1$, $\Delta x'_2$, and $\Delta x'_3$, as shown in Fig. 5.5(a). A Cartesian coordinate system can be chosen with one of the corners as the origin and three unit vectors δ_1 , δ_2 , and δ_3 pointing in the three orthogonal directions of the block. In this coordinate system, the position vector of a point p inside the material body is denoted by $\mathbf{X}' = \delta_1 X'_1 + \delta_2 X'_2 + \delta_3 X'_3$.

(a) *Uniaxial extension*

In the uniaxial extension as shown in Fig. 5.5(b), the block (Fig. 5.5(a)) is elongated λ_1 times in the δ_1 direction. The block is transformed to have the dimensions Δx_1 , Δx_2 , and Δx_3 , and the position of the point p is changed to \mathbf{X} with three components given by

$$\begin{aligned} X_1 &= \frac{\Delta x_1}{\Delta x'_1} X'_1 = \lambda_1 X'_1 \\ X_2 &= \frac{\Delta x_2}{\Delta x'_2} X'_2 = \lambda_2 X'_2 \\ X_3 &= \frac{\Delta x_3}{\Delta x'_3} X'_3 = \lambda_3 X'_3. \end{aligned} \quad (5.19)$$

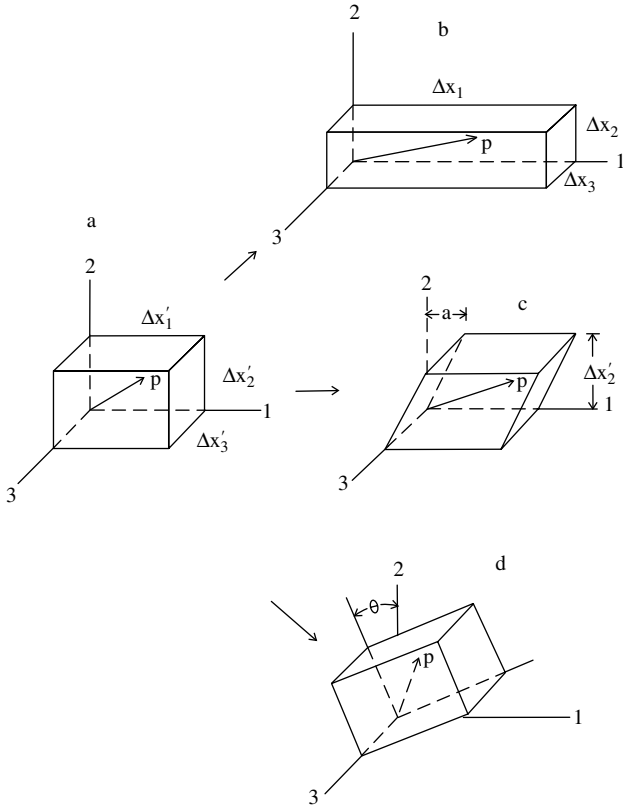


Fig. 5.5 (a) A rectangular block of material at rest. (b) The block under uniaxial extension. (c) The block under simple shear deformation. (d) The block rotated.

Because the elongational deformation is symmetric with respect to the δ_1 direction, $\lambda_2 = \lambda_3$. Substituting Eq. (5.19) into Eq. (5.16), we obtain

$$\mathbf{E} = \begin{pmatrix} \lambda_1 & 0 & 0 \\ 0 & \lambda_2 & 0 \\ 0 & 0 & \lambda_2 \end{pmatrix}. \tag{5.20}$$

As the material is assumed to be incompressible,

$$\lambda_1 \lambda_2^2 = 1. \tag{5.21}$$

Using Eq. (5.21), Eq. (5.20) can be rewritten as

$$\mathbf{E} = \begin{pmatrix} \lambda_1 & 0 & 0 \\ 0 & \frac{1}{\sqrt{\lambda_1}} & 0 \\ 0 & 0 & \frac{1}{\sqrt{\lambda_1}} \end{pmatrix} \quad (5.22)$$

for uniaxial extension.

(b) *Simple shear*

For a simple shear as shown in Fig. 5.5(c), the top plane of the block sliding along the δ_1 direction over a distance, a , with reference to the bottom plane

$$X_1 = X'_1 + \frac{a}{\Delta x'_2} X'_2 = X'_1 + \lambda X'_2 \quad (5.23a)$$

$$X_2 = X'_2 \quad (5.23b)$$

$$X_3 = X'_3 \quad (5.23c)$$

where $\lambda = a/\Delta x'_2$ is the simple shear strain. Substituting Eq. (5.23) into Eq. (5.16), we obtain

$$\mathbf{E} = \begin{pmatrix} 1 & \lambda & 0 \\ 0 & 1 & 0 \\ 0 & 0 & 1 \end{pmatrix} \quad (5.24)$$

for simple shear.

(c) *Solid-body rotation*

Consider the rectangular block shown in Fig. 5.5(a) as a rigid (solid) body. A rotation of the solid body around the δ_3 direction is shown in Fig. 5.5(d). For a rotational angle θ ,

$$X_1 = X'_1 \cos \theta - X'_2 \sin \theta \quad (5.25a)$$

$$X_2 = X'_1 \sin \theta + X'_2 \cos \theta \quad (5.25b)$$

$$X_3 = X'_3. \quad (5.25c)$$

Substituting Eq. (5.25) into Eq. (5.16), we obtain

$$\mathbf{E} = \begin{pmatrix} \cos \theta & -\sin \theta & 0 \\ \sin \theta & \cos \theta & 0 \\ 0 & 0 & 1 \end{pmatrix}. \quad (5.26)$$

For a solid-body rotation, the material body is not deformed; the distance from the origin of the coordinate system to the p point does not change. Yet for a solid-body rotation, $\mathbf{E} \neq \mathbf{\delta}$, according to Eq. (5.26). The tensor \mathbf{E} describes a situation involving deformation [cases (a) and (b)], rotation [case (c)], or both. A way to eliminate the rotational element needs to be found.

Related to the deformation of the material body is the change in length of $d\mathbf{X}'$. We define the length ratio of the change from $d\mathbf{X}'$ to $d\mathbf{X}$ as

$$\mu = \frac{|d\mathbf{X}|}{|d\mathbf{X}'|} \quad (5.27)$$

or from Eq. (5.14)

$$\mu^2 = \frac{d\mathbf{X} \cdot d\mathbf{X}}{d\mathbf{X}' \cdot d\mathbf{X}'}. \quad (5.28)$$

The substitution of Eq. (5.18) into Eq. (5.28) gives

$$\begin{aligned} \mu^2 &= \frac{(\mathbf{E} \cdot d\mathbf{X}') \cdot (\mathbf{E} \cdot d\mathbf{X}')}{d\mathbf{X}' \cdot d\mathbf{X}'} \\ &= \frac{d\mathbf{X}' \cdot \mathbf{E}^T \cdot \mathbf{E} \cdot d\mathbf{X}'}{|d\mathbf{X}'|^2} \\ &= \mathbf{u}' \cdot \mathbf{C} \cdot \mathbf{u}' \end{aligned} \quad (5.29)$$

where Eq. (5.15) has been used for the last equality and \mathbf{C} , called the Cauchy tensor, is given by

$$\mathbf{C} = \mathbf{E}^T \cdot \mathbf{E}. \quad (5.30)$$

The Cauchy tensor is a device for describing the change in length at any point of the material body. Equation (5.29) indicates that in performing such a function the Cauchy tensor operates on the unit vector \mathbf{u}' at some time t' in the past. However, the stress tensor is always measured with respect to the present form of the material body or the deformed state. Thus, there is the need to find a deformation tensor that operates on the unit vector at the present time. This can be done by using the inverse of \mathbf{E} , \mathbf{E}^{-1} , to express $d\mathbf{X}'$ in terms of $d\mathbf{X}$, namely,

$$d\mathbf{X}' = \mathbf{E}^{-1} \cdot d\mathbf{X} \quad (5.31)$$

where

$$\mathbf{E}^{-1} = (\nabla \mathbf{X}')^T. \quad (5.32)$$

Substituting Eq. (5.31) into Eq. (5.28), we obtain

$$\mu^2 = \frac{d\mathbf{X} \cdot d\mathbf{X}}{d\mathbf{X} \cdot (\mathbf{E}^{-1})^T \cdot \mathbf{E}^{-1} \cdot d\mathbf{X}} = \frac{1}{\mathbf{u} \cdot \mathbf{B}^{-1} \cdot \mathbf{u}} \quad (5.33)$$

where

$$\mathbf{u} = \frac{d\mathbf{X}}{|d\mathbf{X}|} \quad (5.34)$$

and \mathbf{B} , called the Finger tensor, is given by

$$\mathbf{B}^{-1} = (\mathbf{E}^{-1})^T \cdot \mathbf{E}^{-1} \quad (5.35a)$$

or

$$\mathbf{B} = \mathbf{E} \cdot \mathbf{E}^T. \quad (5.35b)$$

A direct way for obtaining the Finger tensor, which also describes the deformation, is to consider the change in a local area. In Fig. 5.4, we can follow the change of either the area $d\mathbf{A}'$ or the length $d\mathbf{X}'$ to achieve the same purpose. $d\mathbf{A}'$ and $d\mathbf{X}'$ are related by the volume dV'

$$dV' = d\mathbf{A}' \cdot d\mathbf{X}'. \quad (5.36)$$

Just as Eq. (5.27) defines the length ratio of the change from $d\mathbf{X}'$ to $d\mathbf{X}$, we can define the area ratio of the change from $d\mathbf{A}'$ to $d\mathbf{A}$ as

$$\nu = \frac{|d\mathbf{A}|}{|d\mathbf{A}'|} \quad (5.37)$$

or

$$\nu^2 = \frac{d\mathbf{A} \cdot d\mathbf{A}}{d\mathbf{A}' \cdot d\mathbf{A}'}. \quad (5.38)$$

Similar to Eq. (5.36), we have

$$dV = d\mathbf{A} \cdot d\mathbf{X}. \quad (5.39)$$

Using the assumption of incompressibility, namely $dV' = dV$, we have

$$d\mathbf{A}' \cdot d\mathbf{X}' = d\mathbf{A} \cdot d\mathbf{X}. \quad (5.40)$$

Substituting Eq. (5.18) into Eq. (5.40), we obtain

$$d\mathbf{A}' = d\mathbf{A} \cdot \mathbf{E}. \quad (5.41)$$

The substitution of Eq. (5.41) into Eq. (5.38) gives

$$\nu^2 = \frac{|d\mathbf{A}|^2}{d\mathbf{A} \cdot \mathbf{E} \cdot \mathbf{E}^T \cdot d\mathbf{A}}. \quad (5.42)$$

Using the Finger tensor as defined by Eq. (5.35), Eq. (5.42) is rewritten as

$$\frac{1}{\nu^2} = \mathbf{n} \cdot \mathbf{B} \cdot \mathbf{n} \quad (5.43)$$

where

$$\mathbf{n} = \frac{d\mathbf{A}}{|d\mathbf{A}|}. \quad (5.44)$$

Physically, the Finger tensor \mathbf{B} describes the change in area at a certain point in the material body and operates on the unit vector \mathbf{n} in the deformed state or at the present time. This is what we hope to have for relating to the stress tensor, which is measured with respect to the present form of the material body.

For the three kinds of material body motions shown in Fig. 5.5, we calculate the Cauchy and Finger tensors below:

(a) *Uniaxial extension*

Substituting Eq. (5.22) into Eqs. (5.30) and (5.35), we obtain

$$\begin{aligned} \mathbf{C} = \mathbf{B} &= \begin{pmatrix} \lambda_1 & 0 & 0 \\ 0 & \frac{1}{\sqrt{\lambda_1}} & 0 \\ 0 & 0 & \frac{1}{\sqrt{\lambda_1}} \end{pmatrix} \begin{pmatrix} \lambda_1 & 0 & 0 \\ 0 & \frac{1}{\sqrt{\lambda_1}} & 0 \\ 0 & 0 & \frac{1}{\sqrt{\lambda_1}} \end{pmatrix} \\ &= \begin{pmatrix} \lambda_1^2 & 0 & 0 \\ 0 & \frac{1}{\lambda_1} & 0 \\ 0 & 0 & \frac{1}{\lambda_1} \end{pmatrix}. \end{aligned} \quad (5.45)$$

It is clear that for uniaxial extension $\mathbf{C} = \mathbf{B}$ because $\mathbf{E} = \mathbf{E}^T$.

(b) Simple shear

With \mathbf{E} given by Eq. (5.24), Eqs. (5.30) and (5.35) become, respectively:

$$\begin{aligned}\mathbf{C} &= \begin{pmatrix} 1 & 0 & 0 \\ \lambda & 1 & 0 \\ 0 & 0 & 1 \end{pmatrix} \begin{pmatrix} 1 & \lambda & 0 \\ 0 & 1 & 0 \\ 0 & 0 & 1 \end{pmatrix} \\ &= \begin{pmatrix} 1 & \lambda & 0 \\ \lambda & 1 + \lambda^2 & 0 \\ 0 & 0 & 1 \end{pmatrix}\end{aligned}\quad (5.46)$$

$$\begin{aligned}\mathbf{B} &= \begin{pmatrix} 1 & \lambda & 0 \\ 0 & 1 & 0 \\ 0 & 0 & 1 \end{pmatrix} \begin{pmatrix} 1 & 0 & 0 \\ \lambda & 1 & 0 \\ 0 & 0 & 1 \end{pmatrix} \\ &= \begin{pmatrix} 1 + \lambda^2 & \lambda & 0 \\ \lambda & 1 & 0 \\ 0 & 0 & 1 \end{pmatrix}.\end{aligned}\quad (5.47)$$

(c) Solid-body rotation

The substitution of Eq. (5.26) into Eqs. (5.30) and (5.35) gives

$$\mathbf{C} = \mathbf{B} = \begin{pmatrix} 1 & 0 & 0 \\ 0 & 1 & 0 \\ 0 & 0 & 1 \end{pmatrix} = \boldsymbol{\delta}.\quad (5.48)$$

Both the Cauchy and Finger tensors are unit tensors. This means that, as expected, the solid-body rotation does not deform the material.

5.3 A neo-Hookean Material

In Chapter 4, we discussed Hooke's law (Eq. (4.6)) for a small strain in one dimension. As long as the applied strain is very small, Eq. (4.6) is valid for a solid material. Here, we generalize it in three dimensions. It appears logical that the stress tensor is linearly proportional to the deformation tensor,⁵ that is,

$$\boldsymbol{\tau} = -G\mathbf{B}.\quad (5.49)$$

Here the sign is chosen by taking compression to be positive. For an incompressible material, the total stress tensor is given by

$$\mathbf{T} = P\mathbf{1} - G\mathbf{B}. \quad (5.50)$$

The mechanical property represented by Eq. (5.50) is often called neo-Hookean.

We apply Eq. (5.50) to the uniaxial-extension case with \mathbf{d}_1 being the direction of extension. From Eqs. (5.45) and (5.50), we have

$$\mathbf{T} = \begin{pmatrix} P - G\lambda_1^2 & 0 & 0 \\ 0 & P - \frac{G}{\lambda_1} & 0 \\ 0 & 0 & P - \frac{G}{\lambda_1} \end{pmatrix} \quad (5.51)$$

and the normal-stress difference

$$\begin{aligned} \sigma &= T_{11} - T_{22} = T_{11} - T_{33} \\ &= -G \left(\lambda_1^2 - \frac{1}{\lambda_1} \right) \end{aligned} \quad (5.52)$$

which is identical to Eq. (2.22) with $G = nkT/V$ (see Appendix 8.B). Thus, Eq. (5.50) is a suitable equation for the stress-strain behavior of a rubber. Extensive investigations^{6,7} have also shown that the equation is in good agreement with experimental results of the rubber for moderate deformations.

For a small uniaxial deformation, λ_1 is very close to 1, i.e.

$$\lambda_1 = 1 + \epsilon; \quad \epsilon \ll 1. \quad (5.53)$$

Substituting Eq. (5.53) into Eq. (5.52), we obtain

$$\sigma = - \lim_{\epsilon \rightarrow 0} 3G\epsilon \quad (5.54)$$

Young's modulus E is defined by

$$E = - \lim_{\epsilon \rightarrow 0} \frac{\sigma}{\epsilon}. \quad (5.55)$$

Thus, for an incompressible isotropic material,

$$E = 3G. \quad (5.56)$$

Applying the neo-Hookean Eq. (5.50) to the simple shear deformation case, we obtain from Eq. (5.47)

$$T_{12} = T_{21} = -G\lambda \quad (5.57)$$

$$T_{11} - T_{22} = -G\lambda^2 \quad (5.58)$$

and

$$T_{22} - T_{33} = 0. \quad (5.59)$$

The above results indicate that the stress-strain relation is linear for the shear component (Eq. (5.57)) while the first normal-stress difference becomes very large when the applied shear strain λ is greater than 1 (Eq. (5.58)). The occurrence of the first normal-stress difference is unexpected from the viewpoint of linear viscoelasticity (Eq. (4.6)). It is related to the so-called rod-climbing phenomenon,¹ namely, the observation that a polymeric liquid climbs a rotating shaft.

Comparing Eqs. (5.56) and (5.57), one sees that Young's modulus is three times the shear modulus for an incompressible isotropic solid.

5.4 A Newtonian Fluid

For a fluid that does not possess any elastic property, what needs to be measured is the deformation rate, instead of the total strain. Such a fluid has no memory of past deformations. Thus, we need to express the *present* changing rate of the Finger tensor \mathbf{B} , while moving the past point position \mathbf{X}' in \mathbf{B} infinitely close to its present position \mathbf{X} . Mathematically, these two ideas can be expressed as

$$\begin{aligned} \dot{\gamma}_{ij} &= \lim_{\mathbf{x}' \rightarrow \mathbf{x}} \frac{\partial B_{ij}}{\partial t} \\ &= \lim_{\mathbf{x}' \rightarrow \mathbf{x}} \frac{\partial}{\partial t} \sum_k \frac{\partial X_i}{\partial X'_k} \frac{\partial X_j}{\partial X'_k} \\ &= \lim_{\mathbf{x}' \rightarrow \mathbf{x}} \sum_k \left[\left(\frac{\partial}{\partial t} \frac{\partial X_i}{\partial X'_k} \right) \frac{\partial X_j}{\partial X'_k} + \frac{\partial X_i}{\partial X'_k} \left(\frac{\partial}{\partial t} \frac{\partial X_j}{\partial X'_k} \right) \right] \\ &= \sum_k \left[\frac{\partial V_i}{\partial X_k} \delta_{jk} + \delta_{ik} \frac{\partial V_j}{\partial X_k} \right] \\ &= \frac{\partial V_i}{\partial X_j} + \frac{\partial V_j}{\partial X_i}. \end{aligned} \quad (5.60)$$

The equation for a Newtonian fluid can be written in three-dimensional space as

$$\boldsymbol{\tau} = -\eta \dot{\boldsymbol{\gamma}} \quad (5.61)$$

or

$$\mathbf{T} = P\boldsymbol{\delta} - \eta \dot{\boldsymbol{\gamma}} \quad (5.62)$$

where the components of the rate-of-strain tensor $\dot{\boldsymbol{\gamma}}$ are given by Eq. (5.60). The application of the constitutive equation — Eq. (5.62) — to the simple-shear case gives

$$\mathbf{T} = \begin{pmatrix} P & -\eta\dot{\gamma} & 0 \\ -\eta\dot{\gamma} & P & 0 \\ 0 & 0 & P \end{pmatrix} \quad (5.63)$$

where

$$\dot{\gamma} = \frac{\partial V_1}{\partial X_2} + \frac{\partial V_2}{\partial X_1}. \quad (5.64)$$

From Eq. (5.63), the simple-shear result in one dimension (Eq. (4.3)) is obtained, i.e.

$$T_{12} = -\eta\dot{\gamma}. \quad (5.65)$$

We also see from Eq. (5.63) that the Newtonian fluid does not give rise to a normal-stress difference for simple shear.

In the case of uniaxial extension,

$$V_i = \dot{\lambda}_i X_i; \quad \text{for } i = 1, 2, 3. \quad (5.66)$$

The substitution of Eq. (5.66) into Eq. (5.60) gives

$$\dot{\boldsymbol{\gamma}} = 2 \begin{pmatrix} \dot{\lambda}_1 & 0 & 0 \\ 0 & \dot{\lambda}_2 & 0 \\ 0 & 0 & \dot{\lambda}_3 \end{pmatrix}. \quad (5.67)$$

For an incompressible fluid with density ρ ,

$$\frac{d\rho}{dt} = -\rho \boldsymbol{\nabla} \cdot \mathbf{V} = -\rho \sum_i \frac{\partial V_i}{\partial X_i} = 0. \quad (5.68)$$

Thus,

$$\dot{\lambda}_1 + \dot{\lambda}_2 + \dot{\lambda}_3 = 0. \quad (5.69)$$

Because of the symmetry of the deformation,

$$\dot{\lambda}_2 = \dot{\lambda}_3. \quad (5.70)$$

Using Eqs. (5.69) and (5.70), Eq. (5.67) is rewritten as

$$\dot{\mathbf{y}} = 2 \begin{pmatrix} \dot{\lambda}_1 & 0 & 0 \\ 0 & -\frac{\dot{\lambda}_1}{2} & 0 \\ 0 & 0 & -\frac{\dot{\lambda}_1}{2} \end{pmatrix}. \quad (5.71)$$

The substitution of Eq. (5.71) into Eq. (5.62) gives

$$\mathbf{T} = \begin{pmatrix} P - 2\eta\dot{\lambda}_1 & 0 & 0 \\ 0 & P + \eta\dot{\lambda}_1 & 0 \\ 0 & 0 & P + \eta\dot{\lambda}_1 \end{pmatrix} \quad (5.72)$$

from which

$$T_{11} - T_{22} = T_{11} - T_{33} = -3\eta\dot{\lambda}_1. \quad (5.73)$$

From the comparison of Eqs. (5.65) and (5.73), we see that the tensile viscosity is three times the shear viscosity. This is Trouton's well-known rule, which is analogous to the relation of Young's modulus being three times the shear modulus for an isotropic incompressible material.

Appendix 5.A — Tensor Operations

Here, we use Eq. (5.7) as an example for discussing the operations related to a tensor. The dot in Eq. (5.7) represents the multiplication of a tensor by a vector, and the product is a vector. In Eq. (5.7), the unit vector \mathbf{n} forms a dot product with only the left unit vector in each dyad term of the tensor \mathbf{T} . With $\mathbf{n} \cdot \mathbf{x} = n_x$, $\mathbf{n} \cdot \mathbf{y} = n_y$, and $\mathbf{n} \cdot \mathbf{z} = n_z$, Eq. (5.7) is rewritten as

$$\begin{aligned} \mathbf{t}_n = & \mathbf{x}(n_x T_{xx} + n_y T_{yx} + n_z T_{zx}) + \mathbf{y}(n_x T_{xy} + n_y T_{yy} + n_z T_{zy}) \\ & + \mathbf{z}(n_x T_{xz} + n_y T_{yz} + n_z T_{zz}). \end{aligned} \quad (5.A.1)$$

Sometimes for convenience, the tensor is expressed in terms of a matrix as

$$\mathbf{T} = \begin{pmatrix} T_{xx} & T_{xy} & T_{xz} \\ T_{yx} & T_{yy} & T_{yz} \\ T_{zx} & T_{zy} & T_{zz} \end{pmatrix}. \quad (5.A.2)$$

The matrix representation is convenient because dot-product multiplication is equivalent to standard matrix multiplication. In terms of the matrix representation, Eq. (5.7) is expressed as

$$\begin{aligned}
 \mathbf{t}_n &= \mathbf{n} \cdot \mathbf{T} \\
 &= (n_x \ n_y \ n_z) \begin{pmatrix} T_{xx} & T_{xy} & T_{xz} \\ T_{yx} & T_{yy} & T_{yz} \\ T_{zx} & T_{zy} & T_{zz} \end{pmatrix} \\
 &= (n_x T_{xx} + n_y T_{yx} + n_z T_{zx} \quad n_x T_{xy} + n_y T_{yy} + n_z T_{zy} \quad n_x T_{xz} + n_y T_{yz} + n_z T_{zz})
 \end{aligned} \tag{5.A.3}$$

In Eq. (5.A.3) the vector \mathbf{n} at the left of the dot is represented by a row. The multiplication of the row with the matrix forms another row, which represents a vector. In the matrix representation, the dot product between two vectors is represented by the multiplication of a row on the left and a column on the right.

The tensor \mathbf{T} may also be concisely written as

$$\mathbf{T} = \sum_i \sum_j \delta_i \delta_j T_{ij} \tag{5.A.4}$$

where 1, 2, and 3 represent x , y , and z , respectively and δ_1 , δ_2 , and δ_3 represent the unit vectors \mathbf{x} , \mathbf{y} , and \mathbf{z} , respectively. And the unit vector \mathbf{n} is expressed as

$$\mathbf{n} = \sum_i \delta_i n_i. \tag{5.A.5}$$

Then, Eq. (5.7) may be written as

$$\begin{aligned}
 \mathbf{t}_n &= \mathbf{n} \cdot \mathbf{T} \\
 &= \sum_i \delta_i n_i \cdot \sum_k \sum_l \delta_k \delta_l T_{kl} \\
 &= \sum_i \sum_l n_i T_{il} \delta_l \\
 &= \delta_1 (n_1 T_{11} + n_2 T_{21} + n_3 T_{31}) + \delta_2 (n_1 T_{12} + n_2 T_{22} + n_3 T_{32}) \\
 &\quad + \delta_3 (n_1 T_{13} + n_2 T_{23} + n_3 T_{33}).
 \end{aligned} \tag{5.A.6}$$

The result of Eq. (5.A.6) is the same as those of Eqs. (5.A.1) and (5.A.3).

There are a few special second-order tensors, which are noteworthy:

(1) If

$$T_{ij} = T_{ji}$$

\mathbf{T} is a symmetric tensor.

(2) If

$$\mathbf{T} = \sum_i \sum_j \delta_i \delta_j T_{ij} \quad (5.A.7a)$$

the transpose of \mathbf{T} is defined by

$$\mathbf{T}^T = \sum_i \sum_j \delta_i \delta_j T_{ji}. \quad (5.A.7b)$$

If \mathbf{T} is a symmetric tensor, $\mathbf{T} = \mathbf{T}^T$.

(3) The components of a tensor can be formed from the components of two vectors, two as a pair for one component. Take two vectors \mathbf{v} and \mathbf{w} . The tensor formed from \mathbf{v} and \mathbf{w} is called the dyadic product of \mathbf{v} and \mathbf{w} . The symbol to represent it is simply \mathbf{vw} :

$$\mathbf{vw} = \sum_i \sum_j \delta_i \delta_j v_i w_j. \quad (5.A.8)$$

Note that $\mathbf{vw} \neq \mathbf{wv}$. But

$$(\mathbf{vw})^T = \mathbf{wv} \quad (5.A.9)$$

(4) If the components of the tensor are given by the Kronecker delta δ_{ij} ($\delta_{ij} = 1$ if $i = j$; $\delta_{ij} = 0$ if $i \neq j$), the tensor is called the unit or identity tensor, often denoted by

$$\delta = \sum_i \sum_j \delta_i \delta_j \delta_{ij}. \quad (5.A.10)$$

The single dot product of two tensors \mathbf{S} and \mathbf{T} is a tensor and is expressed as

$$\begin{aligned} \mathbf{S} \cdot \mathbf{T} &= \sum_i \sum_j \sum_k \sum_l \delta_i \delta_j \cdot \delta_k \delta_l S_{ij} T_{kl} \\ &= \sum_i \sum_j \sum_k \sum_l \delta_{jk} \delta_i \delta_l S_{ij} T_{kl} \\ &= \sum_i \sum_l \delta_i \delta_l R_{il} \end{aligned} \quad (5.A.11)$$

where

$$R_{il} = \sum_j S_{ij} T_{jl}. \quad (5.A.12)$$

The product of two tensors with two dots between them (the double dot product) is a scalar and is defined by the following:

$$\begin{aligned} \mathbf{S} : \mathbf{T} &= \sum_i \sum_j \sum_k \sum_l \delta_i \delta_j : \delta_k \delta_l S_{ij} T_{kl} \\ &= \sum_i \sum_j \sum_k \sum_l (\delta_j \cdot \delta_k) (\delta_i \cdot \delta_l) S_{ij} T_{kl} \\ &= \sum_i \sum_j \sum_k \sum_l \delta_{jk} \delta_{il} S_{ij} T_{kl} \\ &= \sum_i \sum_j S_{ij} T_{ji} \\ &= \sum_i R_{ii}. \end{aligned} \quad (5.A.13)$$

References

1. Bird R. B., Armstrong, R. C., and Hassager, O., *Dynamics of Polymeric Liquids*, Vol. 1 (2nd edn), Chapter 9, Wiley, New York (1987).
2. Astarita, G., and Marrucci, G., *Principles of Non-Newtonian Fluid Mechanics*, McGraw-Hill, New York (1974).
3. Malvern, L. E., *Introduction to the Mechanics of a Continuous Medium*, Prentice-Hall, Englewood Cliffs, NJ (1969).
4. Aris, R., *Vectors, Tensors, and the Basic Equations of Fluid Mechanics*, Prentice-Hall, Englewood Cliffs, NJ (1962).
5. Rivlin, R. S., *Phil. Trans. Roy. Soc. (London)* **A240**, 459; 491; 509 (1948).
6. Treloar, R. G., *The Physics of Rubber Elasticity*, (3rd edn) Clarendon Press, Oxford (1975).
7. Anthony, R. L., Caston, R. H., and Guth, E., *J. Phys. Chem.* **46**, 826 (1942).

Chapter 6

Molecular Theory of Polymer Viscoelasticity — Elastic Dumbbell Model

6.1 Introduction

In Chapter 3, we used the Rouse model for a polymer chain to study the diffusion motion and the time-correlation function of the end-to-end vector. The Rouse model was first developed to describe polymer viscoelastic behavior in a dilute solution.¹ In spite of its original intention, the theory successfully interprets the viscoelastic behavior of the entanglement-free polymer melt or blend-solution system.^{2,3} The Rouse theory, developed on the Gaussian chain model, effectively simplifies the complexity associated with the large number of intra-molecular degrees of freedom and describes the slow dynamic viscoelastic behavior — slower than the motion of a single Rouse segment.

As discussed in Chapter 3, there are two equivalent ways to describe the Brownian motions of the polymer chain: the Langevin equation and the Smoluchowski equation. For describing the viscoelastic properties, the Smoluchowski equation is more convenient.^{4,5} As a Rouse chain can have many bead-spring segments, it still contains much complexity. Here, we first treat the special simple case of modeling the polymer chain as a dumbbell with two beads connected by a harmonic spring (see Fig. 6.1). The model is often referred to as the elastic dumbbell. The structural simplicity of the elastic dumbbell facilitates demonstration of the theoretical derivations and explanation of the corresponding physical meanings. In Chapter 7, the theoretical result obtained here will be expanded for the Rouse chain, which can have a finite large number of bead-spring segments. The validity of the Rouse theory, as demonstrated by close agreement with experimental results, will be shown in Chapter 11.

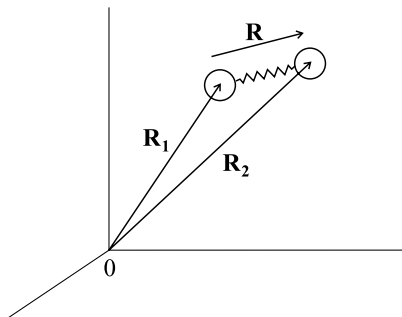


Fig. 6.1 An elastic dumbbell.

6.2 The Smoluchowski Equation for an Elastic Dumbbell

For the dumbbell, as shown in Fig. 6.1, we assume that the two beads have an identical mass m and radius a . Their position vectors are indicated by \mathbf{R}_1 and \mathbf{R}_2 , respectively. Then the “configuration vector” between the two beads is given by

$$\mathbf{R} = \mathbf{R}_2 - \mathbf{R}_1 . \quad (6.1)$$

We assume that the fluid system under consideration has n such dumbbells per unit volume. Each moving bead experiences a friction force which is proportional, with an opposite sign, to the velocity difference between the bead and the fluid flow. The proportionality constant is referred to as the friction constant ζ . In Chapter 3, we studied the special case where there is no fluid flow. Here, a non-zero fluid flow velocity needs to be included for the rheological study. If the polymer chain is surrounded by the solvent, Stoke’s law gives $\zeta = 6\pi\eta_s a$ where η_s is the solvent viscosity.⁶ In a concentrated-solution or melt system, ζ is a parameter that has absorbed all the intermolecular and intersegmental interactions, and depends strongly on temperature, as noted in Chapter 3. In the usual theoretical study of a dynamic problem in the concentrated-solution or melt system, where both the hydrodynamic interaction and excluded volume effect are absent,^{4,7–9} the diameter of the bead is ignored; the bead is treated as a point, and the friction constant just as a parameter. For describing the viscoelastic properties, the elastic dumbbell model and the Rouse model are mean-field theories. The bulk viscoelastic quantity is simply the sum of the statistically-averaged values

from individual model molecules. The friction constant is a basic element of such a mean field.

The fluid velocity field is assumed to be homogeneous and can be expressed as

$$\mathbf{V} = \mathbf{V}_0 + \mathbf{K} \cdot \mathbf{X} \quad (6.2)$$

where \mathbf{V}_0 is a constant, \mathbf{X} is the position vector, and

$$\mathbf{K} = (\nabla \mathbf{V})^T \quad (6.3)$$

which does not change with position, but can change with time. We can make the homogeneous-field assumption because the size of the fluid particle is much smaller than the macroscopic length scale. In the homogeneous flow, the stress tensor is also independent of position. The velocity gradient tensor \mathbf{K} is traceless for an incompressible fluid (Eq. (5.68)).

As seen in Chapter 3, the force constant on the harmonic spring is of entropic origin. The spring forces on bead 1 and bead 2, denoted by \mathbf{F}_1 and \mathbf{F}_2 , respectively, are given by

$$\mathbf{F}_1 = -\frac{\partial V}{\partial \mathbf{R}_1} = \frac{3kT}{R^2} \mathbf{R} = \mathbf{S} \quad (6.4)$$

$$\mathbf{F}_2 = -\frac{\partial V}{\partial \mathbf{R}_2} = -\mathbf{S} \quad (6.5)$$

where \mathbf{S} , referred to as the connector force, has the same direction as \mathbf{R} , and V is the potential of the harmonic spring given by

$$V = \frac{3kT}{2R^2} (\mathbf{R}_2 - \mathbf{R}_1)^2 \quad (6.6)$$

with R^2 denoting the mean square distance between the two beads ($\langle \mathbf{R}^2 \rangle$).

The center-of-mass position of the elastic dumbbell is defined by

$$\mathbf{R}_c = \frac{\mathbf{R}_1 + \mathbf{R}_2}{2}. \quad (6.7)$$

Let $\Psi(\mathbf{R}_1, \mathbf{R}_2) d\mathbf{R}_1 d\mathbf{R}_2$ represent statistically the number of dumbbells that will be found within the configuration range from \mathbf{R}_1 to $\mathbf{R}_1 + d\mathbf{R}_1$ for bead 1 and from \mathbf{R}_2 to $\mathbf{R}_2 + d\mathbf{R}_2$ for bead 2. For a homogeneous flow with no concentration gradient, the configurational distribution of the dumbbells is expected to be independent of the locations of the dumbbells; and we can write

$$\Psi(\mathbf{R}_1, \mathbf{R}_2, t) d\mathbf{R}_1 d\mathbf{R}_2 = \phi(\mathbf{R}_c) \psi(\mathbf{R}, t) d\mathbf{R}_c d\mathbf{R} \quad (6.8)$$

where $\phi(\mathbf{R}_c)$ is the concentration distribution of elastic dumbbells and can be equated with n ; and $\psi(\mathbf{R}, t)$ is the distribution function for the internal configuration at time t . As the Jacobian between $d\mathbf{R}_1 d\mathbf{R}_2$ and $d\mathbf{R}_c d\mathbf{R}$ is one, we can write¹⁰

$$\Psi(\mathbf{R}_1, \mathbf{R}_2, t) = n\psi(\mathbf{R}, t). \quad (6.9)$$

As defined above, $\psi(\mathbf{R}, t)d\mathbf{R}$ is the probability that a randomly selected dumbbell from the fluid system will be in the configuration range \mathbf{R} to $\mathbf{R} + d\mathbf{R}$, and $\psi(\mathbf{R}, t)$ is normalized as

$$\int \psi(\mathbf{R}, t)d\mathbf{R} = 1. \quad (6.10)$$

Then the average value of any dynamic quantity $M(\mathbf{R})$ can be defined by

$$\langle M(t) \rangle = \int M(\mathbf{R})\psi(\mathbf{R}, t)d\mathbf{R}. \quad (6.11)$$

Let the fluid flow velocities at the positions \mathbf{R}_1 and \mathbf{R}_2 be \mathbf{V}_1 and \mathbf{V}_2 , respectively (Eq. (6.2)). Based on Eq. (3.18), we can write the equations of motion for the two beads as

$$\begin{aligned} \zeta(\dot{\mathbf{R}}_1 - \mathbf{V}_1) &= -\frac{\partial}{\partial \mathbf{R}_1}(kT \ln \Psi + V) \\ &= -kT \frac{\partial}{\partial \mathbf{R}_1} \ln \Psi + \mathbf{F}_1 \end{aligned} \quad (6.12)$$

$$\zeta(\dot{\mathbf{R}}_2 - \mathbf{V}_2) = -kT \frac{\partial}{\partial \mathbf{R}_2} \ln \Psi + \mathbf{F}_2. \quad (6.13)$$

Substituting Eqs. (6.2), (6.4), and (6.5) into Eqs. (6.12) and (6.13); and using Eqs. (6.1), (6.7), and (6.9), we can rewrite Eqs. (6.12) and (6.13) in terms of \mathbf{R}_c and \mathbf{R} as

$$\dot{\mathbf{R}} = \mathbf{K} \cdot \mathbf{R} - \frac{2kT}{\zeta} \frac{\partial}{\partial \mathbf{R}} \ln \psi - \frac{2\mathbf{S}}{\zeta} \quad (6.14)$$

and

$$\dot{\mathbf{R}}_c = \mathbf{V}_0 + \mathbf{K} \cdot \mathbf{R}_c. \quad (6.15)$$

Equation (6.15) indicates that the center of mass follows the fluid flow. This result is expected from the assumption made in Eq. (6.9). The continuity

equation for $\Psi(\mathbf{R}_1, \mathbf{R}_2, t)$ is

$$\begin{aligned} \frac{\partial \Psi}{\partial t} &= -\frac{\partial}{\partial \mathbf{R}_1} \cdot \dot{\mathbf{R}}_1 \Psi - \frac{\partial}{\partial \mathbf{R}_2} \cdot \dot{\mathbf{R}}_2 \Psi \\ &= -\frac{\partial}{\partial \mathbf{R}_c} \cdot \dot{\mathbf{R}}_c \Psi - \frac{\partial}{\partial \mathbf{R}} \cdot \dot{\mathbf{R}} \Psi \end{aligned} \quad (6.16)$$

where the second equality results from direct substitution of using Eqs. (6.1) and (6.7). With the substitution of Eqs. (6.9) and (6.15), the first term on the right-hand side of Eq. (6.16) becomes

$$\begin{aligned} -n \frac{\partial}{\partial \mathbf{R}_c} \cdot \dot{\mathbf{R}}_c \psi(\mathbf{R}) &= -n \frac{\partial}{\partial \mathbf{R}_c} \cdot (\mathbf{V}_0 + \mathbf{K} \cdot \mathbf{R}_c) \psi(\mathbf{R}) \\ &= -n(\text{Tr} \mathbf{K}) \psi(\mathbf{R}) = 0 \end{aligned} \quad (6.17)$$

where we have used Eq. (5.68) for the last equality. Thus, Eq. (6.16) becomes

$$\frac{\partial \psi(\mathbf{R})}{\partial t} = -\frac{\partial}{\partial \mathbf{R}} \cdot \dot{\mathbf{R}} \psi(\mathbf{R}). \quad (6.18)$$

Substituting Eq. (6.14) into Eq. (6.18), we obtain the diffusion equation — the Smoluchowsky equation — for $\psi(\mathbf{R})$

$$\frac{\partial \psi(\mathbf{R})}{\partial t} = -\frac{\partial}{\partial \mathbf{R}} \cdot \left([\mathbf{K} \cdot \mathbf{R}] \psi - \frac{2kT}{\zeta} \frac{\partial \psi}{\partial \mathbf{R}} - \frac{2\mathbf{S}\psi}{\zeta} \right). \quad (6.19)$$

This equation describes how the distribution function $\psi(\mathbf{R})$ changes with time under the velocity field \mathbf{K} . When $\mathbf{K} = 0$, the form of Eq. (6.19) becomes similar to that of Eq. (3.15).

To obtain the average value of a physical quantity $\langle M \rangle$, it is not necessary to first calculate the distribution function $\psi(\mathbf{R})$ from Eq. (6.19) and then substitute it into Eq. (6.11). From Eq. (6.11)

$$\frac{d\langle M \rangle}{dt} = \int M \frac{\partial \psi}{\partial t} d\mathbf{R}. \quad (6.20)$$

Substituting Eq. (6.18) into Eq. (6.20), and by means of integration by parts, we obtain

$$\begin{aligned} \frac{d\langle M \rangle}{dt} &= -\int \frac{\partial}{\partial \mathbf{R}} \cdot (\dot{\mathbf{R}} \psi M) d\mathbf{R} + \int \dot{\mathbf{R}} \psi \cdot \frac{\partial M}{\partial \mathbf{R}} d\mathbf{R} \\ &= \left\langle \dot{\mathbf{R}} \cdot \frac{\partial M}{\partial \mathbf{R}} \right\rangle. \end{aligned} \quad (6.21)$$

In Eq. (6.21), we have used the Gauss divergence theorem and the condition that $\psi(\mathbf{R}) = 0$ on the surface at $R = \infty$.

Substituting Eq. (6.14) into Eq. (6.21) and by using integration by parts and the Gauss divergence theorem, we obtain

$$\frac{d\langle M \rangle}{dt} = \left\langle \mathbf{K} \cdot \mathbf{R} \cdot \frac{\partial M}{\partial \mathbf{R}} \right\rangle + \frac{2kT}{\zeta} \left\langle \frac{\partial}{\partial \mathbf{R}} \cdot \frac{\partial M}{\partial \mathbf{R}} \right\rangle - \frac{2}{\zeta} \left\langle \mathbf{S} \cdot \frac{\partial M}{\partial \mathbf{R}} \right\rangle. \quad (6.22)$$

We shall be particularly interested in the case where

$$M = \mathbf{R}\mathbf{R}. \quad (6.23)$$

Substituting Eq. (6.23) into Eq. (6.22), we obtain

$$\frac{d\langle \mathbf{R}\mathbf{R} \rangle}{dt} = \mathbf{K} \cdot \langle \mathbf{R}\mathbf{R} \rangle + \langle \mathbf{R}\mathbf{R} \rangle \cdot \mathbf{K}^T + \frac{4kT}{\zeta} \boldsymbol{\delta} - \frac{4}{\zeta} \langle \mathbf{R}\mathbf{S} \rangle. \quad (6.24)$$

To get the last term of Eq. (6.24), we use the fact that \mathbf{R} and \mathbf{S} are in the same direction (Eq. (6.4)).

Defining

$$\langle \mathbf{R}\mathbf{R} \rangle_{(1)} = \frac{d\langle \mathbf{R}\mathbf{R} \rangle}{dt} - \mathbf{K} \cdot \langle \mathbf{R}\mathbf{R} \rangle - \langle \mathbf{R}\mathbf{R} \rangle \cdot \mathbf{K}^T. \quad (6.25)$$

Equation (6.24) is rewritten as

$$\langle \mathbf{R}\mathbf{R} \rangle_{(1)} = \frac{4kT}{\zeta} \boldsymbol{\delta} - \frac{4}{\zeta} \langle \mathbf{R}\mathbf{S} \rangle. \quad (6.26)$$

With the homogeneous flow assumption, whereby $\nabla \langle \mathbf{R}\mathbf{R} \rangle = 0$, the definition of $\langle \mathbf{R}\mathbf{R} \rangle_{(1)}$ as given by Eq. (6.25) is the same as the codeformational time derivative or convected time derivative shown in Appendix 6.A.

When $\mathbf{K} = 0$ and the fluid system is in the equilibrium state, $d/dt \langle \mathbf{R}\mathbf{R} \rangle = 0$, and Eq. (6.24) gives

$$\langle \mathbf{R}\mathbf{S} \rangle_{eq} = kT\boldsymbol{\delta}. \quad (6.27)$$

If $\mathbf{S} = H\mathbf{R}$, the force constant H is obtained from Eq. (6.27) to be $3kT/R^2$, which is identical to the entropic force constant used in Eqs. (3.31) and (6.4).

6.3 Rheological Constitutive Equation of the Elastic Dumbbell Model

Below, we shall consider the contribution of the dumbbell molecule to the stress tensor of the fluid. If the fluid system is a polymer solution, the total stress tensor of the system can be separated into two parts: \mathbf{T}_s from the solvent and \mathbf{T}_p from the polymer.

$$\begin{aligned}\mathbf{T} &= \mathbf{T}_s + \mathbf{T}_p \\ &= (P_s \boldsymbol{\delta} + \boldsymbol{\tau}_s) + (P_p \boldsymbol{\delta} + \boldsymbol{\tau}_p) \\ &= P \boldsymbol{\delta} + \boldsymbol{\tau}\end{aligned}\tag{6.28}$$

where the definition given by Eq. (5.10) is used, giving

$$P = P_s + P_p\tag{6.29}$$

and

$$\boldsymbol{\tau} = \boldsymbol{\tau}_s + \boldsymbol{\tau}_p = -\eta_s \dot{\boldsymbol{\gamma}} + \boldsymbol{\tau}_p.\tag{6.30}$$

In Eq. (6.30), η_s is the solvent viscosity (see Eq. (5.61)), and

$$\dot{\boldsymbol{\gamma}} = \nabla \mathbf{V} + (\nabla \mathbf{V})^T.\tag{6.31}$$

For $\mathbf{K} = 0$, $\mathbf{T} = P \boldsymbol{\delta}$. In a polymer melt or concentrated solution, $\boldsymbol{\tau}_s$ is either zero or negligible in comparison with $\boldsymbol{\tau}_p$. In Eq. (6.28), \mathbf{T}_p from the dumbbell contains two parts: (a) Any plane in the fluid has the probability of being crossed by a dumbbell at any moment, and in general, a tensile force will be transmitted across the plane by the spring connector; (b) A particular bead of the dumbbell can move across the plane, carrying a certain momentum. The contributions of the connectors and the beads to \mathbf{T}_p are denoted by \mathbf{T}_p^c and \mathbf{T}_p^b , respectively.

(a) Contribution from tension in the connector¹¹

Consider a plane which moves with the local velocity \mathbf{V} in the fluid. Let the direction of the selected plane be denoted by the unit vector \mathbf{n} . Set up a cube which contains an average of only one dumbbell and has a volume of $1/n$. The plane cuts across the middle of the cube as shown in Fig. 6.2. If a dumbbell with the configuration vector \mathbf{R} is randomly thrown into the cube (in other words, its center of mass may, with equal probability, reach

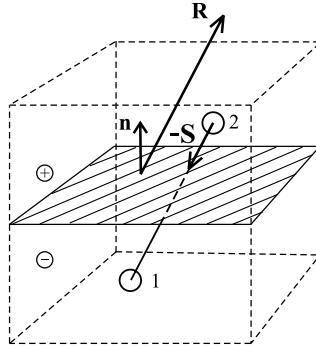


Fig. 6.2 A dumbbell with bond vector \mathbf{R} intersecting an arbitrary plane (shaded) of area $(1/n)^{2/3}$ in a suspension of dumbbells. The plane is moving with the local velocity and has the direction represented by the unit vector \mathbf{n} . The $(-)$ side of the plane exerts a force $-\mathbf{S} = \mathbf{F}_2$ (Eq. (6.5)) to the $(+)$ side through the bond. The dashed lines indicate a cube of volume $1/n$.

at any point inside the cube), the probability that the dumbbell will cross the plane is

$$\frac{\text{Projection of } \mathbf{R} \text{ along the direction of } \mathbf{n}}{\text{side length of the cube}} = \frac{|\mathbf{n} \cdot \mathbf{R}|}{n^{-1/3}}. \quad (6.32)$$

At the same time, the probability that the configuration of the dumbbell is in the range \mathbf{R} to $\mathbf{R} + d\mathbf{R}$ is $\psi(\mathbf{R}, t)d\mathbf{R}$. Thus, the probability that a dumbbell in the range \mathbf{R} to $\mathbf{R} + d\mathbf{R}$ will cross the plane is $|\mathbf{n} \cdot \mathbf{R}|(n^{1/3})\psi(\mathbf{R}, t) d\mathbf{R}$. If bead 2 is on the $(+)$ side of the plane, $|\mathbf{n} \cdot \mathbf{R}| = \mathbf{n} \cdot \mathbf{R}$ and the force exerted on the $(+)$ side from the $(-)$ side is $-\mathbf{S}$; if bead 1 is on the $(+)$ side, $|\mathbf{n} \cdot \mathbf{R}| = -\mathbf{n} \cdot \mathbf{R}$ and the force exerted on the $(+)$ side from the $(-)$ side is \mathbf{S} . Thus, the expectation value of the force exerted from the $(-)$ side to the $(+)$ side of the cube (see Fig. 6.2) through the dumbbell is

$$-n^{1/3} \int (\mathbf{n} \cdot \mathbf{R})\mathbf{S}\psi(\mathbf{R}, t)d\mathbf{R}. \quad (6.33)$$

Dividing this value by the area of the plane $(1/n)^{2/3}$ gives the force per unit area

$$-n \int (\mathbf{n} \cdot \mathbf{R})\mathbf{S}\psi(\mathbf{R}, t)d\mathbf{R} = -n \left[\mathbf{n} \cdot \int \mathbf{R}\mathbf{S}\psi(\mathbf{R}, t)d\mathbf{R} \right]. \quad (6.34)$$

The expectation value given by Eq. (6.34) needs to be equal to $\mathbf{n} \cdot \mathbf{T}_p^c$ (see Eq. (5.7)). Thus the contribution of the connector of the dumbbell to the

stress tensor is

$$\begin{aligned}\mathbf{T}_p^c &= -n \int \mathbf{R}\mathbf{S}\psi(\mathbf{R}, t)d\mathbf{R} \\ &= -n\langle\mathbf{R}\mathbf{S}\rangle.\end{aligned}\quad (6.35)$$

(b) *Contribution due to bead motion*

Because of the momentum it carries, any bead moving across a plane will contribute to the stress tensor. To obtain the value contributed by this mechanism, we first ask how many “1” beads with velocity $\dot{\mathbf{R}}_1$ will, in a unit time, pass through any chosen plane of area S and direction \mathbf{n} . This value is the product of the number of dumbbells per unit volume n and the volume of the parallelepiped, as shown in Fig. 6.3, namely,

$$n[(\dot{\mathbf{R}}_1 - \mathbf{V}_1) \cdot S\mathbf{n}]. \quad (6.36)$$

Then the momentum carried across the shaded plane (Fig. 6.3) is

$$n[(\dot{\mathbf{R}}_1 - \mathbf{V}_1) \cdot S\mathbf{n}]m(\dot{\mathbf{R}}_1 - \mathbf{V}_1). \quad (6.37)$$

Thus, the expectation value of the momentum flux is

$$nm \iint [\mathbf{n} \cdot (\dot{\mathbf{R}}_1 - \mathbf{V}_1)(\dot{\mathbf{R}}_1 - \mathbf{V}_1)] \Xi(\dot{\mathbf{R}}_1, \dot{\mathbf{R}}_2) d\dot{\mathbf{R}}_1 d\dot{\mathbf{R}}_2 \quad (6.38)$$

where $\Xi(\dot{\mathbf{R}}_1, \dot{\mathbf{R}}_2)$ is the velocity distribution function, which is assumed to be described by the Maxwellian distribution. Including the contribution

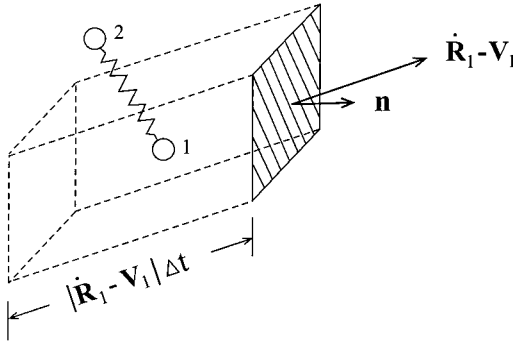


Fig. 6.3 A bead of a dumbbell carries its momentum in crossing an arbitrary surface (shaded) moving with the local velocity, contributing to the stress tensor.

from “2” beads, we obtain the total value

$$nm \iint \mathbf{n} \cdot \left[\sum_{i=1}^2 (\dot{\mathbf{R}}_i - \mathbf{V}_i)(\dot{\mathbf{R}}_i - \mathbf{V}_i) \right] \Xi(\dot{\mathbf{R}}_1, \dot{\mathbf{R}}_2) d\dot{\mathbf{R}}_1 d\dot{\mathbf{R}}_2. \quad (6.39)$$

This expectation value must be equal to $\mathbf{n} \cdot \mathbf{T}_p^b$. Thus,

$$\mathbf{T}_p^b = n \iint \left[\sum_{i=1}^2 m(\dot{\mathbf{R}}_i - \mathbf{V}_i)(\dot{\mathbf{R}}_i - \mathbf{V}_i) \right] \Xi(\dot{\mathbf{R}}_1, \dot{\mathbf{R}}_2) d(\dot{\mathbf{R}}_1 - \mathbf{V}_1) d(\dot{\mathbf{R}}_2 - \mathbf{V}_2). \quad (6.40)$$

Substituting the Maxwellian distribution and $\dot{\mathbf{R}}_i - \mathbf{V}_i = \mathbf{v}_i$ into Eq. (6.40), we obtain

$$\begin{aligned} \mathbf{T}_p^b &= \frac{n \iint \left(\sum_{i=1}^2 m \mathbf{v}_i \mathbf{v}_i \right) \exp \left(- \sum_{i=1}^2 m \mathbf{v}_i^2 / 2kT \right) d\mathbf{v}_1 d\mathbf{v}_2}{\iint \exp \left(- \sum_{i=1}^2 m \mathbf{v}_i^2 / 2kT \right) d\mathbf{v}_1 d\mathbf{v}_2} \\ &= 2nkT\boldsymbol{\delta}. \end{aligned} \quad (6.41)$$

Thus the motions of the beads only contribute to the normal stress.

Combining the contributions of \mathbf{T}_p^c and \mathbf{T}_p^b , as given by Eqs. (6.35) and (6.41), we have

$$\mathbf{T}_p = -n\langle \mathbf{RS} \rangle + 2nkT\boldsymbol{\delta}. \quad (6.42)$$

And Eq. (6.28) may be written as

$$\mathbf{T} = \mathbf{T}_s + \mathbf{T}_p = \mathbf{T}_s - n\langle \mathbf{RS} \rangle + 2nkT\boldsymbol{\delta}. \quad (6.43)$$

At equilibrium, $\mathbf{T}_s = P_s\boldsymbol{\delta}$, and $\langle \mathbf{RS} \rangle_{eq} = kT\boldsymbol{\delta}$ (Eq. (6.27)), so

$$\mathbf{T} = P_s\boldsymbol{\delta} - nkT\boldsymbol{\delta} + 2nkT\boldsymbol{\delta} = P\boldsymbol{\delta}. \quad (6.44)$$

Thus $P = P_s + nkT$ or

$$P_p = nkT. \quad (6.45)$$

Therefore, from Eqs. (6.28), (6.42), and (6.45), we obtain

$$\boldsymbol{\tau}_p = -n\langle \mathbf{RS} \rangle + nkT\boldsymbol{\delta} \quad (6.46)$$

and

$$\boldsymbol{\tau} = \boldsymbol{\tau}_s + \boldsymbol{\tau}_p = -\eta_s \dot{\boldsymbol{\gamma}} - n\langle \mathbf{RS} \rangle + nkT\boldsymbol{\delta}. \quad (6.47)$$

Equation (6.47) was first derived by Kramers.¹²

By eliminating the $\langle \mathbf{RS} \rangle$ term between Eqs. (6.26) and (6.47), we obtain

$$\boldsymbol{\tau} = -\eta_s \dot{\boldsymbol{\gamma}} + \frac{n\zeta}{4} \langle \mathbf{RR} \rangle_{(1)} \quad (6.48)$$

which is referred to as the Giesekus expression for the stress tensor.¹³ As we are mainly interested in the concentrated-solution or melt system, we shall neglect the solvent viscosity term in Eq. (6.48).

$$\boldsymbol{\tau} = \boldsymbol{\tau}_p = \frac{n\zeta}{4} \langle \mathbf{RR} \rangle_{(1)}. \quad (6.49)$$

So far, in deriving Eqs. (6.26) and (6.47), we have only used the relation that \mathbf{R} and \mathbf{S} are in the same direction. By substituting the Hooke relation, Eq. (6.4), into Eq. (6.46), we obtain

$$\boldsymbol{\tau} = \boldsymbol{\tau}_p = \frac{-3nkT}{R^2} \langle \mathbf{RR} \rangle + nkT \boldsymbol{\delta}. \quad (6.50)$$

By performing the convected differentiation operation (see Appendix 6.A), Eq. (6.50) is transformed to

$$\begin{aligned} \boldsymbol{\tau}_{(1)} &= \frac{-3nkT}{R^2} \langle \mathbf{RR} \rangle_{(1)} + nkT \boldsymbol{\delta}_{(1)} \\ &= \frac{-3nkT}{R^2} \langle \mathbf{RR} \rangle_{(1)} - nkT \dot{\boldsymbol{\gamma}} \end{aligned} \quad (6.51)$$

where $\boldsymbol{\delta}_{(1)} = -\boldsymbol{\gamma}_{(1)} = -\dot{\boldsymbol{\gamma}}$ is given by Eq. (6.A.26). By eliminating $\langle \mathbf{RR} \rangle_{(1)}$ between Eqs. (6.49) and (6.51), we obtain the constitutive equation for the elastic dumbbell model:

$$\boldsymbol{\tau} + s \boldsymbol{\tau}_{(1)} = -\eta \dot{\boldsymbol{\gamma}} = -\eta \boldsymbol{\gamma}_{(1)} \quad (6.52)$$

where

$$\eta = nkTs \quad (6.53)$$

and s is the relaxation-time constant for the elastic dumbbell:

$$s = \frac{\zeta R^2}{12kT}. \quad (6.54)$$

Equation (6.52) has the exact form of a “convected Maxwell model.” Therefore, many results from continuum mechanics can be applied to Eq. (6.52) directly. The relevant aspects of continuum mechanics are discussed in Appendix 6.A. The rheological tensors in Eq. (6.52) are all evaluated by following a particular fluid particle at any “current” moment t . Since a particular fluid point is followed, t may be replaced by a past time t' .

For a certain fluid particle (\mathbf{X}, t) , we multiply each term in Eq. (6.52) by $\mathbf{E}(\mathbf{X}, t, t')$, which is placed on the left side, and by $\mathbf{E}(\mathbf{X}, t, t')^T$, which is placed on the right:

$$\begin{aligned} & \mathbf{E}(t, t') \cdot \boldsymbol{\tau}(t') \cdot \mathbf{E}(t, t')^T + s\mathbf{E}(t, t') \cdot \boldsymbol{\tau}_{(1)}(t') \cdot \mathbf{E}(t, t')^T \\ & = -\eta\mathbf{E}(t, t') \cdot \boldsymbol{\gamma}_{(1)}(t') \cdot \mathbf{E}(t, t')^T. \end{aligned} \quad (6.55)$$

Equation (6.55) may be rewritten as (see Eqs. (6.A.14), (6.A.19), and (6.A.21))

$$\boldsymbol{\tau}_{[0]}(t, t') + s\boldsymbol{\tau}_{[1]}(t, t') = -\eta\boldsymbol{\gamma}_{[1]}(t, t') \quad (6.56)$$

which is

$$\boldsymbol{\tau}_{[0]}(t, t') + s\frac{\partial}{\partial t'}\boldsymbol{\tau}_{[0]}(t, t') = -\eta\boldsymbol{\gamma}_{[1]}(t, t'). \quad (6.57)$$

Equation (6.57) is an inhomogeneous first-order linear differential equation of the tensor $\boldsymbol{\tau}_{[0]}$ in the range $-\infty < t' < t$. With the condition that $\boldsymbol{\tau}_{[0]}$ is finite at $t' = -\infty$, we may obtain the solution for $\boldsymbol{\tau}_{[0]}$. $\boldsymbol{\tau}_{[0]}(t, t) = \boldsymbol{\tau}(t)$, as the convected coordinates coincide with the fixed coordinates when $t' = t$. Thus,

$$\begin{aligned} \boldsymbol{\tau}(t) &= -\int_{-\infty}^t \frac{\eta}{s} \exp[-(t-t')/s] \boldsymbol{\gamma}_{[1]}(t, t') dt' \\ &= -\int_{-\infty}^t nkT \exp[-(t-t')/s] \boldsymbol{\gamma}_{[1]}(t, t') dt'. \end{aligned} \quad (6.58)$$

Using integration by parts, Eq. (6.58) may be transformed to

$$\boldsymbol{\tau}(t) = \int_{-\infty}^t \frac{nkT}{s} \exp[-(t-t')/s] \boldsymbol{\gamma}_{[0]}(t, t') dt' \quad (6.59)$$

where $\boldsymbol{\gamma}_{[0]}(t, t')$ is given by Eq. (6.A.6). Equations (6.58) and (6.59) are different from Eqs. (4.14) and (4.15) in that the former equations, involving three dimensions, can be used for large deformations; the latter, with stress and strain expressed as scalar quantities, are limited to small deformations.

6.4 Applications of the Constitutive Equation

We shall illustrate the applications of the constitutive Eq. (6.59) in two cases: stress relaxation following a step shear deformation and steady-state shear flow.

(a) Stress relaxation

For a step shear deformation applied at $t' = 0$, the displacement functions are

$$\begin{aligned} X'_1 &= X_1 && \text{for } t' > 0 \\ X'_1 &= X_1 - \lambda X'_2 && \text{for } t' < 0 \\ X'_2 &= X_2 && \text{for all } t' \\ X'_3 &= X_3 && \text{for all } t'. \end{aligned} \quad (6.60)$$

Applying Eq. (5.16) to Eq. (6.60), we obtain

$$\mathbf{E} = \begin{pmatrix} 1 & 0 & 0 \\ 0 & 1 & 0 \\ 0 & 0 & 1 \end{pmatrix} \quad \text{for } t' > 0 \quad (6.61a)$$

and

$$\mathbf{E} = \begin{pmatrix} 1 & \lambda & 0 \\ 0 & 1 & 0 \\ 0 & 0 & 1 \end{pmatrix} \quad \text{for } t' < 0. \quad (6.61b)$$

Substituting Eq. (6.61) into Eq. (6.A.6), we obtain

$$\boldsymbol{\gamma}_{[0]} = 0 \quad \text{for } t' > 0 \quad (6.62a)$$

and

$$\boldsymbol{\gamma}_{[0]} = \begin{pmatrix} -\lambda^2 & -\lambda & 0 \\ -\lambda & 0 & 0 \\ 0 & 0 & 0 \end{pmatrix} \quad \text{for } t' < 0. \quad (6.62b)$$

Substituting Eq. (6.62) into Eq. (6.59), we obtain

$$\boldsymbol{\tau}(t) = \begin{pmatrix} \tau_{11}(t) & \tau_{12}(t) & 0 \\ \tau_{21}(t) & 0 & 0 \\ 0 & 0 & 0 \end{pmatrix} \quad (6.63)$$

where the shear stress is

$$\tau_{12}(t) = \tau_{21}(t) = -\lambda nkT \exp\left(-\frac{t}{s}\right) \quad (6.64a)$$

or the shear relaxation modulus

$$G(t) = -\frac{\tau_{12}(t)}{\lambda} = nkT \exp\left(-\frac{t}{s}\right) \quad (6.64b)$$

and the first normal-stress difference is

$$\tau_{11}(t) - \tau_{22}(t) = \tau_{11}(t) = -\lambda^2 nkT \exp\left(-\frac{t}{s}\right) \quad (6.65)$$

while the second normal-stress difference $\tau_{22}(t) - \tau_{33}(t)$ is zero. The shear relaxation modulus of the elastic dumbbell model (Eq. (6.64b)) does not show a strain dependence and is equivalent to the linear viscoelastic result, Eq. (4.28). However, Eq. (6.65) is a nonlinear result.

(b) Steady-state shear flow

In maintaining a steady-state shear flow, the displacement functions are given by

$$X'_1 = X_1 - \dot{\lambda}_0(t - t')X_2 \quad (6.66a)$$

$$X'_2 = X_2 \quad (6.66b)$$

$$X'_3 = X_3. \quad (6.66c)$$

Applying Eq. (5.16) to Eq. (6.66), we obtain

$$\mathbf{E} = \begin{pmatrix} 1 & \dot{\lambda}_0(t - t') & 0 \\ 0 & 1 & 0 \\ 0 & 0 & 1 \end{pmatrix}. \quad (6.67)$$

The substitution of Eq. (6.67) into Eq. (6.A.6) gives

$$\boldsymbol{\gamma}_{[0]} = - \begin{pmatrix} \dot{\lambda}_0^2(t - t')^2 & \dot{\lambda}_0(t - t') & 0 \\ \dot{\lambda}_0(t - t') & 0 & 0 \\ 0 & 0 & 0 \end{pmatrix}. \quad (6.68)$$

Substituting Eq. (6.68) into Eq. (6.59), we obtain

$$\boldsymbol{\tau} = \begin{pmatrix} \tau_{11} & \tau_{12} & 0 \\ \tau_{21} & 0 & 0 \\ 0 & 0 & 0 \end{pmatrix} \quad (6.69)$$

where the shear stress is

$$\tau_{12} = \tau_{21} = -nkTs\dot{\lambda}_0 \quad (6.70a)$$

or the viscosity

$$\eta_0 = -\frac{\tau_{12}}{\dot{\lambda}_0} = nkTs \quad (6.70b)$$

and the first normal-stress coefficient is given by

$$\Psi_1 = -\frac{(\tau_{11} - \tau_{22})}{\dot{\lambda}_0^2} = 2nkTs^2 \quad (6.71)$$

while the second normal-stress coefficient $\Psi_2 = -(\tau_{22} - \tau_{33})/\dot{\lambda}_0^2$ is zero.

The viscosity result (Eq. (6.70b)) is the same as what will be obtained from substituting the relaxation modulus (Eq. (6.64b)) into the linear viscoelastic relation (Eq. (4.30)). Similar to Eq. (6.65), Eq. (6.71) is a non-linear result.

Equation (6.70) indicates that the viscosity is independent of the shear rate $\dot{\lambda}_0$. However, it is well known that the polymeric liquid exhibits non-Newtonian behavior, namely, that the viscosity value decreases with increasing shear rate after the rate reaches a certain value. This discrepancy is a weak point of the elastic dumbbell model and arises from an inherent weakness in the Gaussian distribution assumed for the connector vector. We can see the cause of this deficiency from the following analysis of how the dumbbell configuration changes with shear rate.

Under steady shear at a certain rate, the mean square end-to-end distance of an elastic dumbbell is given by

$$\langle \mathbf{R}^2 \rangle = \text{Tr} \langle \mathbf{R}\mathbf{R} \rangle. \quad (6.72)$$

Taking the trace of Eq. (6.50) and substituting the result into Eq. (6.72), we obtain

$$\begin{aligned} \frac{\langle \mathbf{R}^2 \rangle}{\langle \mathbf{R}^2 \rangle_{eq}} &= 1 - \frac{\text{Tr}(\boldsymbol{\tau})}{3nkT} \\ &= 1 + \frac{2(s\dot{\lambda}_0)^2}{3} \end{aligned} \quad (6.73)$$

where, for the second equality, Eq. (6.69) has been used. Equation (6.73) indicates that the elastic dumbbell can be stretched to become infinitely long by increasing the shear rate. Such a situation, of course, cannot occur in reality as the end-to-end distance of a polymer chain can at most be stretched to its backbone-contour length, which is limited by very rigid chemical bonds. The infinite extensibility of the elastic-dumbbell connector is related to the predicted constant viscosity value at all shear rates.

Theoretically, Eq. (6.58) is applicable in both the linear and nonlinear regions, as Eqs. (5.49) and (5.61) are for the elastic and viscous limits, respectively. One can note that as the relaxation time s becomes

infinitely long or infinitely short, Eq. (6.58) reduces to Eqs. (5.49) or (5.61), respectively.

In the linear region, the viscoelastic properties, $G'(\omega)$, $G''(\omega)$, J_e^0 etc., can be obtained from the relaxation modulus using Eq. (6.58) or (6.59) just as they can from the linear viscoelastic relations given in Chapter 4. The relaxation modulus of the elastic dumbbell model contains only a single relaxation time (Eq. (6.64)). This result is clearly too simple and is inconsistent with the observed viscoelastic spectrum whose relaxation-time distribution usually has a considerable width. However, the study of the elastic dumbbell model in this chapter shows the basic theoretical steps required to treat the Rouse chain, which consists of a finite large number of bead-spring segments. As the elastic dumbbell model gives a theoretical form which is equivalent to the convected Maxwell model, the Rouse model yields a form which is equivalent to the convected generalized Maxwell model. In addition, all the relaxation times are expressed in terms of the molecular parameters in the Rouse model.

Appendix 6.A — Codeformational (Convected) Time Derivative

We can label a particle or a point in a material system by giving its position \mathbf{X} (with the Cartesian components X_1, X_2, X_3) at the present time t and denoting it as (\mathbf{X}, t) . The position of the particle (\mathbf{X}, t) at a past time t' is called \mathbf{X}' . The motion of the material is then given by the displacement function:

$$\mathbf{X}' = \mathbf{X}'(\mathbf{X}, t, t') \tag{6.A.1}$$

which tells the position \mathbf{X}' of each particle (\mathbf{X}, t) for all past times t' . The displacement function is continuous and can be inverted to give

$$\mathbf{X} = \mathbf{X}(\mathbf{X}', t, t'). \tag{6.A.2}$$

In Chapter 5, we defined the deformation gradient tensor \mathbf{E} , Cauchy tensor \mathbf{C} , and Finger tensor \mathbf{B} , respectively, as

$$\mathbf{E}(\mathbf{X}, t, t') = (\nabla' \mathbf{X})^T \tag{6.A.3}$$

$$\mathbf{C}(\mathbf{X}, t, t') = \mathbf{E}^T \cdot \mathbf{E} \tag{6.A.4}$$

$$\mathbf{B}(\mathbf{X}, t, t') = \mathbf{E} \cdot \mathbf{E}^T \tag{6.A.5}$$

where (\mathbf{X}, t, t') denotes a material point or particle (\mathbf{X}, t) at a past time t' . Corresponding to the role of the Finger strain tensor \mathbf{B} described in Chapter 5, we define the relative strain tensor $\boldsymbol{\gamma}_{[0]}(\mathbf{X}, t, t')$ as

$$\boldsymbol{\gamma}_{[0]}(\mathbf{X}, t, t') = \boldsymbol{\delta} - \mathbf{B} = \boldsymbol{\delta} - \mathbf{E} \cdot \mathbf{E}^T \quad (6.A.6)$$

which is zero for a rigid-body rotation or when $t' = t$.

We consider the convected coordinate system embedded in a flowing fluid and deforming with it. The convected coordinates denoted by $\hat{X}^1, \hat{X}^2, \hat{X}^3$ remain the same for all the times and exactly coincide with the Cartesian coordinates X_1, X_2, X_3 at time t . Thus, we can label the fluid particle either by the variables $\hat{X}^1, \hat{X}^2, \hat{X}^3$ or with the variables X_1, X_2, X_3 , and t .

Let $d\mathbf{X}'$ be the vector between two neighboring fluid particles at time t' and $\hat{\mathbf{g}}_i$ be the base vector tangent to the \hat{X}^i -coordinate curve ($\hat{\mathbf{g}}_i$ is a function of (\mathbf{X}, t, t') or $(\hat{X}^1, \hat{X}^2, \hat{X}^3, t')$ and referred to as the convected base vector). Then $d\mathbf{X}'$ can be either expressed as

$$d\mathbf{X}' = \sum_{j=1}^3 \boldsymbol{\delta}_j dX'_j \quad (6.A.7)$$

or as

$$d\mathbf{X}' = \sum_{i=1}^3 \hat{\mathbf{g}}_i d\hat{X}^i \quad (6.A.8)$$

where

$$\begin{aligned} \hat{\mathbf{g}}_i &= \frac{\partial \mathbf{X}'}{\partial \hat{X}^i} \\ &= \frac{\partial}{\partial \hat{X}^i} \left(\sum_j \boldsymbol{\delta}_j X'_j \right) \\ &= \frac{\partial}{\partial X_i} \left(\sum_j \boldsymbol{\delta}_j X'_j \right) \\ &= \sum_j \boldsymbol{\delta}_j \frac{\partial X'_j}{\partial X_i} \\ &= \sum_j \boldsymbol{\delta}_j D_{ji} \\ &= \mathbf{D} \cdot \boldsymbol{\delta}_i \end{aligned} \quad (6.A.9)$$

with \mathbf{D} defined by

$$\mathbf{D}(\mathbf{X}, t, t') = (\nabla \mathbf{X}')^T \quad (6.A.10)$$

which is the inverse of \mathbf{E} , i.e.

$$\mathbf{D} \cdot \mathbf{E} = \boldsymbol{\delta}. \quad (6.A.11)$$

The stress tensor of the fluid particle (\mathbf{X}, t) at time t' , $\boldsymbol{\tau}(\mathbf{X}, t, t')$, can be expanded either in terms of unit vectors at the present time t and Cartesian components τ_{ij} or in terms of the convected base vectors at position \mathbf{X}' and time t' and contravariant components $\hat{\tau}^{ij}$ as shown in the following:

$$\begin{aligned} \boldsymbol{\tau}(\mathbf{X}, t, t') &= \sum_i \sum_j \boldsymbol{\delta}_i \boldsymbol{\delta}_j \tau_{ij} \\ &= \sum_i \sum_j \hat{\mathbf{g}}_i \hat{\mathbf{g}}_j \hat{\tau}^{ij} \\ &= \sum_i \sum_j (\mathbf{D} \cdot \boldsymbol{\delta}_i) (\mathbf{D} \cdot \boldsymbol{\delta}_j) \hat{\tau}^{ij} \\ &= \mathbf{D} \cdot \boldsymbol{\tau}_{[0]} \cdot \mathbf{D}^T \end{aligned} \quad (6.A.12)$$

where Eq. (6.A.9) has been used, and

$$\boldsymbol{\tau}_{[0]} = \sum_i \sum_j \boldsymbol{\delta}_i \boldsymbol{\delta}_j \hat{\tau}^{ij} \quad (6.A.13)$$

whose components associated with the unit vectors at the present time t are equivalent to the contravariant components of $\boldsymbol{\tau}(\mathbf{X}, t, t')$. We need to express the contravariant components $\hat{\tau}^{ij}$ in terms of the Cartesian components τ_{ij} . Using Eq. (6.A.11), this transformation can be obtained from Eq. (6.A.12) as

$$\boldsymbol{\tau}_{[0]}(\mathbf{X}, t, t') = \mathbf{E}(\mathbf{X}, t, t') \cdot \boldsymbol{\tau}(\mathbf{X}, t, t') \cdot \mathbf{E}^T(\mathbf{X}, t, t'). \quad (6.A.14)$$

When $t = t'$, $\boldsymbol{\tau}_{[0]}$ is equal to $\boldsymbol{\tau}(\mathbf{X}, t, t)$.

Both $\boldsymbol{\gamma}_{[0]}$ and $\boldsymbol{\tau}_{[0]}$ are codeformational rheological tensors. They can describe the deformation and the stress response to a deformation without interference from the rigid-body rotation (see Chapter 5). In other words, these tensors and their time derivatives, integrations, and combinations

allow us to establish an objective constitutive equation. The expressions for the time derivatives of $\boldsymbol{\gamma}_{[0]}$ and $\boldsymbol{\tau}_{[0]}$ are derived in the following:

We shall first consider the changing rate of \mathbf{D} and \mathbf{E} with time, following the fluid particle (\mathbf{X}, t) . From Eq. (6.A.10),

$$\begin{aligned}
 \frac{\partial}{\partial t'} \mathbf{D}(\mathbf{X}, t, t') &= \sum_i \sum_j \delta_i \delta_j \frac{\partial}{\partial t'} \frac{\partial X'_i}{\partial X_j} \\
 &= \sum_i \sum_j \delta_i \delta_j \frac{\partial}{\partial X_j} \frac{\partial X'_i}{\partial t'} \\
 &= \sum_i \sum_j \delta_i \delta_j \frac{\partial}{\partial X_j} V'_i(\mathbf{X}, t, t') \\
 &= \sum_i \sum_j \delta_i \delta_j \sum_s \left(\frac{\partial V'_i}{\partial X'_s} \right) \left(\frac{\partial X'_s}{\partial X_j} \right) \\
 &= \sum_i \sum_j \delta_i \delta_j \sum_s (\nabla \mathbf{V})_{si} D_{sj} \\
 &= (\nabla \mathbf{V})^T \cdot \mathbf{D}.
 \end{aligned} \tag{6.A.15}$$

Here, it is understood that \mathbf{D} and $\nabla \mathbf{V}$ are evaluated at t' for the fluid particle (\mathbf{X}, t) .

From Eq. (6.A.11),

$$\frac{\partial}{\partial t'} (\mathbf{E} \cdot \mathbf{D}) = \frac{\partial \mathbf{E}}{\partial t'} \cdot \mathbf{D} + \mathbf{E} \cdot \frac{\partial \mathbf{D}}{\partial t'} = 0. \tag{6.A.16}$$

Using Eqs. (6.A.11) and (6.A.15), we obtain from Eq. (6.A.16)

$$\begin{aligned}
 \frac{\partial \mathbf{E}}{\partial t'} &= -\mathbf{E} \cdot \left(\frac{\partial \mathbf{D}}{\partial t'} \right) \cdot \mathbf{E} \\
 &= -\mathbf{E} \cdot (\nabla \mathbf{V})^T \cdot \mathbf{D} \cdot \mathbf{E} \\
 &= -\mathbf{E} \cdot (\nabla \mathbf{V})^T.
 \end{aligned} \tag{6.A.17}$$

The partial time derivative of Eq. (6.A.6) is defined as

$$\begin{aligned}
 \boldsymbol{\gamma}_{[1]}(\mathbf{X}, t, t') &= \frac{\partial \boldsymbol{\gamma}_{[0]}}{\partial t'} \\
 &= - \left(\frac{\partial \mathbf{E}}{\partial t'} \right) \cdot \mathbf{E}^T - \mathbf{E} \cdot \left(\frac{\partial \mathbf{E}^T}{\partial t'} \right).
 \end{aligned} \tag{6.A.18}$$

Substituting Eq. (6.A.17) into Eq. (6.A.18), we obtain

$$\begin{aligned}\boldsymbol{\gamma}_{[1]}(\mathbf{X}, t, t') &= \mathbf{E} \cdot [(\nabla \mathbf{V})^T + \nabla \mathbf{V}] \cdot \mathbf{E}^T \\ &= \mathbf{E} \cdot \boldsymbol{\gamma}_{(1)} \cdot \mathbf{E}^T \\ &= \mathbf{E} \cdot \dot{\boldsymbol{\gamma}} \cdot \mathbf{E}^T\end{aligned}\quad (6.A.19)$$

where

$$\boldsymbol{\gamma}_{(1)}(\mathbf{X}, t, t') = (\nabla \mathbf{V})^T + \nabla \mathbf{V} = \dot{\boldsymbol{\gamma}}. \quad (6.A.20)$$

Similarly, using Eq. (6.A.17), the partial time derivative of Eq. (6.A.14) is written as

$$\boldsymbol{\tau}_{[1]} = \frac{\partial \boldsymbol{\tau}_{[0]}}{\partial t'} = \mathbf{E} \cdot \boldsymbol{\tau}_{(1)} \cdot \mathbf{E}^T \quad (6.A.21)$$

where $\boldsymbol{\tau}_{(1)}$ is called the contravariant convected derivative of $\boldsymbol{\tau}$ and is defined by

$$\boldsymbol{\tau}_{(1)}(\mathbf{X}, t, t') = \frac{\partial \boldsymbol{\tau}}{\partial t'} - \boldsymbol{\tau} \cdot (\nabla \mathbf{V}) - (\nabla \mathbf{V})^T \cdot \boldsymbol{\tau}. \quad (6.A.22)$$

As $t' \rightarrow t$, $\boldsymbol{\tau}_{(1)}(\mathbf{X}, t) = D\boldsymbol{\tau}/Dt - \boldsymbol{\tau} \cdot \nabla \mathbf{V} - (\nabla \mathbf{V})^T \cdot \boldsymbol{\tau}$, where D/Dt is the “material time derivative,” which gives the time rate of change following a fluid particle. It is understood that in the equations above, \mathbf{D} , \mathbf{E} , $\nabla \mathbf{V}$, $\boldsymbol{\tau}_{(1)}$ are all functions of t' and the particle (\mathbf{X}, t) . We can summarize the results of Eqs. (6.A.19) and (6.A.21) by using an arbitrary symmetric second-order tensor $\mathbf{A}(\mathbf{X}, t, t')$, as shown below:

$$\mathbf{A}_{[0]}(\mathbf{X}, t, t') = \mathbf{E} \cdot \mathbf{A} \cdot \mathbf{E}^T \quad (6.A.23)$$

$$\mathbf{A}_{[1]}(\mathbf{X}, t, t') = \frac{\partial \mathbf{A}_{[0]}}{\partial t'} = \mathbf{E} \cdot \mathbf{A}_{(1)} \cdot \mathbf{E}^T \quad (6.A.24)$$

where $\mathbf{A}_{(1)}$ is called the contravariant convected derivative of \mathbf{A} and is defined by

$$\mathbf{A}_{(1)}(\mathbf{X}, t, t') = \frac{\partial \mathbf{A}}{\partial t'} - \mathbf{A} \cdot \nabla \mathbf{V} - (\nabla \mathbf{V})^T \cdot \mathbf{A}. \quad (6.A.25)$$

When Eq. (6.A.6) is substituted into Eq. (6.A.24) ($\boldsymbol{\gamma}_{[0]}$ as $\mathbf{A}_{[0]}$), the $\boldsymbol{\delta}$ term becomes zero. In this case, Eq. (6.A.6) is equivalent to $-\mathbf{E} \cdot \boldsymbol{\delta} \cdot \mathbf{E}^T = -\mathbf{E} \cdot \boldsymbol{\delta} \cdot \mathbf{E}^T$ when compared with Eq. (6.A.23); in other words, $\mathbf{A} = -\boldsymbol{\delta}$ is

to be substituted into Eq. (6.A.25) to obtain $\boldsymbol{\gamma}_{(1)}$, i.e.

$$\begin{aligned}\boldsymbol{\delta}_{(1)} &= -\boldsymbol{\gamma}_{(1)} \\ &= -[\nabla\mathbf{V} + (\nabla\mathbf{V})^T] \\ &= -\dot{\boldsymbol{\gamma}}.\end{aligned}\tag{6.A.26}$$

An important concept in continuum mechanics is the objectivity, or admissibility, of the constitutive equation.⁶ There are the covariant and contravariant ways of achieving objectivity. The molecular theories: the elastic dumbbell model of this chapter, the Rouse model to be studied in the next chapter, and the Zimm model^{5,14} which includes the preaveraged hydrodynamic interaction, all give the result equivalent to the contravariant way. In this appendix, we limit our discussion of continuum mechanics to what is needed for the molecular theories studied in Chapters 6 and 7. More detailed discussions of the subject, particularly about the convected coordinates, can be found in Refs. 5 and 6.

References

1. Rouse, P. E. Jr., *J. Chem. Phys.* **21**, 1271 (1953).
2. Lin, Y.-H., *Macromolecules* **19**, 168 (1986).
3. Lin, Y.-H., and Juang J.-H., *Macromolecules* **32**, 181 (1999).
4. Doi, M., and Edwards, S. F., *The Theory of Polymer Dynamics*, Oxford Univ. Press (1986).
5. Bird, R. B., Curtiss, C. F., Armstrong, R. C., and Hassager, O., *Dynamics of Polymeric Liquids, Vol. 2, Kinetic Theory*, (2nd edn). Wiley, New York (1987).
6. Bird, R. B., Armstrong, R. C., and Hassager, O., *Dynamics of Polymeric Liquids, Vol. 1, Fluid Mechanics*, (2nd edn). Wiley, New York (1987).
7. Flory, P. J., *Principles of Polymer Chemistry*, Cornell Univ. Press, Ithaca (1953).
8. de Gennes, P. G., *Scaling Concepts in Polymer Physics*, Cornell Univ. Press, Ithaca (1979).
9. Edwards, S. F., and Freed, K. F., *J. Chem. Phys.* **61**, 1189 (1974); Freed, K. F., and Edwards, S. F., *J. Chem. Phys.* **61**, 3626 (1974).
10. McQuarrie, D. A., *Statistical Mechanics*, Harper & Row, New York (1976).
11. A more general method of derivation can be found in Ref. 4.
12. Kramers, H. A., *Physica* **11**, 1 (1944).
13. Giesekus, H., *Rheol. Acta* **2**, 50 (1962).
14. Zimm, B. H., *J. Chem. Phys.* **24**, 269 (1956).

Chapter 7

Molecular Theory of Polymer Viscoelasticity — The Rouse Model

7.1 The Smoluchowski Equation of the Rouse Model

The elastic dumbbell model studied in Chapter 6 is both structurally and dynamically too simple for a polymer. However, the derivation of its constitutive equation illustrates the main theoretical steps involved. In this chapter we shall apply these theoretical results to a Gaussian chain (or Rouse chain) containing many bead-spring segments (Rouse segments).¹ First we obtain the Smoluchowski equation for the bond vectors.² After transforming to the normal coordinates, the Smoluchowski equation for each normal mode is equivalent in form to the equation for the elastic dumbbell.

Consider the Rouse chain containing N identical beads as shown in Fig. 3.2. Each bead in the Rouse chain plays the same role as the bead in the elastic dumbbell. Denote the Hooke constant of the spring by $3kT/b^2$ where b^2 represents the mean square length of the spring or bond $\langle \mathbf{b}^2 \rangle$. Relative to a certain point O in space, the position vectors of the beads are denoted by $\{\mathbf{R}_n\} = (\mathbf{R}_1, \mathbf{R}_2, \dots, \mathbf{R}_N)$. Then the center-of-mass position of the chain is given by

$$\mathbf{R}_c = \frac{1}{N} \sum_{n=1}^N \mathbf{R}_n. \quad (7.1)$$

Relative to the center of mass, the positions of the beads are given by

$$\{\mathbf{d}_n\} = \{\mathbf{R}_n - \mathbf{R}_c\}. \quad (7.2)$$

And the bond vectors are defined by

$$\mathbf{b}_s = \mathbf{R}_{s+1} - \mathbf{R}_s = \mathbf{d}_{s+1} - \mathbf{d}_s; \quad s = 1, 2, \dots, N-1 \quad (7.3)$$

We shall need to go back and forth between the beads and the bonds through Eq. (7.3). To avoid the confusion, we shall use the following index convention:

- n, m for numbering the beads from 1 to N
- $s, t, u \dots$ for numbering the bonds from 1 to $N - 1$.

With this convention, the upper limit of a summation is understood to be either N or $N - 1$, if not indicated.

Using Eqs. (7.1) and (7.3), one easily obtains

$$\mathbf{d}_N = \frac{1}{N} \sum_{s=1}^{N-1} s \mathbf{b}_s. \quad (7.4)$$

Thus

$$\mathbf{d}_n = \mathbf{d}_N - \sum_{s=n}^{N-1} \mathbf{b}_s = \sum_{s=1}^{N-1} \frac{s}{N} \mathbf{b}_s - \sum_{s=n}^{N-1} \mathbf{b}_s. \quad (7.5)$$

From Eqs. (7.1), (7.3) and (7.5), the relations between $\{\mathbf{R}_n\}$ and $(\{\mathbf{b}_s\}, \mathbf{R}_c)$ can be expressed as

$$\mathbf{b}_s = \sum_{n=1}^N C_{sn} \mathbf{d}_n = \sum_{n=1}^N C_{sn} \mathbf{R}_n \quad (7.6)$$

$$\mathbf{R}_c = \frac{1}{N} \sum_{n=1}^N \mathbf{R}_n \quad (7.1)$$

and

$$\mathbf{R}_n = \sum_{s=1}^{N-1} B_{ns} \mathbf{b}_s + \mathbf{R}_c \quad (7.7)$$

or

$$\mathbf{d}_n = \sum_{s=1}^{N-1} B_{ns} \mathbf{b}_s$$

where

$$C_{sn} = \delta_{s+1,n} - \delta_{s,n} \quad (7.8)$$

$$\begin{aligned}
 B_{ns} &= \frac{s}{N} && \text{for } s < n \\
 &= \frac{s}{N} - 1 && \text{for } s \geq n.
 \end{aligned}
 \tag{7.9}$$

From Eqs. (7.8) and (7.9), we obtain the following relations for any s :

$$\sum_{n=1}^N C_{sn} = \sum_{n=1}^N (\delta_{s+1,n} - \delta_{s,n}) = 0
 \tag{7.10}$$

$$\sum_{n=1}^N B_{ns} = 0.
 \tag{7.11}$$

By using Eq. (7.10), the substitution of Eq. (7.7) into Eq. (7.6) gives

$$\begin{aligned}
 \mathbf{b}_s &= \sum_{n=1}^N C_{sn} \mathbf{R}_n = \sum_{n=1}^N C_{sn} \left(\mathbf{R}_c + \sum_{t=1}^{N-1} B_{nt} \mathbf{b}_t \right) \\
 &= \sum_{n=1}^N \sum_{t=1}^{N-1} C_{sn} B_{nt} \mathbf{b}_t.
 \end{aligned}
 \tag{7.12}$$

Since $\{\mathbf{b}_s\}$ is an independent set of vectors,

$$\sum_{n=1}^N C_{sn} B_{nt} = \delta_{st}.
 \tag{7.13}$$

Equation (7.13) can also be shown by carrying out the matrix multiplication with C_{sn} and B_{nt} substituted by Eqs. (7.8) and (7.9), respectively. Substituting Eqs. (7.1) and (7.6) into Eq. (7.7), we obtain

$$\mathbf{R}_n = \sum_{m=1}^N \left(\frac{1}{N} + \sum_{s=1}^{N-1} B_{ns} C_{sm} \right) \mathbf{R}_m.
 \tag{7.14}$$

Thus

$$\sum_{s=1}^{N-1} B_{ns} C_{sm} = \delta_{nm} - \frac{1}{N}.
 \tag{7.15}$$

Using Eq. (7.8), one shows

$$\begin{aligned}
 \sum_{n=1}^N C_{sn} C_{tn} &= \sum_{n=1}^N C_{sn} C_{nt}^T = A_{st} \\
 &= 2\delta_{st} - \delta_{s+1,t} - \delta_{s-1,t}
 \end{aligned}
 \tag{7.16}$$

where (A_{st}) is the $(N - 1) \times (N - 1)$ Rouse matrix, which we have seen in Chapter 3 (Eq. (3.45)). The eigenvalues of the Rouse matrix are given by (Appendix 3.A)

$$a_p = 4 \sin^2 \left(\frac{p\pi}{2N} \right); \quad p = 1, 2, \dots, N - 1. \quad (7.17); (3.46)$$

As discussed in Chapter 3, each bead of the Rouse chain, under ceaseless collisions with fast moving small molecules and/or microstructural segments, is undergoing Brownian motion. At the same time the bead at \mathbf{R}_n is affected by both the tensile forces on the n th and $(n - 1)$ th bonds. According to the same definition used in Eqs. (6.4) and (6.5), the total force asserted on the n th bead by the springs is expressed as

$$\begin{aligned} \mathbf{F}_n &= \mathbf{S}_n - \mathbf{S}_{n-1} = - \sum_{s=1}^{N-1} (\delta_{s+1,n} - \delta_{s,n}) \mathbf{S}_s \\ &= - \sum_{s=1}^{N-1} C_{sn} \mathbf{S}_s \end{aligned} \quad (7.18)$$

where Eq. (7.8) is used for the last equality, and the tensile force on the s th bond is given by

$$\mathbf{S}_s = \frac{3kT}{b^2} \mathbf{b}_s. \quad (7.19)$$

Similar to the elastic dumbbell case, the equation of motion for any bead in the Rouse chain is written as

$$\zeta(\dot{\mathbf{R}}_n - \mathbf{V}_0 - \mathbf{K} \cdot \mathbf{R}_n) = -kT \frac{\partial}{\partial \mathbf{R}_n} \ln \Psi + \mathbf{F}_n \quad (7.20)$$

where $\Psi(\{\mathbf{R}_n\}, t)$ is the configurational distribution function. For a homogeneous flow with no concentration gradient, similar to Eq. (6.9) in the elastic dumbbell case, the configurational distribution function of the Rouse chain Ψ may be written as

$$\Psi(\{\mathbf{R}_n\}, t) = n\psi(\{\mathbf{b}_s\}, t) \quad (7.21)$$

where n is the number of Rouse chains per unit volume of the polymeric liquid.

Summing Eq. (7.20) over n and then dividing the result by N , we obtain

$$\frac{\zeta}{N} \sum_{n=1}^N \dot{\mathbf{R}}_n = \frac{\zeta}{N} \sum_{n=1}^N (\mathbf{V}_0 + \mathbf{K} \cdot \mathbf{R}_n) - \frac{kT}{N} \sum_{n=1}^N \frac{\partial}{\partial \mathbf{R}_n} \ln \Psi + \frac{1}{N} \sum_{n=1}^N \mathbf{F}_n. \quad (7.22)$$

Substituting Eqs. (7.1), (7.18) and (7.21) into Eq. (7.22), we obtain

$$\zeta \dot{\mathbf{R}}_c = \zeta (\mathbf{V}_0 + \mathbf{K} \cdot \mathbf{R}_c) - \frac{kT}{N} \sum_{n=1}^N \left[\left(\frac{\partial \ln \psi}{\partial \mathbf{R}_c} \right) \left(\frac{\partial \mathbf{R}_c}{\partial \mathbf{R}_n} \right) + \sum_{s=1}^{N-1} \left(\frac{\partial \ln \psi}{\partial \mathbf{b}_s} \right) \left(\frac{\partial \mathbf{b}_s}{\partial \mathbf{R}_n} \right) \right] - \frac{1}{N} \sum_{n=1}^N \sum_{s=1}^{N-1} C_{sn} \mathbf{S}_s. \quad (7.23)$$

Using Eq. (7.10) from Eq. (7.6), we obtain

$$\sum_{n=1}^N \frac{\partial \mathbf{b}_s}{\partial \mathbf{R}_n} = \sum_{n=1}^N C_{sn} = 0. \quad (7.24)$$

Using the result of Eq. (7.24) and the assumption that $\psi(\{\mathbf{b}_s\}, t)$ is not a function of \mathbf{R}_c , Eq. (7.23) becomes

$$\dot{\mathbf{R}}_c = \mathbf{V}_0 + \mathbf{K} \cdot \mathbf{R}_c \quad (7.25)$$

which is equivalent to Eq. (6.15) in the elastic dumbbell case. This result is expected from assuming Eq. (7.21). Substituting Eqs. (7.7), (7.18) and (7.21) into Eq. (7.20), we obtain

$$\zeta \left[\dot{\mathbf{R}}_c + \sum_{s=1}^{N-1} B_{ns} \dot{\mathbf{b}}_s \right] = \zeta \left[\mathbf{V}_0 + \mathbf{K} \cdot \left(\mathbf{R}_c + \sum_{s=1}^{N-1} B_{ns} \mathbf{b}_s \right) \right] - kT \sum_{s=1}^{N-1} \left(\frac{\partial \ln \psi}{\partial \mathbf{b}_s} \right) \left(\frac{\partial \mathbf{b}_s}{\partial \mathbf{R}_n} \right) - \sum_{s=1}^{N-1} C_{sn} \mathbf{S}_s. \quad (7.26)$$

Using Eqs. (7.6) and (7.25), Eq. (7.26) is rewritten as

$$\zeta \sum_{s=1}^{N-1} B_{ns} \dot{\mathbf{b}}_s = \zeta \mathbf{K} \cdot \sum_{s=1}^{N-1} B_{ns} \mathbf{b}_s - kT \sum_{s=1}^{N-1} \left(\frac{\partial \ln \psi}{\partial \mathbf{b}_s} \right) C_{sn} - \sum_{s=1}^{N-1} C_{sn} \mathbf{S}_s. \quad (7.27)$$

Multiplying Eq. (7.27) by C_{tn} which is placed on the left side and summing the result over n , we obtain

$$\zeta \sum_{n=1}^N \sum_{s=1}^{N-1} C_{tn} B_{ns} \dot{\mathbf{b}}_s = \zeta \mathbf{K} \cdot \sum_{n=1}^N \sum_{s=1}^{N-1} C_{tn} B_{ns} \mathbf{b}_s - kT \sum_{s=1}^{N-1} \left(\frac{\partial \ln \psi}{\partial \mathbf{b}_s} \right) \sum_{n=1}^N C_{tn} C_{sn} - \sum_{n=1}^N \sum_{s=1}^{N-1} C_{tn} C_{sn} \mathbf{S}_s. \quad (7.28)$$

Using Eqs. (7.13) and (7.16), Eq. (7.28) is rewritten as

$$\dot{\mathbf{b}}_t = \mathbf{K} \cdot \mathbf{b}_t - \frac{1}{\zeta} \sum_{s=1}^{N-1} A_{st} \left(kT \frac{\partial \ln \psi}{\partial \mathbf{b}_s} + \mathbf{S}_s \right). \quad (7.29)$$

Equation (7.29) for the Rouse chain is equivalent to Eq. (6.14) for the elastic dumbbell. However, Eq. (7.29) indicates that the motions of $N - 1$ bond vectors are coupled with each other through the Rouse matrix (A_{st}).

After the equation of motion for the bonds (Eq. (7.29)) is obtained, we need to express the continuity equation for Ψ in terms of $\{\mathbf{b}_s\}$ to obtain the Smoluchowski equation. Similar to Eq. (6.16), we have

$$\frac{\partial \Psi}{\partial t} = - \sum_{n=1}^N \frac{\partial}{\partial \mathbf{R}_n} \cdot \dot{\mathbf{R}}_n \Psi. \quad (7.30)$$

Using Eqs. (7.1), (7.6), and (7.7), which relate $\{\mathbf{R}_n\}$ and $(\{\mathbf{b}_s\}, \mathbf{R}_c)$, and Eqs. (7.10) and (7.11), Eq. (7.30) is rewritten as

$$\frac{\partial \Psi}{\partial t} = - \frac{\partial}{\partial \mathbf{R}_c} \cdot \dot{\mathbf{R}}_c \Psi - \sum_{s=1}^{N-1} \frac{\partial}{\partial \mathbf{b}_s} \cdot \dot{\mathbf{b}}_s \Psi. \quad (7.31)$$

Similar to the first term of Eq. (6.16) being zero, the first term of Eq. (7.31) disappears with the substitution of Eq. (7.21). Thus, Eq. (7.31) becomes

$$\frac{\partial \psi}{\partial t} = - \sum_{s=1}^{N-1} \frac{\partial}{\partial \mathbf{b}_s} \cdot \dot{\mathbf{b}}_s \psi. \quad (7.32)$$

By using Eq. (7.19), the substitution of Eq. (7.29) into Eq. (7.32) gives

$$\frac{\partial \psi}{\partial t} = - \sum_{s=1}^{N-1} \frac{\partial}{\partial \mathbf{b}_s} \cdot \left[(\mathbf{K} \cdot \mathbf{b}_s) \psi - \frac{1}{\zeta} \sum_{t=1}^{N-1} A_{st} \left(kT \frac{\partial \psi}{\partial \mathbf{b}_t} + \frac{3kT}{b^2} \mathbf{b}_t \psi \right) \right]. \quad (7.33)$$

This equation is equivalent to Eq. (6.19) for the elastic dumbbell and is the Smoluchowski equation for the Rouse chain under the flow field \mathbf{K} . In this equation, the Rouse matrix (A_{st}) couples the motions of the bond vectors $\{\mathbf{b}_s\}$. Transforming to normal coordinates is the normal procedure used to decouple the motions. As shown in Chapter 3, the transformation

to normal coordinates $\{\mathbf{q}_t\}$ is given by

$$\mathbf{b}_s = \sum_{t=1}^{N-1} U_{st} \mathbf{q}_t \quad (7.34); (3.47)$$

where (U_{st}) is the orthogonal matrix (Eq. (3.48)) that diagonalizes the Rouse matrix, i.e.

$$\sum_{t=1}^{N-1} U_{ts} U_{tu} = \sum_{t=1}^{N-1} U_{st}^T U_{tu} = \delta_{su} \quad (7.35); (3.49)$$

and

$$\sum_{s=1}^{N-1} \sum_{t=1}^{N-1} U_{ps}^T A_{st} U_{tu} = a_p \delta_{pu} \quad (7.36)$$

where the eigenvalues $\{a_p\}$ are given by Eq. (7.17).

Using Eq. (7.35), the inverse of Eq. (7.34) is given by

$$\mathbf{q}_u = \sum_{s=1}^{N-1} U_{us}^T \mathbf{b}_s. \quad (7.37)$$

Then, using Eq. (7.37),

$$\frac{\partial}{\partial \mathbf{b}_s} = \sum_{u=1}^{N-1} \left(\frac{\partial}{\partial \mathbf{q}_u} \right) \left(\frac{\partial \mathbf{q}_u}{\partial \mathbf{b}_s} \right) = \sum_{u=1}^{N-1} U_{us}^T \frac{\partial}{\partial \mathbf{q}_u}. \quad (7.38)$$

Using Eqs. (7.34) and (7.38), Eq. (7.33) is expressed as

$$\begin{aligned} \frac{\partial \psi}{\partial t} &= - \sum_s \sum_u U_{su} \frac{\partial}{\partial \mathbf{q}_u} \cdot \left\{ \left(\mathbf{K} \cdot \sum_v U_{sv} \mathbf{q}_v \right) \psi \right. \\ &\quad \left. - \frac{1}{\zeta} \sum_t A_{st} \left(kT \sum_w U_{tw} \frac{\partial \psi}{\partial \mathbf{q}_w} + \frac{3kT}{b^2} \sum_w U_{tw} \mathbf{q}_w \psi \right) \right\} \\ &= - \sum_v \sum_u \left(\sum_s U_{vs}^T U_{su} \right) \frac{\partial}{\partial \mathbf{q}_u} \cdot (\mathbf{K} \cdot \mathbf{q}_v) \psi \\ &\quad + \sum_u \sum_w \left(\sum_t \sum_s U_{us}^T A_{st} U_{tw} \right) \left(\frac{kT}{\zeta} \frac{\partial}{\partial \mathbf{q}_u} \cdot \frac{\partial \psi}{\partial \mathbf{q}_w} + \frac{3kT}{\zeta b^2} \frac{\partial}{\partial \mathbf{q}_u} \cdot \mathbf{q}_w \psi \right). \end{aligned} \quad (7.39)$$

Using Eqs. (7.35) and (7.36), Eq. (7.39) is rewritten as

$$\frac{\partial \psi}{\partial t} = - \sum_u \frac{\partial}{\partial \mathbf{q}_u} \cdot \left[(\mathbf{K} \cdot \mathbf{q}_u) \psi - \frac{a_u}{\zeta} \left(kT \frac{\partial \psi}{\partial \mathbf{q}_u} + \frac{3kT}{b^2} \mathbf{q}_u \psi \right) \right]. \quad (7.40)$$

We assume that Eq. (7.40) has a solution of the form

$$\psi(\{\mathbf{q}_s\}, t) = \prod_{s=1}^{N-1} \psi_s(\mathbf{q}_s, t) \quad (7.41)$$

where $\psi_s(\mathbf{q}_s, t)$ is normalized by

$$\int \psi_s(\mathbf{q}_s, t) d\mathbf{q}_s = 1. \quad (7.42)$$

The substitution of Eq. (7.41) into Eq. (7.40) gives

$$\begin{aligned} & \sum_{u=1}^{N-1} \left(\prod_{t \neq u} \psi_t \right) \frac{\partial \psi_u}{\partial t} \\ &= - \sum_{u=1}^{N-1} \left(\prod_{t \neq u} \psi_t \right) \frac{\partial}{\partial \mathbf{q}_u} \cdot \left[(\mathbf{K} \cdot \mathbf{q}_u) \psi_u - \frac{a_u}{\zeta} \left(kT \frac{\partial \psi_u}{\partial \mathbf{q}_u} + \frac{3kT}{b^2} \mathbf{q}_u \psi_u \right) \right]. \end{aligned} \quad (7.43)$$

Dividing both sides of Eq. (7.43) by $\psi_1 \psi_2 \dots \psi_{N-1}$, we obtain an equation which is expressed as a collection of groups, each of which contains only one of the coordinates $\{\mathbf{q}_s\}$. The only way this equation can be satisfied is to let each of these groups be a simple function of time $E_u(t)$. That is,

$$\begin{aligned} \frac{\partial \psi_u}{\partial t} = - \frac{\partial}{\partial \mathbf{q}_u} \cdot \left[(\mathbf{K} \cdot \mathbf{q}_u) \psi_u - \frac{a_u}{\zeta} \left(kT \frac{\partial \psi_u}{\partial \mathbf{q}_u} + \frac{3kT}{b^2} \mathbf{q}_u \psi_u \right) \right] + E_u(t) \psi_u \\ u = 1, 2, \dots, N-1. \end{aligned} \quad (7.44)$$

If Eq. (7.44) is integrated over the whole \mathbf{q}_u space, the left side becomes zero because of the normalization condition (Eq. (7.42)), and the first term on the right side becomes zero because ψ_u vanishes as $\mathbf{q}_u \rightarrow \infty$. Hence $E_u(t)$ must be zero. Then Eq. (7.44) becomes the same as Eq. (6.19) if ψ_u is replaced by ψ , \mathbf{q}_u by \mathbf{R} , a_u by 2, and $(3kT/b^2)\mathbf{q}_u$ by \mathbf{S} .

Then, following the derivation steps from Eq. (6.19) to Eq. (6.26), we obtain from Eq. (7.44) the following results, which are equivalent to

Eqs. (6.24) and (6.26) for an elastic dumbbell:

$$\frac{d\langle \mathbf{q}_u \mathbf{q}_u \rangle}{dt} = \mathbf{K} \cdot \langle \mathbf{q}_u \mathbf{q}_u \rangle + \langle \mathbf{q}_u \mathbf{q}_u \rangle \cdot \mathbf{K}^T + \frac{2a_u kT}{\zeta} \boldsymbol{\delta} - \frac{6a_u kT}{\zeta b^2} \langle \mathbf{q}_u \mathbf{q}_u \rangle \quad (7.45)$$

or

$$\langle \mathbf{q}_u \mathbf{q}_u \rangle_{(1)} = \frac{2a_u kT}{\zeta} \boldsymbol{\delta} - \frac{6a_u kT}{\zeta b^2} \langle \mathbf{q}_u \mathbf{q}_u \rangle. \quad (7.46)$$

7.2 Rheological Constitutive Equation of the Rouse Model

In Chapter 6, we derived the stress tensor for the elastic dumbbell model. By following the derivation steps given there, one obtains the following result for the Rouse chain model with N beads per chain, which is equivalent to Eq. (6.50) for the elastic dumbbell model:

$$\boldsymbol{\tau} = -\frac{3nkT}{b^2} \sum_{s=1}^{N-1} \langle \mathbf{b}_s \mathbf{b}_s \rangle + n(N-1)kT\boldsymbol{\delta}. \quad (7.47)$$

In Eq. (7.47), we have neglected the solvent contribution as we are mainly interested in the concentrated-solution or melt system. The first term of Eq. (7.47) arises from the tensile force on the bonds, and the second term from the momenta associated with the moving beads. Substituting Eqs. (7.34) and (7.35) into Eq. (7.47), we obtain

$$\begin{aligned} \boldsymbol{\tau} &= -\frac{3nkT}{b^2} \sum_s \sum_t \sum_u U_{st} U_{su} \langle \mathbf{q}_t \mathbf{q}_u \rangle + n(N-1)kT\boldsymbol{\delta} \\ &= -\frac{3nkT}{b^2} \sum_{u=1}^{N-1} \langle \mathbf{q}_u \mathbf{q}_u \rangle + n(N-1)kT\boldsymbol{\delta}. \end{aligned} \quad (7.48)$$

We rewrite Eq. (7.48) as

$$\boldsymbol{\tau} = \sum_{u=1}^{N-1} \boldsymbol{\tau}^u \quad (7.49)$$

with

$$\boldsymbol{\tau}^u = -\frac{3nkT}{b^2} \langle \mathbf{q}_u \mathbf{q}_u \rangle + nkT\boldsymbol{\delta}. \quad (7.50)$$

Following the procedure for obtaining Eq. (6.52) from Eqs. (6.26) and (6.50), one obtains the following result from Eqs. (7.46) and (7.50):

$$\boldsymbol{\tau}^u + s_u \boldsymbol{\tau}_{(1)}^u = -nkT s_u \boldsymbol{\gamma}_{(1)} = -nkT s_u \dot{\boldsymbol{\gamma}} \quad (7.51)$$

where s_u is the relaxation time for the u th Rouse mode of motion and is given by

$$s_u = \frac{\zeta b^2}{6a_u kT}. \quad (7.52)$$

Following the steps for obtaining Eq. (6.57), we rewrite Eq. (7.51) as

$$\boldsymbol{\tau}_{[0]}^u(t, t') + s_u \frac{\partial}{\partial t'} \boldsymbol{\tau}_{[0]}^u(t, t') = -nkT s_u \boldsymbol{\gamma}_{[1]}(t, t'). \quad (7.53)$$

Just as Eqs. (6.58) and (6.59) were obtained in Chapter 6, the integral forms of Eq. (7.53) can be obtained. Then, with Eq. (7.49), the integral form of the constitutive equation for the Rouse chain model is given by (with u replaced by p)

$$\boldsymbol{\tau}(t) = -nkT \int_{-\infty}^t \sum_{p=1}^{N-1} \exp\left[-\frac{(t-t')}{s_p}\right] \boldsymbol{\gamma}_{[1]}(t, t') dt' \quad (7.54)$$

or

$$\boldsymbol{\tau}(t) = nkT \int_{-\infty}^t \sum_{p=1}^{N-1} \frac{1}{s_p} \exp\left[-\frac{(t-t')}{s_p}\right] \boldsymbol{\gamma}_{[0]}(t, t') dt'. \quad (7.55)$$

Substituting Eq. (7.17) into Eq. (7.52), s_p is rewritten as

$$s_p = \frac{\zeta b^2}{24kT \sin^2(p\pi/2N)}; \quad p = 1, 2, \dots, N-1 \quad (7.56)$$

which can also be expressed as

$$s_p = \frac{K \pi^2 M^2}{24N^2 \sin^2(p\pi/2N)} \quad (7.57)$$

where K is the frictional factor given by Eq. (3.57). The molecular-weight independence and temperature dependence of K have been discussed in Chapter 3.

Similar to the elastic dumbbell case, we can obtain the various viscoelastic properties from the constitutive equation of the Rouse model. The main difference between the two models is that the elastic dumbbell

model contains only one relaxation time, while the Rouse model has multiple relaxation times, the number of which is equal to the number of bonds (springs) in a single chain.

For the shear relaxation modulus, the Rouse model gives

$$G(t) = nkT \sum_{p=1}^{N-1} \exp\left(-\frac{t}{s_p}\right). \quad (7.58)$$

The shear viscosity of the Rouse model can be obtained by substituting Eq. (7.58) into Eq. (4.30) or, as Eq. (6.70) was obtained, it can be calculated by substituting the steady-state shear deformation into Eq. (7.55). These two different calculations give the same result:

$$\begin{aligned} \eta_0 &= nkT \sum_{p=1}^{N-1} s_p \\ &= nkT \sum_{p=1}^{N-1} \frac{\zeta b^2}{6kT a_p} \\ &= \frac{n\zeta b^2(N^2 - 1)}{36} \end{aligned} \quad (7.59)$$

where for the last equality Eq. (7.A.5) is used. As in the elastic dumbbell case, the Rouse model does not predict the non-Newtonian behavior of viscosity.

Similarly, the steady-state compliance J_e^0 is obtained as

$$\begin{aligned} J_e^0 &= nkT \sum_{p=1}^{N-1} \frac{s_p^2}{\eta_0^2} \\ &= \frac{n(\zeta b^2)^2 \sum_{p=1}^{N-1} 1/a_p^2}{36kT \eta_0^2} \\ &= \frac{2N^2 + 7}{5nkT(N^2 - 1)} \end{aligned} \quad (7.60)$$

where for the last equality Eqs. (7.A.6) and (7.59) are used.

For a polymer melt, $n = \rho N_A / M$, where ρ is the density and N_A the Avogadro number. When the condition $N \gg 1$ holds, for easy comparison

with experimental results of polymer melts, Eq. (7.59) may be written as

$$\begin{aligned}\eta_0 &= \frac{\rho N_A \zeta b^2 N^2}{36M} \\ &= K \left(\frac{\rho RT \pi^2}{36} \right) M\end{aligned}\quad (7.61)$$

and Eq. (7.60) be written as

$$J_e^0 = \frac{2M}{5\rho RT}.\quad (7.62)$$

The Rouse model has the same defects in the nonlinear region as the elastic dumbbell model because they share the same basic assumptions. However, in the linear region the Rouse model accurately describes the viscoelastic properties of the concentrated or melt system whose molecular weight is not high enough for entanglements to form. The successful predictions of the theory include the most basic aspects: the molecular-weight dependence of the relaxation times and the line shape of viscoelastic responses (relaxation modulus, viscoelastic spectrum and creep compliance) over the entropic region as detailed in the Chapters 11 and 14.

Appendix 7.A — Eigenvalues and the Inverse of the Rouse Matrix

While Eq. (7.16) gives the $(N-1) \times (N-1)$ Rouse matrix with the eigenvalues $\{a_p\}$ given by Eq. (7.17) (see Appendix 3.A), another $(N-1) \times (N-1)$ symmetric matrix (K_{st}) can be formed from (B_{ns}):

$$K_{st} = \sum_{n=1}^N B_{ns} B_{nt} = \sum_{n=1}^N B_{sn}^T B_{nt} \quad (7.A.1)$$

which sometimes is referred to as the Kramers matrix.³ Using Eq. (7.9), (K_{st}) is obtained as

$$\begin{aligned}K_{st} &= \frac{s(N-t)}{N} && \text{if } s \leq t \\ &= \frac{t(N-s)}{N} && \text{if } t \leq s.\end{aligned}\quad (7.A.2)$$

Using Eqs. (7.10), (7.11), (7.13), and (7.15), the matrix (K_{st}) is shown to be the inverse of the Rouse matrix (A_{st}) as follows:

$$\begin{aligned}
 \sum_{t=1}^{N-1} K_{st} A_{tu} &= \sum_{t=1}^{n-1} \left(\sum_{n=1}^N B_{sn}^T B_{nt} \right) \left(\sum_{m=1}^N C_{tm} C_{mu}^T \right) \\
 &= \sum_{n=1}^N \sum_{m=1}^N B_{sn}^T C_{mu}^T \left(\sum_{t=1}^{N-1} B_{nt} C_{tm} \right) \\
 &= \sum_n \sum_m C_{um} B_{ns} \left(\delta_{nm} - \frac{1}{N} \right) \\
 &= \sum_n C_{un} B_{ns} - \frac{1}{N} \left(\sum_m C_{um} \right) \left(\sum_n B_{ns} \right) \\
 &= \delta_{su}.
 \end{aligned} \tag{7.A.3}$$

Denote the matrices obtained from diagonalizing (A_{st}) and (K_{st}) by (A'_{st}) and (K'_{st}) , respectively. Then, using the trace-invariance property of a matrix, the following relations are obtained:

$$\begin{aligned}
 \sum_{s=1}^{N-1} A'_{ss} &= \sum_s a_s = \sum_s 4 \sin^2 \left(\frac{s\pi}{2N} \right) \\
 &= \sum_s A_{ss} = 2(N-1)
 \end{aligned} \tag{7.A.4}$$

$$\begin{aligned}
 \sum_{s=1}^{N-1} K'_{ss} &= \sum_s \frac{1}{a_s} = \sum_s \frac{1}{4 \sin^2(s\pi/2N)} \\
 &= \sum_s K_{ss} = \frac{N^2 - 1}{6}
 \end{aligned} \tag{7.A.5}$$

$$\begin{aligned}
 \sum_{s=1}^{N-1} K'^2_{ss} &= \sum_s \frac{1}{a_s^2} = \sum_s \sum_t K_{st} K_{ts} \\
 &= \frac{(N^2 - 1)(2N^2 + 7)}{180}
 \end{aligned} \tag{7.A.6}$$

where, for the last equality of Eq. (7.A.4), Eq. (7.16) is used, and for the last equalities of Eqs. (7.A.5) and (7.A.6), Eq. (7.A.2) is used. Equations (7.A.5) and (7.A.6) are used, respectively, in obtaining the expressions for

the zero-rate shear viscosity η_0 (Eq. (7.59)) and the steady-state compliance J_e^0 (Eq. (7.60)) of the Rouse model.

References

1. Rouse, P. E., Jr., *J. Chem. Phys.* **21**, 1272 (1953).
2. See Chapter 6 and references therein.
3. Kramers, H. A., *Physica* **11**, 1 (1944); Bird, R. B., Curtiss, C. F., Armstrong, R. C., and Hassager, O., *Dynamics of Polymeric Liquids*, Vol. 2 (2nd edn.), Wiley, New York (1987), p. 24.

Chapter 8

Molecular Theory of Polymer Viscoelasticity — Entanglement and the Doi–Edwards (Reptation) Model

8.1 Introduction

The so-called chain entanglement which occurs in a concentrated long-chain polymeric liquid is a kind of intermolecular interaction. Unlike other types of intermolecular interactions, it does not involve an energetic change and is purely an entropic, topological phenomenon. Because of this reason, chain entanglement does not give rise to a change in the electron density distribution. As a result, polymer chain entanglement cannot be observed by microscopes or static scattering or absorption spectroscopies. Chain entanglement mainly affects polymer chain motions. Thus, its presence can be detected by the slow-down of polymer dynamics and is clearly visible in several viscoelastic properties.

An example is the molecular-weight dependence of zero-shear viscosity as shown in Fig. 4.7 for various nearly monodisperse polymers. As the molecular weight increases above a critical value M_c , the viscosity increases much more rapidly than in the low-molecular-weight region below M_c , exhibiting the well-known 3.4 power law.^{1,2}

Another strong indication of the entanglement effect is the observation of a clear plateau in the linear relaxation modulus $G(t)$ ^{3,4} and storage modulus spectrum $G'(\omega)$ ⁵ when the polymer has a sufficiently high molecular weight and is nearly monodisperse (Figs. 4.6 and 4.9). As the molecular weight decreases, the modulus plateau disappears gradually. In the region of molecular weight where the polymer chains are long enough to be described by the Gaussian chain model and yet not long enough to form entanglements, the Rouse model (Chapter 7) accurately describes the line shapes of linear viscoelastic responses (over the entropic region; Chapters 11 and 14). In this low-molecular-weight region, there is no detectable modulus

plateau; and the Rouse theory does not involve any *structural* interactions (entanglements) among chains. This correlation strongly suggests that the appearance of the modulus plateau at high molecular weight should be due to the occurrence of entanglements among the chains. The larger the molecular weight, the longer the time needed to relax any deviation from the equilibrium state of entanglement, such as that caused by a step strain in the stress relaxation measurement. Thus, the plateau region stretches further toward the longer time (for $G(t)$) or toward the lower frequency (for $G'(\omega)$) with increasing molecular weight, as shown in Figs. 4.6 and 4.9.

Entanglement has long been considered equivalent to temporary or non-chemical “cross-link”.⁶ If we assume that each entanglement is permanent and use the theory of rubber elasticity (Chapter 2), the molecular weight of an entanglement strand (the chain section between two adjacent entanglement points), often referred to as the entanglement molecular weight M_e , can be calculated from the plateau modulus G_N as^{3,7,8}

$$M_e = \frac{\rho RT}{G_N}. \quad (8.1)$$

As discussed below in this chapter, the Doi–Edwards theory⁹ models entanglements as slip-links. Having taken the effects of chain slippage through the links into account, the theory gives:

$$M_e = \frac{4}{5} \left(\frac{\rho RT}{G_N} \right). \quad (8.2)$$

Experimental results of various polymers show that the critical molecular weight M_c is about 2.4 times the value of M_e (determined according to Eq. (8.2)). This observation indicates the close relation between M_c and M_e .

On the basis of the experimental results of polymer viscoelasticity as explained above, it has long been believed that chain entanglements occur in a concentrated long-chain system.

The close relation between the viscoelastic properties and the chain dynamics of a polymeric liquid has long been recognized. The Rouse theory describes the viscoelastic properties of an entanglement-free polymer in terms of the Rouse normal modes of motion (Chapter 7). A promising way to describe the entanglement effect for a high-molecular-weight polymer had not appeared until 1971 when de Gennes suggested the idea of reptation.¹⁰ He suggested that a linear flexible chain moved in a network as if a “snake” crawled in a “thin tube” and that the only motions allowed for the chain

were associated with the displacement of certain “defects” (stored length) along the chain. Since entanglements, even though different from permanent cross-links, can last very long, de Gennes suggested that the idea of chain reptation might be applicable to a polymer melt system to describe the constraint effect of entanglement on the chain motions. In 1978–1979, Doi and Edwards combined the idea of chain reptation with the mechanical properties of a concentrated polymer system and developed a very successful molecular rheological constitutive equation. A linear viscoelastic theory (referred to as the extended Doi–Edwards theory or as the extended reptation theory^a) has further been developed (Chapter 9)¹¹ by incorporating additional intramolecular relaxation processes in the theoretical framework of the Doi–Edwards theory. The extended reptation theory quantitatively and consistently explains different aspects of the linear viscoelastic properties of linear flexible polymers, including the 3.4 power law and the close relation between M_c and M_e as mentioned above.^{4,12–14} Such successes were quite unexpected, considering that the extended reptation theory as well as the Doi–Edwards theory is a mean-field theory. Quantitative analyses of experimental results in terms of the extended reptation theory will be discussed in Chapter 10. As shown in Chapter 11, the concentration dependence of entanglement is quantitatively determined by analyzing the viscoelastic spectra of the blend solution systems in terms of the theory.¹⁵ A further development of the Doi–Edwards theory for the nonlinear region will be studied in Chapter 12.^{13,16} The successes of the linear and nonlinear extended theories should be attributed to the foundation layed down by the Doi–Edwards theory. In this chapter, we shall study the basic elements in the Doi–Edwards theory.

8.2 The Primitive Chain

Entanglement represents a nonpermanent structural interaction among different chains in a polymer. In general, at the most fundamental level, a problem that involves many molecules is extremely difficult. Doi and

^aAs the theory is based on the theoretical framework of the Doi–Edwards theory, it is referred to as the extended Doi–Edwards theory from the theoretical consideration; at the same time, since the theory includes the intramolecular motions on top of the reptation process, physically it is referred to as the extended reptation theory. Considering that the Doi–Edwards theory covers the nonlinear region, while the extended reptation theory is limited to the linear region, the term “extended reptation theory” is used throughout this book instead of the extended Doi–Edwards theory.

Edwards adopted a mean-field assumption and simplified a multi-chain problem to a single-chain problem. In doing so, they introduced the concept of the so-called *primitive chain*. In a concentrated system, each chain is pictured as moving independently in a “tube,” representing the constraint effect due to entanglements with the surrounding chains. As a person’s shadow follows his movement, the tube associated with a chain moves with the chain. The *central line* of the tube associated with a polymer chain is defined as the primitive chain (or primitive path). The segments of the real chain wriggle around its primitive chain. The wriggling motions determine the fundamental statistical and dynamical properties of the primitive chain. The wriggling motions progress rapidly; however, their movement amplitudes are limited by the tube diameter a . The tube, like entanglements, is invisible and is conceived to describe how chain entanglements constrain the movement of a chain.

There are other equivalent ways to represent the effect of the tube. As shown in Fig. 8.1, a polymer chain constrained inside a tube of diameter a is equivalent to a chain passing through a sequence of slip-links separated apart by a statistically equal space, a . Each slip-link represents an entanglement with another chain nearby. The links only allow the chain to slide along itself forward or backward. The straight line connecting two adjacent links is regarded as equivalent to the central line of the tube; and

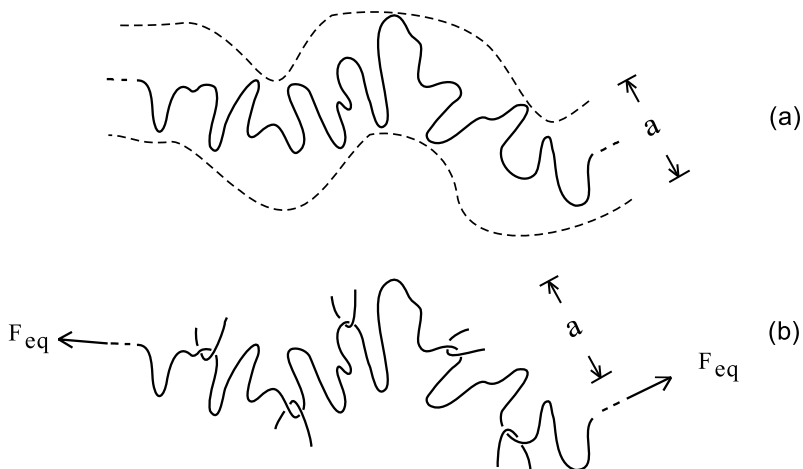


Fig. 8.1 Equivalence of (a) the tube picture and (b) the slip-link picture with the hypothetical tensile force $F_{eq} = 3kT/a$ pulling at both chain ends in describing the constraint effect of entanglement on the movement of a polymer chain.

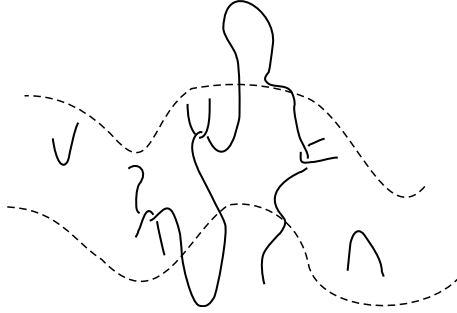


Fig. 8.2 In the slip-link model, a hypothetical tensile force $F_{eq} = 3kT/a$ pulling at both chain ends is necessary to keep the polymer chain constrained by the slip-links; otherwise, the polymer chain will soon shrink along the primitive path and “leak” out from the space between the slip-links or, so to speak, leak out of the tube.

its length, a , is regarded as a step length (also referred to as the entanglement distance) of the primitive chain. The segments of the real polymer chain between two adjacent links wriggle in the direction perpendicular to the primitive path. To use the slip-link picture, it is necessary to assume that tensile forces of the magnitude $F_{eq} = 3kT/a$ (see Appendix 8.A) are applied to both ends of the chain so that the amplitude of the segmental wriggling motions will be basically kept within the tube diameter. Otherwise, the chain could “leak” out through the spaces between the links or, so to speak, leak out of the tube, as shown in Fig. 8.2; and the slip-links would lose the effect of constraining the motions of the chain. The slip-link picture with the tensile forces applied at both chain ends is equivalent to the tube picture.⁹ The primitive chain as defined above has the following two characteristics:

(a) In the equilibrium state, the configuration of the primitive chain is a sequence of random walks. Namely, the primitive chain can be regarded as a freely jointed chain consisting of segments (steps) with length equal to the distance, a , between two adjacent links (the links being equivalent to the joints). Then the mean square end-to-end distance of the polymer chain denoted by R^2 is equal to aL where L is the total contour length of the primitive chain. As the polymer is a Gaussian chain by itself, $R^2 = N_o b^2$ where N_o is the number of Rouse segments per chain and b denotes the root mean square length of a Rouse segment. Then the number of steps on the primitive chain is

$$N \left(= \frac{M}{M_e} \right) = \frac{L}{a} = \frac{R^2}{a^2} = \frac{N_o b^2}{a^2}. \quad (8.3)$$

This equation also implies that each entanglement strand is sufficiently long to be described by a Gaussian chain model, i.e.

$$a^2 = N_e b^2 \quad (8.4)$$

where N_e is the number of Rouse segments per entanglement strand. Equation (8.3) is the most fundamental assumption in the Doi–Edwards theory. (Note: In the Doi–Edwards papers, b was defined as the effective bond length of the real chain.⁹ b can be, as done here, regarded as the root mean square length of the Rouse segment, with the corresponding changes in meaning for N_o and N_e . The use of the Rouse segment, also later adopted by Doi and Edwards,^{16,17} is more convenient for further development of the theory and analyses of the experimental results in terms of the extended theories in the later chapters.)

(b) The Brownian motion of the primitive chain is reptational. The primitive chain moves along itself forward or backward randomly. In other words, each point on the primitive chain follows its immediate neighbor in movement. The important exception is the two chain ends. As the primitive chain moves forward, the “head” can choose its direction randomly; in reverse, as the primitive chain moves backward, the “end” can also choose its direction randomly. This random process of moving forward and backward can be described in terms of the curvilinear diffusion constant defined by

$$D_{cv} = \frac{\langle \Delta S^2 \rangle}{2\Delta t} \quad (8.5)$$

where ΔS is the curvilinear length the primitive chain moves in a short time interval Δt (see Appendix 3.D). At the same time, according to the Einstein relation (Eq. (3.9)),

$$D_{cv} = \frac{kT}{N_o \zeta} \quad (8.6)$$

where ζ is the friction constant of the Rouse segment or bead (also see Appendix 9.A).

8.3 Diffusion Motion

Here, we shall relate the translational diffusion motion of the center of mass of a polymer chain to the curvilinear diffusion constant. Experimentally, the translational diffusion constant can readily be measured.^{18–21}

Doi and Edwards considered the primitive chain as a freely jointed chain with step length a . The positions of the joints (or links) can be labeled as

$$\{\mathbf{R}_n\} = (\mathbf{R}_1, \mathbf{R}_2, \dots, \mathbf{R}_N). \quad (8.7)$$

Then $|\mathbf{R}_n - \mathbf{R}_{n-1}| = a$. Assume that in a time interval Δt , the primitive chain jumps forward or backward with equal probability one step of length a . Then the curvilinear diffusion constant can be defined by

$$D_{cv} = \frac{a^2}{2\Delta t}. \quad (8.8)$$

And the equations of motion can be written as:

$$\mathbf{R}_n(t + \Delta t) = \mathbf{R}_{n+1}(t) \frac{(1 + \xi(t))}{2} + \mathbf{R}_{n-1}(t) \frac{(1 - \xi(t))}{2} \quad (8.9)$$

for $n = 2, 3, \dots, N - 1$

$$\mathbf{R}_1(t + \Delta t) = \mathbf{R}_2(t) \frac{(1 + \xi(t))}{2} + [\mathbf{R}_1(t) + \mathbf{r}(t)] \frac{(1 - \xi(t))}{2} \quad (8.10)$$

$$\mathbf{R}_N(t + \Delta t) = [\mathbf{R}_N(t) + \mathbf{r}(t)] \frac{(1 + \xi(t))}{2} + \mathbf{R}_{N-1}(t) \frac{(1 - \xi(t))}{2} \quad (8.11)$$

where $\xi(t) = -1$ when the primitive chain jumps forward and $\xi(t) = 1$ when it jumps backward, and $\mathbf{r}(t)$ is a vector of random orientation of length $|\mathbf{r}(t)| = a$.

The center of mass of the polymer chain at time t and $t + \Delta t$ can be defined, respectively, by

$$\mathbf{R}_c(t) = \frac{1}{N} \sum_{n=1}^N \mathbf{R}_n(t) \quad (8.12)$$

$$\mathbf{R}_c(t + \Delta t) = \frac{1}{N} \sum_{n=1}^N \mathbf{R}_n(t + \Delta t). \quad (8.13)$$

By subtracting Eq. (8.12) from Eq. (8.13), into both of which Eqs. (8.9)–(8.11) have been substituted, we obtain

$$\begin{aligned} \mathbf{R}_c(t + \Delta t) - \mathbf{R}_c(t) &= \frac{1}{N} \{[\mathbf{R}_N(t) - \mathbf{R}_1(t)]\xi(t) + \mathbf{r}(t)\} \\ &= \frac{1}{N} [\mathbf{R}(t)\xi(t) + \mathbf{r}(t)] \end{aligned} \quad (8.14)$$

where $\mathbf{R}(t) = \mathbf{R}_N(t) - \mathbf{R}_1(t)$ is the end-to-end vector of the polymer chain. Then the time-correlation function of the center-of-mass velocity can be

written as

$$\begin{aligned}
 \langle \mathbf{V}_c(t) \cdot \mathbf{V}_c(t') \rangle &= \frac{1}{\Delta t^2} \langle [\mathbf{R}_c(t + \Delta t) - \mathbf{R}_c(t)] \cdot [\mathbf{R}_c(t' + \Delta t) - \mathbf{R}_c(t')] \rangle \\
 &= \frac{1}{\Delta t^2 N^2} [\langle \xi(t) \xi(t') \mathbf{R}(t) \cdot \mathbf{R}(t') \rangle + \langle \mathbf{r}(t) \cdot \mathbf{r}(t') \rangle \\
 &\quad + \langle \xi(t) \mathbf{R}(t) \cdot \mathbf{r}(t') \rangle + \langle \xi(t') \mathbf{R}(t') \cdot \mathbf{r}(t) \rangle] \\
 &= \frac{1}{\Delta t^2} \left[\frac{a^2}{N} \delta_{tt'} + \frac{a^2}{N^2} \delta_{tt'} \right]. \tag{8.15}
 \end{aligned}$$

For obtaining the above result, we have used the following relations:

$$\langle \xi(t) \xi(t') \mathbf{R}(t) \cdot \mathbf{R}(t') \rangle = \langle \xi(t) \xi(t') \rangle \langle \mathbf{R}(t) \cdot \mathbf{R}(t') \rangle = N a^2 \delta_{tt'} \tag{8.16}$$

$$\langle \mathbf{r}(t) \cdot \mathbf{r}(t') \rangle = a^2 \delta_{tt'} \tag{8.17}$$

and the condition that $\mathbf{R}(t)$ and $\mathbf{r}(t)$ are totally uncorrelated.

The second term of Eq. (8.15) is much smaller than the first term and can be neglected. We can obtain the mean square displacement of the center of mass from time 0 to t by integrating Eq. (8.15) over t and t' . Then, by substituting the result of the double integration into Eq. (3.40), we obtain

$$\begin{aligned}
 6D_G t &= \sum_{t'} \sum_{t''} \frac{a^2}{N} \delta_{t't''} \\
 &= \left(\frac{a^2}{\Delta t} \right) \frac{t}{N} = \frac{2D_{cv} t}{N}. \tag{8.18}
 \end{aligned}$$

For the last equality, Eq. (8.8) has been used.

From Eq. (8.18)

$$D_G = \frac{D_{cv}}{3N}. \tag{8.19}$$

Using Eqs. (8.3), (8.4) and (8.6), Eq. (8.19) can be written as

$$D_G = \frac{kTN_e}{3\zeta N_o^2}. \tag{8.20}$$

This result shows that the diffusion constant of a long polymer chain in a concentrated system, because of the constraint effect of entanglement, is inversely proportional to the square of the molecular weight. This molecular-weight dependence is distinctively different from the result, $D_G \propto M^{-1}$, given by the Rouse model (Chapter 3) and its observation is often regarded as the indication of the reptational motion.¹⁸ As shown in

Chapter 10, the scaling relation $D_G \propto M^{-2}$ for entangled nearly monodisperse polymers has been widely observed.

8.4 Relaxation Modulus

In Chapter 4, we studied the fundamental importance of the relaxation modulus $G(t)$ in linear viscoelasticity. Here, we shall show how the theoretical form of $G(t)$ in the Doi-Edwards model is derived in terms of molecular structural and dynamic parameters. In the Doi-Edwards theory the study of $G(t)$ includes the nonlinear region. However, we shall postpone full discussion of $G(t)$ in the nonlinear region until Chapter 12.

In describing the entanglement effect in terms of the slip-link picture, we have mentioned that, at both ends of the chain in the equilibrium state, a tensile force F_{eq} (Fig. 8.1b) needs to be applied to keep the chain “extended” so that the chain will not leak out of the tube (Fig. 8.2). Under such a condition, the primitive chain can maintain its contour length L . The magnitude of F_{eq} can be calculated according to the elementary theory of chain statistical mechanics. As shown in Appendix 8.A, the tensile force that keeps a Gaussian chain section with n segments at a length of l is $(3kT/nb^2)l$. Now the primitive-chain contour length is L ; thus,

$$F_{eq} = \left(\frac{3kT}{N_e b^2} \right) L = \frac{3kT}{a}. \quad (8.21)$$

This force should be equal to the tensile force on each entanglement strand which, following the same arguments, is given by $(3kT/N_e b^2)a = 3kT/a$. Thus, the two are consistent.

In Chapters 6 and 7, we showed that the average contribution to the stress tensor from a segment with length vector \mathbf{R} and tensile force \mathbf{F} is $-\langle \mathbf{R}\mathbf{F} \rangle$. For a particular entanglement strand with the length vector denoted by \mathbf{r}_i and with n_i segments, the tensile force is $\mathbf{F}_i = (3kT/n_i b^2)\mathbf{r}_i$. Thus, for a polymer system where there are c identical chains per unit volume and each chain has N entanglement strands, the stress tensor at a certain time, t , is expressed as

$$\mathbf{T}(t) = -3ckT \sum_{i=1}^N \left\langle \frac{\mathbf{r}_i(t)\mathbf{r}_i(t)}{n_i(t)b^2} \right\rangle + P\mathbf{\delta}. \quad (8.22)$$

In Eq. (8.22), we have neglected the contribution from the momentum transfer, which being isotropic, even if not negligible, can be absorbed in p .

Assume that, at time $t \leq 0$, the polymeric liquid system is in the equilibrium state, and a particular chain constrained by the slip-links in the system has a configuration as shown in Fig. 8.3(a). At $t = 0$, a step deformation \mathbf{E} is applied to the system, and the configuration of the chain together with the slip-links is immediately changed to that shown in Fig. 8.3(b). At this stage, the stress tensor is given by:

$$\mathbf{T} = -3ckT \sum_{i=1}^N \left\langle \frac{\mathbf{r}'_i \mathbf{r}'_i}{n'_i b^2} \right\rangle + p\delta \quad (8.23)$$

where

$$\mathbf{r}'_i = \mathbf{E} \cdot \mathbf{r}_i \quad (8.24)$$

and n'_i is the number of segments in the i th entanglement strand. (Note: Following the notation of Doi and Edwards, the apostrophe mark “'” is used to indicate the state after the application of the deformation \mathbf{E} , which is opposite to the way it is used in Chapter 5, where the apostrophe mark indicates the state before deformation (Eq. (5.18))). Because the chain has not had a chance to slide through the slip-links, n'_i is equal to its equilibrium value, n_i (i.e. the value before the deformation is applied). Thus, the tensile force on the i th entanglement strand becomes:

$$\mathbf{F}'_i = \left(\frac{3kT}{n_i b^2} \right) \mathbf{r}'_i. \quad (8.25)$$

Because \mathbf{r}'_i is affected by the applied deformation, and n_i has not changed, the tensile forces on the different entanglement strands are no longer balanced by one another along the primitive chain. In such a situation, the chain must slide through the slip-links to readjust the segmental distribution $\{n_i\}$ along the chain. In this readjustment process, entanglement strands with higher tensile forces will pull segments from those with lower tensile forces. This dynamic process will end in a time $t = T_{eq}$ when the tensile forces along the whole primitive chain become balanced and equal to its equilibrium value $3kT/a$ (Eq. (8.21)), reaching a state as shown in Fig. 8.3(c). Denote the number of segments in the i th entanglement strand at the end of the readjustment process by n''_i . Then from the equilibrium equation

$$|\mathbf{F}_i| = \frac{3kT}{n''_i b^2} |\mathbf{r}'_i| = \frac{3kT}{a} \quad (8.26)$$

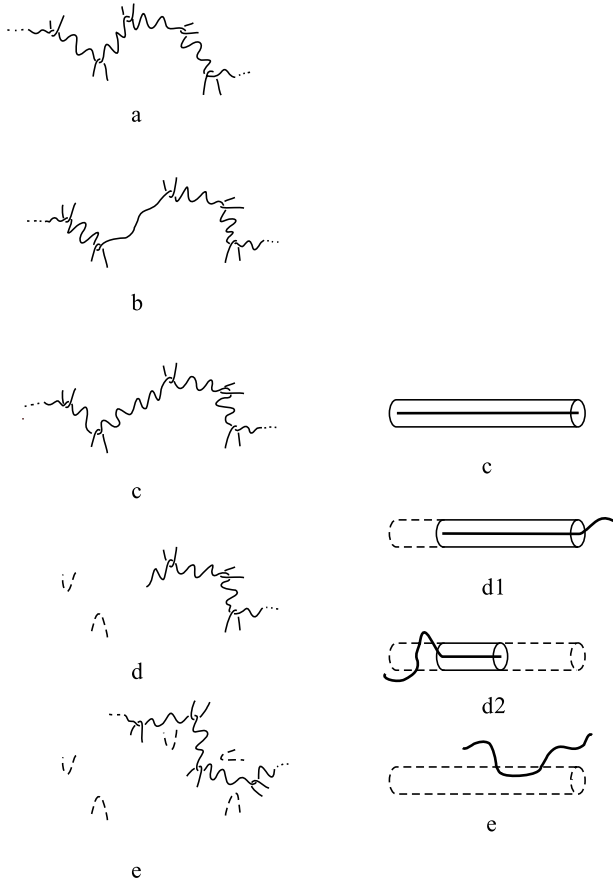


Fig. 8.3 Schematic illustration of the entanglement configuration on a polymer chain and its relaxation following a step deformation. (a) The equilibrium state before a deformation is applied. (b) Immediately after the application of a step deformation at time $t = 0$, entanglement strands of the chain are either stretched or compressed. (c) At $t \sim T_{eq}$, the readjustment of the segmental distribution balances the tensile force along the primitive chain and recovers its equilibrium contour length. At this stage, the conformation of the primitive chain is in a non-equilibrium state; the positions of the slip-links are not in a random configuration (the non-random slip-links at this stage are referred to as the original slip-links). On the right, an equivalent deformed tube is shown (shown as a straight tube to symbolize its anisotropy; the deformed tube at this stage is referred to as the original tube). (d) By reptation, the chain disengages from the original slip-links. Illustrated in terms of the tube picture on the right, (d1) and (d2): As the chain reptates right and left, those parts of the original tube which have been reached by the chain ends disappears (indicated by the dashed lines). (e) Finally the chain disengages from all the original slip-links and forms a new set of slip-links with other chains, returning to the equilibrium state, which is statistically equivalent to (a). On the right, the original tube vanishes or the chain is totally out of the original tube.

we obtain

$$n_i'' = \frac{a|\mathbf{r}'_i|}{b^2} = \frac{a|\mathbf{E} \cdot \mathbf{r}_i|}{b^2}. \quad (8.27)$$

At the same time, the contour length of the primitive chain, L'' , recovers its equilibrium value, L . Thus,

$$L'' = \sum_{i=f}^l |\mathbf{r}'_i| = L = \frac{N_o b^2}{a} \quad (8.28)$$

where the limits of summation, f and l , represent the first and the last entanglement strands of the polymer chain at $t = T_{eq}$. Using Eq. (8.27), the number of entanglement strands is obtained as

$$N'' = l - f = \frac{N_o}{\langle n_i'' \rangle} = \frac{N_o b^2}{\langle |\mathbf{E} \cdot \mathbf{r}_i| \rangle a}. \quad (8.29)$$

If the unit vector along \mathbf{r}_i is denoted by \mathbf{u}_i ;

$$\mathbf{r}_i = a\mathbf{u}_i. \quad (8.30)$$

Equation (8.29) can be rewritten as

$$N'' = \frac{N_o b^2}{\langle |\mathbf{E} \cdot \mathbf{u}| \rangle a^2}. \quad (8.31)$$

Through the equilibration process of segmental redistribution among the different entanglement strands, the stress tensor given by Eq. (8.23) is changed to a new form at $t = T_{eq}$. Using Eqs. (8.3), (8.24), (8.27), (8.30) and (8.31), the stress tensor at $t = T_{eq}$ is obtained as

$$\begin{aligned} \mathbf{T} &= -3cN''kT \left\langle \frac{\mathbf{r}'_i \mathbf{r}'_i}{n_i'' b^2} \right\rangle + P\delta \\ &= -3cNkT \left\langle \frac{(\mathbf{E} \cdot \mathbf{u})(\mathbf{E} \cdot \mathbf{u})}{|\mathbf{E} \cdot \mathbf{u}|} \right\rangle \langle |\mathbf{E} \cdot \mathbf{u}| \rangle^{-1} + P\delta. \end{aligned} \quad (8.32)$$

From Eq. (8.32), the modulus value at $t = T_{eq}$, as a function of deformations \mathbf{E} , can be calculated. The chain-slippage mechanism involved in the above modeling leads to two effects: one is the process of equilibrating the segmental distribution along the primitive chain; the other is the reduction of the number of entanglement strands. In Eq. (8.32), the equilibration process of the segmental redistribution is related to $|\mathbf{E} \cdot \mathbf{u}|$ inside the first $\langle \dots \rangle$, which is from Eq. (8.27); and the reduction of the number of entanglement strands is related to $\langle |\mathbf{E} \cdot \mathbf{u}| \rangle^{-1}$, which is from Eq. (8.31).

For a simple shear step deformation,

$$\mathbf{E} = \begin{pmatrix} 1 & \lambda & 0 \\ 0 & 1 & 0 \\ 0 & 0 & 1 \end{pmatrix} \quad (8.33)$$

the xy component of the stress tensor can be obtained from Eq. (8.32) as

$$T_{xy} = \tau_{xy} = -3cNkT \frac{\left\langle \left((u_x + \lambda u_y) u_y \right) / \sqrt{(u_x + \lambda u_y)^2 + u_y^2 + u_z^2} \right\rangle}{\left\langle \sqrt{(u_x + \lambda u_y)^2 + u_y^2 + u_z^2} \right\rangle} \quad (8.34)$$

where u_x , u_y , and u_z are the components of the unit vector \mathbf{u} in the x , y , and z directions. To calculate the shear stress T_{xy} from Eq. (8.34) at different values of the applied strain λ , we make the transformation to spherical coordinates (r , θ , ϕ):

$$\begin{aligned} u_x &\rightarrow \sin \theta \cos \phi \\ u_y &\rightarrow \sin \theta \sin \phi \\ u_z &\rightarrow \cos \theta \end{aligned}$$

and perform averaging over all orientations for $\langle \dots \rangle$, i.e.

$$\langle \dots \rangle \rightarrow \frac{1}{4\pi} \int_0^{2\pi} \int_0^\pi \dots \sin \theta \, d\theta \, d\phi.$$

In the nonlinear region, T_{xy} can only be calculated numerically (by a computer program). In the linear region, where all the second order terms and beyond in Eq. (8.34) can be neglected, we obtain

$$\tau_{xy} = -\frac{4}{5}cNkT\lambda. \quad (8.35)$$

We define the modulus G_N by

$$G_N = -\frac{\tau_{xy}}{\lambda} = \frac{4}{5}cNkT. \quad (8.36)$$

Equation (8.36) becomes Eq. (8.2) for a polymer melt; and as mentioned above, G_N is smaller by a factor of $4/5$ than the result based on the theory of rubber elasticity (Eq. (8.1)), where each entanglement is treated as a permanent cross-link. The reduction factor $4/5$ is entirely due to the segmental redistribution along the primitive chain. From Eq. (8.31), it can be shown that $N'' = N$ in the linear region; in other words, the reduction of the number of entanglement strands occurs only in the nonlinear region.

The chain-slippage effects are responsible for the theoretical form given by Eq. (8.32). For a comparison, we consider the situation where each slip-link is replaced by a permanent cross-link. In this situation, the equilibrium time constant T_{eq} is irrelevant, and n'_i remains equal to n_i . Using Eqs. (8.4) and (8.30), we obtain from Eqs. (8.23) and (8.24)

$$\mathbf{T} = -3cNkT\langle(\mathbf{E} \cdot \mathbf{u})(\mathbf{E} \cdot \mathbf{u})\rangle + P\boldsymbol{\delta}. \quad (8.37)$$

As shown in Appendix 8.B, Eq. (8.37) is equivalent to Eq. (5.50) with $G = cNkT$ and to the result of rubber elasticity obtained in Chapter 2. In the linear region, Eq. (8.1) is obtained from Eq. (8.37).

8.5 Relaxation of Stress by Reptation

Equation (8.32) gives the stress, and thus modulus, of a well entangled polymeric liquid at $t = T_{eq}$, following a step deformation at $t = 0$. At this stage, as shown in Fig. 8.3(c), the configuration of slip-link positions or the distribution of entanglement-strand orientations is not random like that of the equilibrium state before the application of the step deformation. Only when the configuration has recovered from the non-random situation to the equilibrium random state (statistically equivalent to that of Fig. 8.3(a)), can the extra stress at $t = T_{eq}$ relax back to zero. To reach this stress-free state, each chain in the polymeric liquid system needs to be totally out of the non-random configuration of slip-links, through which it has been entangled with neighboring chains (or, equivalently, out of the deformed or statistically anisotropic tube), and re-forms a new random configuration of entanglements with other chains (or, equivalently, re-forms a new statistically isotropic tube). As described by the reptation mechanism in the section on diffusion motion and as represented in Fig. 8.3(d) (Figs. 8.3(d1), and 8.3(d2)), the polymer chain will move back and forth along itself and eventually get out of the deformed tube totally and reach the equilibrium state in which the orientations of the newly formed entanglement strands are totally random (Fig. 8.3(e)). By considering the reptation mechanism, the stress relaxation functional form is derived as follows: First, for the physical quantity of interest, the equation of motion will be formulated.

The segmental distribution along the primitive chain has reached the equilibrium state at $t = T_{eq}$. In this state, by using Eq. (8.27), Eq. (8.32)

can be rewritten as

$$\mathbf{T} = -3ckT \sum_{i=f}^l \left\langle \frac{\mathbf{u}'_i \mathbf{r}'_i}{a} \right\rangle + P\delta \quad (8.38)$$

where $\mathbf{u}'_i = \mathbf{r}'_i/|\mathbf{r}'_i|$ is the orientation of the i th entanglement strand. We shall replace the discrete representation of the primitive chain (namely, the one consisting of entanglement-strand steps) by the continuous one (namely, the central line of the tube). In doing so, the summation over the entanglement strands will be replaced by integration along the primitive path, s ; and the unit vector of the entanglement strand, $\mathbf{u}'_i(t)$, will be replaced by the unit vector $\mathbf{u}(s, t) = \partial \mathbf{R}(s, t)/\partial s$ which represents the tangential direction along the contour-length coordinate s (i.e. $\sum \mathbf{u}'_i(t) \mathbf{r}'_i(t) \rightarrow \int_0^L \mathbf{u}(s, t) \mathbf{u}(s, t) ds$). Then, Eq. (8.38) can be rewritten as

$$\mathbf{T} = -\frac{3ckT}{a} \int_0^L \langle \mathbf{u}(s, t) \mathbf{u}(s, t) \rangle ds + P\delta. \quad (8.39)$$

By absorbing the isotropic part of the integrand into the pressure term, Eq. (8.39) can be expressed as

$$\mathbf{T} = -\frac{3ckT}{a} \int_0^L \mathbf{S}(s, t) ds + P\delta \quad (8.40)$$

where

$$\mathbf{S}(s, t) = \left\langle \mathbf{u}(s, t) \mathbf{u}(s, t) - \frac{\delta}{3} \right\rangle. \quad (8.41)$$

Assume in a short time step Δt the primitive chain moves a curvilinear distance Δs . Then

$$\mathbf{u}(s, t + \Delta t) = \mathbf{u}(s + \Delta s, t). \quad (8.42)$$

As Δs can be positive or negative and is random, its distribution is characterized by the moments

$$\langle \Delta s \rangle = 0; \quad \langle \Delta s^2 \rangle = 2D_{cv} \Delta t. \quad (8.43)$$

As $\mathbf{S}(s, t)$ is a function of $\mathbf{u}(s, t)$ (Eq. (8.41)), and because of Eq. (8.42) with Δs being random

$$\mathbf{S}(s, t + \Delta t) = \langle \mathbf{S}(s + \Delta s, t) \rangle. \quad (8.44)$$

Using Eq. (8.43), the right hand side of Eq. (8.44) is expanded as

$$\begin{aligned}
 \mathbf{S}(s, t + \Delta t) &= \left\langle \mathbf{S}(s, t) + \Delta s \frac{\partial \mathbf{S}(s, t)}{\partial s} + \frac{1}{2} \Delta s^2 \frac{\partial^2 \mathbf{S}(s, t)}{\partial s^2} + \dots \right\rangle \\
 &= \mathbf{S}(s, t) + \langle \Delta s \rangle \frac{\partial \mathbf{S}(s, t)}{\partial s} + \frac{1}{2} \langle \Delta s^2 \rangle \frac{\partial^2 \mathbf{S}(s, t)}{\partial s^2} \\
 &= \mathbf{S}(s, t) + D_{cv} \Delta t \frac{\partial^2 \mathbf{S}(s, t)}{\partial s^2}.
 \end{aligned} \tag{8.45}$$

That is

$$\frac{\partial \mathbf{S}(s, t)}{\partial t} = D_{cv} \frac{\partial^2 \mathbf{S}(s, t)}{\partial s^2}. \tag{8.46}$$

At both ends of the chain, the distribution of \mathbf{u} is random so that

$$\mathbf{S}(s, t) = \left\langle \mathbf{u}\mathbf{u} - \frac{\delta}{3} \right\rangle = 0 \quad \text{at } s = 0; L. \tag{8.47}$$

Equation (8.46), with the above boundary condition, describes the relaxation process from the state of Fig. 8.3(c) to the state of Fig. 8.3(d) and then to that of Fig. 8.3(e). The relaxation from Fig. 8.3(b) to Fig. 8.3(c) is finished in time T_{eq} . Because T_{eq} is in general much shorter than the characteristic time of the relaxation process described by Eq. (8.46), the state of Fig. 8.3(c) is assumed as the initial state ($t = 0$); namely, $\mathbf{S}(s, t = 0)$ (compare Eq. (8.32) with Eqs. (8.40) and (8.41)) is assumed as

$$\mathbf{S}(s, t = 0) = \left\langle \frac{(\mathbf{E} \cdot \mathbf{u})(\mathbf{E} \cdot \mathbf{u})}{|\mathbf{E} \cdot \mathbf{u}|} \right\rangle \langle |\mathbf{E} \cdot \mathbf{u}| \rangle^{-1} - \frac{\delta}{3} \equiv \mathbf{Q}(\mathbf{E}). \tag{8.48}$$

With this initial condition and the boundary condition given by Eq. (8.47), the solution of the differential equation, Eq. (8.46), is derived in terms of normal modes as:

$$\mathbf{S}(s, t) = \mathbf{Q}(\mathbf{E}) \sum_{p=\text{odd}} \frac{4}{p\pi} \sin\left(\frac{p\pi s}{L}\right) \exp\left(\frac{-tp^2}{T_d}\right) \tag{8.49}$$

where

$$T_d = \frac{L^2}{D_{cv}\pi^2} \tag{8.50}$$

is the characteristic time for the disentanglement process.

Substituting Eq. (8.49) into Eq. (8.40), one obtains

$$\mathbf{T}(t) = -\frac{3cLkT}{a}\mathbf{Q}(\mathbf{E}) \sum_{p=\text{odd}} \frac{8}{p^2\pi^2} \exp\left(\frac{-p^2t}{T_d}\right) + P\delta \quad (8.51)$$

which can be rewritten as

$$\mathbf{T}(t) = -\frac{15}{4}G_N\mathbf{Q}(\mathbf{E})\mu(t) + P\delta \quad (8.52)$$

with

$$G_N = \frac{4}{5}\frac{cLkT}{a} = \frac{4}{5}cNkT \quad (8.53)$$

as given by Eq. (8.36), and

$$\mu(t) = \sum_{p=\text{odd}} \frac{8}{p^2\pi^2} \exp\left(\frac{-p^2t}{T_d}\right). \quad (8.54)$$

The relaxation modulus $G(t)$ that follows a step shear strain in the linear region can be obtained from Eqs. (8.52)–(8.54) as

$$G(t) = G_N\mu(t). \quad (8.55)$$

It will be shown from analyzing the experimental results (Chapter 10) that G_N is the so-called plateau modulus.

Substituting Eqs. (8.3), (8.4), and (8.6) into Eq. (8.50), T_d can be rewritten as

$$T_d = \frac{\zeta N_o^3 b^2}{\pi^2 k T N_e} = K \frac{M^3}{M_e} \quad (8.56)$$

where K is the frictional factor that has been defined by Eq. (3.57). As with the Rouse theory, the Doi–Edwards theory has been developed on the same frictional-factor basis. The Doi–Edwards theory, however, having taken the constraint effect of entanglement into account, gives a structural factor for the longest relaxation time quite different from that of the Rouse theory. The former is proportional to M^3 and inversely proportional to M_e ; the latter is proportional to M^2 . As the relaxation-time distributions are also quite different, the line shapes of the relaxation modulus $G(t)$ predicted by the two theories are characteristically different. As we shall see in Chapter 9, the Doi–Edwards theory has provided the basic structural element for the plateau in $G(t)$ to appear.

Substituting Eqs. (8.53)–(8.56) into Eqs. (4.30) and (4.63), one obtains the zero-shear viscosity η_0 and the steady-state compliance J_e^0 , respectively, as

$$\eta_0 = \frac{\pi^2}{15} K \left(\frac{\rho R T M^3}{M_e^2} \right) \quad (8.57)$$

$$J_e^0 = \frac{3}{2} \left(\frac{M_e}{\rho R T} \right). \quad (8.58)$$

The $\eta_0 \propto M^3$ relation of Eq. (8.57) is still different from the experimental observation $\eta_0 \propto M^{3.4}$ (Fig. 4.7), while Eq. (8.58) agrees with the basic molecular-weight independence of J_e^0 in the high-molecular-weight region (Fig. 4.12). A detailed comparison of Eqs. (8.57) and (8.58) with the Rouse theory and the extended reptation theory as well as experimental results will be discussed in Chapter 10.

Appendix 8.A — Tension in a Gaussian Chain Between Two Fixed Points

From Chapter 1, we know that the probability for the end-to-end vector to be \mathbf{R} in a Gaussian chain with N Gaussian (or Rouse) segments is given by

$$\Phi(\mathbf{R}, N) \propto \exp \left(\frac{-3\mathbf{R}^2}{2Nb^2} \right). \quad (8.A.1)$$

Then the free energy of the Gaussian chain can be written as

$$\begin{aligned} A &= -kT \ln(\Phi) + C \\ &= kT \left(\frac{3\mathbf{R} \cdot \mathbf{R}}{2Nb^2} \right) + C \end{aligned} \quad (8.A.2)$$

where C is a constant. Define the tensile force on the Gaussian chain with both ends fixed at positions 1 and 2 as

$$\mathbf{F} = \mathbf{F}_1 = -\mathbf{F}_2 \quad (8.A.3)$$

with \mathbf{F} pointing in the same direction as \mathbf{R} . In order to know the tensile force \mathbf{F} , we calculate, using Eq. (8.A.2), the change in free energy dA caused by an infinitesimal increment in \mathbf{R} .

$$dA = \left(\frac{3kT}{Nb^2} \right) \mathbf{R} \cdot d\mathbf{R}. \quad (8.A.4)$$

The free energy change is related to the tensile force \mathbf{F} by

$$dA = \mathbf{F} \cdot d\mathbf{R}. \quad (8.A.5)$$

Thus, from the last two equations,

$$\left[\mathbf{F} - \left(\frac{3kT}{Nb^2} \right) \mathbf{R} \right] \cdot d\mathbf{R} = 0 \quad (8.A.6)$$

This scalar product must be equal to zero for any infinitesimal increment $d\mathbf{R}$. Thus,

$$\mathbf{F} = \left(\frac{3kT}{Nb^2} \right) \mathbf{R}. \quad (8.A.7)$$

Appendix 8.B — Equivalent Expressions for Rubber Elasticity

Equation (5.50) with $G = cNkT$ and Eq. (8.37) are equivalent, if we prove

$$\langle (\mathbf{E} \cdot \mathbf{u})(\mathbf{E} \cdot \mathbf{u}) \rangle = \frac{\mathbf{B}}{3}. \quad (8.B.1)$$

In a chosen Cartesian coordinate system where the components of the unit vector \mathbf{u} are denoted by $\{u_i\}$ ($i = 1, 2,$ and 3), the ij component of $\langle (\mathbf{E} \cdot \mathbf{u})(\mathbf{E} \cdot \mathbf{u}) \rangle$ is written as

$$\begin{aligned} \langle (\mathbf{E} \cdot \mathbf{u})_i (\mathbf{E} \cdot \mathbf{u})_j \rangle &= \left\langle \left(\sum_k E_{ik} u_k \right) \left(\sum_l E_{jl} u_l \right) \right\rangle \\ &= \sum_k \sum_l E_{ik} E_{jl} \langle u_k u_l \rangle \\ &= \sum_k \sum_l E_{ik} E_{jl} \frac{\delta_{kl}}{3} \\ &= \frac{1}{3} \sum_k E_{ik} E_{jk} = \frac{1}{3} \sum_k E_{ik} E_{kj}^T. \end{aligned} \quad (8.B.2)$$

Using the definition of the Finger tensor (Eq. (5.35)), Eq. (8.B.1) is proven.

References

1. Fox, T. G., and Flory, P. J., *J. Phys. Colloid Chem.* **55**, 221 (1951).
2. Berry, G. C., and Fox, T. G., *Adv. Polym. Sci.* **5**, 261 (1968).
3. Mark, H., and Tobolsky, A. V., *Physical Chemistry of High Polymeric Systems* Interscience, New York (1950).

4. Lin, Y.-H., *Macromolecules* **19**, 159 (1986).
5. Onogi, S., Masuda, T., and Kitagawa, K., *Macromolecules* **3**, 109 (1970).
6. Lodge, A. S., *Trans. Faraday Soc.* **52**, 120 (1956).
7. Ferry, J. D., *Viscoelastic Properties of Polymers (3rd edn)*, Wiley, New York (1980).
8. Graessley, W. W., *Adv. Polym. Sci.* **16**, 1 (1974).
9. Doi, M., and Edwards, S. F., *J. Chem. Soc., Faraday Trans. 2*, **74**, 1789 (1978); **74**, 1802 (1978); **74**, 1818 (1978); and **75**, 38 (1979).
10. de Gennes, P.-G., *J. Chem. Phys.* **55**, 572 (1971).
11. Lin, Y.-H., *Macromolecules*, **17**, 2846 (1984).
12. Lin, Y.-H., *Macromolecules* **19**, 159 (1986); **19**, 168 (1986); **22**, 1437 (1989).
13. Lin, Y.-H., *J. Non-Newtonian Fluid Mech.*, **23**, 163 (1987).
14. Lin, Y.-H., *Makromol. Chem., Macromol. Symp.* **56**, 1 (1992).
15. Lin, Y.-H., *Macromolecules* **20**, 885 (1987).
16. Doi, M., *J. Polym. Sci., Polym. Phys. Ed.* **18**, 1005 (1980).
17. Doi, M., and Edwards, S. F., *The Theory of Polymer Dynamics*, Oxford Univ. Press (1986).
18. Klein, J., *Nature* **271**, 143 (1978).
19. Mills, P. J., Green, P. F., Palmstrom, C. J., Mayer, J. W., and Kramer, E. J., *Appl. Phys. Lett.* **45**, 958 (1984); Green, P. F., Palmstrom, C. J., Mayer, J. W., and Kramer, E. J., *Macromolecules* **18**, 501 (1985); Green, P. F., and Kramer, E. J., *Macromolecules* **19**, 1108 (1986).
20. Pearson, D. S., Ver Strate, G., von Meerwall, E., and Schilling, F. C., *Macromolecules* **20**, 1133 (1987); Pearson, D. S., Fetters, L. J., Graessley, W. W., Ver Strate, G., and von Meerwall, E., *Macromolecules* **27**, 711 (1994).
21. Lodge, T. P., Rotstein, N. A., and Prager, S., *Advances in Chemical Physics* **LXXIX** (ed. I. Prigogine and S. A. Rice). Wiley, New York (1990), and references therein.

Chapter 9

Molecular Theory of Polymer Viscoelasticity — The Extended Reptation Model

9.1 Intramolecular Processes

As discussed in the last chapter, the Doi–Edwards theory describes how the stress initiated by a step deformation relaxes by the reptational process after the equilibration time T_{eq} of the segmental redistribution along the primitive chain. As will be shown below, the reptational process plays the most important role in the terminal region of the relaxation modulus.

Without theoretical analysis, we can clearly identify at least three relaxation processes by simply looking at the experimental results of the stress relaxation curves. Shown in Fig. 9.1 are two relaxation modulus curves of a nearly monodisperse polystyrene sample ($M_w = 422,000$; $M_w/M_n = 1.05$) whose molecular weight is much greater than the entanglement molecular weight M_e : One of the curves, $G(t)$ or $G(\lambda \rightarrow 0, t)$, is in the linear region; the other at the shear strain $\lambda = 5$, $G(\lambda = 5, t)$, is in the nonlinear region (also see Fig. 12.3). The two curves are superposed in the terminal region by shifting the $G(\lambda = 5, t)$ curve upwards along the modulus axis by a factor that is the inverse of the so-called damping factor. This will be discussed below. The kind of nonlinear result shown in Fig. 9.1 was first reported and extensively studied by Osaki *et al.*^{1–5}

The $G(t)$ curve in Fig. 9.1 shows two distinct relaxation processes separated by a plateau.^{6,7} The first one has been called the transition process (denoted by $\mu_A(t)$ below)^a while the second is called the terminal process (denoted by $\mu_C(t)$ below). As shown in Figs. 4.6 and 4.9, the plateau widens, and the two relaxation processes separate further apart as the molecular weight increases. For a nonlinear relaxation modulus $G(\lambda, t)$ as

^aSee the note at the end of this chapter for a clarification of the term “transition region”.

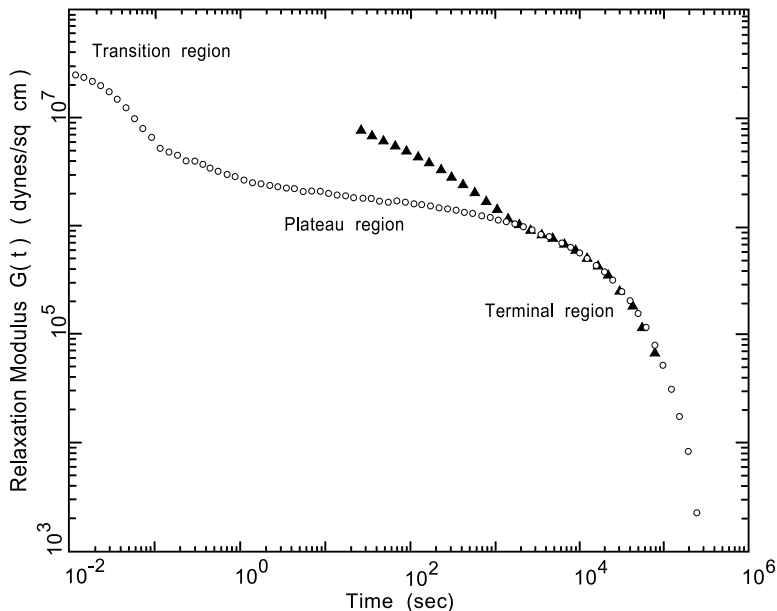


Fig. 9.1 Relaxation modulus $G(\lambda, t)$ in the linear ($\lambda \rightarrow 0$; $\circ\circ\circ$) and nonlinear ($\lambda = 5$; $\blacktriangle\blacktriangle\blacktriangle$) regions of a nearly monodisperse polystyrene melt ($M_w = 4.22 \times 10^5$). The $G(\lambda = 5, t)$ curve was measured at a temperature different from the reference temperature (127.5°C) of the shown $G(\lambda \rightarrow 0, t)$ master curve; as shown the $G(\lambda = 5, t)$ curve has been shifted along both the time axis and the modulus axis to superpose on the $G(\lambda \rightarrow 0, t)$ curve in the terminal region. (See Fig. 12.3 for the results of $G(\lambda = 0.2, t)$ and $G(\lambda = 5, t)$, both measured at the same temperature.)

shown in Fig. 9.1, there appears a distinctive relaxation process (denoted by $\mu_B^*(t, \lambda)$ below, which is also the notation used in its theoretical study in Chapter 12) in the time region corresponding to the $G(t)$ plateau. At the same time, the relaxation curves $G(\lambda, t)$ at different λ values are superposable onto the $G(t)$ curve in the terminal region by a vertical shift. From the superposition, the λ dependence of the shifting factor, $h(\lambda) = G(\lambda, t)/G(\lambda \rightarrow 0, t)$, can be obtained, which is often referred to as the damping function (also see Chapter 12). As shown in Fig. 9.2,^{8,9} and as reported by Osaki *et al.*,^{4,5} Vrentas *et al.*,¹⁰ and Pearson,¹¹ the measured damping factors are in close agreement with the Doi–Edwards curve calculated using Eq. (8.34). It is important to point out that the theoretical $h(\lambda)$ curve does not involve a single fitting parameter and, as confirmed by experimental results, is independent of molecular weight and the type of polymer. In other words, $h(\lambda)$ is universal for nearly monodisperse

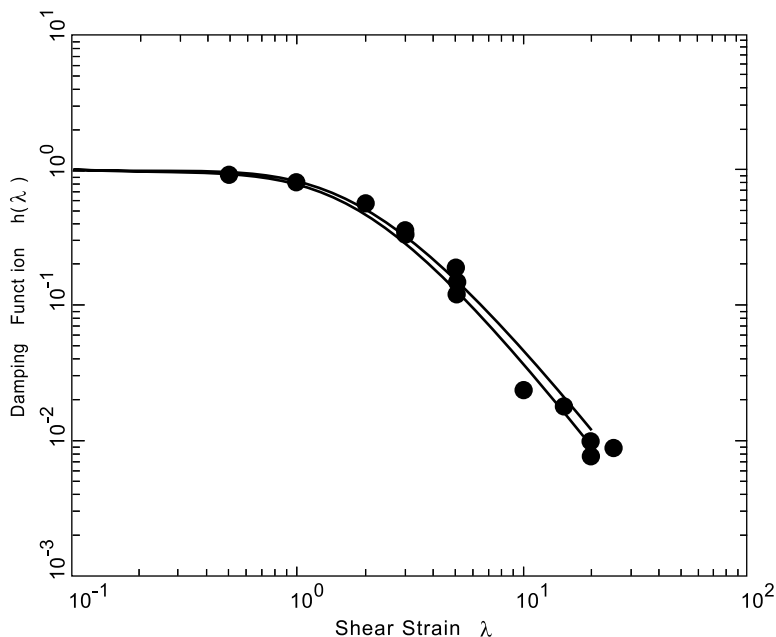


Fig. 9.2 Comparison of the damping functions: the measured values (\bullet) and the curve calculated from Eq. (8.34) (the lower line) and that calculated from Eq. (12.17) with the independent alignment approximation (the upper line).

polymers in the entanglement region. This result, a very successful aspect of the Doi–Edwards theory, supports that the reptational process discussed in the last chapter applies to the terminal region of $G(t)$. In Fig. 9.1, the $G(t)$ and $G(\lambda = 5, t)$ curves are superposed in the terminal region by taking the damping factor into account.

As described above, we can clearly observe three distinct relaxation processes. It is obvious that to fully describe the relaxation modulus, $G(t)$ or $G(t, \lambda)$, we need to consider other processes in addition to the reptational process. These additional processes may suggest the answer for the deviation of the observed scaling, $\eta \propto M^{3.4}$, from the prediction of the *pure* reptational chain model, $\eta \propto M^3$.

Doi¹² has proposed a theory, which will be discussed in detail in Chapter 12, describing $\mu_B^*(t, \lambda)$ as the relaxation of tension on the primitive chain. The theory predicts that the $\mu_B^*(t, \lambda)$ process is not observable in the linear region, which has been found to be in agreement with experiment.⁸ However, corresponding to the dynamics of $\mu_B^*(t, \lambda)$, there is a process

(denoted by $\mu_B(t)$ below) affecting $G(t)$ in the linear region. This process was first theoretically studied by Doi^{13,14} and then by Lin.¹⁵ Although the $\mu_B(t)$ and $\mu_B^*(t, \lambda)$ processes have the same dynamic origin, their mechanisms for affecting the relaxation modulus are different. Because the molecular dynamics for $\mu_B(t)$ is the same as that of $\mu_B^*(t, \lambda)$, either $\mu_B(t)$ or $\mu_B^*(t, \lambda)$ occurs in the time region of the plateau in $G(t)$.

Considering the transition of the stress level given by Eq. (8.37) to that given by Eq. (8.32), Lin¹⁵ has proposed that a minor process $\mu_X(t)$ exists between the $\mu_A(t)$ process region and the plateau region, namely, the $\mu_B(t)$ process region.

In summary, four processes in order of increasing relaxation time, $\mu_A(t)$, $\mu_X(t)$, $\mu_B(t)$, and $\mu_C(t)$, have been identified. Below, we shall follow Lin's steps¹⁵ in showing the molecular dynamics these four processes represent and how they occur in $G(t)$.

9.2 Contour Length Fluctuations of the Primitive Chain

According to the Doi–Edwards theory, after time $t = T_{eq}$ following a step deformation at $t = 0$, the stress relaxation is described by Eqs. (8.52)–(8.56). In obtaining these equations, it is assumed that the primitive-chain contour length is *fixed* at its equilibrium value at all times. And the curvilinear diffusion of the primitive chain relaxes momentarily the orientational anisotropy (as expressed in terms of the unit vector $\mathbf{u}(s, t) = \partial \mathbf{R}(s, t) / \partial s$), or the stress anisotropy, on the portion of the tube that is reached by either of the two chain ends. The theory based on these assumptions, namely, the Doi–Edwards theory, is called the *pure* reptational chain model. In reality, the primitive-chain contour length should not be fixed, but rather fluctuates (stretches and shrinks) because of thermal (Brownian) motions of the segments.

Doi and Edwards treated the polymer chain as a Gaussian chain in the time region $t < T_{eq}$. They assumed that the equilibration process of segmental redistribution took place before T_{eq} . Even though they did not deal with the dynamic behavior of the equilibration process, they used the Gaussian chain model to obtain the stress at the end of the equilibration process (Eq. (8.32)). To be consistent, the dynamic aspect of the Gaussian chain picture needs to be included for $t > T_{eq}$.

While considering the thermal motions of the segments, the stretch-and-shrink motion of the primitive-chain contour length will help relax the tube stress at both ends of the tube. This effect occurs because when a chain moves out of the tube due to a stretching of the contour length following a

shrink, it can pick a random direction. Thus, the size of the tube-end region that can be affected by this relaxation process is determined by the fluctuation amplitude of the contour length. To include both the contour length fluctuation process and the reptational process as causes for the stress relaxation, we need to consider two important aspects: (1) The contour length fluctuation is a Rouse-like motion with a characteristic relaxation time τ_B which is much shorter than the characteristic time T_d of the reptational process because τ_B is proportional to M^2 (Chapters 3 and 7) while T_d is proportional to M^3 (T_d will be denoted by τ_C^0 below, standing for the *pure* reptation). (2) Both the contour length fluctuation and the reptational motion occur simultaneously. To obtain a theoretical expression for $G(t)$ which is simple in form, one hopes to separate the contributions of the two kinds of motions. In other words, we hope to express the stress relaxation as a sum of two *decoupled* processes. The decoupling of the two contributions can be achieved by following a scheme of “thought experiment” as described below:

We first regard the fixed primitive-chain contour length L in Eqs. (8.3) and (8.51) as the time average of the fluctuating length $L(t)$. In other words,

$$L(t) = \langle L(t) \rangle + \delta L(t) = L + \delta L(t) \quad (9.1)$$

where $\delta L(t)$ represents the fluctuation; $\langle \delta L(t) \rangle = 0$. Thus, the length $L(t)$ plays two roles here. On the one hand, its average as defined in Eq. (9.1) represents the original tube length (at $t = T_{eq}$) whose tube stress is to be relaxed (in other words, the relaxation strength at $t = T_{eq}$ is proportional to the average length L). On the other hand (see Eq. (9.2)), its length fluctuation motion relaxes the tube stress in the tube end regions. As the chain ends migrate because of the reptational motion, the contour length fluctuation causes additional relaxation of the tube stress whenever the fluctuation amplitude allows the chain ends to encounter the original tube (Fig. 9.3).

To sort out such a complicated dynamic situation, we first assume that the primitive chain is “nailed down” at some central point of the chain, i.e. the reptational motion is “frozen”; only the contour length fluctuation is allowed. This is equivalent to setting $\tau_C^0 \rightarrow \infty$ while allowing the contour length fluctuation $\delta L(t)$ to occur with a finite characteristic relaxation time τ_B . In this hypothetical situation, the portion of the tube that still possesses tube stress at $t \approx \tau_B$ is reduced to a shorter length L_o , because of the fluctuation $\delta L(t)$. Then, at $t < \tau_B$, the tube length that still possesses tube stress can be defined by

$$L(t) = L_o + \overline{\delta L}(t). \quad (9.2)$$

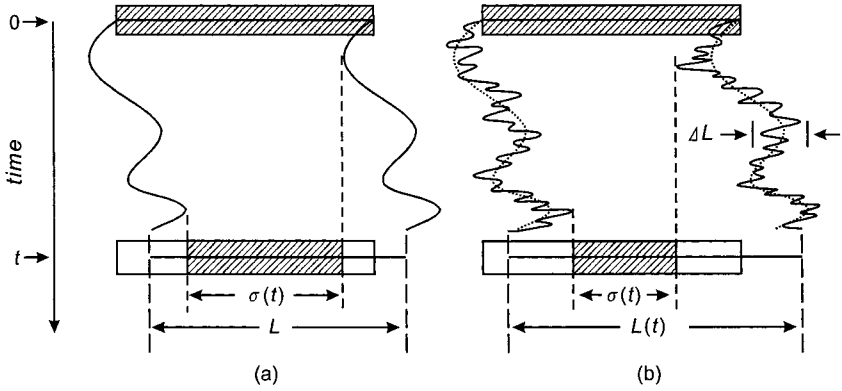


Fig. 9.3 The Brownian motion of a primitive chain: (a) with fixed contour length, and (b) with fluctuating contour length. The oblique lines denote the region that has not been reached by either end of the primitive chain. The length of the region $\sigma(t)$ decreases faster in (b) than in (a). $\Delta L \sim \delta L = N_o^{0.5}b$ (see Eqs. (9.4) and (9.8)). Reproduced, by permission, from Ref. 13.

In other words, $\overline{\delta L}(t)$ relaxes to zero at $t \approx \tau_B$. Because $\overline{\delta L}(t)$ remains in the original tube at $t < \tau_B$, we can regard it as the length of $\delta L(t)$ that is still correlated to its original $\delta L(0)$. In other words, we regard $\overline{\delta L}(t)$ as the projection of $\delta L(t)$ to $\delta L(0)$, i.e.

$$\overline{\delta L}(t) = \frac{\langle \delta L(0)\delta L(t) \rangle}{\langle |\delta L(0)|^2 \rangle^{1/2}}. \quad (9.3)$$

As shown in Appendix 9.A, from considering the polymer chain as a Gaussian chain consisting of N_o segments with the root mean square length b , the functional form for $\overline{\delta L}(t)$ is derived as

$$\overline{\delta L}(t) = \sqrt{N_o}b\mu_B(t) \quad (9.4)$$

where

$$\mu_B(t) = \sum_{p=\text{odd}} \frac{8}{\pi^2 p^2} \exp\left(-\frac{p^2 t}{\tau_B}\right) \quad (9.5)$$

with

$$\tau_B = \frac{\zeta b^2 N_o^2}{3\pi^2 kT} = \frac{K}{3} M^2 \quad (9.6)$$

where the frictional factor K is given by Eq. (3.57).

The tube stress on $\overline{\delta L}(t)$ relaxes according to Eqs. (9.4)–(9.6) under the condition $\tau_C^o \rightarrow \infty$. In reality, τ_C^o cannot be infinitely long. We still need to look for the relaxation functional form for the tube stress on L_o (Eq. (9.2)). Although the contour length fluctuation and the reptational motion occur simultaneously, we can keep using the theoretical form given by Eqs. (9.4)–(9.6) for the $\overline{\delta L}(t)$ relaxation if we regard τ_B to be *infinitely short* compared to a finite τ_C^o when we look for the theoretical form for the relaxation of the tube stress on L_o . This statement is valid because regarding τ_B to be finite and τ_C^o to be infinitely long (the assumption in obtaining Eqs. (9.4)–(9.6)) is equivalent to regarding τ_B to be infinitely short and τ_C^o to be finite, both being equivalent to setting $\tau_B/\tau_C^o \rightarrow 0$. $\tau_B/(\tau_C^o \rightarrow \infty)$ is fundamentally related to $(\tau_B \rightarrow 0)/\tau_C^o$ by a time shift. As the time-temperature superposition principle^{16,17} can be applied in composing a master curve (As detailed in Chapter 14, the thermorheological simplicity or time-temperature superposition principle holds if only the so-called entropic region — defined in Sec. 9.3 — of a viscoelastic response is involved; by definition, all the Rouse-segment-based dynamic processes as considered here occur in the entropic region.), such a time shift has no effect on the *line shape* of the whole $G(t)$ curve, which is of our present concern. Because the condition $\tau_B/\tau_C^o \rightarrow 0$ separates the two processes so far apart, it serves our objective to express the stress relaxation in two decoupled terms. In the reptational mechanism that allows Eqs. (8.52)–(8.56) to be derived, it is assumed that *as soon as* any point on the original tube is reached by the chain end, the tube stress between that point and the original tube end is totally relaxed. Because τ_B here is regarded as infinitely short compared to τ_C^o , the primitive-chain contour length *instantly* reaches its “minimum” length L_o at any moment. Thus, by the reptational process — the curvilinear diffusion — the primitive chain only need to get out of a tube of length L_o in effect to complete the relaxation of the whole tube stress. To account for this effect, we just change the pure reptational time $\tau_C^o (= T_d)$ given by Eq. (8.50) to τ_C given by

$$\tau_C = \frac{L_o^2}{\pi^2 D_{cv}} \quad (9.7)$$

where the curvilinear diffusion constant D_{cv} , unaffected by the contour length fluctuation, remains inversely proportional to the number of Rouse beads of the polymer chain.

In summary, under the assumed condition $\tau_B/\tau_C^o \rightarrow 0$, which allows us to keep Eqs. (9.4)–(9.6) as the functional form for the relaxation of the

tube stress on $\overline{\delta L}(t)$, we have to change the pure reptational time τ_C^o to τ_C given by Eq. (9.7) for the relaxation of the tube stress on the tube length L_o .

At $t = T_{eq}$, the tube stress resides over the whole tube length — the average contour length of the primitive chain L (Eqs. (8.3) and (8.51)). From Eq. (9.2) we have

$$L = L(t \approx T_{eq} \approx 0) = L_o + \overline{\delta L}(0) = L_o + \delta L \quad (9.8)$$

where, according to Eq. (9.4),

$$\delta L = \overline{\delta L}(0) = \sqrt{N_o}b. \quad (9.9)$$

Thus, L in the expression (Eqs. (8.53)) for the G_N used in Eq. (8.55) is separated into two parts: δL and L_o . The tube stress on δL is to be relaxed according to Eqs. (9.4)–(9.6) while that on L_o is to be relaxed by the reptational process with the time constant τ_C given by Eq. (9.7). Instead of Eqs. (8.53)–(8.56), the *linear* relaxation modulus $G(t)$ for $t \geq T_{eq}$ is now given by

$$G(t) = \frac{4cLkT}{5a} \left[\frac{\delta L}{L} \mu_B(t) + \frac{L_o}{L} \mu_C(t) \right] \quad (9.10)$$

where $\mu_B(t)$ is given by Eqs. (9.5) and (9.6); and $\mu_C(t)$, equivalent to Eq. (8.54) with T_d or τ_C^o replaced by τ_C (Eq. (9.7)), is given by

$$\mu_C(t) = \sum_{p=\text{odd}} \frac{8}{\pi^2 p^2} \exp\left(\frac{-p^2 t}{\tau_C}\right). \quad (9.11)$$

Using Eqs. (8.3), (8.6) (8.56), (9.8) and (9.9), τ_C can be obtained from Eq. (9.7) as

$$\begin{aligned} \tau_C &= \frac{\zeta N_o}{\pi^2 kT} \left(\frac{N_o b^2}{a} - \sqrt{N_o}b \right)^2 \\ &= \frac{\zeta b^2 N_o^3}{\pi^2 kT N_e} \left(1 - \sqrt{\frac{N_e}{N_o}} \right)^2 \\ &= K \frac{M^3}{M_e} \left(1 - \sqrt{\frac{M_e}{M}} \right)^2. \end{aligned} \quad (9.12)$$

Using Eqs. (8.3), (9.8) and (9.9), Eq. (9.10) is rewritten as

$$G(t) = G_N(B\mu_B(t) + C\mu_C(t)) \quad (9.13)$$

where G_N is given by Eq. (8.53) or (8.2), B is the relative fluctuation amplitude given by

$$B = \frac{\delta L}{L} = \sqrt{\frac{M_e}{M}} \quad (9.14)$$

and C is given by

$$C = \frac{L_o}{L} = 1 - B. \quad (9.15)$$

Hence, $G(t)$ as given by Eq. (9.13) is a sum of two relaxation processes, i.e. two separate or decoupled relaxation terms and is applicable to the stress relaxation for $t \geq T_{eq}$.

Note that Eq. (9.13) contains two features related to the molecular-weight dependence of the line shape of the relaxation modulus: (1) Both B and C are functions of the normalized molecular weight M/M_e . With decreasing molecular weight, the relaxation strength B for the contour-length-fluctuation process increases, while the relaxation strength C for the reptational process which has been corrected for the contour-length-fluctuation effect decreases. (2) The relaxation time ratio, τ_C/τ_B , obtained from Eqs. (9.6) and (9.12):

$$\frac{\tau_C}{\tau_B} = 3 \frac{M}{M_e} \left(1 - \sqrt{\frac{M_e}{M}} \right)^2 \quad (9.16)$$

is a function of the normalized molecular weight M/M_e and decreases with decreasing molecular weight. These two features indicate that the line shape of $G(t)$ for $t \geq T_{eq}$ is a universal function of the normalized molecular weight and that the plateau region in $G(t)$ will diminish with decreasing molecular weight. We shall further discuss the molecular-weight dependence of $G(t)$'s line shape below and in Chapter 10, where an extensive comparison between theory and experiment is made.

9.3 Relaxation Processes before $t \approx T_{eq}$

In general, the slower the mode of motion, the larger the length scale involved. So far in this chapter, we have studied the $\mu_B(t)$ and $\mu_C(t)$ processes in $G(t)$. $\mu_B(t)$ represents an intramolecular motion that involves the whole chain, and $\mu_C(t)$ is related to the diffusion motion of the whole

chain. In $G(t)$, besides these two processes, there are two readily identifiable faster processes, $\mu_X(t)$ and $\mu_A(t)$, as mentioned in the beginning of this chapter. Either of these two fast processes involves only a section or a part of the chain.

(a) *The $\mu_X(t)$ process*

At $t \approx T_{eq}$ following the application of a step shear strain at $t = 0$, the modulus G_N is given by Eq. (8.53) (also see Eq. (9.13)), which is derived from Eq. (8.32). As shown in Chapter 8, the equilibration process of the segmental redistribution along the primitive chain relaxes the stress given by Eq. (8.23) or (8.37) to that given by Eq. (8.32). In the linear region of the step shear strain, from Eq. (8.37) one obtains the modulus

$$G_N^* = cNkT = \frac{\rho RT}{M_e} \quad (9.17)$$

G_N^* is greater than G_N by a factor of 5/4. Thus, in the linear region, the decline of the modulus from G_N^* to G_N is due to the chain slippage through the entanglement links, which is driven by the equilibration of the segmental distribution. The chain-slippage mechanism was described in the derivation from Eq. (8.23) to Eq. (8.32). It was pointed out in Chapter 8 that in the linear region, the number of entanglement strands is not reduced as a result of chain slippage. We refer to the transition $G_N^* \rightarrow G_N$ as the $\mu_X(t)$ process with a characteristic time τ_X which can be regarded as equivalent to T_{eq} in the *linear* region. Consistent with $\tau_B (> T_{eq})$ being longer than $\tau_X (\approx T_{eq})$, the $\mu_X(t)$ process equilibrates segmental distribution among neighboring entanglement strands while the $\mu_B(t)$ process involves the whole polymer chain. Since G_N^* is greater than G_N by $G_N/4$, the proper way to add the $\mu_X(t)$ process to Eq. (9.13) is as follows:

$$G(t) = G_N \left[1 + \frac{1}{4} \mu_X(t) \right] [B\mu_B(t) + C\mu_C(t)]. \quad (9.18)$$

The theoretical functional form for $\mu_X(t)$ is not known. It has been assumed that the decay of $\mu_X(t)$ is a single exponential. Because $\mu_X(t)$ affects the $G(t)$ line shape only in a minor way, such a simple assumption basically does not affect the quantitative nature of the comparison of experimental results with the whole $G(t)$ equation, as will be discussed in Chapter 10.

(b) The $\mu_A(t)$ process

In the whole process of obtaining Eq. (9.18), we have considered only the deformation or orientation of entanglement strands along the primitive path and the associated relaxation processes. In a time shorter than required for the chain slippage through any entanglement link to have a chance to occur, the deformation of the chain segments towards all directions, including the directions perpendicular to the primitive path, adds values to the initial modulus $5G_N/4$ given in Eq. (9.18). Here, the relaxation process of the additional modulus is the Rouse motion of an entanglement strand with both ends fixed — the Rouse–Mooney normal modes of motion, which is treated in Appendix 9.B. The functional form of the relaxation process is given by Eqs. (9.B.24)–(9.B.26).

One sees that the end of relaxation in Eq. (9.B.24) occurs when $\mu_A(t)$ diminishes to zero, and that the modulus value of Eq. (9.B.24) at the end of relaxation matches the initial value of Eq. (9.18). Thus, we can combine Eqs. (9.18) and (9.B.24) as

$$G(t) = G_N[1 + \mu_A(t)] \left[1 + \frac{1}{4}\mu_X(t)\right] [B\mu_B(t) + C\mu_C(t)] \quad (9.19)$$

where $\mu_A(t)$ is given by Eqs. (9.B.25) and (9.B.26). Equation (9.19) covers the whole range of relaxation times from the transition region (the $\mu_A(t)$ -process region) to the terminal region (the $\mu_C(t)$ -process region). The smallest structural unit involved in the theoretical development that leads to Eq. (9.19) is the Rouse segment. Because of the close relationship between the entropic-force constant of the Rouse segment and the modulus, the region where a Rouse-segment-based molecular theory, such as Eq. (9.19), is applicable may be referred to as the entropic region. It is expected that Eq. (9.19) ceases to be applicable in the time region shorter than the characteristic reorientation time of a single Rouse segment or equivalently the relaxation time of the highest Rouse–Mooney normal mode $\sim \zeta b^2/24kT = K\pi^2 m^2/24$. At such short time scales, the stress-relaxation process (often referred to as the α -, glassy- or structural-relaxation process) is much influenced by the energetic interactions between segments (both intra-molecular and inter-molecular) at the microstructural level, whose size scales are considerably smaller than that of a Rouse segment. This short-time region is studied in detail in Chapter 14 and is referred to as the energetic region. Before Chapter 14, comparisons between theories and experiments will be limited to the entropic region. Theoretically a boundary between the two separate regions can be defined as occurring at the

modulus $\rho RT/m$ with m being the molecular weight of a Rouse segment. For polystyrene, the boundary occurs at 4×10^7 dynes/cm² corresponding to $m \approx 850$ as detailed in Appendix 13.A.

9.4 Universality of the $G(t)$ Line Shape in Terms of the Extended Reptation Theory (ERT)

As noted previously in this chapter, Eqs. (9.13)–(9.16) indicate that the line shape of the $G(t)$ curve is a universal function of the normalized molecular weight M/M_e in the region covered by the $\mu_B(t)$ and $\mu_C(t)$ processes. The relaxation times τ_B and τ_C can also be normalized with respect to the relaxation time of the lowest mode of the $\mu_A(t)$ process, $\tau_A^1 (= KM_e^2/6$, from Eq. (9.B.20) for a sufficiently large N_e). The relaxation-time ratios are expressed as:

$$\frac{\tau_C}{\tau_A^1} = 6 \left(\frac{M}{M_e} \right)^3 \left(1 - \sqrt{\frac{M_e}{M}} \right)^2 \quad (9.20)$$

$$\frac{\tau_B}{\tau_A^1} = 2 \left(\frac{M}{M_e} \right)^2. \quad (9.21)$$

The fact that these two relaxation-time ratios are a universal function of M/M_e indicates that the universality of the $G(t)$ line shape extends to the $\mu_A(t)$ process region. $\mu_X(t)$ is situated between $\mu_A(t)$ and the processes $\mu_B(t)$ and $\mu_C(t)$. Thus, although we do not have the theoretical form for $\mu_X(t)$, its characteristic time τ_X normalized with respect to τ_A^1 should also be a function of the normalized molecular weight M/M_e . From the $G(t)$ line shape analysis in terms of Eq. (9.19) as discussed in detail in Chapter 10, it has been found that τ_X is best described by

$$\tau_X = 0.55KM_eM \quad (9.22)$$

or

$$\frac{\tau_X}{\tau_A^1} \approx 3 \frac{M}{M_e}. \quad (9.23)$$

The structural factors of the relaxation times τ_A^1 , τ_X , τ_B and τ_C ; and the hierarchy and universality among them as discussed above are viewed from a different angle in Appendix 9.D. Through dimensional analysis, it is shown that all of these are characteristics inherently contained in the extended slip-link model.

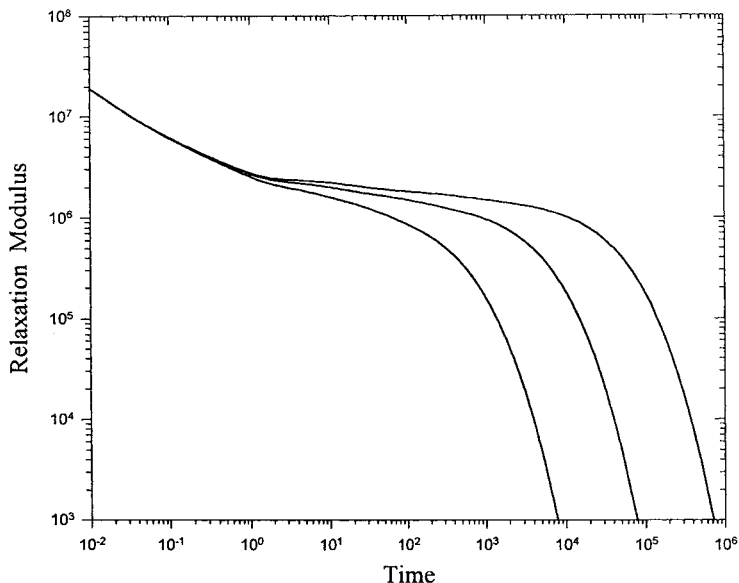


Fig. 9.4 Relaxation modulus $G(t)$ curves calculated by convoluting Eq. (9.19) with the Schulz molecular-weight distribution for $M_w/M_n = 1.05$ (i.e. $Z = 20$; see Eqs. (10.3) and (10.4)) at molecular weights: $M_w/M_e = 10, 20$, and 40 as they would be for polystyrene ($G_N = 2 \times 10^6$ dyne/sq cm; $M_e = 13,500$). The frictional factor K for the $\mu_X(t)$, $\mu_B(t)$ and $\mu_C(t)$ processes is set at 5×10^{-9} and the frictional factor (denoted by K') for the $\mu_A(t)$ process is set at $K' = 3.3K$ (see Chapter 10 for details of the ratio K'/K).

Equation (9.19) accurately describes the observed characteristics associated with the transformation of the $G(t)$ line shape with changing molecular weight. To illustrate the capability of the theory in describing these characteristics, the relaxation modulus curves calculated from Eq. (9.19) at $M_w/M_e = 10, 20$ and 40 , all with the polydispersity of $M_w/M_n = 1.05$, are shown in Fig. 9.4 for comparison with the experimental results, as shown in Fig. 4.6. In Chapter 10, in terms of the theory, quantitative analyses of the relaxation modulus curves of a series of nearly monodisperse polystyrene samples will be described in detail.

9.5 Zero-Shear Viscosity and Steady-State Compliance

Using the equations of linear viscoelasticity (Eqs. (4.30) and (4.63)), the zero-shear viscosity, η_0 , and the steady-state compliance, J_e^0 , can be numerically calculated from Eq. (9.19) by a computer program. If the molecular

weight is greater than $\sim 5M_e$, the contributions of the $\mu_A(t)$ and $\mu_X(t)$ processes to η_0 and J_e^0 are negligible because of their relatively short relaxation times. From Eq. (9.19) with the $\mu_A(t)$ and $\mu_B(t)$ processes neglected or Eq. (9.13), η_0 and J_e^0 are derived as

$$\eta_0 = K \frac{\pi^2 \rho RT}{15} \frac{M^3}{M_e^2} \left[\left(1 - \sqrt{\frac{M_e}{M}} \right)^3 + \frac{1}{3} \left(\sqrt{\frac{M_e}{M}} \right)^3 \right] \quad (9.24)$$

$$J_e^0 = \frac{3M_e}{2\rho RT} \frac{(1 - \sqrt{M_e/M})^5 + \frac{1}{9}(\sqrt{M_e/M})^5}{[(1 - \sqrt{M_e/M})^3 + \frac{1}{3}(\sqrt{M_e/M})^3]^2}. \quad (9.25)$$

Equation (9.24) closely approximates the observed $\eta_0 \propto M^{3.4}$ relation over a wide region of molecular weight above $5M_e$. J_e^0 is highly sensitive to the molecular-weight distribution. As a result, the measured values of nearly monodisperse polymers in the high-molecular-weight region ($> 7M_e$) are about 1.7 times greater than the values calculated from Eq. (9.25) which is for ideal monodispersity. In Chapter 10, we shall further compare the experimental results of η_0 and J_e^0 with the theoretical results calculated with and without both the $\mu_A(t)$ and $\mu_X(t)$ processes.

The effect of the primitive-chain contour length fluctuation was first considered by Doi.¹³ In an approach which was meant to be an approximation, Doi obtained the zero-shear viscosity and the steady-state compliance as

$$\eta_0 = K \frac{\rho RT}{3} \frac{M^3}{M_e^2} \left[\left(1 - \sqrt{\frac{M_e}{M}} \right)^3 + \frac{1}{5} \left(\sqrt{\frac{M_e}{M}} \right)^3 \right] \quad (9.26)$$

$$J_e^0 = \frac{9M_e}{5\rho RT} \frac{(1 - \sqrt{M_e/M})^5 + \frac{1}{9}(\sqrt{M_e/M})^5}{[(1 - \sqrt{M_e/M})^3 + \frac{1}{5}(\sqrt{M_e/M})^3]^2}. \quad (9.27)$$

Equations (9.26) and (9.27) are similar to Eqs. (9.24) and (9.25), respectively. Doi's calculation was mainly for the molecular-weight dependence of the zero-shear viscosity and the steady-state compliance. Because of the approximations involved in his approach, Doi's results do not converge to the Doi-Edwards theory (Eqs. (8.57) and (8.58)) at infinitely high molecular weight as Eqs. (9.24) and (9.25) do.

Taking the contour-length-fluctuation effect into account, Doi¹⁴ obtained another expression for the viscosity

$$\eta_0 = K \frac{\pi^2 \rho RT}{15} \frac{M^3}{M_e^2} \left(1 - 1.47 \sqrt{\frac{M_e}{M}} \right)^3. \quad (9.28)$$

Although Eq. (9.28) converges to the Doi–Edwards theory at infinitely high molecular weight, it predicts a slope of $\log(\eta_0)$ vs $\log(M)$ which is much steeper than the 3.4 observed over a wide molecular-weight region.¹⁵

9.6 Note: A Clarification of the Term “Transition Region”

In general, the transition region refers to the time or frequency region, where the magnitude of the measured modulus changes from glasslike to rubberlike. Ferry has explained why the term “transition” should not be confused with the glass transition by pointing out that no change in the thermodynamic state of the material such as occurs when the glass transition temperature is traversed. Still, its use in the literature is sometimes confusing. Basically it appears that the term “transition region” has been used to indicate different zones depending on whether mainly theory or experiment is under discussion. The Rouse–Mooney process $\mu_A(t)$ as detailed in Appendix 9.B has been used to describe the viscoelastic behavior in the transition region (see p. 247 of Ref. 17).¹⁸ The point where the modulus starts to rise from the plateau has been used to indicate the onset of the transition region (see also Figs. 12–9 of Ref. 17).¹⁸ For these reasons, the first-process region in the $G(t)$ shown in Fig. 9.1 has been denoted as the transition region and the dynamics that occurs in this region as the transition process — referring to the $\mu_A(t)$ process. As indicated by the theoretical derivation given in Appendix 9.B, $\mu_A(t)$ is a purely entropy-driven process. The entropic nature of $\mu_A(t)$ appears inconsistent with its being associated with the transition from glasslike to rubberlike, as the transition state should possess a certain degree of glassiness and cannot be entirely of entropic nature. The term “transition region” used by Inoue *et al.*^{19–21} refers to the frequency region where a simple stress optical rule (the rubbery one) does not hold due to significant contribution from the glassy component, which follows another stress optical rule (the glassy one). The transition region as referred to by Inoue *et al.* typically occurs around $\sim 10^8$ dynes/cm². Consistent with the analysis of Inoue *et al.*, the frequency where $G'(\omega) = 10^8$ dynes/cm² has often been used as a gauge of the location of the transition region, because it is a value intermediate between those characteristic of the glasslike and rubberlike states (see p. 323 of Ref. 17). In the case of polystyrene, this modulus level is higher than those where the first three modes of motion in $\mu_A(t)$ occur by about ten to 40 times. This large discrepancy and the entropic nature of $\mu_A(t)$ suggest that referring the first-process region in the $G(t)$ shown in Fig. 9.1

(where $\mu_A(t)$ occurs) as the transition region may not be entirely proper. On the one hand for making links with some reports in the literature and on the other hand for distinguishing the difference, the transition region may be divided into two zones: the transition region (I) for the region around $G'(\omega) = 10^8$ dynes/cm², where both the glassy and rubbery components coexist; and the transition region (II), where the purely entropic process $\mu_A(t)$ is applicable. Thus, more precisely, the transition region indicated in Fig. 9.1 stands for the transition region (II).

Appendix 9.A — Contour Length Fluctuations of the Primitive Chain

The time-correlation function $\langle \delta L(0)\delta L(t) \rangle$ of Eq. (9.3) will be derived by considering the polymer chain as a Gaussian chain consisting of N_o segments each with the root mean square length b . Let $S_n(t)$ be the contour “position” of the n th bead relative to a certain reference point on the primitive path. Then the contour length of the primitive chain at time t is given by

$$L(t) = S_{N_o}(t) - S_0(t). \quad (9.A.1)$$

The equilibrium average of $L(t)$, $L = \langle L(t) \rangle$, is defined by Eq. (8.3).

The motion of $S_n(t)$ is described by the following Langevin equation:

$$\zeta \frac{\partial}{\partial t} S_n(t) = \frac{3kT}{b^2} \frac{\partial^2}{\partial n^2} S_n(t) + f_n(t) \quad (9.A.2)$$

where $f_n(t)$ is the random fluctuation force that is Gaussian characterized by the moments (see Chapter 3):

$$\langle f_n(t) \rangle = 0; \quad \langle f_n(t)f_m(t') \rangle = 6\zeta kT \delta(t - t') \delta(n - m) \quad (9.A.3)$$

when the contour length fluctuation is considered; or

$$\langle f_n(t) \rangle = 0; \quad \langle f_n(t)f_m(t') \rangle = 2\zeta kT \delta(t - t') \delta(n - m) \quad (9.A.3')$$

when the curvilinear diffusion is considered.²² The difference in physical meaning between Eqs. (9.A.3) and (9.A.3') is explained as follows:

The force constant, $3kT/b^2$, used in Eq. (9.A.2) originates from the entropy related to the number of microstructural configurations in a Rouse segment. The microstructural configurations have to be considered in three-dimensional space. Involving three-dimensional space is related to the idea that the size of the Rouse segment, $\sim b$, is much smaller than the tube

diameter, a . In accordance with this picture, each segment on the chain receives thermal agitations or fluctuation forces from all directions in the volume $\sim La^2$ pervaded by the chain. Fluctuation forces perpendicular to as well as parallel to the primitive path contribute to the fluctuation of $L(t)$. It is easy to imagine that the movements towards the wall of the tube or even somewhat leaking out of the tube by some local segments will shorten the length $L(t)$. Thus, we need to include fluctuation forces from all directions in three-dimensional space even though we are considering the length fluctuation only along the primitive path. Because of the Gaussian chain statistics, the effects of fluctuation forces in any three mutually-perpendicular directions are the same. As a result, there is the factor 6 in Eq. (9.A.3). In summary, the use of Eq. (9.A.3) is consistent with the entropic force constant $3kT/b^2$ in Eq. (9.A.2).

The fluctuation forces also cause the curvilinear diffusion along the primitive path. However, because of the constraint effect of the tube, the “positive” and “negative” fluctuation forces perpendicular to the primitive path cancel each other out when averaged over a time period longer than required for a segment to travel over an entanglement distance, and thus make no net contribution to the curvilinear diffusion and the translational diffusion of the center of mass. Thus, in the study of the curvilinear diffusion, Eq. (9.A.3') should be used, instead of Eq. (9.A.3).

As discussed in the Doi–Edwards theory (Chapter 8), a fictitious tensile force F_{eq} given by Eq. (8.21) must be assumed to apply at both chain ends. Hence the boundary condition for Eq. (9.A.2) is

$$\frac{3kT}{b^2} \frac{\partial}{\partial n} S_n(t) = F_{eq} \quad \text{at } n = 0; N_o \quad (9.A.4)$$

or

$$\frac{\partial}{\partial n} S_n(t) = l \quad \text{at } n = 0; N_o \quad (9.A.5)$$

with

$$l = \frac{b^2}{a}. \quad (9.A.6)$$

Equation (9.A.2) has the following type of solution which satisfies the boundary condition.

$$S_n(t) = X_o(t) + \left(n - \frac{N_o}{2}\right) l + \left(\frac{2}{N_o}\right)^{1/2} \sum_p X_p(t) \cos\left(\frac{p\pi n}{N_o}\right) \quad \text{for } p = 1, 2, \dots \quad (9.A.7)$$

where

$$X_o(t) = \frac{1}{N_o} \int_0^{N_o} S_n(t) dn \quad (9.A.8)$$

represents the position of the “curvilinear center of the chain” along the primitive path. To study the motion of $X_o(t)$ (the curvilinear diffusion motion of the chain), Eq. (9.A.3') is to be used for the fluctuation force in Eq. (9.A.2), as explained above. Using Eq. (9.A.8), we obtain from substituting Eq. (9.A.7) into Eq. (9.A.2) the equation of the $X_o(t)$ motion

$$\zeta \frac{\partial}{\partial t} X_o(t) = \frac{1}{N_o} \int_0^{N_o} f_n(t) dn. \quad (9.A.9)$$

The solution of Eq. (9.A.9) gives rise to Eq. (8.6).

For decoupling the $\mu_B(t)$ and $\mu_C(t)$ processes as in Eq. (9.13), we first “freeze” the curvilinear diffusion motion by setting $\tau_C^o \rightarrow \infty$. For such a consideration, $X_o(t)$ can be eliminated from Eq. (9.A.7). As explained above, in studying the intramolecular modes of motion that cause the contour length fluctuation of the primitive chain, Eq. (9.A.3) is to be used for the fluctuation force. Substituting Eq. (9.A.7) into Eq. (9.A.2) and then following the procedure as given in Appendix 3.C, we obtain

$$\langle X_p(0)X_p(t) \rangle = \frac{N_o^2 b^2}{\pi^2 p^2} \exp(-\lambda_p t) \quad (9.A.10)$$

where

$$\lambda_p = \frac{p^2}{\tau_B} \quad (9.A.11)$$

with

$$\tau_B = \frac{\zeta b^2 N_o^2}{3\pi^2 kT}. \quad (9.A.12)$$

From Eqs. (9.1), (9.A.1) and (9.A.7), we obtain

$$\delta L(t) = L(t) - N_o l = -2 \left(\frac{2}{N_o} \right)^{1/2} \sum_{p=\text{odd}} X_p(t) \quad (9.A.13)$$

and

$$\langle \delta L(0) \delta L(t) \rangle = \frac{8}{N_o} \sum_{p=\text{odd}} \langle X_p(0) X_p(t) \rangle. \quad (9.A.14)$$

The random fluctuation $\mathbf{g}_n(t)$ is the same as defined by Eqs. (3.34) and (3.35); and

$$\left(M_{st} \right) = \begin{pmatrix} 1 & -1 & 0 & 0 & \cdot & \cdot & 0 \\ -1 & 2 & -1 & 0 & 0 & \cdot & 0 \\ 0 & -1 & 2 & -1 & 0 & \cdot & 0 \\ \cdot & \cdot & \cdot & \cdot & \cdot & \cdot & \cdot \\ \cdot & \cdot & \cdot & \cdot & \cdot & \cdot & \cdot \\ 0 & \cdot & \cdot & \cdot & 0 & -1 & 2 & -1 \\ 0 & 0 & \cdot & \cdot & \cdot & 0 & -1 & 1 \end{pmatrix} \quad (9.B.6)$$

is referred to as the Rouse–Mooney matrix, which as shown in Appendix 9.C, has the eigenvalues:

$$a_p = 4 \sin^2 \left(\frac{p\pi}{2N_e} \right); \quad p = 0, 1, 2, \dots, N_e - 1. \quad (9.B.7)$$

The transformation from the bond vectors $\{\mathbf{b}_s\}$ to the normal coordinates $\{\mathbf{q}_p\}$ which diagonalizes the Rouse–Mooney matrix is expressed by

$$\mathbf{b}_s = \sum_{p=0}^{N_e-1} U_{sp} \mathbf{q}_p. \quad (9.B.8)$$

As shown in Appendix 9.C,

$$U_{s0} = \frac{1}{\sqrt{N_e}} \quad \text{for all } s \quad (9.B.9)$$

$$U_{sp} = \sqrt{\frac{2}{N_e}} \cos \left(\frac{(s+1/2)p\pi}{N_e} \right) \quad \text{for } p = 1, 2, 3, \dots, N_e - 1.$$

In terms of the normal coordinates, the Langevin equation is rewritten as:

$$\frac{d\mathbf{q}_p}{dt} = -\frac{1}{\tau_p^e} \mathbf{q}_p + \mathbf{h}_p(t) \quad \text{for } p = 1, 2, 3, \dots, N_e - 1 \quad (9.B.10)$$

where

$$\tau_p^e = \frac{\zeta b^2}{3kT a_p} \quad (9.B.11)$$

and the random fluctuation $\mathbf{h}_p(t)$ are characterized by the following moments:

$$\langle \mathbf{h}_p(t) \rangle = 0 \quad (9.B.12)$$

$$\langle \mathbf{h}_p(t') \mathbf{h}_q(t'') \rangle = \delta \frac{8kT}{\zeta} \sin^2 \left(\frac{p\pi}{2N_e} \right) \delta_{pq} \delta(t' - t''), \quad (9.B.13)$$

which turn out to have the same forms as those for the free Rouse chain (Eqs. (3.52) and (3.53) with N replaced by N_e).

(U_{sp}) being an orthogonal matrix, the substitution of Eq. (9.B.8) into Eq. (9.B.2) gives

$$\boldsymbol{\sigma}(t) = -\frac{3kT}{b^2} \sum_{p=0}^{N_e-1} \langle \mathbf{q}_p(t) \mathbf{q}_p(t) \rangle. \quad (9.B.14)$$

From the inverse of the transformation expressed by Eq. (9.B.8), we obtain

$$\mathbf{q}_0 = \frac{1}{\sqrt{N_e}} \sum_{s=0}^{N_e-1} \mathbf{b}_s(t) = \frac{1}{\sqrt{N_e}} \mathbf{R}_e \quad (9.B.15)$$

which is independent of time as \mathbf{R}_e is assumed fixed. The time independence of \mathbf{q}_0 is consistent with $\tau_0 = \infty$ (corresponding to $a_0 = 0$ as given by Eq. (9.B.7)). Using Eq. (9.B.15), Eq. (9.B.14) is rewritten as

$$\boldsymbol{\sigma}(t) = -\frac{3kT}{N_e b^2} \langle \mathbf{R}_e \mathbf{R}_e \rangle - \frac{3kT}{b^2} \sum_{p=1}^{N_e-1} \langle \mathbf{q}_p(t) \mathbf{q}_p(t) \rangle. \quad (9.B.16)$$

Equation (9.B.10) has the solution

$$\mathbf{q}_p(t) = \mathbf{q}_p(0) \exp \left(-\frac{t}{\tau_p^e} \right) + \int_0^t \mathbf{h}_p(t') \exp \left[-\frac{(t-t')}{\tau_p^e} \right] dt'. \quad (9.B.17)$$

Using Eqs. (9.B.12) and (9.B.13), we obtain from Eq. (9.B.17)

$$\langle \mathbf{q}_p(t) \mathbf{q}_p(t) \rangle = \langle \mathbf{q}_p(0) \mathbf{q}_p(0) \rangle \exp \left(-\frac{2t}{\tau_p^e} \right) + \delta \left(\frac{b^2}{3} \right) \left[1 - \exp \left(-\frac{2t}{\tau_p^e} \right) \right]. \quad (9.B.18)$$

Before the step deformation \mathbf{E} is applied, the system is in an equilibrium state. Following the same procedure as used in deriving Eq. (3.54), an equivalent result can be obtained, which in turn allows us to define

$$\langle |\mathbf{q}_p^o|^2 \rangle = \langle \mathbf{q}_p^o(0) \cdot \mathbf{q}_p^o(0) \rangle = b^2. \quad (9.B.19)$$

Using Eq. (9.B.19), the following expression may be obtained

$$\begin{aligned} \langle \mathbf{q}_p(0)\mathbf{q}_p(0) \rangle &= \langle (\mathbf{E} \cdot \mathbf{q}_p^o)(\mathbf{E} \cdot \mathbf{q}_p^o) \rangle \\ &= \langle |\mathbf{q}_p^o|^2 \rangle \langle (\mathbf{E} \cdot \mathbf{u})(\mathbf{E} \cdot \mathbf{u}) \rangle_{\mathbf{u}} \\ &= b^2 \langle (\mathbf{E} \cdot \mathbf{u})(\mathbf{E} \cdot \mathbf{u}) \rangle_{\mathbf{u}} \end{aligned} \quad (9.B.20)$$

where $\langle \dots \rangle_{\mathbf{u}}$ denotes averaging over all orientation of \mathbf{u} . Using Eq. (9.B.20), from substituting Eq. (9.B.18) into Eq. (9.B.16), we obtain

$$\begin{aligned} \boldsymbol{\sigma}(t) &= -\frac{3kT}{N_e b^2} \langle \mathbf{R}_e \mathbf{R}_e \rangle \\ &\quad - 3kT \sum_{p=1}^{N_e-1} \left[\left\langle (\mathbf{E} \cdot \mathbf{u})(\mathbf{E} \cdot \mathbf{u}) - \frac{\delta}{3} \right\rangle_{\mathbf{u}} \exp\left(-\frac{2t}{\tau_p^e}\right) + \frac{\delta}{3} \right]. \end{aligned} \quad (9.B.21)$$

Using the equation

$$\langle \mathbf{R}_e \mathbf{R}_e \rangle = \langle (\mathbf{E} \cdot \mathbf{R}_e^o)(\mathbf{E} \cdot \mathbf{R}_e^o) \rangle_{\mathbf{u}} = N_e b^2 \langle (\mathbf{E} \cdot \mathbf{u})(\mathbf{E} \cdot \mathbf{u}) \rangle_{\mathbf{u}}, \quad (9.B.22)$$

we obtain from Eq. (9.B.21) the stress relaxation of a system with C entanglement strands per unit volume in the time region $t < \tau_X$ following a step shear deformation at $t = 0$:

$$\begin{aligned} T_{\alpha\beta}(t) &= -3CKT \left[1 + \sum_{p=1}^{N_e-1} \exp\left(-\frac{2t}{\tau_p^e}\right) \right] \langle (\mathbf{E} \cdot \mathbf{u})_{\alpha} (\mathbf{E} \cdot \mathbf{u})_{\beta} \rangle_{\mathbf{u}} \\ &= -3cNkT \left[1 + \sum_{p=1}^{N_e-1} \exp\left(-\frac{2t}{\tau_p^e}\right) \right] \langle (\mathbf{E} \cdot \mathbf{u})_{\alpha} (\mathbf{E} \cdot \mathbf{u})_{\beta} \rangle_{\mathbf{u}} \end{aligned} \quad (9.B.23)$$

where c is the number of polymer chains per unit volume, with N entanglement strands per chain.

The relaxation modulus $G(t)$ in the linear region is obtained from Eq. (9.B.23) as

$$G(t) = cNkT[1 + \mu_A(t)] \quad (9.B.24)$$

where

$$\mu_A(t) = \sum_{p=1}^{N_e-1} \exp\left(-\frac{t}{\tau_A^p}\right) \quad (9.B.25)$$

with

$$\begin{aligned} \tau_A^p &= \frac{\tau_p^e}{2} = \frac{\zeta b^2}{24kT \sin^2(\pi p/2N_e)} \\ &= \frac{K \pi^2 M_e^2}{24N_e^2 \sin^2(\pi p/2N_e)}. \end{aligned} \quad (9.B.26)$$

The frictional factor K is given by Eq. (3.57).

When $N_e \rightarrow \infty$, Eq. (9.B.26) can be reduced as

$$\begin{aligned} \tau_A^p &= \frac{\zeta N_e^2 b^2}{6\pi^2 kT p^2} \\ &= \frac{K M_e^2}{6p^2}. \end{aligned} \quad (9.B.27)$$

The combination of Eqs. (9.B.24), (9.B.25) (with $N_e \rightarrow \infty$) and (9.B.27) is in agreement with the result obtained from the continuous model in which Eq. (9.B.2) is replaced by

$$\boldsymbol{\sigma}(t) = -\frac{3kT}{b^2} \int_0^{N_e} \left\langle \left(\frac{\partial \mathbf{r}_n(t)}{\partial n} \right) \left(\frac{\partial \mathbf{r}_n(t)}{\partial n} \right) \right\rangle dn. \quad (9.B.28)$$

And the Langevin equation has the same expression as given by Eq. (3.C.1) (with \mathbf{R}_n replaced by \mathbf{r}_n) except under different boundary conditions — changing from free to fixed boundary conditions. In the continuous model with $\mathbf{r}_0 = 0$ and $\mathbf{r}_{N_e} = \mathbf{R}_e$, the transformation to the normal coordinates $\mathbf{X}_p(t)$ ($p = 1, 2, \dots, \infty$) is performed according to

$$\mathbf{r}_n(t) = \frac{n}{N_e} \mathbf{R}_e + \left(\frac{2}{N_e} \right)^{1/2} \sum_p \mathbf{X}_p(t) \sin \left(\frac{pn\pi}{N_e} \right). \quad (9.B.29)$$

Appendix 9.C — Eigenvalues and Eigenvectors of the Rouse–Mooney Matrix

We consider the Rouse–Mooney matrix (M_{st}) of the dimension $z \times z$. The z eigenvalues $\{a_s\}$ of the matrix are the roots of the equation obtained by setting the determinant $D_z = |M_{st} - a\delta_{st}|$ equal to zero, i.e.

$$D_z = \begin{vmatrix} x-1 & -1 & 0 & 0 & \cdot & \cdot & 0 \\ -1 & x & -1 & 0 & \cdot & \cdot & 0 \\ 0 & -1 & x & -1 & 0 & \cdot & 0 \\ \cdot & \cdot & \cdot & \cdot & \cdot & \cdot & \cdot \\ \cdot & \cdot & \cdot & \cdot & \cdot & \cdot & \cdot \\ 0 & 0 & \cdot & \cdot & 0 & -1 & x & -1 \\ 0 & 0 & \cdot & \cdot & \cdot & 0 & -1 & x-1 \end{vmatrix} = 0 \quad (9.C.1)$$

where

$$x = 2 - a. \quad (9.C.2)$$

From Eq. (19.C.1), the recursion relation is found as follows

$$D_z = xD_{z-1} - D_{z-2} \quad (9.C.3)$$

with

$$D_2 = x^2 - 2x \quad (9.C.4)$$

and

$$D_3 = \begin{vmatrix} x-1 & -1 & 0 \\ -1 & x & -1 \\ 0 & -1 & x-1 \end{vmatrix} = (x^2 - 1)(x - 2). \quad (9.C.5)$$

Eq. (9.C.3) is identical in form to the recursion relation (Eq. (3.A.3)) for the Rouse matrix. Setting $x = 2 \cos \theta = \exp(i\theta) + \exp(-i\theta)$ and following a procedure similar to that used in Appendix 3.A, the $z(= N_e)$ eigenvalues are obtained as

$$a_0 = 0 \quad (9.C.6a)$$

and

$$a_p = 4 \sin^2 \left(\frac{p\pi}{2N_e} \right); \quad \text{for } p = 1, 2, \dots, N_e - 1. \quad (9.C.6b)$$

Eqs. (9.C.6a) and (9.C.6b) together may be expressed by Eq. (9.B.7).

Following a procedure similar to that used in the Rouse matrix case, the normalized eigenvectors $\{C_k^p\}$ ($k = 0, 1, 2, \dots, N_e - 1$) corresponding to the respective eigenvalues given above are obtained as

$$C_k^0 = \frac{1}{\sqrt{N_e}} \quad \text{at all } k \text{ if } p = 0 \quad (9.C.7a)$$

and

$$C_k^p = \sqrt{\frac{2}{N_e}} \cos\left(\frac{(k + 1/2)p\pi}{N_e}\right) \quad \text{for } p = 1, 2, \dots, N_e - 1. \quad (9.C.7b)$$

Equation (9.C.7) leads to the transformation expressed by Eq. (9.B.9).

Appendix 9.D — Hierarchy and Universality among the Inherent Characteristic Times in the (Extended) Slip-Link Model

It is generally true that in a physical system a slower process is associated with a larger length scale. For Brownian motion, this is particularly clear and can be expressed by the following scaling relation:

$$\tau_k \approx \frac{L_k^2}{D_k} \quad (9.D.1)$$

based on dimensional analysis with τ_k , L_k and D_k denoting a characteristic time, length and diffusion constant, respectively. To make use of Eq. (9.D.1), a relevant length scale needs to be identified first. The diffusion constant conjugate to the length scale can be selected from the few obvious choices: $D = kT/\zeta$, D/N_o and D/N_e according to whether a physical justification can be made. For instance in the Rouse model, two characteristic lengths can be identified: the Rouse-segment length b and the end-to-end distance of the chain $R = (N_o b^2)^{1/2}$. These two length scales indicate two characteristic times:

$$\tau_0 \approx \frac{b^2}{D} = \frac{\zeta b^2}{kT} = K\pi^2 m^2 \quad (9.D.2)$$

$$\tau_r \approx \frac{R^2}{(D/N_o)} = \frac{\zeta N_o^2 b^2}{kT} = K\pi^2 M^2 \quad (9.D.3)$$

where the diffusion constants of a single Rouse bead and of the Rouse chain as a whole are given by $D = kT/\zeta$ and D/N_o , respectively (N in Eq. (3.41) is replaced by N_o here). τ_0 is of the order of the correlation time

for reorientation of a single Rouse segment; and except for a proportional constant τ_r is equivalent to the relaxation time of the first Rouse normal mode (Eq. (3.55) or (7.56)).

Additional characteristic times are expected to arise from the introduction of the length scales a and L into the slip-link model as defined by Eq. (8.3). In addition to τ_0 , the characteristic times in the slip-link model can be identified as

$$\tau_1 \approx \frac{a^2}{(D/N_e)} = \frac{\zeta N_e^2 b^2}{kT} = K\pi^2 M_e^2 \quad (9.D.4)$$

$$\tau_2 \approx \frac{a^2}{(D/N_o)} = \frac{\zeta N_e N_o b^2}{kT} = K\pi^2 M_e M \quad (9.D.5)$$

$$\tau_3 \approx \frac{R^2}{(D/N_o)} = \frac{\zeta N_o^2 b^2}{kT} = K\pi^2 M^2 \approx \tau_r \quad (9.D.6)$$

$$\tau_4^o \approx \frac{L^2}{(D/N_o)} = \frac{\zeta N_o^3 b^2}{kTN_e} = K\pi^2 \frac{M^3}{M_e}. \quad (9.D.7)$$

Theoretically, the length scale a can be defined in either the three-dimensional space or along the primitive chain (curvilinear contour); however, R is defined in the three-dimensional space and L defined along the curvilinear contour. In the Doi–Edwards theory, D/N_o is the curvilinear diffusion constant D_{cv} (Eq. (8.6)); in other words, it is defined along the curvilinear contour. Thus from the viewpoint of the Doi–Edwards theory, τ_3 as defined by Eq. (9.D.6) involving R and D_{cv} “mixes” the two different sorts of space (the three-dimensional space versus the curvilinear contour), which should be forbidden. Indeed, a τ_3 -characterized dynamic process is not expected to occur as a result of introducing *only* Eq. (8.3) as τ_3 is independent of L and a . A τ_3 -characterized dynamic process cannot occur in the Doi–Edwards theory (pure-reptation model) with the imposed restriction that the length of L remains fixed. The solution of the Langevin equation for the primitive chain — allowing the length of L to fluctuate — gives the characteristic time of the contour-length fluctuations (a Rouse-like motion), τ_B , which differs from τ_3 by a proportional constant (Appendix 9.A).

Using Eqs. (9.D.4)–(9.D.7), the ratios of the four characteristic times can be expressed as

$$\frac{\tau_4^o}{\tau_3} \propto \frac{\tau_3}{\tau_2} \propto \frac{\tau_2}{\tau_1} \propto \frac{N_o}{N_e} = \frac{M}{M_e}, \quad (9.D.8)$$

all being proportional to the normalized molecular weight M/M_e or N_o/N_e . Except for a proportional constant, τ_4^o is equivalent to the *pure* reptation time of the Doi–Edwards theory. The contour length fluctuation affects the relaxation mechanism for the stress on the primitive chain in the way as illustrated in Fig. 9.3. Because of this effect, the length L is shortened by the amplitude of the contour length fluctuation, δL , in the same sense as Eq. (9.7). In other words, the Eq. (9.D.7) for τ_4^o is modified to become

$$\tau_4 \approx \frac{(L - \delta L)^2}{(D/N_o)} = \frac{\zeta N_o^3 b^2}{kTN_e} \left(1 - \sqrt{\frac{N_e}{N_o}}\right)^2 = K\pi^2 \frac{M^3}{M_e} \left(1 - \sqrt{\frac{M_e}{M}}\right)^2. \quad (9.D.9)$$

All the functional forms of the relaxation processes and relaxation strengths have been derived except that $\mu_X(t/\tau_X)$ is assumed to be a single exponential decay with the characteristic time τ_X . As pointed out in Sec. 9.3.a, the existence of the $\mu_X(t)$ process is theoretically clear; it is responsible for the decline in modulus from G_N^* to G_N — corresponding to the relaxation strength 1/4 incorporated into in Eq. (9.18). It is also clearly supported by comparing theory with experiment (compare Figs. 2 and 3 with Figs. 8 and 9 of Ref. 15). It has been shown theoretically (Sec. 9.3) that the $\mu_X(t)$ process arises from the chain slipping through entanglement links to release uneven local chain tension — i.e. to equilibrate the segmental distribution between *neighboring* entanglement strands. Unlike the $\mu_B(t)$ process involving the fluctuations of the whole chain molecule, the $\mu_X(t)$ process involves local dynamics in separate sections of the chain, whose length scale should be of the same order of magnitude as the entanglement distance a . Corresponding to this process, $L_k \approx a$ should be used in Eq. (9.D.1). At the same time, the curvilinear diffusion constant D/N_o instead of D/N_e should be chosen as the conjugate diffusion constant for the reason that dynamically chain slippage has occurred. Therefore, except for a proportional constant, τ_X is expected to be equivalent to τ_2 as given by Eq. (9.D.5). Note that after the chain slippage through entanglement links has occurred, the only diffusion constant that can be chosen for D_k in Eq. (9.D.1) is D/N_o — as used in Eqs. (9.D.5)–(9.D.7) and (9.D.9) for obtaining τ_2 , τ_3 , τ_4^o and τ_4 , respectively.

As explained in Sec. 9.4, the application of the universality covering the $\mu_B(t) - \mu_C(t)$ region and the $\mu_A(t)$ region to the $\mu_X(t)$ process requires that the scaling relation $\tau_X \propto KM_e^{2-m}M^m$ be satisfied. Then from the $G(t)$ line-shape analyses of nearly monodisperse polystyrene samples with

different molecular weights, $m = 1$ and the coefficient 0.55 in Eq. (9.22) were obtained. The above analysis showing $\tau_X \approx \tau_2$ with τ_2 given by Eq. (9.D.5) supports the structural factor obtained for τ_X .

Thus, τ_1 , τ_2 , τ_3 and τ_4 are equivalent to τ_A^1 , τ_X , τ_B and τ_C , respectively, except for a proportional constant. With τ_4^0 replaced by τ_4 , Eq. (9.D.8) may be rewritten as

$$\frac{\tau_4}{\tau_1} \approx \left(\frac{M}{M_e} \right)^3 \left(1 - \sqrt{\frac{M_e}{M}} \right)^2, \quad (9.D.10)$$

$$\frac{\tau_3}{\tau_1} \approx \left(\frac{M}{M_e} \right)^2, \quad (9.D.11)$$

and

$$\frac{\tau_2}{\tau_1} \approx \frac{M}{M_e} \quad (9.D.12)$$

which are equivalent to Eqs. (9.20), (9.21) and (9.23), respectively, except for a proportional constant. Thus, the above analyses based on the scaling relation Eq. (9.D.1) show that the hierarchy and universality among and the structural factors of the characteristic times of the ERT processes are naturally inherent in the extended slip-link model — extended as τ_3 given by Eq. (9.D.6) is allowed and Eq. (9.D.9) is used to replace Eq. (9.D.7).

References

1. Einaga, Y., Osaki, K., Kurata, M., Kimura, S., and Tamura, M., *Polym. J.* **2**, 550 (1971).
2. Fukuda, M., Osaki, K., and Kurata, M., *J. Polym. Sci. Phys. Ed.* **13**, 1563 (1975).
3. Osaki, K., Bessho, N., Kojimoto, T., and Kurata, M., *J. Rheol.* **23**, 617 (1979).
4. Osaki, K., and Kurata, M., *Macromolecules* **13**, 671 (1980).
5. Osaki, K., Nishizawa, K., and Kurata, M., *Macromolecules* **15**, 1068 (1982).
6. Mark, H., and Tobolsky, A. V., *Physical Chemistry of High Polymeric Systems*, Interscience, New York (1950).
7. Lin, Y.-H., *Macromolecules* **19**, 159 (1986).
8. Lin, Y.-H., *J. Non-Newtonian Fluid Mech.* **23**, 163 (1987).
9. Lin, Y.-H., *J. Rheol.* **28**, 1 (1984).
10. Vrentas, C. M., and Graessley, W. W., *J. Rheol.* **26**, 359 (1982).
11. Pearson, D. S., *Rubber Chem. Tech.* **60**, 439 (1987).
12. Doi, M., *J. Polym. Sci., Polym. Phys. Ed.* **18**, 1005 (1980).

13. Doi, M., *J. Polym. Sci., Polym. Lett. Ed.* **19**, 265 (1981).
14. Doi, M., *J. Polym. Sci., Polym. Phys. Ed.* **21**, 667 (1983).
15. Lin, Y.-H., *Macromolecules* **17**, 2846 (1984).
16. Tobolsky, A. V., *J. Apply. Phys.* **27**, 673 (1956).
17. Ferry, D. J., *Viscoelastic Properties of Polymers* (3rd edn), Wiley, New York (1980).
18. Kramer, O., and Ferry, J. D., *Science and Technology of Rubber*, Chapter 5, edited by F. R. Eirich, Academic Press, New York (1978).
19. Inoue, T., Okamoto, H., and Osaki, K., *Macromolecules* **24**, 5670 (1991).
20. Okamoto, H., Inoue, T., and Osaki, K., *J. Polym. Sci.: Part B: Polym. Phys.* **33**, 417 (1995).
21. Inoue, T., and Osaki, K., *Macromolecules* **29**, 1595 (1996).
22. Doi, M., and Edwards, S. F., *The Theory of Polymer Dynamics*, Chapter 6, Oxford Univ. Press (1986).
23. Mooney, M., *J. Polym. Sci.* **34**, 599 (1959).

Chapter 10

Comparison of the Extended Reptation Theory (ERT) with Experiments

Much information about the viscoelastic properties of flexible linear polymers as related to entanglement has been obtained from the experimental studies of well characterized nearly monodisperse samples prepared by anionic polymerization or fractionation. Most of the earlier results can be found in the book by Ferry¹ and in its references. A review article by Ferry covered the key research works from 1930 to 1970.² We may summarize the main advancements made in this earlier period as follows: (1) the observation of the general line-shape pattern of the linear relaxation modulus $G(t)$ (or viscoelastic spectrum $G'(\omega)$ & $G''(\omega)$; as the linear relaxation modulus and viscoelastic spectrum are equivalent, we shall mention either one of the two in this and the next chapters, with the understanding that the same is also applied to the other; we shall also omit the word “linear” if it is well understood from the context that the linear region is being considered) from the transition region (II) to the terminal region and its transformation with changing molecular weight (see Figs. 4.6, 4.9 and 4.10); (2) the determination of the entanglement molecular weight M_e from the plateau modulus observed in $G(t)$ (before the publication of the Doi–Edwards theory, Eq. (8.1) was used instead of Eq. (8.2)); (3) the observation of the 3.4 power law of the zero-shear viscosity η_0 and the basic molecular-weight independence of the steady-state compliance J_e^0 in the high-molecular-weight region (Figs. 4.7 and 4.12); and (4) the determinations of the critical molecular weights M_c and M'_c from the molecular-weight dependence of η_0 and J_e^0 , respectively, and their close relations with the M_e value.

These results pointed out several aspects of universality in polymer viscoelasticity and led to some theoretical modelings.³ However, a promising way to describe the entanglement effect in a concentrated long-chain system had not appeared until de Gennes suggested the idea of reptation

in 1971. Only during and after the advent of the Doi–Edwards theory, did meaningful quantitative comparison between theory and experiment become possible as for the damping function $h(\lambda)$. The extended reptation theory (ERT), whose development on the theoretical framework of the Doi–Edwards theory was described in Chapter 9, provides a $G(t)$ function which can be expressed as a universal form in terms of the normalized molecular weight M/M_e , covering the whole range from the transition region (II) to the terminal region. It was pointed out in Chapter 9 that the ERT accurately describes the characteristics of transformation of the $G(t)$ line shape with changing molecular weight and that it explains the molecular-weight dependence of η_0 and J_e^0 . In this chapter we shall describe and discuss detailed aspects of the quantitative comparison between the ERT and experimental results.

10.1 Effects of the Molecular-Weight Distribution of the Sample

The functional form of the relaxation modulus $G(t)$ as given by Eq. (9.19) together with Eqs. (9.5), (9.6), (9.11), (9.12), (9.14), (9.15), (9.B.18), (9.B.20) and (9.22) is for an “ideally monodisperse sample” in the entanglement region. Equation (9.12) indicates that the relaxation time of the main process in $G(t)$ — the terminal process $\mu_C(t)$ — is strongly dependent on the molecular weight. Thus, to compare the measured $G(t)$ line shapes with the theory, we need to take the molecular-weight distribution into account, even though the studied samples are nearly monodisperse (typically with $M_w/M_n < 1.1$). This consideration involves the so-called blending law. The simplest kind of blending law is the linear additivity of the contributions from the different molecular-weight components in the distribution. Assuming such a blending law is equivalent to the *mean-field* assumption (in the sense that the bulk viscoelastic properties can be expressed in terms of the behavior associated with a single chain) which the ERT as well as the Doi–Edwards theory has been developed on. The mean field assumed from the very beginning of the Doi–Edwards theory is represented by the clear definition of the primitive chain (Eq. (8.3)). Thus, the mean field has much to do with the tube diameter a and its associated entanglement molecular weight M_e (Eq. (8.4)) which is determined from the plateau modulus (Eq. (8.2)). In addition, Eq. (8.3) plays a crucial role in the derivations of the expressions for τ_C^0 and τ_C as studied in Chapters 8 and 9. In a nearly monodisperse system of sufficiently high

molecular weight, a molecular weight-independent plateau modulus can be determined to give a well-defined value for M_e and thus for the tube diameter a as well. This observation indicates that in such a system all polymer chains, in spite of their small differences in molecular weight, “feel” the same tube-diameter size. This deduction also implies that the *linear-additivity rule* can be applied in the case of a nearly monodisperse sample if the mean-field assumption itself is valid in an ideally monodisperse system. Thus, it is logical to linearly convolute Eq. (9.19) with the nearly monodisperse distribution of the sample to calculate $G(t)$ for comparison with the experimental result. In the case of a broadly polydisperse sample, no clear plateau in $G(t)$ can be observed. This phenomenon suggests that Eq. (9.19) probably may not be used to analyze the $G(t)$ line shape of a broadly polydisperse sample by using the linear-additivity rule. In Chapter 11, blend systems consisting of two nearly monodisperse components with quite different molecular weights will be studied, revealing the complexity of an additional effect — the tube-dilation effect — involved in their $G(t)$ ’s.

In this chapter, all the results of nearly monodisperse systems presented show that the linear-additivity rule is well followed, except mainly for one sample, whose molecular weight is the highest among the studied. The deviation from the linear-additivity rule for this particular sample is small yet clearly detectable. The deviation was found to be due to the presence of a low-molecular-weight tail in the otherwise “perfectly” nearly monodisperse distribution of the sample. Because this effect has some bearing on the actual approach taken to analyze the $G(t)$ line shapes of the less perfect samples, we briefly discuss it below.

The $G(t)$ line shape of a nearly monodisperse high-molecular-weight sample will change somewhat when the sample is blended with a *small* amount of polymer with a considerably smaller molecular weight, yet still greater than M_e . The plateau region in $G(t)$ is still clearly observable in such a blend system. However, the small change in the $G(t)$ line shape will not follow the linear-additivity rule. In our discussion below, we shall refer to the added low-molecular-weight polymer as component one and the host or major component as component two. If the amount of component one is very small, such a blend can be functionally approximated as equivalent to a nearly monodisperse system with a low-molecular-weight tail or vice versa. Because component-one’s molecular weight is much smaller than component-two’s, the still clearly observable plateau is to be associated with component two. As the amount of component one is very small, the tube diameter felt by component-two’s chains remains (virtually) the same.

The unchanged tube diameter means that the terminal relaxation time associated with component two remains the same. But a small amount of tube stress on component-two's chains will relax in a time much shorter than the terminal relaxation time as the fast-moving component-one's chains reptate away from component-two's chains. This additional relaxation — not caused by the reptational motions of component-two's chains themselves — slightly enhances the declining rate in the plateau region. The relaxation of the tube stress on the component-one chains also basically occurs in the plateau region. Because there is only residual amount of component one, the apparent effect of this relaxation would basically amount to enhancing slightly the decline rate in the plateau region.

In the plateau region, since the absolute value of the reciprocal slope $|\Delta t/\Delta G|$ is large, a small “wrong” additional decline of the modulus ΔG in the plateau region can lead to a large error in time Δt . Thus, as the relaxation-time scale is transformed to the molecular-weight scale in the analysis of the $G(t)$ line shape, the presence of a small amount of component one can artificially broaden the molecular-weight distribution if the sample system is regarded as a nearly monodisperse system rather than a binary blend. This effect somewhat contaminates the line-shape analysis in one case discussed below, where the studied nearly monodisperse sample contains a low-molecular-weight tail. This effect will be further discussed when the comparison of theory with experiment is made for zero-shear viscosity.

A stronger effect of different nature will occur if the amount of component one is not small. In this case the tube diameter felt by component-two's chains becomes larger (this is referred to as the tube dilation effect) while that felt by component-one's chains remains the same as in a monodisperse situation. This effect is based on the observation that the terminal relaxation time associated with component two is shortened by the presence of a significant amount of component one (as discussed in detail in Chapter 11, corresponding to the tube dilation, an apparent larger entanglement molecular weight denoted by M_e'' can be defined which leads to a smaller τ_C value when M_e in Eq. (9.12) is substituted by M_e''). As also pointed out by Doi and Edwards,⁴ the tube is a dynamic concept rather than static. In a system of broad molecular-weight distribution, chains of different molecular weights feel different effective tube diameter sizes. A longer chain feels a larger tube diameter because of relatively higher reptational mobility of the shorter chains in its surroundings, while the shortest chain in the system feels the same tube-diameter size as in a monodisperse

system. The distribution of tube-diameter sizes felt by components of different molecular weights contributes greatly to the disappearance of a clear modulus plateau in a commercial polymer, whose molecular weight distribution is generally very broad. To apply Eq. (9.19) to a broadly polydisperse polymer by using the linear-additivity rule is bound to fail. Because the tube-dilation effect is truly a many-body problem even from the view-point of the tube model, the blending law for a broadly polydisperse polymer is very complicated. However, the tube-dilation effect, as it occurs in blend systems consisting of two nearly monodisperse components with very different molecular weights, can be studied profitably in a systematic way as described in Chapter 11.

10.2 Analysis of the $G(t)$ Line Shape

In practice, two approaches have been found to take the molecular-weight distribution into account in comparing Eq. (9.19) with the measured $G(t)$ line shapes of nearly monodisperse polymers:

One is to convolute Eq. (9.19) with a distribution consisting of multiple discrete components whose molecular weights and weight fractions are adjustable parameters under the constraint that the weight-average molecular weight is kept equal to the value determined from the sample characterization. That is

$$W(M) = \sum_i W_i \delta(M - M_i) \quad (10.1)$$

with

$$M_w = \sum_i W_i M_i \quad (10.2)$$

where W_i is the weight fraction of the component with molecular weight M_i , and M_w is the weight-average molecular weight of the sample. These parameters are adjusted in fitting the measured $G(t)$ to the calculated with a nonlinear, least-squares fitting computer program.

The other approach is to assume that the molecular-weight distribution is described by the Schulz distribution^{5,6} given by

$$W(M) = \frac{Z^{Z+1}}{\Gamma(Z+1)} \frac{M^Z}{M_n^{Z+1}} \exp \left[-\frac{ZM}{M_n} \right] \quad (10.3)$$

where Γ is the gamma function and

$$\frac{Z+1}{Z} = \frac{M_w}{M_n}. \quad (10.4)$$

Equation (10.4) indicates that the polydispersity of the Schulz distribution is characterized by the single parameter, Z . In this approach for a certain polymer sample, a series of $G(t)$ curves are first calculated by convoluting Eq. (9.19) with Eq. (10.3) at different Z values. Then, the optimum Z value is determined by the best superposition of the measured on the calculated $G(t)$ curve. In calculating the $G(t)$ curve at a certain Z value, the M_n value used in Eq. (10.3) is first calculated from Eq. (10.4) with the known M_w value of the sample.

Most anionically-polymerized high-molecular-weight samples ($> \sim 10M_e$ for polystyrene) usually contain a low-molecular-weight tail. This is a characteristic of high-molecular-weight samples synthesized anionically, which is likely caused by the presence of just a trace amount of impurity during polymerization. The plateau region in $G(t)$ of a sample is wide if its molecular weight is high. Thus, it takes only a very small amount of the low-molecular-weight tail to cause a noticeable additional decline of the modulus in the plateau region, which can lead to an artificial broadening of the molecular-weight distribution extracted from the nonlinear, least-squares fitting to the $G(t)$ curve — an effect which was explained above. In this case, the first approach has been found more appropriate.

For polystyrene polymers with a molecular weight smaller than $\sim 10M_e$, the modulus plateau region is not that flat and declines more quickly with decreasing molecular weight. As explained in Chapter 9 and will further be seen from the analysis of the $G(t)$ line shapes shown below, the main reason for this observed phenomenon is that the four relaxation processes, $\mu_A(t)$, $\mu_X(t)$, $\mu_B(t)$ and $\mu_C(t)$, are getting closer to one another in time. In the low-molecular-weight region, because of the closeness and even overlapping of the four processes, it is difficult to do the nonlinear, least-squares fitting of the first approach; instead, the approach of using the Schulz distribution has been found to be very efficient and satisfactory. It became very apparent in the actual doing that the adjustment of the single parameter Z in the Schulz distribution could unequivocally lead to a very close matching of the calculated and measured $G(t)$ curves from the terminal region to the transition region (II).

For a series of studied polystyrene samples with a molecular weight less than $10M_e$,⁷ the best Schulz distributions obtained from the closest

matching of the calculated and measured $G(t)$ line shapes have the Z values corresponding to a polydispersity of $M_w/M_n < 1.04$ in good agreement with the values obtained from the characterization of the samples.

For two nearly monodisperse polystyrene samples of $M_w = 1.79 \times 10^5$ and 4.22×10^5 (these two samples are denoted by NBS and F40, respectively),⁷ the $G(t)$ line-shape analyses were made by doing the nonlinear, least-squares fitting in terms of a distribution consisting of three discrete molecular-weight components (Eq. (10.1)). The polydispersity obtained from the line-shape analysis for the NBS sample was $M_w/M_n = 1.08$, in good agreement with the value 1.07 measured with the gel permeation chromatograph (GPC); while that for F40 was $M_w/M_n = 1.16$, which is somewhat greater than an apparent GPC value of 1.05. As explained above, the discrepancy in the case of F40 is due to the low-molecular-weight tail in the distribution as revealed by an independent GPC measurement.⁷ This discrepancy also has much to do with the “pitfalls” likely to occur in any nonlinear, least-squares fitting which would cause the *uniqueness or exact correctness* of the obtained “best” set of the adjustable parameters to be questioned. Here, the assumed distribution of three *discrete* components cannot represent completely the true distribution which should be continuous. At the same time, the number of involved fitting parameters is not small. This combination makes the obtained distribution easily distorted by errors in the measured curve. Here the main error source, as explained above, is the additional declining rate in the plateau region due to the low-molecular-weight tail in the studied sample. These factors lead to the artificially larger polydispersity in the molecular-weight distribution obtained from the nonlinear, least-squares $G(t)$ fitting of F40. In support of this explanation, the frictional factor K for F40 obtained from this $G(t)$ fitting is about 30% smaller than the average value obtained for the samples with molecular weight $< 10M_e$. The smaller K value and the broader molecular-weight distribution in the case of F40 are both artificial outcomes of the nonlinear, least-squares fitting of $G(t)$. As explained further in the comparison of theory and experiment for the zero-shear viscosity below, these two artificial effects cancel each other out in the integration of $G(t)$ (Eq. (4.30)), giving a viscosity value which agrees closely with the predicted value. The 30% reduction of the K value in the case of F40 is unlikely due to the molecular-weight error in the sample characterization. Based on Eq. (9.12), an error of 10% in the weight-average molecular weight can cause an uncertainty of $\sim 30\%$ in the K value obtained from the $G(t)$ curve analysis. The expected accuracy (a few percent at

most) of the sample's molecular-weight value makes it an unlikely factor. Furthermore, if the molecular-weight error were the cause, a corresponding 30% reduction should have been observed in the viscosity value. A similar explanation as given above for the F40 sample can account partially for the 30% reduction in K obtained from the $G(t)$ curve analysis for the NBS sample. As NBS's molecular weight is less than half of F40's, the flatness of the plateau in $G(t)$ of the former is greatly reduced. Thus, the artificial broadening of the molecular-weight distribution obtained from the $G(t)$ line-shape analysis for NBS is not as noticeable as that occurring to F40. Some inherent broader molecular-weight distribution of the NBS sample also contribute to the polydispersity obtained from its $G(t)$ line-shape analysis.

The results of the $G(t)$ curve analyses for the samples: F40, F10, F4 and F2 are shown in Figs. (10.1)–(10.4). These results show the typical close agreement between theory and experiment (see Ref. 7 for more comparisons of the calculated with the measured $G(t)$ curves). In these figures, the

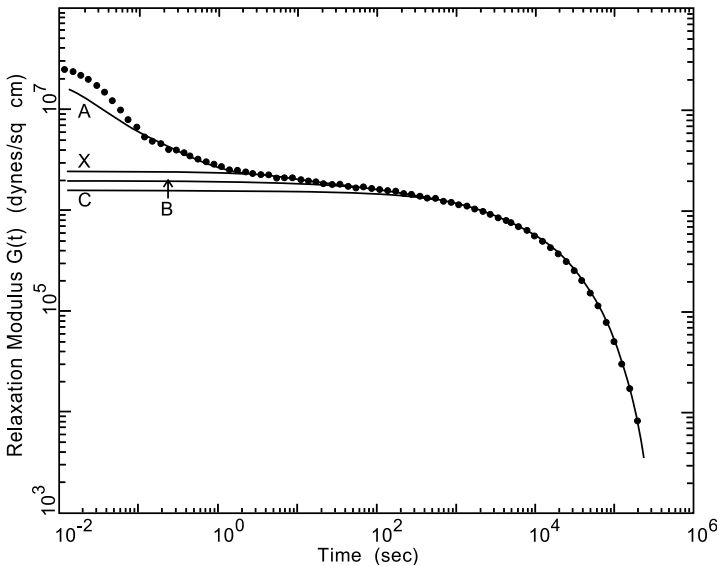


Fig. 10.1 Comparison of the measured (dots) and the calculated (line) relaxation modulus for the F40 sample. Also shown are the separate contributions of the $\mu_A(t)$, $\mu_X(t)$, $\mu_B(t)$ and $\mu_C(t)$ processes (line A is calculated with all four processes in Eq. (9.19) included, line X is calculated without $\mu_A(t)$, line B is calculated without $\mu_A(t)$ and $\mu_X(t)$, and line C is calculated without $\mu_A(t)$, $\mu_X(t)$ and $\mu_B(t)$; thus, the portion between line A and line X is the contribution of the $\mu_A(t)$ process, and so forth).

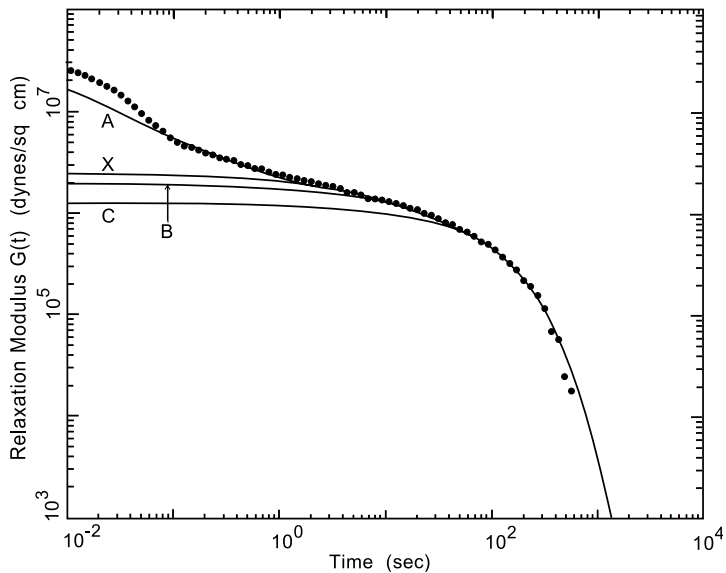


Fig. 10.2 Same as Fig. 10.1 for the F10 sample.

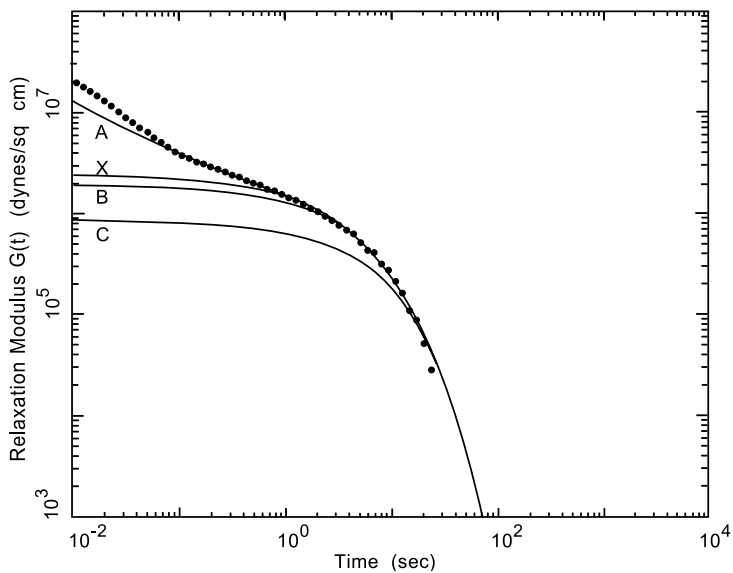


Fig. 10.3 Same as Fig. 10.1 for the F4 sample.

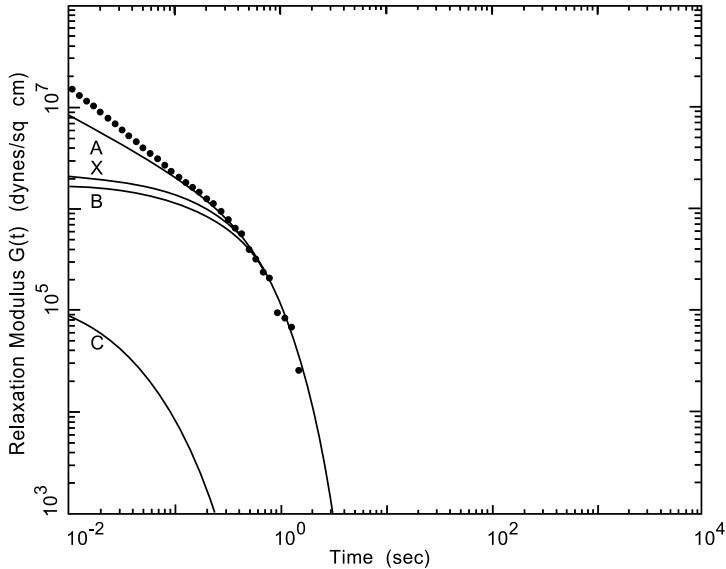


Fig. 10.4 Same as Fig. 10.1 for the F2 sample.

separate contributions from the $\mu_A(t)$, $\mu_X(t)$, $\mu_B(t)$ and $\mu_C(t)$ processes to the total $G(t)$ are also shown. In the short time region, deviations of the measured curves from the calculated are expected as we have not included in the theory the sub-Rouse-segmental dynamic process (the glassy-relaxation process), which is, as pointed out in Chapter 9, much affected by the energetic interactions among microstructural segments. Furthermore as pointed out in Chapter 4, the experimental data at times shorter than 0.1–0.2 sec are not expected to be accurate considering the compliance of the transducer and the step deformation rise time.

In the region of the low relaxation modes of the $\mu_A(t)$ process, it has been shown that the calculated $G(t)$ curve is very much independent of the N_e value used in the calculation (see Eqs. (9.19), (9.B.24)–(9.B.26)) as long as the N_e value is sufficiently large. For the shown $G(t)$ curves, $N_e = 10$ was used in the calculation. As far as the region of the low $\mu_A(t)$ modes is concerned, the fact that $N_e = 10$ is sufficiently large is demonstrated by the close agreement between two $G(t)$ curves calculated with the same frictional factor, one with $N_e = 10$ and the other with $N_e = \infty$ ($N_e = \infty$ is equivalent to using Eq. (9.B.27); see Figs. 3 and 10 of Ref. 8). As will be further discussed below, the frictional factor in the $\mu_A(t)$ process is

determined by matching the calculated and the measured in the region of the low $\mu_A(t)$ modes. (Note: The N_e value depends on the molecular weight for the Rouse segment m , i.e. $N_e = M_e/m$. The value of m for polystyrene obtained by different methods is $780 \sim 900$,⁹⁻¹⁵ (see Appendix 13.A) from which N_e should be about 16. However, using $N_e = 10$ here does not cause any difference in the obtained frictional factor for the $\mu_A(t)$ process.)

Here, we need to point out some detailed aspects of the procedure involved in the analysis of the $G(t)$ curves. In analyzing the $G(t)$ curves measured at a certain temperature in terms of Eq. (9.19), the parameters K and M_e are involved in addition to the parameters related to the molecular-weight distribution as discussed above. The expressions for the relaxation times contain both K and M_e while the plateau modulus G_N is related to M_e only. Thus, before K is finally determined from the $G(t)$ analysis, M_e has to be first determined from the plateau modulus. This process was carried out in the following way: An M_e value was first calculated from the literature value of G_N according to Eq. (8.2). The obtained M_e value was used for calculating all the $G(t)$ curves required during the nonlinear, least-squares fitting to the measured $G(t)$ curve of a high-molecular-weight sample (such as F40) whose modulus plateau was wide and clear. Then, a new value of the plateau modulus G_N was determined from the least-squares fitting. The obtained plateau modulus was used to calculate a new M_e value to be used in repeating the nonlinear, least-squares fitting process. Theoretically this procedure will be repeated until the obtained G_N value is consistent with the M_e value entered in the calculation of the $G(t)$ curves. As the finally determined G_N value was in very close agreement with the literature value which had been used initially, the convergence was quickly reached. The plateau modulus values in literature^{1,16} have often been obtained from integrating the peak in the terminal region of the loss-modulus spectrum. The determination from matching the measured and calculated $G(t)$ curves with a nonlinear least-squares fitting program should be considered as the most direct method. The two results are in close agreement with each other: for polystyrene $M_e = 13,500$ is obtained from the direct method⁷ while $M_e = 13,300$ is obtained from the integration method.¹⁶

Using the finally determined M_e value for polystyrene (13,500 corresponding to $G_N = 2 \times 10^6$ dyn/cm² at 127.5°C), the K value for each polystyrene sample was then determined from the $G(t)$ analysis under the constraint that the weight-average molecular weight of the distribution used in the calculation is fixed at the known value of the sample. From fitting

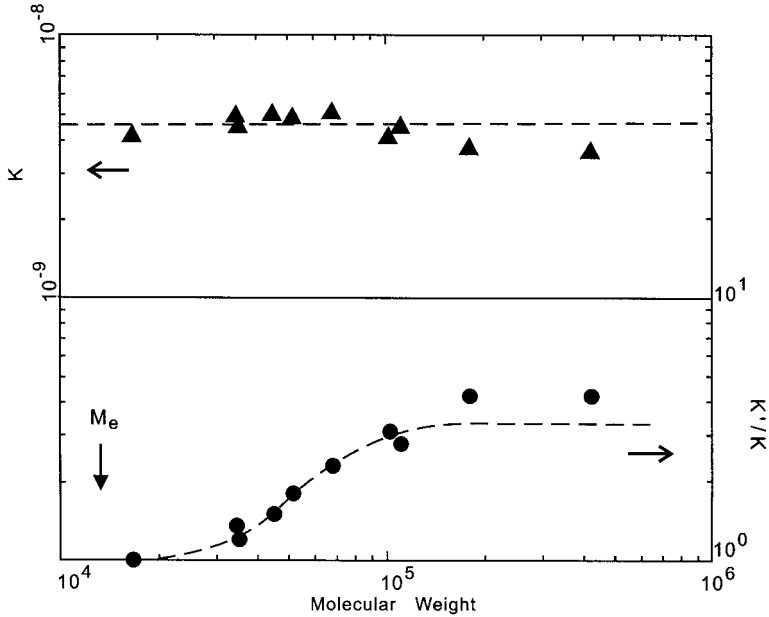


Fig. 10.5 K and K'/K values as a function of molecular weight M_w that have been obtained from the line-shape analysis of the measured $G(t)$ curves at 127.5°C .

to the $G(t)$ curves of different samples measured at the same temperature, the K values at different molecular weights were obtained. As indicated by the results at 127.5°C shown in Fig. 10.5, the K value in the $\mu_C(t)$, $\mu_B(t)$ and $\mu_X(t)$ processes is found independent of molecular weight as expected from the theory; however, the K (denoted by K' below) value in the $\mu_A(t)$ process is different as will be explained and discussed below.

The K values of the F40 and NBS samples are about 30% smaller than the average of the K values determined for the samples in the molecular-weight region below $10M_e$. As explained above, this small yet noticeable reduction of the K value is mainly related to the molecular-weight distribution rather than caused by an error in the weight-average molecular weights of the samples. Above $10M_e$ ($> 135,000$ for polystyrene), K' is independent of molecular weight and is greater than K by a factor of about 4.2. Corrected for the 30% reduction in K in the case of NBS and F40, the K'/K ratio becomes about 3.3 above $10M_e$. Below $10M_e$ the ratio K'/K declines gradually with decreasing molecular weight and reaches 1 as the molecular weight approaches M_e . From the close agreements between

the calculated and measured $G(t)$ curves as shown in Figs. 10.1–10.4, the obtained K and K' values as a function of molecular weight are uniquely determined.

That the obtained frictional factor K is, as expected, independent of molecular weight is a vitally important result of the analysis of the $G(t)$ curves. The very good description of the line shapes of the $G(t)$ curves by the theory would be totally meaningless if the obtained K values were not independent of molecular weight. The significance will be further demonstrated when the comparison of theory with experiment is made for the zero-shear viscosity.

What is surprising is the obtained molecular-weight dependence of K' . K'/K being greater than one indicates that the friction constant for motions involving a length scale smaller than the tube diameter and restricted inside the tube is greater than that for motions along the primitive path involving length scales greater than the tube diameter. Amazingly this difference disappears, i.e. $K'/K \rightarrow 1$, as the molecular weight approaches the M_e value. This phenomenon is very significant as it indicates very reasonably that there is no difference between K and K' or no motional anisotropy when the entanglement becomes absent. In other words, the difference between the frictional factors K and K' has much to do with the degree of entanglement per chain, i.e. M/M_e . As shown in Fig. 10.5, when the normalized molecular weight M/M_e is sufficiently large (> 10), the ratio K'/K reaches a plateau value. Such an effect can be explained in terms of the extra free volume generally associated with the chain ends. The extra free volume at either chain end is always available to the motions along the primitive path. On the other hand, the portion of the extra free volume available to the $\mu_A(t)$ modes of motion of a particular chain depends on the concentration of chain ends belonging to polymer chains in its surroundings. Thus, the K' value extracted from the $\mu_A(t)$ process is molecular weight-dependent. The same dependence of K'/K on the normalized molecular weight is also observed in binary-blend solutions as will be detailed in Chapter 11. The dependence of K'/K on M/M_e will be further discussed in Chapter 14 as related to the dependence of the glass transition temperature T_g on M/M_e (Sec. 14.6) and the universal dependence of K' on the temperature difference from the glass transition point $\Delta T = T - T_g$ in the polystyrene system (Sec. 14.9).

The $G(t)$ curves shown in Figs. 10.1–10.4 were measured with the System Four mechanical spectrometer manufactured by Rheometrics, Inc. When oscillatory measurements for storage and loss moduli were made

with this instrument, both the strain signal of the servo system and the stress signal from the transducer were correlated with a standard sine wave to calculate the in-phase and out-of-phase components. Because of these correlation steps, the obtained storage- and loss-modulus spectra as a function of frequency should be more free of noise than the relaxation-modulus curves. To confirm the measurements and analyses of the $G(t)$ curves as shown above, the storage- and loss-modulus spectra of the studied sample were also measured. Consistent agreements between theory and experiment were obtained. The comparisons of the measured with the calculated storage-modulus spectra $G'(\omega)$ corresponding to those comparisons shown in Figs. 10.2–10.4 are shown in Figs. 10.6–10.8. The theoretical $G'(\omega)$ curves have been calculated with the same values of the Z parameter and the K'/K ratio as those used in calculating the corresponding $G(t)$ curves. Because the experimental $G'(\omega)$ spectra were obtained at temperatures somewhat lower than 127.5°C , the K values used in the calculations are significantly different. One can notice that significant deviations of the measured from the calculated $G(t)$ curves occur at modulus

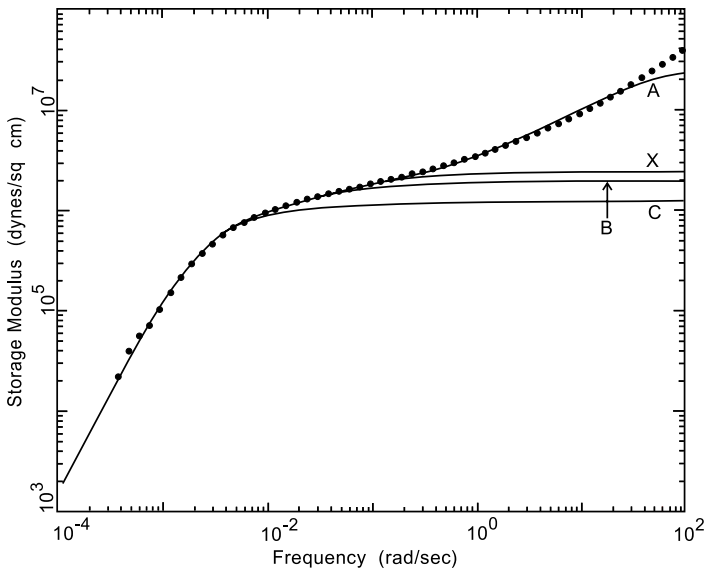


Fig. 10.6 Comparison of the measured (dots) and calculated (line) storage-modulus spectra for the F10 sample. Also shown are the separate contributions of the $\mu_A(t)$, $\mu_X(t)$, $\mu_B(t)$ and $\mu_C(t)$ processes (see Fig. 10.1 for the calculation of the A, X, B, and C lines).

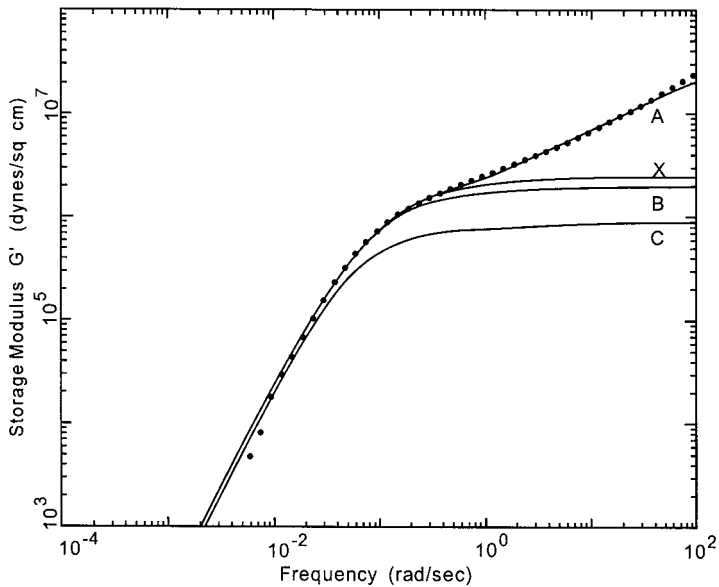


Fig. 10.7 Same as Fig. 10.6 for the F4 sample.

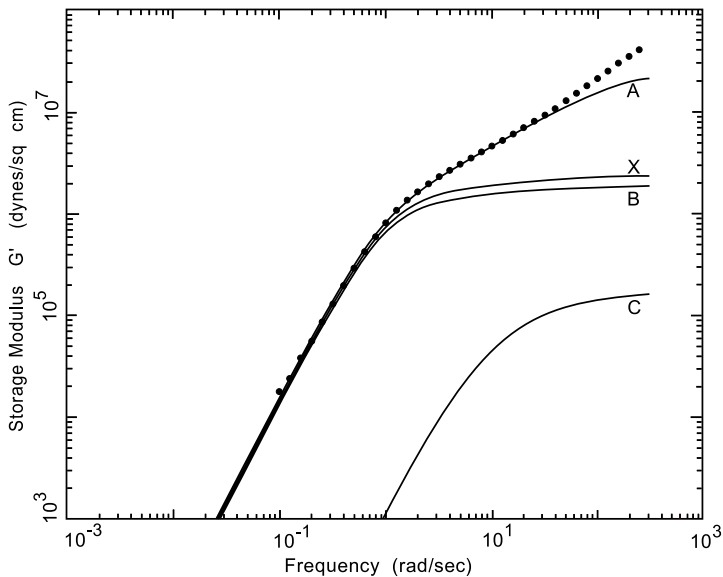


Fig. 10.8 Same as Fig. 10.6 for the F2 sample.

values $> \sim 6 \times 10^6$ dynes/cm² — except in the case of F2 — while deviations do not occur in the comparisons between calculated and measured $G'(\omega)$ spectra until a higher modulus level ($> \sim 1.2 \times 10^7$ dynes/cm²). The difference is mainly due to the effects associated with the compliance of the transducer and the step deformation rise time in the $G(t)$ measurements, which have been accounted for or are absent in the $G'(\omega)$ measurements. Disregarding the difference in the high-modulus (short-time or high-frequency) region, quantitative consistency is observed between the results shown in Figs. 10.2–10.4 and those shown in Figs. 10.6–10.8. The same level of quantitative consistency has been observed for the other samples which have also been studied and whose obtained K and K'/K values are included in Fig. 10.5. Because of its low molecular weight (only $1.24M_e$), F2 has a very weak $\mu_C(t)$ process allowing its $G(t)$ to decline rapidly at early times; as a result, the measured $G(t)$ starts to deviate from the calculated at a smaller modulus level than in the other cases. A similar effect is observed in the comparison of the measured and calculated $G'(\omega)$ spectra of F2. Aside from this, the same level of quantitative consistency between $G(t)$ and $G'(\omega)$ is also observed in the case of F2.

As explained in the Appendix 10.A, $G''(\omega)$ spectra are intrinsically not suitable for testing the validity of the ERT or the Rouse theory if the line-shape analyses are to cover only the entropic region.

10.3 Zero-Shear Viscosity and Steady-State Compliance

Through Eqs. (4.30) and (4.63), the zero-shear viscosity η_0 and the steady-state compliance J_e^0 are related to the relaxation modulus $G(t)$. In the high molecular weight region ($> \sim 5M_e$), both the $\mu_A(t)$ and $\mu_X(t)$ processes relax much faster than the $\mu_C(t)$ process and contribute negligibly to η_0 and J_e^0 . With the $\mu_A(t)$ and $\mu_X(t)$ processes neglected, the zero-shear viscosity and the steady-state compliance are given by Eqs. (9.24) and (9.25), respectively. It is clear from Eqs. (9.24) and (9.25) that the viscosity value is affected by the frictional factor K , which is strongly dependent on temperature, and a structural factor; while the steady-state compliance, being independent of K , is only affected by a structural factor. The structural factors of η_0 and J_e^0 are related to the functional form of the relaxation modulus $G(t)$, which is in turn determined by the structural factors of the relaxation times (Eqs. (9.6) and (9.12)) and the relaxation strengths (B and C as given by Eqs. (9.14) and (9.15)).

Both Eqs. (9.24) and (9.25) are for ideal monodispersity. As η_0 is proportional to the first moment of the relaxation-time distribution (Eq. (4.65)) while J_e^0 is proportional to the second moment (Eq. (4.66)), the former is far less sensitive to the molecular-weight distribution than the latter. If the molecular-weight distribution of a sample is nearly monodisperse, its η_0 value is little affected by the distribution while its J_e^0 value is significantly affected.

What has been said above about the effect of molecular-weight distribution on η_0 and J_e^0 is similarly applicable to the low-molecular-weight region where the contributions of the $\mu_A(t)$ and $\mu_X(t)$ processes cannot be neglected. The analytical expressions for η_0 and J_e^0 cannot be obtained from the full expression of the relaxation modulus (Eq. (9.19)). Yet theoretical values of η_0 and J_e^0 , including the contributions of $\mu_A(t)$ and $\mu_X(t)$, can be numerically calculated with a computer program.

(a) *Zero-shear viscosity*

For showing the *main* effect of molecular-weight distribution on the viscosity value η_0 , especially in the high molecular-weight region, it is sufficient to use the Doi–Edwards equation (Eqs. (8.54)–(8.56)) instead of Eq. (9.19). Using the Doi–Edwards equation, it can be easily shown by linearly adding the contributions from the different molecular-weight components that $\eta_0 \propto M_w M_z M_{z+1}$ ¹⁷ instead of $\eta_0 \propto M_w^3$. As $M_{z+1} > M_z > M_w$, the width of the distribution of a nearly monodisperse polymer can lead to a viscosity value slightly higher than that of an ideally monodisperse polymer at the same weight-average molecular weight. If the studied samples of different molecular weights are equally nearly monodisperse, the viscosity values for all the samples will increase more or less equally by a small amount due to the narrow distribution of molecular weight; the obtained molecular-weight dependence of viscosity will be practically the same as that obtained for “ideally monodisperse samples”.

As shown above, the $G(t)$ line shapes of a series of polystyrene samples at different molecular weights above M_e are well described by convoluting Eq. (9.19) with a nearly monodisperse distribution. Furthermore, the frictional factor K obtained from the analysis of the $G(t)$ curves measured at the same temperature is independent of molecular weight. Thus, we expect to obtain good agreement between theory and experiment for the

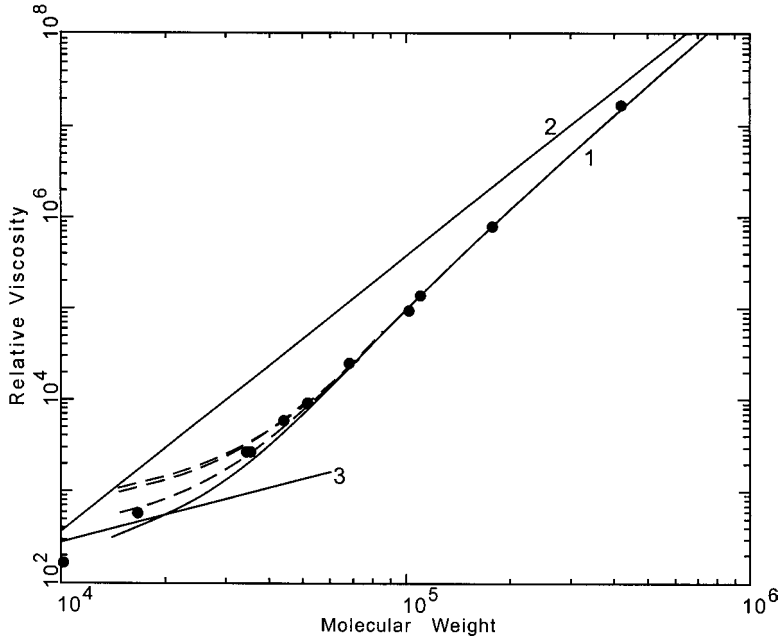


Fig. 10.9 Comparison of the measured viscosity values (\bullet ; without the so-called T_g correction) of nearly monodisperse polystyrene samples and those calculated from Eq. (9.24) (solid line 1), from the Doi-Edwards theory (solid line 2), from the Rouse theory (solid line 3), and from integrating numerically Eq. (9.19) with $K'/K = 1$ (the bottom dashed line), $K'/K = 3$ (the middle dashed line), and $K'/K = 5.5$ (the top dashed line).

zero shear-viscosity over the whole molecular-weight region above M_e if we numerically calculate η_0 from the full expression for $G(t)$. This expectation is confirmed by the comparison of the measured viscosity values with the calculated curves¹⁸ as shown in Fig. 10.9 (the experimental points are without the so-called T_g or free volume correction; see below).

Six theoretical viscosity curves calculated with the same K value are shown in Fig. 10.9: curve 1 is calculated from Eq. (9.24); curve 2 from the Doi-Edwards theory (Eq. (8.57)); curve 3 from the Rouse theory (Eq. (7.61)); and three dashed lines calculated numerically from integrating Eq. (9.19) with $K'/K = 1$, 3.3, and 5.5, respectively. The ratio of $K'/K = 5.5$ was obtained by multiplying $K'/K = 3.3$ by a factor which was estimated from comparing the areas obtained from integrating

$G(t)$ in the $\mu_A(t)$ region with and without the apparent long-time tail of the glassy-relaxation process. The long-time tail means the difference between the measured and the calculated $G(t)$ curves as can be seen in Figs. 10.1–10.4 in the short-time region. As pointed out earlier, the short-time regions (< 0.1 sec) of the measured $G(t)$ curves are not accurate, to replace $K'/K = 3.3$ with $K'/K = 5.5$ in the numerical calculation of the zero shear viscosity was intended to be an apparent, rough correction for the contribution of the glassy-relaxation process (also referred to as the internal-viscosity contribution^a). In Chapter 14, the whole glassy-relaxation process is included in the full-range line-shape fitting analyses of the viscoelastic responses at different temperatures to as low as the glass transition point T_g . As indicated by the results obtained in Chapter 14, the correction turns out to be roughly right for the temperature (127.5°C) at which the $G(t)$ curves are obtained. As further discussed in Sec. 14.13, using $K'/K = 5.5$ in the numerical calculation amounts to only a fraction of the correction for the contribution of the internal viscosity at temperatures close to T_g . The difference between the viscosity curves calculated with $K'/K = 3.3$ and 5.5 is very small and is only barely noticeable in the very low-molecular-weight region $< M_e$. Thus, the contribution of internal viscosity to the zero shear viscosity is negligibly small for the considered range of molecular weights (i.e. $\geq M_e$) at temperatures sufficiently high above T_g . In the high-molecular-weight region, curve 1 (Eq. (9.24)) merges with the curves calculated numerically with $K'/K = 1, 3.3$ and 5.5. The comparison of experimental results with the ERT in Fig. 10.9 is made by allowing the the experimental data points to shift along the vertical axis until the best superposition on the theoretical curve is obtained in the high-molecular-weight region ($> 8 \times 10^4$ where no difference between curve 1 and curves calculated with $K'/K = 1, 3.3,$ and 5.5 can be discerned). As expected from the results shown in Fig. 10.5 that K is independent of molecular weight and that K'/K declines gradually from a plateau value of 3.3 in the

^aHere, the “internal viscosity” is defined as the contribution of the glassy-relaxation process to the zero-shear viscosity. This definition is different from the common understanding of the term used in literature,^{19,20} although both have similar notions as to the existence of an effect of fast sub-Rouse-segmental motions on polymer viscoelasticity. In the literature the term “internal viscosity” generally refers to the effect that would lead to a plateau value of the intrinsic viscosity at high frequencies.

high-molecular-weight region to 1 as the molecular weight approaches M_e , the experimental η_0 results is in good agreement with curve 1 in the high-molecular-weight region and gradually shifts from the curve of $K'/K = 3.3$ (or $K'/K = 5.5$) to the curve of $K'/K = 1$.

As shown in Fig. 10.9, the viscosity data points of the F40 and NBS samples as well as those of the other samples are closely on the theoretical curve, without showing a reduction of 30% which occurs to the K values (Fig. 10.5) obtained from the analyses of the $G(t)$ curves of the two samples. Due to the modification of the zero-shear viscosity by a narrow molecular-weight distribution as discussed above, the effect on the viscosity from the 30% reduction in K is largely cancelled out by the artificial broadening of the molecular-weight distribution extracted from the $G(t)$ line-shape analysis.

Because of the molecular-weight dependence of the glass transition temperature T_g or free volume in the polymer melt, it has been a common practice to correct the measured *isothermal* viscosity data to the values corresponding to temperatures of equal distance from individual T_g values of the samples (i.e. at the same $\Delta T = T - T_g$).^{1,21} This so-called T_g correction allows the viscosity data to be compared under the condition of presumably the same friction constant or frictional factor so that the structural factor of η_0 (i.e. a certain function of molecular weight) can be determined. As T_g reaches a plateau value^{22,23} when the molecular weight is sufficiently high, the correction is smaller with increasing molecular weight. The correction affects the η_0 values noticeably mainly in the molecular-weight region below $\sim 2M_c$. After the T_g correction, the molecular-weight dependence of viscosity has the empirical relations: $\eta \propto M$ below the critical molecular weight M_c , in apparent agreement with the Rouse theory, and $\eta_0 \propto M^{3.4}$ above M_c . As K is independent of molecular weight to as low as M_e , the decline of the K'/K ratio from 3.3 to 1, starting around $M/M_e = 10$, should be related to the gradual increase in free volume (or decrease of T_g) with decreasing molecular weight. In other words, the η_0 curve calculated with $K'/K = 3.3$ (or 5.5) should correspond to the molecular dependence of η_0 obtained after the T_g correction. Indeed, as shown in Fig. 10.10,¹⁸ the theoretical curve of $\log(\eta_0)$ vs. $\log(M_w)$ calculated with $K'/K = 3.3$ (or 5.5) and with $M_e = 13,500$ for polystyrene as the only input parameter has a critical bending point very close to the M_c value (33,000) as reported in the literature for polystyrene,^{1,21,22,24,25} a slope of 1 below M_c , and a

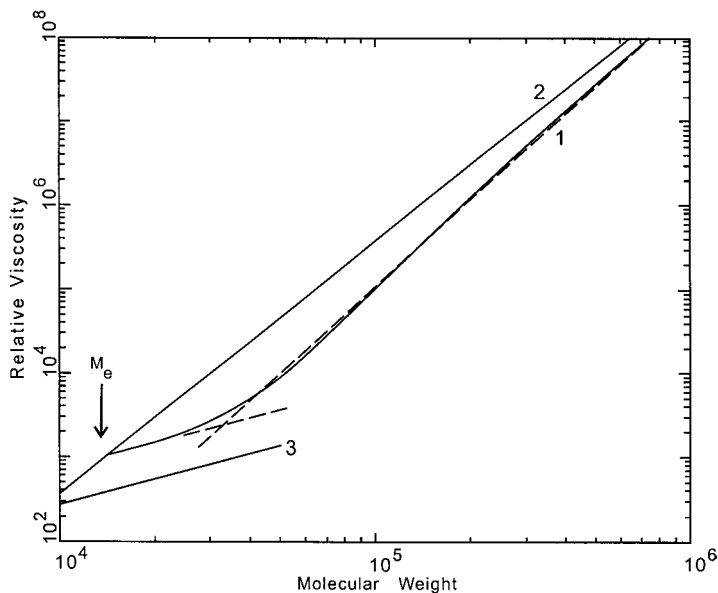


Fig. 10.10 Comparison of the theoretical curve (solid line 1) obtained from integrating numerically Eq. (9.19) with $K'/K = 5.5$ and the power law relations $\eta_0 \propto M^{3.4}$ above M_c and $\eta_0 \propto M$ below M_c (the dashed lines). $M_e = 13,500$ is used in the calculation giving $M_c = 33,000$. Also shown are the curves of the Doi–Edwards theory (solid line 2) and the Rouse theory (solid line 3).

form above M_c which can be closely approximated by the well-known 3.4 power law.

The experimental observation of $\eta_0 \propto M$ (after the T_g correction) in the molecular-weight region below M_c has often been used to indicate that in this region the viscoelastic behavior is described by the Rouse theory and the system is free of entanglement, and that M_c is the onset point of entanglement.^{1,17,21} However, the theoretical curve with $K'/K = 3.3$ or 5.5, while being linearly proportional to M below M_c , is higher by a factor of about 3 than the Rouse curve calculated with the same K as shown in Figs. 10.9 and 10.10. Even the theoretical curve with $K'/K = 1$ as well as the experimental data point at the molecular weight of $1.24M_e < M_c$ — without the T_g correction — is higher than the Rouse line. These results indicate that the polymer melt is not free of entanglement between M_e and M_c as often thought on the basis of the observed molecular-weight dependence of the corrected η_0 below M_c . In other words, while the Rouse

theory predicts $\eta_0 \propto M$, the reverse is not true. This conclusion is further confirmed by the direct observation of the onset of entanglement at M_e by monitoring the deviation of the viscoelastic spectrum from the Rouse theory in Chapter 11 and the comparison of the viscosity data at M_c with the results of diffusion measurements discussed later in this chapter.

(b) *Steady-state compliance*

As the steady-state compliance J_e^0 is sensitive to the molecular-weight distribution, the experimental results of the nearly monodisperse samples are higher than the theoretical values for ideal monodispersity. Shown in Fig. 10.11 is the comparison of the experimental data of J_e^0 (the experimental results shown in Fig. 10.11 are consistent with those shown in Fig. 4.12) with four theoretical curves: curve 1 is calculated from Eq. (9.25); curves 2 and 3 are numerically calculated from the substitution of Eq. (9.19) into

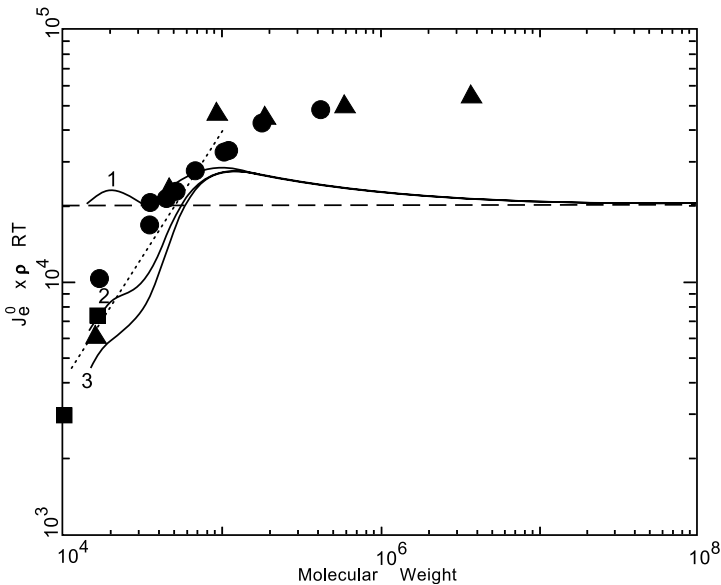


Fig. 10.11 Comparison of the steady-state compliance data, $J_e^0 \times \rho RT$, of nearly monodisperse polystyrene samples (\bullet and \blacksquare from Ref. 18; \blacktriangle from Ref. 33) and those calculated from Eq. (9.25) (solid line 1), from the Doi-Edwards theory (the dashed line), from the Rouse theory (the dotted line), and calculated numerically from substituting Eq. (9.19) into Eq. (4.63) with $K'/K = 1$ (line 2), and $K'/K = 3.3$ (line 3).

Eq. (4.63) with $K'/K = 1$ and 3.3, respectively; the dashed line is the Doi-Edwards theory (Eq. (8.58)); and the dotted line is the Rouse theory (Eq. (7.62)). There is no difference among curves 1, 2, and 3 in the high-molecular-weight region, $> \sim 10M_e$. Curve 1 does not predict the observed decline of J_e^0 with decreasing molecular weight in the low-molecular-weight region. Curves 2 and 3, both of which contain the contributions of the $\mu_A(t)$ and $\mu_X(t)$ processes, predict the bending point M'_c ($\approx 7M_e$) accurately and a decline of J_e^0 with decreasing molecular weight below M'_c . Below M'_c , the actual theoretical curve should transit gradually from the curve of $K'/K = 3.3$ to the curve of $K'/K = 1$.

The experimental data points are above the theoretical curves because of the finite molecular-weight distribution of the samples, even though they are very narrow. The gradual decline of J_e^0 with increasing molecular weight above M'_c as predicted by the theory is not directly reflected by the data points, whose molecular-weight dependence appears flat. As revealed from the $G(t)$ line-shape analysis as well as the GPC characterization of the sample, the molecular-weight distribution of a higher-molecular-weight nearly monodisperse sample is broader than that of a lower-molecular-weight one. In fact the trend of molecular-weight distribution broadening with increasing molecular weight is generally true for samples synthesized anionically. The apparent flatness of the J_e^0 that results in the molecular-weight region $> M'_c$ actually indicates that J_e^0 for ideal monodispersity should decline slightly with increasing molecular weight, as indicated by curves 1, 2 and 3. Below M'_c , both curves 2 and 3 are below the Rouse line. In the low molecular weight region, the inclusion of the glassy-relaxation component in $G(t)$ would also make the J_e^0 values smaller. These two effects, cancelling out the broadening effect due to the finite molecular-weight distribution of the samples, make the J_e^0 data points below M'_c very close to the Rouse line calculated for ideal monodispersity (also see Fig. 4.12). This close agreement with the Rouse line is merely a coincidence.

We can conclude that the ERT has accurately explained the molecular-weight dependence of the zero-shear viscosity and the steady-state compliance and their respective transition points M_c and M'_c . This success is indeed the logical consequence of the success of the theory in analyzing the $G(t)$ curves of the studied samples, a vitally important aspect of which is the molecular-weight independence of the frictional factor K . From the analysis of the $G(t)$ curves, it is revealed that entanglements exist between M_e and M_c . This point will be further confirmed by the

comparison of the diffusion data with the viscosity data through the ERT as discussed below.

10.4 Viscoelasticity and Diffusion

We can rewrite Eq. (8.20) as given by the Doi–Edwards theory for the diffusion constant D_G as

$$D_G = K_d M^{-2} \quad (10.5)$$

with

$$K_d = \frac{K_\infty M_e}{3\pi^2 K} \quad (10.6)$$

where K_∞ is the ratio of the mean-square end-to-end distance of the polymer chain to the molecular weight

$$K_\infty = \frac{R^2}{M} \quad (10.7)$$

which can be determined from the neutron scattering of the polymer melt system with the probed chain labelled with deuterium. As the diffusion constant of a polymer D_G characterizes the translational motion of the center of mass, it should not be affected by the intramolecular chain motions that affect the viscoelastic behavior. Thus, in spite of the importance of the intramolecular motions for the viscoelastic behavior as studied in Chapter 9 and above, D_G should remain described by Eqs. (10.5) and (10.6). Both the M_e and K values in Eq. (10.6) can be determined from the analysis of the $G(t)$ curves in terms of Eq. (9.19) as shown previously in this chapter. Thus, the K_d value can be predicted by using the values of K , M_e and K_∞ obtained from analyzing the experimental data of viscoelasticity and scattering for comparison with the value determined from direct measurements of the diffusion constant on the basis of Eq. (10.5). This comparison would give a very important test to the ERT.

The $D_G \propto M^{-2}$ scaling relation (Eq. (10.5)) has been extensively observed.^{26,27} Kramer *et al.*^{28,29} using the forward recoil spectrometry and the marker displacement technique have obtained very consistent diffusion results for polystyrene. Shown in Fig. 10.12 is the tracer diffusion constant in a polystyrene matrix of molecular weight $P = 2 \times 10^7$ obtained with the two techniques at 174°C. It has been experimentally shown by Green and Kramer³⁰ that if the diffusing-chain molecular weight M is sufficiently high ($> 100,000$), the tracer diffusion constant is the same as the self-diffusion

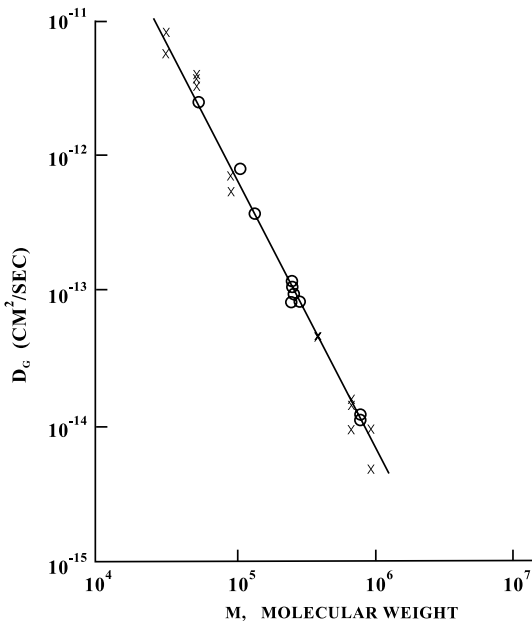


Fig. 10.12 The molecular-weight dependence of the tracer diffusion constant obtained for the nearly monodisperse polystyrene samples in a polystyrene matrix of molecular weight $P = 2 \times 10^7$ at 174°C . The solid line represents $D_G = 0.008M^{-2}$. Reproduced, by permission, from Ref. 28.

constant (i.e. when $P = M$). The diffusion constant characterizes the translational motion of the center of mass of the polymer chain, and should not be affected by the intramolecular motions. Thus, while the stress relaxation in the terminal region is much shortened by the primitive-chain contour length fluctuation if the molecular weight is not large, the diffusion constant, if not affected by the so-called constraint release processes, is related only to the *pure* reptation time. For instance, at $M = 55,000$, the pure reptation time is longer than the terminal relaxation time by a factor of 3.9.³¹ Because of this difference, while, as shown previously in this chapter, the linear viscoelasticity is not susceptible to the constraint release effect as long as the sample is nearly monodisperse, the diffusion constant in the low molecular weight region ($< 100,000$ for polystyrene) is somewhat enhanced by the effect. Since we are interested in comparing the viscoelastic data with the diffusion results, we consider the tracer diffusion data as shown in Fig. 10.12. The diffusion constant for a high-molecular-weight nearly monodisperse polystyrene polymer was measured by Bueche using the radiolabeling technique.³² After Bueche's result is corrected to 174°C

by using the temperature dependence of viscosity data,³³ the obtained K_d value is in close agreement with the values obtained by Kramer *et al.* The average of these studies gives $K_d = 8 \times 10^{-3} \text{ cm}^2\text{g}/(\text{s mol}^2) \pm 13\%$ at 174°C .³⁴

Besides from the analysis of $G(t)$ as shown in Sec. 10.2, the frictional factor K can be obtained from the viscosity data using Eq. (9.24) in the high-molecular-weight region where the contributions of the $\mu_A(t)$ and $\mu_X(t)$ processes to viscosity are negligible. From the data of Plazek and O'Rourke³³ at $M_w = 0.94 \times, 1.89 \times,$ and 6.0×10^5 , one obtains $K = 3.2 \times, 2.4 \times,$ and 2.7×10^{-12} , respectively, at 174°C . As explained in Sec. 10.3, the polydispersity of a nearly monodisperse polymer causes its viscosity to be slightly higher than that of an ideally monodisperse one at the same weight-average molecular weight. Equation (9.24) being for ideal monodispersity, a correction should be made to the above obtained K values. The bulk of correction can be made if the M_w/M_n values of the samples are known. While being not given, the M_w/M_n values of the three samples can be estimated from matching their measured steady-state compliance J_e^0 values³³ with those calculated from Eq. (4.63) wherein the $G(t)$ is first calculated from convoluting Eq. (9.19) with the Schulz distribution (Eq. (10.3)) using the Z value as the only adjustable parameter. In this way, $Z = 23, 20$ and 10 (correspondingly, $M_w/M_n = 1.04, 1.05$ and 1.1) are obtained for the three samples, respectively. Then the correction factors for K due to polydispersity can be obtained by comparing the viscosity values calculated from Eq. (9.24) and from integrating numerically the $G(t)$ calculated from convoluting Eq. (9.19) with the Schulz distribution using the above obtained Z values, both kinds of calculations being done with the same (weight-average) molecular weight and K for each sample. The thus obtained correction factors are 1.24, 1.22 and 1.34 for the three samples, respectively. That the first sample, while having a Z value slightly larger than the second one, has a slightly larger correction factor is due to the fact that at its molecular weight the $\mu_A(t)$ and $\mu_X(t)$ processes can still make a small noticeable contribution to viscosity. The K values corrected by these factors are $2.6 \times, 2.0 \times,$ and 2.0×10^{-12} , respectively. In the same way, the K values of the three samples at 127.5°C are obtained to be $5.7 \times, 4.9 \times,$ and 5.8×10^{-9} , respectively. Using the ratio of the average values of the two sets of K values, we obtain $K = 1.9 \times 10^{-12}$ at 174°C from the K value at 127.5°C obtained from analyzing $G(t)$ (4.7×10^{-9} ; the average over the samples with M_w between 3.4×10^4 and 1.1×10^5 as shown in Fig. 10.5). The above obtained K values are in close agreement with one another, at both 174 and 127.5°C , further supporting K being independent

of molecular weight as shown in Fig. 10.5. Using the average of the K values at 174°C in Eq. (10.6) gives $K_d = 9.2 \times 10^{-3}$, in close agreement with the value 8×10^{-3} obtained directly from the diffusion measurements.

Shortly after the Doi-Edwards theory was published, Graessley¹⁷ proposed using the viscosity value at M_c to calculate the K value on the basis of the Rouse theory

$$K = \frac{36\eta_0(M = M_c)}{\pi^2 \rho RT M_c} \quad (10.8)$$

and then calculate through Eq. (10.6) the K_d value for comparison with that obtained from the diffusion measurements. Since the diffusion measurements were made on samples in the molecular-weight region where the glass transition temperature T_g does not change with molecular weight, the viscosity value at M_c to be entered into Eq. (10.8) has to be first corrected for the T_g difference at M_c .

Graessley's approach for checking the validity of the diffusion constant of the Doi-Edwards theory (Eqs. 10.5 and 10.6) was based on the traditional belief that there was no entanglement at a molecular weight smaller than M_c . However, the results as shown earlier in this chapter: (1) the quantitative analysis of the $G(t)$ curves in terms of Eq. (9.19) indicating that the frictional factor K is independent of molecular weight to as low as just above M_e (Fig. 10.5) and (2) the molecular-weight dependence of the viscosity being well described by the ERT over the whole molecular-weight region above M_e (Fig. 10.9) clearly indicate that entanglement already occurs in the molecular-weight region between M_e and M_c . As shown in Figs. 10.9 and 10.10, the theoretical η_0 curve with $K'/K = 3.3$ or 5.5, which is equivalent to having the T_g correction made, is about 3 times greater than the Rouse value in the region of M_e to M_c . Therefore, we should see that the K_d value calculated from $\eta_0(M_c)$ using Eqs. (10.6) and (10.8) will be too small by a factor of about 3 in comparison with the value determined from the diffusion measurements. Indeed that is what happens.³⁴ From the viscosity results of Plazek and O'Rourke,³³ one obtains the value of $\eta_0(M_c = 33,000)$, after the T_g correction at 174°C, to be in the close neighborhood of 2,810P. Corresponding to the T_g -corrected value of $\eta_0 = 2,930P$ for $M_c = 35,000$ at 174°C reported by Lodge *et al.*²⁷ $\eta_0 = 2,760P$ for $M_c = 33,000$. These two $\eta_0(M_c = 33,000)$ values are in close agreement. Using the value of $\eta_0(M_c)$, K_d is calculated to be 2.3×10^{-3} through Eqs. (10.6) and (10.8), which is smaller than the K_d values determined from the diffusion measurements by a factor of about 3.5.

10.5 Summary

To conclude the experimental tests of the ERT as covered in this chapter, the K values of polystyrene at 127.5 and 174°C obtained from different sources: (a) $G(t)$ line-shape analyses of a series of nearly monodisperse samples at 127.5°C; (b) viscosity data of nearly monodisperse samples with different molecular weights at both 127.5 and 174°C; (c) full-range creep-compliance $J(t)$ analyses of a nearly monodisperse sample ($M_w = 4.69 \times 10^4$); and (d) calculation from the K_d value (Eqs. (10.5) and (10.6)) obtained by diffusion measurements at 174°C, are listed in Table 10.1 for a comprehensive comparison. While (a), (b) and (d) have been detailed in this chapter, (c) is from the study as detailed in Chapter 14. As the temperature dependences of viscosity — reflecting the temperature dependence of K — at different molecular weights are closely superposable,³³ K being independent of molecular weight at 127.5 and 174°C as shown in Table 10.1 is equally valid at any temperature between. The K values at 127.5°C listed in the first row of the table represent the viscoelastic results of totally 11 samples of different molecular weights ranging from 3.4×10^4 to 6×10^5 . These values, with an average of 4.9×10^{-9} , have a standard deviation of only 10%. In contrast, the ratio between the viscosity at the highest molecular weight (6×10^5) and that at the lowest (3.4×10^4) covered in Table 10.1 exceeds four orders of magnitude. Furthermore, the K values are obtained independently by different types of viscoelastic measurements — strain-controlled and stress-controlled. Considering the extremely stringent nature of these tests, the molecular-weight independence of K is regarded as rigorously proven.

As shown by the above analyses of the viscoelasticity and diffusion data in terms of the ERT, the paradox between the scaling relations $\eta_0 \propto M^3$ and $D_G \propto M^{-2}$ predicted by the pure reptational model, that occurs in their comparison with the experimental results, is resolved. Furthermore, the relation between viscoelasticity and diffusion as given by the ERT is quantitatively supported by the data of polystyrene. The analysis of the viscosity data at M_e in relation to the K_d value obtained from the diffusion measurements also supports the ERT. Considering the different nature of the experiments of viscoelasticity and diffusion, the quantitative agreement between these two kinds of data as analyzed in terms of the ERT is remarkable and thus indeed significant.

The existence of entanglement in between M_e and M_c will be further supported by the study in Chapter 11 — the direct observation of the onset of entanglement at M_e by monitoring the initial deviation of the viscoelastic

Table 10.1 Frictional factor K values obtained by analyzing the results of $G(t)$ ⁷, $J(t)$ ³⁵, viscosity³³ and diffusion^{28–30} at 127.5 and/or 174°C.

	From $G(t)$ a series of samples 3.4×10^4 $\leq M_w \leq 1.1 \times 10^5$	From $J(t)$ $M_w = 4.69 \times 10^4$	From Viscosity			From	Average*
			$M_w = 9.4 \times 10^4$	$M_w = 1.89 \times 10^5$	$M_w = 6.0 \times 10^5$	Diffusion	
$K(127.5^\circ\text{C}) \times 10^9$	$4.7 \pm 8\%$	4.8	5.7	4.9	5.8	(5.3) [†]	$4.9 \pm 10\%^{\ddagger}$
$K(174^\circ\text{C}) \times 10^{12}$	(2.2) [†]	(2.3) [†]	2.6	2.0	2.0	2.5	$2.3 \pm 14\%$

*The average values are obtained from averaging over the values not enclosed in a bracket.

[†]Values in a bracket are calculated from the shown values at the other temperature using the ratio of the two average K values.

[‡]The average is calculated with equal weighting accorded to each of the totally 11 samples, whose K values extracted from viscoelastic results are contained in this row.

spectrum from the Rouse theory as the molecular weight or concentration increases from the entanglement-free region.

Appendix 10.A — The Reason Why $G''(\omega)$ Should Be Excluded from the Line-Shape Analysis in Terms of the Rouse Theory or the ERT If Only the Entropic Region Is to Be Covered

The most basic structural unit in the Rouse theory and the ERT is the Rouse segment, which has a length scale considerably greater than that of the microstructure. Thus, both theories do not intend to describe the fast dynamics associated with chain sections shorter than a Rouse segment — the glassy-relaxation process. As opposed to the dynamic processes described by the ERT or the Rouse theory being entropic in origin, the sub-Rouse-segmental process as observed in the relaxation modulus $G(t)$ is dominantly affected by the energetic interactions among microstructural segments (Chapter 14). The number of Rouse segments per unit volume determines the highest rubbery (entropic) modulus value to which a measured stress-relaxation modulus $G(t)$ can be attributed, which in general is of the order of magnitude $\sim 5 \times 10^7$ dynes/cm². The fast sub-Rouse-segmental dynamics is responsible for the relaxation of $G(t)$ in the short-time region covering the range from $\sim 10^{10}$ to $\sim 5 \times 10^7$ dynes/cm² as will be detailed in Chapter 14. With the initial modulus virtually at the level of a glass, this fast relaxation is much related to the glass-transition phenomenon. In summary, the full-range $G(t)$ of a polymer encompasses an energetic-interaction-driven (or simply as energy-driven) process occurring in the short-time region and entropy-driven dynamic processes in the long-time region. The analyses of the line shapes of the viscoelastic spectra in terms of the ERT or/and the Rouse theory as detailed in this chapter and the next are obviously intended to be limited to the entropic region. We have to make sure that the long-time tail of the glassy-relaxation process does not interfere with the analyses or contaminate the analyses, so to speak. The following explains why the loss-modulus spectrum $G''(\omega)$ should not be considered in such a line-shape analysis for extracting reliable unambiguous information:

To simplify the explanation, we can express $G(t)$ in the following form:

$$G(t) = A_0 \exp(-t/\tau_0) + \sum_i S_i \exp(-t/\tau_i) \quad (10.A.1)$$

where the first term represents the glassy-relaxation process and the second term represent the collection of the different processes or normal modes as contained in the ERT or the Rouse theory. Usually the glassy-relaxation process is described not by a single exponential decaying function but rather by a stretched exponential form (see Chapter 14). However, for our present purpose, the assumption of a single exponential decay is sufficient to illustrate the main point in a simpler and clearer way. Here, it is also understood that the relaxation strength A_0 is much larger than the sum $\sum_i S_i$ and τ_0 is much smaller than the smallest, denoted by τ_v , in the set of relaxation times $\{\tau_i\}$. In this analysis we may regard τ_0 as equivalent to the average glassy-relaxation time $\langle\tau\rangle_G$ — namely, $\tau_0 \approx \langle\tau\rangle_G$. As can be seen in Chapter 14 for polystyrene, $A_0 \approx 10^{10}$ dynes/cm² while $\sum_i S_i \approx 4 \times 10^7$ dynes/cm²; and τ_v/τ_0 exceeds ~ 10 at the glass transition point T_g and increases with increasing temperature — by ~ 26 times as the temperature increases from T_g to 40K above T_g . As the $G(t)$ functional forms of the Rouse theory and the ERT are known as given in Chapters 7 and 9, respectively, the relaxation-time distributions: $\{S_i\}$ and $\{\tau_i\}$ can be calculated accurately in both the entanglement-free and entangled cases (see Appendix 14.A for details). In the line-shape analysis of a measured $G(t)$, $G'(\omega)$ or $G''(\omega)$ curve (or spectrum) in terms of the ERT or the Rouse theory, the region that is free of the glassy-relaxation process and safe from its contamination must be identified first. We shall refer to this region as the *safe* entropic region below. As the $G(t)$ and $G'(\omega)$ line shapes are near mirror images of each other (see Fig. 4.13 and Appendix 14.A; the frequency domain is inverted to the time domain as $0.7/\omega \rightarrow t$), the safe region in $G'(\omega)$ is basically equivalent to that in $G(t)$. Thus, in the analysis given below, we only need to discuss the difference between the $G'(\omega)$ and $G''(\omega)$ cases. For identifying the safe entropic region, obviously we have to examine the influence of the glassy-relaxation process in the frequency region where the two types of processes may overlap: $\omega\tau_0 < 1$ ($\omega^2\tau_0^2 \ll 1$) and $\{\omega\tau_i\}$ from $\gtrsim 1$ to $\gg 1$. In this region, as $\omega^2\tau_0^2 \ll 1$, we may express $G'(\omega)$ and $G''(\omega)$ as

$$G'(\omega) = A_0\omega^2\tau_0^2 + \sum_i S_i \frac{\omega^2\tau_i^2}{1 + \omega^2\tau_i^2} \quad (10.A.2)$$

and

$$G''(\omega) = A_0\omega\tau_0 + \sum_i S_i \frac{\omega\tau_i}{1 + \omega^2\tau_i^2}. \quad (10.A.3)$$

Clearly, the effect of the glassy relaxation attenuates much faster in $G'(\omega)$ ($\sim A_0\omega^2\tau_0^2$) than in $G''(\omega)$ ($\sim A_0\omega\tau_0$) with decreasing ω . As A_0 is very

large, even though $\omega\tau_0 < 1$, $A_0\omega\tau_0$ is still substantial. As a result, the frequency region which can already be designated as the safe entropic region in $G'(\omega)$ is still much under the influence of the glassy relaxation in $G''(\omega)$. It turns out that substantial contamination by the glassy relaxation in $G''(\omega)$ extends deeply into the region where relaxations of fast dynamic processes in the ERT or the Rouse theory have extensively occurred. By contrast, the influence of the glassy-relaxation process in $G'(\omega)$ is basically limited to the close neighborhood of the reciprocal(s) of its relaxation time(s). Thus from this analysis, we can draw a general conclusion: if only the entropic region of a polymer viscoelastic spectrum is included in the line-shape analysis in terms of a Rouse-segment-based molecular theory, the results of $G''(\omega)$ should not be considered because of its extensive contamination by the glassy relaxation. This is the reason why only the analyses of $G(t)$ and/or $G'(\omega)$ in terms of the ERT or the Rouse theory are shown in Chapters 10 and 11. In the original papers,^{7,8,18} the measured $G''(\omega)$ spectra have been compared with the calculated curves — calculated using the fitting parameters obtained from the analyses of the corresponding $G(t)$ curves or $G'(\omega)$ spectra — showing the large discrepancies arising due to the contamination effect.

In Chapter 14, two functional forms for the relaxation modulus $G(t)$ over its full dynamic range are given: one by incorporating a stretched exponential form for the glassy-relaxation process into the ERT (for entangled systems) and the other into the Rouse theory (for entanglement-free systems). The full range of creep compliance $J(t)$ curves or $G^*(\omega)$ spectra (both $G'(\omega)$ and $G''(\omega)$) of nearly monodisperse polystyrene samples covering both the energetic and entropic regions have been successfully analyzed in terms of either of the two $G(t)$ functional forms. In this scheme of analysis, either the ERT or the Rouse theory is deployed as the frame of reference. Having taken both the glassy-relaxation process and the ERT dynamic processes or the Rouse modes of motion into account, both the $G'(\omega)$ and $G''(\omega)$ spectra can be quantitatively analyzed over the modulus range from $\sim 10^{10}$ to $\sim 10^4$ dynes/cm². In other words, in this case $G''(\omega)$ can be included in the analysis as safely as $G'(\omega)$.

References

1. Ferry, D. J., *Viscoelastic Properties of Polymers* (3rd edn). Wiley, New York (1980).
2. Ferry, J. D., *Macromolecules* **16**, 5237 (1991).
3. Graessley, W. W., *Adv. Polym. Sci.* **16**, 1 (1974).

4. Doi, M., and Edwards, S. F., *The Theory of Polymer Dynamics*, Oxford Univ. Press (1986).
5. Schulz, G. V., *Z. Phys. Chem. Abt. B* **43**, 25 (1939).
6. Tung, L. H., in *Polymer Fractionation* (ed. M. Cantow), Academic Press, New York (1967).
7. Lin, Y.-H., *Macromolecules* **19**, 159 (1986).
8. Lin, Y.-H., *Macromolecules* **17**, 2846 (1984).
9. Wignall, G. D., Schelten, J., and Ballard, D. G. H., *J. Appl. Cryst.* **7**, 190 (1974).
10. Ballard, D. G. H., Rayner, M. G., and Schelten, J., *Polymer* **17**, 349 (1976).
11. Norisuye, T., and Fujita, H., *Polym. J.* (Tokyo) **14**, 143 (1982).
12. Inoue, T., Okamoto, H., and Osaki, K., *Macromolecules* **24**, 5670 (1991).
13. Inoue, T., and Osaki, K., *Macromolecules* **29**, 1595 (1996).
14. Lin, Y.-H., and Lai, C. S., *Macromolecules* **29**, 5200 (1996).
15. Lai, C. S., Juang, J.-H., and Lin, Y.-H., *J. Chem. Phys.* **110**, 9310 (1999); Lin, Y.-H., and Luo, Z.-H., *J. Chem. Phys.* **112**, 7219 (2000).
16. Fetters, L. J., Lohse, D. J., Richter, D., Witten, T. A., and Zirkel, A., *Macromolecules* **27**, 4639 (1994).
17. Graessley, W. W., *J. Polym. Sci., Polym. Phys. Ed.* **18**, 27 (1980).
18. Lin, Y.-H., *Macromolecules* **19**, 168 (1986).
19. Massa, D. J., Schrag, J. L., and Ferry, J. D., *Macromolecules* **4**, 210 (1971).
20. Noordermeer, J. W. M., Ferry, J. D., and Nemoto, N., *Macromolecules* **8**, 672 (1975).
21. Berry, G. C., and Fox, T. G., *Adv. Polym. Sci.* **5**, 261 (1968).
22. Fox, T. G., and Loshaek, S., *J. Polym. Sci.* **15**, 371 (1955).
23. Lin, Y.-H., *Macromolecules* **23**, 5292 (1990).
24. Allen, V. R., and Fox, T. G., *J. Chem. Phys.* **41**, 337 (1964).
25. Stratton, R. A., *J. Colloid Interface Sci.* **22**, 517 (1966).
26. Pearson, D. S., Ver Strate, G., von Meerwall, E., and Schilling, F. C., *Macromolecules* **20**, 1133 (1987); Pearson, D. S., Fetters, L. J., Graessley, W. W., Ver Strate, G., and von Meerwall, E., *Macromolecules* **27**, 711 (1994).
27. Lodge, T. P., Rotstein, N. A., and Prager, S., *Advances in Chemical Physics* **LXXIX** (ed. I. Prigogine and S. A. Rice), Wiley, New York (1990), and references therein.
28. Mills, P. J., Green, P. F., Palmstrom, C. J., Mayer, J. W., and Kramer, E. J., *Appl. Phys. Lett.* **45**, 957 (1984). The measurement temperature 170°C in this paper has been corrected to be 174°C in Ref. 27.
29. Green, P. F., Palmstrom, C. J., Mayer, J. W., and Kramer, E. J., *Macromolecules* **18**, 501 (1985).
30. Green P. F., and Kramer, E. J., *Macromolecules* **19**, 1108 (1986).
31. Lin, Y.-H., *Macromolecules* **18**, 2779 (1985). In this paper, the analysis of the comparison of the viscoelastic data with the diffusion data was made at 170°C, which should have been 174°C (see Refs. 28 and 30).
32. Bueche, F., *J. Chem. Phys.* **48**, 1410 (1968).
33. Plazek, D. J., and O'Rourke, V. M., *J. Polym. Sci., Polym. Phys. Ed.* **9**, 209 (1971).
34. Lin, Y.-H., *Macromolecules* **24**, 5346 (1991).
35. Plazek, D. J., *J. Phys. Chem.* **69**, 3480 (1965).

Chapter 11

ERT vs. Rouse Theory, Concentration Dependence and Onset of Entanglement, and Tube Dilation

11.1 Introduction

In general, one uses the simple solvent of small molecules to prepare a polymer solution. In such a system, there are two effects: hydrodynamic interaction¹⁻³ and excluded volume effect^{1,4,5} which can complicate the theoretical description or analysis of the entanglement effect on the polymer chain dynamic and viscoelastic behavior. To avoid these two effects, we can prepare for study a sample system which contains two components of the same kind of polymer: one with a molecular weight M_2 much greater than the entanglement molecular weight M_e (referred to as component two) and the other with a molecular weight M_1 smaller than M_e (referred to as component one). Because a component-one chain is too short to entangle with other chains, as far as the constraint effect of entanglement on the dynamics of component-two's chains is concerned, we can treat such a low-molecular-weight component as the solvent. Such a blend system is thus referred to as a blend *solution*. With dilution, the entanglement molecular weight and the associated entanglement distance increase.

In a blend solution, the interaction parameter χ of the Flory-Huggins theory is zero (the chain end effect is negligible) and independent of temperature. Otherwise, a temperature-dependent χ can lead to a thermorheologically complex behavior of the polymer solution system, which would disallow the application of the time-temperature superposition principle. A theoretical analysis^{5,6} indicates that if $M_1^2 \gg M_2$, the system is free of the excluded volume effect that will cause the component-two chain to expand; in other words, the chain coil remains Gaussian. Here, we consider polystyrene blend solutions with M_1 slightly smaller than M_e ($= 13,500$ for polystyrene). In such a system, the condition $M_1^2 \gg M_2$ can be easily satisfied. Furthermore, the solvent, being chains of more than ten Rouse

segments (the molecular weight for a Rouse segment is about 850^{7-9}), serves as a viscoelastic medium to component-two's chains rather than a viscous one. At the same time, the identical segments of both components with the same average surroundings have the same mobility (or friction constant). Thus, the hydrodynamic interaction is not expected to occur in the blend solution. Without both effects, the basic short-range (shorter than the entanglement strand) Rouse dynamic behavior of both components in the blend solution is expected to be the same as that in the pure melt containing a single component.

The Doi–Edwards theory was built on the primitive chain concept which is defined by Eq. (8.3). Its relation with the key physical quantities can be summarized in the following equations:

$$aL = R^2 = Na^2 = N_o b^2 = \frac{M}{M_e} a^2 \quad (11.1)$$

$$M_e = \frac{4}{5} \frac{\rho RT}{G_N} \quad (11.2)$$

and

$$a^2 = K_\infty M_e \quad (11.3)$$

where K_∞ is given by Eq. (10.7). In other words, the tube diameter or the entanglement distance, a , is related to the entanglement molecular weight M_e determined from the plateau modulus G_N . The increase of the entanglement molecular weight with dilution will be reflected by the concentration dependence of the plateau modulus. By simple argument, the entanglement molecular weight of the blend solution M'_e is given by

$$M'_e = \frac{M_e}{W_2} \quad (11.4)$$

where W_2 is the weight fraction of component two.

Equations (9.14), (9.15), (9.20), (9.21), and (9.23) indicate that the relaxation strengths B and C , as well as the normalized relaxation times τ_C/τ_A^1 , τ_B/τ_A^1 , and τ_X/τ_A^1 , are functions of the normalized molecular weight M/M_e . Thus, the *line shape* of the relaxation modulus $G(t)$ changes with concentration. As shown below, the viscoelastic behavior of the entangled component in the concentrated blend solution is well described by Eq. (9.19) with the entanglement molecular weight M_e replaced by M'_e , which is given by Eq. (11.4).¹⁰ This means that $G(t)$ is universal among monodisperse melt systems and blend solution systems, as all the $G(t)$ curves are described by

a general form (Eq. (9.19)) expressed in terms of the normalized molecular weight M_2/M'_e (M_2/M'_e includes the special case of M/M_e when $W_2 = 1$; the experimental proof of the universality in the case of $W_2 = 1$ was shown in Chapter 10).

In the blend solution system, the viscoelastic behavior of the solvent component (component one) is described by the Rouse theory, regardless of the concentration. It will be shown below that the viscoelastic behaviors of both components are described by the Rouse theory as the whole system is free of entanglement when component-two's molecular weight is smaller than the entanglement molecular weight M'_e (i.e. $M_2 < M'_e$ for small W_2). By monitoring the deviation of component-two's viscoelastic response from the Rouse theory as W_2 increases, the onset point of entanglement can be determined and is found to be in close agreement with Eq. (11.4).

When the molecular weights of both components in a blend are greater than the entanglement molecular weight M_e , a new idea, tube dilation — a dynamic aspect of the tube associated with the high-molecular-weight component, needs to be introduced.

11.2 Entanglement Region

(a) Theory

The entanglement molecular weight for component two in a blend solution, M'_e , increases as component-one's weight fraction W_1 increases. We can imagine preparing a blend solution in the following way: Start with the pure component-two polymer (i.e. $W_2 = 1$) which forms entanglements extensively because $M_2 \gg M_e$. We cut half of the chains to sections of equal length slightly shorter than M_e to serve as solvent molecules, while keeping the other half of the chains intact. In a solution prepared this way, each point along an uncut (long) chain now has a one-half chance of encountering a short chain (solvent chain) and a one-half chance of encountering a long chain. It takes a chain section of M_e length on a long chain in the original pure melt to form one entanglement with another chain; now in the blend solution, based on probability, it will take a section of $2M_e$ length on the long chain to form one entanglement with another long chain. Thus the entanglement molecular weight in the blend solution, M'_e , should change with weight fraction W_2 according to Eq. (11.4).

Therefore, for a blend solution where the viscoelastic behavior of component one is described by the Rouse theory (Eq. (7.58)) and that of

component two by the ERT (Eq. (9.19)); the theoretical form of the total relaxation modulus $G(t)$ is given by

$$\begin{aligned}
 G(t) = & W_1 \int A_1(M) G_R(t, M) dM \\
 & + W_2 \frac{4\rho RT}{5M'_e} [1 + \mu_A(t)] \\
 & \times \int A_2(M) \left[1 + \frac{1}{4} \exp(-t/\tau_X) \right] \left[B\mu_B(t/\tau_B) + C\mu_C(t/\tau_C) \right] dM
 \end{aligned} \tag{11.5}$$

In Eq. (11.5), $A_1(M)$ and $A_2(M)$ are the nearly monodisperse molecular weight distributions of components one and two, respectively; $G_R(t)$ is the relaxation modulus of the Rouse theory, given by Eqs. (7.57) and (7.58); and $\mu_A(t)$, $\mu_B(t)$, $\mu_C(t)$, B , C , τ_A^p , τ_X , τ_B and τ_C have the same functional forms as given in Chapter 9 (Eqs. (9.B.25), (9.5), (9.11), (9.14), (9.15), (9.B.26), (9.22), (9.6) and (9.12), respectively) but with all the M_e quantities appearing in the equations replaced by M'_e (Eq. (11.4)). When $W_1 = 0$, the second term of Eq. (11.5) becomes identical to Eq. (9.19), which can be regarded as a special case of Eq. (11.5).

(b) Comparison of theory and experiment

The linear relaxation moduli and viscoelastic spectra have been studied for a series of concentrated polystyrene blend solutions consisting of two nearly monodisperse components: F1 ($M_w = 1.03 \times 10^4$) as component one and X ($X = P7: M_w = 6.8 \times 10^4$; F10: $M_w = 1.00 \times 10^5$; F35: $M_w = 3.55 \times 10^5$; F80: $M_w = 7.75 \times 10^5$) as component two.¹⁰ The blend solutions were prepared at the weight-fraction ratios of P7/F1 = 50/50 and 75/25; F10/F1 = 50/50 and 75/25; F35/F1 = 50/50; and F80/F1 = 50/50. In these systems, the component-one polymer with a molecular weight slightly below the entanglement molecular weight M_e is free of entanglement yet long enough to be described by the Rouse theory while component-two polymers, which all have a weight-average molecular weight M_{w2} greater than M'_e , are well entangled. The viscoelastic-spectrum line shapes of these blend solutions have been analyzed in terms of Eq. (11.5) as shown below.

For convenience of discussion, the friction factor in the $G_R(t)$ process is denoted by K'' (Eq. (7.57)), in the $\mu_A(t)$ process by K' (Eq. (9.B.26)), and in τ_X (Eq. (9.22)), τ_B (Eq. (9.6)), and τ_C (Eq. (9.12)) by K . In a *homogeneous* blend, all components are in the same average environment.

Thus, the first and second terms of Eq. (11.5) are expected to have the same frictional factor, i.e. $K'' = K$. If the second term of Eq. (11.5) behaves the same in the concentrated blend solution as in the pure-melt system (i.e. when $W_1 = 0$ in Eq. (11.5)), whose study was described in the last chapter, the same molecular-weight dependence of K'/K (Fig. 10.5) should be followed with the molecular weight expressed in terms of the normalized molecular weight: M_w/M_e for the melt and M_{w2}/M'_e for the blend solution. Indeed, as shown in Fig. 11.1, the molecular-weight dependences of the melt and blend-solution systems have been observed to be the same.¹⁰ The dependence of K'/K on M/M_e (or M_2/M'_e) can be described by the empirical equation:

$$\frac{K'}{K} = \frac{2.525}{\exp[-0.643[(M/M_e) - 4.567]] + 1} + 0.769. \quad (11.6)$$

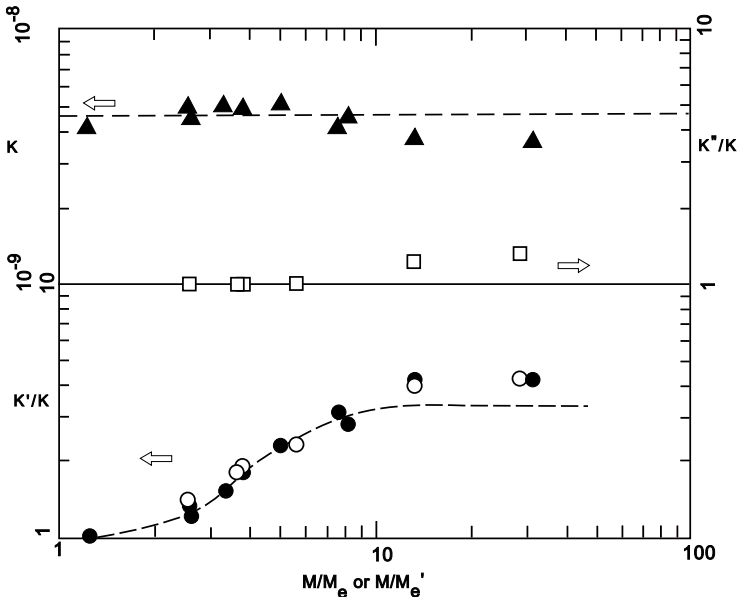


Fig. 11.1 K (▲) for the nearly monodisperse (polystyrene) melts (from Ref. 11b; same as shown in Fig. 10.5), K''/K (□) for the X/F1 blend solutions (from Ref. 10), and K'/K : (●) for the nearly monodisperse melts (from Ref. 11b; same as shown in Fig. 10.5) and (○) for the X/F1 blend solutions (from Ref. 10) as a function of the normalized molecular weight: M_w/M_e for the melt and M_w/M'_e for the blend solution.

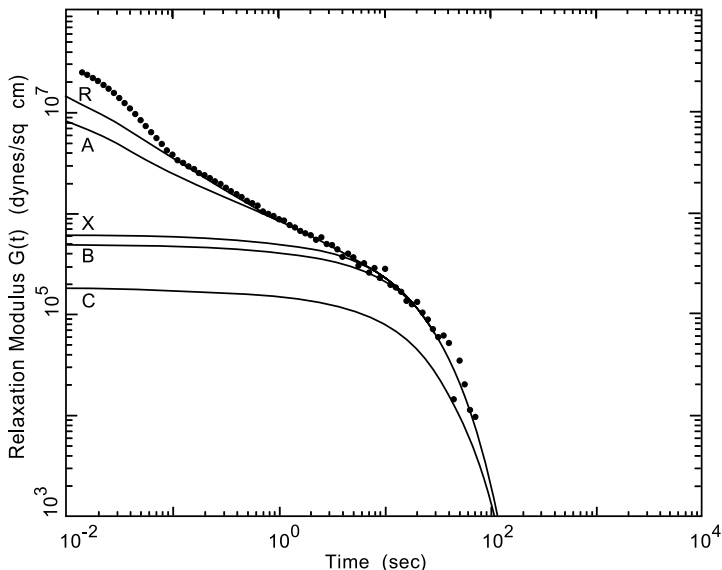


Fig. 11.2 Comparison of the measured (dots) and the calculated (line) relaxation modulus, $G(t)$, for the P7/F1 = 50/50 sample. Also shown are the separate contributions of the free-Rouse-chain process of F1 (the portion between lines R and A; line A is calculated by setting $W_1 = 0$), and the $\mu_A(t)$, $\mu_X(t)$, $\mu_B(t)$, and $\mu_C(t)$ processes of P7 (see Fig. 10.1 for the calculation of lines A, X, B and C). The calculation is made with $K = 10^{-8}$, $K'/K = 1.4$, and $K''/K = 1$.

Four representative relaxation moduli or viscoelastic spectra are shown in Figs. 11.2–11.5, indicating the typical consistent and quantitative agreement between theory and experiment. As noted for the melt system in Chapter 10, aside from the effects associated with the compliance of the transducer and the step deformation rise time in the relaxation-modulus case, the difference between the measured and the calculated in the short-time or high-frequency region is due to the glassy-relaxation process. All of the shown calculated spectra are obtained with $M'_e = 27,000$ (as given by Eq. (11.4) for $W_1/W_2 = 50/50$) and by setting the number of Rouse segments per entanglement strand to $N'_e = 20$, and the number of Rouse segments per free Rouse chain of F1 to $N_R = 8$ (corresponding to $M_w = 10,300$). It has been shown that these spectra are identical to those calculated by setting $N'_e = 40$ and $N_R = 16$ over the whole region where the measured and the calculated closely agree with each other (see Figs. 1 and 2 of Ref. 10). In other words, the N'_e and N_R values used in the calculation are sufficiently large (also see Chapter 10).

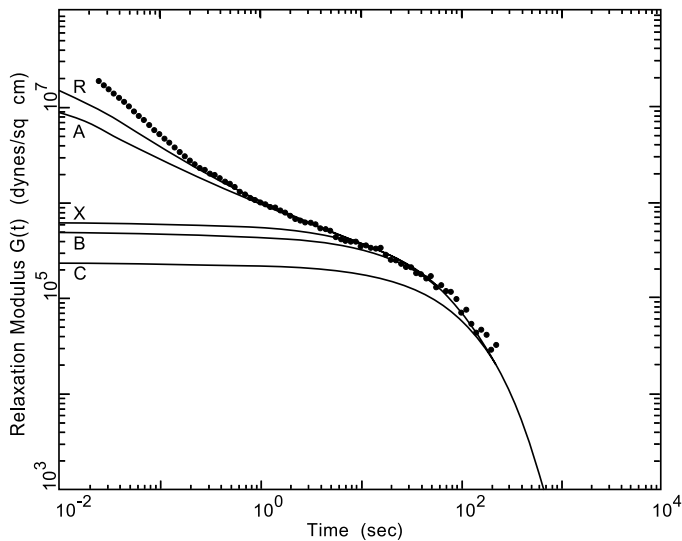


Fig. 11.3 Same as Fig. 11.2 for the F10/F1 = 50/50 sample. The calculation is made with $K'/K = 1.8$ and $K''/K = 1$.

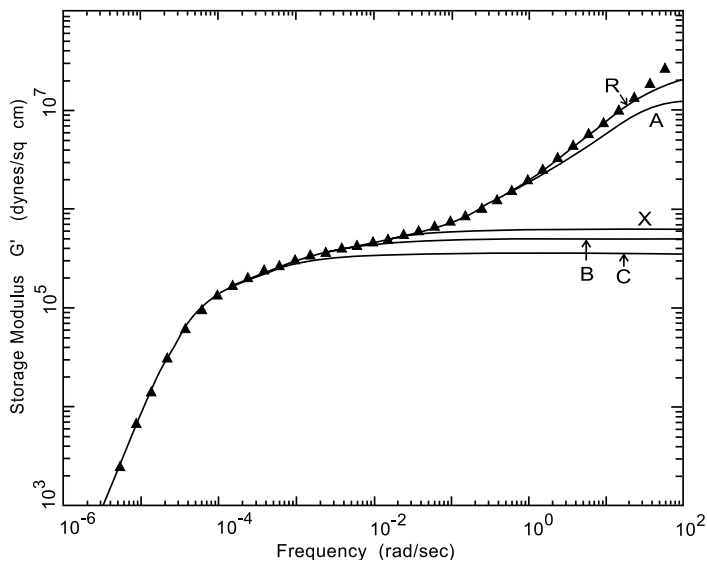


Fig. 11.4 Same as Fig. 11.2 for the storage-modulus spectrum, $G'(\omega)$, of the F35/F1 = 50/50 sample. The calculation is made with $K'/K = 4.1$ and $K''/K = 1.2$.

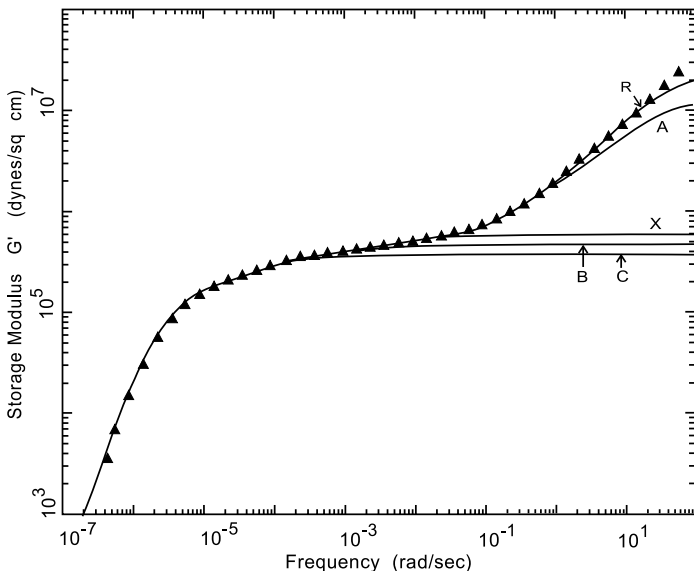


Fig. 11.5 Same as Fig. 11.2 for the storage-modulus spectrum, $G'(\omega)$, of the F80/F1 = 50/50 sample. The calculation is made with $K'/K = 4.2$ and $K''/K = 1.3$.

Furthermore, in the line-shape analyses of these viscoelastic spectra, the molecular-weight distributions of P7, F10, F35, and F80 included in the calculations are identical, respectively, to those extracted from the line-shape analyses of the spectra of the pure melt systems,¹¹ some of which have been shown in Chapter 10. Thus, the close agreements between theory and experiment in the line-shape analyses have been achieved under the consistency of maintaining the same molecular-weight distributions of the samples between the pure-melt and blend-solution systems. Thus, in a quantitative way, the universality of viscoelastic spectrum is shown extending over the melt and blend-solution systems in accordance with Eq. (11.5) with the molecular weight normalized with respect to M_e for the melt and M'_e for the blend solution.

This universality has also been illustrated by Watanabe *et al.* in another way.¹² They compared the line shapes of the viscoelastic spectra of a nearly monodisperse polystyrene melt (sample L161 with $M_w = 1.72 \times 10^5$ and $M_w/M_n = 1.07$) and a blend solution (consisting of two nearly monodisperse polystyrene polymers: L407 with $M_w = 4.27 \times 10^5$ and $M_w/M_n = 1.05$ as component two and sample L10 with $M_w = 1.05 \times 10^4$ and $M_w/M_n = 1.08$ as component one; the weight-fraction ratio of the blend is

L407/L10 = 40/60) whose normalized molecular weights, $M_w/M_e = 12.74$ for the melt and $M_{w,L407}/M'_e = 12.65$ for the blend solution, are nearly identical. Corresponding to the same normalized molecular weight, the viscoelastic-spectrum line shapes of the two systems agree with each other very well as shown in Fig. 11.6 (Fig. 7 of Ref. 12). L10 with a molecular weight $M_w < M_e$ serves as a solvent in the blend solution and only contributes to the very high frequency region, which is outside the region of line-shape comparison shown in Fig. 11.6. Although the line-shape comparison of Fig. 11.6 is illustrative in showing the universality of the viscoelastic spectrum, it may be affected somewhat by a possible small difference between the molecular-weight distributions of the two systems.

The transformation of the viscoelastic spectrum with changing concentration is well explained in terms of Eq. (11.5) with M'_e given by Eq. (11.4).

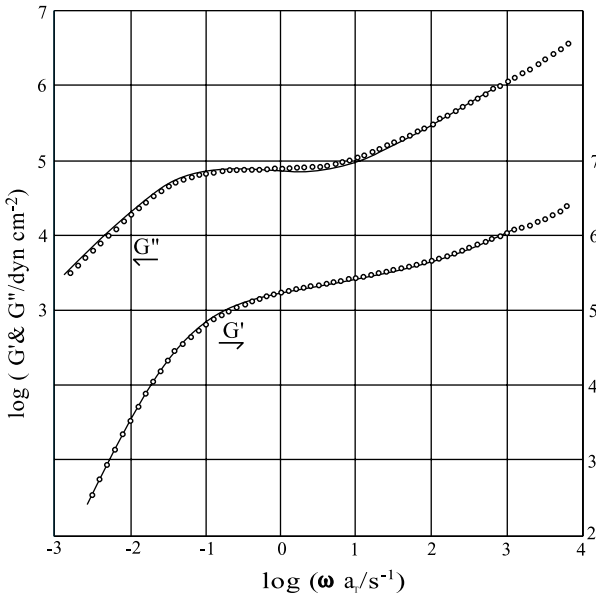


Fig. 11.6 Comparison of the shapes of the storage- and loss-modulus spectra of the polystyrene sample L161 in melt (—) and of the blend solution L407/L10 = 40/60 (o o o), both having nearly the same normalized molecular weight: $M_w/M_e = 12.74$ for the former; and $M_{w,L407}/M'_e = 12.65$ for the latter. For the line-shape comparison, the spectra of the L161 sample are shifted downward along the modulus axis by a factor of $W_2^2 = (0.4)^2$ by Watanabe *et al.*¹² in accordance with Eq. (11.7). Reproduced, by permission, from Ref. 12.

It is illuminative to point out two characteristics in the transformation. One is the decrease in the plateau modulus (denoted by G'_N for the blend solution) with dilution. From Eqs. (11.4) and (11.5), one obtains the concentration dependence of G'_N as

$$G'_N = G_N W_2^2. \quad (11.7)$$

The agreement between the experimental results and Eq. (11.7) is within 5% for the studied blend-solution samples.¹⁰ The second point is the diminishing of the modulus-plateau zone with decreasing W_2 . The increase in entanglement molecular weight M'_e with decreasing W_2 affects the line shape of the viscoelastic spectrum through the relaxation strengths B and C (Eqs. (9.14) and (9.15)) and the relaxation-time ratios τ_C/τ_A^1 , τ_B/τ_A^1 , τ_X/τ_A^1 (Eqs. (9.20), (9.21), (9.23)). As W_2 decreases, the relaxation-time ratios decrease and bring all the relaxation processes closer in time; particularly, the separation between the transition zone (II) and the terminal zone is narrowed by the decrease in the ratio τ_C/τ_A^1 . While the decrease in W_2 reduces the width of the modulus plateau, B increases and C decreases, both changes enhancing the importance of the $\mu_B(t)$ process. These changes reduce the flatness of the modulus plateau. As shown in Fig. 11.7, the comparison of the viscoelastic spectra of pure F10, F10/F1 = 75/25, and F10/F1 = 50/50, all quantitatively described by Eq. (11.5) (including Eq. (9.19) for pure F10), clearly illustrates the effects of dilution on the spectrum line shape.

A very important result of the line-shape analysis of the viscoelastic spectra in terms of Eq. (11.5) for the concentrated blend solutions is that the obtained K'' and K values are, as expected, the same (Fig. 11.1). The sensitivity of the determination of the K''/K ratio is rather high. As shown in Fig. 3 of Ref. 10, a 50% change in the K''/K ratio value can cause a clearly noticeable difference between the measured and calculated spectra; the possible error of the shown K''/K ratio values in Fig. 11.1 should be no more than about 20%. The close agreement between K'' and K means that the ERT, developed on the framework of the Doi–Edwards theory (Chapter 9), has bridged the gap between the Doi–Edwards theory and the Rouse theory. One may think that the linkage is quite miraculous because the tube (or the primitive chain defined by Eq. (8.3)) introduced in the Doi–Edwards theory is an *assumed* mean field which is structurally one level larger than the mean field assumed in the Rouse theory (i.e. the Rouse segment and its associated friction constant). The linkage not only supports the validity of the primitive-chain idea, but also

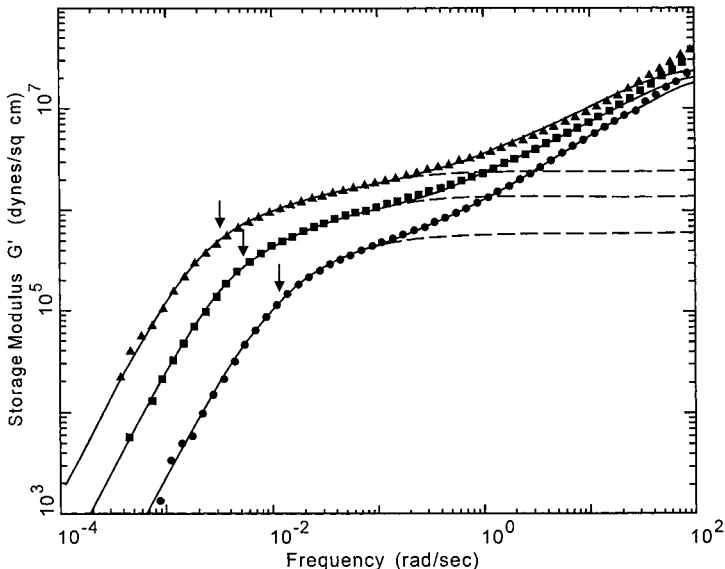


Fig. 11.7 Comparison of the storage-modulus spectra (both the calculated (lines) and the measured) of the F10 (\blacktriangle), F10/F1 = 75/25 (\blacksquare) and F10/F1 = 50/50 (\bullet) samples. The arrows indicate the frequencies $\omega_C = 1/\tau_C$ where the τ_C values are calculated from Eq. (9.12) with $K = 1 \times 10^{-8}$ and M_e replaced by $M'_e = M_e \times W_2^{-1}$. The dashed lines indicate the separations of the contributions of the free-Rouse-chain process of F1 and the $\mu_A(t)$ process from those of the $\mu_X(t)$, $\mu_B(t)$ and $\mu_C(t)$ processes; in other words, the high frequency limits of the dashed lines occur at $(5/4)G_N W_2^2$ (see Eq. (11.5)).

supports that the Doi-Edwards theory has provided the right theoretical framework in which the additional dynamic processes can be properly incorporated.

In this section, we have shown the results of the quantitative analyses of the viscoelastic spectra in the concentrated region where chain entanglements are extensive. These results, as well as those described in Chapter 10 for the melt system, give the molecular-weight dependence of K'/K shown in Fig. 11.1, suggesting that entanglements start at the molecular weight M_e for the melt system and M'_e for the blend solution. It is important to observe directly whether this is indeed so. To show the onset of entanglement, we shall first study the low-concentration region of the blend-solution system and the low-molecular-weight region of the one-component melt system where the whole system is expected to be free of entanglement.

11.3 Entanglement-Free Region and Onset of Entanglement

As discussed above, the entanglement molecular weight M'_e in a concentrated blend solution is given by Eq. (11.4). If the concentration W_2 is smaller than the critical concentration W_c , defined by

$$W_c = \frac{M_e}{M_{w2}} \quad (11.8)$$

then $M_{w2} < M'_e$ and the solution should be free of entanglement for both the low- and high-molecular-weight components.¹³ The relaxation modulus of such an entanglement-free blend solution may be described by a linear combination of two Rouse relaxation processes corresponding to the two components.

$$G(t) = W_1 \int A_1(M) G_R(t, M) dM + W_2 \int A_2(M) G_R(t, M) dM \quad (11.9)$$

where $G_R(t, M)$ is the relaxation modulus given by Eqs. (7.57) and (7.58) and $A_1(M)$ and $A_2(M)$ are the nearly monodisperse molecular-weight distributions of component one and component two, respectively.

A series of polymer blend solutions, denoted by samples A, B, C and D, were prepared by blending two nearly monodisperse polystyrene polymers: G10 (component two with $M_w = 1.03 \times 10^5$ and $M_w/M_n = 1.01$) and G1 (component one with $M_w = 9.1 \times 10^3$ and $M_w/M_n = 1.02$) at the weight-fraction ratios $W_1/W_2 = 95/5, 80/20, 70/30$ and $60/40$, respectively.¹³ Shown in Fig. 11.8 are the molecular-weight distributions for the G1/G10 blend solutions calculated using the Schulz function (Eqs. (10.3) and (10.4)) with $Z = 50$ for G1 and $Z = 90$ for G10. $Z = 50$ and $Z = 90$ for the two separate components were chosen to give the M_w/M_n values in agreement with the values obtained from the sample characterizations of G1 and G10, respectively. The entanglement molecular weights M_e ($= 13,500$ for polystyrene) and M'_e (Eq. (11.4)) for all the blend-solution samples are indicated in Fig. 11.8. Figure 11.8(a) shows that both components in sample A are free of entanglement. Figures 11.8(b)–(d) indicate that while the G1 component remains free of entanglement, the degree of entanglement among G10's chains (namely, M_{w2}/M'_e) increases with the increase in W_2 from sample B to sample D.

As shown in Fig. 11.9, the storage-modulus spectrum of sample A is well described by the Rouse theory: Eq. (11.9) with the molecular weight distribution ($W_1 A_1(M)$ and $W_2 A_2(M)$) shown in Fig. 11.8(a). In the calculation

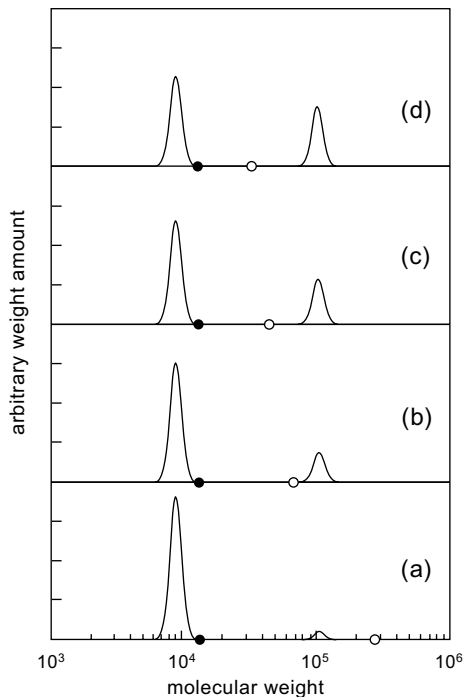


Fig. 11.8 The molecular-weight distribution calculated using the Schulz function (Eqs. (10.3) and (10.4) with $Z = 50$ for $G1$ and $Z = 90$ for $G10$) for the $G1/G10 = 95/5$ (a), $80/20$ (b), $70/30$ (c), and $60/40$ (d) blend solution samples. M_e and M'_e for each blend solution are indicated by \bullet and \circ points, respectively.

of the spectrum, the number of Rouse segments per chain N is taken as the integer of the ratio M/m where m , set to be 850 for polystyrene,^{7–9,13} is the molecular weight for a Rouse segment. Due to the weak molecular-weight dependence of the relaxation times, and of the relaxation-time distribution in the Rouse model, the calculated spectrum is very insensitive to the molecular-weight distribution of either of the two nearly monodisperse components as long as it is sufficiently narrow. For instance, as long as $Z \geq 50$, virtually no change in the spectrum can be discerned as the Z value varies. This insensitivity removes any concern that some difference in the calculated spectrum might be caused by a small uncertainty in the molecular-weight distribution.

No shift along the modulus axis is involved in obtaining the very close superposition of the measured and calculated spectra as shown in Fig. 11.9. This indicates that the force constant on the Rouse segment, which gives

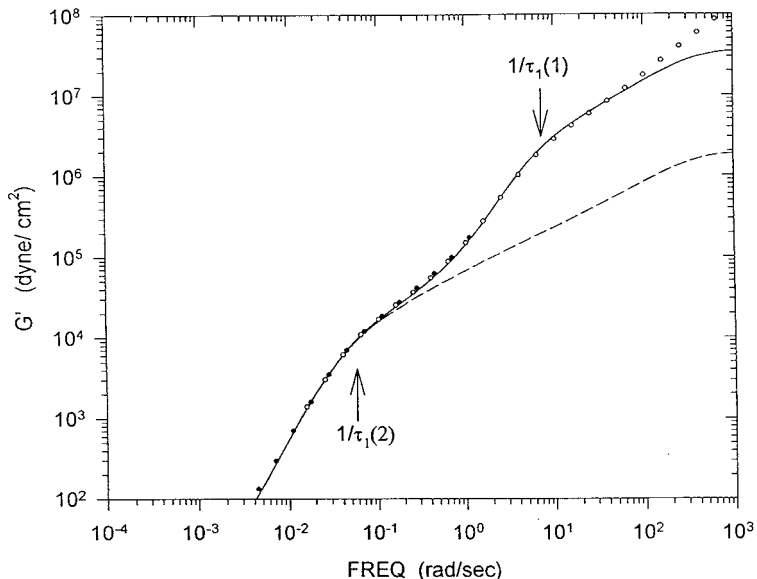


Fig. 11.9 Comparison of the measured storage-modulus spectrum (\circ and \bullet) and that calculated from the Rouse theory (solid line) for sample A. The dashed line indicates the separation of the contributions from the G1 and G10 components. The arrow at $1/\tau_1(1)$ indicates the frequency that is the reciprocal of the relaxation time of the first Rouse mode of the G1 component calculated from Eq. (7.57) with $K = 1 \times 10^{-8}$, whereas the arrow at $1/\tau_1(2)$ indicates the same for the G10 component.

rise to the modulus, is of entropic origin as it is defined statistically. In Fig. 11.9, the dashed line (calculated by setting $W_1 = 0$) indicates the separation of the contributions from the G10 and G1 components. It is clear that the two “bumps” on the storage-modulus spectrum correspond to the main viscoelastic responses of the two components in the blend solution: the high-frequency one for the G1 component and the low-frequency one for the G10 component. The accurate prediction by the theory of the relative positions of the two bumps and their shapes clearly illustrates that, in the entanglement-free region, the molecular-weight dependence (i.e. $\tau_1 \propto M^2$) and the p dependence (i.e. $\tau_p \propto 1/\sin^2(p\pi/2N)$) of the viscoelastic relaxation times in the blend solution are well described by the Rouse theory.

Entanglements among component-two’s chains will eventually occur as W_2 increases above a certain point. As they occur, the constraint effect due to entanglement will render the spectrum in the low-frequency region where the main viscoelastic response of component two occurs no longer described by the Rouse theory. Assuming that entanglements never did occur to

component two, the hypothetical viscoelastic spectra for samples B, C, and D can be calculated from Eq. (11.9). Since component-one's chains remain free of entanglement regardless of the concentration, the region around the high-frequency bump in each of the measured spectra remain well described by the Rouse theory. Thus, the Rouse viscoelastic response of component one can be used as the internal reference by matching the measured and calculated spectra over the high-frequency bump region. In doing the superposition, only shifting along the frequency axis is allowed. Then, with the internal reference set this way, the deviation of the measured spectra of samples B, C and D from Eq. (11.9) in the low-frequency region will reflect the influence of entanglement on component-two's viscoelastic behavior. As expected, the deviation becomes larger with increasing W_2 . As shown in Fig. 11.10, in each case the measured storage-modulus spectrum and the

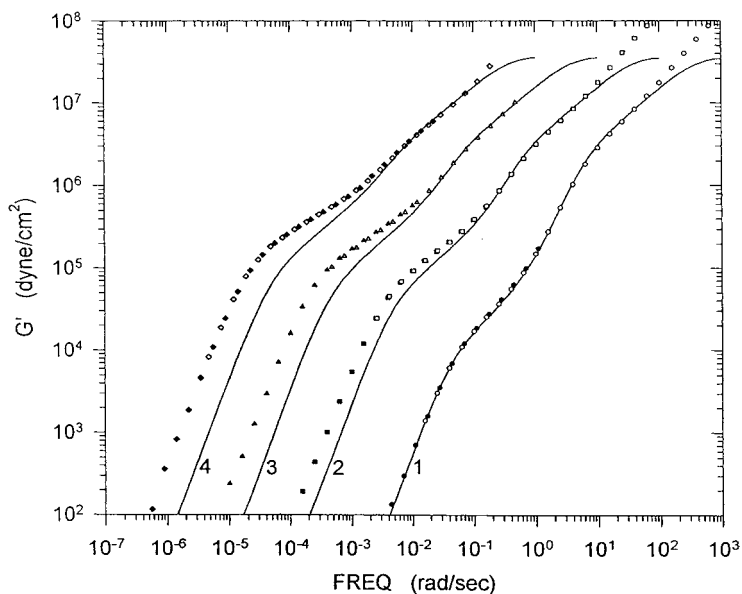


Fig. 11.10 Comparison of the measured storage-modulus spectra of samples A (\circ and \bullet), B (\square and \blacksquare), C (\triangle and \blacktriangle), and D (\diamond and \blacklozenge) with those calculated (solid lines) using the Rouse theory for both the G1 and G10 components. In calculating the spectra, the frictional factor K is set to be 10^{-8} for sample A (line 1); 10^{-7} for sample B (line 2); 10^{-6} for sample C (line 3); and 10^{-5} for sample D (line 4) to avoid overlapping of the lines and the data points. The comparison is made for each sample by shifting the measured spectrum along the frequency axis to match the calculated in the high-frequency bump region.

calculated are parallel with each other in the low-frequency region (both the calculated and measured lines of $\log(G')$ versus $\log(\omega)$ are straight and have the expected slope of 2; see Chapter 4). The measured line is more remote toward the lower-frequency side from the calculated as W_2 increases. The shift factor obtained from superposing the two parallel lines by moving only along the frequency axis can be used to characterize the degree of deviation. Because of the use of the internal reference, the frequency-shift factor determined this way for component two is free of any change of the frictional factor due to any outside influence, such as a change in temperature or concentration; in other words, it reflects entirely the change in the structural factor of relaxation-time (mainly of the slowest mode) which is caused by the occurrence of entanglements. In Fig. 11.11, the frequency-shift factors at different concentrations W_2 are shown. By extrapolating the shift factors towards the smaller W_2 region, the point where the extrapolation line crosses the no-shift line can be determined. This point, denoted by W_c^o , can be regarded as the highest concentration where a change in the structural factor of relaxation-time due to entanglement has not yet occurred, or as the onset point of entanglement. W_c^o occurs in the close neighborhood of W_c calculated according to Eq. (11.8). This means that,

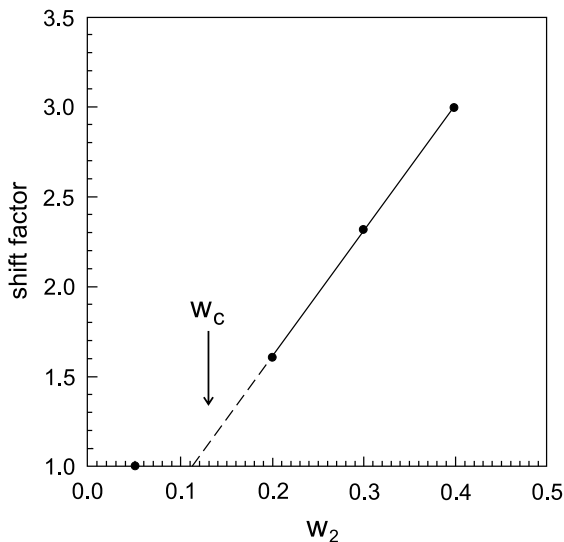


Fig. 11.11 Frequency-shift factor as caused by the entanglement effect versus the weight fraction of component two, W_2 . The arrow indicates the predicted W_c value from Eq. (11.8).

if M_{w2} is the variable, and W_2 is kept at a fixed value in the blend solution, entanglements start to occur within the experimental error at M'_e given by Eq. (11.4).

Equation (11.9) includes the special case of pure melt containing only one nearly monodisperse component (i.e. by setting either W_1 or $W_2 = 1$) whose molecular weight M_w is smaller than M_e . Shown in Fig. 11.12 is the comparison of the storage-modulus spectrum of a nearly monodisperse polystyrene polymer F1 whose molecular weight is $0.76M_e$ ($M_w = 1.03 \times 10^4$; $M_w/M_n = 1.01$), with that calculated from Eq. (11.9) using the Schulz molecular-weight distribution with $Z = 90$.¹⁴ As long as Z is above 50, no change in the calculated spectrum can be discerned with a change in Z . Except for the very-high-frequency region where the glassy-relaxation process has a significant contribution to the measured spectrum, the measured and calculated spectra are in close agreement over the whole range of modulus (i.e. below $\sim 5 \times 10^6$ dynes/sq cm; the small molecular weight of the F1 sample makes the higher-modulus (or -frequency) region particularly susceptible to the contribution of the glassy-relaxation process). On the other hand, it is very clear from Fig. 11.13¹⁴ that such

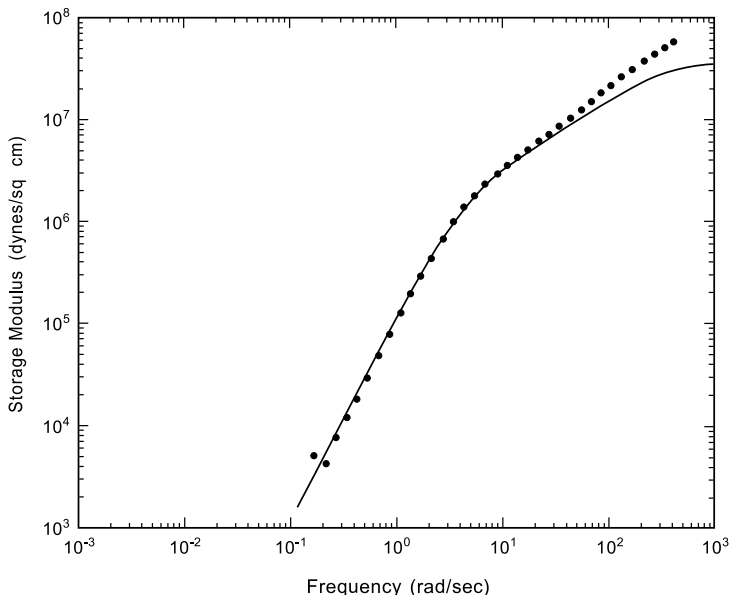


Fig. 11.12 Comparison of the measured (dots) storage-modulus spectrum and the calculated (line) from the Rouse theory for sample F1.

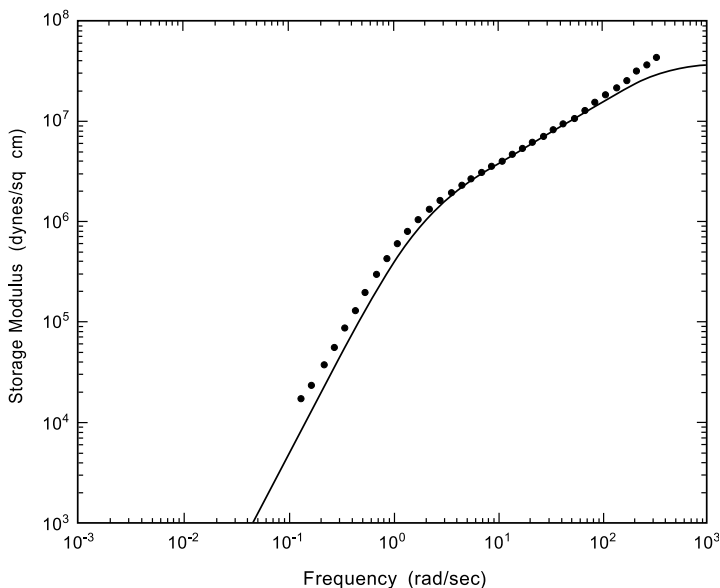


Fig. 11.13 Comparison of the measured (dots) storage-modulus spectrum and the calculated (line) from the Rouse theory for sample F2.

a close agreement between the measured spectrum and the Rouse theory (calculated with $Z = 50$) cannot be obtained for a nearly monodisperse polystyrene melt F2 whose molecular weight is $1.24M_e$ ($M_w = 1.67 \times 10^4$; $M_w/M_n = 1.02$). Similar to the results shown in Fig. 11.10, Fig. 11.13 shows that the measured spectrum in the low-frequency region deviates toward the lower-frequency side from the calculated while both spectra match in the high-frequency region. This slow-down phenomenon, occurring mainly to the slowest Rouse mode of motion, is a sign of entanglement. In fact, as shown in Figs. 10.4 and 10.8, the spectrum of F2 can be well described by Eq. (9.19), which contains the constraint effect of chain entanglement (the $\mu_C(t)$ process). From the results shown in Figs. 11.12 and 11.13, the initial deviation from the Rouse theory, signifying the onset of entanglement, should occur at a molecular weight between those of F1 and F2, namely, between 10,300 and 16,700. In other words, the onset of entanglement should occur at a point very close to the entanglement molecular weight M_e ($= 13,500$ for polystyrene) for the one-component melt. This result is in agreement with the finding that the onset of entanglement occurs in the close neighborhood of M_e' for the blend solution.

Denote the molecular weight at the onset of entanglement as M_e^o for the pure-melt system and as $M_e^{o'}$ for the blend-solution system. From the close agreement between the onset molecular weight of entanglement and the entanglement molecular weight for both the pure-melt system and the blend-solution system, M_e and M_e^o as well as M_e' and $M_e^{o'}$ can be regarded as equivalent. Considering the independence of the Rouse theory and the Doi–Edwards theory, the equivalence of M_e and M_e^o (M_e' and $M_e^{o'}$) is indeed very significant as the determination of M_e (M_e') is ultimately based on the slip-link idea in the Doi–Edwards theory (Eqs. (8.2) and (11.4)) while M_e^o ($M_e^{o'}$) is determined by monitoring the deviation of the measured spectrum at a molecular weight in the neighborhood of M_e (or M_e') from the Rouse theory. In other words, the agreement between M_e and M_e^o (M_e' and $M_e^{o'}$) puts the Rouse theory and the Doi–Edwards theory on the same footing. On the basis of this agreement, one would suggest that the basic assumptions in the Doi–Edwards theory, the primitive chain (Eq. (8.3)) and the slip-link picture, be considered as much of a “first principle” as the Rouse theory is in polymer dynamics and viscoelasticity. This suggestion is strongly enforced by the agreement between the frictional factors K and K'' (Fig. 11.1), indicating that the ERT bridges the gap between the Rouse theory and the Doi–Edwards theory, a conclusion discussed earlier in this chapter.

The onset of entanglement occurring at M_e rather than at M_c is consistent with the viscosity value in the molecular-weight region between M_e and M_c being higher by a factor of about three (after the T_g correction) than that predicted on the basis of the Rouse theory,¹⁵ as discussed in detail in Chapter 10. Another linkage between the Rouse theory and the Doi–Edwards theory was made in Chapter 10 by the agreement between the diffusion-proportional constant K_d (Eqs. (10.5) and (10.6)) obtained from the diffusion measurements and the value calculated from the frictional factor K obtained from the viscosity value at M_c in terms of the Rouse theory and corrected for the factor three mentioned above.

The direct observation of the onset molecular weight of entanglement at M_e (M_e') breaks the traditional belief that chain entanglements start to occur at M_c .^{16–18} The traditional idea was based on the observation that the zero-shear viscosity (after the T_g correction) below the critical point M_c has an apparent molecular-weight dependence as that given by the Rouse theory ($\propto M$). This misconception was mainly caused by the failure to notice that the integration of the relaxation modulus (Eq. (4.30))

for obtaining the viscosity can even out vital entanglement-related details in the relaxation modulus or equivalently in the viscoelastic spectrum.

11.4 Tube Dilation

As the molecular weight of the solvent component (component one) in the blend solution is raised above the entanglement molecular weight M_e , the viscoelastic behavior of the blend system (the system with $M_{w2} > M_{w1} > M_e$ is referred to as the binary blend) becomes much more complicated. Because component one is affected by chain entanglement in the binary blend, its viscoelastic behavior cannot be described by the Rouse theory, and it can no longer be treated simply as a solvent. However, if M_{w1} , while being greater than M_e , is sufficiently smaller than M_{w2} , component one can possess some solvent characteristics as far as the constraint effect of entanglement on the dynamics of component two is concerned. As a result, the *effective* entanglement molecular weight (denoted as M_e'') for the terminal relaxation of component two, which becomes faster than that of the pure component-two melt, is neither M_e nor M_e' (as given by Eq. (11.4)), but between. Such a phenomenon of M_e'' being larger than M_e is referred to as tube dilation. This phenomenon is clearly observed by monitoring the shift in time or frequency in superposing the viscoelastic spectra of a binary blend and its pure component-two melt in the terminal region, both spectra being measured at the same temperature.¹⁹

Two nearly monodisperse polystyrene polymers: F80 ($M_w = 7.75 \times 10^5$) and F35 ($M_w = 3.55 \times 10^5$) were chosen as component two in preparing the binary-blend samples for study. The relaxation-modulus curves of the binary blends: F80/NBS (NBS $M_w = 1.79 \times 10^5$), F80/F10 (F10 $M_w = 1.00 \times 10^5$), F80/F4 (F4 $M_w = 4.49 \times 10^4$), F35/F10, F35/S8 (S8 $M_w = 8.3 \times 10^4$), F35/S6 (S6 $M_w = 6.04 \times 10^4$) and F35/F4 at two different concentrations $W_2/W_1 = 75/25$ and $50/50$ were measured and analyzed.¹⁹ In order to determine accurately the time-shift factor in the terminal region of $G(t)$ between a binary blend and its pure component-two melt, either right before or after the measurement of a binary blend, the pure component-two sample (i.e. either pure F80 or pure F35) was measured under the same condition. As shown in Fig. 10.5, the frictional factor K at a constant temperature remains constant at all molecular weights to as low as just above M_e . Thus, since the polymer samples used as component one in preparing the binary blends all have a molecular weight $> M_e$, the

frictional factor K for the terminal relaxation remains the same; any time shift in the terminal region between a binary blend and its pure component-two melt should be entirely due to a change in the entanglement-related structural factor.

If the frictional factor K in a blend *solution* were the same as that in its pure component-two melt, the terminal-relaxation-time ratio of the two systems could be obtained from Eq. (9.12) as

$$\frac{\tau'_C}{\tau_C} = \frac{M_e}{M'_e} \left[\frac{1 - (M'_e/M_{w2})^{1/2}}{1 - (M_e/M_{w2})^{1/2}} \right]^2 \tag{11.10}$$

where τ'_C is for the blend solution and τ_C for the pure melt. In Fig. 11.14, the measured and calculated relaxation curves of the pure F80 melt are compared with the curves of the F80/Y binary-blend series (Y = NBS, F10, F4 and $W_2/W_1 = 0.5/0.5$), measured at the same temperature, and the theoretical curve of the blend solution with F80 as component two

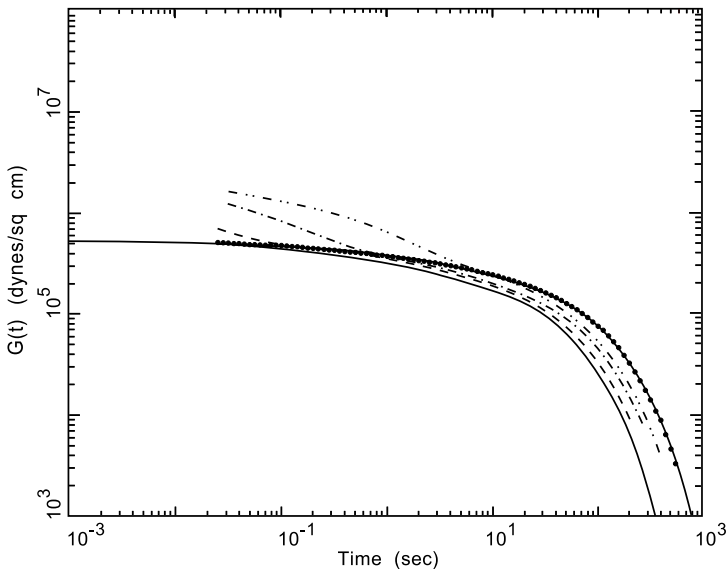


Fig. 11.14 Comparison of the calculated and measured relaxation modulus $G(t)$ curves in the terminal region: the upper solid line is the calculated for the F80 melt, which has been multiplied by a factor of $1/4(= W_2^2)$ for comparison with other curves; the lower solid line is calculated for the concentrated solution of F80 at $W_2 = 0.5$ ($M'_e = M_e/0.5$); ($\bullet \bullet \bullet$) is the measured $G(t)$ of the F80 melt multiplied by $1/4$; ($- \cdot -$) is the measured $G(t)$ of the F80/NBS = 50/50 blend; ($- - -$) is the measured $G(t)$ of the F80/F10 blend; and ($- - -$) is the measured $G(t)$ of the F80/F4 blend.

($W_2/W_1 = 0.5/0.5$) calculated with the same frictional factor as used in the calculation for the pure F80 melt. In the figure, both the measured and calculated curves of the pure F80 melt have been shifted down along the modulus axis by a factor of $W_2^2 = 0.25$ (see Appendix 11.A) so that all the curves are compared at the same modulus level in the terminal region.

Figure 11.14 clearly shows that as component-one's molecular weight decreases, the terminal relaxation of the binary blend shifts from that of the pure F80 melt toward that of the blend solution. All the relaxation curves shown in Fig. 11.14 are superposable in the terminal region by shifting along the time axis. The superposition is possible in practice, but not rigorously correct in theory; thus the obtained shift factors are apparent effective values. Denote the terminal relaxation time for a binary blend by τ_C'' which plays an equivalent role to τ_C (Eq. (9.12)) for the pure F80 melt. Then the time-shift factor obtained from the superposition between a binary-blend's curve and pure F80's can be expressed as τ_C''/τ_C . The relaxation-time ratio τ_C'/τ_C calculated from Eq. (11.10) should be the limiting value of τ_C''/τ_C as M_1 becomes low enough ($< M_e$) for serving as a solvent.

Shown in Fig. 11.15 are the shift factors τ_C''/τ_C , which have been obtained in the way described above for the F80/Y = 50/50 blend series, as a function of component-one's molecular weight for four series of binary blends: F80/Y at $W_2/W_1 = 0.75/0.25$ and $0.5/0.5$; and F35/Y at $W_2/W_1 = 0.75/0.25$ and $0.5/0.5$. Two important results can be obtained from the data shown in Fig. 11.15: First, as expected, the shift factor τ_C''/τ_C approaches the limiting value, τ_C'/τ_C , calculated from Eq. (11.10) as component-one's molecular weight becomes smaller than M_e . Second, by extrapolation toward the higher side of component-one's molecular weight, the shift factor τ_C''/τ_C reaches 1 (i.e. no shift) *far before* component-two's molecular weight is reached. Regarding a nearly monodisperse system as equivalent to a binary-blend system whose two components have the same molecular weight, we can easily see that the above result of τ_C''/τ_C reaching 1 "early" indicates that the general idea of the so-called constraint-release mechanism, as shared in the various versions,²⁰⁻²⁶ predicting a shortening of the terminal relaxation time even for a monodisperse system, cannot be valid. In fact, this result from a very different angle supports strongly the previously-drawn conclusion (Chapter 10) that the mean-field assumption which Eq. (9.19) as well as the Doi-Edwards theory is based on is rigorously valid for a (nearly) monodisperse system.

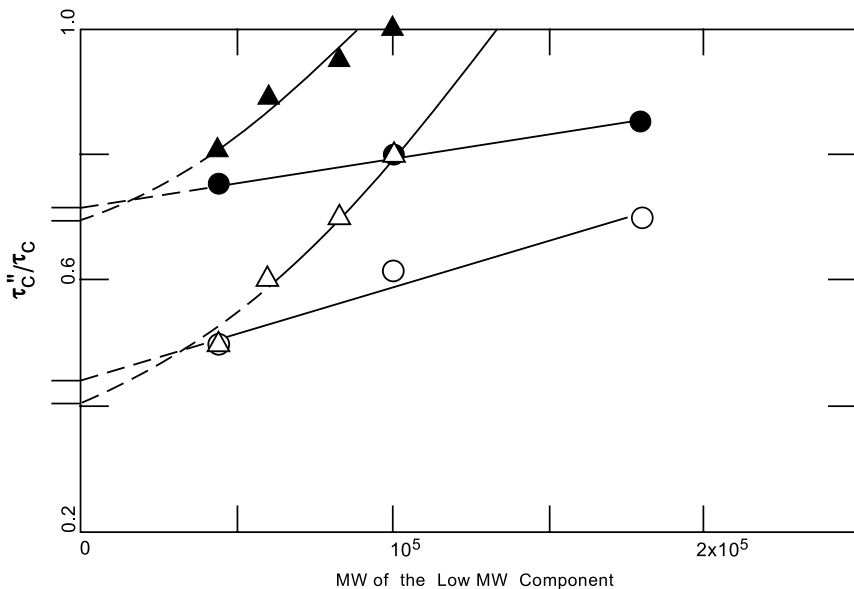


Fig. 11.15 The apparent time-shift factor, τ_C''/τ_C , as a function of the molecular weight (MW) of the low MW component (denoted by Y) in the binary blends: F80/Y = 75/25 (\bullet); F80/Y = 50/50 (\circ); F35/Y = 75/25 (\blacktriangle); and F35/Y = 50/50 (\triangle). The horizontal lines on the vertical axis indicate the theoretical τ_C''/τ_C values calculated from Eq. (11.10) as the limiting values for the four series of blend samples.

By using an equation analogous to Eq. (11.10), which relates the shift factor τ_C'/τ_C to M_e' , an effective entanglement molecular weight M_e'' corresponding to the ratio τ_C''/τ_C for a binary blend can be obtained. Shown in Fig. 11.16 are the M_e''/M_e values for the F80/Y binary blend series with $W_2/W_1 = 0.5/0.5$ as a function of component-one's molecular weight. In agreement with the results shown in Fig. 11.15, M_e''/M_e reaches the value 2 when component-one's molecular weight approaches zero; on the higher side, M_e''/M_e reaches 1 far before F80's molecular weight is reached.

As discussed in this section, the tube-dilation effect, i.e. $M_e''/M_e > 1$, mainly occurs in the terminal-relaxation region of component two in a binary blend. This effect means that the basic mean-field assumption of the Doi-Edwards theory (Eq. (8.3)) has a dynamic aspect when the molecular-weight distribution of the polymer sample is not narrow. This additional dynamic effect causes the viscoelastic spectrum of a broadly polydisperse sample to be much more complicated to analyze in terms of the tube model, and is the main factor which prevents Eq. (9.19) from being applied

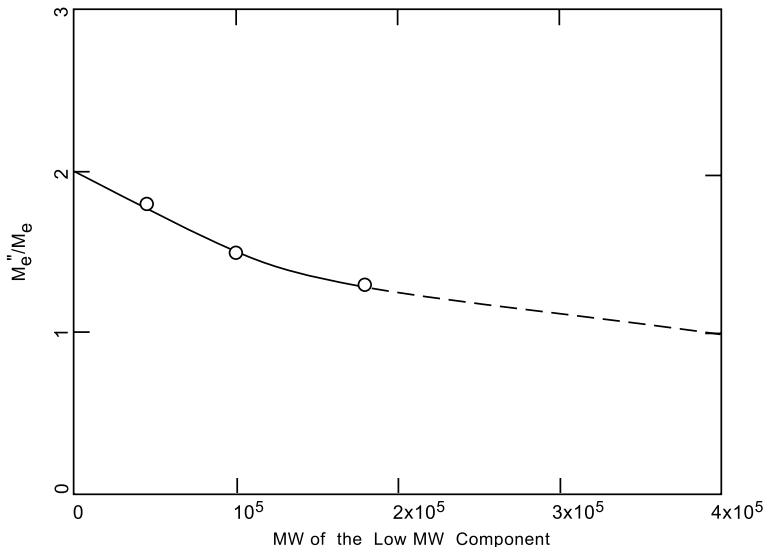


Fig. 11.16 The apparent M_e''/M_e values as a function of the molecular weight of the low MW component (Y) in the F80/Y = 50/50 blends.

directly to commercial polymers. On the other hand, by monitoring the tube-dilation effect as a function of component-one's molecular weight in a binary-blend system, the conclusion that the mean-field assumption in the Doi-Edwards theory and Eq. (9.19) for the (nearly) monodisperse system is valid, which has been drawn from the extensive, consistently quantitative studies of nearly monodisperse samples (Chapter 10), is further confirmed. One may consider this confirmation independent of Eq. (9.19) or (11.5) because one can analyze the tube-dilation effect in the binary blend systems without really involving Eq. (11.5), as done in this section, and reach the same conclusion.

Appendix 11.A — Basic Form of the Blending Law in a Binary Blend^{10,19}

For a blend system consisting of two monodisperse components whose molecular weights are both greater than M_e and far apart from each other (i.e. $M_2 \gg M_1 > M_e$), the blending law can be basically described by the following relaxation-modulus function (not covering the time region of the

$\mu_A(t)$ and $\mu_X(t)$ processes)

$$\begin{aligned}
 G(t) = G_N W_1 & \left[B_1 \mu_B \left(\frac{t}{\tau_{B1}} \right) + C_1 \mu_C \left(\frac{t}{\tau_{C1}} \right) \right] \\
 & + G_N W_2 [W_1 T(t) + W_2] \left[B_2 \mu_B \left(\frac{t}{\tau_{B2}} \right) + C_2 \mu_C \left(\frac{t}{\tau_{C2}} \right) \right]
 \end{aligned} \tag{11.A.1}$$

where B_1 , C_1 , τ_{B1} , and τ_{C1} are for component one and B_2 , C_2 , τ_{B2} , and τ_{C2} for component two; and B , C , $\mu_B(t)$, $\mu_C(t)$, τ_B and τ_C have the same definitions as given by Eqs. (9.14), (9.15), (9.5), (9.11), (9.6) and (9.12), respectively. In the above equation, $T(t)$ is a decaying function for the tube-renewal process that takes place on a component-two chain as the component-one chains originally entangled with it disentangle and reptate away. From the analyses of measured spectra in terms of Eq. (11.A.1), $T(t)$, assumed to be a single exponential, is found to have a characteristic time τ_t that is about seven times larger than τ_{C1} . At the same time, while B_1 , C_1 , τ_{B1} and τ_{C1} are not affected by the presence of component two and keep their respective values in the pure melt state, B_2 , C_2 , τ_{B2} and τ_{C2} are affected by the tube dilation due to the much faster reptation motions of the component-one chains. The tube-dilation effect can be accounted for by changing the M_e quantity that occurs in the expressions for B_2 , C_2 , τ_{B2} and τ_{C2} to an apparent effective value $M_e'' (> M_e)$ as discussed in the section on tube dilation of this chapter. For two components which are actually *nearly* monodisperse in an experiment, the convolution over their respective molecular-weight distributions can be done to Eq. (11.A.1) in the same way as done to Eq. (11.5), however, without including the effect of component-one's molecular-weight distribution on $T(t)$.

When component-one's molecular weight is below M_e , the viscoelastic response of component one is described by the Rouse theory, and τ_t (proportional to τ_{C1} if the component-one chain reptates) can be equated to zero as the component-one chains lose the reptational mechanism. Then Eq. (11.A.1) is transformed to

$$G(t) = W_1 G_R(t, M_1) + G'_N \left[B_2 \mu_B \left(\frac{t}{\tau_{B2}} \right) + C_2 \mu_C \left(\frac{t}{\tau_{C2}} \right) \right] \tag{11.A.2}$$

where $G_R(t, M_1)$ is given by Eqs. (7.57) and (7.58) and

$$G'_N = G_N W_2^2 = \frac{4\rho RT}{5M_e'} W_2 \tag{11.A.3}$$

with

$$M_e' = \frac{M_e}{W_2}. \quad (11.A.4)$$

Equation (11.A.2) together with Eqs. (11.A.3) and (11.A.4) is consistent with Eq. (11.5). Equation (11.A.4), being the same as Eq. (11.4), is in agreement with the expectation that, as M_1 becomes smaller than M_e , the binary blend becomes a blend solution with component one serving as the solvent. With this change, the M_e (or M_e'') quantity in all the expressions for B_2 , C_2 , τ_{B2} and τ_{C2} is replaced by M_e' as given by Eq. (11.A.4).

While the blending law — Eq. (11.A.1) — leads to the theoretical expression for a monodisperse blend solution (Eq. (11.5)) in a natural way as discussed above, it is also consistent with the theory for a monodisperse melt system (Eq. (9.19)) and the linear-additivity rule assumed in testing the theory with the experimental results of nearly monodisperse samples (Chapter 10). Equation (11.A.1) can be reduced to the equation for a monodisperse melt system in three ways: (a) by setting $W_1 = 0$; (b) by setting $W_2 = 0$; and (c) by taking $M_2 \rightarrow M_1$ (or $M_1 \rightarrow M_2$). The first two ways are obvious. The third way requires some explanation. Equation (11.A.1) has to become independent of W_1 or W_2 when $M_1 = M_2$. This can occur only if $T(t)$ becomes independent of time and equal to 1. Hence, Eq. (11.A.1) and the monodisperse theory (Eq. (9.19) or Eq. (9.13)) have to be consistent in the third way. $T(t)$ becoming 1 as $M_1 \rightarrow M_2$ suggests that when M_1 and M_2 are sufficiently close to each other, the linear-additivity rule for the contributions from the two components becomes applicable by setting $W_1 T(t) + W_2 = 1$ in Eq. (11.A.1).

References

1. Doi, M., and Edwards, S. F., *The Theory of Polymer Dynamics*, Oxford Univ. Press (1986).
2. Bird, R. B., Curtiss, C. F., Armstrong, R. C., and Hassager, O., *Dynamics of Polymeric Liquids, Kinetic Theory*, Vol. 2 (2nd edn.), Wiley, New York (1987).
3. Zimm, B. H., *J. Chem. Phys.* **24**, 269 (1956).
4. Flory, P. J., *Principles of Polymer Chemistry*, Cornell Univ. Press, Ithaca (1953).
5. de Gennes, P. G., *Scaling Concepts in Polymer Physics*, Cornell Univ. Press, Ithaca (1979).

6. Kirste, R., and Lehnen, B., *Makromol. Chem.* **177**, 1137 (1976); Westermann, S., Willner, L., Richter, D., and Fetters, L. J., *Macromol. Chem. Phys.* **201**, 500 (2000).
7. Wignall, G. D., Schelten, J., and Ballard, D. G. H., *J. Appl. Cryst.* **7**, 190 (1974); Ballard, D. G. H., Rayner, M. G., and Schelten, J., *Polym.* **17**, 349 (1976); Norisuye, T., and Fujita, H., *Polym. J.* (Tokyo) **14**, 143 (1982).
8. Inoue, T., Okamoto, H., and Osaki, K., *Macromolecules* **24**, 5670 (1991); Inoue, T., and Osaki, K., *Macromolecules* **29**, 1595 (1996).
9. Lin, Y.-H., and Lai, C. S., *Macromolecules* **29**, 5200 (1996); Lai, C. S., Juang, J.-H., and Lin, Y.-H., *J. Chem. Phys.* **110**, 9310 (1999); and Lin, Y.-H., and Luo, Z.-H., *J. Chem. Phys.* **112**, 7219 (2000).
10. Lin, Y.-H., *Macromolecules* **20**, 885 (1987).
11. Lin, Y.-H., (a) *Macromolecules* **17**, 2846 (1984); (b) **19**, 159 (1986).
12. Watanabe, H., Sakamoto, T., and Kotaka, T., *Macromolecules* **18**, 1436 (1985).
13. Lin, Y.-H., and Juang, J.-H., *Macromolecules* **32**, 181 (1999).
14. Lin, Y.-H., *Macromolecules* **19**, 168 (1986); as shown in Figs. 11.12 and 11.13, the theoretical curves are recalculated with $m = 850$ for each Rouse segment.
15. Lin, Y.-H., *Macromolecules* **24**, 5346 (1991).
16. Ferry, D. J., *Viscoelastic Properties of Polymers* (3rd edn.), Wiley, New York (1980).
17. Berry, G. C., and Fox, T. G., *Adv. Polym. Sci.* **5**, 261 (1968).
18. Graessley, W. W., *J. Polym. Sci., Polym. Phys. Ed.* **18**, 27 (1980).
19. Lin, Y.-H., *Macromolecules* **22**, 3075 (1989); **22**, 3080 (1989).
20. Klein, J., *Macromolecules* **11**, 853 (1978).
21. Daoud, M., and de Gennes, P.-G., *J. Polym. Sci., Polym. Phys. Ed.* **17**, 1971 (1979).
22. Graessley, W. W., *Adv. Polym. Sci.* **47**, 67 (1982).
23. Marrucci, M., *J. Polym. Sci., Polym. Phys. Ed.* **23**, 159 (1985).
24. Viovy, J. L., *J. Phys. (Les Ulis, Fr.)* **46**, 847 (1985).
25. Rubinstein, M., Helfand, E., and Pearson, D. S., *Macromolecules* **20**, 822 (1987).
26. des Cloizeaux, J., *Macromolecules* **23**, 3992 (1990).

Chapter 12

Molecular Theory of Polymer Viscoelasticity — Nonlinear Relaxation Modulus of Entangled Polymers

In the Doi–Edwards theory as studied in Chapter 8, the stress *right after* the equilibrium time T_{eq} following the initial application of a step deformation (Eq. (8.32)) was derived by allowing the polymer chain to slide through the slip-links in order to equilibrate the segmental distribution along the primitive path. The Doi–Edwards theory is concerned mainly with the stress relaxation after T_{eq} by the reptational motion of the polymer chain. In the time region $> T_{eq}$, the strain dependence of the modulus — the damping function $h(\lambda)$ — is well predicted by the Doi–Edwards theory (Fig. 9.2).

The ERT developed on the basis of the Doi–Edwards theory shows that the linear relaxation modulus $G(t)$ contains four processes: $\mu_A(t)$, $\mu_X(t)$, $\mu_B(t)$ and $\mu_C(t)$ (Eq. (9.19)). It was shown in Chapter 10 that the ERT explains various *linear* viscoelastic properties consistently and quantitatively. In the linear $G(t)$, the process $\mu_X(t)$, responsible for the change in the shear modulus from $\rho RT/M_e$ (Eqs. (8.1) and (8.37)) to $G_N = 4\rho RT/5M_e$ (Eq. (8.36)), equilibrates the segmental distribution along the primitive path. In other words, in the linear region of strain, τ_X is equivalent to T_{eq} . However, in the nonlinear region, T_{eq} is quite different.

In the linear $G(t)$, after time τ_X , the modulus is further relaxed to zero by the $\mu_B(t)$ and $\mu_C(t)$ processes. However, in the nonlinear relaxation modulus, the relaxation phenomenon in the time region corresponding to the $\mu_B(t)$ process is quite different. It has been shown theoretically by Doi¹ that in this time region the tensile forces along the primitive chain, arising from uneven segmental distribution, contribute greatly to the total stress. The relaxation of the chain tension is described by the same equation of motion as the $\mu_B(t)$ process and thus involves the whole chain. In the nonlinear relaxation modulus, T_{eq} is equivalent to τ_B and thus much longer than τ_X .

12.1 Chain-Tension Relaxation

For the nonlinear relaxation modulus, the relaxation phenomenon in the time region corresponding to the $\mu_A(t)$ process is complicated and difficult to study both theoretically and experimentally. Because of the finite extensibility of an entanglement strand in a polymer, a theoretical treatment of the $\mu_A(t)$ process based on the Gaussian chain model will not be so valid in the nonlinear region. Experimentally in the nonlinear region of strain, the high stress level corresponding to the high modulus in the $\mu_A(t)$ -process region easily overloads the transducer. Thus, for the study of the nonlinear relaxation modulus, we shall not consider the time region corresponding to the $\mu_A(t)$ process. Experimentally, one can avoid the $\mu_A(t)$ -process region by making measurements at a temperature sufficiently high so that the relaxation of the $\mu_A(t)$ process is faster than the actual deformation rate occurring in a step-strain experiment, i.e. $\sim 1/\epsilon$ where ϵ is the rise time of the step strain (see Chapter 4).

Consider a single chain having N entanglement strands with the slip-link positions at $\mathbf{R}_0, \mathbf{R}_1, \dots, \mathbf{R}_N$. Let the number of Rouse segments on the i th entanglement strand be denoted by N_i . Then the total number of Rouse segments of the chain is

$$\sum_i N_i = N_o. \quad (12.1)$$

The stress tensor $\mathbf{T}(t)$ following a step deformation \mathbf{E} applied at $t = 0$ is given by (Eq. (8.23) with \mathbf{r}'_i replaced by $\mathbf{r}_i(t)$ and n'_i by $N_i(t)$)

$$\mathbf{T}(t) = -3ckT \sum_i \left\langle \frac{\mathbf{r}_i(t)\mathbf{r}_i(t)}{N_i(t)b^2} \right\rangle + P\delta \quad (12.2)$$

where

$$\mathbf{r}_i(t) = \mathbf{R}_i(t) - \mathbf{R}_{i-1}(t). \quad (12.3)$$

Letting the index n represent the n th Rouse segment in the entanglement strand between \mathbf{R}_{i-1} and \mathbf{R}_i , Doi assumes for $t \gtrsim \tau_A^1$ (see Eq. (9.B.26))

$$\mathbf{R}_i(t) - \mathbf{R}_{i-1}(t) = \mathbf{v}_n^i(t)N_i(t)\langle l_n^i(t) \rangle \quad (12.4)$$

where $\mathbf{v}_n^i(t)$ is unit vector in the direction of $\mathbf{R}_i(t) - \mathbf{R}_{i-1}(t)$ and $N_i(t)\langle l_n^i(t) \rangle$ is the distance between \mathbf{R}_i and \mathbf{R}_{i-1} . In the Doi-Edwards model, the length of an entanglement strand $|\mathbf{R}_i(t) - \mathbf{R}_{i-1}(t)|$ is assumed to remain the same before this particular strand is reached by either of the two chain ends

through the reptational motion. Thus, the length $N_i(t)\langle l_n^i(t) \rangle$ associated with an entanglement strand which is not close to the chain ends does not change with time for $t < T_{eq}$. However, during $t < T_{eq}$, both $N_i(t)$ and $\langle l_n^i(t) \rangle$ change individually with time as the chain slippage through the entanglement links is taking place to equilibrate the segmental distribution along the primitive path. At the same time, while the total number of Rouse segments in the chain $\sum_i N_i(t) = N_o$ is a constant, the number of entanglement strands per chain, N , changes with time because Eq. (8.29) indicates that disentanglement occurs in the nonlinear region.

Using Eqs. (12.3) and (12.4), Eq. (12.2) can be expressed as

$$\begin{aligned} \mathbf{T}(t) &= -\frac{3ckT}{b^2} \sum_i N_i(t) \langle \mathbf{v}_n^i(t) \mathbf{v}_n^i(t) \rangle \langle l_n^i(t) \rangle^2 + P\delta \\ &= -\frac{3ckT}{b^2} \int_0^{N_o} dn \langle \mathbf{v}_n(t) \mathbf{v}_n(t) \rangle \langle l_n(t) \rangle^2 + P\delta. \end{aligned} \quad (12.5)$$

In making the assumption of Eq. (12.4), one has allowed the averaging over orientation for $\mathbf{v}_n \mathbf{v}_n$ to be separated from the tensile-stress magnitude ($\propto \langle l_n(t) \rangle^2$) on each Rouse segment as expressed in Eq. (12.5). Furthermore, in changing the summation over the entanglement strands to the integration over the whole chain segments $\int_0^{N_o} dn$ in Eq. (12.5), $N_i(t)$ is replaced by its average. Applying these assumptions is equivalent to making the so-called independent alignment approximation.² With these assumptions, the *local* differences among entanglement strands have been ignored. These assumptions lead to some small discrepancies from the exact situation, as can be seen in the following:

Let S_n be the point on the primitive-chain contour corresponding to the n th Rouse segment. Denote the positions of S_n in three-dimensional space before and after a step deformation \mathbf{E} is applied as $\mathbf{R}^o(S_n)$ and $\mathbf{R}(S_n(t))$, respectively. Then, before the application of \mathbf{E} , the length vector $l_n^o \mathbf{v}_n^o$ along the primitive chain corresponding to the n th Rouse segment is given by

$$l_n^o \mathbf{v}_n^o = \frac{\partial}{\partial n} \mathbf{R}^o(S_n) \quad (12.6)$$

with

$$l_n^o = \left| \frac{\partial \mathbf{R}^o(S_n)}{\partial n} \right| \quad (12.7)$$

and

$$\mathbf{v}_n^o = \frac{(\partial \mathbf{R}^o(S_n))/\partial n}{|(\partial \mathbf{R}^o(S_n))/\partial n|}. \quad (12.8)$$

And at time t following the initial application of \mathbf{E} , the length vector corresponding to the n th Rouse segment is given by

$$\frac{\partial}{\partial n} \mathbf{R}(S_n(t)) = \mathbf{v}_n(t) l_n(t). \quad (12.9)$$

Since $\mathbf{R}(S_n(t))$ changes affinely with the deformation \mathbf{E} , the *initial* value of $l_n(t)$ and $\mathbf{v}_n(t)$ (i.e. the values at $t \approx \tau_A^1$ and denoted by l'_n and \mathbf{v}'_n) are

$$l'_n = \left| \frac{\partial}{\partial n} \mathbf{E} \cdot \mathbf{R}^o(S_n) \right| = l_n^o |\mathbf{E} \cdot \mathbf{v}_n^o| \quad (12.10)$$

and

$$\mathbf{v}'_n = \frac{\mathbf{E} \cdot \mathbf{v}_n^o}{|\mathbf{E} \cdot \mathbf{v}_n^o|}. \quad (12.11)$$

Then, from Eqs. (12.10) and (12.11), one obtains

$$\langle l'_n \rangle = \langle l_n^o \rangle \langle |\mathbf{E} \cdot \mathbf{v}_n^o| \rangle = l \langle |\mathbf{E} \cdot \mathbf{u}| \rangle_{\mathbf{u}} \equiv \alpha(\mathbf{E}) l \quad (12.12)$$

and

$$\begin{aligned} \langle \mathbf{v}'_n \mathbf{v}'_n \rangle &= \left\langle \frac{(\mathbf{E} \cdot \mathbf{v}_n^o)(\mathbf{E} \cdot \mathbf{v}_n^o)}{|\mathbf{E} \cdot \mathbf{v}_n^o|^2} \right\rangle \\ &= \left\langle \frac{(\mathbf{E} \cdot \mathbf{u})(\mathbf{E} \cdot \mathbf{u})}{|\mathbf{E} \cdot \mathbf{u}|^2} \right\rangle_{\mathbf{u}} \end{aligned} \quad (12.13)$$

where \mathbf{v}_n^o is denoted by the unit vector \mathbf{u} which appears in Eqs. (8.32) and (8.37), as it represents the orientation of an entanglement strand in the equilibrium state; and $\langle l_n^o \rangle$ (the average value before deformation) is replaced by the equilibrium value l , which is given by

$$l = \frac{b}{\sqrt{N_e}} \quad (12.14)$$

for $N_e l = a$. Substituting Eqs. (12.12) and (12.13) into Eq. (12.5), one then has the stress at $t \approx \tau_A^1$

$$\begin{aligned} \mathbf{T}(t \approx \tau_A^1) &= -\frac{3ckT}{b^2} N_o l^2 \left\langle \frac{(\mathbf{E} \cdot \mathbf{u})(\mathbf{E} \cdot \mathbf{u})}{|\mathbf{E} \cdot \mathbf{u}|^2} \right\rangle_{\mathbf{u}} \alpha(\mathbf{E})^2 + P\delta \\ &= -3cNkT \left\langle \frac{(\mathbf{E} \cdot \mathbf{u})(\mathbf{E} \cdot \mathbf{u})}{|\mathbf{E} \cdot \mathbf{u}|^2} \right\rangle_{\mathbf{u}} \alpha(\mathbf{E})^2 + P\delta \end{aligned} \quad (12.15)$$

where, for the last equality, Eqs. (8.3) and (12.14) have been used.

The discrepancy between Eq. (12.15) and the exact result, Eq. (8.37), is not large as

$$\left\langle \frac{(\mathbf{E} \cdot \mathbf{u})(\mathbf{E} \cdot \mathbf{u})}{|\mathbf{E} \cdot \mathbf{u}|^2} \right\rangle_{\mathbf{u}} \langle |\mathbf{E} \cdot \mathbf{u}|^2 \rangle_{\mathbf{u}}^2 \approx \langle (\mathbf{E} \cdot \mathbf{u})(\mathbf{E} \cdot \mathbf{u}) \rangle_{\mathbf{u}}. \quad (12.16)$$

A comparison between $\langle (\mathbf{E} \cdot \mathbf{u})(\mathbf{E} \cdot \mathbf{u}) / |\mathbf{E} \cdot \mathbf{u}|^2 \rangle_{\mathbf{u}} \alpha(\mathbf{E})^2$ and $\langle (\mathbf{E} \cdot \mathbf{u})(\mathbf{E} \cdot \mathbf{u}) \rangle_{\mathbf{u}}$ as a function of shear strain and uniaxial extension/compression strain is shown in Figs. 12.1 and 12.2, respectively.

Equation (12.5) contains two relaxation processes: $\langle \mathbf{v}_n(t) \mathbf{v}_n(t) \rangle$ is to be randomized or relaxed by the chain reptational motion, and the change in $\langle l_n(t) \rangle^2$ with time represents the chain-tension relaxation. The former is much slower than the latter if the molecular weight is large. At $t \approx T_{eq}$, the chain-tension relaxation process ends and $\langle l_n(t) \rangle$ returns to its equilibrium value l ; the stress tensor $\mathbf{T}(t \approx T_{eq})$ becomes

$$\mathbf{T}(t \approx T_{eq}) = -3cNkT \left\langle \frac{(\mathbf{E} \cdot \mathbf{u})(\mathbf{E} \cdot \mathbf{u})}{|\mathbf{E} \cdot \mathbf{u}|^2} \right\rangle_{\mathbf{u}} + p\delta \quad (12.17)$$

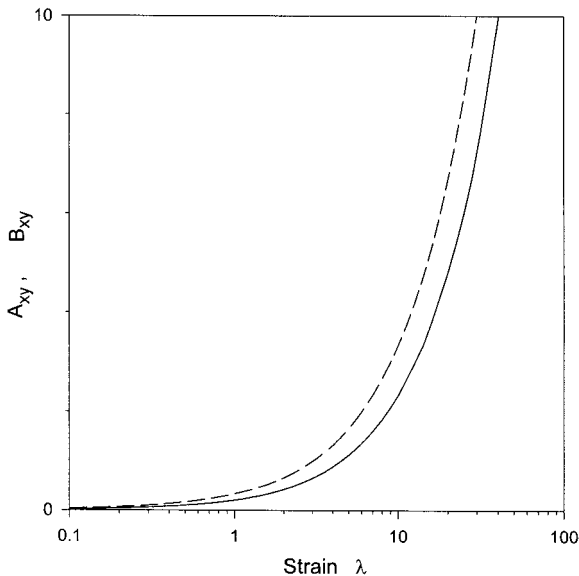


Fig. 12.1 Comparison of $\langle (\mathbf{E} \cdot \mathbf{u})(\mathbf{E} \cdot \mathbf{u}) / |\mathbf{E} \cdot \mathbf{u}|^2 \rangle_{\mathbf{u}} \alpha(\mathbf{E})^2$ (denoted by \mathbf{A} ; solid line) and $\langle (\mathbf{E} \cdot \mathbf{u})(\mathbf{E} \cdot \mathbf{u}) \rangle_{\mathbf{u}}$ (denoted by \mathbf{B} ; dashed line) as a function of strain λ for simple shear deformation (\mathbf{E} given by Eq. (5.24)).

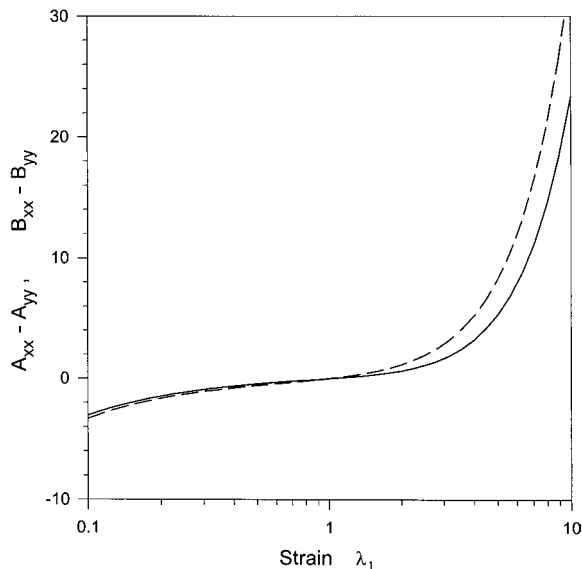


Fig. 12.2 Comparison of $\langle (\mathbf{E} \cdot \mathbf{u})(\mathbf{E} \cdot \mathbf{u}) / |\mathbf{E} \cdot \mathbf{u}|^2 \rangle \alpha(\mathbf{E})^2$ (denoted by \mathbf{A} ; solid line) and $\langle (\mathbf{E} \cdot \mathbf{u})(\mathbf{E} \cdot \mathbf{u}) \rangle$ (denoted by \mathbf{B} ; dashed line) as a function of strain λ_1 for uniaxial extension/compression deformation (\mathbf{E} given by Eq. (5.22)).

which is an approximation to Eq. (8.32), as

$$\begin{aligned} \left\langle \frac{(\mathbf{E} \cdot \mathbf{u})(\mathbf{E} \cdot \mathbf{u})}{|\mathbf{E} \cdot \mathbf{u}|^2} \right\rangle_{\mathbf{u}} &\equiv \mathbf{Q}'(\mathbf{E}) + \frac{\delta}{3} \\ &\approx \left\langle \frac{(\mathbf{E} \cdot \mathbf{u})(\mathbf{E} \cdot \mathbf{u})}{|\mathbf{E} \cdot \mathbf{u}|} \right\rangle_{\mathbf{u}} \langle |\mathbf{E} \cdot \mathbf{u}| \rangle_{\mathbf{u}}^{-1} \equiv \mathbf{Q}(\mathbf{E}) + \frac{\delta}{3}. \end{aligned} \quad (12.18)$$

$\mathbf{Q}'(\mathbf{E})$ represents the result of the independent alignment approximation. A comparison of $\mathbf{Q}(\mathbf{E})$ with $\mathbf{Q}'(\mathbf{E})$ as well as with experimental results through the damping function $h(\lambda)$ for step shear will be presented in the next section.

The relaxation of $\langle l_n(t) \rangle^2$, which occurs mainly in the time domain from τ_A^1 to T_{eq} , has been obtained by Doi¹ as in the following. From Eq. (9.A.2) with the substitution of $l_n(t) = S_n(t) - S_{n-1}(t)$, we have

$$\zeta \frac{\partial}{\partial t} \langle l_n(t) \rangle = \frac{3kT}{b^2} \frac{\partial^2}{\partial n^2} \langle l_n(t) \rangle \quad (12.19)$$

with the boundary condition (Eq. (9.A.5))

$$\langle l_n(t) \rangle = l \quad \text{at } n = 0; N_0. \quad (12.20)$$

Using Eq. (12.12) as the initial condition, Eq. (12.19) is solved as

$$\langle l_n(t) \rangle = l \left[1 + (\alpha(\mathbf{E}) - 1) \sum_{p=\text{odd}} \frac{4}{\pi p} \sin\left(\frac{p\pi n}{N_o}\right) \exp\left(-\frac{tp^2}{\tau_B^*}\right) \right] \quad (12.21)$$

where τ_B^* is identical to τ_B given by Eqs. (9.6) or (9.A.12)

$$\tau_B^* = \tau_B = \frac{\zeta b^2 N_o^2}{3\pi^2 kT} = \frac{K}{3} M^2. \quad (12.22)$$

As the relaxation time of $\langle \mathbf{v}_n(t) \mathbf{v}_n(t) \rangle$ is much longer than τ_B if the molecular weight is large, during the time $t \leq \tau_B$ one may temporarily replace it by $\mathbf{Q}'(\mathbf{E}) + \delta/3$ (Eqs. (12.13) and (12.18)). Letting the term $\delta/3$ be absorbed in the pressure terms, for $t \leq \tau_B$ we have from Eq. (12.5)

$$\mathbf{T}(t) = -\frac{3ckT}{b^2} \mathbf{Q}'(\mathbf{E}) \int_0^{N_o} dn \langle l_n(t) \rangle^2 + P\delta. \quad (12.23)$$

Substituting Eq. (12.21) into Eq. (12.23) and carrying out the integration, one obtains

$$\mathbf{T}(t) = -\frac{3cN_o kT}{N_e} \mathbf{Q}'(\mathbf{E}) \mu_B^*(t, \mathbf{E}) + P\delta \quad (12.24)$$

where

$$\mu_B^*(t, \mathbf{E}) = \sum_{p=\text{odd}} \frac{8}{\pi^2 p^2} \left[1 + (\alpha(\mathbf{E}) - 1) \exp\left(-\frac{p^2 t}{\tau_B^*}\right) \right]^2. \quad (12.25)$$

Equation (12.25) indicates that $\mu_B^*(t, \mathbf{E})$ relaxes from a strength of $(\alpha(\mathbf{E}))^2$ at $t \approx \tau_A^1 \ll \tau_B$ to the constant of 1 at $t > \tau_B$. The two processes $\mu_B^*(t, \mathbf{E})$ and $\mu_B(t)$ have the same dynamic origin; their relaxation times τ_B^* and τ_B are the same, both obtained from the same equation of motion (Eq. (9.A.2)).

While the $\mu_B^*(t, \mathbf{E})$ relaxation is going on, the relatively slow relaxation of $\langle \mathbf{v}_n \mathbf{v}_n \rangle$ by the reptational motion also gets under way. At $t \approx \tau_B^*$ when the primitive chain has recovered its equilibrium contour length, the effect of the contour length fluctuation on the terminal relaxation should basically be the same as that in the linear region. In other words, the relaxation of $\langle \mathbf{v}_n(t) \mathbf{v}_n(t) \rangle$ should be described by Eqs. (9.11) and (9.12). Thus from Eq. (12.24), we write the stress relaxation after $t \approx \tau_A^1$ as

$$\mathbf{T}(t) = -3cNkT \mathbf{Q}'(\mathbf{E}) \mu_B^*(t, \mathbf{E}) \mu_C(t) + P\delta. \quad (12.26)$$

As pointed out above, $\mu_B(t)$ and $\mu_B^*(t, \mathbf{E})$ have the same dynamic origin. However, $\mu_B^*(t, \mathbf{E})$ relaxes the extra tension residing in every part of the primitive chain while $\mu_B(t)$ relaxes the tube stress only in the tube end regions. In the linear region, $\alpha(\mathbf{E}) = 1$; thus, the $\mu_B^*(t, \mathbf{E})$ process is not observable (see Eq. (12.25)). In the nonlinear region, the contribution of the chain tension to the total stress is very large; the $\mu_B(t)$ process (see Eq. (9.13)) is “wiped out” or overshadowed by the $\mu_B^*(t, \mathbf{E})$ process. Particularly in the high-molecular-weight region, where the relaxation strength of the $\mu_B(t)$ process (Eq. (9.14)) is relatively small in comparison with that of the $\mu_C(t)$ process (Eq. (9.15)), the $\mu_B(t)$ process can be ignored. By neglecting the contribution of the $\mu_B(t)$ process, the stress relaxation in the *terminal region* can be obtained from Eq. (8.52) with $\mu(t)$ given by Eq. (8.54) to be replaced by $\mu_C(t)$ given by Eqs. (9.11) and (9.12)

$$\mathbf{T}(t) = -3cNkT\mathbf{Q}(\mathbf{E})\mu_C(t) + P\delta. \quad (12.27)$$

Since $\mathbf{Q}(\mathbf{E}) \approx \mathbf{Q}'(\mathbf{E})$, one may combine Eqs. (12.26) and (12.27) as

$$\mathbf{T}(t) = -3cNkTK(\mathbf{E})\mu_B^*(t, \mathbf{E})\mu_C(t) + P\delta \quad (12.28)$$

with

$$\mathbf{K}(\mathbf{E}) = \mathbf{Q}(\mathbf{E}) \quad (12.29)$$

or

$$\mathbf{K}(\mathbf{E}) = \mathbf{Q}'(\mathbf{E}) \quad (12.30)$$

when the independent alignment approximation is used.

12.2 Comparison of Theory and Experiment

In Fig. 12.3, the relaxation modulus of a nearly monodisperse polystyrene of $M_w = 4.22 \times 10^5$ (F40) at the step shear strain $\lambda = 5$ is compared with that in the linear region ($\lambda = 0.2$), both being measured at the same temperature. In the nonlinear relaxation modulus, as expected from Eq. (12.28), two distinctive relaxation processes are visible; in addition to the terminal relaxation, a faster process occurs in the time region corresponding to the plateau in the linear $G(t)$. The linear and nonlinear relaxation curves are superposable in the terminal region as one of the two curves is allowed to shift along the modulus axis (as explained below, a small shift toward the

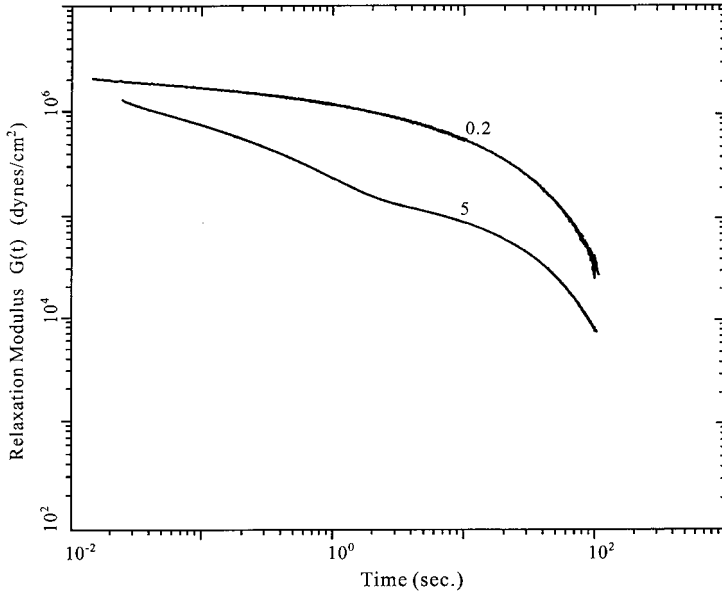


Fig. 12.3 Comparison of the relaxation modulus $G(t, \lambda)$ at $\lambda = 0.2$ (in the linear region) and at $\lambda = 5$ (in the nonlinear region) of nearly monodisperse polystyrene sample F40 ($M_w = 4.22 \times 10^5$), both measured at the same temperature ($\sim 167^\circ\text{C}$).

shorter time is required for moving the linear curve to superpose on the nonlinear curve in the case of $\lambda = 5$).

(a) Damping function

In making the superposition of two relaxation-modulus curves in the terminal region, the shift factor along the modulus axis defined by

$$h(\lambda) = \frac{G(t, \lambda)}{G(t, \lambda \rightarrow 0)} \quad \text{for } t > T_{eq} \quad (12.31)$$

is often referred to as the damping function. The damping function can be calculated from $\mathbf{Q}(\mathbf{E})$ (see Eq. (8.34)), or from $\mathbf{Q}'(\mathbf{E})$ when the independent alignment approximation is used (Eq. (12.18)). In Fig. 9.2, the calculated $h(\lambda)$ curves, with and without the independent alignment approximation, are compared with the measured values for the F40 sample. Some small shift along the time axis corresponding to a reduction of the relaxation time at a step shear strain $\lambda \geq 5$ is required to make a good superposition. The shown $h(\lambda)$ values measured at large strains (≥ 5) were obtained by allowing

such a time shift. A greater time shift is required for a greater strain. At the strain $\lambda = 5$, a time shift of about 15% can be observed. Although this effect has not been clearly expected in the Doi–Edwards theory, some disentanglement caused by a large deformation (see Eq. (8.29)) may lead to a small shortening of the reptation time. This effect can be seen by replacing M_e of Eq. (9.12) by a greater effective value due to disentanglement caused by a large deformation. Except for the small time shift involved at a very large strain, the agreement between the calculated and measured $h(\lambda)$ values is very good. The successful prediction of the damping function by the Doi–Edwards theory is very significant as no fitting parameter is involved in the calculation. In other words, the damping function is universal. Indeed the close agreement between theory and experiment for $h(\lambda)$ has been observed for different polymers.^{3–8}

(b) *Line shape of relaxation modulus*

The nonlinear relaxation modulus as shown in Fig. 12.3 contains two distinctive relaxation processes. It is both interesting and important to see how well the relative positions of the two relaxation processes are described by Eq. (12.28) together with Eqs. (9.11), (9.12), (12.22) and (12.25). In Figs. 12.4–12.7, we compare the measured relaxation moduli at $\lambda = 3$ and 5 with those calculated from Eq. (12.28) for two nearly monodisperse polystyrene samples: F40 and F80 ($M_w = 7.75 \times 10^5$). The molecular-weight distributions of the two samples included in the calculation are identical to those that have been extracted from the analyses of their respective linear viscoelastic spectra as described in detail in Chapter 10. The decrease in the modulus from the linear $G(t)$ in the terminal region is determined by the damping factor $h(\lambda)$, for which the close agreement between theory and experiment has been shown in Fig. 9.2. As shown in Figs. 12.4–12.7, the comparisons of the measured nonlinear relaxation curves with the calculated are made by matching in the terminal region to obtain the actual damping factors shown in Fig. 9.2. Overall, the agreement between theory and experiment is good; however, some discrepancies can be observed. At $\lambda = 3$, the theoretical curves in the $\mu_B^*(t, \mathbf{E})$ -process region underestimate the measured, by about the same degree for both the F40 and F80 samples. These discrepancies may arise from assumptions made in deriving Eq. (12.25) as discussed in the last section. The difference between theory and experiment appears related to the $\alpha(\mathbf{E})$ value, calculated from Eq. (12.12) at $\lambda = 3$, being too small.

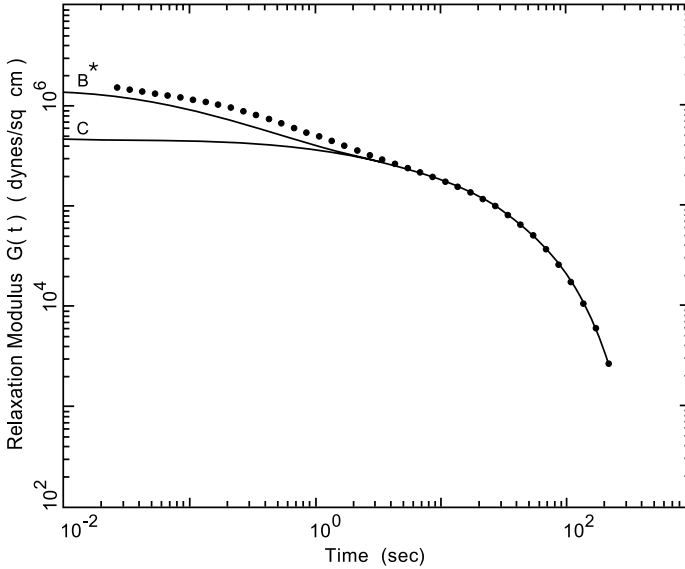


Fig. 12.4 Comparison of the measured (dots) and the calculated (line) relaxation modulus $G(t, \lambda)$ at $\lambda = 3$ for sample F40. The curves are calculated from Eq. (12.28); the portion between line B* and line C is the contribution of the $\mu_B^*(t, \mathbf{E})$ process, while below line C is the contribution of the $\mu_C(t)$ process.

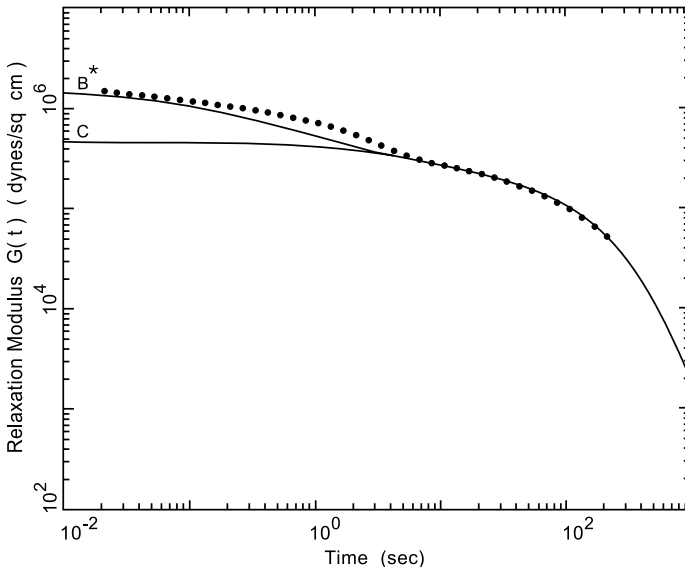


Fig. 12.5 Same as Fig. 12.4 for sample F80.

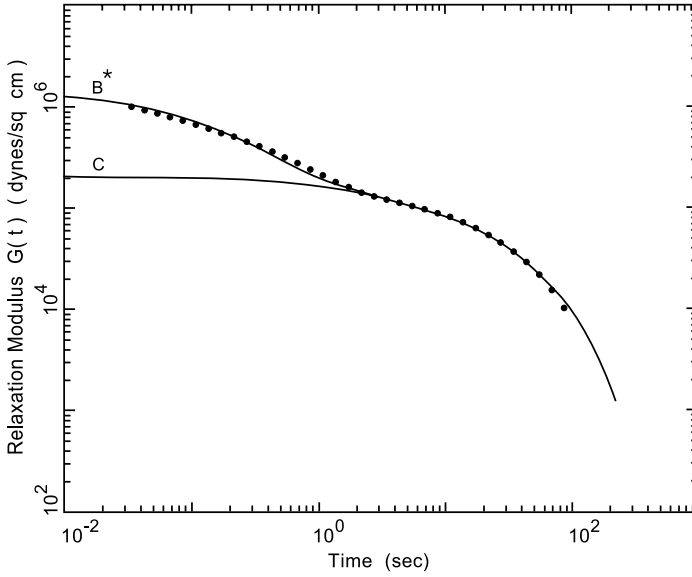
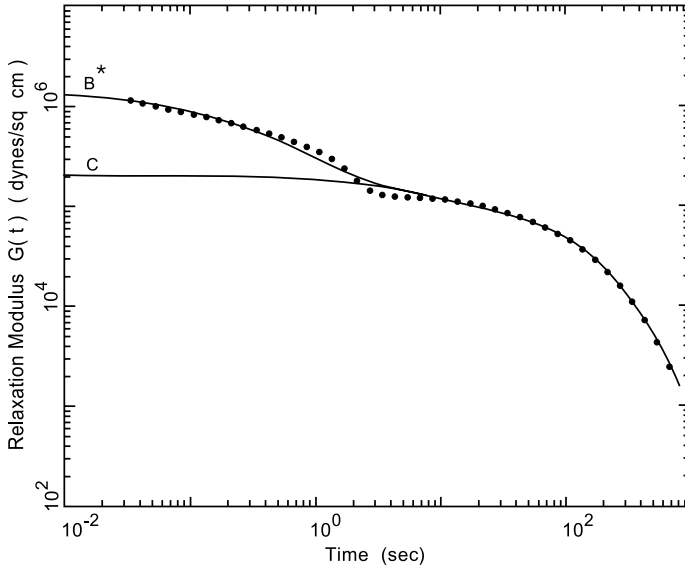
The molecular-weight dependence of τ_C is given by Eq. (9.12) for both the linear and nonlinear relaxation moduli. As pointed out above, it has been observed experimentally that τ_C decreases by a small amount $\sim 15\%$ at $\lambda = 5$, most likely due to disentanglement caused by the large strain. Bearing this small reduction in τ_C , one still sees in Figs. 12.6 and 12.7 that the relative positions of the $\mu_B^*(t, \mathbf{E})$ and $\mu_C(t)$ processes are reasonably well described by Eq. (12.28) for both samples with *very different molecular weights*. This agreement supports that the molecular-weight dependence of the relaxation-time ratio of the two processes is well given by

$$\frac{\tau_C}{\tau_B^*} = 3 \frac{M}{M_e} \left(1 - \sqrt{\frac{M_e}{M}} \right)^2 \quad (12.32)$$

which is obtained from Eqs. (9.12) and (12.22). Equation (12.32) is the same as Eq. (9.16) for the relaxation-time ratio between $\mu_B(t)$ and $\mu_C(t)$ in the linear $G(t)$. As the role of the $\mu_B(t)$ process in the linear $G(t)$ has been well proven in Chapter 10, the observation that Eq. (12.32) is well followed in the nonlinear $G(t)$ supports that $\tau_B^* = \tau_B$ and that $\mu_B(t)$ and $\mu_B^*(t, \mathbf{E})$ have the same dynamic origin. This conclusion is expected from the modeling that leads to Eq. (12.25).

For making a comparison of the roles of the various dynamic processes in the linear and nonlinear regions, we show in Fig. 12.8 the linear and nonlinear (at $\lambda = 5$) $G(t)$ curves, both calculated and measured, for the F40 sample. In this figure, the nonlinear $G(t)$ curve is shifted upward along the modulus axis (by a factor that is equivalent to the reciprocal of the damping factor) so that its terminal region is superposed on the linear $G(t)$ curve. The theoretical curve for the linear $G(t)$ is calculated using Eq. (9.19) while that for the nonlinear $G(t)$ is calculated using Eq. (12.28). The comparison illustrates the relative positions (or roles) of the involved processes: $\mu_B^*(t, \mathbf{E})$ — nonlinear, $\mu_B(t)$ — linear, $\mu_C(t)$ — linear and nonlinear, $\mu_A(t)$ — linear, and $\mu_X(t)$ — linear. The linear and nonlinear $G(t)$'s are linked in the terminal region (the $\mu_C(t)$ process) by the damping factor.

Finally, we shall mention the slip-stick melt fracture phenomenon⁹ — a phenomenon often observed in polymer extrusion — which is much related to the relative positions of the $\mu_B^*(t, \mathbf{E})$ and $\mu_C(t)$ processes. The phenomenon is a well-known problem in the polymer processing industry because it limits the output of polymer through an extruder. In a capillary flow, the decline of the viscosity observed as the shear rate (or flow rate) increases from the Newtonian region is much related to the damping factor

Fig. 12.6 Same as Fig. 12.4 for sample F40 at $\lambda = 5$.Fig. 12.7 Same as Fig. 12.4 for sample F80 at $\lambda = 5$.

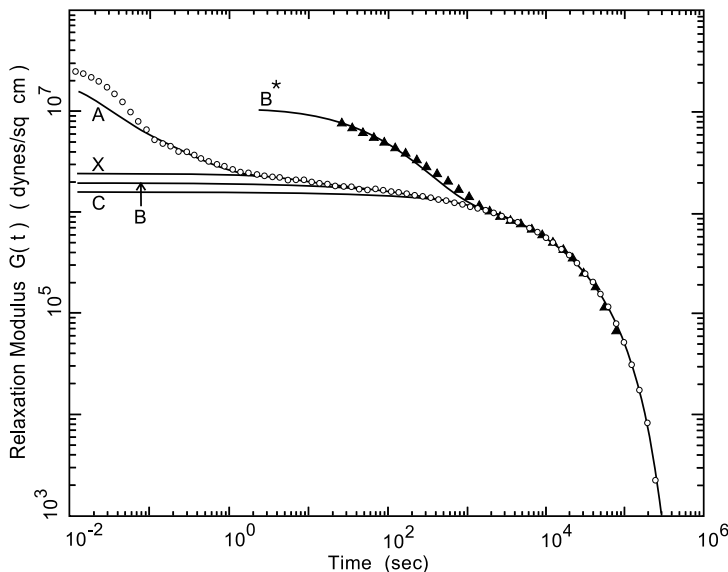


Fig. 12.8 Comparison of the linear and nonlinear (at $\lambda = 5$) $G(t)$ line shapes, measured (\circ for the linear; \blacktriangle for $\lambda = 5$) and calculated (lines), for sample F40. Also shown are the separate contributions of the $\mu_A(t)$, $\mu_X(t)$, $\mu_B(t)$, $\mu_B^*(t, \mathbf{E})$ and $\mu_C(t)$ processes (see Figs. 10.1 and 12.6).

associated with the $\mu_C(t)$ process. In a high, but not extremely high, shear-rate region where still only the contribution of the $\mu_C(t)$ process needs to be considered, the shear stress will eventually *decline* with the increasing shear rate because of the damping factor. In this rate region, the “viscosity” is negative, indicating instability. As the shear rate increases further to become comparable to $1/\tau_B^*$, the chain tension begins to contribute to the total shear stress significantly and causes the stress to rise again. Thus a dip in the flow curve is created. When the two processes $\mu_B^*(t, \mathbf{E})$ and $\mu_C(t)$ grow further apart with increasing molecular weight according to Eq. (12.32), the dip becomes wider and deeper, and more observable. The maximum point before the dip in the flow curve represents the onset of instability. It has been shown that the instability point corresponds to the onset of the slip-stick melt fracture phenomenon. There is the tendency for the dip to be smeared out by the molecular-weight distribution of the sample. The wider and deeper dip for a larger molecular weight has a higher chance to survive the smearing-out effect. Thus, the slip-stick melt fracture phenomenon is more prone to occur at a higher molecular weight

in agreement with experimental results. The details of the explanation for the slip-stick melt fracture phenomenon in terms of the molecular dynamic processes can be found in the original studies,^{7,10-13} from which one sees that the slip-stick melt fracture is a universal phenomenon for flexible linear polymers.

References

1. Doi, M., *J. Polym. Sci., Polym. Phys. Ed.* **18**, 1005 (1980).
2. Doi, M., and Edwards, S. F., *J. C. S. Faraday II* **74**, 1802 (1978); II **74**, 1818 (1978).
3. Osaki, K., and Kurata, M., *Macromolecules* **13**, 671 (1980).
4. Osaki, K., Nishizawa, K., and Kurata, M., *Macromolecules* **15**, 1068 (1982).
5. Vrentas, C. M., and Graessley, W. W., *J. Rheol.* **26**, 359 (1982).
6. Lin, Y.-H., *J. Rheol.* **28**, 1 (1984).
7. Lin, Y.-H., *J. Non-Newtonian Fluid Mech.* **23**, 163 (1987).
8. Pearson, D. S., *Rubber Chem. Tech.* **60**, 439 (1987).
9. Vinogradov, G. V., Malkin, A. Ya, Yanovskii, G. Yu, Borisenkova, E. K., Yarlykov, B. V., and Berezhnaya, G. V., *J. Polym. Sci. Part A-2* **10**, 1061 (1972).
10. Edwards, S. F., *Rheol. Acta* **29**, 493 (1990).
11. Lin, Y.-H., *J. Rheol.* **29**, 605 (1985).
12. McLeish, T. C. B., and Ball, R. C., *J. Polym. Sci., Phys. Ed.* **24**, 1735 (1986).
13. Lin, Y.-H., *Makromol. Chem., Macromol. Symp.* **56**, 1 (1992).

Chapter 13

Number of Entanglement Strands per Cubed Entanglement Distance, n_t

13.1 Introduction

How the existence of chain entanglement was initially suggested by several important viscoelastic observations has been reviewed in Chapter 8. Chain entanglements occur to any kind of flexible polymer as long as the concentration of the polymer system is sufficiently high and the chain length sufficiently long. In the previous chapters, the universality of chain entanglement as reflected by its effect on various viscoelastic properties has been extensively and consistently analyzed and demonstrated in terms of the molecular theories. The most prominent aspects of universality in polymer viscoelasticity related to entanglement include: (1) The linear relaxation modulus $G(t)$ is a universal function of the normalized molecular weight M/M_e where M_e is determined from the plateau modulus. The molecular-weight dependence of the zero-shear viscosity (including the well-known 3.4 power law) as well as that of the steady-state compliance is a logical consequence of the universality of $G(t)$. (2) In the well-entangled region, the damping function is independent of molecular weight and the polymer type, and thus is a universal function. The theories predicting these two important aspects of universality are ultimately based on the slip-link model of the Doi–Edwards theory. A very important element of the slip-link model is the entanglement strand with the associated quantities: the entanglement molecular weight M_e and the entanglement distance a . The universality as brought out by the studies mentioned above strongly suggest that there should be some fundamental universal relation among the entanglement strand and several basic polymer physical quantities such as density and the characteristic ratio C_∞ (or K_∞).

The viscoelastic response functions $G(t)$ and $G'(\omega)$ studied so far have basically been limited to the entropic (rubbery) region, both theoretically and experimentally. For polystyrene,^{1,2} the entropic region occurs below the modulus level $\sim 4 \times 10^7$ dynes/cm². The studied molecular theories have been developed using the Rouse segment as the most basic structural unit; in other words, it is assumed that the polymer behaves as a Gaussian chain. As long as we are only interested in polymer dynamic or viscoelastic behaviors corresponding to length scales above or comparable to the entanglement distance, this assumption is expected to be valid on the basis of the central limit theorem. In the next five chapters, studies will be extended into the energetic region (short-time or high-frequency), with modulus values ranging from $\sim 4 \times 10^7$ to $\sim 10^{10}$ dynes/cm²; this assumption as applied to length scales near and at that of the Rouse segment will be investigated. Some results of the studies, as will be used in the discussion presented in this chapter, are briefly summarized in the following:

The relaxation modulus $G(t)$ that is relevant to the topic discussed in this chapter is limited to the linear-response region and to time scales longer than the relaxation time of the highest Rouse or Rouse–Mooney normal mode. In other words, only the entropic region of a linear relaxation modulus $G(t)$ is of concern; the glassy relaxation that occurs in the short-time region is excluded from consideration. In modeling the linear relaxation modulus of a polymer over only the entropic region, a chain consisting of N Fraenkel segments³ gives rise to nearly the same result as a chain consisting of N Rouse segments⁴ (detailed in Chapter 17). In other words, limiting our consideration to linear viscoelasticity at entropic-dynamics time scales, a Fraenkel segment may be regarded as equivalent to a Rouse segment. At the same time, as far as modeling the polymer chain conformation is concerned, a freely jointed chain consisting of N Kuhn segments may be regarded as equivalent to a chain consisting of N sufficiently rigid Fraenkel segments. Thus, the Fraenkel segment is capable of playing a dual role: either as the Rouse segment or as the Kuhn segment. Through their individual equivalence to the Fraenkel segment, the sizes of the Rouse and Kuhn segments become equivalent. Indeed, the studies^{1,2,5–14} as briefly explained in Appendix 13.A has indicated that the sizes of the Rouse and Kuhn segments experimentally determined in accordance with their roles as defined above are the same within experimental error. Thus, for the present discussion purpose, we may consider the polymer chain either as a linkage of freely jointed Kuhn segments, each of length b , or as a linkage of Rouse segments, each with

the root mean square length b . The Kuhn and Rouse segments will be treated as equivalent — mainly their sizes are of concern here — and used interchangeably.

13.2 Theoretical Basis and Experimental Support for n_t Being a Universal Constant

As in the previous chapters, it has been assumed that the number of (Kuhn) segments per entanglement strand, N_e , is sufficiently large so that the mean square end-to-end distance of an entanglement strand can be expressed as

$$a^2 = N_e b^2 = C_\infty \frac{M_e}{m_o} b_o^2 = K_\infty M_e \quad (13.1)$$

where C_∞ is the characteristic ratio, m_o is the average mass per chemical segment, b_o is the average length per chemical bond, and $K_\infty = R^2/M$ where R^2 is the mean square end-to-end distance $\langle \mathbf{R}^2 \rangle$ of a freely jointed chain or a Gaussian chain of molecular weight M . The importance of Eqs. (8.3) and (13.1) cannot be over-emphasized; we recall their frequent use in deriving the reptation time and the damping function in the Doi–Edwards theory (Chapter 8), in obtaining the functional form for the primitive-chain contour length fluctuation process as well as the terminal relaxation time in the ERT (Chapter 9) and in describing the chain-tension relaxation process by Doi (Chapter 12).

The plateau modulus of a polymer melt G_N is proportional to the number of entanglement strands per unit volume n_v :

$$G_N = \frac{4\rho RT}{5M_e} = \frac{4}{5} n_v kT \quad (13.2)$$

with

$$n_v = \frac{\rho N_A}{M_e} \quad (13.3)$$

where ρ is the polymer density, N_A the Avogadro number, and k the Boltzmann constant. Because of the universality of chain entanglement as summarized in Sec. 13.1, a certain one-to-one correspondence should exist between the entanglement distance a and n_v . A logical way is to calculate a quantity which is independent of dimension. This consideration led to proposing that the number of entanglement strands per cubed

entanglement distance denoted by n_t :

$$n_t = n_v a^3 = \frac{\rho N_A}{M_e} (\sqrt{K_\infty M_e})^3 \quad (13.4)$$

should be a universal constant.¹⁵ Every quantity in Eq. (13.4) can be independently determined by experimental measurements: M_e from the measured value of the plateau modulus (Eq. (13.2)), and K_∞ from the R^2 value obtained mainly from the small-angle neutron scattering (SANS) measurement on the polymer melt or from the light scattering measurement or the intrinsic viscosity measurement of the dilute solution system under the θ condition. Shown in Tables 13.1 and 13.2 are the measured ρ , K_∞ , and M_e (or G_N) values of two sets of polymers at two different temperatures,

Table 13.1 Molecular and rheological characteristics for polymers at 413 K. See Table 13.3 for the polymers denoted by the abbreviations. As defined in the text, ρ in g/cm^3 ; G_N in MPa; K_∞ in nm^2/molg ; and a in nm. Reproduced, with permission, from Ref. 16.

Polymer	ρ	G_N	$K_\infty \times 10^2$	a	M_e	n_t
PE	0.78	2.60	1.25	3.22	828	18.98
PEB-2	0.79	2.21	1.21	3.44	976	19.65
PEB-4.6	0.79	1.90	1.15	3.62	1139	19.74
PE0	1.06	1.80	0.81	3.62	1624	18.64
PEB-7.1	0.79	1.55	1.05	3.83	1398	19.11
PEB-9.5	0.79	1.40	1.05	4.04	1552	20.18
PEB-10.6	0.79	1.30	1.06	4.21	1674	21.29
1,4-PBd	0.83	1.25	0.88	3.99	1815	17.37
PEB-11.7	0.79	1.20	0.95	4.16	1815	18.89
alt-PEB	0.79	0.95	0.83	4.36	2284	17.31
PEB-17.6	0.80	0.90	0.91	4.71	2433	20.65
PEB-24.6	0.80	0.67	0.80	5.12	3276	19.66
alt-PEB	0.80	0.52	0.69	5.41	4226	18.02
HHPP	0.81	0.52	0.69	5.44	4279	18.32
a-PP	0.79	0.47	0.67	5.57	4623	17.76
PEB-32	0.80	0.43	0.69	5.95	5124	19.81
1,4-PI	0.83	0.42	0.63	5.83	5429	18.19
PIB	0.85	0.32	0.57	6.45	7288	18.78
PMMA	1.13	0.31	0.43	6.52	10013	18.86
PEB-39.3	0.81	0.30	0.65	6.90	7371	21.55
PEB-40.9	0.81	0.29	0.60	6.80	7652	19.90
H ₂ -3,4-PI	0.81	0.22	0.53	7.31	10114	18.87
PS	0.97	0.20	0.43	7.60	13309	19.24
PDMS	0.90	0.20	0.46	7.50	12293	18.46
PEE	0.81	0.20	0.51	7.50	11084	18.46
PVCH	0.92	0.068	0.32	11.2	38966	20.07

Av. $19.14 \pm 5.7\%$

Table 13.2 Same as Table 13.1. For polymers at 298 K. Reproduced, with permission, from Ref. 16.

Polymer	ρ	G_N	$K_\infty \times 10^2$	a	M_e	n_t
1,4-PEB	0.90	1.15	0.88	3.68	1543	17.35
alt-PEP	0.86	1.15	0.92	3.70	1475	17.58
PEB-17.6	0.86	1.12	0.93	3.75	1522	18.00
PEB-14	0.86	1.12	0.93	3.75	1522	17.97
PEB-24.6	0.86	0.69	0.80	4.46	2482	18.54
alt-PEB	0.86	0.58	0.73	4.62	2942	17.36
HHPP	0.88	0.52	0.69	4.81	3347	17.56
a-PP	0.85	0.48	0.66	4.83	3518	16.45
PEB-32	0.86	0.44	0.64	4.99	3888	16.62
PEB-39.3	0.86	0.38	0.62	5.30	4507	17.17
H ₂ -50-PI	0.86	0.35	0.63	5.56	4876	18.23
1.4PI	0.90	0.35	0.60	5.51	5097	17.80
PIB	0.92	0.32	0.57	5.69	5686	17.93
PEB-40.9	0.86	0.30	0.55	5.59	5709	15.90
PDMS	0.97	0.20	0.42	6.37	9613	15.70
H ₂ -3,4-PI	0.88	0.19	0.46	6.52	9160	15.99
PEE	0.87	0.18	0.49	6.80	9536	17.20
1,4-1,2-PBd	0.84	0.87	0.80	3.87	1880	16.24
62-PBd	0.89	0.81	0.73	3.98	2178	15.50
cis-PBd	0.90	0.76	0.76	4.22	2347	17.32
PPOX	1.00	0.70	0.60	4.12	2832	14.85
cis-PI	0.91	0.58	0.68	4.60	3120	17.18
PVE	0.89	0.57	0.66	4.53	3091	16.10
50-PI	0.89	0.41	0.55	4.85	4317	14.25
1,4-PEB	0.89	0.29	0.54	5.75	6090	16.79
PMA	1.11	0.25	0.44	6.19	8801	18.05
H ₂ -1,4-MYRC	0.85	0.14	0.43	7.24	12077	16.13
1,4-MYRC	0.89	0.10	0.40	8.39	17681	17.93
H ₂ -64-MYRC	0.85	0.10	0.41	8.30	16828	17.34
64-MYRC	0.89	0.07	0.37	9.65	24874	19.35

Av. 17.02 \pm 6.6%

413K and 298 K, which have been compiled by Fetters *et al.*¹⁶ Also shown in the two tables are the calculated values of a (according to Eq. (13.1)) and n_t (according to Eq. (13.4)). The abbreviations in the first column of the tables denote polymers shown in Table 13.3. The two tables show that while the plateau modulus G_N , a key viscoelastic property, can differ by a factor as large as 38 (between PE and PVCH), the n_t value is constant. The averages of n_t in Tables 13.1 and 13.2 are 19.14 and 17.02 with only 5.7% and 6.6% for the standard deviation δ , respectively. The two average n_t values differ by about 13%, which, though still small, is somewhat larger than their standard deviations. Thus n_t appears to have a very weak temperature dependence, which may arise from a small

Table 13.3 Polymers represented by the abbreviations used in Tables 13.1 and 13.2. Reproduced, with permission, from Ref. 16.

PE	polyethylene (the PE G_N^0 is from an extrapolation involving values for the PEB-x samples (see below where x ranged from 2 to 19.7)
PEB-x	poly(ethylene-co-butene) (the integer (x) denotes the number of ethyl branches per 100 backbone carbons; these have been made by the hydrogenation of polybutadienes of varying vinyl content; these copolymers have a minimum to two ethylene units between two 1-butene units as a consequence of the 1,4-units in the parent polybutadienes; thus, PEB-2 is equivalent to an 8 wt % EB and PEB-50 to polybutene)
PEO	poly(ethylene oxide)
62-PBd	1,2-1,4-polybutadiene \sim 62/30/8 vinyl/ <i>trans/cis</i>
<i>cis</i> -PBd	1,4-polybutadiene \sim 96% <i>cis</i> constant
1,4-PBd	1,4-polybutadiene \sim 50/40/10 <i>trans/cis</i> /vinyl
1,4-1,2-PBd	copolymer of 1,4-polybutadiene and 1,2-polybutadiene 60/40; parent material of PEB-14
<i>cis</i> -PI	1,4-polyisoprene \sim 100% <i>cis</i> content; natural rubber
1,4-PI	1,4-polyisoprene \sim 75/20/5 <i>cis/trans</i> /3,4
<i>alt</i> -PEP	essentially alternating poly(ethylene-co-propylene); hydrogenated 1,4-PI
1,4-PEB	1,4-poly(ethylbutadiene) \sim 75/20/5 <i>cis/trans</i> /3,4
<i>alt</i> -PEB	essentially alternating poly(ethylene-co-1-butene); hydrogenated 1,4-PEB
HHPP	head-to-head polypropylene; hydrogenated poly(2,3-dimethylbutadiene)
a-PP	atactic (in the Bernoullian sense) polypropylene; hydrogenated P2MP
PIB	polyisobutylene
PMA	poly(methyl acrylate)
PMMA	poly(methyl methacrylate)(\sim 75% syndio-tactic)
H ₂ -3,4-PI	copolymer of poly(isopropylethylene) and poly(1-methyl-1-ethylethylene) 75/25; hydrogenated 3,4-PI
PS	polystyrene
PVCH	poly(vinylcyclohexane) from the hydrogenation of polystyrene
PDMS	poly(dimethylsiloxane)
PVE	poly(vinylethylene) or 1,2-polybutadiene
PEE	poly(ethylethylene); hydrogenated PVE
50-PI	polyisoprene copolymer containing 50%-1,4 units and 50%-3,4 units
H ₂ 50-PI	hydrogenated version of 50-PI
1,4-MYRC	1,4-polymycene 97/3 1,4/3,4
H ₂ -1,4-MYRC	hydrogenated 1,4-MYRC
64-MYRC	1,4-3,4 polymycene 64/36 1,4/3,4; parent of H ₂ 64-MYRC
H ₂ 64-MYRC	hydrogenated version of 64-MYRC

deviation from the ideal fundamental assumptions (Eqs. (13.1) and (13.2)) involved in obtaining Eq. (13.4). Nevertheless, the results clearly indicate that n_t is a universal constant, regardless of the great diversity in microstructure.

13.3 Concentration Dependence of n_t

Consider the blend-solution system whose universal viscoelastic behavior has been extensively studied in Chapter 11. Here we replace the weight fraction W_1 of the solvent component by ϕ . Then for the blend solution we have the entanglement molecular weight:

$$M'_e = \frac{M_e}{\phi} \quad (13.5)$$

and the plateau modulus:

$$G'_N = \frac{4}{5} \frac{\phi \rho RT}{M'_e} = \frac{4}{5} \frac{\rho RT}{M_e} \phi^2. \quad (13.6)$$

Using Eqs. (13.1), (13.3), and (13.5), the number of entanglement strands per unit volume and entanglement distance in the blend solution, denoted by n'_v and a' respectively, are obtained as

$$n'_v = \frac{\phi \rho N_A}{M'_e} = n_v \phi^2 \quad (13.7)$$

$$a'^2 = K_\infty M'_e = \frac{a^2}{\phi}. \quad (13.8)$$

Corresponding to Eq. (13.4), the number of entanglement strands per cubed entanglement distance for the blend solution is now defined by

$$n'_t = n'_v a'^3. \quad (13.9)$$

By using Eq. (13.4), the substitution of Eqs. (13.7) and (13.8) into Eq. (13.9) gives

$$n'_t = n_t \sqrt{\phi}. \quad (13.10)$$

Thus, due to the presence of the solvent molecules, the number of entanglement strands per cubed entanglement distance decreases with dilution.

13.4 Packing of Polymer Chains

The fact that n_t is a universal constant for the pure-melt system indicates that the constraint effect of entanglement on the viscoelastic behavior is mainly due to the long length of the polymer chain and basically has nothing to do with the microstructure of the polymer. Regarding each segment as a Kuhn segment, we can assume that each segment is cylindrical-shaped,

with length b and diameter d . The size of a Kuhn segment considered here contains the average contribution of free volume, which necessarily exists among segments. Taking the average n_t to be 18 and by considering the packing of the Kuhn segments in a volume a^3 , we have

$$\frac{\pi}{4}d^2bN_e = \frac{a^3}{18}. \quad (13.11)$$

Using Eq. (13.1), we obtain from Eq. (13.11)

$$N_e = 200 \left(\frac{d}{b} \right)^4 \quad (13.12)$$

which indicates that the number of Kuhn segments per entanglement strand N_e is solely determined by and very sensitive to the aspect ratio d/b of the Kuhn segment; the thinner the freely jointed chain (or the Gaussian chain), the smaller the number of segments in one entanglement strand. Physically, this relation is indeed a very reasonable expectation. Although the microstructural details are ignored in using the Kuhn segment and N_e to obtain Eq. (13.12), whether both the aspect ratio b/d and N_e are universal constants remains to be seen. As discussed extensively in the previous chapters, the viscoelastic behavior of an entangled polymer is universal as expressed in terms of the normalized molecular weight M/M_e (or M/M'_e). Whether universality can extend into the size scale below M_e (for instance, N_e being a universal constant) is not now known. We may say that there is currently a not well-understood gap existing between the Rouse-segment size scale and the entanglement-strand size scale. Some progresses in this area have recently been made as summarized in Appendix 13.A. However, how valid or useful the above analysis in terms of the aspect ratio of the Kuhn segment is, remains to be confirmed by more experimental studies. For polystyrene and cis-polyisoprene, whose M_e and m (or M_K) values are both available (see Tables 13.1–13.3 and Table 1 of Ref. 2), the N_e values agree well with each other: 16 for PS and 17 for cis-PIP. By contrast, the N_e value for polyisobutylene similarly obtained appears somewhat larger (20–36), with a larger uncertainty.

13.5 Some Comments

From the view point that a plateau modulus G_N can only be clearly measured in a nearly monodisperse high-molecular-weight sample, the number of entanglement strands per cubed entanglement distance n_t , which

is calculated using the G_N value, has a clear definition only in the high-molecular-weight region. However, the extensive analysis of the viscoelastic behavior in terms of the ERT shows that M_e does not change with molecular weight decreasing to as low as just above M_e (Chapters 10 and 11). Furthermore, it has been shown in Chapter 11 that, within a small experimental error, the onset of entanglement M_e^o is equivalent to the entanglement molecular weight M_e determined from the plateau modulus according to Eq. (13.2).^{17,18} These results suggest that Eq. (13.4) for n_t remain applicable in the molecular-weight region where a clear modulus plateau is not visible, as long as $M > M_e$. What really affects the polymer viscoelasticity as the molecular weight decreases (such as the gradual disappearance of a clear modulus plateau as M becomes less than about $7M_e$) is not an entanglement-related structural change which would affect n_t , but the decline of the reptation influence and the simultaneous increase in the importance of the primitive-chain-contour-length-fluctuation effect (Chapters 9 and 10).

When Fetters *et al.* reported the voluminous data covering a wide range of G_N (Tables 13.1 and 13.2), they offered another interpretation for n_t as a universal constant. They started with the idea that the larger the dimension of a chain coil, the greater the volume it sweeps out, and the greater the number of other chains it will encounter with which it might entangle. They defined the volume pervaded by the chain as

$$V_{sp} = A \langle R_g^2 \rangle^{3/2} = A \left[\frac{C_\infty M b_o^2}{6m_o} \right]^{3/2} \quad (13.13)$$

where A is a constant of order unity. And they considered the situation that N_{sp} chains, each with molecular weight M , would fill a volume V_{sp} :

$$N_{sp} = \frac{V_{sp} \rho N_A}{M}. \quad (13.14)$$

Then, they defined M_e (which they also linked with the plateau modulus G_N according to Eq. (13.2) as described below) as the molecular weight of a chain at which $N_{sp} = 2$, that is, when there is just one other chain in the spanned volume. Since V_{sp} is proportional to a^3 at $M = M_e$, the argument naturally leads to an equation equivalent to Eq. (13.4), disregarding the difference in the proportional constant. The arbitrariness of setting $N_{sp} = 2$ at $M = M_e$ is absorbed in the proportional constant as well. Fetters *et al.* started by setting N_{sp} equal to 2 at the onset of entanglement, which they assumed to be M_e , and then they moved on to link this M_e with the plateau

modulus G_N according to Eq. (13.2), which is really experimentally defined in the high-molecular-weight region. In view of the result that the onset of entanglement M_e^o is equivalent to the entanglement molecular weight M_e as shown in Chapter 11 and further pointed out above, the argument of Fetters *et al.* might appear equivalent to Lin's. Since entanglement in a monodisperse polymer melt involves many chains, even in the region where entanglements have just begun to occur, it seems somewhat arbitrary to set $N_{sp} = 2$, i.e. only involving two chains, at the onset of entanglement. In effect, as long as N_{sp} is held to be a constant, an equation equivalent to Eq. (13.4) will be obtained. Then, what should N_{sp} be at $M = M_e$? As pointed out above, n_t is only related to the structural aspect which remains the same as long as $M > M_e = M_e^o$.

Appendix 13.A — The Rouse Segment vs. the Kuhn Segment

In its original definition, the Rouse segment is regarded as an artificial structural unit and its size can be arbitrarily chosen for describing slow polymer viscoelastic behavior.¹⁹ When we are interested in the fast dynamic processes in polymer viscoelasticity, such as those that would be theoretically treated as the high Rouse or Rouse–Mooney modes of motion (Chapter 7 and Appendix 9.B), the size of a Rouse segment becomes an issue. The Rouse-segment size of concern here is the smallest Rouse-segment size that can be determined experimentally in accordance with its definition (as in the Rouse theory for polymer viscoelasticity). Related to this subject are the early studies of the Kuhn segment based on the determination of the persistence length by neutron scattering.^{12–14} A logical question to ask is what the relative sizes of the Rouse and Kuhn segments are as determined experimentally in accordance with their respective definitions. While the distribution based on the freely jointed chain is Gaussian (Eq. (1.42)) only when the chain is long (large N), the Gaussian distribution of the Rouse-chain model (Eq. (1.48)) occurs between any two beads in the chain. This difference seems to suggest that it may take a certain number of segments — Kuhn segments — in the freely jointed chain model to form one Rouse segment. But the studies as briefly summarized in the following indicate they are actually nearly of the same size:

If the molecular weight of a Rouse segment, m , is known, the upper modulus bound $G'_R(\omega \rightarrow \infty) = \rho RT/m$ (or in terms of Young's modulus,

$E'_R(\omega \rightarrow \infty) = 3\rho RT/m$ as used in Refs. 1 and 2) for the range of $G'(\omega)$ (or equivalently $G(t)$; see Appendix 10.A) where either the Rouse theory or the ERT is applicable can be predicted. As detailed in Chapter 14, a relaxation modulus $G(t)$ functional form can be assumed to be the sum of an energy-driven process (the glassy relaxation) and entropy-driven modes of motion or processes as well described by the Rouse theory or the ERT. In such a scheme,^{20,21} $G(t)$ is partitioned at the modulus $\rho RT/m$ into the energetic (short-time and high-modulus) and entropic (long-time and low-modulus) regions. As the transition from the former to the latter is basically smooth, one cannot unambiguously extract the value of $\rho RT/m$ from analyzing a measured viscoelastic response alone. Making use of the observed two different coexisting stress optical rules: one applicable to the fast glassy-relaxation region and the other to the slow rubbery (or entropic) region, Inoue and Osaki have obtained the $E'_R(\omega \rightarrow \infty) = 3\rho RT/m$ values for different polymers by analyzing dynamic mechanical and birefringence results together.^{1,2,5,6} From the obtained $E'_R(\omega \rightarrow \infty)$ values they have calculated the m values for different polymers. They have also calculated the molecular-weight values of the Kuhn segment, M_K (Sec. 1.4), from the unperturbed mean square end-to-end and fully extended end-to-end distances of their studied polymers.² They have found that the m and M_K values are the same within experimental errors. Through a theoretical analysis interrelating the depolarized photon-correlation and viscoelastic results of polystyrene concentrated-solution and melt systems, the dynamics and size of a “Rouse” segment have been studied. The value of m estimated from the study is close to the value obtained by Inoue *et al.* for polystyrene. As the Rouse-segment and Kuhn-segment pictures are allowed to be interchanged in the analysis, the study is basically consistent with the conclusion of Inoue and Osaki. For polystyrene, Inoue *et al.* have obtained $m = 850$ and $M_K = 840$ consistent with the values (780–900) obtained by different studies, including persistence-length measurements by neutron scattering.^{7–14} In the later chapters, $m (= M_K) = 850$ will be used in all the analyses of the results of polystyrene.

Due to its entropic spring potential, the Rouse segment is infinitely stretchable (Sec. 6.4.b) and is artificially soft. In spite of this unphysical nature, the Rouse-segment-based molecular theories: the Rouse theory and the ERT are quantitatively successful in describing polymer viscoelastic responses over the entropic region as extensively shown in Chapters 10 and 11. The Kuhn segment as defined in the freely jointed chain model is totally rigid, which is mainly useful for describing the conformation of

a polymer chain — a static property. The excessive softness of a Rouse segment is in sharp contrast to the total rigidity of a Kuhn segment. As m is nearly equal to M_K , this contrast represents a paradox. Trying to understand this paradox, Inoue and Osaki² have suggested that the Rouse segment likely includes contributions from complicated motions, not included in the Rouse-chain model as originally developed. In Chapter 17, stress relaxations of Fraenkel chains obtained by Langevin equation-based Monte Carlo simulations have been analyzed.⁴ As detailed in that chapter, the analyses have given rise to a theoretical basis for resolving the paradox. The physical essence of the basis is that the Fraenkel segment plays a dual role: as the Rouse segment in a Gaussian chain for describing the entropic relaxation process in $G(t)$ and as the Kuhn segment in a freely jointed chain for describing the chain conformation.

References

1. Inoue, T., Okamoto, H., and Osaki, K., *Macromolecules* **24**, 5670 (1991).
2. Inoue, T., and Osaki, K., *Macromolecules* **29**, 1595 (1996).
3. Fraenkel, G. K., *J. Chem. Phys.* **20**, 642 (1952).
4. Lin, Y.-H., and Das, A. K., *J. Chem. Phys.* **126**, 074902 (2007).
5. Inoue, T., Hayashihara, H., Okamoto, H., and Osaki, K., *J. Polym. Sci., Part B: Polym. Phys.* **30**, 409 (1992).
6. Okamoto, H., Inoue, T., and Osaki, K., *J. Polym. Sci., Part B: Polym. Phys.* **33**, 417 (1995).
7. Lin, Y.-H., *J. Polym. Res.* **1**, 51 (1994).
8. Lin, Y.-H., and Lai, C. S., *Macromolecules* **29**, 5200 (1996).
9. Lai, C. S., Juang, J.-H., and Lin, Y.-H., *J. Chem. Phys.* **110**, 9310 (1999).
10. Lin, Y.-H., and Luo, Z.-H., *J. Chem. Phys.* **112**, 7219 (2000).
11. Lin, Y.-H., *J. Phys. Chem.* **109**, 17670 (2005).
12. Wignall, G. D., Schelten, J., and Ballard, D. G. H., *J. Appl. Cryst.* **7**, 190 (1974).
13. Ballard, D. G. H., Rayner, M. G., and Schelten, J., *Polymer* **17**, 349 (1976).
14. Norisuye, T., and Fujita, H., *Polym. J. (Tokyo)* **14**, 143 (1982).
15. Lin, Y.-H., *Macromolecules* **20**, 3080 (1987).
16. Fetters, L. J., Lohse, D. J., Richter, D., Witten, T. A., and Zirkel, A., *Macromolecules* **27**, 4639 (1994).
17. Lin, Y.-H., *Macromolecules* **19**, 159; 168 (1986).
18. Lin, Y.-H., and Juang, J.-H., *Macromolecules* **32**, 181 (1999).
19. Rouse, P. E., Jr., *J. Chem. Phys.* **21**, 1272 (1953).
20. Lin, Y.-H., *J. Phys. Chem. B* **109**, 17654 (2005).
21. Lin, Y.-H., *J. Phys.: Condens. Matter* **19**, 466101 (2007).

Chapter 14

Glass Transition-Related Thermorheological Complexity in Polystyrene Melts

14.1 Introduction

In the short-time or high-frequency region of the viscoelastic response (relaxation modulus $G(t)$, viscoelastic spectrum $G^*(\omega)$ or creep compliance $J(t)$) of a polymer melt with modulus values in the range from $\sim 10^7$ to $\sim 10^{10}$ dynes/cm² (or compliance values in the range from $\sim 10^{-7}$ to $\sim 10^{-10}$ cm²/dyne) the chain dynamics (often referred to as the glassy-, structural- or α -relaxation) is much affected by energetic interactions among microstructural segments.¹⁻⁴ For simplicity we refer to this region as the energetic region. By contrast, the long-time (low-frequency) region with modulus values below $\sim 10^7$ dynes/cm² (corresponding to compliance values larger than $\sim 10^{-7}$ cm²/dyne), where the Rouse-segment-based molecular theories: the ERT and the Rouse theory, are quantitatively applicable⁵⁻⁹ as extensively shown in Chapters 10 and 11, is referred to as the entropic region. Experimental results¹⁰⁻¹⁸ indicate that the temperature dependence of the time scales of (or dynamics in) the energetic region is in general stronger than that of the entropic region. The effect that the time (or frequency)-temperature superposition principle is not applicable when the whole time range covering both the regions is considered is generally referred to as the thermorheological complexity.

The energetic region has rarely been studied for two reasons: one experimental and the other theoretical. Experimentally, accurate measurements of $G(t)$ or $G^*(\omega)$ over the energetic region require an extremely stiff transducer, which, due to lack of enough sensitivity, is in general not suitable for the commonly studied entropic region. For this reason, the experimental $G(t)$ and $G^*(\omega)$ results studied in Chapters 10 and 11 are confined to the

entropic region. As opposed to the ERT and the Rouse theory describing very successfully the viscoelastic relaxation over the entropic region, a molecular theory applicable in the energetic region does not exist. Due to these difficulties, the thermorheological complexity has seldom been studied and analyzed. The thermorheological complexity in polystyrene samples was first investigated by Plazek performing extensive creep compliance measurements. Using a frictionless magnetic bearing, Plazek was able to measure the creep compliance $J(t)$ as small as $\sim 10^{-10}$ cm²/dyne and obtain the $J(t)$ curves over five decades in time scale in a single measurement run in the best cases. Plazek's $J(t)$ results contain rich information about the glassy-relaxation process as well as the associated thermorheological complexity.

Plazek's $J(t)$ results have been analyzed through a scheme using the successful description of the viscoelastic relaxation over the entropic region in terms of the Rouse theory (for entanglement-free systems) or the ERT (for entangled systems) as the frame of reference. In this scheme, the glassy-relaxation process $A_G\mu_G(t)$ [or $A_G^f\mu_G(t)$; Eq. (14.2) or (14.6) and Eq. (14.3)] represented by the stretched exponential or Kohlrausch, Williams, and Watts (KWW) function^{19–21} is incorporated into either of the two theories. The creep compliance is related to the relaxation modulus by the convolution integral Eq. (4.73). With the $G(t)$ functional form given, $J(t)$ can be calculated by means of Eq. (4.73) for comparison with the experimental curves. The convolution integral equation may be solved numerically by the method of Hopkins and Hamming^{22,23} as detailed in Appendix 4.A.

The consistently quantitative capabilities of the ERT and the Rouse theory as detailed in Chapters 10–11 should be exploited, which led to developing the above sketched scheme of analysis. With respect to either of the two theories as the frame of reference, the fast glassy-relaxation process can be studied in perspective. The vital basis for using the ERT as the reference frame in the study of entangled systems is the result that the frictional factor K is independent of molecular weight as expected theoretically (Sec. 10.5). In accord with K carrying the temperature dependence of all the relaxation times in the ERT, the time–temperature superposition principle holds within the entropic region of entangled systems. K being independent of molecular weight, the temperature dependence of the glassy-relaxation time with respect to that of K is expected to behave in a certain universal way. As detailed below, the same can be said about using the Rouse theory as the reference frame for an entanglement-free system.

With the ERT and the Rouse theory successfully applied to the entropic region, $J(t)$ line shapes over the whole time range have been quantitatively analyzed in a systematic way as the KWW form for the glassy relaxation $A_G\mu_G(t)$ is included.

14.2 $G(t)$ Functional Forms

(a) *Entangled case*

Incorporating the glassy-relaxation process $A_G\mu_G(t)$ into the ERT, the relaxation modulus $G(t)$ for a nearly monodisperse entangled sample is expressed as

$$G(t) = G_N F(t) \int f(M) G_E(M, t) dM \quad (14.1)$$

with $G_N G_E(M, t)$ being equal to the right side of Eq. (9.18) and

$$F(t) = 1 + \mu_A(t/\tau_A) + A_G\mu_G(t/\tau_G). \quad (14.2)$$

In Eq. (14.1), $f(M)$ is the molecular-weight distribution of the sample under study, which may be expressed in terms of the Schulz distribution (Eq. (10.3)). The functional forms and relaxation times of the different processes contained in the ERT: $\mu_A(t)$, $\mu_X(t)$, $\mu_B(t)$ and $\mu_C(t)$ have been detailed in Chapter 9. As shown in Chapter 10, the frictional factor K in the three processes: $\mu_X(t)$, $\mu_B(t)$ and $\mu_C(t)$, is independent of molecular weight as expected from the theory. However, the frictional factor in the Rouse–Mooney process $\mu_A(t)$, as denoted by K' , is found greater than K by a factor R_K that depends on the normalized molecular weight M/M_e (Eq. (11.6)) for the polystyrene system. As it turns out, the predetermined $R_K(M/M_e)$ factor plays a very important role in obtaining or discovering the universality of the T_g -related dynamics and thermorheological complexity of the polystyrene system studied in this chapter. The glassy-relaxation process, with the relaxation strength given by A_G , is expressed by the stretched exponential (KWW) function

$$\mu_G(t/\tau_G) = \exp[-(t/\tau_G)^\beta]; \quad 0 < \beta \leq 1, \quad (14.3)$$

which is widely known to describe closely the structural relaxation characteristic of glass-forming liquids or polymer melts. With the relaxation

given by (Eq. (14.3)), the average glassy-relaxation time is defined by

$$\langle \tau \rangle_G = \int_0^\infty \mu_G(t/\tau_G) dt = \frac{\tau_G}{\beta} \Gamma(1/\beta) \quad (14.4)$$

where Γ is the gamma function. Then, the glassy-relaxation time as a function of temperature relative to the time scales of the $\mu_A(t)$, $\mu_X(t)$, $\mu_B(t)$ and $\mu_C(t)$ processes, which are all proportional to the frictional factor K — including $K' = R_K K$ in $\mu_A(t)$ — can be characterized in terms of the structural-growth parameter defined by:

$$s = \frac{\langle \tau \rangle_G}{K}. \quad (14.5)$$

The combination of Eqs. (14.1)–(14.5) may be used to analyze the $J(t)$ results of entangled systems, with s treated as a temperature-dependent fitting parameter, which has the unit Da^2 .

(b) *Entanglement-free case*

As shown in Chapter 11, in an entanglement-free melt or blend solution the viscoelastic spectrum is quantitatively described by the Rouse theory over the entropic region. The onset of entanglement has been observed by monitoring the initial deviation from the Rouse theory as the molecular weight or concentration increases. The observed onset molecular weight of entanglement is in close agreement with the entanglement molecular weight, M_e or M'_e (Eq. (11.4)) calculated from the plateau modulus (Eqs. (8.2) and (11.A.3)). Furthermore, the $G(t)$ and $G'(\omega)$ line shapes of a series of entangled blend solutions have been quantitatively analyzed in terms of the linear combination of the ERT and the Rouse theory, respectively, multiplied by the weight fractions of the entangled and entanglement-free components (Eq. (11.5)). As shown by the quantitative line-shape analyses, the frictional factor K in the ERT is the same as that in the Rouse theory within a small possible experimental error ($< 20\%$). In other words, the two theories are on the same footing at the Rouse-segmental level. Thus, Eq. (14.5) is equally applicable in an entanglement-free system as long as its molecular weight is greater than that of a Rouse segment. Then, corresponding to Eqs. (14.1)–(14.4) for a nearly monodisperse entangled polymer melt, the relaxation modulus for an entanglement-free melt is expressed by

$$G(t) = A_G^f \mu_G(t) + \rho RT \int \frac{f(M)}{M} \mu_R(t, M) dM. \quad (14.6)$$

In Eq. (14.6), $\mu_R(t, M)$ representing the Rouse relaxation for the component with molecular weight M is expressed by

$$\mu_R(t, M) = \sum_{p=1}^{N-1} \exp\left(-\frac{t}{\tau_p}\right) \quad (14.7)$$

(in accordance with Eq. (7.58) with the notation s_P being replaced by τ_p here) with the relaxation times $\{\tau_p\}$ given by Eq. (7.56) or (7.57). And A_G^f is the full relaxation strength of the glassy relaxation and is related to A_G of Eq. (14.2) by $A_G^f = A_G \rho RT / M_e = (5/4) A_G G_N$. Incorporating $A_G \mu_G(t)$ into the ERT or $A_G^f \mu_G(t)$ into the Rouse theory is intended as a phenomenological description. As the relaxation times of $\mu_X(t)$, $\mu_B(t)$ and $\mu_C(t)$ are all much longer than the slowest in $\mu_G(t)$, it makes no practical difference to express the glassy relaxation either as the $A_G \mu_G(t)$ term inside $F(t)$ (Eq. (14.2)) or as a separate term $A_G^f \mu_G(t)$ in Eq. (14.6).

The number of the Rouse segments per chain with molecular weight M as contained in Eq. (7.56) or (7.57) can be defined as

$$N = \text{cint}(M/m) + 1 \quad (14.8)$$

where the function $\text{cint}(x)$ converts a number x to an integer by rounding the fractional part of x . For the analyses of polystyrene systems, $m = 850$ as given in Appendix 13.A is used.

In terms of the $G(t)$ functional forms given above, the $J(t)$ curves of two entangled (samples A and B) and one entanglement-free (sample C) nearly monodisperse samples (Plazek) and the $G^*(\omega)$ spectra of four entanglement-free nearly monodisperse samples (L10, A5000, A2500 and A1000; Inoue *et al.*¹⁵) have been analyzed quantitatively and consistently. The weight average molecular weights of all these samples are given in Table 14.1. As the ultimate significance of the studies presented in this chapter is based on the literal applications of the Rouse theory and the ERT, the analyses are explained and discussed in detail.

14.3 $J(t)$ Line-Shape Analyses of Entangled Systems

(a) *Line-shape fitting procedure*

The successful application of the ERT to the entropic region of the viscoelastic response of entangled systems has been shown by extensive analyses of the $G(t)$ and $G'(\omega)$ results (Chapter 10). As expected from this, the $J(t)$ line shape (at a certain temperature) of an entangled sample over the

Table 14.1 Characteristics: M_w , M_w/M_n and T_g (based on DSC and defined at $\tau_S = 1,000$ sec) and parameters: A_G^f , β and Z extracted by analyzing the creep-compliance $J(t)$ curves or viscoelastic spectra $G^*(\omega)$ of the polystyrene samples, whose structural-relaxation times τ_S , structural-growth parameters s' and frictional factors K' are displayed, respectively, in Figs. 14.13, 14.14 and 14.15. Also shown are the K values at 127.5°C of samples A, B, C and F2 along with the average value of K shown in Table 10.1; and the M_w , M_w/M_n , and T_g (DCS) of F2. The reference theory used in each analysis is indicated.

Sample	M_w	Z (M_w/M_n)	Theory	K (s/Da ²) (127.5°C)	$A_G^f \times 10^{-9}$ dynes/cm ²	β	T_g (°C) ($\tau_S = 1,000$ sec)	T_g (°C)* (DSC)	Displayed in Figs. 14.13, 14.14 or 14.15
A	46,900	20(1.05)	ERT	4.8×10^{-9}	12.95	0.41	97	97.1	τ_S , s' , K' from $J(t)$
B	122,000	20(1.05)	ERT	†	9.73	0.41	98.0 ₃ (99.5 ₅ ‡)	100	τ_S , s' , K' from $J(t)$
C	16,400	20(1.05)	Rouse	4.15×10^{-9}	9.93	0.42	93.8	93.8	τ_S , s' , K' from $J(t)$
F2	16,700	120(1.01)	ERT	4.0×10^{-9}				93.9	
Average value from Table 10.1 M_w from 3.4×10^4 to 6×10^5			ERT	$4.9 \times 10^{-9} \pm 10\%$					
L10	10,500	50(1.02)	Rouse		9.93	0.42	90.0 ₃	90	τ_S , s' , K' from $G^*(\omega)$
A5000	5,970	50(1.02)	Rouse		10.9	0.42	81.6 ₄	82	τ_S , s' , K' from $G^*(\omega)$
A2500	2,630	20(1.05)	Rouse		10.9	0.42	59.4 ₃	59.6	τ_S , s' , K' from $G^*(\omega)$
A1000	1,050	(1.13)			11.5	0.36	6.2 ₂		τ_S from $G^*(\omega)$

*Read from Fig. 14.12.

†Because s-B is contaminated by residual plasticizers, its K value at 127.5°C is not listed.

‡Correction for the contamination by the residual plasticizers has been made, which is explained in Sec. 14.12.

rubber(like)-to-fluid region is well described by Eq. (14.1) with a properly chosen polydispersity parameter Z for the Schulz distribution $f(M)$. A full-range $J(t)$ curve can be calculated through Eq. (4.73) from Eq. (14.1) with K fixed at a certain value and a set of A_G , β and s parameters as contained in Eqs. (14.2)–(14.5). The A_G , β and s parameters mainly affect the short-time/small-compliance region ($< \sim 5 \times 10^{-7}$ cm²/dyne). In the initial stage of the fitting procedure, the line shape of $J(t)$ is the main concern. Full-range $J(t)$ curves calculated with A_G , β and s as adjustable parameters are allowed to be shifted along the time axis (log scale) to find the one that best fits the $J(t)$ line shape measured at a certain temperature. In this way close fittings to the $J(t)$ line shapes of samples A and B at different temperatures are obtained as shown in Figs. 14.1 and 14.2, respectively.^a Of particular importance are the temperature-dependent s values extracted from the $J(t)$ line-shape fitting analyses. The experimental $J(t)$ results shown in Figs. 14.1 and 14.2 are those shown in Fig. 1 of Ref. 10 and Fig. 7 of Ref. 11, respectively, which have all been reduced using 100°C as the reference temperature for the compliance (i.e. multiplied by $\rho T / \rho_0 T_0$ with ρ_0 being the density at $T_0 = 373$ K). Accordingly, all the theoretical $J(t)$ curves are calculated at $\rho T / \rho_0 T_0 = 1$. Following Plazek's notation, a thus calculated $J(t)$ is denoted by $J_p(t)$; the corresponding relaxation modulus $G(t)$ is denoted by $G_p(t)$. In Figs. 14.1 and 14.2, all the theoretical $J_p(t)$ curves are calculated with $K = 5 \times 10^{-9}$; and the experimental data points (at individual temperatures) are superimposed on the calculated curves by a shift along the time axis. The time coordinate axis with respect to which all the $J_p(t)$ curves calculated with the same K are shown is referred to as a K -normalized time coordinate axis; and a time scale on it as a K -normalized time scale. 5×10^{-9} is nearly the K value of polystyrene at 127.5°C (see Table 10.1). Thus, Figs. 14.1 and 14.2 use a mixed reference system: 100°C as the reference temperature for the compliance coordinate (for $\rho T / \rho_0 T_0 = 1$) and 127.5 (± 0.4)°C for the K -normalized time coordinate. Being wavy, each $J_p(t)$ curve has three bending points: two concaves and one convex as shown in the figures. Each bending point being a characteristic position in the two-dimensional plot of $\log J_p(t)$ vs. $\log t$, matching the calculated and measured curves around each bending point allows the absolute value of compliance (independent of temperature as all being at the reference temperature 100°C) and the K -normalized time scale (dependent on temperature) to be determined. And the simultaneous

^aFigures 14.1, 14.2 and 14.7 are formed by superimposing the experimental data points on the calculated curves using commercially available graphics software.

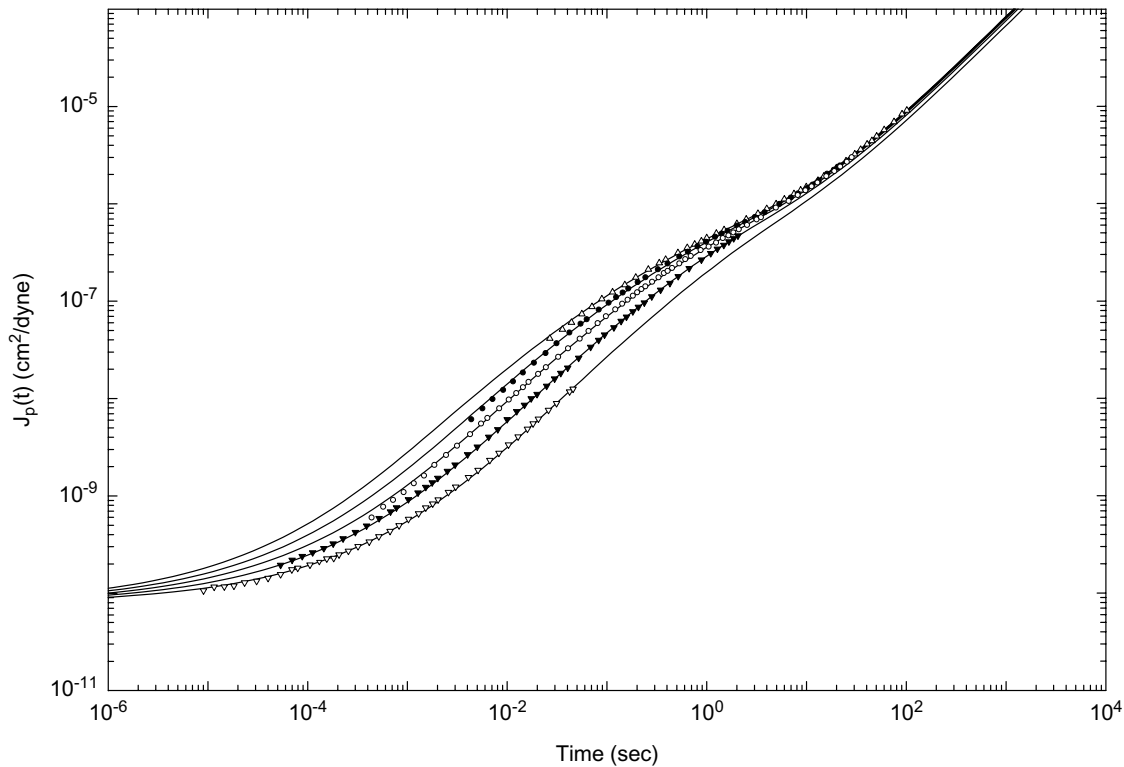


Fig. 14.1 Creep compliance $J_p(t)$ data of sample A measured at 114.5 (Δ); 109.6 (\bullet); 104.5 (\circ); 100.6 (\blacktriangledown); and 97 (∇) $^\circ$ C superimposed on the corresponding theoretical curves (solid lines; from left to right, respectively) calculated using $K = 5 \times 10^{-9}$, $G_N = 1.89 \times 10^6$ dyn/cm 2 , and the A_G , β and s values obtained as explained in the text and listed in Tables 14.1 and 14.2.

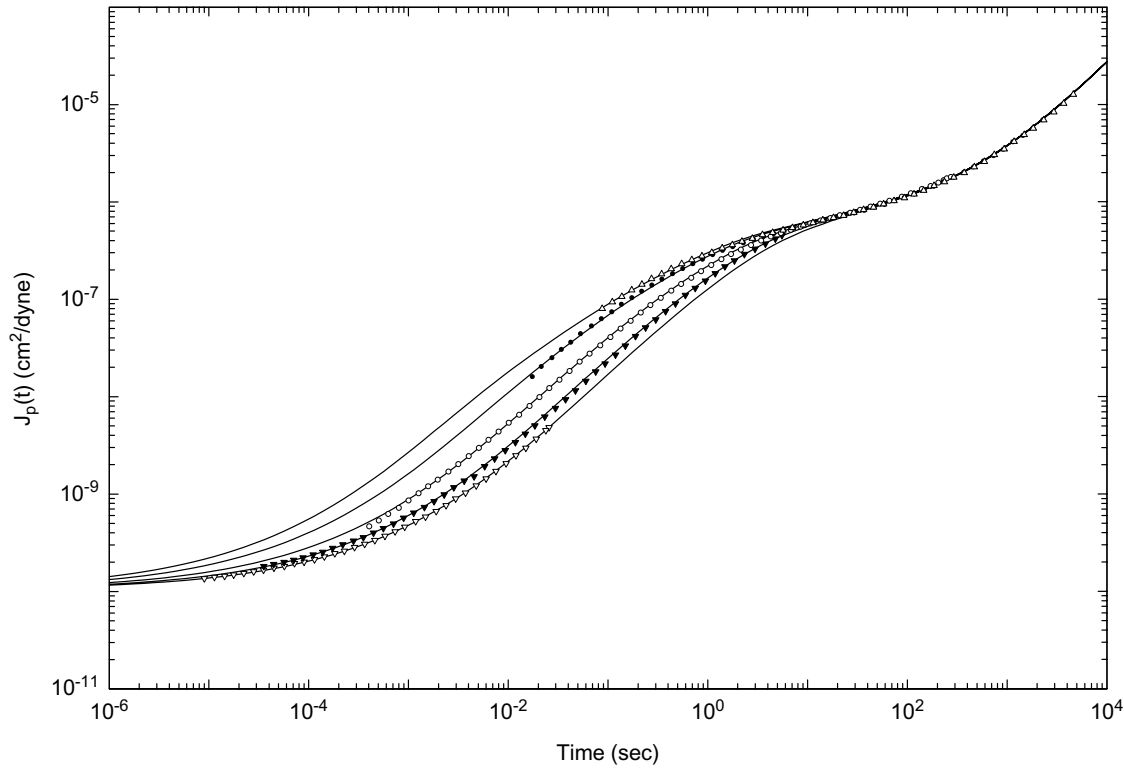


Fig. 14.2 Creep compliance $J_p(t)$ data of sample B measured at 119.8 (Δ); 113.8 (\bullet); 105.5 (\circ); 101.0 (\blacktriangledown); and 98.3 (∇) $^\circ\text{C}$ superimposed on the corresponding theoretical curves (solid lines; from left to right, respectively) calculated using $K = 5 \times 10^{-9}$, $G_N = 1.89 \times 10^6$ dyn/cm 2 , and the A_G , β and s values obtained as explained in the text and listed in Tables 14.1 and 14.2.

matching over two bending points is a key criterion for determining the line shape of $J_p(t)$. For the shown close agreements between the calculated and measured $J_p(t)$ curves, in the case of sample A, no shift along the compliance axis is required at different temperatures. In the case of sample B, no shift along the compliance axis is required at 105.5, 101.0 and 98.3°C, while a shift of the experimental data upwards by $\sim 5\%$ has been made (for a slightly better agreement than can be achieved without making such a shift) at 119.8 and 113.8°C. From each superposition, a time-scale shift factor SF is obtained, which, when multiplied by 5×10^{-9} , gives the K value at the corresponding temperature. Thus determined K values at different temperatures are listed in Table 14.2. For sample A at 125°C and sample B at 134.5°C, the measured $J_p(t)$ curves cover the region with compliance from $\sim 4 \times 10^{-7}$ to $\sim 3 \times 10^{-5}$ cm²/dyne, which, as discussed below, can only be used to determine their K values. As trustworthy s values for sample A at 125°C and sample B at 134.5°C are not obtainable, their full-range $J_p(t)$ curves are not calculated and shown in Figs. 14.1 and 14.2. The K value of sample A at 127.5°C as shown in Tables 10.1, 14.1 and 14.2 is calculated from its K value at 125°C using the viscosity ratio of the sample between the two temperatures.¹²

(b) *Fitting parameters*

In analyzing the $J_p(t)$ line shapes as described above, conditions have to be satisfied to ensure that the close fittings at different temperatures as shown in Figs. 14.1 and 14.2 are unique and physically meaningful. This is best explained through discussing one by one the parameters M_e , K , K' (or $R_K(M)$), Z , m , A_G , β , and s involved in describing the $J_p(t)$ line shapes over eight decades in time scale in one case and nine decades in the other case. As explained below, some of these parameters have been predetermined; some are uniquely determined in a particular region of $J_p(t)$; and some may be regarded as equivalent to predetermined ones. As detailed below, K and Z correlate with the *time scale* and *line shape*, respectively, of the region of $J_p(t)$ with compliance $> \sim 5 \times 10^{-7}$ cm²/dyne; s with the *time scale* of $J_p(t)$ over the region $< \sim 5 \times 10^{-7}$ cm²/dyne; and A_G and β with the *line shape* of $J_p(t)$ over the region $< 10^{-8}$ cm²/dyne.

The entanglement molecular weight M_e has been predetermined from the plateau modulus — a static property. An error in the M_e value will lead to an error in the obtained K value as both M_e and K appear in the equations for the relaxation times τ_A , τ_X , τ_B and τ_C as pointed out

Table 14.2 Structural and dynamic quantities: s' , K , K' and τ_S extracted by analyzing the experimental $J(t)$ curves of samples A and B at different temperatures.

Sample A					Sample B				
Temp (°C)	K (s/Da ²)	$K' = 1.61K$ (s/Da ²)	$s' = s/1.61$ (Da ²)	τ_S (s)	Temp (°C)	K (s/Da ²)	$K' = 3.16K$ (s/Da ²)	$s' = s/3.16$ (Da ²)	τ_S (s)
97	9.84×10^{-4}	1.58×10^{-3}	35,090	1,000	[98.0 ₃]*	$[4.40_3 \times 10^{-4}]$	$[1.39 \times 10^{-3}]$	[39,930]	[1,000]
100.6	9.7×10^{-5}	1.56×10^{-4}	17,560	49.4	98.3	3.6×10^{-4}	1.14×10^{-3}	38,060	779
104.5	1.2×10^{-5}	1.93×10^{-5}	10,150	3.53	101	6.02×10^{-5}	1.9×10^{-4}	24,500	83.9
109.6	1.2×10^{-6}	1.93×10^{-6}	6,244	0.217	103.3	1.52×10^{-5}	4.79×10^{-5}	18,640	16.1
114.5	1.96×10^{-7}	3.16×10^{-7}	3,903	0.0222	105.5	5.43×10^{-6}	1.72×10^{-5}	13,033	4.03
125	9.08×10^{-9}	1.46×10^{-8}			113.8	1.49×10^{-7}	4.71×10^{-7}	5,474	4.64×10^{-2}
127.5	4.8×10^{-9}	7.68×10^{-9}			119.8	2.61×10^{-8}	8.25×10^{-8}	2,867	4.26×10^{-3}
					134.5	8×10^{-10}	2.53×10^{-9}		

*Values listed in brackets at this temperature are calculated from the equations obtained by least-squares fittings to the values determined at different temperatures; see the text.

in Chapter 10. The M_e value used in the $J_p(t)$ line-shape analyses is the value 13,500 that has been well determined and used in the extensive $G(t)$ and $G'(\omega)$ line-shape analyses over the entropic region as detailed in Chapter 10.

$Z = 20$ is obtained for both samples A and B giving $M_w/M_n = 1.05$ which is within the range expected for a nearly monodisperse sample as those falling between $Z = 30$ and 120 extracted from the $G(t)$ and $G'(\omega)$ curves over the terminal region (Chapter 10). The Z parameter mainly correlates with the *line shape* over the portions of $J_p(t)$ with compliance $> \sim 5 \times 10^{-7}$ cm²/dyne but not with their *time scales*, with which the K value is sensitively correlated. Possible small uncertainties in Z virtually have no effect on the obtained K value.

The K'/K ratios, being determined by the time scale of the $\mu_A(t)$ process relative to those in the plateau-terminal region (the $\mu_X(t)$, $\mu_B(t)$ and $\mu_C(t)$ processes) have been extracted from the $G(t)$ and $G'(\omega)$ line-shape analyses (Chapters 10 and 11) and shown to be closely described by the empirical Eq. (11.6). The K'/K values used in the analyses of the $J_p(t)$ curves of samples A and B are calculated from Eq. (11.6).

The molecular weight of a Rouse segment, m , has been determined independently (see Appendix 13.A). The m value mainly affects the interface between the energetic region (dominated by the $A_G\mu_G(t)$ process) and the entropic region (described by the $\mu_A(t)$, $\mu_X(t)$, $\mu_B(t)$ and $\mu_C(t)$ processes in the ERT). The separation between $A_G\mu_G(t)$ and $\mu_A(t)$ in Eqs. (14.1) and (14.2) represents a discontinuity as the separation between the first and second terms of Eq. (14.6) does. The same discontinuity is also embodied in Inoue's analyses of dynamic mechanical and birefringence results (Appendix 13.A). Using Eqs. (14.1)–(14.5) (or Eqs. (14.3)–(14.7)) for the $J_p(t)$ line-shape analyses, we have substituted a discontinuity for a smooth transition as should occur in reality. The discontinuity picture can be considered as a first-order approximation and should work well if the location of the discontinuity as represented by the m value is properly determined. The discontinuity approximation and the value $m = 850$ used in the calculations are supported by the close agreements between the calculated and the measured $J_p(t)$ curves as shown in Figs. 14.1 and 14.2 (and Fig. 14.7).

The K value is well determined by the *time scales* of the portions of $J_p(t)$ with compliance $> \sim 5 \times 10^{-7}$ cm²/dyne. The accuracy of the obtained K value may be illustrated by the value obtained for sample A at 127.5°C being in close agreement the values obtained previously (Table 10.1). At the same time, the Z value, being sensitive mainly to the line shape of

$J_p(t)$ over the same region, is well within the expected range. Thus, to the same effect, we may regard K and Z as predetermined parameters as M_e , $R_K(M)(K'/K$ or K' with K determined) and m are. In other words, A_G , β , and s are the main fitting variables, which affect $J_p(t)$ only over the short-time/small-compliance region. The end result is the seamlessly quantitative and consistent descriptions of the $J_p(t)$ curves at different temperatures over the whole time range.

Among the three variables A_G , β , and s , A_G is basically dictated by the glassy modulus, the reciprocal of the glassy compliance J_G , and β is determined by the $J_p(t)$ line shape over the small-compliance region, $< 10^{-8}$ cm²/dyne. The determination of s (Eq. (14.5)), which sensitively correlates with the K -normalized time scales of the $J_p(t)$ curve in the $10^{-8} \sim 5 \times 10^{-7}$ cm²/dyne region and is effectively *decoupled* from how A_G and β are obtained. Figure 14.3 compares three $J_p(t)$ curves calculated at three different β values: 0.36, 0.41 and 0.46; all with $A_G = 5482$ and $s = 56,550$ as obtained for sample A at 97°C. The one with $\beta = 0.41$ is the

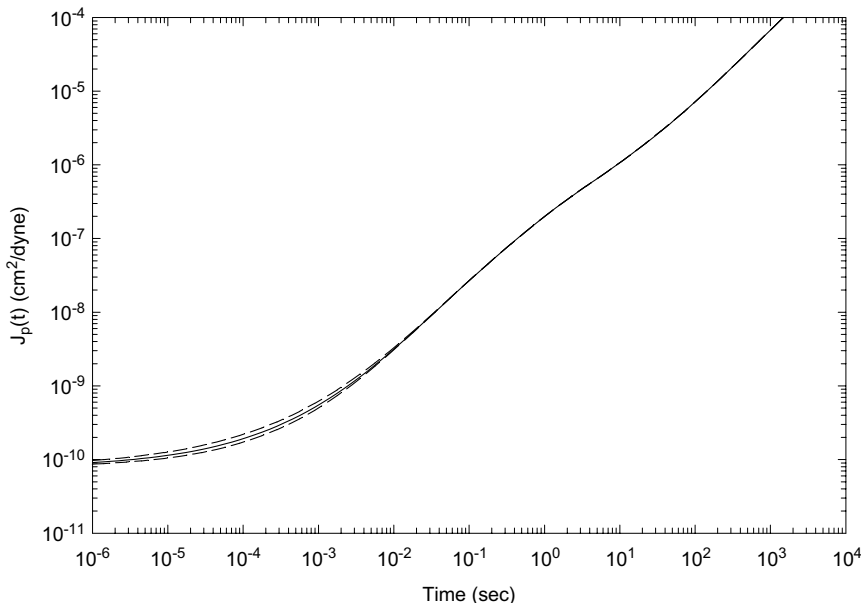


Fig. 14.3 Comparison of the $J_p(t)$ curves calculated using $A_G = 5,482$ and $s = 56,550$ at $\beta = 0.36$ (upper dashed line), 0.41 (solid line) and 0.46 (lower dashed line); the one at $\beta = 0.41$ is the same as the calculated curve shown in Fig. 14.1 for sample A at 97°C.

calculated curve shown in Fig. 14.1 for sample A at 97°C. The comparison illustrates the sensitivity of the $J_p(t)$ line shape over the small-compliance region ($< 10^{-8}$ cm²/dyne) to changes in β . From comparing the differences among the curves calculated at three different β values and the close agreement of the calculated $\beta = 0.41$ curve with the experimental points shown in Fig. 14.1, the uncertainty of $\beta = 0.41$ should be well within ± 0.02 . Figure 14.3 also illustrates the independence of the $J_p(t)$ curve over the s -sensitive region $10^{-8} \sim 5 \times 10^{-7}$ cm²/dyne from variations in β as pointed out above.

Thus, s values at different temperatures can be uniquely obtained by fitting the calculated $J_p(t)$ curves closely to the measured ones as shown in Figs. 14.1 and 14.2 with A_G and β well determined by the small-compliance region. In other words, the whole thermorheological complexity in $J_p(t)$ of the polystyrene samples is reduced to the simple temperature dependence of the obtained s values as shown in Fig. 14.4. This reduction is of particular

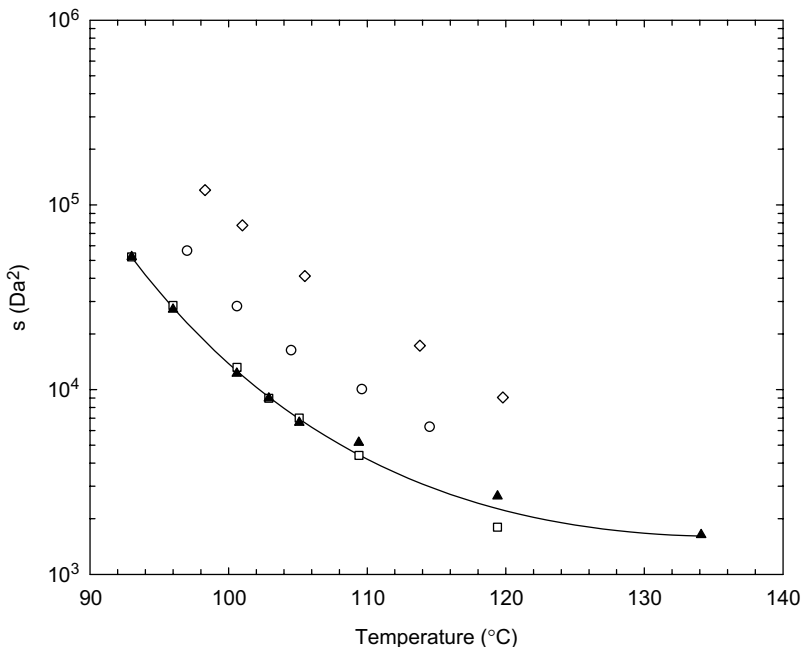


Fig. 14.4 s values as a function of temperature of samples A (o), B (◇) and C (□) determined by the $J_p(t)$ line-shape analyses; ▲ determined by matching the calculated and experimental J_{ep}^0 values; the solid line is the best fit of the modified VTF equation to the ▲ data points).

significance as we notice in Figs. 14.1 and 14.2 that the shift with temperature in the $\sim 5 \times 10^{-7}$ cm²/dyne region is not as large as that in the $\sim 10^{-8}$ cm²/dyne region. One observes that the shift with temperature changes gradually with time scale (K -normalized) between the two regions. This time-scale dependence of the shift factor in $J_p(t)$ is referred to as the temporally uneven thermorheological complexity as it occurs over a considerably wide range, larger than two decades of time scale. The temporal unevenness over the range is fully and uniquely described by adjusting the single parameter s as indicated above. Concurrently, the simple temperature dependence of s has a clear physical meaning: the temperature dependence of the glassy-relaxation process being stronger than that of the entropy-driven ones. This is clearly illustrated in Fig. 14.5 by the comparison of the $G_p(t)$ curves — with time scale normalized by

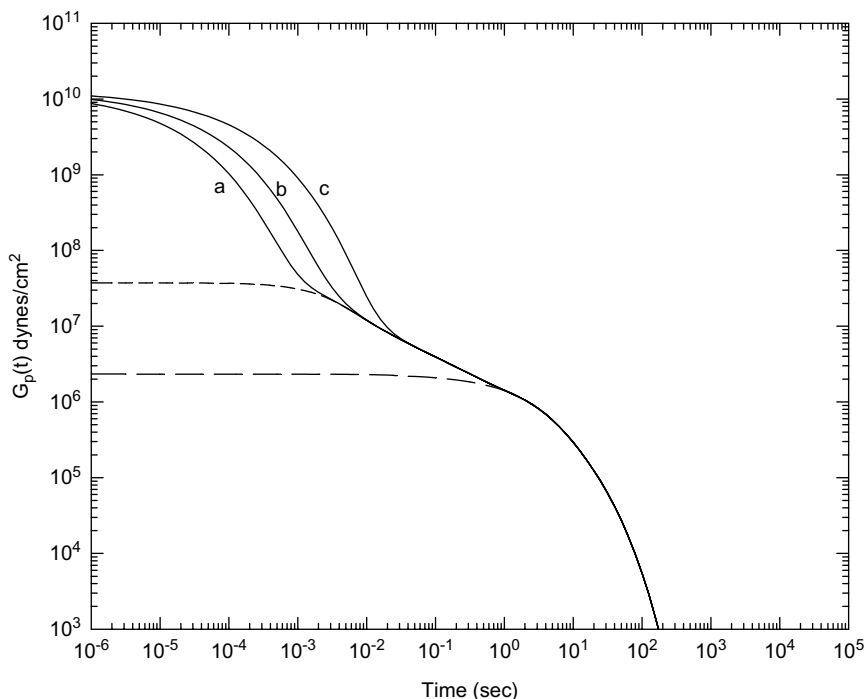


Fig. 14.5 Comparison of the $G_p(t)$ curves (solid lines) corresponding to three $J_p(t)$ curves shown in Fig. 14.1 for sample A: a for 114.5°C; b for 104.5°C; and c for 97°C. The short-dash line is calculated without the $A_G\mu_G(t)$ process; the long-dash line is calculated without both the $A_G\mu_G(t)$ and $\mu_A(t)$ processes.

$K = 5 \times 10^{-9}$ — corresponding to the three $J_p(t)$ curves of sample A at 114.5, 104.5 and 97°C shown in Fig. 14.1. In contrast to the temporal unevenness of thermorheological complexity in $J_p(t)$, the shift factor in $G_p(t)$ changes quite abruptly from the value over the glassy-relaxation region to that over the entropic region. As will be shown below, the temporal unevenness of thermorheological complexity in $J_p(t)$ arises from the smearing of the different processes by the convolution integral Eq. (4.73).

On the surface, there are eight parameters involved in fitting the calculated $J_p(t)$ curves quantitatively to the measured ones over the whole time range. The above discussion explains why the *whole* thermorheological complexity in $J_p(t)$ is uniquely represented by the simple change in s with temperature. All the other parameters can be determined independently beforehand or by analyzing $J_p(t)$ with respect to line shape or time scale in a specific region, which is insensitive to changes in s .

The obtained K value of sample A at 127.5°C as well as the A_G and β values for samples A and B are listed in Table 14.1. Due to the contamination by residual plasticizers, the K value of sample B is not listed for comparison and the A_G of sample B is about 25% smaller than that of sample A. As discussed below (Sec. 14.9 and 14.10), the small decrease in the K and A_G values due to the contamination in sample B basically does not affect the conclusion that will be developed based on its s values obtained at different temperatures.

Here, it should be stressed that the theoretical basis for the scheme that enables the $J_p(t)$ results to be quantitatively analyzed is ultimately the frictional factor K in the ERT being independent of molecular weight as expected. The ERT having met this crucial criterion for its validity, theoretically there is no limit to the time range of $J_p(t)$ that can be analyzed, depending on the molecular weight of the sample under study.

(c) *Smearing Effect in $J(t)$*

Shown in Fig. 14.6 is the comparison of the curves of $\log G_p(t)$ and $\log J_p(t)^{-1}$ vs. $\log t$ calculated with $K = 5 \times 10^{-9}$ using the s value corresponding to 114.5°C for sample A. One sees that the $G_p(t)$ curve has clear line-shape features showing the separate processes as given in Eqs. (14.1) and (14.2), while the solution of the convolution integral Eq. (4.73) for calculating $J_p(t)$ smears the separate features greatly. To illustrate this further, both the $G_p(t)$ and $J_p(t)^{-1}$ curves calculated without the contribution of the $A_G\mu_G(t)$ process are shown for comparison with the full curves.

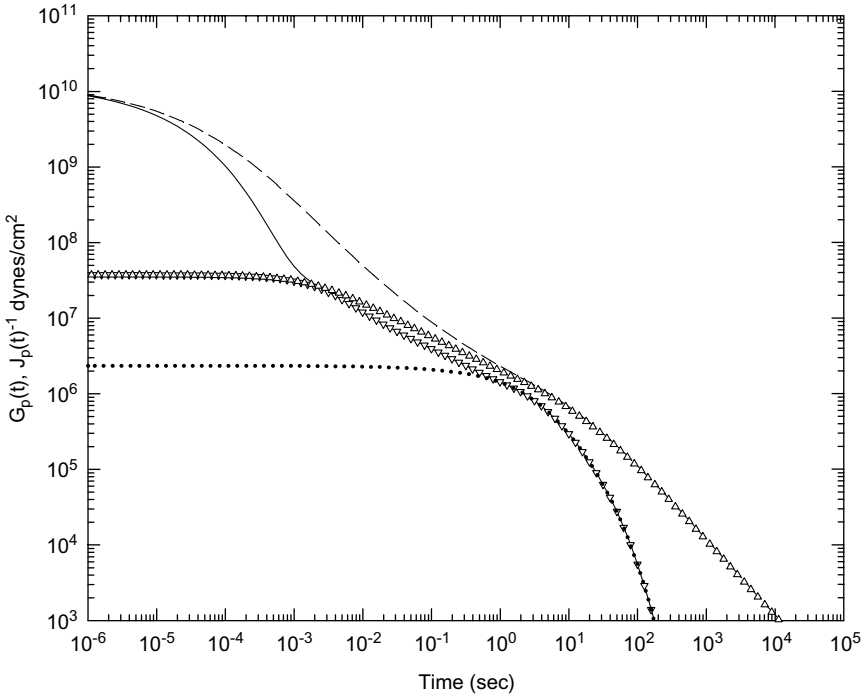


Fig. 14.6 Comparison of the $G_p(t)$ (solid line) and $J_p(t)^{-1}$ (dashed line) curves for sample A at 114.5°C (the same $G_p(t)$ as curve a shown in Fig. 14.5; the same $J_p(t)$ as the corresponding one shown in Fig. 14.1). Also shown are the $G_p(t)$ (∇) and $J_p(t)^{-1}$ (Δ) curves calculated without the $A_G\mu_G(t)$ process, and the $G_p(t)$ curve (dotted line) calculated without both the $A_G\mu_G(t)$ and $\mu_A(t)$ processes.

Clearly, the contribution of $A_G\mu_G(t)$ to $J_p(t)$ extends its influence to the (K -normalized) time scale of the $\mu_A(t)$ process; in contrast, the $A_G\mu_G(t)$ and $\mu_A(t)$ processes in $G_p(t)$ are localized in their individual time-scale regions and are well separated. Thus, the stronger temperature dependence of the $\mu_G(t)$ process can much affect $J_p(t)$ in the time-scale region of the $\mu_A(t)$ process. In other words, in $J_p(t)$ the effect of the increase in s with decreasing temperature extends to the region around $\sim 5 \times 10^{-7}$ cm²/dyne instead of being localized in the region of the glassy relaxation $\mu_G(t)$. As the effect diminishes gradually with increasing time scale, the temperature dependence of the time scale in the region around $\sim 5 \times 10^{-7}$ cm²/dyne is not as strong as that in the glassy-relaxation region — this is the temporal unevenness of the thermorheological complexity in $J_p(t)$ pointed out

above. The unevenness has been first observed by Plazek (see Fig. 9 of Ref. 11) saying “The divergence seen in the region of the ‘knee’ of the reduced (recoverable compliance) curve indicates that all of the retardation mechanisms do not have the same temperature dependence.” Indeed, this observation was an unusual discovery as Plazek stated “This discrepancy would not have been detected without a large range of time scale (of measurement).” However, without the help of a valid molecular theory as the base, this observed phenomenon had remained unexplained for many years. Now it is clear that the intricacy arises mainly from the smearing effect of the convolution integral (Eq. (4.73)) and the source of the whole phenomenon is traced back to a physical effect that can be simply stated: the glassy relaxation having a stronger temperature dependence — as evidently shown in Fig. 14.5. For sample B, a similar comparison of the curves of $\log G_p(t)$ and $\log J_p(t)^{-1}$ vs. $\log t$ as that shown in Fig. 14.6 is observed as it should. In the case of sample A, the glassy-relaxation process has a small effect on the flow region of $J_p(t)$. The effect is more noticeable in sample A than in sample B, because the terminal region of the former with a smaller molecular weight is closer to the glassy-relaxation region in time scale than that of the latter. The effect becomes more obvious as s becomes larger with decreasing temperature (see Fig. 14.1). In an entanglement-free system as studied below with a molecular weight being even smaller, the $J_p(t)$ curves at different temperatures become even more featureless because of the smearing effect. To ensure the uniqueness and correctness of the $J_p(t)$ line-shape analyses in the entanglement-free case, consistencies with the analyses of the results of steady-state compliance J_e^0 and viscosity η_0 have to be checked as detailed below.

14.4 Analyses of $J(t)$, J_e^0 and η_0 in an Entanglement-Free System

The $J(t)$ curves of an entanglement-free system can be analyzed in terms of Eqs. (14.3)–(14.8) in the same way as those of the entangled systems in terms of Eqs. (14.1)–(14.5). For an entangled system, a full discussion of the uniqueness and significance of the involved parameters or fitting parameters and their predeterminations or determinations have been given in Sec. 14.3.b. In an entanglement-free system, the number of parameters is reduced as the ratio K'/K and the entanglement molecular weight M_e are not involved. As far as the glassy-relaxation process is concerned, the involved fitting parameters in entangled and entanglement-free systems are

the same. Thus, the discussion of fitting parameters given in Sec. 14.3.b is equally applied to entanglement-free systems.

Given the facts that sample C has a molecular weight just slightly above the entanglement molecular weight M_e and a molecular-weight distribution not extremely narrow, it is not immediately clear whether it is an entangled or entanglement-free system. For achieving quantitative agreements between the calculated and measured results for both $J(t)$ and J_e^0 of sample C, the following factors need to be evaluated and determined: (1) The choice of the functional form — i.e. Eq. (14.1) or Eq. (14.6) or even a linear combination of Eqs. (14.1) and (14.6) (namely, using Eq. (11.5) as the reference frame) if the system behaves as an entangled blend solution. (2) The Z parameter for the molecular weight distribution $f(M)$. (3) The A_G (or A_G^f) and β values for the glassy-relaxation process. They can best be found by a process of trial and error until consistent quantitative agreements are obtained. For sample C, it has been found that the combination of Eq. (14.6) and $Z = 20$ gives the best result. The use of Eq. (14.6) and the choice $Z = 20$ are closely related to each other. In view of sample C's M_w value being above M_e (13,500), Eq. (14.1) instead of Eq. (14.6) should be used. However, sample C's molecular-weight distribution, though nearly monodisperse, is broad enough to have a sufficient total amount of components with molecular weights below M_e , rendering the system entanglement-free by dilution. With $Z = 20$ ($M_w/M_n = 1.05$), sample C has 21 wt% of the distribution below M_e . The dilution increases the entanglement molecular weight from M_e to $M_e' = 17,090$ as calculated from Eq. (11.4). As $M_e' > M_w$, sample C immerses in an entanglement-free state. By contrast, because of its extremely narrow molecular weight distribution, F2 does not exhibit signs of entanglement dilution even though it has a similar weight-average molecular weight ($M_w = 16,700$):^b The viscoelastic responses $G(t)$ and $G'(\omega)$ of F2 clearly could not be described by the Rouse theory over the entropic region (Chapter 10). Instead they have been successfully analyzed in terms of the ERT with $Z = 120$ ($M_w/M_n < 1.01$) and $K'/K = 1$. In Table 14.1, the frictional factor K of F2 obtained from the analysis presented in Chapter 10 is also listed for later discussions.

As s increases in sample C, the time scale of the glassy-relaxation process becomes closer to those of the Rouse modes of motion; and the steady-state compliance J_e^0 is predicted to decline according to Eq. (4.66). For sample C,

^bCorrection: The F2 sample with $M_w = 16,700$ was wrongly referred to as F1 in Ref. 4. Both F1 and F2 are samples studied in Refs. 6 and 7.

a computer program can be set up to scan through a wide range of s to calculate a large set of J_e^0 values (Eq. (4.63)), from which those matching with the values determined experimentally at different temperatures can be identified. The A_G^f and β values listed in Table 14.1 for sample C allow consistent and quantitative matching of the calculated results with the $J(t)$ line shapes from 93 to 119.4°C and the J_e^0 values from 93 to 134.1°C obtained by Plazek. The A_G^f and β values are, respectively, uniquely dictated by the compliance values and line shapes of $J(t)$ at 93 and 96°C — namely, the short-time/low-compliance region of $J(t)$. As shown in Table 14.1, the β value of sample C is consistent with those obtained for samples A and B. And the A_G^f value for sample C is between those for samples A (corresponding to $A_G = 5,482$) and B (corresponding to $A_G = 4,119$). As indicated above, the A_G^f value of sample B being smaller is due to the contamination by residual plasticizers. A_G^f of sample C being smaller than that of sample A should be at least partly due to its smaller molecular weight. Furthermore, the A_G^f and β values of sample C are in close agreement with those of three nearly monodisperse entanglement-free polystyrene melts, L10, A5000 and A2500 (Table 14.1), obtained by analyzing their viscoelastic spectra using the same scheme, as will be presented below.

100°C has been used as the reference temperature at which all the calculated and measured viscoelastic quantities of sample C are compared after being adjusted by multiplying them by the factor $\rho T / \rho_0 T_0$. As in the entangled systems studied above, the adjusted $J(t)$ is denoted by $J_p(t)$; and the corresponding viscoelastic quantities $G(t)$, J_e^0 and η_0 are denoted by $G_p(t)$, J_{ep}^0 and η_p , respectively. Thus, the experimental J_e^0 values listed in Table II of Ref. 12 are first adjusted by multiplying them by $\rho T / \rho_0 T_0$. With the A_G^f and β values determined for sample C, the s values at different temperatures are determined by matching the calculated J_{ep}^0 with the adjusted experimental values. These s values are then used to calculate the $J_p(t)$ line shapes — calculated with $\rho T / \rho_0 T_0 = 1$ — for comparison with the adjusted measured curves (those shown in Fig. 1 of Ref 12). In general, the agreements between the thus calculated $J_p(t)$ curves and the measured are very close. The s values (shown in Fig. 14.4) obtained by matching the calculated J_{ep}^0 values with the measured ones have been modified slightly in some cases to obtain a better agreement between the calculated and measured $J_p(t)$ line shapes as shown in Fig. 14.7. Each of the theoretical $J_p(t)$ curves is first calculated with $K = 10^{-4}$. In superposing the calculated $J_p(t)$ on the measured at a certain temperature, shifting only along the log-time axis is allowed. From each superposition, a time-scale shift

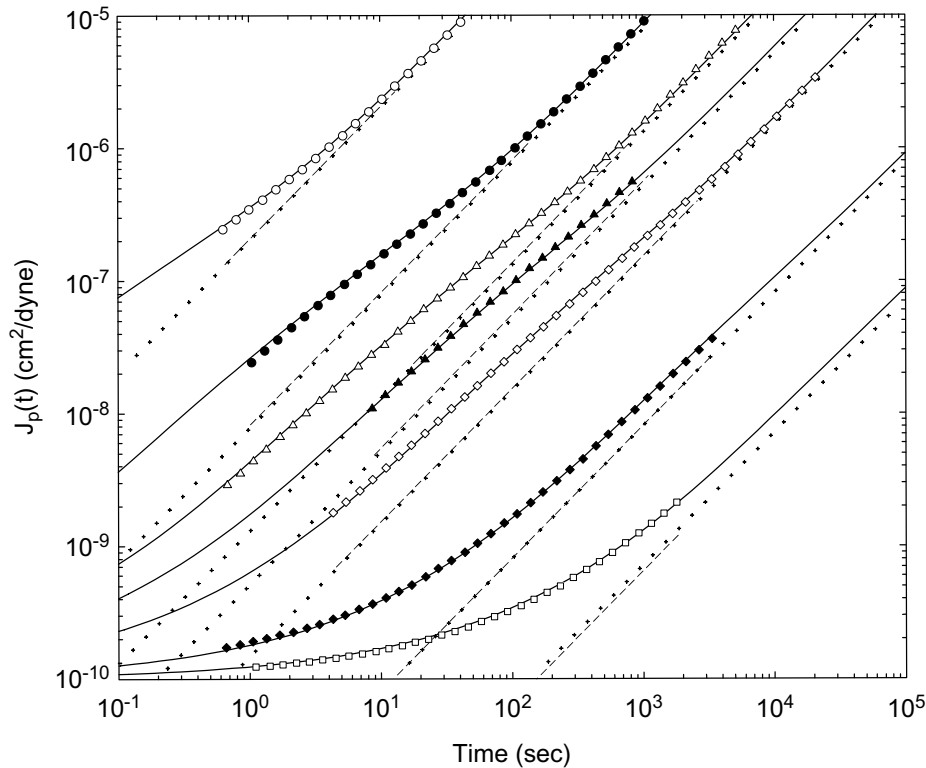


Fig. 14.7 Creep compliance $J_p(t)$ data of sample C measured at 119.4 (\circ); 109.4 (\bullet); 105.1 (Δ); 102.9 (\blacktriangle); 100.6 (\diamond); 96 (\blacklozenge); and 93 (\square) $^\circ$ C superimposed on the theoretical curves (solid line; left to right, respectively) calculated with the s and K values at the corresponding temperatures as listed in Table 14.3; and the A_G^f and β values obtained as explained in the text and listed in Table 14.1. Also shown are the individual comparisons between the experimental (dashed line) and calculated (+ + +) long-time $J_p(t)$ limits, t/η_p , at the corresponding temperatures.

factor SF is obtained, which when multiplied by 10^{-4} gives the K value at the corresponding temperature. Except for the results at 134.1°C , s values obtained by fitting the calculated to the measured $J_p(t)$ line shapes and the corresponding K values at different temperatures are listed in Table 14.3. At 134.1°C , due to the lack of an experimental $J_p(t)$ curve, the s value obtained by matching the calculated and experimental J_{ep}^0 values is listed in Table 14.3. The K value at 134.1°C has been determined in an indirect way using the *viscosity enhancement factors* at different temperatures that can be calculated from the s values as explained in the following:

In general the glassy relaxation of a polymer is orders of magnitude faster than the terminal relaxation if its molecular weight is not particularly small. The contribution of the glassy relaxation to the zero-shear viscosity η_p — referred to as the *internal viscosity* (Sec. 10.3.a) — is thus negligible if the molecular weight of the sample is sufficiently large. In the case of sample C whose molecular weight is not large, the contribution of the internal viscosity to η_p cannot be neglected. At low temperatures, its viscosity is particularly enhanced by the presence of the glassy-relaxation process. Using the obtained s values, including the one at 134.1°C , the viscosity values of sample C containing the internal-viscosity contributions can be calculated, as listed under the $\eta_P(K = 10^{-4})$ column in Table 14.3 with K set at 10^{-4} . Enhancements due to the glassy-relaxation process at different temperatures can be numerically evaluated by comparing the $\eta_P(K = 10^{-4})$ values with that calculated with the same K value but without the glassy-relaxation process (i.e. setting $A_G^f = 0$ in the calculation; the first row of Table 14.3). The extent of enhancement is expressed as the ratio $\eta_P(K = 10^{-4}) / \eta_p(K = 10^{-4}; A_G^f = 0)$, whose values are also listed in Table 14.3. The contribution of the internal viscosity is only 11% at 134.1°C and increases gradually more rapidly with decreasing temperature, enhancing the viscosity by a factor of 4.6 at 93°C . As shown in Fig. 14.8, the large viscosity enhancement due to the glassy-relaxation process at a low temperature is reflected by the large shift of the corresponding $J_p(t)$ curve in the flow (long-time) region to larger K -normalized time scales ($K = 10^{-4}$ for all calculated curves) from one at a high temperature.

Dividing a measured viscosity value by the product of $\rho T / \rho_0 T_0$ and $\eta_p(K = 10^{-4}) / \eta_p(K = 10^{-4}; A_G^f = 0)$, a reduced viscosity value, denoted by η_R , is obtained. The η_R value, without the contribution of the internal viscosity and independent of the small change in modulus with temperature, is linearly proportional to K . Then, the K value at 134.1°C can be calculated by multiplying the K values at other temperatures by the ratio

Table 14.3 Structural and dynamic quantities extracted by analyzing the experimental $J(t)$ curves of sample C at different temperatures.

Temp (°C)	$s' = s$ (Da ²)	$K' = K$ (s/Da ²)	$\log \eta_p$ ($K = 10^{-4}$)	$\eta_p / \eta_p (A_G = 0)$ ($K = 10^{-4}$)	$\rho T / \rho_0 T_0$	$\log \eta_0^{\ddagger}$ exp.	$\log \eta_0$ calcd	$\log J_e^{0\ddagger}$ exp.	$\log J_e^0$ calcd	τ_S (s)
$A_G = 0$			10.159	1						
134.1	(16,40)*	(1.06×10^{-9})	(10.205)	(1.111)	1.072	5.257	(5.261)	-6.75	(-6.75)	(3.13×10^{-5})
127.5		$[4.15 \times 10^{-9}]^{\dagger}$								$[1.28 \times 10^{-4}]^{\dagger}$
119.4	18,00	3.09×10^{-8}	10.210	1.125	1.042	6.730	6.717	-6.79	-6.75	1.00×10^{-3}
109.4	44,00	6.89×10^{-7}	10.275	1.306	1.021	8.116	8.122	-6.90	-6.87	5.46×10^{-2}
105.1	70,00	3.6×10^{-6}	10.331	1.486	1.012	8.882	8.893	-6.96	-6.98	4.54×10^{-1}
102.9	89,90	8.33×10^{-6}	10.370	1.626	1.008	9.270	9.294	-7.05	-7.05	1.35
100.6	13,200	2.45×10^{-5}	10.442	1.919	1.003	9.820	9.832	-7.16	-7.19	5.82
96	28,500	2.89×10^{-4}	10.633	2.979	0.993	11.088	11.090	-7.54	-7.57	1.48×10^2
93.7 ₆	$[43,960]^{\dagger}$	$[1.19 \times 10^{-3}]^{\dagger}$								$[1,000]^{\dagger}$
93	52,300	2.08×10^{-3}	10.825	4.635	0.987	12.156	12.138	-7.94	-7.94	1.96×10^3

*The s value at 134.1°C is determined by matching the calculated and experimental J_{ep}^0 values. All the values in brackets at 134.1°C are derived from the thus determined s value as detailed in the text.

[†]Calculated from the equations obtained by least-squares fittings to the values determined at different temperatures; see the text.

[‡]Values obtained from Table II of Ref. 12.

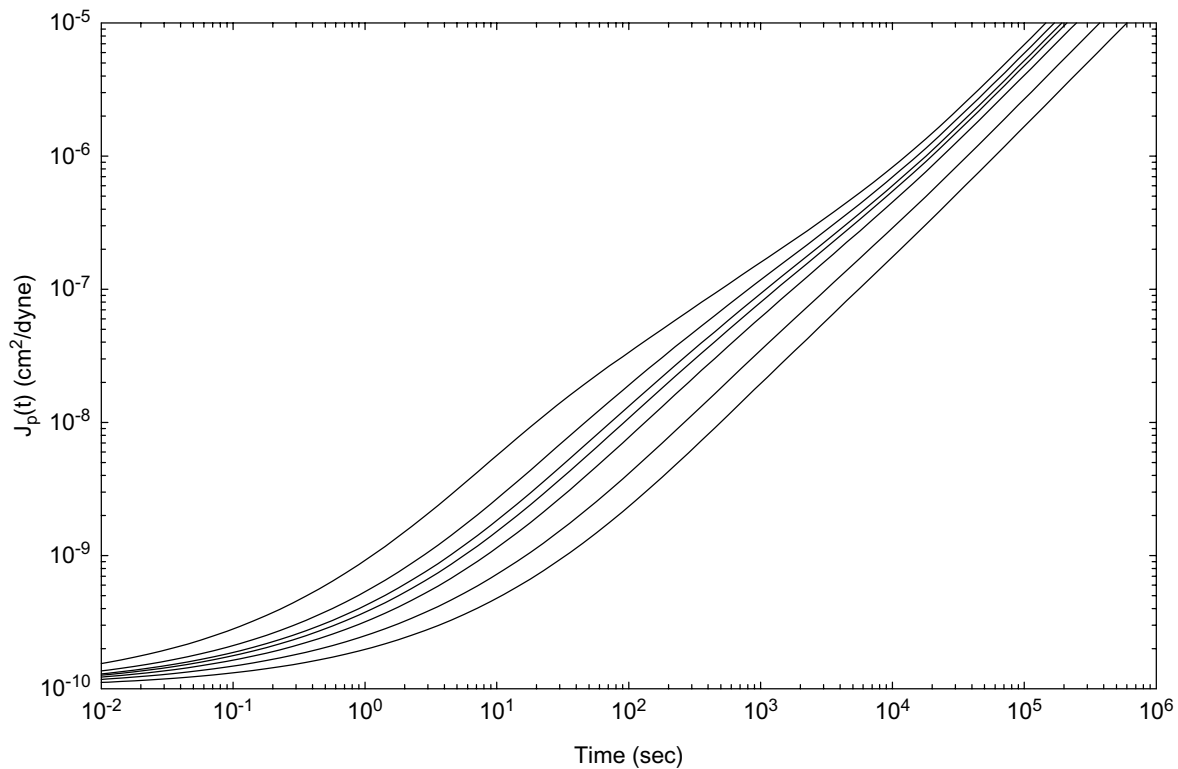


Fig. 14.8 Comparison of creep compliance $J_p(t)$ curves of sample C calculated using $K = 10^{-4}$ and the s values (listed in Table 14.3) corresponding to the calculated curves shown in Fig. 14.7 (lines from left to right corresponding to 119.4, 109.4, 105.1, 102.9, 100.6, 96 and 93 °C, respectively).

$\eta_R(134.1^\circ\text{C})/\eta_R(t^\circ\text{C})$. In this way, the average K value at 134.1°C obtained from the K values at seven other temperatures is 1.06×10^{-9} with a standard deviation of only 3.5%. As any substantial error in s can cause a large error in the calculated η_R values, especially at low temperatures, the small standard deviation implies that the s values are consistently and correctly obtained from the $J_p(t)$ line-shape analyses.

The inclusion of the glassy-relaxation process allows us to adjust the s values such that the calculated $J_p(t)$ line shapes are fitted closely to the measured curves and the calculated and experimental J_{ep}^0 values are matched at different temperatures. Still, whether concurrently the calculated viscosity values containing the internal-viscosity contributions are in agreement with the values measured at different temperatures need to be checked. Multiplying the $\eta_P(K = 10^{-4})$ values by the shift factor SF (equivalent to $K/10^{-4}$) and the ratio $\rho T/\rho_0 T_0$ gives the theoretical viscosity values at the corresponding temperatures, as listed under the $\eta_0(\text{calcd})$ column in Table 14.3. The $\eta_0(\text{calcd})$ values, including at 134.1°C , are in close agreement with the measured values as listed under the $\eta_0(\text{exp})$ column in Table 14.3, confirming the validity of the analysis. The validity is equivalently confirmed by the agreements between the calculated and measured $J_p(t)$ long-time limits t/η_p at different temperatures as shown in Fig. 14.7.

The two sets of s values as a function of temperature: one obtained from the analyses of the J_{ep}^0 data and the other obtained by analyzing the $J_p(t)$ curves, are in close agreement (Fig. 14.4), indicating the consistency between the two sets of analyses. The consistency is equivalently indicated by the close agreement between the experimental J_e^0 values and those calculated using the s values obtained from the $J_p(t)$ line-shape analyses, as listed in Table 14.3 and shown in Fig. 14.9. This agreement explains quantitatively the decline in J_e^0 of a low-molecular-weight sample with temperature decreasing towards T_g as due to the temperature dependence of the glassy-relaxation process being stronger than that of the entropy-driven modes of motion.

The K values shown in Table 14.3 for sample C can be well fitted by the Vogel–Tammann–Fulcher (VTF) equation^{24–26} or the Williams–Landel–Ferry (WLF) equation.²⁷ From the VTF equation with the parameters obtained from the fitting, the K values at 127.5 and 93.7°C are calculated and listed in Table 14.3, with the former also listed in Table 14.1. The result of K (and τ_S) at 93.7°C is used in sections 14.8 and 14.10.a where the structural relaxation time and the length scale at T_g are defined or studied.

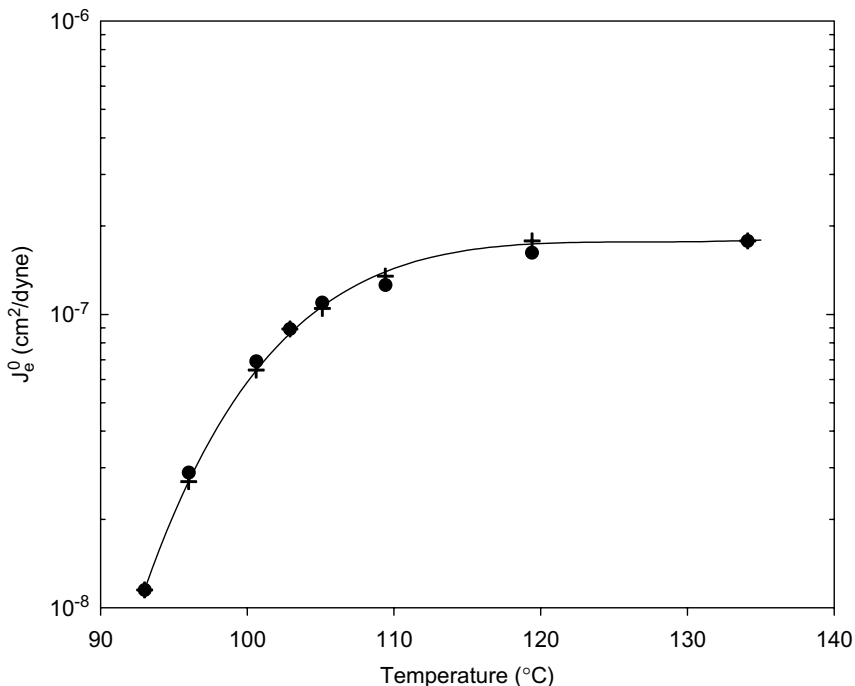


Fig. 14.9 Comparison of the measured J_e^0 values (●) of sample C with those calculated (+) using the s values obtained from the $J_p(t)$ line-shape analyses and the curve calculated from the empirical functional form $\log(J_e^0) = a + b/x + c/x^2 + d/x^3$ (x being the temperature in °C) best fitted to the calculated values. Note: As the $J_p(t)$ curve at 134.1°C is not available for analysis to obtain the s value, the J_e^0 value at 134.1°C used in the least-squares fitting is the experimental value itself.

14.5 Analyses of the $G^*(\omega)$ Spectra of Entanglement-Free Systems

The $G^*(\omega)$ spectra of L10, A5000, and A2500 are quantitatively analyzed in terms of Eqs. (14.3)–(14.8) just as the $J_p(t)$ line shapes of sample C have been. The calculation of $G^*(\omega)$ from a $G(t)$ functional form can be accurately carried out numerically according to the procedure described in Appendix 14.A. In the case of A1000, as the contribution of the Rouse modes of motion is negligible due to its very small molecular weight — about that of a single Rouse segment $m = 850$ — $G^*(\omega)$ is analyzed in

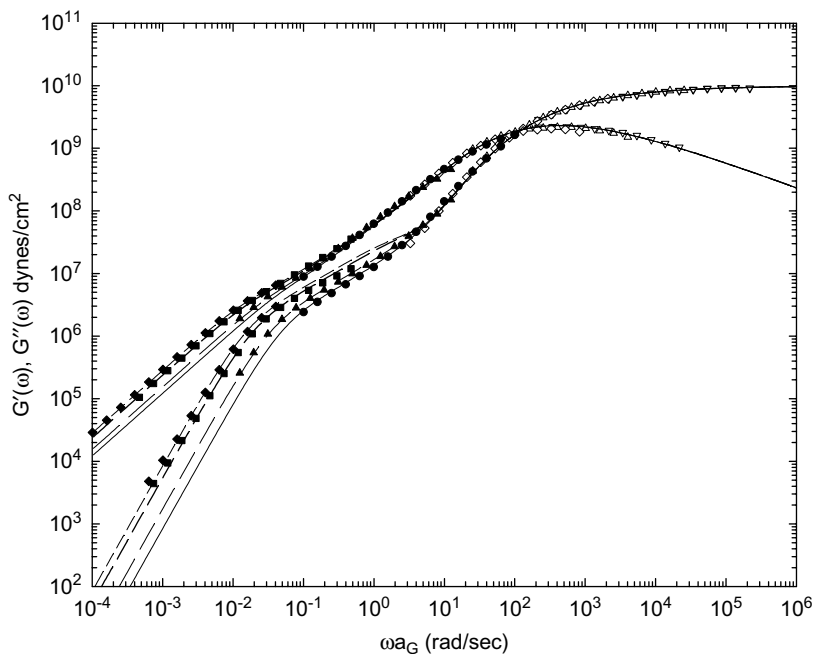


Fig. 14.10 The viscoelastic spectra $G^*(\omega)$ of L10 measured at different temperatures (∇ at 92°C ; Δ at 95°C ; \diamond at 99°C ; \bullet at 105°C ; \blacktriangle at 110°C ; \blacksquare at 120°C ; and \blacklozenge at 130°C) composed together by matching all the spectra over the glassy-relaxation region (using 105°C ($\Delta T = 15\text{K}$) as the reference temperature) and superimposed on the corresponding calculated curves (the glassy-relaxation region: solid line; the entropic region: solid line at 105°C ($\Delta T = 15\text{K}$), long-dash line at 110°C ($\Delta T = 20\text{K}$), medium-dash line at 120°C ($\Delta T = 30\text{K}$), and short-dash line at 130°C ($\Delta T = 40\text{K}$)).

terms of only a stretched exponential function for the glassy relaxation (Eq. (14.3)). Comparisons of the calculated and measured $G^*(\omega)$ spectra are shown in Fig. 14.10 for L10. And those for samples, A5000, A2500 and A1000 are shown in Fig. 14.11.

In these figures, the spectrum at a certain temperature is chosen for each sample as the reference (for instance 105°C for L10), with which the line shapes of the spectra measured at different temperatures are matched over the glassy region to form a composite spectrum. From such a process, the time-scale shift factors a_G with respect to the reference spectrum

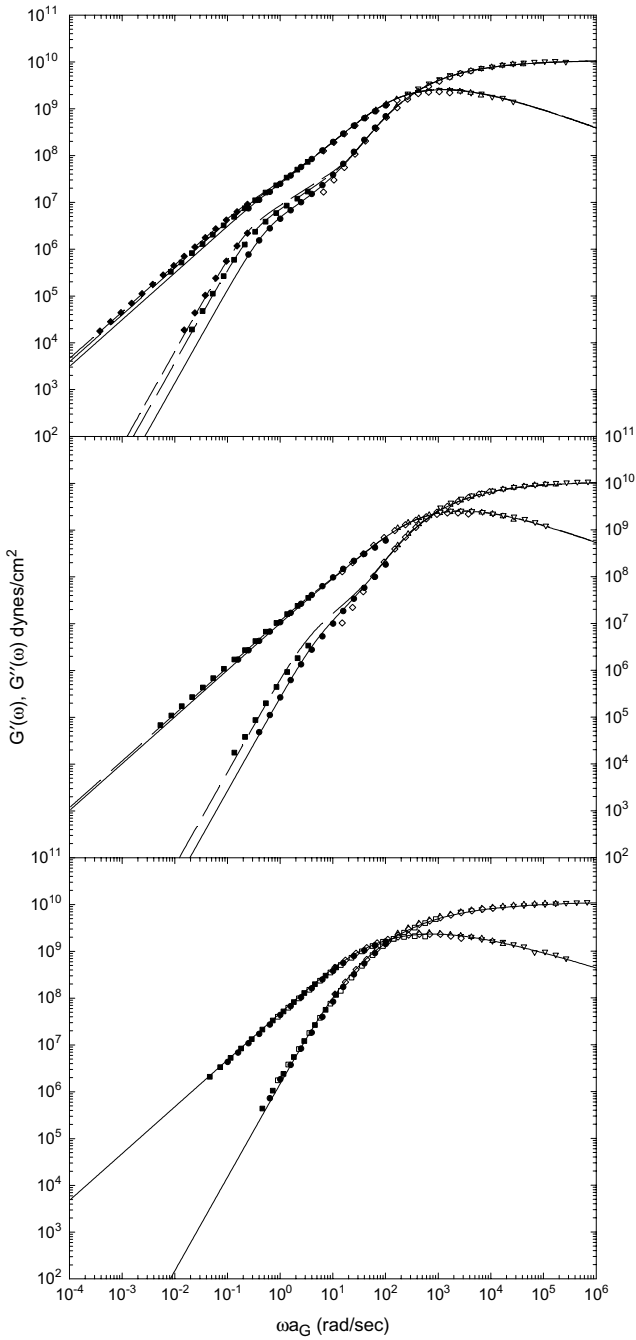


Fig. 14.11 (Figure on facing pages) Top: The viscoelastic spectra $G^*(\omega)$ of A5000 measured at different temperatures (∇ at 85°C; Δ at 88°C; \diamond at 92°C; \bullet at 100°C; \blacksquare 110°C; and \blacklozenge at 120°C) composed together by matching all the spectra over the glassy-relaxation region (using 100°C as the reference temperature) and superimposed on the corresponding calculated curves (the glassy-relaxation region: solid line; the entropic region: solid line at 100°C, long-dash line at 110°C, and short-dash line at 120°C). Middle: The viscoelastic spectra $G^*(\omega)$ of A2500 measured at different temperatures (∇ at 62°C; Δ at 65°C; \diamond at 70°C; \bullet at 80°C; and \blacksquare at 90°C) composed together by matching all the spectra over the glassy-relaxation region (using 80°C as the reference temperature) and superimposed on the corresponding calculated curves (the glassy-relaxation region: solid line; the entropic region: solid line at 80°C, and long-dash line at 90°C). Bottom: The viscoelastic spectra $G^*(\omega)$ of A1000 measured at different temperatures (∇ at 5°C; Δ at 10°C; \diamond at 15°C; \square at 20°C; \bullet at 25°C; and \blacksquare at 30°C) composed together by matching all the spectra over the glassy-relaxation region (using 25°C as the reference temperature) and superimposed on the calculated curve (solid line).

are obtained at different temperatures.^c For each sample, the average glassy-relaxation time at the reference temperature, $\langle\tau\rangle_G^0$, is determined by matching the calculated spectrum with the composite spectrum over the glassy-relaxation region. The $\langle\tau\rangle_G$ values at different temperatures are then calculated by multiplying the obtained $\langle\tau\rangle_G^0$ values by the shift factors a_G for each sample. Concurrently, the parameters A_G^f and β are extracted by fitting the calculated line shapes to the composite spectra over the glassy-relaxation region. As listed in Table 14.1, the values of A_G^f and β obtained for L10, A5000 and A2500 are consistent with those of samples A, B and C. The M_w/M_n value of A1000 indicates that its molecular-weight distribution is broader than those of the other samples. With its small M_w value, A1000 should contain components with chain lengths as short as and shorter than the length scale associated with the glassy-relaxation process in a typical polystyrene sample with chain length of at least several times larger than a Rouse segment. As a result, its glassy-relaxation

^cIt may not be entirely proper to shift the viscoelastic spectra along the log-modulus axis over the glassy-relaxation region in accordance with the theory of rubber elasticity (i.e. using $\rho_0 T_0 / \rho T$ as the shift factor) to form the composite spectra. At the same time the largest temperature differences between the spectra measurements are no more than 25K and no superposition indicates a shift along the log-modulus axis is needed. Thus, the spectra at different temperatures are superposed on each chosen reference spectrum by shifting them only along the log-frequency axis. Technically, this is slightly different from the analyses of the creep compliance $J(t)$ and the steady-state compliance J_e^0 which have all been made on the results reduced along the compliance axis by the multiplication factor $\rho T / \rho_0 T_0$ using 100°C as the reference temperature. However, any discrepancies that may arise from this difference are expected to be negligibly small for the reasons as just explained above.

time distribution is directly broadened by its molecular-weight distribution, leading to a β value smaller than those for the other samples.

The $G^*(\omega)$ line shapes of L10, A5000 and A2500 in the entropic (or Rouse) region are affected by their molecular-weight distributions, though not in a sensitive way. It is sufficient to just use the Z values in the Schulz molecular-weight distributions corresponding to the respective M_w/M_n values listed by Inoue *et al.*¹⁵ without any further adjustment to calculate the $G^*(\omega)$ spectra. The thus calculated spectra match closely with the measured ones (Figs. 14.10 and 14.11), confirming the molecular weight value (850) of a Rouse segment of polystyrene.

Just as in the cases of samples A, B and C, $\langle\tau\rangle_G$ (or structural-relaxation times τ_S ; see Eq. (14.10)) of L10, A5000 and A2500 can be separated into two decoupled quantities: the structural-growth parameter s and the frictional factor K . As in the $J_p(t)$ line-shape analyses, s is entirely determined by the line shape of the $G^*(\omega)$ spectrum that spans over both the glassy-relaxation and entropic regions, while K is calculated from the time-scale shift factor. However, the way in which the $G^*(\omega)$ spectra at different temperatures are presented in Figs. 14.10 and 14.11 is “opposite” to that in which the $J_p(t)$ (Figs. 14.1, 14.2 and 14.8) and $G_p(t)$ (Fig. 14.5) curves are shown. The $G^*(\omega)$ spectra are matched with one another over the glassy-relaxation region, while the $J_p(t)$ and $G_p(t)$ curves are composed together using the same frictional factor K in calculating the shown theoretical curves. Thus, here the shift factor a_G is first used to calculate $\langle\tau\rangle_G$ (or τ_S); then the frictional factor K is calculated from Eq. (14.5) using the s value determined by the line-shape analysis. By contrast, K (as well as $K' = R_K K$ in the cases of samples A and B) is first calculated directly from the time-scale shift factor obtained by matching the calculated and experimental $J_p(t)$ curves.

14.6 Dynamic Anisotropy in Entangled Systems

The K values obtained by analyzing the viscoelastic results of polystyrene samples with different molecular weights from 3.4×10^4 to 6×10^5 in terms of the ERT give an average of 4.9×10^{-9} with a standard deviation of 10% at 127.5°C (Table 10.1). With $M_w = 1.24M_e$ the K value of F2 is only about 20% below the average value (Table 14.1). As opposed to the molecular-weight independence of K extending to a molecular weight virtually as low as just above M_e , T_g starts to decrease with decreasing molecular weight

around $11M_e$ as shown in Fig. 14.12.^{28,29} From the conventional viewpoint of the relation between viscoelastic dynamics and T_g as related to free volume, the contrast represents a paradox. As discussed briefly in Chapter 10, the paradox can be explained by the physical picture that the free volume at both chain ends is always available to the modes of motion along the primitive path — namely the $\mu_X(t)$, $\mu_B(t)$ and $\mu_C(t)$ processes — whose relaxation times are all proportional to K . Such a mechanism may allow K to be disengaged from dependence on the average free volume in the bulk and become independent of molecular weight. Thus, it has been proposed that the decrease in T_g with decreasing molecular weight in the entangled region should be related to the molecular-weight dependence of the ratio $K'/K = R_K(M/M_e)$ — as described by the empirical Eq. (11.6) in the case of polystyrene. Equation (11.6) has been obtained by fitting the empirical function to the K'/K ratios obtained by analyzing the $G(t)$ and $G'(\omega)$ line shapes of nearly monodisperse polystyrene samples. From a plateau value 3.3 at high molecular weights, $R_K(M/M_e)$ declines gradually

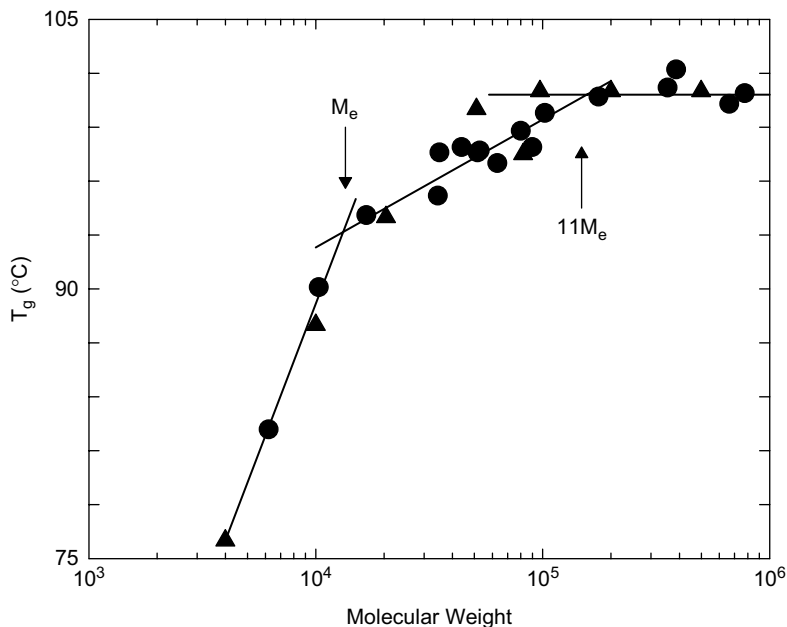


Fig. 14.12 Glass transition points (T_g) of nearly monodisperse polystyrene samples with different molecular weights: (●) data measured by differential scanning calorimetry (Ref. 28) and (▲) data measured by differential thermal analysis (Ref. 29; all moved up by 1°C).

with decreasing molecular weight below $M/M_e = 10$ and reaches 1 as $M/M_e \rightarrow 1$. K'/K being greater than 1 indicates that the dynamics in an entangled system is anisotropic: $\mu_A(t/\tau_A)$ describes the chain motion of an entanglement strand with both ends fixed. Thus, unlike K being for the modes of motion along the primitive path that are always facilitated by the free volume at both chain ends, K' should be like T_g , sensitive to the average free volume in the bulk. Consistent with such a picture is the observation that T_g starts to decrease from its plateau value with decreasing molecular weight at around the same molecular weight as $R_K(M/M_e)$ does in the case of polystyrene.

The temperature dependences of s for samples A, B, and C are shown together in Fig. 14.4. Very significantly, while different molecular theories — the ERT and the Rouse theory — are involved in the analyses for the entangled and entanglement-free systems, the s values of samples A, B and C change with temperature in a similar way relative to their individual T_g . This similarity turns out to be the prelude to the consistency and relationships among them as will be discussed in Sec. 14.9. The observation of such results is not surprising considering the conclusion derived from the study of the blend solutions in Chapter 11: the ERT and the Rouse theory are on the same footing at the Rouse-segmental level as the frictional factor K in both theories are the same within a possible error of no more than 20%. Concurrently, it supports that Eq. (14.5) is generally applicable and indicates that the thermorheological complexity should occur so long as the molecular weight is greater than the Rouse segment size.

Neglecting the small difference in T_g between samples A and B, it had been pointed out² that their s values at the same temperature basically followed the molecular-weight dependence of K'/K — namely, $R_K(M/M_e)$ as given by Eq. (11.6). This molecular-weight dependence of s is also borne out by the analysis that has included sample C's results and taken the T_g differences into account as given in Sec. 14.9.⁴ As can be observed in Fig. 14.12, T_g of sample C is considerably smaller than the plateau value at high molecular weights due to its relatively low molecular weight. That s and K'/K have the same molecular-weight dependence should be closely related to the fact that the $\mu_G(t)$ and $\mu_A(t)$ processes are next to each other along the time axis. To eliminate this molecular-weight dependence of s , one may define

$$s' = \frac{s}{(K'/K)} = \frac{\langle \tau \rangle_G}{K'} \quad (14.9)$$

in which Eq. (14.5) is used for the second equality.

As detailed in Chapter 10, the quantitative analyses of the relaxation modulus and viscoelastic spectrum of sample F2 in terms of the ERT have yielded $K'/K = 1$ within a small experimental error ($<10\%$). This result as well as the calculation using Eq. (11.6) (Fig. 11.1) indicates $K'/K = 1$ as $M_w \rightarrow M_e$. When the tube or topological constraint of entanglement is disappearing and the Rouse theory becomes applicable at M_e , to have $K' = K$ is physically meaningful as it indicates that the dynamics in the system becomes isotropic as it should. As the molecular weights of both sample C and F2 are so close to M_e and their K values are nearly the same (Table 14.1), the s value of sample C may be regarded as equivalent to that of F2. One may do so particularly because there is no difference between s and s' for F2 as $K'/K = 1$. Conversely, a pair of *fictional* s' and K' may be defined as $s' = s$ and $K' = K$ for sample C (even though there is only one frictional factor in an entanglement-free system). As it turns out in the T_g -related universal behaviour studied in this chapter (Sec. 14.9), the frictional factor K and the structural-growth parameter s in sample C play, respectively, the same roles as K' and s' in the entangled systems: samples A and B. For presenting these results altogether, K and s of sample C are also denoted by K' and s' , respectively. Similarly, the notation $K' = K$ and $s' = s$ may always be used in the entanglement-free region of molecular weight. This notation system is also used in comparing the analysis-obtained results of entanglement-free systems L10, A5000 and A2500 (Sec. 14.5) against those of samples A, B and C, as studied later in this chapter. Thus, whenever the notation K' or s' for any of the entanglement-free systems is used in this chapter (in a figure or the text), automatically its K or s value is meant or used.

14.7 Comparison of the A_G^f and β Values Extracted from the $J(t)$ and $G^*(\omega)$ Line Shapes

The values of the glassy-relaxation strength A_G^f and stretching parameter β extracted by analyzing the $J(t)$ (or $J_p(t)$; in what follows, often no distinction will be made between notations with and without the subscript p , particularly in discussions, as the difference between the quantities they represent being insignificantly small) curves of samples A, B and C and the $G^*(\omega)$ spectra of L10, A5000, A2500 and A1000 are listed together in Table 14.1 for comparison. Because of the contamination by residual plasticizers, the somewhat smaller A_G^f value of sample B may be excluded from the comparison. Considering some differences in molecular weight and

temperature, the A_G^f and β values of samples A and C are consistent with those of L10, A5000 and A2500. As sample C and L10 have comparable molecular weights and the analyses of their results are made at temperatures very close to each other (100 vs. 105°C), the close agreement between them is particularly impressive. On the basis of Boltzmann's superposition principle, the agreement indicates the consistency between the $J(t)$ and $G^*(\omega)$ results in the glassy-relaxation region. In view of the special technical requirement for making accurate measurements of $J(t)$ of very low compliance or $G^*(\omega)$ of very high modulus in the glassy-relaxation region, it should be very rare to observe such an agreement — the only one of this kind to the author's knowledge. The agreement also signifies that the two sets of results from two independent laboratories support each other.

As the A_G^f value is dictated by $J(0)^{-1}$, the line shape of the glassy-relaxation process is mainly characterized by the stretching parameter β . The significance of the consistency between the β values obtained from the $J(t)$ and $G^*(\omega)$ line-shape analyses is much more than what meets one's eye — namely, much more than the consistency merely in the glassy-relaxation region — as explained in the following: The convolution integral (Eq. (4.73)) that converts $G(t)$ into $J(t)$ smears the separate processes in $G(t)$ giving a much more featureless $J(t)$ line shape. The smearing effect has been clearly illustrated by the comparison of the $G(t)$ and $J(t)^{-1}$ curves calculated with and without the glassy-relaxation process included as shown in Fig. 14.6. By contrast, such a smearing effect basically does not occur in converting $G(t)$ into $G^*(\omega)$ as the storage modulus spectrum $G'(\omega)$ is a near mirror image of $G(t)$ if $0.7t^{-1}$ is regarded as equivalent to ω (see Fig. 4.13 and Appendix 14.A). Thus, the analysis of the $J(t)$ line shape for extracting the glassy-relaxation process is a much more challenging task than that of the $G^*(\omega)$ line shape. Without a correct functional form (either the ERT or the Rouse theory) for the entropic dynamic processes as the *base* (as the frame of reference), the glassy-relaxation process cannot be properly extracted by analyzing the $J(t)$ curves. As the ERT being used for an entangled polystyrene system, the correctness includes the predetermined ratio $K'/K = R_K(M/M_e)$ as given by Eq. (11.6). Including this, we may summarize that the success of the ERT serving as the reference frame in the $J(t)$ line-shape analyses for the entangled polystyrene systems are testified to by agreements between theory and experiment in three aspects: (1) the quantitative description of the $J(t)$ line shapes over the full range at different temperatures (Figs. 14.1 and 14.2); (2) the frictional factor K obtained for sample A being in quantitative agreement with the values

obtained previously and shown independent of molecular weight as expected theoretically (Table 10.1); and (3) the correctness of the predetermined $R_K(M/M_e)$ values for samples A and B as calculated from Eq. (11.6), which is strongly indicated by the obtained β values being consistent with those obtained for sample C, L10, A5000 and A2500 (Table 14.1).

14.8 T_g Defined by the Structural Relaxation

Time $\tau_S = 1,000$ sec

The structural- (or α -) relaxation time τ_S may be somewhat arbitrarily defined by the time when the ratio between the contribution of the glassy-relaxation process (G) to the relaxation modulus $G(t)$ and the total contributed by all the entropic processes (R), G/R , reaches 3.² Physically, this means that G/R has decayed nearly by factor of e (2.72) from ~ 10 , which is the G/R ratio at the relaxation time ($t = \tau_A^{15}$) of the highest Rouse–Mooney mode when the temperature is at the glass transition point. At the same time, the contribution from the glassy component in such a state is still significant. The structural-relaxation time defined this way is basically equivalent physically to that defined by³

$$\tau_S = 18 \langle \tau \rangle_G. \quad (14.10)$$

The structural-relaxation time as given by Eq. (14.10) is also in close agreement with the α -relaxation time defined in a usual way:^{3,4} the time at which the relaxation modulus reaches 10^8 dynes/cm² (see Figs. 14.17 and 14.18).^d The structural-relaxation time defined by Eq. (14.10), besides reflecting the effect of the glassy relaxation on the bulk mechanical properties, has the virtue of following exactly the temperature dependence of the

^dIn Figs. 14.17 and 14.18 it is shown that the point in time at which $G(t) = 10^8$ dynes/cm² is very close to the structural relaxation τ_S defined by Eq. (14.10). As given in Ref. 1 (p. 323), the frequency where $G'(\omega) = 10^8$ dynes/cm² — denoted by ω_{GR} here — is usually regarded as the characteristic rate of the glass-rubber transition. The rationale for Eq. (14.10) is explained in the text and detailed in Ref. 2; its validity is supported by $\tau_S = 1,000$ sec at the calorimetrically determined T_g . The rationale for using $G'(\omega) = 10^8$ dynes/cm² as the criterion for determining ω_{GR} is that it is a value intermediate between those characteristic of the rubberlike and glasslike states. As can be seen in Fig. 14.22, $\omega_S = 0.7/\tau_S$ is very close to ω_{GR} . This is consistent with what has been pointed out in Ref. 1: corresponding to $G'(\omega) = 10^8$ dynes/cm² at ω_{GR} , $G(t) = 0.8 \times 10^8$ dynes/cm² at $t = 1/\omega_{GR}$. The difference between a characteristic time defined by the point in time at which $G(t) = 10^8$ dynes/cm² and a corresponding characteristic rate defined by the frequency at which $G'(\omega) = 10^8$ dynes/cm² is quite small. Thus, the structural relaxation time as defined by Eq. (14.10) basically has the same physical meaning corresponding to that given to ω_{GR} .

glassy-relaxation process. The other definitions are somewhat affected by changes in the line shape of the viscoelastic response with temperature — namely, affected by the thermorheological complexity.

Using Eq. (14.9), the structural-relaxation time given by Eq. (14.10) may be rewritten as

$$\tau_S = 18sK = 18s'K'. \quad (14.11)$$

By analyzing the $J(t)$ line shape of sample A at the calorimetric T_g (97°C), the structural-relaxation time $\tau_S = 1,000$ sec is obtained. In the literature, τ_S reaching 100–1,000 sec has been used as the criterion for defining T_g .^{30–32} In view of the τ_S value of sample A at its calorimetric T_g , $\tau_S = 1,000$ sec is also used for defining the glass-transition points T_g of samples B and C, which will be used in the analyses and discussions of their results. As shown in Table 14.1, the thus defined T_g for samples A and C are consistent with the calorimetric values which are read from Fig. 14.12. Including at the thus defined T_g , the dynamic and structural quantities at different temperatures: K , K' , s' and τ_S obtained by analyzing the $J_p(t)$ curves of sample A are listed in Table 14.2.

As sample B is contaminated by residual plasticizers, its frictional factor K is smaller than that of a normal sample as expected. Because of the contamination, the T_g value of sample B has been estimated by Plazek¹¹ to be smaller than that of a normal sample of the same molecular weight by about one degree. The T_g of sample C is smaller than that of sample A because of its smaller molecular weight. The contamination by residual plasticizers in sample B may be treated in a similar way causing its T_g to become smaller; in other words, the $\tau_S = 1,000$ sec criterion is used to define the T_g of sample B *as it is*. From the s and K values extracted by analyzing the $J_p(t)$ curve of sample B at the lowest temperature (98.3°C), $\tau_S = 779$ sec is obtained, which is a little smaller than the criterion value. The temperature at which $\tau_S = 1,000$ sec is calculated by extrapolation using the VTF equation best-fitted to the analysis-obtained τ_S values at different temperatures. The T_g determined this way for sample B is 98.0°C. Then from the best fit of the VTF equation to the K values of sample B at different temperatures, the K value at this temperature (T_g) has been obtained as listed in Table 14.2. The s and s' values at T_g are then calculated from Eq. (14.11) using the thus obtained τ_S and K values. The K , K' ($= 3.16K$), s' and τ_S values of sample B at different temperatures including those at T_g are listed in Table 14.2.

In the case of sample C, by interpolation — using the best fit of the VTF equation to the τ_S values listed in Table 14.3 — $\tau_S = 1,000$ sec is

obtained at 93.7°C, which is then regarded as the T_g . Then, as also listed in Table 14.3, the K' (= K) and s' (= s) values of sample C at this temperature can be obtained from their values at different temperatures by interpolation — using the best-fit VTF equation for K and the best-fit modified-VTF equation (the form as given by Eq. (14.13)) for s .

For L10, A5000, A2500, as the longest τ_S values extracted from the data of Inoue *et al.* are around 100–200 sec, their T_g values are determined by extrapolation using the best fit of the VTF equation to the available data. As shown in Table 14.1, these T_g values are consistent with the calorimetric values as closely as those of samples A, B and C are. In the case of A1000, the τ_S results at different temperatures are fitted to the VTF equation, from which the T_g point where $\tau_S = 1,000$ sec is determined by interpolation.

The T_g defined by the criterion $\tau_S = 1,000$ sec as explained above serves as a common *reference point* for the different samples, with respect to which the obtained τ_S , s' and K' results may be compared in proper perspective.

14.9 Dependences of τ_S , s' and K' on $\Delta T = T - T_g$

The analysis-obtained results of samples A, B and C strongly suggest that the τ_S and s' values of the three samples depend on how far the temperature is from each individual T_g . Using the T_g defined by $\tau_S = 1,000$ sec for each sample (Table 14.1), the τ_S values of samples A, B and C as a function of the temperature difference from T_g , $\Delta T = T - T_g$, are displayed in Fig. 14.13. In spite of the fact that sample C has a significantly lower T_g due to its smaller molecular weight and that sample B is contaminated by residual plasticizers, the τ_S values of the three samples fall closely on the same curve. Note that both τ_S and T_g of sample B are determined for the sample as it is (contaminated). Apparently, the contamination in sample B by plasticizers is so low that sample B has kept the T_g -related nature of polystyrene. The close agreement among the three samples strongly supports the use of ΔT to account for the differences in T_g . The τ_S values of the three samples can be collectively well fitted to the VTF equation:

$$\log(\tau_S) = a_\tau + \frac{b_\tau}{(\Delta T + t_\tau)} \quad (14.12)$$

as demonstrated in Fig. 14.13 by the close agreement between the data points and the curve calculated with the best-fit parameters $a_\tau = -11.5045$, $b_\tau = 539.3497$ and $t_\tau = 37.1827$.

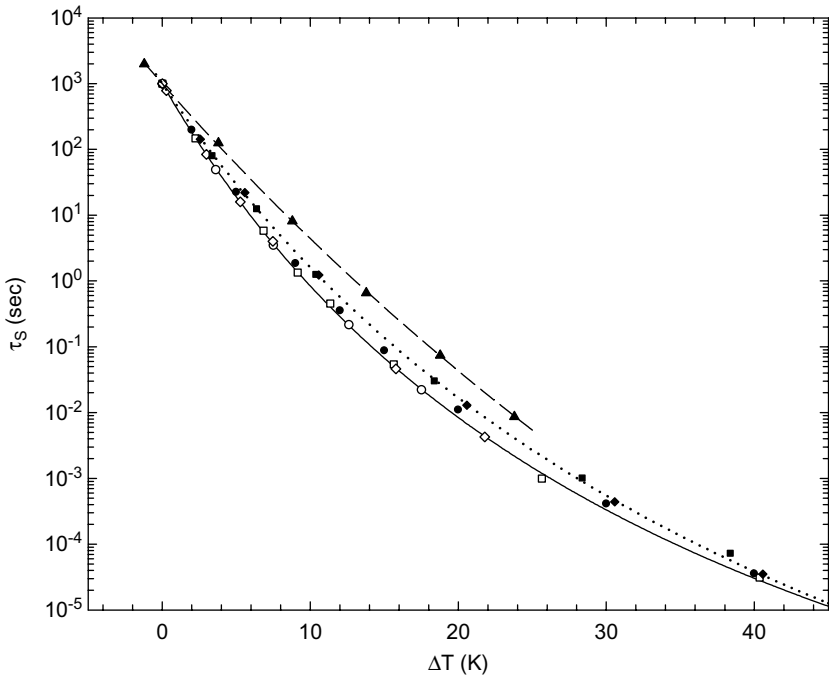


Fig. 14.13 Mutually consistent ΔT dependences of the structural-relaxation times τ_S of samples A (\circ), B (\diamond) and C (\square) are shown collectively. The solid line is calculated from the VTF equation (Eq. (14.12)) which best fits the data points of samples A, B and C collectively. Also shown are the τ_S data points of L10 (\bullet), A5000 (\blacksquare), A2500 (\blacklozenge , with the best-fit VTF curve represented by the dotted line) and A1000 (\blacktriangle , with the best-fit VTF curve represented by the dashed line).

In Fig. 14.14, the s' data points of samples A, B and C as a function of ΔT are shown to fall closely on the same curve. The ΔT dependence of s' of the three samples can be collectively well fitted to a modified VTF form:

$$\log(s') = c_1 + c_2(\Delta T + t_s) + \frac{c_3}{\Delta T + t_s}. \quad (14.13)$$

The curve shown in Fig. 14.14 is calculated with the best-fit parameters $c_1 = -4.2189$, $c_2 = 0.0364$, $c_3 = 375.6136$ and $t_s = 55.0922$.

The consistency of the ΔT dependences of s' and τ_S individually falling on the same curves implies that the same consistency should be applicable to K' as well according to Eq. (14.11); indeed so as illustrated in Fig. 14.15. The ΔT dependences of K' of samples A, B and C can be collectively fitted to the VTF equation of the form given by Eq. (14.12) with

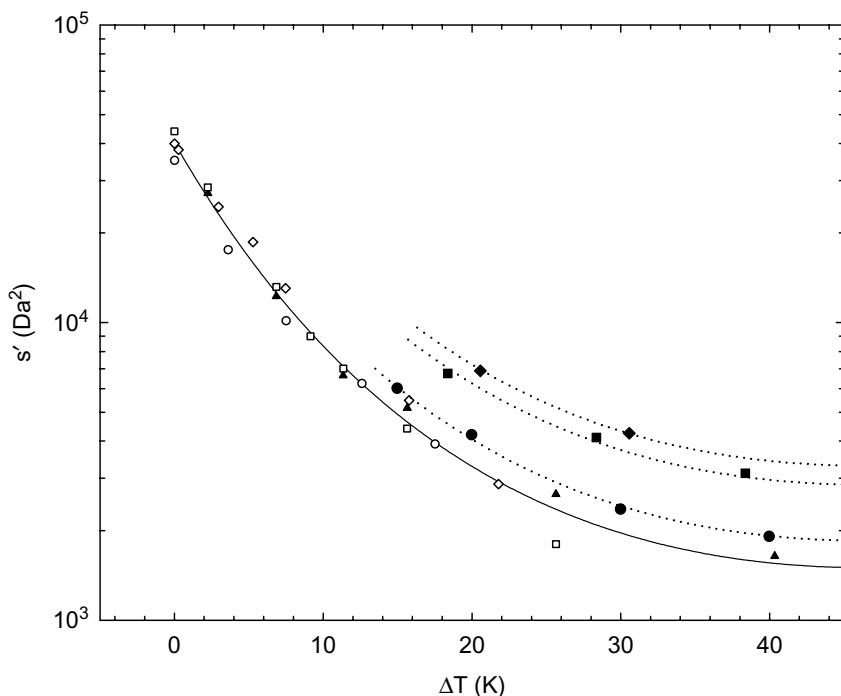


Fig. 14.14 Mutually consistent ΔT dependences of s' values of samples A (\circ), B (\diamond) and C (\square determined by the $J_p(t)$ line-shape analyses; \blacktriangle determined by matching with the experimental J_{ep}^0 values) are shown collectively. The solid line is calculated from the modified VTF equation (Eq. (14.13)) which best fits the data points of samples A, B and C collectively. Also shown are the s' data points of L10 (\bullet), A5000 (\blacksquare) and A2500 (\blacklozenge). The dotted lines individually represent the universal curve multiplied by a factor (1.23, 1.9 and 2.2) superposing on the data points of L10, A5000 and A2500, respectively.

the notations τ_S , a_τ , b_τ and t_τ replaced by K' , a_K , b_K and t_K , respectively. The curve shown in Fig. 14.15 is calculated with the best-fit parameters $a_K = -15.3931$, $b_K = 536.9037$ and $t_K = 42.8976$. The K' values of samples A, B and C as a function of ΔT falling on the same curve indicates that the molecular-weight dependence of T_g is directly related to the molecular-weight dependence of K' . This is exactly what has been proposed (Secs. 10.2 and 10.3) and further explained in Sec. 14.6 in the context of this chapter. In the meanwhile, K is independent of molecular weight at and above 127.5°C (Sec. 10.5). Therefore, as opposed to the consistency in the ΔT dependence of K' among samples A, B and C, their K values do not, as expected, have a common ΔT dependence.

(a) T_g -related universality in polystyrene

It is remarkable that the τ_S , s' and K' data points of samples A, B and C as a function of ΔT individually fall *naturally* on the same curves as shown in Figs. 14.13, 14.14 and 14.15, respectively. These results suggest a T_g -related universality. Although there are only three samples involved, such universality can indeed be claimed within the polystyrene system, because of the universal nature of the elements involved in the quantitative analyses of the $J(t)$ results of the three samples. These elements have been studied in diverse parts of Chapters 9–11 and this chapter; they are summarized here:

(1) The validity of the ERT and the universality it represents have been well tested as presented in Chapters 10–11. The success of the ERT is further summarized in Sec. 14.7 with the additional supports obtained from the study presented in this chapter. The success of the ERT being crucially testified to by the molecular-weight independence of K , there is no limit to the time range of $J(t)$ that can be analyzed, depending on the molecular

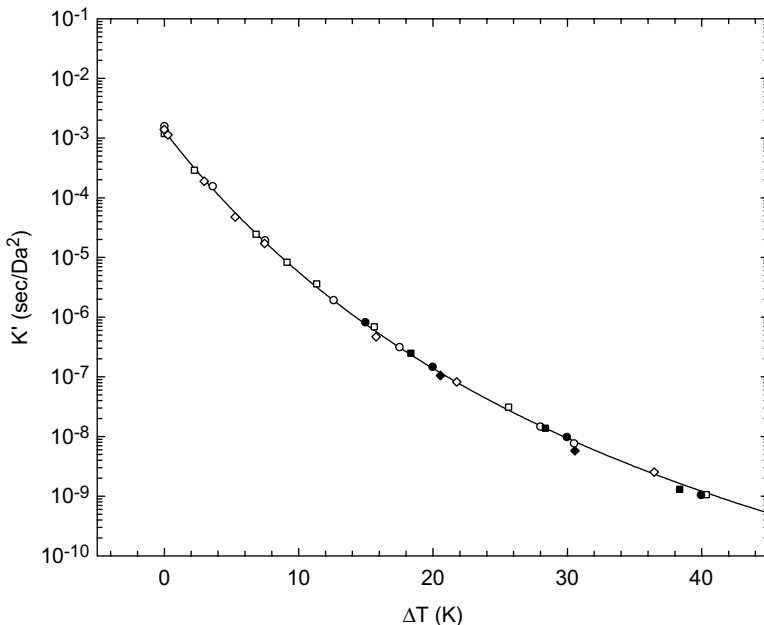


Fig. 14.15 Mutually consistent ΔT dependences of K' values of samples A (\circ), B (\diamond) and C (\square) are shown collectively. The solid line is calculated from the VTF equation which best fits the data points of samples A, B and C collectively. Also shown are the K' data points of L10 (\bullet), A5000 (\blacksquare) and A2500 (\blacklozenge).

weight of the studied sample. On such a basis, the quantitatively successful analyses of $J(t)$ results in the single case of sample A have all the ingredients for generalizing the success to polymers of other molecular weights. Furthermore, the results of samples B and C support such a generalization.

(2) Sample B is contaminated by residual plasticizers; as a result, its obtained K value is appreciably smaller than the average value of normal samples as expected. However, its K'/K ratio as can be calculated from Eq. (11.6), which represents the predetermined universal normalized molecular-weight dependence of K'/K in polystyrene, is not expected to be affected — as both K' and K being affected to the same degree. The predicted K'/K ratio of sample B is 3.16 and that of sample A is 1.61. As explained in Sec. 14.6, one can regard sample C as having $K'/K = 1$ — basically equivalent to F2, an entangled system with $K'/K = 1$ which is nearly the value ($K'/K = 1.04$) obtained by substituting $M/M_e = 1.24$ for F2 into Eq. (11.6). These K'/K ratios are used to calculate s' and K' from s and K , respectively, of the three samples as explained in Sec. 14.6. Thus, it is under the condition of maintaining consistency with the universality of K'/K predetermined for polystyrene (Eq. (11.6)) that the common curves of s' and K' shared by the three samples are obtained.

(3) The close agreements between the τ_S , s' and K' results of sample C as a function of $\Delta T = T - T_g$ and those of samples A and B should not be surprising even though two different molecular theories are independently involved. These agreements can be expected on the basis of the conclusion that the ERT and the Rouse theory are on the same footing at the Rouse segmental level as derived in Sec. 11.2.b (also see Sec. 14.2.b).

A comment should be made about the contamination by residual plasticizers in sample B. Its T_g value is determined by the criterion $\tau_S = 1,000$ sec for the sample as it is; at the same time, the obtained quantities τ_S , s' and K' are also associated with sample B as it is. Because the contamination is at a very low level, the T_g -related dynamic process of sample B is dominated by the characteristics of polystyrene. Thus, the results of τ_S , s' and K' as a function of $\Delta T = T - T_g$ of sample B as shown in Figs. 14.13, 14.14 and 14.15 can be regarded as equivalent to those of a “normal sample B”.

On the basis of the universal nature of three elements explained above, the common curves of τ_S , s' and K' shared by samples A, B and C can be regarded as representing a T_g -related universality applicable within polystyrene system, entangled or not. As shown below, departure from

the universality occurs as the molecular weight becomes smaller than $M_w \approx 12,000$, nearly 30% below that of sample C.

In the above discussions, one observes that the predetermined factor $R_K(M/M_e)$ (Eq. (11.6)) plays a very important role interfacing the ΔT - or T_g -related universality occurring in the short-time region (the $\mu_G(t) - \mu_A(t)$ region) and the other universality of topological nature — topological constraints of entanglements — occurring in the long-time region (the $\mu_X(t) - \mu_B(t) - \mu_C(t)$ region). Specifically, on the one hand, the universal ΔT dependences of s' and K' cannot be obtained without $R_K(M/M_e)$; on the other hand, K' is obtained from multiplying K , which is independent of molecular weight at and above 127.5°C , by the factor $R_K(M/M_e)$.

(b) *Deviations from the T_g -related universality*

The τ_S values for the four samples, L10, A5000, A2500 and A1000, obtained from their $G^*(\omega)$ line-shape analyses are shown in Fig. 14.13 along with the results obtained for samples A, B and C. The τ_S results of L10, A5000 and A2500 shown in Fig. 14.13 indicate that deviation from the universal curve increases gradually with decreasing molecular weight, moving towards the curve for A1000; the largest change occurs between A2500 and A1000. The data points of L10 cling closely to the universal curve, suggesting that the universality of the ΔT dependence of τ_S should extend to a molecular weight between sample C and L10. The s' and K' values of L10 are similarly close to or virtually on their respective universal curves as shown below.

The structural-growth parameter s' and the frictional factor K' for L10, A5000 and A2500 can only be extracted from a $G^*(\omega)$ spectrum that spans both the glassy-relaxation and entropic regions simultaneously. As the $G^*(\omega)$ spectra measured by Inoue *et al.*¹⁵ at low temperatures ($\Delta T < 14\text{K}$) cover only the glassy-relaxation region, the numbers of data points of s' and K' extractable from the $G^*(\omega)$ spectra are considerably less than that of τ_S . As s' decreases with increasing temperature, the entropic region of the spectrum shifts further away from the glassy-relaxation region — according to Eq. (14.11) (or (14.9)), K' increases with decreasing s' as τ_S (or $\langle \tau \rangle_G$) being kept fixed — as shown in Figs. 14.10 and 14.11.

Shown in Figs. 14.14 and 14.15, respectively, are the s' and K' values of L10, A5000 and A2500 in comparison with the results of samples A, B and C as well as the calculated universal curves. The K' values of the low-molecular-weight samples are virtually all on the universal curve, with slightly noticeable deviation towards the lower side only in the case

of A2500. The successful use of ΔT to account for the change in T_g with molecular weight is indeed extraordinary in the case of K' , considering the large drops in these samples' T_g values from the plateau at high molecular weights (decreasing by ~ 10 , 18 and 40K in L10, A5000 and A2500, respectively; Table 14.1). As the K' values of these samples closely follow the universal curve, the deviation of s' from the universal curve to the higher side is mainly correlated with τ_S deviating towards the same side according to Eq. (14.11).

As shown in Fig. 14.14, the s' data points of L10 appear to have just begun deviating from the universality. When multiplied by a constant, the calculated universal curve can be shifted upwards to superpose well on the s' data points of L10, A5000 and A2500 individually as shown by the dotted lines in Fig. 14.14. By extrapolating the thus obtained multiplication factors, it is estimated that deviation from the universal curve begins around $M_w = 12,000$, which is between the M_w value of L10 and the M_e value. Thus, although the universal curve is applicable to both entangled (samples A and B) and entanglement-free (samples C) systems as shown in the last section, the entanglement-free region in which it is applicable is quite narrow.

(c) Comparison of the $G^*(\omega)$ spectra of sample C and L10

For further illustrating the consistency between the $J(t)$ and $G^*(\omega)$ results, the $G_p^*(\omega)$ spectra of sample C have been calculated using the s' and K' values obtained by analyzing its $J_p(t)$ curves and shown in Fig. 14.16 for comparison with the $G^*(\omega)$ spectra of L10 (Fig. 14.10). In both Figs. 14.10 and 14.16, spectra at equivalent ΔT values are shown for a one-to-one comparison. As the reference temperature chosen in Fig. 14.10 for L10 is equivalent to $\Delta T = 15\text{K}$, the spectra shown in Fig. 14.16 for sample C are superposed on each other over the glassy-relaxation region with the reference chosen at 108.8°C ($\Delta T = 15\text{K}$). Both L10 and sample C being free of entanglement with some difference in molecular weight, the great similarity between the two sets of spectra at equivalent ΔT values is expected based on what have been shown in Figs. 14.13–14.15. Figure 14.16 also shows the spectrum of sample C at $\Delta T = 0$ (or at $T_g = 93.8^\circ\text{C}$); the equivalent information for L-10 is not contained in the data of Inoue *et al.* Both being at the same ΔT (15K), the frequency scale of the glassy-relaxation region shown in Fig. 14.10 for L10 is about 25% away from that shown for sample C in Fig. 14.16. At $\Delta T = 15\text{K}$, $\tau_S = 0.089\text{sec}$ (or $\langle\tau\rangle_G = 4.9 \times 10^{-3}\text{sec}$) for L10 as opposed to $\tau_S = 0.069\text{sec}$ (or $\langle\tau\rangle_G = 3.8 \times 10^{-3}\text{sec}$) for sample

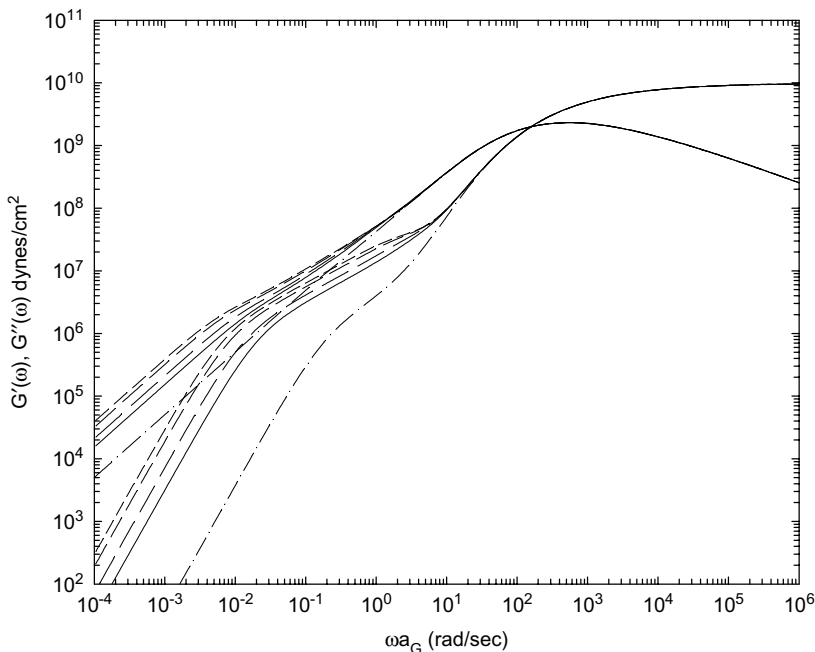


Fig. 14.16 The viscoelastic spectra $G_p^*(\omega)$ of sample C at different temperatures or ΔT calculated using the parameters extracted by analyzing its measured $J_p(t)$ curves and composed together by matching all the spectra over the glassy-relaxation region (using 108.8°C as the reference temperature). The glassy-relaxation region: solid line; the entropic region: dot-dash line at $T_g = 93.8^\circ\text{C}$ ($\Delta T = 0$), solid line at 108.8°C ($\Delta T = 15\text{K}$), long-dash line at 113.8°C ($\Delta T = 20\text{K}$), medium-dash line at 123.8°C ($\Delta T = 30\text{K}$), and short-dash line at 133.8°C ($\Delta T = 40\text{K}$).

C, in accord with the τ_S values of L10 being slightly above the universal curve as shown in Fig. 14.13.

14.10 Structure as Revealed in $G(t)$

(a) Length scale at T_g

With the s' and K' values determined for samples A, B and C (Tables 14.2 and 14.3), the $G_p(t)$ curves of the three samples may be calculated from Eqs. (14.1)–(14.5) (for samples A and B) and Eqs. (14.3)–(14.7) (for sample C). The $G_p(t)$ curves calculated for the three samples at their individual T_g 's are shown together in Fig. 14.17 for a revealing comparison. In the figure, the curves calculated by setting A_G (or A_G^f) = 0 are also shown; in each set of curves, the area between the full curve and the curve with

A_G (or $A_G^f = 0$) represents the contribution of the glassy-relaxation process to the relaxation modulus $G_p(t)$. For samples A and B, the curves calculated without both the glassy relaxation and Rouse–Mooney normal modes are also shown; the area between a thus calculated curve and that with $A_G = 0$ represents the contribution of the Rouse–Mooney normal modes to $G_p(t)$. Also indicated in the figure are the positions of the relaxation times of the Rouse normal modes in sample C and of the Rouse–Mooney normal modes in samples A and B.

The positions of the relaxation times of the normal modes may be used as “graduations” of an internal yardstick for measuring the spatial range (length scale) influenced by the glassy-relaxation process. The p th Rouse (or Rouse–Mooney) normal mode represents the local motion of the chain which includes N/p (or N_e/p) segments, with N (or N_e) being the number of segments per free chain (or per entanglement strand). In other words, the relaxation time of the p th normal mode, τ_p (in the Rouse process of sample C) or τ_A^p (in the Rouse–Mooney process of samples A and B) is associated with the length scale given by³²

$$\lambda_p \approx (a^2/p)^{0.5} \quad (14.14)$$

with a standing for the end-to-end distance in the entanglement-free case or the entanglement distance in the entangled case. The value a may be calculated from the characteristic ratio C_∞ or equivalently K_∞ as given in Table 13.1; one obtains $a = \sqrt{K_\infty M_e} = 7.62$ nm for samples A and B, and $a = \sqrt{K_\infty M_w} = 8.4$ nm for sample C. One sees in Fig. 14.17 that the vertical dotted line at 10^3 sec representing the structural-relaxation time τ_S at T_g passes through between the relaxation times of the seventh and eighth normal modes in all three cases. Using the position of $\tau_S = 10^3$ sec relative to τ_A^7 and τ_A^8 or to τ_7 and τ_8 , the length scale λ at T_g may be calculated from the values of λ_7 and λ_8 (Eq. (14.14)) by interpolation. The λ values so obtained are 2.76, 2.87 and 3.0 nm for samples A, B and C, respectively. These values are consistent with one another; at the same time, they are virtually the same as that estimated by the calorimetric method for polystyrene at T_g .^{33,34}

(b) Change in length scale with ΔT

In accordance with the calculation of the universal curve shown in Fig. 14.13, $\tau_S = 1$ sec at $\Delta T = 9.7$ K. For illustrating the changes in length scale with ΔT occurring in samples A, B and C in perspective, shown in Fig. 14.18 is the comparison of the $G_p(t)$ curves of the three

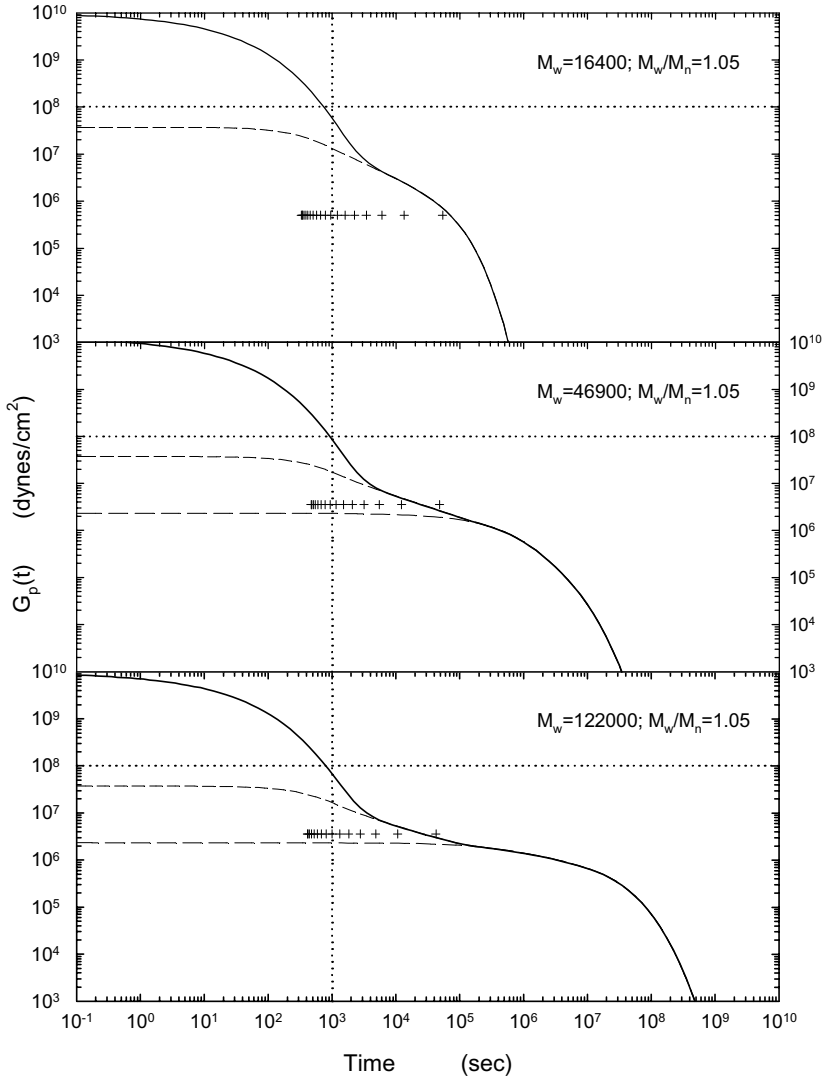


Fig. 14.17 Comparison of the $G_p(t)$ curves of samples A (middle figure), B (bottom one) and C (top one) at individual glass transition points or $\Delta T = 0$. In each figure, the relaxation times of the Rouse–Mooney normal modes (for samples A and B) or the Rouse normal modes (for sample C) are indicated (+); the short-dash line is calculated with A_G^f or $A_G = 0$; and the long-dash line is calculated with $A_G = 0$ and the contribution of the Rouse–Mooney normal modes set to zero. The vertical dotted line represents the structural-relaxation time $\tau_S = 1,000$ sec. The individual points in time at which the three $G_p(t)$ curves cross the horizontal dotted lines at 10^8 dyn/cm² represent the structural- (or α -) relaxation times as usually defined, which are all very close to $\tau_S = 1,000$ sec.

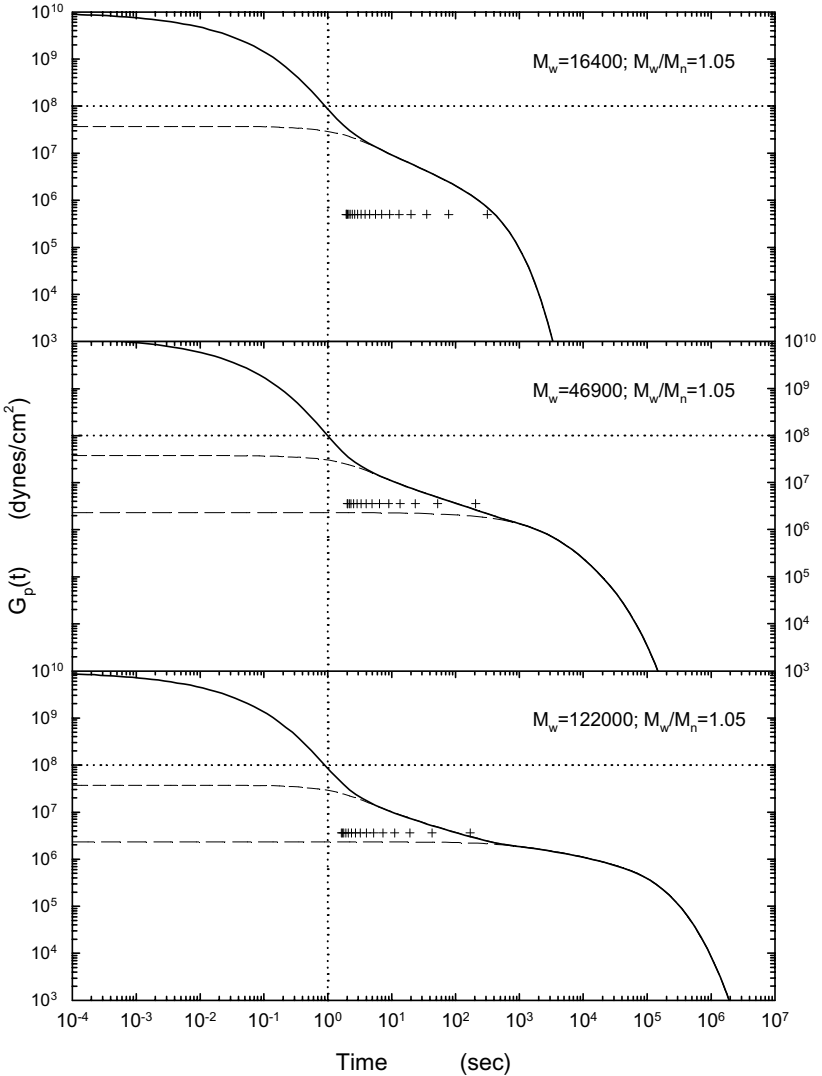


Fig. 14.18 Comparison of the $G_p(t)$ figures of samples A (middle figure), B (bottom one) and C (top one) at $\Delta T = 9.7\text{K}$. In each figure, the relaxation times of the Rouse–Mooney normal modes (for samples A and B) or the Rouse normal modes (for sample C) are indicated (+); the short-dash line is calculated with A_G^f or $A_G = 0$; and the long-dash line is calculated with $A_G = 0$ and the contribution of the Rouse–Mooney normal modes set to zero. The vertical dotted line represents the structural-relaxation time $\tau_S = 1$ sec. The individual points in time at which the three $G_p(t)$ curves cross the horizontal dotted lines at 10^8 dyn/cm² represent the structural- (or α -) relaxation times as usually defined, which are all very close to $\tau_S = 1$ sec.

samples calculated at $\Delta T = 9.7\text{K}$. The parameters: s' and K' used to calculate the $G_p(t)$ curve for each of the samples are obtained from the values determined at different temperatures by interpolation using the best-fit equations. As shown in the figure, the vertical dotted line at 1 sec representing the structural-relaxation time occurs before the relaxation time of the highest Rouse or Rouse–Mooney mode by about an equal distance along the $\log t$ axis in all three cases — equivalent to $\log 1.9$, $\log 2.0$ and $\log 1.6$ for samples C, A and B, respectively. Clearly, the consistency among the three samples observed at $\Delta T = 0$ (Fig. 14.17) holds at $\Delta T = 9.7\text{K}$ as well. $\tau_S = 1$ sec being shorter than the motional time of a single Rouse segment means that the length scale associated with the structural-relaxation process is shorter than the Rouse-segmental length of ~ 2 nm, indicating a rubbery state. By contrast, the length scale reaches ~ 3 nm at $\Delta T = 0$, indicating *vitrification* at the Rouse-segmental level.

14.11 Frictional Slowdown and Structural Growth

As indicated by the universal ΔT dependence of K' shown in Fig. 14.15, the molecular-weight dependence of K' and that of T_g are directly related with each other. The consistency of the ΔT dependence of s' among the three samples indicates that the molecular-weight dependence of K' extends into the time scales of the glassy-relaxation process according to Eq. (14.11). In other words, after the correction for differences in T_g is made to both the $\mu_A(t)$ (or $\mu_R(t)$) and $\mu_G(t)$ processes by expressing K' and s' as a function of ΔT , they become independent of molecular weight. This also means that the molecular-weight dependence of T_g in the entanglement region is directly related to the (same) molecular-weight dependence of the fast dynamic processes $\mu_A(t)$ and $\mu_G(t)$. Note that while the ΔT dependences of $\mu_A(t)$ (or $\mu_R(t)$) and $\mu_G(t)$ either separately or as a whole are independent of molecular weight, the difference in time scale between $\mu_A(t)$ (or $\mu_R(t)$) and $\mu_G(t)$ decreases with decreasing ΔT — due to the increase in s' as further discussed in the following:

While K' is a frictional factor, s' having the unit Da^2 is a structural factor. Thus the ΔT dependence of s' (Fig. 14.14) and that of K' (Fig. 14.15) are of different physical nature. With decreasing ΔT , the former represents the growth of a T_g -related (dynamic) structure while the latter represents purely the frictional slowdown of the Rouse segment. The structural relaxation ($\mu_G(t)$) with relaxation time defined by Eq. (14.11) contains the effects of both the frictional slowdown and structural growth while the $\mu_A(t)$ or $\mu_R(t)$ process is only affected by the frictional slowdown. As a result, the

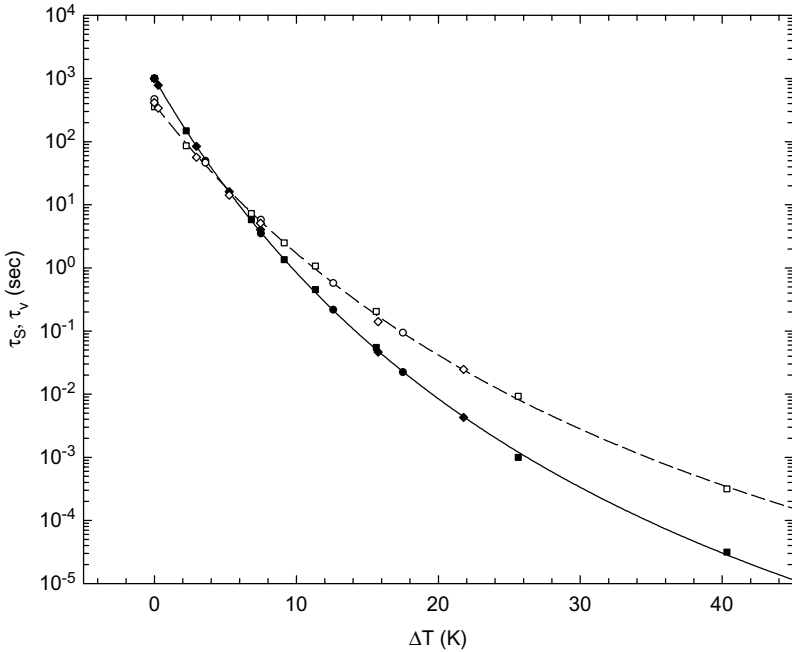


Fig. 14.19 Comparison between the collective dependence of τ_S of samples A, B and C (τ_S : \bullet for A, \blacklozenge for B and \blacksquare for C) on ΔT and that of τ_v (τ_v : \circ for A, \diamond for B and \square for C). The lines (solid line for τ_S and dashed line for τ_v) are calculated from the two VTF equations which individually best fit the τ_S and τ_v data of the three samples collectively.

time scale of τ_S relative to those of $\{\tau_A^p\}$ or $\{\tau_p\}$ changes with ΔT as observed in the comparison of Figs. 14.17 and 14.18. This effect is further illustrated in Fig. 14.19 by the comparison of τ_S and the Rouse-segmental motional time τ_v over a wide ΔT range. τ_v is defined by

$$\tau_v = \frac{K' \pi^2 m^2}{24} \quad (14.15)$$

with $m = 850$ being the mass for a Rouse segment. When $N = M/m$ or $N_e = M_e/m$ is sufficiently large for $(N-1)/N \approx 1$ or $(N_e-1)/N_e \approx 1$ to be valid as in the polystyrene case, Eq. (14.15) is virtually of no difference from the relaxation time of the highest Rouse or Rouse–Mooney normal mode (Eq. (7.57) for the Rouse modes in the case of sample C with $K = K'$; Eq. (9.B.26) for the Rouse–Mooney modes in the case of samples A and B with K replaced by $K' = R_K K$). In Fig. 14.19, one sees the ΔT dependence of τ_S crossing that of τ_v ; and the crossing occurs at $\Delta T = 4.9\text{K}$ where $\tau_S = \tau_v = 20.5\text{sec}$. The results shown in Figs. 14.17, 14.18 and 14.19

altogether indicate that corresponding to the time scale of τ_S increasing with ΔT decreasing, the T_g -related length scale increases gradually and reaches ~ 3 nm at $\Delta T = 0$ (or at T_g) in the same way for all the three studied samples. This universal behavior within the polystyrene system is expected on the basis of the universal curves of τ_S , s' and K' as a function of ΔT as shown in Figs. 14.13–14.15, respectively.

Because of the clear physical pictures embodied in the ERT and the Rouse theory used as the reference frames, the time scale and length scale of the glassy-relaxation process can be characterized unambiguously as both increasing with temperature decreasing towards T_g . The shown universality covering both the entangled and entanglement-free cases are significant in at least two aspects: Firstly, it supports the conclusion that the ERT and the Rouse theory are on the same footing at the Rouse-segmental level as derived from their sharing the same frictional factor K in Chapter 11. In other words, if this conclusion derived in Chapter 11 were not true, that both the entangled and entanglement-free systems share the same universal curves associated with τ_S , s' and K' , respectively, could not have been observed. Secondly, it strongly indicates the importance of the yardstick roles played by the time scale and length scale associated with a Rouse segment. Using them as reference points, both the time scale and length scale of the glassy-relaxation process can be monitored as a function of temperature decreasing towards the glass transition point.

14.12 K Values in the Close Neighborhood of T_g

As the time coordinates in Figs. 14.17–14.19 are expressed in terms of real-time scale (sec), the relaxation times as contained or shown in these figures are ultimately determined by the K values. As the temperature is approaching T_g ($\Delta T \lesssim 20$ K; in this temperature region $\tau_S \gtrsim 10^{-2}$ sec), because $K' = R_K K$ ($K' = 1.61$ K for sample A; $K' = 3.16$ K for sample B; and $K' = K$ for sample C) K has to change with ΔT in such a way that the corresponding K' values exhibit the universal behavior shown in Fig. 14.15. In other words, with the temperature approaching T_g , K becomes influenced by the T_g changing with molecular weight (Fig. 14.12). This has to be reconciled with the fact that K is independent of molecular weight at and above 127.5°C . As shown in Fig. 14.20 and explained in the following, the comparison of the K values as a function of temperature between samples A, B and C illustrates such a transition.

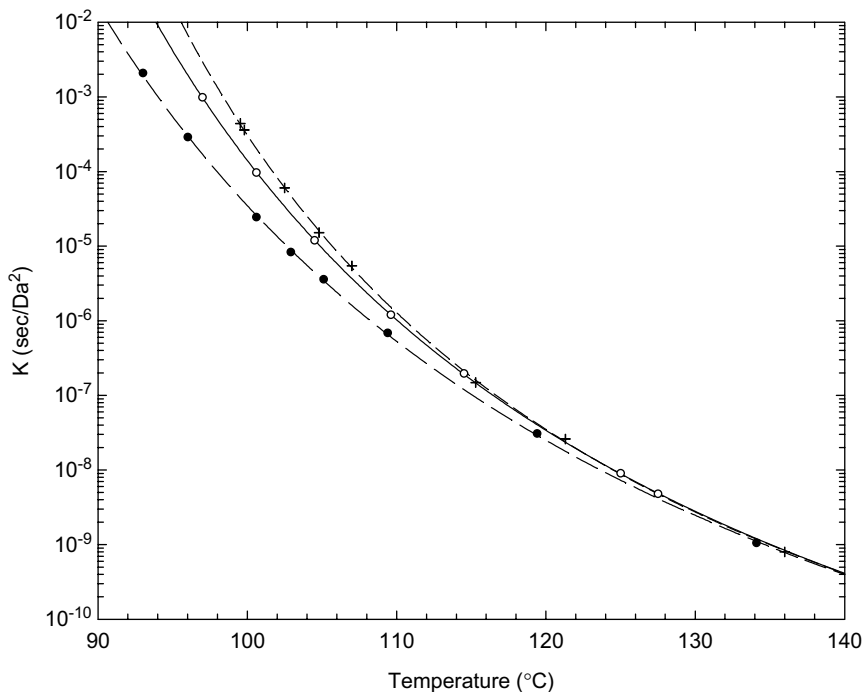


Fig. 14.20 Comparison of the K values of sample A (\circ), sample C (\bullet), and the hypothetically uncontaminated sample B ($+$) as a function of temperature (see the text). The lines are calculated from the VTF equations which individually best fit the experimental data of each of the three samples: solid line for sample A, long-dash line for sample C, and short-dash line for the hypothetically uncontaminated sample B.

Sample C and F2 have similar M_w values and nearly the same K value at 127.5°C (Table 14.1). As described by the Rouse theory, the viscoelastic response of sample C is characterized by a single frictional factor K — isotropic dynamically. In the case of F2, because its molecular weight is so close to M_e , $K = K'$ within a small experimental error — virtually isotropic dynamically. Thus, the difference in the physical meaning of K between sample C and F2 should be very small. On the basis of these obtained results, the K values of sample C and F2 as a function of temperature are expected to be very close to each other. The pattern that the K values of samples A and C diverge as the temperature approaching T_g and merge at high temperatures ($\gtrsim 130^\circ\text{C}$) as shown in Fig. 14.20 should similarly occur between sample A and F2. At 127.5°C, the K values (Table 14.1) for sample C and F2 are about 17–20% smaller than the average value $K = 4.9 \times 10^{-9} \pm$

10% obtained for samples with molecular weights ranging from 3.4×10^4 to 6.0×10^5 (Table 10.1). The K values for sample C and F2 being 17–20% smaller is most likely due to the effect of T_g being substantially smaller than the plateau value at high molecular weights (by $\sim 6\text{K}$). In any case, these differences in K are so small that these results actually support the ERT and the Rouse theory being on the same footing at the Rouse-segmental level.

Because sample B is contaminated by residual plasticizers, the K values of sample B cannot be directly compared with those listed in Table 10.1. To illustrate the point made above, the curve calculated from the VTF equation best-fitted to the K values of sample B is shifted to the higher-temperature side by 1.5K in Fig. 14.20. The temperature shift is to account for the decrease in T_g due to the contamination by residual plasticizers. The magnitude of the shift has been chosen such that after the shift, the curve superposes closely on the best-fit VTF curve of sample A over the region above $\sim 115^\circ\text{C}$. The magnitude of the shift is basically in accord with that ($\sim 1\text{K}$) estimated by Plazek. The superposition satisfies naturally the expectation (based on the results shown in Table 10.1) that the K value of the “uncontaminated sample B” be in close agreement with that of sample A at 127.5°C . After such a shift, the best-fit VTF curve of sample B begins to rise above that of sample A below $\sim 115^\circ\text{C}$, illustrating the divergence similar to but smaller than that between samples A and C. If we use the universal value $K' = 1.35 \times 10^{-3}$ predicted at $\Delta T = 0$ (see Fig. 14.15), the K value at T_g for the “uncontaminated sample B” should be $4.27 \times 10^{-4} (= K'/3.16)$, which occurs at 99.5°C on the shifted best-fit VTF curve of sample B. This T_g value is consistent with the sum of the shift (1.5K) and the T_g value of sample B (98.0°C) determined by the criterion $\tau_S = 1,000$ sec. In summary, as determined by the criterion $\tau_S = 1,000$ sec, the T_g values for sample A, “uncontaminated sample B”, and sample C are 97, 99.6 and 93.8°C , respectively; these values are consistent with the calorimetric values listed in Table 14.1., which are read from Fig. 14.12.

The analysis-obtained results of K shown above suggest that the free volume decreasing with decreasing temperature that eventually leads to the glass transition can be separated into two stages as explained in the following: the free volume at either of the two chain ends being always available to the motions along the primitive path, has been given as the explanation for the isothermal frictional factor K being independent of molecular weight at and above 127.5°C (for $M \geq 3.4 \times 10^4$; Secs. 10.2 and 14.6). At the same time, the universal ΔT dependence of K' (Fig. 14.15) has been explained as due to K' being solely dependent on the average free volume in the bulk, which is affected by two factors: the number of

chain ends per unit volume and the chain-end free volume. The former factor is inversely proportional to molecular weight and the latter factor decreases with decreasing temperature. The former factor makes both the glass transition point T_g and K' start to decline with decreasing molecular weight around the same point ($\sim 11M_e$; Figs. 10.5 (or 11.1) and 14.12). With decreasing temperature, the glass transition occurs — i.e. arriving at T_g — as the decreasing average free volume in the bulk reaches a certain minimum value. These explanations and the transition of K from being independent of molecular weight to being affected by a molecular-weight change around $\Delta T = 20\text{K}$ (for $M \gtrsim 3.4 \times 10^4$ as suggested by the results shown in Table 10.1 and Fig. 10.20) together suggest that the chain-end free volume in affecting T_g manifests in two stages. At $\Delta T > \sim 20\text{K}$, the isothermal average free volume in the bulk of a polystyrene is directly proportional to the number of chain ends per unit volume while the isothermal chain-end free volume remains the same — i.e. independent of molecular weight. This is the first stage as characterized by K being independent of molecular weight. In the temperature region of $\Delta T < \sim 20\text{K}$, the isothermal chain-end free volume becomes affected by how far the temperature is above T_g . This second stage is characterized by the isothermal frictional factor K becoming molecular weight-dependent, which can be considered as a sort of positive feedback effect: as the average free volume in the bulk is reduced below a certain critical value, its further decrease with decreasing temperature can induce an additional decrease in the isothermal chain-end free volume. This will not occur in a system whose average free volume in the bulk is still above the critical value due to a smaller molecular weight. Thus, as the temperature decreases the system with a higher molecular weight enters the second stage earlier as indicated in Fig. 14.20.

14.13 Internal Viscosity and Zero Shear Viscosity

As might be suggested by the Rouse theory (Eq. (7.61)), the zero-shear viscosity η_0 data of polymer melts had been analyzed in terms of the assumption that the viscosity could be expressed as the product of a structural factor and a frictional factor.³⁴ Considering the existence of the thermorheological complexity in different polymers, fundamentally such an assumption is not expected to hold particularly at temperatures close to the glass transition point. As shown in Sec. 10.3.a, the molecular-weight dependence of the zero-shear viscosity calculated by integrating Eq. (9.19) with $K'/K = 3.3$ (or 5.5) is in close agreement with the well-known empirical structural

factors: $\eta_0 \propto M$ below M_c and $\eta_0 \propto M^{3.4}$ above M_c .^{35–38} In the calculation of viscosity, the contribution of the glassy-relaxation process (the internal viscosity) is not included when $K'/K = 3.3$ is used or insufficiently accounted for when $K'/K = 5.5$ is used particularly at temperatures close to T_g . As $T \rightarrow T_g$, the contribution of the internal viscosity to η_0 increases greatly; and its percentage of the total η_0 value is particularly large if the molecular weight is not significantly larger than M_c . This can be illustrated by considering the F2 case, in which the values of the ratio η_p/η_p ($A_G = 0$) at different temperatures should be very similar to those of sample C listed in Table 14.3. As can be estimated using the listed η_p/η_p ($A_G = 0$) values of sample C, the contribution of the internal viscosity to the total η_0 value increases from around 10% at $\Delta T \approx 40\text{K}$ to about 80% at $\Delta T = 0$. Thus, the comparison of the molecular-weight dependence of viscosity calculated from Eq. (9.19) using $K'/K = 3.3$ (or 5.5) with the empirical structural factors: $\eta_0 \propto M$ below M_c and $\eta_0 \propto M^{3.4}$ above M_c as detailed in Sec. 10.3.a is meaningful only if made at temperatures sufficiently high above T_g . From the experimental point of view, a meaningful comparison can be made also only at sufficiently high temperatures as the empirical structural factors have been constructed on the basis of data measured at temperatures quite high above T_g . That the comparison is meaningful only at temperatures sufficiently high above T_g is also indicated by another effect: As the temperature is very close to T_g , the isothermal frictional factor K itself becomes dependent on molecular weight as shown in Fig. 14.20.

Appendix 14.A — Calculations of the $G'(\omega)$ and $G''(\omega)$ Spectra from a $G(t)$ Functional Form

The storage and loss modulus spectra $G'(\omega)$ and $G''(\omega)$ — such as those of L10, A5000, A2500 and sample C shown in Figs. 14.10, 14.11 and 14.16 — can be accurately calculated from their relaxation-time distributions $H(\tau_n)\Delta \log \tau$ which are first numerically calculated from the theory (Eq. (14.1) or (14.6)). The discrete relaxation times $\{\tau_n\}$ are usually chosen to be equally spaced on a log scale; namely, $\tau_{n+1}/\tau_n = z$ with $z = 10^{\Delta \log \tau}$ being a constant. This is often done by setting the number of discrete relaxation times per decade to a certain integer; a large integer may be chosen if a high resolution is desired or needed.

With the frictional factor K set at a certain value, the $G(t)$ curves of sample C, for example, can be calculated from Eq. (14.6) (in combination with Eqs. (14.3)–(14.5), (14.7) and (14.8)) using the parameters A_G^f , β and

s extracted by analyzing its measured $J(t)$ curves. Instead of calculating the $G(t)$ curves, the same equations and parameters can be used to calculate the $H(\tau_n)\Delta \log \tau$ distributions. In doing so, we consider the Rouse-theory part and the $A_G^f \mu_G(t)$ term in Eq. (14.6) separately. In the former, all the normal modes and their relaxation times are known. Thus, for this portion, a computer program can be constructed to accumulate the relaxation strengths of all the normal modes associated with different molecular-weight components in the sample with relaxation times τ falling in the interval, $\tau_n/\sqrt{z} \leq \tau < \tau_n\sqrt{z}$. In this way, the relaxation-time distribution for the Rouse-theory part at a chosen resolution can be obtained. At the same chosen resolution, the relaxation-time distribution of the $A_G^f \mu_G(t)$ term with $\mu_G(t)$ given by Eq. (14.3) can be calculated numerically.²¹ The total relaxation-time distribution can be formed by summing the distributions obtained for the two separate portions. The obtained total relaxation-time distribution $H(\tau_n)\Delta \log \tau$ can be checked by comparing the $G(t)$ curve calculated numerically according to

$$G(t) = \sum_n H(\tau_n) \exp(-t/\tau_n) \Delta \log \tau \quad (14.A.1)$$

with that calculated directly from Eq. (14.6). With the relaxation-time distribution confirmed this way, the $G'(\omega)$ and $G''(\omega)$ spectra can be calculated numerically in a straightforward manner using their respective expressions:

$$G'(\omega) = \sum_n H(\tau_n) \frac{\omega^2 \tau_n^2}{1 + \omega^2 \tau_n^2} \Delta \log \tau \quad (14.A.2)$$

$$G''(\omega) = \sum_n H(\tau_n) \frac{\omega \tau_n}{1 + \omega^2 \tau_n^2} \Delta \log \tau. \quad (14.A.3)$$

In a similar manner, the relaxation-time distributions and viscoelastic spectra of entangled systems can be calculated from Eq. (14.1) (in combination with Eqs. (14.2)–(14.5)). Although Eq. (14.1) contains an infinite number of terms, the numerical calculation can be done because the contribution of the p th mode in $\mu_B(t)$ as well as in $\mu_C(t)$ diminishes fast with increasing p ($\propto 1/p^2$; Eqs. (9.5) and (9.11)); one may include a sufficient number of terms in the computation to achieve the desired high level of accuracy. However, the computer program involving the ERT is much lengthier because it contains numerous products of two exponentials and of three exponentials. Furthermore, multiplication of two relaxation-time distributions — that associated with the glassy relaxation $A_G \mu_G(t)$ and that associated with the processes contained in the $G_E(t)$ as defined by Eq. (14.1) — is involved. Shown in Figs. 14.21 and 14.22 are the comparisons of the $H(\tau)$

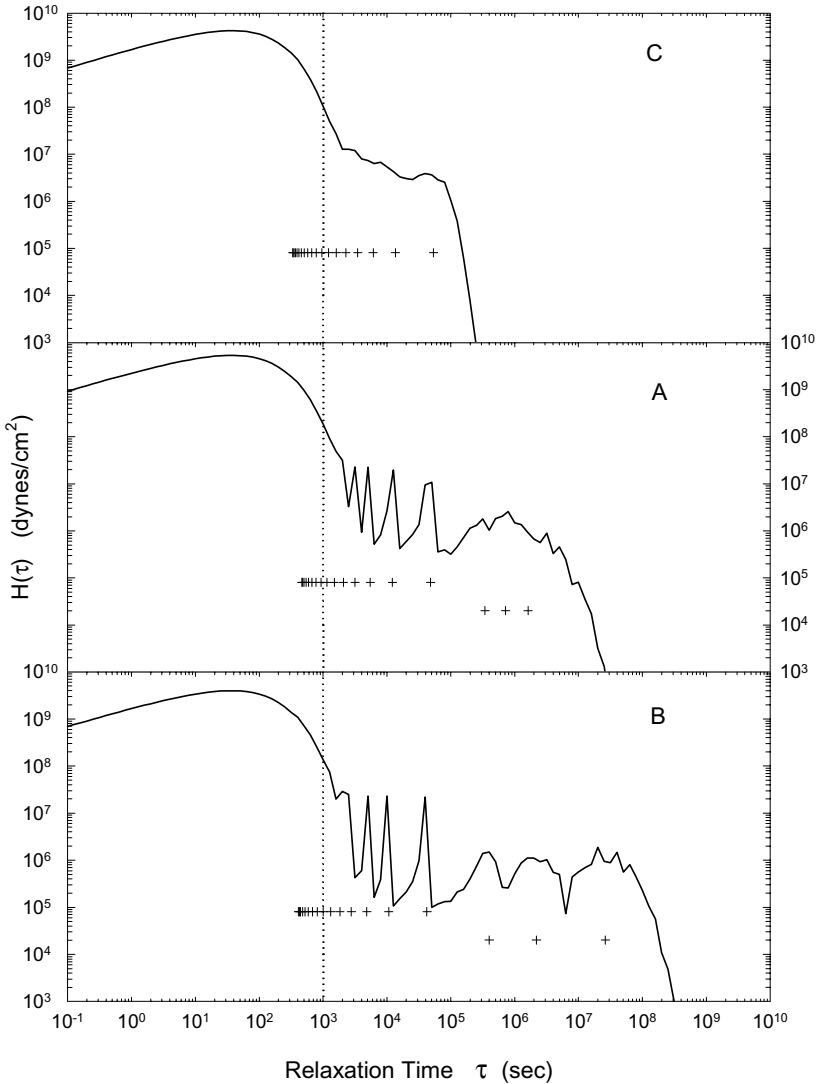


Fig. 14.21 Comparison of the $H(\tau)$ distributions of samples A (middle figure), B (bottom one) and C (top one) at individual glass transition points or $\Delta T = 0$. In each figure, the relaxation times of the Rouse-Mooney normal modes (for samples A and B) or the Rouse normal modes (for sample C) are indicated (upper +). In the entangled cases (samples A and B) the relaxation times of the individual dominant (lowest) modes in the $\mu_X(t)$, $\mu_B(t)$ and $\mu_C(t)$ processes are also indicated (lower +). The vertical dotted line represents the structural-relaxation time $\tau_S = 1,000$ sec.

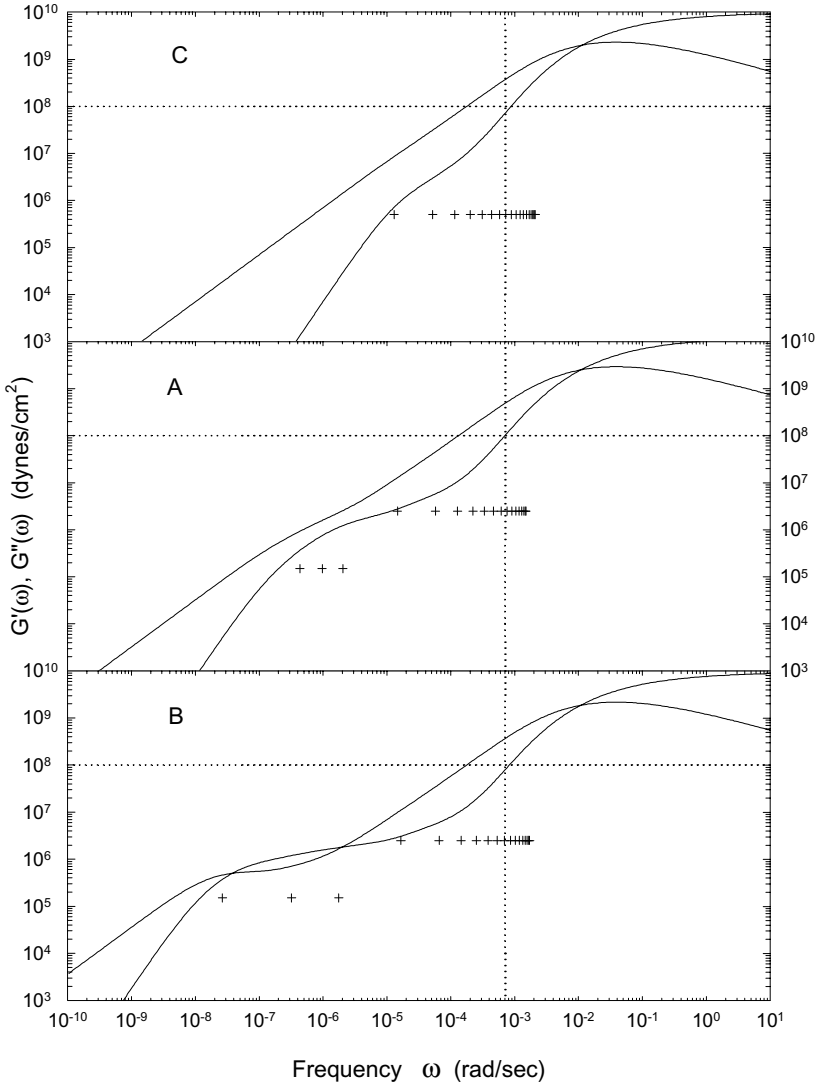


Fig. 14.22 Comparison of the $G'_p(\omega)$ and $G''_p(\omega)$ spectra of samples A (middle figure), B (bottom one) and C (top one) at individual glass transition points or $\Delta T = 0$. In each figure, the relaxation rates (defined as $0.7/\text{relaxation-time}$) of the Rouse–Mooney normal modes (for samples A and B) or the Rouse normal modes (for sample C) are indicated (upper +). In the entangled cases (samples A and B) the relaxation rates of the individual dominant (lowest) modes in the $\mu_X(t)$, $\mu_B(t)$ and $\mu_C(t)$ processes are also indicated (lower +). The vertical dotted line represents the structural-relaxation rate $\omega_S = 0.7 \times 10^{-3}$ rad/sec. The individual frequencies at which the $G'_p(\omega)$ curves of the three samples cross the horizontal dotted lines at 10^8 dyn/cm² represent the traditionally defined structural- (or α -) relaxation rates.

distributions (presented at the resolution of 10 relaxation times per decade) and of the $G'_p(\omega)$ and $G''_p(\omega)$ spectra, respectively, of samples A, B and C at $\Delta T = 0$ — corresponding to the $G_p(t)$ curves shown in Fig. 14.17. In the shown $H(\tau)$ distributions, the correspondences between the peak positions and the relaxation times of the Rouse (in sample C) or Rouse–Mooney (in samples A and B) normal modes as indicated by + can be observed as expected theoretically. Note that the relaxation-time peaks of the Rouse–Mooney normal modes, as being free from the broadening due to the finite width of molecular weight distribution of the sample, is much sharper than those of the Rouse normal modes. However, they are slightly broadened and shifted to shorter times by coupling (modulation) with the relaxation modes contained in the $\mu_X(t)$, $\mu_B(t)$ and $\mu_C(t)$ processes. The relaxation times or rates of the dominant (lowest) modes in the $\mu_X(t)$, $\mu_B(t)$ and $\mu_C(t)$ processes are also indicated in Figs. 14.21 and 14.22; their corresponding relaxation-time peaks are all broadened by the finite width of molecular weight distribution. Some additional fluctuations can be observed in the $H(\tau)$ distributions; they occur because in the numerical calculations the molecular weight distribution (the Schultz distribution; Eq. (10.3)) is represented in a discrete rather than continuous form. However, detailed features are contained in the shown $H(\tau)$ distributions over the entropic region — the normal-mode peaks; and the bumps in the plateau and terminal regions of an entangled system — that are absent from those that have been obtained by conversion from the measured $G(t)$ or $G^*(\omega)$ by procedures involving different orders of approximations.^{1,13,23,39–41} As pointed out in Chapter 4, $G(t)$ and $G'(\omega)$ are near mirror images to each other if the time/frequency inversion is made under $\omega t = 0.7$. Thus, corresponding to the structural-relaxation time occurring at $\tau_S = 1,000$ sec in $G(t)$, the structural-relaxation rate occurs at $\omega_S = 7 \times 10^{-4} \text{sec}^{-1}$ in $G'(\omega)$.

References

1. Ferry, J. D., *Viscoelastic Properties of Polymers* (3rd edn), Wiley, New York (1980).
2. Lin, Y.-H., *J. Phys. Chem. B* **109**, 17654 (2005).
3. Lin, Y.-H., *J. Phys. Chem. B* **109**, 17670 (2005).
4. Lin, Y.-H., *J. Phys.: Condens. Matter* **19**, 466101 (2007).
5. Lin, Y.-H., *Macromolecules* **17**, 2846 (1984).
6. Lin, Y.-H., *Macromolecules* **19**, 159 (1986).
7. Lin, Y.-H., *Macromolecules* **19**, 168 (1986).
8. Lin, Y.-H., *Macromolecules* **20**, 885 (1987).

9. Lin, Y.-H., and Juang, J.-H., *Macromolecules* **32**, 181 (1999).
10. Plazek, D. J., *J. Phys. Chem.* **69**, 3480 (1965).
11. Plazek, D. J., *J. Polym. Sci., Part A-2: Polym. Phys.* **6**, 621 (1968).
12. Plazek, D. J., and O'Rourke, V. M., *J. Polym. Sci. A-2: Polym. Phys.* **9**, 209 (1971).
13. Inoue, T., Okamoto, H., and Osaki, K., *Macromolecules* **24**, 5670 (1991).
14. Inoue, T., Hayashihara, H., Okamoto, H., and Osaki, K., *J. Polym. Sci., Part B: Polym. Phys.* **30**, 409 (1992).
15. Inoue, T., Onogi, T., Yao, M.-L., and Osaki, K., *J. Polym. Sci.: Part B: Polym. Phys.* **37**, 389 (1999).
16. Okamoto, H., Inoue, T., and Osaki, K., *J. Polym. Sci. Part B: Polym. Phys.* **33**, 417 (1995).
17. Schonhals, A., *Macromolecules* **26**, 1309 (1993); Schonhals, A., and Schlosser, E., *Phys. Scr., T.* **49**, 233 (1993).
18. Adachi, K., and Hirano, H., *Macromolecules* **31**, 3958 (1998).
19. Kohlrausch, R., *Annalen der Physik* **91**, 56 (1854); **91**, 179 (1854).
20. Williams, G., and Watts, D. C., *Trans. Faraday Soc.* **66**, 80 (1970).
21. Lindsey, C. P., and Patterson, G. D., *J. Chem. Phys.* **73**, 3348 (1980).
22. Hopkins, I. L., and Hamming, R. W., *J. Appl. Phys.* **28**, 906 (1957); *J. Appl. Phys.* **29**, 742 (1958).
23. Tschoegl, N. W., *The Phenomenological Theory of Linear Viscoelastic Behavior*, Springer-Verlag, Berlin (1989).
24. Vogel, H., *Phys. Z.*, **22**, 645 (1921).
25. Fulcher, G. S., *J. Am. Chem. Soc.* **8**, 339 (1925); *J. Am. Chem. Soc.* **8**, 789 (1925).
26. Tammann, G., and Hesse, G., *Z. Anorg. Allg. Chem.* **156**, 245 (1926).
27. Williams, M. L., Landel, R. F., and Ferry, J. D., *J. Am. Chem. Soc.* **77**, 3701 (1955).
28. Lin, Y.-H., *Macromolecules* **23**, 5292 (1990).
29. Rudin, A., and Burgin, D., *Polymer* **16**, 291 (1975).
30. Angell, C. A., *J. Non-Cryst. Solids* **131–133**, 13 (1991).
31. Angell, C. A., *Science* **267**, 1924 (1995).
32. Doi, M., and Edwards, S. F., *The Theory of Polymer Dynamics*, Oxford Univ. Press (1987).
33. Sillescu, H., *J. Non-Cryst. Solids* **243**, 81 (1999).
34. Hempel, E., Hempel, G., Hensei, A., Schick, C., and Donth, E., *J. Phys. Chem. B* **104**, 2460 (2000).
35. Berry, G. C., and Fox, T. G., *Adv. Polym. Sci.* **5**, 261 (1968).
36. Fox, T. G., and Loshaek, S., *J. Polym. Sci.* **15**, 371 (1955).
37. Allen, V. R., and Fox, T. G., *J. Chem. Phys.* **41**, 337 (1964).
38. Stratton, R. A., *J. Colloid Interface Sci.* **22**, 517 (1966).
39. Masuda, T., Kitagawa, K., Inoue, T., and Onogi, S., *Macromolecules* **3**, 116 (1970).
40. Osaki, K., Kimura, S., and Kurata, M., *J. Polym. Sci.: Polym. Phys. Ed.* **19**, 517 (1981).
41. Watanabe, H., and Kotaka, T., *Macromolecules* **17**, 2316 (1984).

Chapter 15

The Basic Mechanism for the Thermorheological Complexity in Polystyrene Melts

In the previous chapter, the analyses^{1–3} of the thermorheological complexity (TRC) in polystyrene melts^{4–7} in terms of the structural growth parameter s or s' have been studied in detail. The effects of differences in the glass transition temperature T_g among samples with different molecular weights on τ_S , K' and s' can be fully accounted for by expressing them as a function of the temperature difference from T_g , $\Delta T = T - T_g$. τ_S , K' and s' values of samples A, B and C plotted as a function of ΔT fall individually on a common curve representing a T_g -related universality within the polystyrene system, *entangled or not*. It is of great interest to understand the basic mechanism of the TRC;¹ the revealed universality suggests that such an understanding is fundamentally important.

For polystyrene, the frictional factor (K') for the Rouse–Mooney process $\mu_A(t)$ in the ERT is greater than that (K) for the $\mu_X(t)$, $\mu_B(t)$ and $\mu_C(t)$ processes by the *temperature-independent* factor $R_K(M/M_e)$ as given by Eq. (11.6).^{8–10} The frictional factor K in the ERT is independent of molecular weight at and above 127.5°C as expected theoretically and has also been shown to be the same as that in the Rouse theory within small experimental errors¹⁰ (Chapters 10 and 11). In the study of the TRC in polystyrene, as explained in Sec. 14.6, the notation $K' = K$ and $s' = s$ — which also means $R_K = 1$ — has been adopted for an entanglement-free system.³ That is, whenever the notation K' or s' for an entanglement-free system is used, automatically its K or s value is meant or used. As defined by Eq. (14.11), s (or s') may be regarded as representing the K -normalized (or K' -normalized) glassy (or structural)-relaxation time. As $R_K(M/M_e)$ is independent of temperature, either K or K' carries the temperature dependence of the relaxation times of *all* the dynamic processes or modes of motion in the entropic region of a polystyrene melt system, entangled or

not. As s or s' decreases with increasing temperature, the entropic region shifts more away from the glassy-relaxation region (Figs. 14.5, 14.17–14.19), representing the TRC. Thus, the basic mechanism of the TRC may be analyzed in terms of either the pair of s and K or the pair of s' and K' . Because of the universality associated with K' and s' expressed as a function of ΔT , the analysis in terms of K' and s' as done below is systematic and is the preferred representation.

15.1 The Basic Mechanism of the Thermorheological Complexity (TRC)

Equivalent to Eq. (3.57), the frictional factor K' may be expressed as

$$K' = \frac{\zeta' b^2}{kT\pi^2 m^2} = \frac{b^2}{D'\pi^2 m^2} \quad (15.1)$$

where $D' = kT/\zeta'$ denotes the diffusion constant of the Rouse segment. Undergoing Brownian motion, the diffusion constant of the Rouse segment can generally (see Appendix 3.D) be expressed as

$$D' = \frac{kT}{\zeta'} \approx \frac{l^2}{\Delta t} \quad (15.2)$$

where l is the step length that the Rouse segment has moved in a short time interval Δt that can be as short as the segmental collision time-scale. The only criterion for choosing Δt and l is that the steps are independent of one another; then, after a sufficiently large number of steps, the central limit theorem^{11,12} (Chapter 1) ensures convergence to a Gaussian stochastic process. This is an essential element in the Langevin equation as applied to slow chain dynamics. As pointed above, one may also express Eq. (15.2) in terms of the diffusion constant D as corresponding to $K (= \zeta b^2/kT\pi^2 m^2 = b^2/D\pi^2 m^2)$; the two representations differ only by a proportionality constant, R_K . For an entanglement-free system, as the notation $K' = K$ and $s' = s$ is used, $D' = D$ is also adopted.

At high temperatures, there is a wide range down to very small values from which to choose l and Δt satisfying Eq. (15.2); the dynamic process is often referred to as the continuous (small-step) or “free” diffusion.^{13–19} At a temperature close to T_g , the structure is formed with a certain *lifetime* τ_S , which has increased greatly with s' and K' (Eq. (14.11)); then, the smallest independent time step that can be chosen is of the same order of magnitude as the lifetime of the structure $\Delta\tau \approx \tau_S = 18\langle\tau\rangle_G$. We can

choose $\Delta\tau$ as the time step because it is still much shorter than the relaxation times of the low Rouse–Mooney or Rouse normal modes (particularly the first three), $\tau_A^{p=1,2,3}$ or $\tau_{p=1,2,3}$, even at T_g or $\Delta T = 0$ (see Fig. 14.17). In other words, by the time $t \approx \tau_A^{p=1,2,3}$ or $\tau_{p=1,2,3}$, the chain dynamics has regained homogeneity and ergodicity — as indicated by the agreements of experiments with the ERT or the Rouse theory (Chapter 14). Corresponding to $\Delta\tau$ being longer at lower temperatures, a larger length scale denoted by d is expected for the step length as explained in the following:

As K' is determined by the quantitative analysis of a $J(t)$ curve (or $G^*(\omega)$ spectrum), so D' is defined through Eq. (15.1). Corresponding to K' being for the dynamics in the *entropic* region of the viscoelastic response of a polymer melt, D' is a characteristic of the long-time or *diffusion* regime of the mean square segmental displacement. This is an essential element of both the Rouse theory and the ERT (based on the Doi–Edwards theory), predicting the relations between the viscoelasticity of a polymer and its molecular (whole-chain) translational diffusion, D_G . D (or D') is proportional to D_G for an entanglement-free (Rouse) chain (detailed in Chapters 3 and 7); and to D_G and D_{cv} (curvilinear diffusion constant as defined in the Doi–Edwards theory)^{11,20} for a well-entangled chain (detailed in Chapters 8–10) by different structural factors (see Eqs. (3.41), (8.6), (8.20) and (10.5)). Due to Eq. (15.1), the following constraint is imposed on the system:

$$\text{const} = D'K' \approx \left(\frac{d^2}{\Delta\tau} \right) K' \approx \left(\frac{d^2}{\tau_S} \right) K' = \left(\frac{d^2}{18s'} \right) \quad (15.3)$$

where Eq. (14.11) has been used. To maintain $D'K'$ constant, d has to increase by about five times as s' increases from ~ 1500 at temperatures higher than $\sim T_g + 40\text{K}$ to $\sim 40,000$ at T_g as shown in Fig. 14.14. All the relaxation times of the dynamic processes or modes of motion as observed in the viscoelastic response of a polymer over the entropic region are proportional to $K' \propto \zeta'/kT \approx \Delta\tau/d^2$ while the structural relaxation time is $\tau_S \approx \Delta\tau \propto \langle \tau \rangle_G$. With decreasing temperature, $\Delta\tau$ increases more strongly than $\Delta\tau/d^2$ does as d increases with the structural growth parameter s' . This difference in temperature dependence represents the basic mechanism for the TRC. Viscoelastic and dynamic results of glass-forming polymers^{4–7,21–27} generally show a stronger temperature dependence in the short-time (high-frequency) region than that in the long-time (low-frequency) region; thus, the TRC is a general phenomenon. The above described mechanism for the TRC is expected to be generally applicable.

15.2 Breakdown of the Stokes–Einstein Relation (BSE) Sharing the Same Basic Mechanism

As the glass transition temperature T_g is approached from above, fragile glass-forming liquids display an interesting phenomenon: the temperature dependence of the translational diffusion becomes gradually weaker than that of the viscosity η or the rotational relaxation time τ_{rot} . This effect is often referred to as the breakdown of the (Debye–) Stokes–Einstein relation (BSE).^{28–34} The BSE in glass-forming liquids has been actively studied and various models^{33,35–40} have been proposed to explain it. The BSE observed in *o*-Terphenyl (OTP)^{28–32} will be presented in this chapter as a representative example.

Without the entropy-driven modes of motion — as described by either the ERT or the Rouse theory — in OTP, the viscosity can be expressed by

$$\eta \propto \int_0^\infty \mu_G(t) dt = \langle \tau \rangle_G \propto \tau_S \approx \tau_{rot} \approx \Delta\tau. \quad (15.4)$$

What is explained above concerning the diffusion of the Rouse segment in polystyrene melts can similarly be applied to the molecular diffusion D_g in OTP; i.e.

$$D_g \approx \frac{d^2}{\Delta\tau}. \quad (15.5)$$

Thus, from Eqs. (15.4) and (15.5), one sees that $D_g\tau_{rot}$ increases with increasing d as T_g is approached from above, indicating the BSE.

To characterize the BSE, a translational diffusion enhancement factor μ has been defined by

$$\mu = \frac{D_g}{D_{SE}} \quad (15.6)$$

where D_{SE} is the translational-diffusion constant predicted by the Stokes–Einstein relation. As the Stokes–Einstein relation holds at temperatures far above T_g in OTP, its μ value at a temperature T close to T_g may be calculated from

$$\mu(T) = \frac{D_g(T)\tau_{rot}(T)}{D_g(T_{high})\tau_{rot}(T_{high})} \left(\text{or } \frac{D_g(T)\eta(T)/T}{D_g(T_{high})\eta(T_{high})/T_{high}} \right) \quad (15.7)$$

where T_{high} stands for a high temperature in the region where the Stokes–Einstein relation holds.

As s' for the polystyrene system reaches a plateau value of about 1,500 as the temperature is more than 40K above T_g (Fig. 14.14), under the constraint imposed by Eq. (15.3), d should reach a lower limiting value d_0 at high temperatures. Denoting the plateau value of s' at high temperatures by s'_0 , the s' value at a temperature T above T_g may be expressed by

$$s'(T) = s'_0 \left(\frac{d(T)}{d_0} \right)^2. \quad (15.8)$$

Applying the same idea to the translational diffusion enhancement parameter in OTP and substituting Eqs. (15.4) and (15.5) into Eq. (15.7), the μ value at a temperature T above T_g may be expressed by

$$\mu(T) = \left(\frac{d(T)}{d_0} \right)^2. \quad (15.9)$$

The comparison of Eqs. (15.8) and (15.9) indicates that $\mu(T)$ for OTP is equivalent to $s'(T)/s'_0$ for polystyrene melts, reflecting the same mechanism.

The essence in the above comparative analysis of TRC and BSE is that the entropic region of the viscoelastic response of a polystyrene melt is regarded as equivalent to the diffusion regime of the molecular displacement in OTP. This is based on the central limit theorem, which is expected to hold in both types of long-time regimes. They play equivalent roles by serving individually as the reference frame for characterizing the glassy relaxation that occurs in the short-time region. Specifically, just as Eq. (14.9) or (14.11) uses the entropic region of the viscoelastic response of a polystyrene sample as the reference frame (note $1/K' \propto D'$ as indicated by Eq. (15.1)), the calculation of the product $D_g\tau_{rot}$ in the case of OTP amounts to using the diffusion regime as the reference frame.

15.3 Comparison of the TRC and BSE Results

The $\mu(T)$ data for OTP as defined by Eq. (15.7) have been compiled by Mapes *et al.*³² from diffusion results obtained by NMR,²⁸ isothermal desorption³² and the results of rotational relaxation time²⁸ and viscosity.⁴¹ In Fig. 15.1, the $\mu(\Delta T)$ results of OTP^a are compared with the $s'(\Delta T)/s'_0$ values of the three polystyrene samples: A, B and C as a function of $\Delta T = T - T_g$ (Chapter 14). The magnitude of the enhancement factor $\mu(\Delta T)$

^aData of OTP (Ref. 32) provided by Prof. Ediger in digital form are shown in Fig. 15.1.

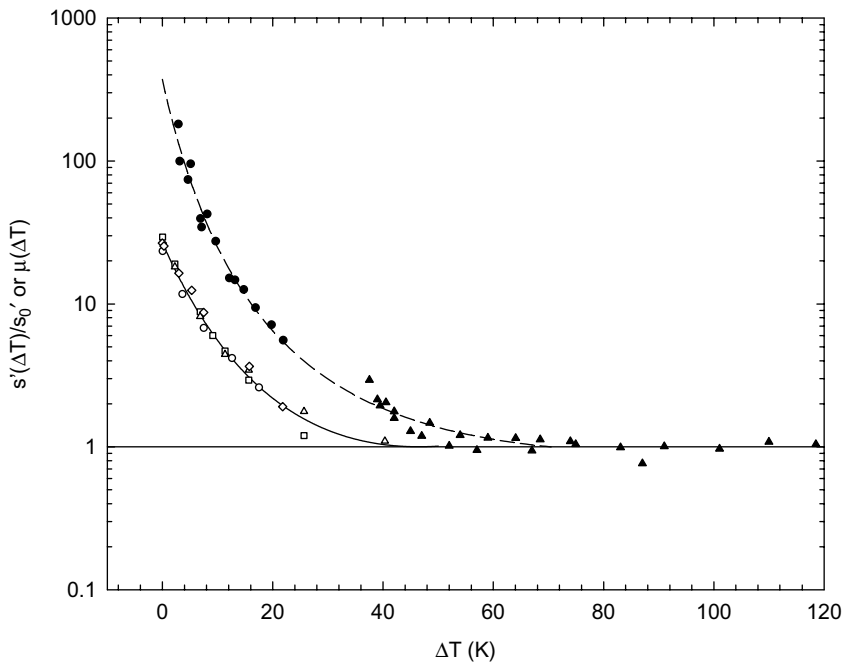


Fig. 15.1 Comparison of the $s'(\Delta T)/s'_0$ values (with $s'_0 = 1,500$) of polystyrene samples: A(\circ), B(\diamond) and C(\square) obtained by analyzing the $J(t)$ line shapes; Δ by matching the calculated and experimental steady-state compliance J_e^0 values with the diffusion enhancement factors $\mu(\Delta T)$ of OTP (\bullet isothermal desorption; \blacktriangle NMR) as a function of $\Delta T = T - T_g$. The solid line is calculated from the modified VTF equation (Eq. (14.13)) which best fits the $s'(\Delta T)/s'_0$ results of the three polystyrene samples collectively. The dashed line represents the curve calculated from the modified VTF equation best fitting the $\mu(\Delta T)$ data of OTP.

being different for different materials, the similarity in shape between the $\mu(\Delta T)$ and $s'(\Delta T)/s'_0$ curves shown in Fig. 15.1 supports the conclusion that $\mu(\Delta T)$ for OTP plays the same role as $s'(\Delta T)/s'_0$ for polystyrene.

The $G^*(\omega)$ spectra of the entanglement-free samples L10, A5000 and A2500 have also been analyzed in terms of the same $G(t)$ functional form, Eq. (14.6), as the $J(t)$ curves of sample C have been. It has been found that the τ_S , s' and K' values of these samples obtained from the analyses deviate more from the respective universal curves with decreasing molecular weight. As shown in Fig. 14.14, the common curve of $\log(s')$ vs. ΔT shared by samples A, B and C can be superposed closely on the data of L10, A5000 and A2500 individually by a vertical shift. By extrapolating the

obtained shift factors to the no-shift point, deviation is estimated to start occurring around $M_w = 12,000$ for polystyrene. The close superposition suggests that these low-molecular-weight samples have the same or very similar dependence of $s'(\Delta T)/s'_0$ on ΔT as shown in Fig. 15.1 for samples A, B and C.

15.4 A Discussion of the Glass Transition as Viewed from the Study of TRC

As studied in Chapter 14, the TRC is closely related to the glass transition; so is the BSE as indicated by various studies.^{14–19,35–38} The implications regarding the glass transition as can be derived by analyzing the TRC may be summarized as in the following:

(a) The stretching parameter β for the glassy-relaxation process obtained by analyzing the $J(t)$ curves or $G^*(\omega)$ spectra of nearly monodisperse polystyrene samples of different molecular weights, entangled and entanglement-free, is consistently within 0.41–0.42 (Table 14.1). It is commonly assumed that the observed nonexponential relaxation is strongly influenced by the underlying energy landscape associated with the structural configurations that the system may adopt^{14–18} — a picture of dynamic heterogeneity.

(b) As indicated by Eq. (14.11), both the increases in s' and K' (Figs. 14.14 and 14.15) contribute to the increase in the structural-relaxation time τ_s with temperature decreasing towards T_g . The increase in K' represents frictional slowdown. As s' has the dimension of Da^2 — playing the same role as the structural factors in the expressions for relaxation times studied in earlier chapters^b — the quantification of s' implies the existence of some structure in the system and its temperature dependence indicates that the mass (size) of the structure increases with decreasing temperature. Traditionally, the existence of some structure in the glass transformation range has been inferred from the change of heat capacity in the neighborhood of T_g as a function of the DSC scanning rate and the sluggishness of the stress relaxation.^{13,14} The gradually larger increase in s' with

^bAs can be seen by comparing the expression $\langle \tau \rangle_G = K's' (= Ks)$ (Eq. 14.11) with the expression of any of the different relaxation times as given by Eqs. (3.62), (7.57), (8.56), (9.12) and (9.B.26).

temperature approaching T_g from above causes an even greater slowdown on the glassy relaxation, by which a glass-forming liquid is characterized as fragile.^{14–18} Thus, the structure growing with decreasing temperature as indicated by the increase in s' greatly contributes to fragility of polystyrene.

(c) s' as a quantity embodying the size aspect of the structure is straightly extracted from the glassy relaxation itself. Being part of a relaxation process, the structure cannot be permanent but rather should be fluctuating or flickering with a certain lifetime. This picture implies that the system is dynamically heterogeneous, which is consistent with (a).

(d) With more structural formation (as a result of increasing s'), the average segment spends an increasing fraction of time in trajectory-reversing collisions with its neighbors — as if a particle with a finite kT being situated inside a cage; as a result, the mean waiting time $\Delta\tau \approx \tau_s$ between two successive jumps becomes longer. The constraint imposed by Eq. (15.3) dictates that as s' increases with temperature decreasing towards T_g , the average length d , over which the segments jump, must increase. The transition from free diffusion to hopping (or activated motions) of the segments starts around 45K above T_g for polystyrene (see Fig. 14.14). With less volume available, more cooperation is needed between neighbors in order for one to escape its initial “cage” in making a jump.^{15,16} The cooperative jump motion has often been inferred from the apparent activation energy associated with τ_s in the neighborhood of T_g being many times larger than the value that can be assigned to a single segment^{14–18,42,43} — such as the value in the high temperature region.

(e) With respect to the length scales of the Rouse (for entanglement-free systems) or Rouse–Mooney (for entangled systems) normal modes, the length scale of the glassy relaxation increasing with s' as the temperature decreases can be monitored (Figs. 14.17–14.19). In this way, the length scale of polystyrene at T_g has been determined to be ~ 3 nm consistently for samples A, B and C.

The above summary gives a general picture of the glassy relaxations of a flexible linear polymer at and near T_g . The general picture has several basic features: the existence of a fluctuating structure (corresponding to an energy-landscape picture), contribution of structural growth to fragility, dynamic heterogeneity, the transition from free diffusion to cooperative hopping or activated motions, the existence of a characteristic length scale at T_g . As the TRC in polystyrene and the BSE in OTP are sharing the same basic mechanism, these basic features may also be regarded as applicable to fragile glass-forming liquids such as OTP. These features have indeed

been suggested, discussed or revealed in various studies of fragile glass-forming liquids.^{13–19,43–55} Furthermore, the study of the TRC allows a new physical meaning to be assigned to the translational-diffusion enhancement factor $\mu(T)$ for fragile glass-forming liquids. Considering that $s'(T)/s'_0$ is equivalent to $\mu(T)$ and that s' has the unit Da^2 , $\mu(T)$ may be regarded as a quantity that reflects the square of an effective or average mass size of some structure growing with temperature decreasing towards T_g .

15.5 Specific Relations with Literature-Reported Studies of BSE

Different studies have been reported to explain the BSE. These studies are based on or lead to dynamic heterogeneity in glass-forming systems. In the following, the specific relations of two models explaining the BSE^{35,50} with the discussed basic mechanism, which is initially derived from the study of the TRC, are pointed out:

(a) For explaining the enhancement of translational diffusion in deeply super-cooled liquids, Stillinger and Hodgdon (S&H)³⁵ have proposed a two-state model. As shown in Appendix 15.A, a one-to-one correspondence between the two-state model formulated by S&H and the hopping picture as represented by Eq. (15.5) can be found. The average length d jumped by the molecule after having waited for an average period $\Delta\tau \approx \tau_S$ since the previous jump is shown to be equivalent to the distance the molecule moves by diffusion in a fluidized domain (with viscosity η_0 inside the domain) over the domain's lifetime t_0 in the S&H model:

$$d^2 \approx D_g \Delta\tau \approx D_g \tau_S = \left(\frac{kT}{6\pi\eta_0 R} \right) t_0 \propto \mu. \quad (15.10)$$

Equation (15.10) agrees with Eq. (15.9) indicating d increasing with decreasing temperature. Either Eq. (15.5) or the two-state model of S&H has reflected that this effect takes place as the temperature decreases towards T_g . Despite their simplicity, either of them has captured the notion — the “hopping” mechanism or the presence of the mobile fraction — that characterizes the collective motions of particles effectively as far as the long-time (diffusion) regime is concerned, therefore explaining the BSE occurring at low temperatures.

(b) Simulations on glass-forming binary mixtures by Yamamoto and Onuki⁵⁰ (Y&O) have shown that the BSE occurs in highly super-cooled

states. Based on the van Hove self-correlation functions concurrently calculated, dynamic heterogeneity has been demonstrated to play an essential role in causing the BSE. The notation τ_α given in Ref. 50 may be regarded as $\Delta\tau$ defined in this chapter; for consistency τ_α of Ref. 50 is replaced by $\Delta\tau$ in the following discussion. At low temperatures where the BSE occurs, at time scales of $\sim \Delta\tau$, the mobile and slow components can be resolved; and the *hopping* of the mobile molecules gives a *dominant* contribution to the mean square displacement $\langle [\Delta\mathbf{r}(t = \Delta\tau)]^2 \rangle$.^c As opposed to clear dynamic heterogeneity at $t \approx \Delta\tau$, with time increasing in the long-time region $t > 10\Delta\tau$, the van Hove correlation function approaches the Gaussian form^d — confirming the central limit theorem. As shown in Ref. 50, $D_g\Delta\tau (= \langle [\Delta\mathbf{r}(\Delta\tau)]^2 \rangle / 6)$ ^e increases with increasing $\Delta\tau$ (or decreasing temperature) from the plateau expected from the Stokes–Einstein relation in the small $\Delta\tau$ (or high temperature) region. Thus, $D_g\Delta\tau$ or $\langle [\Delta\mathbf{r}(\Delta\tau)]^2 \rangle$ of Y&O may be regarded as corresponding to d^2 in Eq. (15.5). Y&O have clearly shown that the BSE is directly related to the increase in $\langle [\Delta\mathbf{r}(\Delta\tau)]^2 \rangle$ with decreasing temperature just as the increase in d^2 is responsible for the TRC and BSE in the basic mechanism studied in this chapter. In other words, the picture revealed by the simulations of Y&O represents an “actual” depiction of the basic mechanism as occurring in a model system. The equivalence is characterized by three key elements: the existence of a structure that is flickering in nature (corresponding to the coexistence of mobile and slow components as shown by Y&O); the validity of the central limit theorem as applied to long times $t \gg \Delta\tau$; and the correspondence between $\langle [\Delta\mathbf{r}(\Delta\tau)]^2 \rangle$ and d^2 , both reflecting molecular hopping at low temperatures.

Appendix 15.A — Comparison with the Two-State Model of BSE

The two-state picture proposed by Stillinger and Hodgdon³⁵ consists of flickering fluidized domains in an essentially solid matrix; in the fluidized domains, stress can be released quickly and the molecule can move faster. The fluidized domains in the SH picture was described in terms of four temperature-dependent average characteristics:

- (1) domain volume v_0 ;
- (2) domain appearance rate per unit volume, r_0 ;

^cSee Fig. 3 of Ref. 50.

^dSee Fig. 5 of Ref. 50.

^eSee Fig. 2 of Ref. 50.

- (3) domain lifetime t_0 ;
 (4) domain internal viscosity η_0 .

η_0 must reflect the fluidized nature of the domains, and thus its magnitude must be substantially less than the macroscopically measured viscosity η . Following SH, as the volume fraction ϕ_0 of the system that is interior to the fluidized domains is given by

$$\phi_0 = r_0 v_0 t_0; \quad (15.A.1)$$

the structural relaxation time τ_S is expressed as

$$\tau_S (\approx \tau_{rot}) = \frac{1}{r_0 v_0} = \frac{t_0}{\phi_0}. \quad (15.A.2)$$

And the viscosity η may be given by

$$\eta \approx G_\infty \tau_S = \frac{G_\infty}{r_0 v_0}. \quad (15.A.3)$$

A key assumption in the SH model is that the system's overall translational diffusion constant D_g is a simple volume average over fluidized domains and surrounding static matrix. Thus,

$$D_g = \phi_0 D_0 + (1 - \phi_0) \times 0 = \phi_0 \left(\frac{kT}{6\pi\eta_0 R} \right) \quad (15.A.4)$$

where the Stokes–Einstein equation is assumed to hold in the fluidized domains; and R is the effective radius of the diffusing molecule. Then using Eqs. (15.A.1) and (15.A.3), the enhancement factor μ as defined by Eq. (15.6) is expressed as

$$\mu = \phi_0 \left(\frac{kT}{6\pi\eta_0 R} \right) \bigg/ \left(\frac{kT}{6\pi\eta R} \right) = r_0 v_0 t_0 \frac{\eta}{\eta_0} \approx G_\infty \frac{t_0}{\eta_0}. \quad (15.A.5)$$

As observed, μ increases with decreasing temperature; so must t_0/η_0 do. Then, using Eqs. (15.A.2) and (15.A.4), we obtain Eq. (15.10) from Eq. (15.5).

References

1. Lin, Y.-H., *J. Phys. Chem. B* **109**, 17654 (2005).
2. Lin, Y.-H., *J. Phys. Chem. B* **109**, 17670 (2005).
3. Lin, Y.-H., *J. Phys.: Condens. Matter* **19**, 466101 (2007).

4. Plazek, D. J., *J. Phys. Chem.* **69**, 3480 (1965).
5. Plazek, D. J., *J. Polym. Sci., Part A-2: Polym. Phys.* **6**, 621 (1968).
6. Plazek, D. J., and O'Rourke, V. M., *J. Polym. Sci. A-2: Polym. Phys.* **9**, 209 (1971).
7. Inoue, T., Onogi, T., Yao, M.-L., and Osaki, K., *J. Polym. Sci.: Part B: Polym. Phys.* **37**, 389 (1999).
8. Lin, Y.-H., *Macromolecules* **17**, 2846 (1984).
9. Lin, Y.-H., *Macromolecules* **19**, 159 (1986).
10. Lin, Y.-H., *Macromolecules* **20**, 885 (1987).
11. Doi, M., and Edwards, S. F., *The Theory of Polymer Dynamics*, Oxford Univ. Press (1986).
12. Reichl, L. E., *A Modern Course in Statistical Physics* (2nd edn), Wiley, New York (1998).
13. Goldstein, M., *J. Chem. Phys.* **51**, 3728 (1969).
14. Angell, C. A., *J. Non-Cryst. Solids* **131–133**, 13 (1991).
15. Angell, C. A., *Science* **267**, 1924 (1995).
16. Stillinger, F. H., *Science* **267**, 1935 (1995).
17. Ediger, M. D., Angell, C. A., and Nagel, S. R., *J. Phys. Chem.* **100**, 13200 (1996).
18. Ediger, M. D., *Annu. Rev. Phys. Chem.* **51**, 99 (2000).
19. Thirumalai, D., and Mountain, R. D., *Phys. Rev. E* **47**, 479 (1993).
20. Doi, M., and Edwards, S. F., *J. Chem. Soc., Faraday Trans. 2*, **74**, 1789 (1978); **74**, 1802 (1978).
21. Plazek, D. J., *Polym. J.* **12**, 43 (1980).
22. Plazek, D. J., *J. Rheol.* **40**, 987 (1996).
23. Inoue, T., Okamoto, H., and Osaki, K., *Macromolecules* **24**, 5670 (1991).
24. Inoue, T., Hayashihara, H., Okamoto, H., and Osaki, K., *J. Polym. Sci. Polym. Phys. Ed.* **30**, 409 (1992).
25. Okamoto, H., Inoue, T., and Osaki, K., *J. Polym. Sci.: Part B: Polym. Phys.* **33**, 417 (1995).
26. Schonhals, A., *Macromolecules* **26**, 1309 (1993); Schonhals, A., and Schlosser, E., *Phys. Scr., T.* **49**, 233 (1993).
27. Adachi, K., and Hirano, H., *Macromolecules* **31**, 3958 (1998).
28. Fujara, F., Geil, B., Sillescu, H., and Fleischer, G. Z., *Phys. B: Condens. Matter* **88**, 195 (1992).
29. Cicerone, M. T., and Ediger, M. D., *J. Phys. Chem.* **97**, 10489 (1993).
30. Kind, R., Liechti, N., Korner, N., and Hülliger, J., *Phys. Rev. B* **45**, 7697 (1992).
31. Chang, I., Fujara, F., Geil, B., Heuberger, G., Mangel, T., and Sillescu, H., *J. Non-Cryst. Solids* **172–174**, 248 (1994).
32. Mapes, M. K., Swallen, S. F., and Ediger, M. D., *J. Phys. Chem. B* **110**, 507 (2006).
33. Chang, I., and Sillescu, H., *J. Phys. Chem. B* **101**, 8794 (1997).
34. Swallen, S. F., Traynor, K., McMahan, R. J., Ediger, M. D., and Mates, T. E., *J. Phys. Chem. B* **113**, 4600 (2009); Swallen, S. F., Bonvallet, P. A., McMahan, R. J., and Ediger, M. D., *Phys. Rev. Lett.* **90**, 015901 (2003).

35. Stillinger, F. H., and Hodgdon, J. A., *Phys. Rev. E* **50**, 2064 (1994).
36. Tarjus, G., and Kivelson, D., *J. Chem. Phys.* **103**, 3071 (1995).
37. Liu, C. Z.-W., and Openheim, I., *Phys. Rev. E* **53**, 799 (1996).
38. Cicerone, M. T., Wagner, P. A., and Ediger, M. D., *J. Phys. Chem. B* **101**, 8727 (1997).
39. Xia, X., and Wolynes, P. G., *J. Phys. Chem.* **105**, 6570 (2001).
40. Jung, Y. J., Garrahan, J. P., and Chandler, D., *Phys. Rev. E* **69**, 061205 (2004).
41. Plazek, D. J., Bero, C. A., and Chay, I. C., *J. Non-Cryst. Solids* **172–174**, 181 (1994).
42. Adam, G., and Gibbs, J. H., *J. Chem. Phys.* **43**, 139 (1965).
43. Sillescu, H., *J. Non-Cryst. Solids* **243**, 81 (1999).
44. Weeks, E. R., Crocker, J. C., Levitt, A. C., Schofield, A., and Weitz, D. A., *Science* **287**, 627 (2000).
45. Mountain, R. D., *J. Chem. Phys.* **102**, 5408 (1995).
46. Sastry, S., Debenedetti, P. G., and Stillinger, F. H., *Nature* **393**, 554 (1998).
47. Debenedetti, P. G., and Stillinger, F. H., *Nature* **410**, 259 (2001).
48. Russell, E. V., and Israeloff, N. E., *Nature* **408**, 695 (2000).
49. Martinez, L.-M., and Angell, C. A., *Nature* **410**, 663 (2001).
50. Yamamoto, R., and Onuki, A., *Phys. Rev. Lett.* **81**, 4915 (1998).
51. Donati, C., Glotzer, S. C., Poole, P. H., Kob, W., and Plimpton, S. J., *Phys. Rev. E* **60**, 3107 (1999).
52. Schroder, T. B., Sastry, S., Dyre, J. C., and Glotzer, S. C., *J. Chem. Phys.* **112**, 9834 (2000).
53. Hempel, E., Hempel, G., Hensei, A., Schick, C., and Donth, E., *J. Phys. Chem. B* **104**, 2460 (2000).
54. Reinsberg, S. A., Qiu, X. H., Wilhelm, M., Spiess, H. W., and Ediger, M. D., *J. Chem. Phys.* **114**, 7299 (2001).
55. Qiu, X. H., and Ediger, M. D., *J. Phys. Chem. B* **107**, 459 (2003).

Chapter 16

Monte Carlo Simulations of Stress Relaxation of Rouse Chains

In Chapters 3, 6 and 7, the two equivalent descriptions of Brownian motion: the Langevin and Smoluchowski equations for an entanglement-free system have been studied in the cases where analytic solutions are obtainable: the time-correlation function of the end-to-end vector of a Rouse chain and the constitutive equation of the Rouse model. When the Brownian motion of a more complicated model is to be studied, where an analytical solution cannot be obtained, the Monte Carlo simulation becomes a useful tool. Unlike the Monte Carlo simulation that is employed to calculate static properties using the Metropolis criterion,^{1,2} the simulation based on the Langevin equation can be used to calculate both static and dynamic quantities.³⁻⁵ In this chapter, the simulation scheme will be introduced and illustrated by applying it to the Rouse chain. The computer simulation results of the Rouse-chain model can be directly compared with the analytical solutions to demonstrate the validity of the simulations. This will serve to validate simulations by the same scheme on systems of which analytical solutions are not available. In Chapters 17 and 18, simulations on entanglement-free Fraenkel chains⁴⁻⁶ are studied giving new understandings at the molecular level of polymer viscoelasticity.

16.1 The Basic Monte Carlo Simulation Scheme as Applied to the Rouse Model

In the Monte Carlo simulation, the continuous change in time, dt , in the Langevin equation is replaced by a small time step, Δt . The changes in the positions $\{\mathbf{R}_n(t)\}$ of the beads of a Rouse chain are slow varying processes as opposed to the fluctuations $\{\mathbf{g}_n(t)\}$ defined by Eqs. (3.34) and (3.35) being instantaneously fast. Thus, with the random displacement $\mathbf{d}_n(t_i)$ of

the n th bead during the i th time step (Δt) defined as

$$\mathbf{d}_n(t_i) = \mathbf{d}_n(i) = \int_{t_i}^{t_i+\Delta t} \mathbf{g}_n(t) dt. \quad (16.1)$$

Equation (3.31) can be replaced by

$$\mathbf{R}_n(t_i + \Delta t) = \mathbf{R}_n(t_i) + \frac{1}{\zeta} \mathbf{F}_n(t_i) \Delta t + \mathbf{d}_n(t_i). \quad (16.2)$$

As derived from the interaction potential Eq. (3.30), the total force $\mathbf{F}_n(t_i)$ asserted on an internal bead by the springs is given by

$$\mathbf{F}_n(t_i) = -\frac{3kT}{b^2} (2\mathbf{R}_n(t_i) - \mathbf{R}_{n+1}(t_i) - \mathbf{R}_{n-1}(t_i)). \quad (16.3)$$

Equivalent to Eq. (16.3), the equations for the end beads (for $n = 1$ or N) can be similarly obtained. Being in a general form, Eq. (16.2) can be used as long as the interaction potential is a coarse-grained one (such as the Fraenkel potential studied in Chapters 17 and 18), from which the sum of spring forces on each bead $\mathbf{F}_n(t_i)$ can be similarly obtained.

Obviously, corresponding to Eq. (3.34), the average of the random displacement for any time step i is

$$\langle \mathbf{d}_n(i) \rangle = \langle \mathbf{d}_n(t_i) \rangle = 0. \quad (16.4)$$

The diffusion constant D of a single Rouse bead, as shown in Appendix 3.D, can be defined by

$$D = \frac{kT}{\zeta} = \frac{d^2}{2\Delta t} \quad (16.5)$$

where d is the step length traversed by a bead during a time step Δt along each of the three Cartesian axes. Using Eqs. (3.35), (16.1) and (16.5), the correlation of $\mathbf{d}_n(i) (= \mathbf{d}_n(t_i))$ at two time steps is obtained as

$$\begin{aligned} & \langle \mathbf{d}_n(i) \mathbf{d}_m(j) \rangle \\ &= \int_{t_i}^{t_i+\Delta t} dt' \int_{t_j}^{t_j+\Delta t} dt'' \langle \mathbf{g}_n(t') \mathbf{g}_m(t'') \rangle \\ &= d^2 \delta \delta_{nm} \delta_{ij} \end{aligned} \quad (16.6)$$

which means that the random steps $\{\mathbf{d}_n(i)\}$ may take up the role played by the random fluctuations $\{\mathbf{g}_n(t)\}$ in the Langevin equation. Equation (16.6)

indicates that a random step taken by a bead in a certain coordinate direction during a certain time step is totally correlated with itself. At the same time, one random step is totally uncorrelated with another, if between the two at least one of the following is true: the two steps are separately taken by two different beads ($n \neq m$); the two steps are in different coordinate directions ($\alpha \neq \beta$, with $\alpha, \beta \equiv x, y$ or z); and the two steps occur separately during two different time steps ($i \neq j$). Each of the three components of $\mathbf{d}_n(i)$ for any bead and any time step, can be calculated by multiplying d by $+1$ or -1 that can be generated randomly with equal probability by a computer.^{1,2} Thus generated random steps $\{\mathbf{d}_n(i)\}$ satisfy the conditions given by Eqs. (16.4) and (16.6). Using Eq. (16.5), Eq. (16.2) may be rewritten as

$$\mathbf{R}_n(i+1) = \mathbf{R}_n(i) + \frac{d^2}{2kT} \mathbf{F}_n(i) + \mathbf{d}_n(i) \quad (16.7)$$

where i denotes some current time step $t_i/\Delta t$, while $i+1$ denotes the next one. For the Rouse model, Eqs. (3.31), (3.34) and (3.35), which collectively define the Langevin equation for the internal beads, are replaced by Eq. (16.7) together with Eqs. (16.3), (16.4) and (16.6) in the Monte Carlo simulation. The equivalent transformation is applied to Eqs. (3.32) and (3.33) for the end beads. In a computer simulation, Eq. (16.7) allows us to calculate the chain configuration of the next time step, $\{\mathbf{R}_n(i+1)\}$, from the current configuration $\{\mathbf{R}_n(i)\}$. As the diffusion constant D is given by Eq. (16.5), the number of steps required for a dynamic response or time-correlation function to relax or decay to a certain extent depends on the d value chosen. Using Eq. (16.5), the relaxation time τ_p as given by Eq. (3.55) can be expressed in units of the time step as

$$\frac{\tau_p}{\Delta t} = \frac{b^2}{6d^2 \sin^2(p\pi/2N)}. \quad (16.8a)$$

In the same way, corresponding to Eq. (7.56),

$$\frac{\tau_p}{\Delta t} = \frac{b^2}{12d^2 \sin^2(p\pi/2N)}. \quad (16.8b)$$

Clearly, a smaller d representing a higher time-scale resolution leads to greater computing-time requirements as a larger number of steps are required for the time-correlation function or relaxation function under simulation to reach the same point in time.

Through Eq. (16.8a) or (16.8b), the time-correlation function $C(t) = \langle \mathbf{R}(0) \cdot \mathbf{R}(t) \rangle$ of the end-to-end vector and the relaxation modulus $G(t)$ calculated from Eqs. (3.59) and (7.58), respectively, may be compared with the corresponding simulation results for a Rouse chain. In the simulation of a time-correlation function, an equilibrium state is first established by running a sufficiently large number of Monte Carlo steps. Then, a time window is set up, within which the time-correlation function may be calculated as explained in the following:

The end-to-end vectors $\{\mathbf{R}(i); i = 1 \text{ to } N_w\}$ of N_w sequential time steps — the time-window set of vectors — are first calculated in an equilibrium state and stored. As the simulation advances one step forward, the first end-to-end vector in the time-window set, $\mathbf{R}(1)$, kept in the storage is discarded and replaced by the second $\mathbf{R}(2)$, the second by the third, \dots , and the last $\mathbf{R}(N_w)$ by the newly generated. Updating the stored time-window set of vectors in the same replacement scheme is repeated a large number of times — one for each advancing step. Before each updating, the dot products of the first end-to-end vector $\mathbf{R}(1)$ and each of the vectors in the set $\{\mathbf{R}(i); i = 1 \text{ to } N_w\}$ are calculated and individually accumulated over many repetitions — for averaging over the number of repetitions. After a sufficiently large number of repetitions, the obtained (time-)averaged values as denoted by $\overline{\mathbf{R}(1) \cdot \mathbf{R}(1)}$, $\overline{\mathbf{R}(1) \cdot \mathbf{R}(2)}$, $\overline{\mathbf{R}(1) \cdot \mathbf{R}(3)} \dots$ are equivalent to $C(0)$, $C(1)$, $C(2)$, \dots respectively, under the ergodic assumption.⁷ As shown in Fig. 16.1, the quantitative agreements between simulations and theory for the end-to-end vector time-correlation function confirm the validity of the Monte Carlo simulation scheme.

16.2 Simulation of the Rouse Relaxation Modulus — Following the Application of a Step Shear Strain

The relaxation modulus $G(t)$ can be calculated by the Monte Carlo simulation after a step shear deformation

$$\mathbf{E} = \begin{pmatrix} 1 & \lambda & 0 \\ 0 & 1 & 0 \\ 0 & 0 & 1 \end{pmatrix} \quad (16.9)$$

is applied in an affine way to the polymer chain in an equilibrium state at $t = 0$. Following the application of \mathbf{E} , the evolution of $\{\mathbf{R}_n(i)\}$ is calculated according to Eq. (16.7), and the stress relaxation of a chain with N beads,

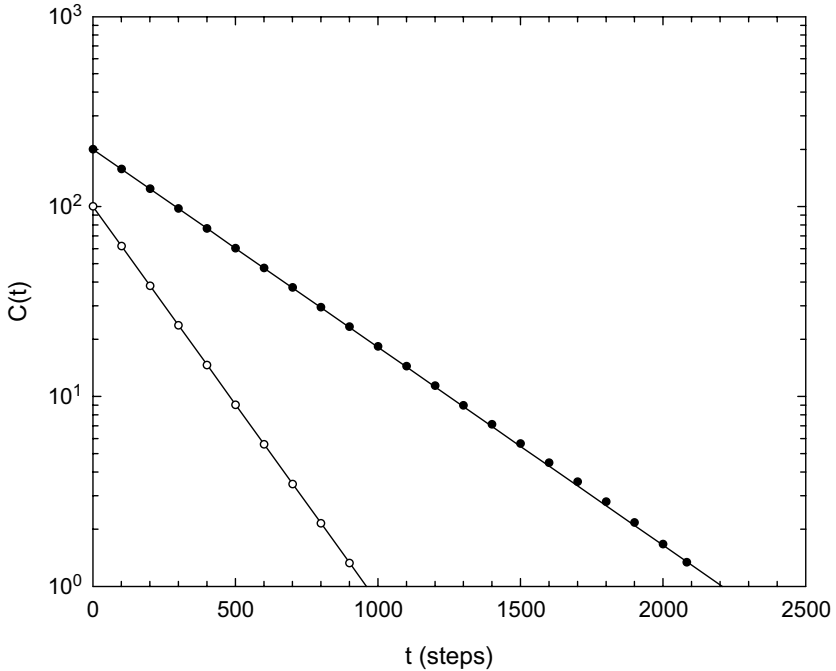


Fig. 16.1 Comparison of the analytical solutions (solid lines) and the Monte Carlo simulations for the time-correlation functions of the end-to-end vector, $C(t) = \langle \mathbf{R}(0) \cdot \mathbf{R}(t) \rangle$, of the Rouse chains with two beads (o) and three beads (•) ($b = 10$ and $d = 0.4$ are used in the simulations.).

normalized per segment, is given by

$$S_{xy}(\lambda, i) = \frac{1}{(N - 1)} \sum_{n=1}^N \langle F_{nx}(i) Y_n(i) \rangle. \quad (16.10)$$

As shown in Appendix 16.A, the expression for the stress tensor given in Eq. (16.10) is equivalent to that expressed in terms of connector force and bond vector in Chapters 6 and 7 (see Eq. (6.35)).

In the simulation, a large number of relaxation processes following a step deformation are repeated and the calculated values of the dynamic quantity $\sum_{n=1}^N F_{nx}(i) Y_n(i)$ at individual time steps (i) are accumulated for averaging as denoted by the angular bracket $\langle \rangle$ in Eq. (16.10). Before a new cycle is started, the simulation must be run for a sufficiently large number of time steps for the system to reach an equilibrium state. To prevent some residual stress from accumulating, the step deformation may

be applied in a cyclic manner. If the \mathbf{E} given by Eq. (16.9) is referred to as a deformation in the x direction and denoted by x , the deformation cycle: $x \rightarrow -x \rightarrow y \rightarrow -y \rightarrow z \rightarrow -z$ is repeated. Following each step deformation, the physically equivalent stress component is monitored and its numerical values at different time steps are registered. The registered values are accumulated for averaging over each cycle and over the number of cycles. Although the cyclic scheme has been used for obtaining the results reported in this chapter (and Chapters 17 and 18), the obtained simulation results are discussed with respect to Eq. (16.9) as the chosen direction of deformation — in other words, the shear stress is denoted by the xy component. With $S_{xy}(\lambda, i)$ (Eq. (16.10)) calculated this way, the normalized relaxation modulus per segment is given by

$$G_S(i) = -\frac{S_{xy}(\lambda, i)}{\lambda}. \quad (16.11)$$

Both the Rouse theory and the Rouse-model Monte Carlo simulation are a mean-field representation, meaning that the stress relaxation is the sum of contributions from all the chains in a unit volume, each represented by its statistically averaged time dependence (Chapters 6 and 7).^{8,9} Thus, simulations as explained above are performed on a single chain.

16.3 Simulation of the Rouse Relaxation Modulus — in an Equilibrium State

In accordance with the fluctuation–dissipation theorem (Appendix 16.B), at low strains λ in the linear region, the normalized relaxation modulus given by Eqs. (16.10) and (16.11) is equivalent to the time-correlation function:

$$\begin{aligned} G_S(i) &= \frac{1}{(N-1)kT} \langle J_{xy}(0)J_{xy}(i) \rangle \\ &= \frac{1}{(N-1)kT} \overline{J_{xy}(0)J_{xy}(i)} \\ &= \frac{1}{I(N-1)kT} \sum_{i_0=1}^I J_{xy}(i_0)J_{xy}(i_0+i) \end{aligned} \quad (16.12)$$

where $J_{xy}(i)$ is the stress component given by

$$J_{xy}(i) = \sum_{n=1}^N F_{nx}(i)Y_n(i). \quad (16.13)$$

In Eq. (16.12), I represents a large number of iterations.^a In the simulation, all the six combinations of $J_{\alpha\beta}(t)$ (with $\alpha \neq \beta$)^b may be used for averaging in the calculation of the time-correlation function; the xy component is used as the representative of the shear stress in all the discussions. The simulation result as obtained through Eqs. (16.10) and (16.11) may be referred to as the step strain-simulated $G_S(t)$, as opposed to the equilibrium-simulated $G_S(t)$ obtained through Eq. (16.12).

16.4 Comparison between Simulation and Theory of the Rouse Model

(a) Step strain-simulated relaxation modulus

The shear relaxation modulus $G_S(t)$ and the first normal-stress difference function $G_{\Psi_1}(t)$, both normalized on a per-segment basis and with kT set to 1, are obtained from the constitutive equation of the Rouse model (Eq. (7.55) with s_p replaced by τ_p) as

$$G_S(t) = \frac{-S_{xy}(t, \lambda)}{\lambda} = \frac{-\tau_{xy}(t, \lambda)}{\lambda n (N-1)} = \frac{1}{(N-1)} \sum_{p=1}^{N-1} \exp\left[-\frac{t}{\tau_p}\right] \quad (16.14)$$

and

$$\begin{aligned} G_{\Psi_1}(t) &= -\frac{S_{xx}(t, \lambda) - S_{yy}(t, \lambda)}{\lambda^2} = -\frac{\tau_{xx}(t, \lambda) - \tau_{yy}(t, \lambda)}{\lambda^2 n (N-1)} \\ &= \frac{1}{(N-1)} \sum_{p=1}^{N-1} \exp\left[-\frac{t}{\tau_p}\right] \end{aligned} \quad (16.15)$$

Several key predictions of the Rouse theory may be summarized as in the following:

- (1) The relaxation time of the p th Rouse normal mode, $\tau_p(N)$, has the N and p dependences as given by Eq. (7.56) or Eq. (16.8b).
- (2) No nonlinear effect in the shear stress relaxation; in other words, $G_S(t)$ as given by Eq. (16.14) is independent of the applied strain λ .

^aCorrection: the typical number of iterations $I \sim 3 \times 10^4$ indicated in Ref. 4 should have been $I \sim 3 \times 10^8$.

^bAt any time-step of simulation computation $J_{\alpha\beta}(t) = J_{\beta\alpha}(t)$ is observed, except for extremely small run-off errors.

- (3) The Lodge–Meissner relation holds; namely, $G_S(t) = G_{\Psi_1}(t)$ as indicated by Eqs. (16.14) and (16.15).
- (4) The second normal-stress difference as defined by $N_2(t, \lambda) = -(S_{yy}(t, \lambda) - S_{zz}(t, \lambda))$ is zero.

These results are exactly confirmed by the simulations; cases (1)–(3) are illustrated in the following: The relaxation time in units of the time step as expressed by Eq. (16.8b) allows one to compare the simulated $G_S(t)$ curve with that calculated from Eq. (16.14). In Fig. 16.2, such a comparison is made for two-bead, five-bead and ten-bead Rouse chains. The perfect agreements between the simulated and theoretical line shapes without any shift along both the modulus and time-step axes confirm the predicted N and p dependences of the relaxation times of the Rouse normal modes. As predicted by the theory, no nonlinear effect can be observed between the

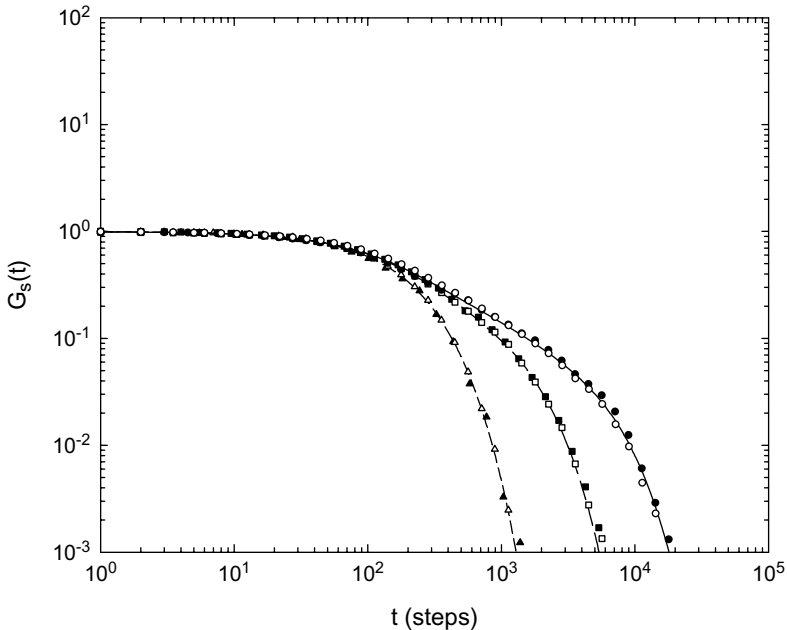


Fig. 16.2 Comparison of the step strain-simulated $G_S(t)$ results of two-bead, five-bead and ten-bead Rouse chains (\blacktriangle for $N = 2$; \blacksquare for $N = 5$; \bullet for $N = 10$) with the equilibrium-simulated $G_S(t)$ curves (\triangle for $N = 2$; \square for $N = 5$; and \circ for $N = 10$) and the Rouse theoretical curves (short-dash line for $N = 2$; long-dash line for $N = 5$; and solid line for $N = 10$).

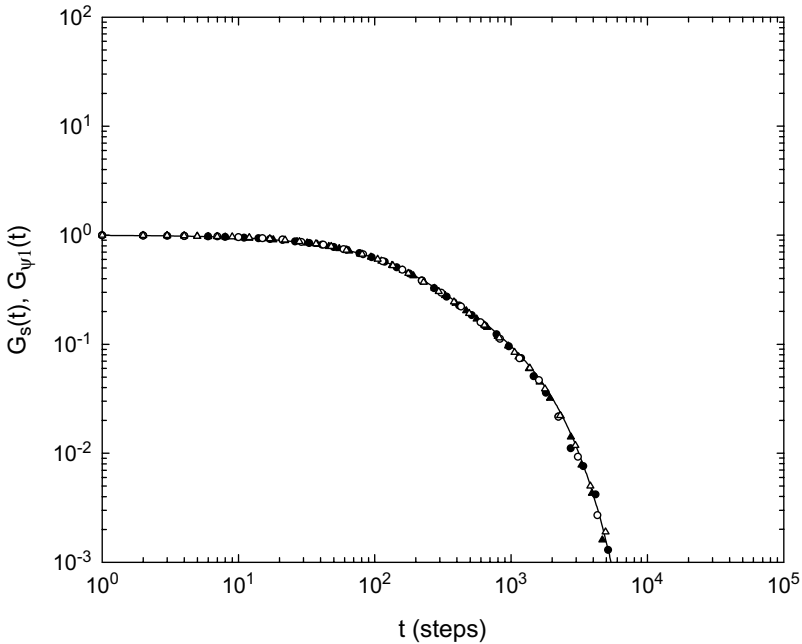


Fig. 16.3 Comparison of the Rouse theory (solid line) and the results of $G_S(t)$ (\circ at $\lambda = 1$ and \triangle at $\lambda = 2$) and $G_{\Psi_1}(t)$ (\bullet at $\lambda = 1$ and \blacktriangle at $\lambda = 2$) obtained from simulations on the five-bead Rouse chain following the application of a step shear strain λ .

$G_S(t)$ curves simulated at $\lambda = 0.5$ and 1 for the Rouse chain model; in other words, the shown step strain-simulated $G_S(t)$ curves are linear results. In Fig. 16.3, the strain independence of $G_S(t)$ and $G_{\Psi_1}(t)$ for a five-bead Rouse chain and the close agreements of the simulation results with the theoretical Rouse curve are shown.

(b) *Equilibrium-simulated relaxation modulus*

Based on the fluctuation–dissipation theorem, the equilibrium-simulated $G_S(t)$ is predicted to be equivalent to the step strain-simulated $G_S(t)$ in the linear region. In Fig. 16.2, the equilibrium-simulated $G_S(t)$ curves for two-bead, five-bead and ten-bead Rouse chains are also shown. These equilibrium-simulated $G_S(t)$ results are in perfect agreement with the step strain-simulated results and the Rouse theoretical curves, illustrating the fluctuation–dissipation theorem as applied to the Rouse model and confirming the validity of the Monte Carlo simulations.

Appendix 16.A — Molecular Expression for the Stress Tensor

Consider a volume V_0 , which contains N beads. There are totally $N(N-1)/2$ pair interactions between the beads, chemically bonded or not. Then Eq. (6.35) can be generalized to express the stress tensor arising from the interactions between the N beads in V_0 as

$$\boldsymbol{\tau} = \frac{1}{2V_0} \sum_{n=1}^N \sum_{m=1}^N \langle \mathbf{F}_{nm} (\mathbf{R}_m - \mathbf{R}_n) \rangle \quad (16.A.1)$$

where \mathbf{F}_{nm} denotes the force that the n th bead exerts on the m th bead (cf. Eq. (6.4) or (6.5)); in the double sum, the terms with $n = m$ being zero, there are in effect only $N(N-1)$ terms; and the double sum is divided by 2 to correct for double counting. The total force exerted on the m th bead is given by:

$$\mathbf{F}_m = \sum_n \mathbf{F}_{nm}. \quad (16.A.2)$$

Using Newton's third law $\mathbf{F}_{nm} = -\mathbf{F}_{mn}$ and Eq. (16.A.2), Eq. (16.A.1) is rewritten as

$$\begin{aligned} \boldsymbol{\tau} &= \frac{1}{2V_0} \left\langle \sum_m \sum_n \mathbf{F}_{nm} \mathbf{R}_m - \sum_m \sum_n \mathbf{F}_{nm} \mathbf{R}_n \right\rangle \\ &= \frac{1}{V_0} \left\langle \sum_m \mathbf{F}_m \mathbf{R}_m \right\rangle. \end{aligned} \quad (16.A.3)$$

When only a single chain is considered as in a mean-field representation, Eq. (16.A.3) reduces to the normalized form given by Eq. (16.10).

Appendix 16.B — Time-Correlation Functional Form for the Relaxation Modulus

In accordance with the fluctuation-dissipation theorem, the self time-correlation function of a physical quantity or the time-correlation function between it and another quantity in an equilibrium system is related to its response to a weak applied external field — weak enough to be in the linear region. Here, after a general proof of the fluctuation-dissipation theorem, the expression of the time-correlation function corresponding to the

relaxation modulus obtained following the application of a step shear strain will be derived.

Consider a time-dependent external field $h(t)$ applied to a system in equilibrium under a potential $V(x)$. For the sake of simplicity, x has been used to denote the whole set of coordinates $\{x_i\}$ appearing in the Smoluchowsky equation. Because the applied field perturbs the system, the average values of physical quantities in the system change from those in the equilibrium state. If the field is weak, the change in any physical quantity is a linear functional of $h(t)$ as expressed by

$$\langle A(t) \rangle_h - \langle A \rangle_0 = \int_{-\infty}^t \mu(t-t') h(t') dt'. \quad (16.B.1)$$

In Eq. (16.B.1), $\langle A(t) \rangle_h$ denotes the value of A at time t when the field $h(t)$ is applied and $\langle A \rangle_0$ is the equilibrium value of A in the absence of the field. As $\mu(t)$ is equivalent to $M(t)$ in Eq. (4.23) if the linear viscoelasticity is being considered, it is referred to as the memory function.^c

The effect of the field on the system may be represented by a perturbation potential as given by

$$V'(x, t) = -h(t)B(x) \quad (16.B.2)$$

where $B(x)$ is the physical quantity conjugate to the field $h(t)$. Then the memory function is related to the time-correlation function between A and B in the absence of the field as given by

$$\mu(t) = -\frac{1}{kT} \frac{d}{dt} \langle A(t)B(0) \rangle_{h=0} \quad (16.B.3)$$

which is called the fluctuation–dissipation theorem.

To prove Eq. (16.B.3), we consider the situation that a constant field h has been applied for so long that the system has reached equilibrium; then the field is switched off at $t = 0$. In this case, Eq. (16.B.1) is rewritten as

$$\langle A(t) \rangle_h = \langle A \rangle_0 + h \int_{-\infty}^0 \mu(t-t') dt' = \langle A \rangle_0 + h\alpha(t) \quad (16.B.4)$$

^c $\mu(t)$ is also called the response function as in Ref. 8. Another reason to refer to $\mu(t)$ as the memory function is to avoid confusion with $G(t)$, $G^*(w)$ and $J(t)$ which are called the viscoelastic response functions in this book.

where

$$\alpha(t) = \int_t^\infty \mu(\tau) d\tau \quad (16.B.5)$$

At $t = 0$, $\langle A(t = 0) \rangle_h$ as defined in Eq. (16.B.4) represents the equilibrium value of A when the constant field h is being applied. $\alpha(t)$ is the relaxation function characterizing the average quantity $\langle A(t > 0) \rangle_h$ changing, in the absence of the field ($h = 0$ for $t > 0$), from $\langle A(t = 0) \rangle_h$ to $\langle A \rangle_0$. If the distribution function $\Psi(x, t)$ in the Smoluchowski equation (Eq. (3.20)) is known, $\langle A(t) \rangle_h$ can be expressed by

$$\langle A(t) \rangle_h = \int A(x) \Psi(x, t) dx. \quad (16.B.6)$$

As there is no applied field for $t > 0$, $\Psi(x, t)$ is related to $\Psi(x, t = 0)$ by the Green function $G(x, x'; t)$ under $h = 0$,

$$\Psi(x, t) = \int G(x, x'; t) \Psi(x', 0) dx'. \quad (16.B.7)$$

As indicated by Eq. (16.B.7), $\Psi(x, t) = G(x, t)$ if the initial condition $\Psi(x', t = 0) = \delta(x - x') = \Pi_n \delta(x_n - x'_n) (= G(x, x'; t = 0))$. In other words, the Green function $G(x, x'; t)$ can be obtained from the Smoluchowski equation as given by Eq. (3.20) with $\Psi(x, t)$ replaced by $G(x, x'; t)$ under the initial condition $G(x, x'; t = 0) = \delta(x - x')$. However, Eq. (3.20) need not be directly involved here. Since the system is at equilibrium in the presence of the field h at $t = 0$,

$$\Psi(x, 0) = \frac{\exp[-(V(x) - hB(x))/kT]}{\int \exp[-(V(x) - hB(x))/kT] dx}. \quad (16.B.8)$$

To terms linear in h , $\Psi(x, 0)$ may be expanded as

$$\begin{aligned} \Psi(x, 0) &= \frac{\exp[-V(x)/kT](1 + hB(x)/kT)}{\int \exp[-V(x)/kT](1 + hB(x)/kT) dx} \\ &= \frac{\exp[-V(x)/kT](1 + hB(x)/kT)}{\int \exp[-V(x)/kT] dx (1 + h\langle B \rangle_0/kT)} \\ &= \frac{\exp[-V(x)/kT][1 + h(B(x) - \langle B \rangle_0)/kT]}{\int \exp[-V(x)/kT] dx} \\ &= \Psi_{eq}(x) \left[1 + \frac{h(B(x) - \langle B \rangle_0)}{kT} \right] \end{aligned} \quad (16.B.9)$$

Using Eqs. (16.B.7) and (16.B.9), Eq. (16.B.6) may be rewritten as

$$\langle A(t) \rangle_h = \int dx \int dx' A(x) G(x, x'; t) \Psi_{eq}(x') \left[1 + \frac{h(B(x') - \langle B \rangle_0)}{kT} \right]. \quad (16.B.10)$$

Using the stationary property of the equilibrium state,

$$\Psi_{eq}(x) = \int G(x, x'; t) \Psi_{eq}(x') dx', \quad (16.B.11)$$

Equation (16.B.10) is further rewritten as

$$\begin{aligned} \langle A(t) \rangle_h &= \int dx A(x) \Psi_{eq}(x) \left[1 - \frac{h\langle B \rangle_0}{kT} \right] \\ &\quad + \frac{h}{kT} \int dx \int dx' A(x) G(x, x'; t) \Psi_{eq}(x') B(x') \\ &= \langle A \rangle_0 - \frac{h}{kT} \langle A \rangle_0 \langle B \rangle_0 + \frac{h}{kT} \langle A(t) B(0) \rangle_0 \end{aligned} \quad (16.B.12)$$

Comparison of Eqs. (16.B.4) and (16.B.12) gives

$$\alpha(t) = \frac{1}{kT} (\langle A(t) B(0) \rangle_0 - \langle A \rangle_0 \langle B \rangle_0) \quad (16.B.13)$$

which in turn leads to Eq. (16.B.3) through Eq. (16.B.5).

For the relaxation of the stress induced by the application of a step strain λ at $t = 0$, Eq. (4.23)^d can be written as

$$\tau_{xy}(t) = \langle J_{xy}(t) \rangle = -\lambda \int_{-\infty}^0 M(t-t') dt' = -\lambda G(t) \quad (16.B.14)$$

as $\lambda(t, t') = 0$ for $t' \geq 0_+$ and $\lambda(t, t') = -\lambda$ for $t \leq 0_-$. Into Eq. (16.B.14), we have incorporated the molecular expression for the shear stress

$$J_{xy}(t) = \frac{1}{V_0} \sum_{n=1}^N F_{nx}(t) Y_n(t) \quad (16.B.15)$$

for a system of N particles and volume V_0 . Note that in the main text, $J_{xy}(t)$ as given by Eq. (16.13) is defined differently: N being the total number of beads in the single chain under simulation without involving the volume. It is convenient to use Eq. (16.13) in the simulations studied in this

^dIf the Rouse chain model being considered, the use of Eq. (7.55) instead of Eq. (4.23) leads to the same result.

chapter and the next two. Here, we consider a general case, which is not limited to the mean-field approach as taken in the Monte Carlo simulations studied in the main text. (The difference arising between using Eq. (16.13) and the complete expression Eq. (16.B.15) needs to be taken into account when a comparison between simulation and experiment is to be made as shown in Fig. 17.7).

From comparing Eqs. (16.B.14) and (16.B.4), the following one-to-one correspondences are obtained:

$$\lambda(t, t' \leq 0_-) \leftrightarrow h \quad \text{or} \quad -\lambda \leftrightarrow h, \quad (16.B.16)$$

$$A(t) \leftrightarrow J_{xy}(t), \quad (16.B.17)$$

$$\mu(t) \leftrightarrow M(t), \quad (16.B.18)$$

$$\alpha(t) \leftrightarrow G(t), \quad (16.B.19)$$

and

$$\langle A \rangle_0 = \langle J_{xy} \rangle_0 = 0. \quad (16.B.20)$$

Using Eqs. (16.B.17), (16.B.19) and (16.B.20), from Eq. (16.B.13) we obtain

$$G(t) = \frac{1}{kT} \langle J_{xy}(t) B(0) \rangle_0. \quad (16.B.21)$$

Substituting Eq. (16.B.16) into Eq. (16.B.2), we obtain the perturbation potential

$$V' = \lambda B(\{\mathbf{R}_n\}) \quad (16.B.22)$$

that has been applied to the system so long that the system is in equilibrium when the field $h = -\lambda$ is turned off at $t = 0$. We need to find the quantity $B(\{\mathbf{R}_n\})$ that is conjugate to $-\lambda$. Physically, the removal of the perturbation potential $V' = \lambda B(\{\mathbf{R}_n\})$ at $t = 0$ can be regarded as equivalent to the application of $U' = -V'$ at $t = 0$ to the system to nullify V' . In obtaining Eqs. (16.B.4 or 16.B.12) and (16.B.14), we have regarded the system at $t > 0$ as free of perturbation ($h = 0$ or $\lambda(t, t' > 0) = 0$). We may also consider the step strain applied at $t = 0$ as a deformation applied to an equilibrium state that remains unperturbed until that moment — as Eq. (4.28) is obtained through Eq. (4.27). Then the step strain applied at $t = 0$ is equivalent to the imposition of the perturbation $U' = -V'$ onto the system.

We can study the perturbation potential that arises from a small step strain applied to an equilibrium system by considering the change in the dynamic free energy. Here, the potential under which the system is in equilibrium at $t \leq 0_-$ is denoted by U . Then the dynamic free energy of the system is defined as

$$\mathcal{A} = \int d\{\mathbf{R}_n\} \Psi (kT \ln \Psi + U). \quad (16.B.23)$$

At equilibrium,

$$\Psi_{eq} = \frac{\exp\left(\frac{-U}{kT}\right)}{Z} \quad (16.B.24)$$

with

$$Z = \int d\{\mathbf{R}_n\} \exp\left(\frac{-U}{kT}\right). \quad (16.B.25)$$

Corresponding to $\Psi = \Psi_{eq}$,

$$\mathcal{A}_{eq} = -kT \log Z \quad (16.B.26)$$

which is the definition of the free energy in equilibrium statistical thermodynamics. If U is independent of time and there is no flux at the boundary, it can be shown that $d\mathcal{A}/dt$ is negative until Ψ reaches Ψ_{eq} .⁸ (Here Ψ_{eq} is redefined by Eq. (16.B.24), as opposed to that given in Eq. (16.B.9).)

As the step strain is applied at $t = 0$, the dynamic free energy of the system becomes

$$\mathcal{A}' = \int d\{\mathbf{R}_n\} \Psi (kT \ln \Psi + U + U') \quad (16.B.27)$$

and the change in the free energy is

$$\delta\mathcal{A} = \int d\{\mathbf{R}_n\} \Psi U' = -\lambda \int d\{\mathbf{R}_n\} \Psi B(\{\mathbf{R}_n\}). \quad (16.B.28)$$

A step shear deformation λ can be regarded as equivalent to a constant strain rate $\lambda/\delta t$ being applied over a very short time interval δt (cf. Eq. (4.27)). The velocity gradient tensor $\mathbf{K} = (\nabla\mathbf{V})^T$ is expressed by

$$\mathbf{K} = \mathbf{xy} \frac{\lambda}{\delta t}. \quad (16.B.29)$$

As $\delta t \rightarrow 0$, \mathbf{K} becomes very large and the evolution of Ψ during the time interval δt (at $t = 0$) is dominated by the term containing \mathbf{K} (see Eqs. (7.20) and (7.30)):

$$\frac{\partial \Psi}{\partial t} = - \sum_n \frac{\partial}{\partial \mathbf{R}_n} \cdot \mathbf{K} \cdot \mathbf{R}_n \Psi. \quad (16.B.30)$$

Then the change in Ψ due to the step deformation λ is given by

$$\begin{aligned} \delta \Psi &= \frac{\partial \Psi}{\partial t} \delta t = - \sum_n \frac{\partial}{\partial \mathbf{R}_n} \cdot (\lambda \mathbf{x} \mathbf{y} \cdot \mathbf{R}_n \Psi) \\ &= - \sum_n \frac{\partial}{\partial X_n} (\lambda Y_n \Psi). \end{aligned} \quad (16.B.31)$$

From Eq. (16.B.23), a differential change in the dynamic free energy related to $\delta \Psi$ is obtained as

$$\delta \mathcal{A} = \int d \{ \mathbf{R}_n \} (kT \ln \Psi + kT + U) \delta \Psi. \quad (16.B.32)$$

Substituting Eq. (16.B.31) into Eq. (16.B.32) and using integration by parts twice, we obtain

$$\begin{aligned} \delta \mathcal{A} &= \int d \{ \mathbf{R}_n \} \sum_n \lambda Y_n \Psi \frac{\partial}{\partial X_n} (kT \ln \Psi + U) \\ &= -\lambda \int d \{ \mathbf{R}_n \} \sum_n F_{nx} Y_n \Psi. \end{aligned} \quad (16.B.33)$$

Equating Eq. (16.B.28) with (16.B.33), we arrive at the result:

$$\lambda \int d \{ \mathbf{R}_n \} \left(B(\{ \mathbf{R}_n \}) - \sum_n F_{nx} Y_n \right) \Psi = 0. \quad (16.B.34)$$

As Eq. (16.B.34) holds for any arbitrary small value of λ ,

$$B(\{ \mathbf{R}_n \}) = \sum_n F_{nx} Y_n = V_0 J_{xy}. \quad (16.B.35)$$

Comparing Eqs. (16.B.17) and (16.B.35), and using Eq. (16.B.20), we conclude that $B = V_0 A$ and $\langle A \rangle_0 = 0$ in applying Eq. (16.B.13) to the case

of linear viscoelasticity. Substituting Eq. (16.B.35) into Eq. (16.B.21), we obtain

$$\begin{aligned} G(t) &= \frac{V_0}{kT} \langle J_{xy}(t) J_{xy}(0) \rangle_0 \\ &= \frac{1}{V_0 kT} \left\langle \left(\sum_{n=1}^N F_{nx}(t) Y_n(t) \right) \left(\sum_{m=1}^N F_{mx}(0) Y_m(0) \right) \right\rangle. \end{aligned} \quad (16.B.36)$$

As $J_{xy}(t)$ is redefined by Eq. (16.13), Eq. (16.B.36) leads to the $G_S(t)$ expression given by Eq. (16.12), which has been normalized on a per-segment basis.

References

1. Allen, M. P., and Tildesley, D. J., *Computer Simulation of Liquids*, Oxford Univ. Press (1991).
2. Frenkel, D., and Smit, B., *Understanding Molecular Simulation*, Academic Press, San Diego (2002).
3. Lin, Y.-H., and Luo, Z.-H., *J. Chem. Phys.* **112**, 7219 (2000).
4. Lin, Y.-H., and Das, A. K., *J. Chem. Phys.* **126**, 074902 (2007).
5. Lin, Y.-H., and Das, A. K., *J. Chem. Phys.* **126**, 074903 (2007).
6. G. K. Fraenkel, *J. Chem. Phys.* **20**, 642 (1952).
7. McQuarrie, D. A., *Statistical Mechanics*, Harper & Row, New York (1976).
8. Doi, M., and Edwards, S. F., *The Theory of Polymer Dynamics*, Oxford Univ. Press (1986).
9. Bird, R. B., Curtiss, C. F., Armstrong, R. C., and Hassager, O., *Dynamics of Polymeric Liquids*, Vol. 2 (2nd edn), Wiley, New York (1987).

Chapter 17

Monte Carlo Simulations of Stress Relaxation of Fraenkel Chains — Linear Viscoelasticity of Entanglement-Free Polymers

In Chapter 16, the Monte Carlo simulations on the Rouse chains have been studied confirming the validity of the simulation scheme by comparing with the theoretical results. Using the same scheme, simulations on the Fraenkel chain model^{1,2} — whose Langevin equation, being nonlinear, lacks an analytical solution — have been carried out, allowing its performance in describing the polymer viscoelastic behavior to be evaluated.^{3,4}

The molecular viscoelastic models — the Rouse model and the extended reptation model — studied in this book are developed using the Rouse segment as the most basic (smallest) structural unit. Analytical solutions for these models have been studied in Chapters 3 and 6–9. As extensively shown in Chapters 10, 11 and 14, these theories are quantitatively successful in describing the viscoelastic response functions (relaxation moduli $G(t)$ and/or viscoelastic spectra $G^*(\omega)$) over the long-time or low-frequency region (the entropic region). In spite of these successes, the unphysical nature of the Rouse segment has long been a concern. As pointed out in Sec. 6.4, a Rouse segment or chain is infinitely extensible as opposed to a real polymer having a finite backbone contour length. The Rouse segment with its entropic-force constant is equivalent to a spring that is too soft. Particularly, the studies^{5–15} as summarized in Appendix 13.A indicating that the Rouse segment and the Kuhn segment are nearly of the same size^a represents a fundamental paradox embedded in the successes of the Rouse-segment-based theories — referred to as the Rouse–Kuhn paradox.

^aNote: In Ref. 3, saying that the Rouse and Kuhn segments are of the same order of magnitude in size is an incomplete description of their relative sizes.

As specifically pointed out in Appendix 13.A, the applicability of a Rouse-segment-based theory (the Rouse theory or the ERT) in the relaxation modulus $G(t)$ is limited to the region below the modulus value $\rho RT/m$. Because of the relationship between the entropic-force constant of the Rouse segment and the modulus, the applicable range of the theory has been referred to as the entropic region. For polystyrene, $m = 850$; the Rouse theory and the ERT are applicable only over the range of modulus below $\sim 4 \times 10^7$ dynes/cm², as clearly illustrated in Figs. 14.17 and 14.18. In other words, the Rouse theory and the ERT are incapable of describing the polymer viscoelastic response over the short-time or high-frequency region where modulus values reach as high as $\sim 10^{10}$ dynes/cm² and dynamic processes are driven by energetic interactions. As presented in Chapter 14, the inadequacy is made up for by incorporating a stretched exponential (KWW) form for the glassy-relaxation process into the ERT or the Rouse theory.^{15–17} As studied in this chapter, the Monte Carlo simulations on Fraenkel chains^{3,4} have led to new fundamental understandings of the polymer viscoelastic behavior at the molecular level. The simulation studies shed light on the main factors behind the inadequacy of the Rouse-segment-based theories and concurrently give rise to a theoretical basis for resolving the Rouse–Kuhn paradox.

17.1 The Fraenkel Chain Model

We can picture an N -bead Fraenkel chain as the chain shown in Fig. 3.2 just as we have pictured an N -bead Rouse chain in Chapters 3 and 7. Here, the only difference is that the spring connecting two beads, instead of being entropic (Eq. (3.30)), is characterized by the Fraenkel potential:

$$U_F = \frac{H_F}{2} \sum_{n=1}^{N-1} \left(\frac{|\mathbf{R}_n - \mathbf{R}_{n+1}|}{b_0} - 1 \right)^2. \quad (17.1)$$

Then the total force asserted on an internal bead by the two immediate springs connected to it is given by

$$\begin{aligned} \mathbf{F}_n(i) = & -\frac{H_F}{b_0^2} (2\mathbf{R}_n(i) - \mathbf{R}_{n+1}(i) - \mathbf{R}_{n-1}(i)) \\ & + \frac{H_F}{b_0} \left[\frac{\mathbf{R}_n(i) - \mathbf{R}_{n-1}(i)}{|\mathbf{R}_n(i) - \mathbf{R}_{n-1}(i)|} + \frac{\mathbf{R}_n(i) - \mathbf{R}_{n+1}(i)}{|\mathbf{R}_n(i) - \mathbf{R}_{n+1}(i)|} \right]. \end{aligned} \quad (17.2)$$

The equivalent equations for the end beads: $n = 1$ or N can be obtained in the same way. In Eqs. (17.1) and (17.2), b_0 represents the tensionless length of the segment; the constant H_F characterizes the rigidity of the segment. For the simulations presented in this chapter, b_0 is set at 1 as the reference length scale and $H_F = 400 kT$ is used. The Langevin equation for a Fraenkel chain can be obtained by substituting Eq. (17.2) into Eq. (16.2) or (16.7). As the (entropic) tensile force on the Rouse segment is replaced by that derived from the Fraenkel potential, the stiffness of the segment is greatly enhanced. With the Fraenkel force being a nonlinear function of the bead positions, the Langevin equation of a Fraenkel chain cannot be solved analytically; the Monte Carlo simulation becomes a crucial means of obtaining its solution.

17.2 Equilibrium-Simulated Relaxation Modulus Curves

The simulations of Fraenkel chains in the equilibrium state give rise to two distinct modes in the relaxation modulus $G_S(t)$ curves as shown in Fig. 17.1 for a five-bead chain — normalized per segment. The “bead” is actually a volume-less point as in the Rouse chain model (Sec. 6.2); with this understanding, it is still referred to as a bead. In Fig. 17.1, the results obtained from simulations with the step length d chosen at 0.01 and 0.03 are compared; a time step for the latter is regarded as equivalent to nine times — the predicted ratio (Eq. (16.8)) — as long as that for the former. The close agreement between the two results indicates that the step length $d = 0.03$ is sufficiently short, causing virtually no distortion in the obtained $G_S(t)$ curve; at the same time, no additional information particularly significant can be gained by choosing the much more time-consuming one, $d = 0.01$. Thus, all the simulations presented in the present chapter and the next are done with $d = 0.03$.

In Fig. 17.2, the equilibrium-simulated $G_S(t)$ curves for two-, five-, ten- and twenty-bead Fraenkel chains are compared; their line shapes are similar to what have been typically observed experimentally (see the $G_p(t)$ curves of sample C shown in Figs. 14.17 and 14.18). In the same figure, these $G_S(t)$ results are also compared with the Rouse theoretical curves — calculated with relaxation times given by Eq. (16.8b) — each for a chain with the corresponding number of beads. In obtaining the shown close superposition of the Rouse theoretical curves on the simulation results over the long-time region, only small shifts need to be applied to the Rouse curves along the log-modulus axis. The multiplication factors corresponding to the shifts

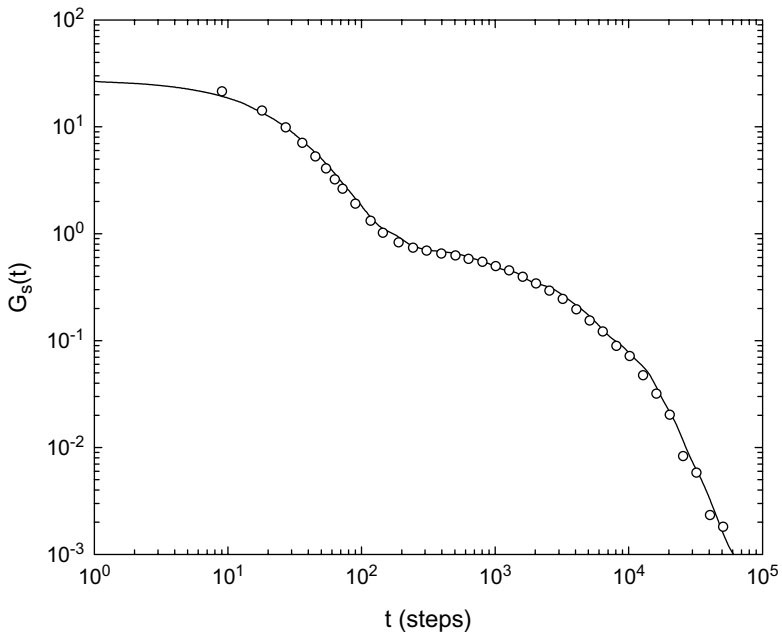


Fig. 17.1 Comparison of the equilibrium-simulated $G_S(t)$ curves of the five-bead Fraenkel chain using the step length $d = 0.01$ (solid line) and $d = 0.03$ (\circ).

are 0.7, 0.85, 0.9, and 0.95 for the two-, five-, ten- and twenty-bead chains, respectively. The trend indicates that the multiplication factor approaches the “perfect” value 1 as the number of beads increases. The shown close agreement of the slow modes with the theoretical $G_S(t)$ curves with only a small shift along the log-modulus axis strongly indicates that the slow mode is well described by the Rouse theory. And clearly the N dependence of the relaxation time as given by Eq. (16.8b) is well followed. Such agreements mean that the slow mode is of entropic nature as the Rouse modes of motion. Considering that the Fraenkel potential between two beads represents a strong energetic interaction and that a Fraenkel segment is much stiffer than a same-size Rouse segment, the emergence of the entropic slow mode is indeed very intriguing. As shown by the analyses described below, the fast mode is an energetic-interaction-driven (or simply as energy-driven) dynamic process while the slow mode is an entropy-driven one. For the sake of simplicity, the Fraenkel dumbbell case has been considered; and the analyses can be extended to a Fraenkel chain with more than two beads.

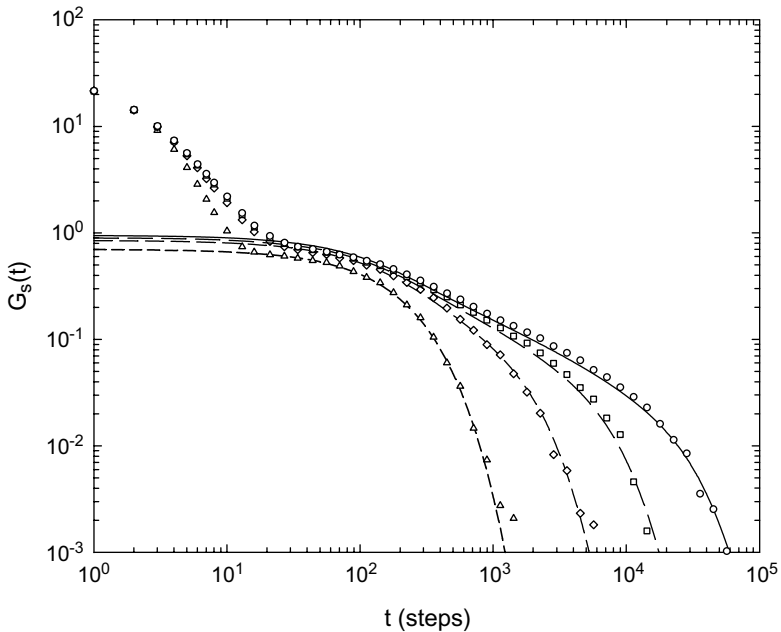


Fig. 17.2 Comparison of the equilibrium-simulated $G_S(t)$ curves of two-bead, five-bead, ten-bead and twenty-bead Fraenkel chains (Δ for $N = 2$; \diamond for $N = 5$; \square for $N = 10$; and \circ for $N = 20$) with the Rouse theoretical curves (short-dash line for $N = 2$; medium-dash line for $N = 5$; long-dash line for $N = 10$; and solid line for $N = 20$). The Rouse theoretical curves have been slightly shifted vertically: multiplied by the factors 0.7, 0.85, 0.9 and 0.95 for $N = 2, 5, 10$ and 20, respectively.

If there is no attractive interaction potential between two beads, the thermal fluctuations in an equilibrium state will eventually separate them far apart. Therefore, at equilibrium, the average distance (or the average distance over a long period of time) between the two beads of a dumbbell is not that corresponding to the tensionless point of the potential between them — namely, when the bond length is equal to b_0 in the Fraenkel-segment case — but larger. There are different ways to define the average distance as will be discussed below; however, this is true in all cases. Hence, the two beads of a dumbbell are more often than not under a tension to bring them closer to each other. The tension is determined by the average kinetic energy associated with the fluctuations built in the Langevin equation (see Appendix 17.A).¹⁸ It is so with a Rouse segment as well as with a Fraenkel segment. Such tensile forces on the segments of a chain play important roles in contributing to the stress tensor of the chain molecule. Because

the Fraenkel potential rises up sharply with a displacement from the tensionless point, the average bond length in the equilibrium state should be larger than b_0 by only a small amount δ_0 . Physically, δ_0 being small has much to do with the existence of the entropy-driven slow mode. With δ_0 being small, as a linear approximation, the tensile force on a segment may be expressed as a linear function of the bond vector as in the Rouse-dumbbell case.

For the Fraenkel dumbbell, the Langevin equation in terms of the bond vector, $\mathbf{b}(t) = \mathbf{R}_2(t) - \mathbf{R}_1(t)$, is given by

$$\frac{d\mathbf{b}(t)}{dt} = - \left(\frac{2}{\zeta} \right) \frac{H_F}{b_0^2} \left[1 - \frac{b_0}{|\mathbf{b}(t)|} \right] \mathbf{b}(t) + \mathbf{g}(t) \tag{17.3}$$

where the fluctuation term is given by $\mathbf{g}(t) = \mathbf{g}_2(t) - \mathbf{g}_1(t)$, with $\mathbf{g}_1(t)$ and $\mathbf{g}_2(t)$ being the fluctuations on beads one and two, respectively, as defined by Eqs. (3.34) and (3.35).

Equation (17.3) can be transformed into the discrete form for simulation in the same way as described in Sec. 16.1. Defining

$$1 - \frac{b_0}{|\mathbf{b}(t)|} = \frac{\delta(t)}{b_0}, \tag{17.4}$$

Equation (17.3) is rewritten as

$$\frac{d\mathbf{b}(t)}{dt} = - \left(\frac{2}{\zeta} \right) \frac{H_F}{b_0^3} \delta(t) \mathbf{b}(t) + \mathbf{g}(t). \tag{17.5}$$

Corresponding to Eq. (17.5), the xy stress component is given by

$$J_{xy}(t) = - \frac{H_F}{b_0^3} \delta(t) b_x(t) b_y(t). \tag{17.6}$$

Substituting Eq. (17.6) into Eq. (16.12), we obtain

$$G_S(t) = \frac{1}{kT} \langle J_{xy}(0) J_{xy}(t) \rangle = \frac{H_F^2}{kT b_0^6} \langle \delta(0) b_x(0) b_y(0) \delta(t) b_x(t) b_y(t) \rangle. \tag{17.7}$$

As expected, the simulation results obtained for the Fraenkel dumbbell based on the combination of Eqs. (16.12) and (16.13) and on Eq. (17.7) are identical. During a simulation, the fluctuation in $\delta(t)$ as defined by Eq. (17.4) can be monitored separately allowing the time correlation function $\langle \delta(0) \delta(t) \rangle$ to be calculated. Physically, $\delta(t)$ approximately represents the deviation of $|\mathbf{b}(t)|$ from b_0 . Any small change in $|\mathbf{b}(t)|$ leads to a large

relative change in $\delta(t)$; for instance, a change in $|\mathbf{b}(t)|$ from 1.005 to 1.01 doubles the value of $\delta(t)$. Thus, compared to the motion associated with the bond vector $\mathbf{b}(t)$ itself (mainly the reorientation motion), $\delta(t)$ represents fast fluctuations with large relative fluctuation amplitude, giving rise to a fast relaxation process in $G_S(t)$ as shown below. As $\delta(t)$ originates from the particular form of the Fraenkel potential and represents the fluctuations in tension along the Fraenkel segment, the fast relaxation mode may very well be referred to as an energy-driven dynamic process. Because of the large difference between the fluctuation rate of $\delta(t)$ and that associated with $b_x(t)b_y(t)$, Eq. (17.7) may be approximated by

$$\begin{aligned} G_S(t) &\approx \frac{H_F^2}{kTb_0^6} \langle \delta(0)\delta(t) \rangle \langle (b_x(0)b_y(0))(b_x(t)b_y(t)) \rangle \\ &= \frac{H_F^2}{kTb_0^6} [\langle \Delta\delta(0)\Delta\delta(t) \rangle + \delta_0^2] \langle (b_x(0)b_y(0))(b_x(t)b_y(t)) \rangle \end{aligned} \quad (17.8)$$

where formally

$$\delta(t) = \Delta\delta(t) + \delta_0 \quad (17.9)$$

with

$$\langle \Delta\delta(t) \rangle = 0; \quad \text{and} \quad \langle \delta(t) \rangle = \delta_0. \quad (17.10)$$

As explained above, the average distance between the two beads is larger than b_0 ; thus δ_0 is greater than zero. Equation (17.8) suggests the coexistence of two distinct relaxation processes in $G_S(t)$. At long times when the correlation function $\langle \Delta\delta(0)\Delta\delta(t) \rangle$ has diminished greatly, $G_S(t)$ as given by Eq. (17.8) enters a slow-relaxation region, which would be described by

$$\frac{1}{kT} \langle J_{xy}(0)J_{xy}(t) \rangle = \frac{H_F^2}{kTb_0^6} [\delta_0^2] \langle (b_x(0)b_y(0))(b_x(t)b_y(t)) \rangle. \quad (17.11)$$

In the short-time region where the process $\langle \Delta\delta(0)\Delta\delta(t) \rangle$ is dominant, the approximation as used in Eq. (17.8) is expected to be good. By contrast, over a long period of time, as the nonvanishing residual fluctuations in $\delta(t)$ are small and more comparable in (relative) magnitude to the slow fluctuations in $b_x(t)b_y(t)$, the approximation expressed as a product of two separate terms δ_0^2 and $\langle (b_x(0)b_y(0))(b_x(t)b_y(t)) \rangle$ in Eq. (17.11) may not be well justified. Nevertheless, the approximate form as given by Eq. (17.8) helps us understand the coexistence of the fast and slow modes of motion as distinctly observed in the simulation results. To illustrate the results and at

the same time somewhat make up for the deficiency of the approximation as represented by Eq. (17.8) in the long-time region, the baseline of $\langle\delta(0)\delta(t)\rangle$ is determined or set in two different ways. Based on either of the two baselines, an approximate $G_S(t)$ curve can be obtained for comparison with the exact result — such comparison analyses help reveal the key physical elements that affect $G_S(t)$. In one case, the natural baseline of $\langle\delta(0)\delta(t)\rangle$ is used, which, denoted by $\delta_N^2 (= \delta_0^2)$, formally according to Eq. (17.8)), is found to be 4×10^{-6} . In the other case, an adjustable parameter δ_x^2 is added to the natural baseline δ_N^2 such that a close fitting to the exact $G_S(t)$ curve (obtained using Eq. (17.7)) is obtained. The best value of δ_x is found to be 0.008. The $G_S(t)$ curves calculated with and without $\delta_x^2 = 6.4 \times 10^{-5}$ added are compared with the exact results in Fig. 17.3. The corresponding $\langle\delta(0)\delta(t)\rangle$ and $\langle\delta(0)\delta(t)\rangle + \delta_x^2$ curves are shown in Fig. 17.4. With $\delta_x^2 = 6.4 \times 10^{-5}$ added, the total baseline becomes $\delta_F^2 = \delta_0^2 + \delta_x^2 = 6.8 \times 10^{-5}$. It is interesting to note that $\delta_F = 0.00825$ is only larger by 10% than the

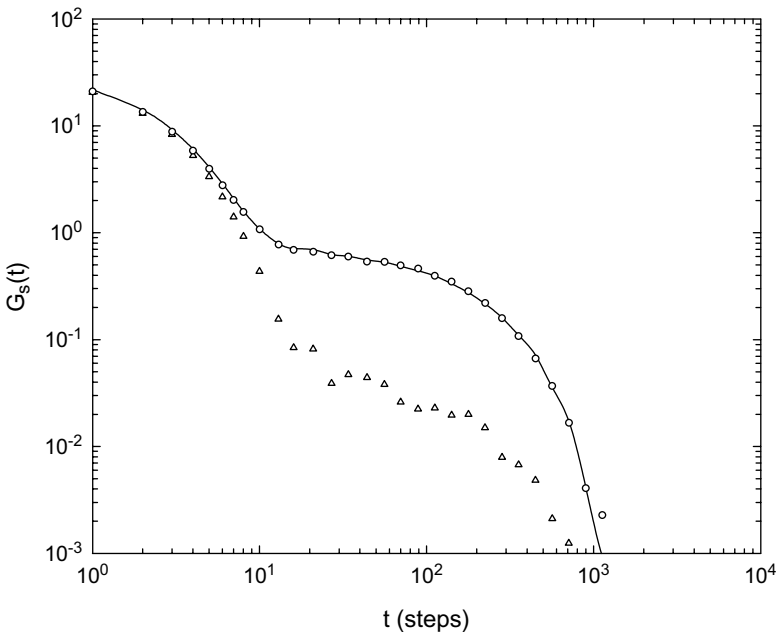


Fig. 17.3 The equilibrium-simulated $G_S(t)$ curves of the Fraenkel dumbbell: exact result (solid line; using Eq. (17.7)) and approximations (Δ , using Eq. (17.8) with $\delta_0^2 = \delta_N^2 = 4 \times 10^{-6}$ as the baseline of $\langle\delta(0)\delta(t)\rangle$); and \circ , using Eq. (17.8) with $\delta_x^2 = 6.4 \times 10^{-5}$ added to the baseline).

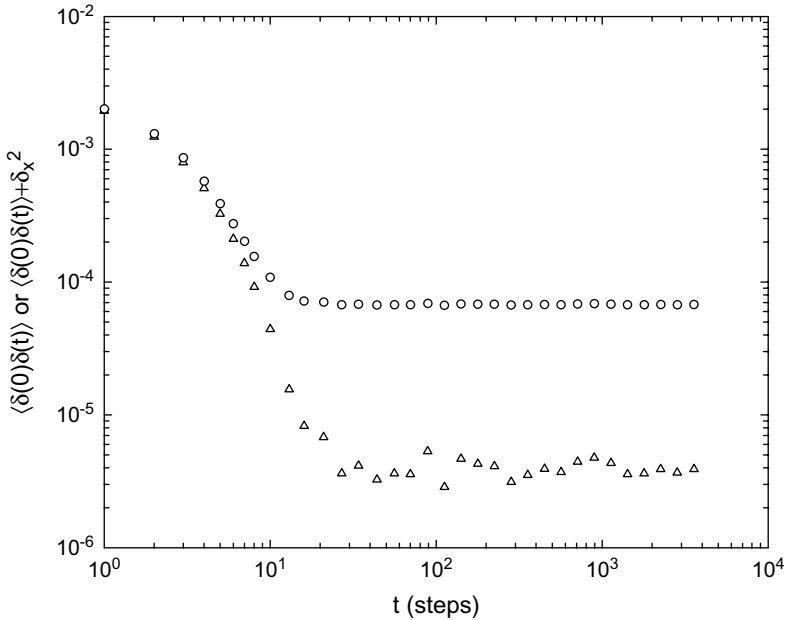


Fig. 17.4 Time-correlation functions $\langle \delta(0)\delta(t) \rangle$ or $\langle \delta(0)\delta(t) \rangle + \delta_x^2$ obtained from simulations on the Fraenkel dumbbell with $\delta(t)$ defined by Eq. (17.4): Δ with $\delta_0^2 = \delta_N^2 = 4 \times 10^{-6}$; and \circ with $\delta_x^2 = 6.4 \times 10^{-5}$ added to the baseline.

value 0.0075 (denoted by δ_V) expected on the basis of the virial theorem.¹⁹ As shown in the Appendix 17.A, the virial theorem is well confirmed by the simulation.

One can notice that the fast declines in the early parts of $G_S(t)$ and $\langle \delta(0)\delta(t) \rangle$ (or $\langle \delta(0)\delta(t) \rangle + \delta_x^2$) occur on the same time scale with negligible difference between the simulation results calculated with and without $\delta_x^2 = 6.4 \times 10^{-5}$ added. Clearly, this is due to the mean square fluctuation magnitude $\langle \delta(0)\delta(0) \rangle$ being much larger than δ_x^2 . For $G_S(t)$, the approximate results are also virtually indistinguishable from the exact one over the most part of the fast-mode region — the early portion. Clearly, these agreements occurring in the short-time region are due to the dominant effect of $\langle \Delta\delta(0)\Delta\delta(t) \rangle$ and indicate that the fast mode in $G_S(t)$ arises from the segment-tension fluctuation $\delta(t)$ — therefore, an energy-driven dynamic process. In the long-time region, large divergences between the curves calculated with and without $\delta_x^2 = 6.4 \times 10^{-5}$ added occur in both $G_S(t)$ and $\langle \delta(0)\delta(t) \rangle$. Because the expression as a product of δ_0^2 and

$\langle (b_x(0)b_y(0))(b_x(t)b_y(t)) \rangle$ (Eq. (17.11)) is not a well-justified approximation as explained above, using the natural baseline δ_N^2 , which is much smaller than the value of δ_V^2 or δ_F^2 , leads to the poorest result. With $\delta_F^2 = 6.8 \times 10^{-5}$ as the baseline, the simulation using the approximate form gives a $G_S(t)$ curve which is virtually indistinguishable from that obtained using the exact form.

The magnitude of δ_0 that appears in Eq. (17.11) may also be studied in a dynamic way as described in the following: Eq. (17.11) represents the time-correlation function of the stress tensor component $J_{xy}(t)$ in the long-time region described by the Langevin equation:

$$\frac{d\mathbf{b}(t)}{dt} = - \left(\frac{2}{\zeta} \right) \frac{H_F \delta_0}{b_0^3} \mathbf{b}(t) + \mathbf{g}(t) \quad (17.12)$$

which is linear and has the same form as that of the Rouse dumbbell:

$$\frac{d\mathbf{b}(t)}{dt} = - \frac{6kT}{\zeta \langle \mathbf{b}^2 \rangle_R} \mathbf{b}(t) + \mathbf{g}(t). \quad (17.13)$$

Thus, the slow mode is expected to behave very similarly to the single mode of motion in the Rouse dumbbell. If the δ_V value as obtained from the virial theorem ($\delta_V = 3kTb_0/H_F$, as from Eq. (17.A.1)) is used for δ_0 , Eq. (17.12) with $b_0 = \langle \mathbf{b}^2 \rangle_R^{1/2} = 1$ becomes identical to Eq. (17.13) and will lead to the same time-correlation function of the bond vector as given by the Rouse dumbbell model (Chapter 3):

$$\langle \mathbf{b}(0) \cdot \mathbf{b}(t) \rangle = \langle \mathbf{b}^2 \rangle_R \exp \left(- \frac{t}{\tau} \right) \quad (17.14)$$

with

$$\tau = \frac{\zeta \langle \mathbf{b}^2 \rangle_R}{6kT} = \frac{\zeta b_0^2}{2H_F(\delta_V/b_0)}. \quad (17.15)$$

The mean square bond length $\langle \mathbf{b}^2 \rangle$ obtained from the simulation of the Fraenkel dumbbell is greater than that of the Rouse dumbbell $\langle \mathbf{b}^2 \rangle_R$ by 1.3%. This will make a small difference in the value of Eq. (17.14) at $t = 0$. As this difference is very small, particularly much smaller than the difference between δ_N , δ_V and δ_F , it can be neglected here. The $\langle \mathbf{b}(0) \cdot \mathbf{b}(t) \rangle$ curve obtained from the simulation of the Fraenkel dumbbell is quantitatively described by a single exponential form just as that of the Rouse dumbbell model but with a relaxation time longer by about 45%. In other words, using the relaxation time of $\langle \mathbf{b}(0) \cdot \mathbf{b}(t) \rangle$ as the criterion for determining the δ_0 value, the best value, denoted by δ_τ , should be 0.0052.

The close match between the approximation and exact $G_S(t)$ curves as shown in Fig. 17.3 is obtained with $\delta_F = 0.00825$, which is only slightly larger than $\delta_V = 0.0075$. As opposed to a slight underestimate in this case, the use of the virial theorem gives an overestimate of the δ_0 value when the relaxation time of the time-correlation function $\langle \mathbf{b}(0) \cdot \mathbf{b}(t) \rangle$ is used as the criterion. Involving only a very slight approximation (see Eq. (17.A.1)) which is unrelated to the approximation — the separation into two time-correlation functions — made in Eq. (17.8), the δ_V value obtained using the virial theorem can be regarded as independent and trustworthy. As opposed to the independence of δ_V , each of the equations (Eqs. (17.8), (17.11) and (17.12)) as involved in estimating the δ_N , δ_τ and δ_F values, contains an approximation which deviates from the true representation in different ways. Thus, the obtained δ_N , δ_τ and δ_F values are not expected to be the same. The δ_N value, which apparently comes from a bad approximation, may be excluded. The obtained δ_τ and δ_F values are within 30% of their average, which is very close to the δ_V value expected based on the virial theorem. These consistencies support that the approximations involved in the above analyses are well justified and confirms the physical picture revealed — the fast mode in $G_S(t)$ is an energy-driven dynamic process and the slow mode is an entropy-driven one as the Rouse relaxation is.

The above analysis can be extended to Fraenkel chains longer than a dumbbell. As detailed in Appendix 17.B, by comparing the simulation results obtained with and without the contribution from couplings between different segments, the above conclusion has been shown to be applicable to a multiple-segment Fraenkel chain as well. The basic nature of the fast mode and that of the slow mode are further confirmed by the studies of the step strain-simulated $G_S(t)$ curves as detailed below.

17.3 Step Strain-Simulated Relaxation Modulus Curves

The step strain-simulated $G_S(t)$ curves obtained at $\lambda = 0.2$ and 0.5 are compared with equilibrium-simulated $G_S(t)$ ones in Fig. 17.5 for the two-, five-, ten- and twenty-bead Fraenkel chains. There are clear differences between the equilibrium-simulated curves and the step strain-simulated at $\lambda = 0.2$ in the cases of two- and five-bead chains, indicating that the fluctuation-dissipation theorem is not fulfilled totally as in the Rouse-chain case. This may be due to $\lambda = 0.2$ not being in the linear region yet as some small differences can be observed between the $G_S(t)$ curves at $\lambda = 0.2$ and 0.5 . In fact, the numerically calculated $G_S(0)$ values as a function of the strain λ

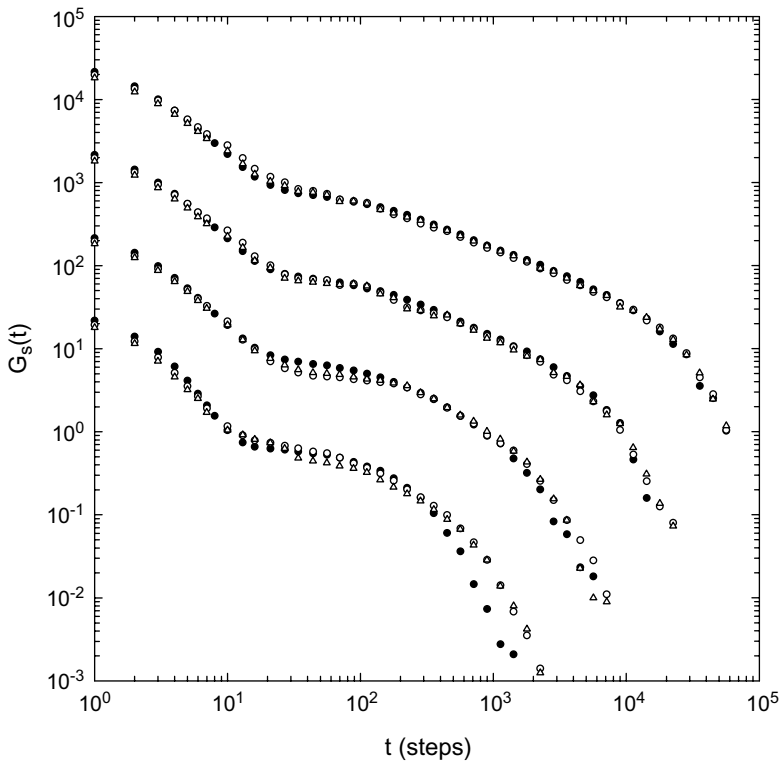


Fig. 17.5 Comparison of the step strain-simulated $G_S(t)$ curves for the two-bead, five-bead, ten-bead and twenty-bead Fraenkel chains at $\lambda = 0.2$ (Δ) and 0.5 (\circ) with the equilibrium-simulated curves (\bullet). To avoid overlapping between different sets of curves, the results of $N = 5, 10$ and 20 have been multiplied by $10, 10^2$ and 10^3 , respectively.

(see Fig. 18.5) indicate that rigorously, the linear region should not extend beyond $\lambda = 0.005$. However, further investigation into decreasing the λ value indicates that this is not the main cause.

As shown in Fig. 17.5, differences between the equilibrium-simulated and step strain-simulated $G_S(t)$ curves occur mainly in the cases of $N = 2$ and 5 ; and virtually no differences can be observed for $N = 10$ and 20 even though $\lambda = 0.2$ and 0.5 are not really in the linear region. In the $N = 2$ case, while the whole shapes of the $G_S(t)$ curves are very similar, differences can be observed in different regions. In the $N = 5$ case, the difference becomes obvious in the early part of the slow mode, where an effect related to the coupling between $\delta(t)$ and $b_x(t)b_y(t)$ — a subject discussed in the

last section — is very likely to occur. The results of $N = 5$ suggests that the coupling between $\delta(t)$ and $b_x(t)b_y(t)$ may be reflected differently in the two types of simulations. This is also suggested by the similarity of trends that can be noticed by comparing Fig. 17.2 and Fig. 17.5, as explained in the following. The results shown in Fig. 17.5 indicates that the agreement between the equilibrium-simulated and step strain-simulated $G_S(t)$ curves becomes much better as N becomes significantly greater than 2. In a similar way as shown in Fig. 17.2, the shifting along the log-modulus axis required for superposing the Rouse theoretical curves on the equilibrium-simulated $G_S(t)$ curves progresses towards the perfect situation — namely, no shifting — as N increases. As may be viewed in terms of the Rouse theory, the number of normal modes (in the slow mode) increases with N . At the same time, the lower modes among them become more removed from the fast mode as N increases. These two effects may improve the *overall decoupling* of the fast and slow modes as N increases. In other words, the trend in Fig. 17.2 suggests that the coupling between $\delta(t)$ and $b_x(t)b_y(t)$ is effectively reduced as the number of modes of motion in the slow mode increases, making the slow mode better described by the Rouse theory. As the difference in coupling may be reduced by the decrease in the coupling itself, this leads to a better agreement between the equilibrium-simulated and step strain-simulated $G_S(t)$ curves as N increases. When $N = 2$ or 5, in spite of the visible differences, an overall agreement between the equilibrium-simulated and step strain-simulated $G_S(t)$ curves is apparent, each revealing clearly two separate modes. Such an overall agreement has been referred to as a quasi-version of the fluctuation–dissipation theorem.

Figure 17.6 shows the mean square segment length $\langle \mathbf{b}^2(t) \rangle$ and its components: $\langle b_x^2(t) \rangle$, $\langle b_y^2(t) \rangle$ and $\langle b_z^2(t) \rangle$ of a five-bead Fraenkel chain as a function of time following the application of the step shear strain $\lambda = 0.5$. Although $\lambda = 0.5$ deviates more from the linear region than $\lambda = 0.2$, these results show more clearly the changing pattern with time while the corresponding $G_S(t)$ curve does not differ from the equilibrium-simulated one very much. Collectively, these results can better serve the illustration purpose, as discussed below, than the results at $\lambda = 0.2$. As shown in Fig. 17.6, the segment length is stretched by the step strain applied at $t = 0$ and relaxes back to its equilibrium value, as opposed to fluctuating around its equilibrium value in an equilibrium state. The dramatic decline in the early part of $\langle \mathbf{b}^2(t) \rangle$ (Fig. 17.6) occurs on the same time scales as that in the early part of $G_S(t)$ (Fig. 17.5). The observed concurrence indicates that the fast mode occurring in the step strain-simulated $G_S(t)$ reflects

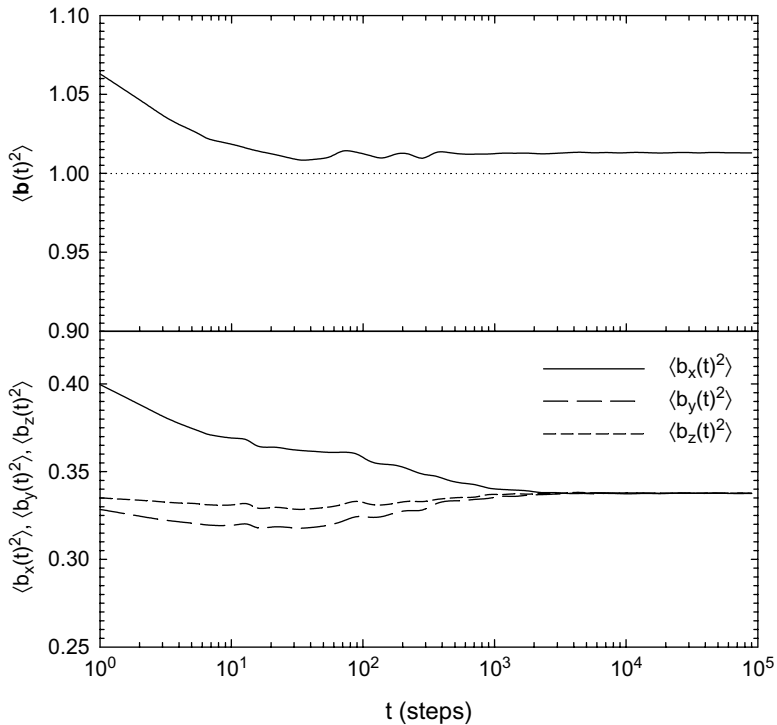


Fig. 17.6 The time-step dependences of $\langle \mathbf{b}^2(t) \rangle$ and the components $\langle b_x^2(t) \rangle$, $\langle b_y^2(t) \rangle$ and $\langle b_z^2(t) \rangle$ for the five-bead Fraenkel chain following a step strain $\lambda = 0.5$.

the decrease in the average segment length back to its equilibrium value and the corresponding reduction in the average tension along the segment. This segment-tension relaxation corresponds to the time-correlation function of segment-tension fluctuation, $\langle \delta(0)\delta(t) \rangle$, as shown in Fig. 17.4. It is interesting to note that right after $\langle \mathbf{b}^2(t) \rangle$ has completed its first decline, it displays signs of overshooting and oscillation around its equilibrium value before reaching its final stable equilibrium value. On the same time scales as the early part of the slow mode in $G_S(t)$, the mean square segment length $\langle \mathbf{b}^2(t) \rangle$ has declined to a level (including the average level in the oscillation zone as can be noticed in Fig. 17.6) that is the same as maintained at all times in an equilibrium-state simulation. However, as opposed to isotropy in the equilibrium state, segmental orientation anisotropy occurs on the same time scales in the system as indicated by the differences among the time dependences of the components $\langle b_x^2(t) \rangle$, $\langle b_y^2(t) \rangle$ and $\langle b_z^2(t) \rangle$. As

orientation does not cause a change in the potential energy of the segment, the anisotropic orientation gives rise to the entropic nature of the slow mode in $G_S(t)$. In the light of the fluctuation–dissipation theorem, corresponding to the *randomization* of segmental orientation (destroying the anisotropy) in the slow-mode region of a step strain-simulated $G_S(t)$, *fluctuations* in segmental orientation should occur at all times in an equilibrium state. It is basically the time-correlation function of the orientation fluctuations that determines the time dependence of the entropic slow mode in an equilibrium-simulated $G_S(t)$, as detailed in Sec. 17.2. The close correlation between the slow mode in $G_S(t)$ and the anisotropic segmental orientation is further shown by analyzing the step strain-simulated results obtained well inside the nonlinear region in Chapter 18.

17.4 Comparison between Simulation and Experiment

Both the Rouse theory (Chapter 7) and the Monte Carlo simulation using the Rouse-chain model (Chapter 16) or the Fraenkel-chain model (this chapter) are based on a mean-field approach to describe the viscoelastic behaviors of entanglement-free polymers. In other words, the relaxation modulus of an entanglement-free polymer system is the sum of contributions from all the chains in a unit volume, each being represented by the statistically averaged time-dependent behavior of a single chain. The quantitatively successful description of experimental results of entanglement-free polymer melts by the Rouse theory as studied in Chapter 11 indicates that the mean-field representation works very well as applied to the entropic region. At the same time as observed in Fig. 17.2, the Rouse theory and the simulation results of Fraenkel chains with $N \gg 2$ agree very well over the entropic region. Besides these theory-vs.-experiment and theory-vs.-simulation agreements over the entropic region, the overall line shape of a simulated $G_S(t)$ curve is very similar to that typically observed experimentally. Thus, it is of great interest to compare simulation and experimental results over the whole time range. Such a comparison would shed light on how well the key features of the relaxation modulus in the short-time region — the structural-relaxation process — can be captured by the Fraenkel-chain model. Intuitively, the mean-field Fraenkel-chain model should be an oversimplified representation of the viscoelastic behavior of a polymer melt over the structural-relaxation region, as interactions among microstructural segments (both intra-molecular and inter-molecular), whose total contribution should be substantial, have not been included.

As presented in Chapter 14, the creep compliance $J(t)$ curves of sample C — an entanglement-free system — have been quantitatively analyzed in terms of the $G(t)$ functional form given by Eq. (14.6), which uses the Rouse theory as the frame of reference. Using the best-fit parameters obtained from the analyses, the $G(t)$ curves of sample C can be faithfully calculated just as those shown in Figs. (14.17) and (14.18) for $\Delta T = T - T_g = 0$ and 9.7K, respectively. Such calculated $G(t)$ curves may be regarded as equivalent to experimentally measured curves for a purpose such as the present one of comparing experiment with simulation. The Monte Carlo simulation being based on the Langevin equation implies that the simulation is for a system that is ergodic. Thus, the $G(t)$ line shape at temperatures sufficiently high above T_g is the one that should be calculated for comparison with the simulation result. Furthermore, as the Monte Carlo simulation is performed on a single chain, the $G(t)$ curve that can be used for comparison with the simulation result should be that for an *ideal* sample system whose chains all have exactly the same molecular weight. The molecular weight for a single Rouse segment, m , being about 850 for polystyrene, sample C with $M_w = 16,400$ corresponds to a chain with 20 beads on average according to Eq. (14.8). The $G(t)$ curve for the ideally monodisperse system with molecular weight M identical to the M_w value of sample C may be calculated using the best-fit parameters obtained for sample C. The calculation is carried out in the same way as the calculations of those shown in Figs. (14.17) and (14.18) except that the convolution of the molecular-weight distribution $f(M)$ in Eq. (14.6) is eliminated. As shown in Fig. 17.7, the equilibrium-simulated $G(t)$ curve for a 20-bead Fraenkel chain with $H_F = 400 kT$ is compared with the “experimental” curve for the ideally monodisperse polystyrene “sample” with molecular weight equal to 16,400 in the high-temperature limit ($T > T_g + 40 \text{ K} = 407 \text{ K}$). Although the experimental $G(t)$ line shape is for $T > 407 \text{ K}$, the modulus is that corresponding to $T = 373 \text{ K}$ (see Chapter 14). As shown, the experimental curve is calculated with the frictional factor $K = 10^{-4}$ — an arbitrarily chosen value. The simulation curve has been superposed on the experimental curve by shifting along both the log-modulus and log-time axes. As the time-scale multiplication factor depends on the K value used in the calculation and the step-length d employed in the simulation, its value is not of particular interest. However, the shift along the log-modulus axis has much to do with the entropic nature of the slow mode as discussed in Sec. 17.2 regarding the results shown in Fig. 17.2. The required vertical multiplication factor for the shown superposition is 4.2×10^7 , which is very close to the

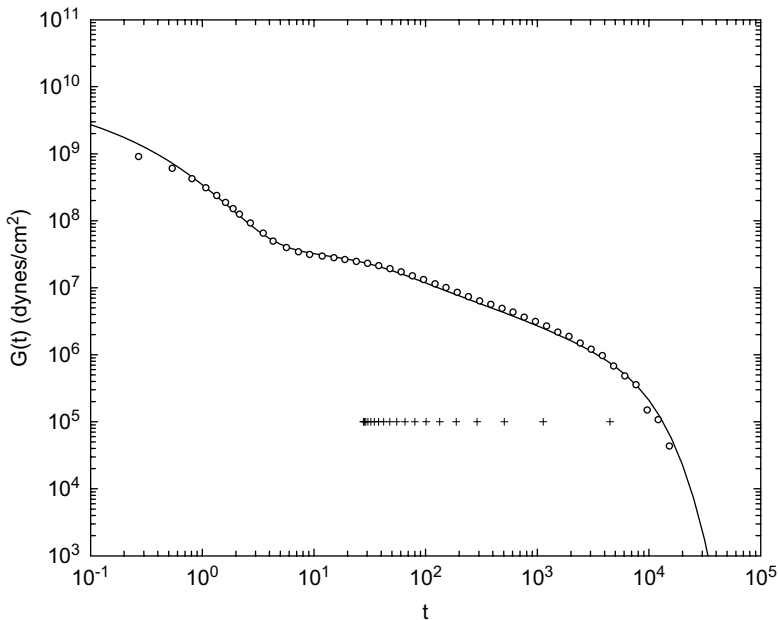


Fig. 17.7 Comparison of the equilibrium-simulated $G(t)$ curve (\circ) for the twenty-bead Fraenkel chain with $H_F = 400kT$ and the predicted “experimental” curve (solid line) for an “ideally monodisperse polystyrene sample” with the molecular weight equivalent to $N = 20$; also shown are the points (+) representing the relaxation times of the 19 Rouse normal modes.

value 3.8×10^7 predicted if the simulated $G(t)$ is in perfect agreement with the Rouse theory over the entropic region. The ratio of $3.8/4.2$ also agrees closely with the multiplication factor 0.95 used to superpose the Rouse theoretical curve on the simulated $G_S(t)$ curve of the 20-bead Fraenkel chain shown in Fig. 17.2. Part of the small difference may be due to the fact that only one adjustable parameter — the shift along the log-modulus axis — is involved in the superposition made in Fig. 17.2 while shifting is allowed along both the log-time and log-modulus axes in Fig. 17.7. The close matching between the experimental and simulated $G(t)$ curves over a wide dynamic range spanning both the energy-driven and entropy-driven modes is indeed very encouraging, considering the simplicity of the model used in the simulation.

$H_F = 400kT$ is somewhat arbitrarily chosen as the model is basically a primitive one. Changing the H_F value mainly affects the modulus level as well as the relaxation in the fast-mode region; an increase

in H_F leads to higher modulus values in the very short-time region and causes a faster decline in the later part of the fast-mode region. As pointed out above, the mean-field Fraenkel-chain model should be too simple to describe adequately the viscoelastic behavior of a polymer melt over the structural-relaxation region, a fine tuning of the H_F value does not appear to serve a particularly meaningful purpose. The important thing is that the Fraenkel-chain model with a finite H_F value gives a generic description of the coexistence of the fast energy-driven and slow entropy-driven modes in the experimental $G(t)$. It is striking to observe an energy-driven mode emerges *naturally* above the short-time region of the slow mode in the simulated $G_S(t)$ curves for entanglement-free Fraenkel chains.

17.5 A Resolution of the Rouse–Kuhn Paradox

As shown in Fig. 17.2, the close agreements between the theoretical and simulated $G_S(t)$ curves over the slow-mode region are each obtained between counterparts (the Rouse chain vs. the Fraenkel chain) with the same number of beads, N . The close agreements between theory and simulation indicate that the size of the Fraenkel segment is the same as that of the Rouse segment. This result strongly suggests that the chain domain that can be properly assigned as a Rouse segment as used in the Rouse theory which successfully describes the *linear* viscoelastic behavior over the entropic region actually can have a considerable degree of rigidity. In other words, the entropic-force constant on each segment is not a required element for the existence of the entropic modes of motion as so well described by the Rouse theory. Physically, the force constants of the various chemical bonds and bond angles (responsible for vibration modes) and the potential barriers impeding internal rotations in the microstructure of the polymer would actually provide such rigidity to a chain domain of the Rouse- or Fraenkel-segment size. Fluctuation in or randomization of segmental orientation gives rise to the slow mode and is responsible for its entropic nature. This is ultimately due to applicability of the virial theorem (Appendix 17.A).

As each segment in a Fraenkel chain becomes totally rigid when $H_F \rightarrow \infty$, the mean-square length $\langle \mathbf{b}^2 \rangle$ of each segment becomes identical to b_0^2 ; in other words, each segment becomes a Kuhn segment and the Fraenkel chain becomes a freely jointed chain. For a Fraenkel chain with $H_F = 400kT$, the $\langle \mathbf{b}^2 \rangle$ value of each segment is larger than b_0^2 by only 1.3%. Under this condition, the difference between the end-to-end distance of a Fraenkel chain and that of the freely jointed chain converted from it by allowing

$H_F \rightarrow \infty$ should be extremely small. Thus, with H_F being not particularly small, one may regard each segment in a Fraenkel chain as equivalent to a Kuhn segment and the Fraenkel chain as a freely jointed chain, as far as the *chain conformation* is concerned.

Summarizing the discussions in the last two paragraphs, clearly the functional form of the Fraenkel potential enables the Fraenkel segment to play a dual role: As opposed to functioning as a Rouse segment as far as the entropic viscoelasticity of a polymer is concerned, a Fraenkel segment behaves as a Kuhn segment as far as the static chain-conformation property is concerned. Thus, the dual role played by the Fraenkel segment resolves the Kuhn–Rouse paradox which has been indicated by the studies summarized in Appendix 13.A. Furthermore, the Fraenkel chain model represents a dramatic improvement over the Rouse chain model in the study of polymer viscoelasticity. The physics behind the coexistence of the two modes in $G_S(t)$ as studied in this chapter represents a significant conceptual advance beyond the scheme of incorporating a glassy-relaxation process into the Rouse theory (Eq. (14.6)) as used for analyzing experimental results in Chapter 14.

Appendix 17.A — Application of the Virial Theorem to the Fraenkel Dumbbell

The average kinetic energy being $kT/2$ for each degree of freedom is a built-in element of the Langevin equation.¹⁸ For simplicity, we consider the Fraenkel dumbbell case; however, the analysis as presented here can be extended to a Fraenkel chain with any number of beads. For a dumbbell, according to the virial theorem $\overline{K} = -\frac{1}{2} \sum_{i=1}^2 \overline{\mathbf{F}_i \cdot \mathbf{R}_i} = (H_F/2b_0^3) \overline{\delta(t) \mathbf{b}(t) \cdot \mathbf{b}(t)}$, where $\overline{K} = 3kT/2$ is the average internal kinetic energy. This relation is well confirmed by the simulation results shown in Fig. 17.8. Since as indicated by simulations, $\mathbf{b}(t) \cdot \mathbf{b}(t)$ in an equilibrium state fluctuates within 10% above and below its mean value, which is larger than b_0^2 by only 1.3%, the virial theorem as applied to the Fraenkel dumbbell can be closely approximated by

$$\frac{H_F}{b_0} \overline{\delta(t)} = 3kT. \quad (17.A.1)$$

For $H_F = 400kT$ and $\overline{\delta(t)} = 0.0075$. In the main text, this $\overline{\delta(t)}$ value is denoted by δ_V .

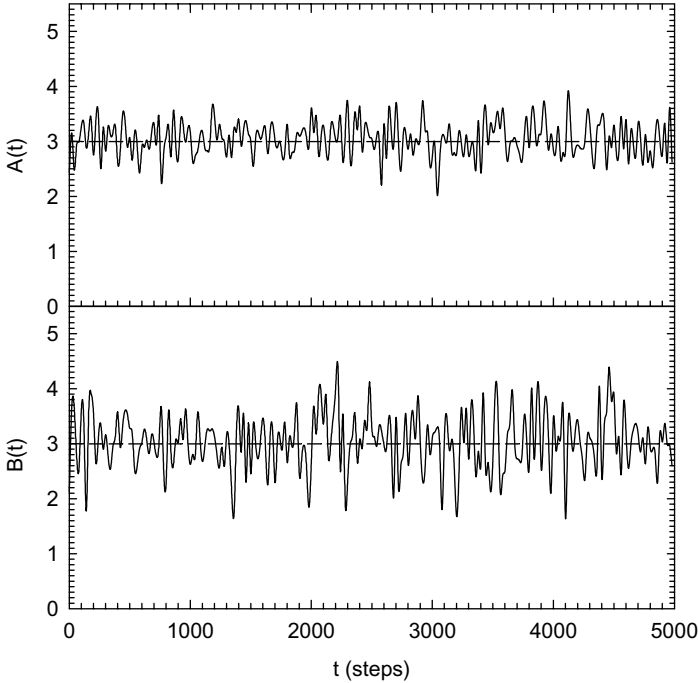


Fig. 17.8 Fluctuations of the internal kinetic energy for a Fraenkel dumbbell calculated in two different ways as represented by $A(t) = -\sum_{i=1}^2 \mathbf{F}_i(t) \cdot \mathbf{R}_i(t)$ and $B(t) = (H_F/b_0^3)\delta(t)\mathbf{b}(t) \cdot \mathbf{b}(t)$, each in a different equilibrium state, giving an average value of 3.073 for A and 3.075 for B ; the dashed lines are drawn at the value of 3 expected based on the virial theorem (with $kT = 1$).

Appendix 17.B — Contribution of the Dynamic Couplings between Different Segments to the Relaxation Modulus

Corresponding to Eq. (17.7) for a dumbbell, the relaxation modulus for an N -bead Fraenkel chain is given by

$$\begin{aligned}
 G_S(t) &= \frac{1}{(N-1)kT} \langle J_{xy}(0)J_{xy}(t) \rangle \\
 &= \frac{H_F^2}{(N-1)kTb_0^6} \left\langle \left(\sum_{i=1}^{N-1} \delta_i(0)b_{ix}(0)b_{iy}(0) \right) \left(\sum_{j=1}^{N-1} \delta_j(t)b_{jx}(t)b_{jy}(t) \right) \right\rangle.
 \end{aligned}
 \tag{17.B.1}$$

As being dynamically correlated, the contributions of the cross-terms (with $i \neq j$) in Eq. (17.B.1) to $G_S(t)$ are not zero.^b Such dynamic cross-correlations also occur in the Rouse-chain model. As it turns out, the sum of the self-terms (with $i = j$) of Eq. (17.B.1) as given by

$$G_S^{\text{self}}(t) = \frac{H_F^2}{(N-1)kTb_0^6} \sum_{i=1}^{N-1} \langle \delta_i(0)b_{ix}(0)b_{iy}(0)\delta_i(t)b_{ix}(t)b_{iy}(t) \rangle, \quad (17.B.2)$$

virtually solely contributes to $G_S(t)$ in the short-time region; in other words, the cross-terms only contribute to the long-time region. This is illustrated by comparing the simulated curves of $G_S(t)$ and $G_S^{\text{self}}(t)$ for a five-bead Fraenkel chain in Fig. 17.9. As there is virtually no difference between

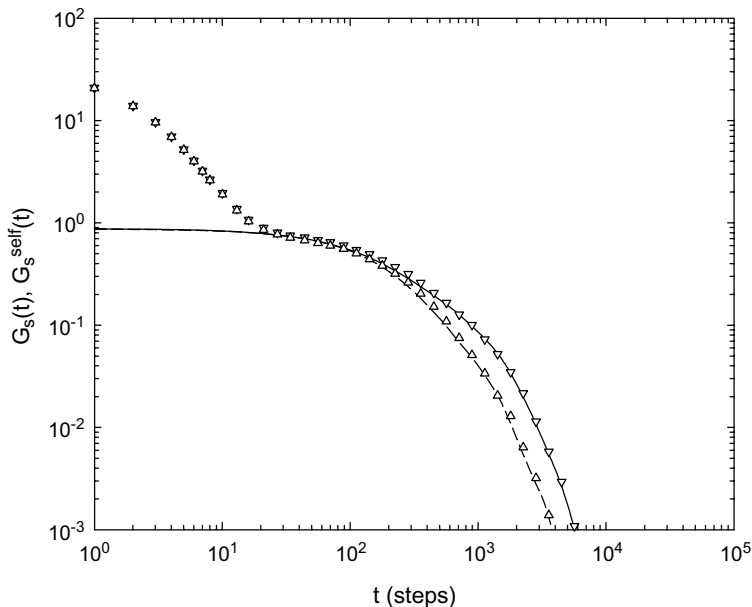


Fig. 17.9 Comparison of the equilibrium-simulated $G_S(t)$ (∇ based on Eq. (17.B.1)) and $G_S^{\text{self}}(t)$ (Δ based on Eq. (17.B.2)) curves for the five-bead Fraenkel chain; also shown are the equilibrium-simulated $G_S(t)$ (solid line) and $G_S^{\text{self}}(t)$ (dashed line) curves for the five-bead Rouse chain. The Rouse curves have been slightly shifted vertically: multiplied by the factor 0.85 as in Fig. 17.2.

^bNote: For the mean square end-to-end vector of a Fraenkel chain, which is a static property, there is no correlation between different segments, just as in the case of the freely jointed chain (Chapter 1).

$G_S(t)$ and $G_S^{\text{self}}(t)$ in the fast-mode region, the short-time region may be analyzed in terms of only Eq. (17.B.2). Since the sum in Eq. (17.B.2) just represents a multiple of the single term in Eq. (17.7), the analysis of tension fluctuations in the Fraenkel dumbbell presented in the main text can be readily applied to an N -bead chain. This means that the fluctuating $\delta_i(t)$ is the dominant factor in the short-time region of $G_S(t)$ for a multiple-segment Fraenkel chain as it is in the Fraenkel-dumbbell case. As opposed to the analysis of the fast mode of an N -bead chain being simplified this way, the contributions of the cross-terms clearly cannot be neglected in the slow-mode region. This and the lack of a good justification for forming a product of $\langle \delta(0)\delta(t) \rangle$ and $\langle (b_x(0)b_y(0))(b_x(t)b_y(t)) \rangle$ (Eq. (17.8)) in the long-time region collectively makes an analysis similar to that done on the Fraenkel dumbbell for the slow mode unwieldy. However, as also shown in Fig. 17.9, the relative weight between the self-term and cross-term components in the Rouse-chain model is virtually the same as in the Fraenkel chain model (over the slow-mode region). The consistency in the internal behavior between the two models further supports that the slow mode behaves virtually just as the Rouse process does. Thus, the conclusion that the fast mode is driven by energetic interactions and the slow mode by entropy as derived from the analysis on the simulation results of the Fraenkel dumbbell, is applicable to multiple-bead Fraenkel chains as well.

References

1. Fraenkel, G. K., *J. Chem. Phys.* **20**, 642 (1952).
2. Bird, R. B., Curtiss, C. F., Armstrong, R. C., and Hassager, O., *Dynamics of Polymeric Liquids*, Vol. 2 (2nd edn), Wiley, New York (1987).
3. Lin, Y.-H., and Das, A. K., *J. Chem. Phys.* **126**, 074902 (2007).
4. Lin, Y.-H., and Das, A. K., *J. Chem. Phys.* **126**, 074903 (2007).
5. Inoue, T., Okamoto, H., and Osaki, K., *Macromolecules* **24**, 5670 (1991).
6. Inoue, T., and Osaki, K., *Macromolecules* **29**, 1595 (1996).
7. Okamoto, H., Inoue, T., and Osaki, K., *J. Polym. Sci.: Part B: Polym. Phys.* **33**, 417 (1995).
8. Wignall, G. D., Schelten, J., and Ballard, D. G. H., *J. Appl. Cryst.* **7**, 190 (1974).
9. Ballard, D. G. H., Rayner, M. G., and Schelten, J., *Polymer* **17**, 349 (1976).
10. Norisuye, T., and Fujita, H., *Polym. J.* (Tokyo) **14**, 143 (1982).
11. Lin, Y.-H., *J. Polym. Res.* **1**, 51 (1994).
12. Lin, Y.-H., and Lai, C. S., *Macromolecules* **29**, 5200 (1996).
13. Lai, C. S., Juang, J.-H., and Lin, Y.-H., *J. Chem. Phys.* **110**, 9310 (1999).
14. Lin, Y.-H., and Luo, Z.-H., *J. Chem. Phys.* **112**, 7219 (2000).

15. Lin, Y.-H., *J. Phys. Chem. B* **109**, 17670 (2005).
16. Lin, Y.-H., *J. Phys. Chem. B* **109**, 17654 (2005).
17. Lin, Y.-H., *J. Phys.: Condens. Matter* **19**, 466101 (2007).
18. McQuarrie, D. A., *Statistical Mechanics*, Harper & Row, New York (1976).
19. Goldstein, H., *Classical Mechanics*, (2nd edn), Addison–Wesley, Reading, MA (1980).

Chapter 18

Monte Carlo Simulations of Stress Relaxation of Fraenkel Chains — Nonlinear Viscoelasticity of Entanglement-Free Polymers

As presented in Chapter 17, the Monte Carlo simulation study of linear viscoelasticity of entanglement-free Fraenkel chains has revealed two distinct dynamic modes in the relaxation modulus $G_S(t)$:¹ (1) The fast mode arises from the fluctuations in segment tension or reflects the relaxation of the segmental tension created by segments being stretched by the applied step shear deformation — an energy-driven dynamic process. (2) The slow mode arises from the fluctuations in segment orientation or represents the randomizations of the strain-induced segmental orientation — an entropy-driven dynamic process. Very significantly, the slow mode is well described by the Rouse theory in all aspects: the magnitude of modulus, the line shape and the N (number of beads) dependence of the relaxation time, particularly when $N \gg 2$. This result means that as far as the slow mode is concerned, one Rouse segment may be replaced by one Fraenkel segment, or vice versa, even though the latter is much stiffer than the former. Furthermore, as indicated by comparing experiment and simulation (Fig. 17.7), the coexistence of the glassy- (structural- or α -) relaxation process (fast energy-driven mode) and the Rouse relaxation mode (slow entropy-driven mode) observed in an entanglement-free polymer melt is explained and their relative time scales are properly described. The shown agreement between simulation and experiment over a wide range spanning both the two modes is consistent with the success of the Rouse theory in explaining the linear viscoelastic response functions of entanglement-free polymer melts in the long-time (low-frequency) or entropic region (Chapters 11 and 14).²⁻⁴ At the same time, it strongly suggests that the Fraenkel-chain model has captured the essential element of the energetic interactions that affect the glassy relaxation in a polymer melt. Describing

in a natural way the emergence of the fast energy-driven mode above the slow Rouse mode in its short-time region, the Fraenkel-chain model represents a dramatic improvement over the Rouse model in the study of linear viscoelasticity. The new understandings in turn suggest that the stress relaxations of Fraenkel chains obtained from the Monte Carlo simulations in the nonlinear region may be profitably analyzed by comparing them with the constitutive equation of the Rouse model (Chapter 7).⁵ In Sec. 16.4, the stress-relaxation results of the Rouse model obtained from the simulations following the application of a step shear deformation have been presented and their perfect agreements with the Rouse theoretical results have been illustrated.

18.1 Effects of the Nonlinearly Enhanced Tensile Force along the Fraenkel Segment

The relaxation modulus $G_S(t)$ and the first normal-stress difference function $G_{\Psi_1}(t)$ (Eqs. (16.14) and (16.15)) of the Rouse model are independent of the applied strain. By contrast, the equivalent dynamic quantities $G_S(t, \lambda)$ and $G_{\Psi_1}(t, \lambda)$ obtained from the Monte Carlo simulations on a five-bead Fraenkel chain at different strains from $\lambda = 0.5$ to 4 are strain-dependent as shown in Fig. 18.1. However, even though both $G_S(t, \lambda)$ and $G_{\Psi_1}(t, \lambda)$ exhibit nonlinear effects, the Lodge–Meissner relation holds perfectly well as can be observed in the same figure. Furthermore, unlike in the Rouse model, the second normal-stress difference $N_2(t, \lambda)$ in the Fraenkel-chain model is not zero as shown in Fig. 18.2. Thus, the Fraenkel-chain model exhibits significant deviations in the nonlinear viscoelastic behavior from the Rouse model, even though its linear relaxation modulus in the long-time region is well described by the Rouse theory. Analyses of these differences as related to the particular form of the Fraenkel potential are given in the following:

A large tensile force along the Fraenkel segment is created when it is significantly stretched by an applied strain, which leads to the stress showing up in the fast mode region. The strain hardening of the fast mode (Fig. 18.1) can be understood by examining the tensile force \mathbf{F}_F along a Fraenkel segment denoted by \mathbf{b} :

$$\mathbf{F}_F = \frac{H_F}{b_0^2} \mathbf{b} - \frac{H_F}{b_0} \left[\frac{\mathbf{b}}{|\mathbf{b}|} \right] = H_F \frac{\delta(t)}{b_0^3} \mathbf{b} \quad (18.1)$$

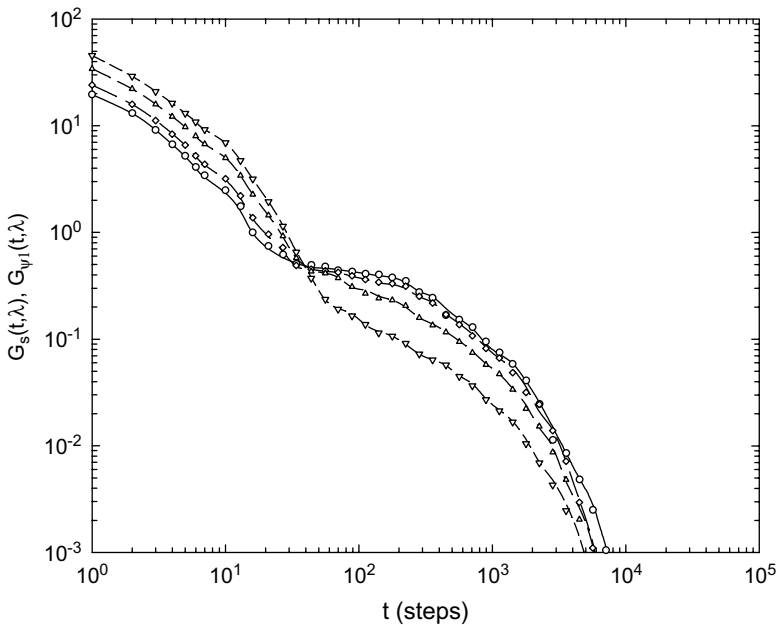


Fig. 18.1 Comparison of the results of $G_S(t, \lambda)$ (solid line at $\lambda = 0.5$; long-dash line at $\lambda = 1$; medium-dash line at $\lambda = 2$; and short-dash line at $\lambda = 4$) and $G_{\Psi_1}(t, \lambda)$ (\circ at $\lambda = 0.5$; \diamond at $\lambda = 1$; \triangle at $\lambda = 2$; and ∇ at $\lambda = 4$) obtained from simulations on the five-bead Fraenkel chain following the application of a step shear strain λ .

where $\delta(t)$ is defined by Eq. (17.4). As shown in Fig. 18.3, right after the application of a step shear strain to the Fraenkel chain in equilibrium, a $|\mathbf{b}(t = 0_+)|$ ($t = 0_+$ is used to denote the state right after the application of a step strain) value larger than b_0 (set equal to 1) on average is created; as a result, the second term of Eq. (18.1) becomes smaller than the first term, leading to a tensile force that will pull the two separated beads back to the equilibrium distance — a recoiling effect. In the simulations under equilibrium conditions as studied in Chapter 17, $\delta(t)$ is used to represent the deviation of the bond length $|\mathbf{b}|$ from the b_0 value in the linear region. In the present nonlinear case, it is better to regard $\delta(t)$ simply as a parameter characterizing the nonlinear enhancement of the tensile force exerted on the segment as the segment is significantly stretched.

A close examination of the calculated values of $G_S(\lambda, t = 0_+)$ (Fig. 18.5) shows that the shear stress increases nonlinearly with the shear strain λ at as low as ~ 0.005 . The calculated $G_S(\lambda, t = 0_+)$ results indicate that

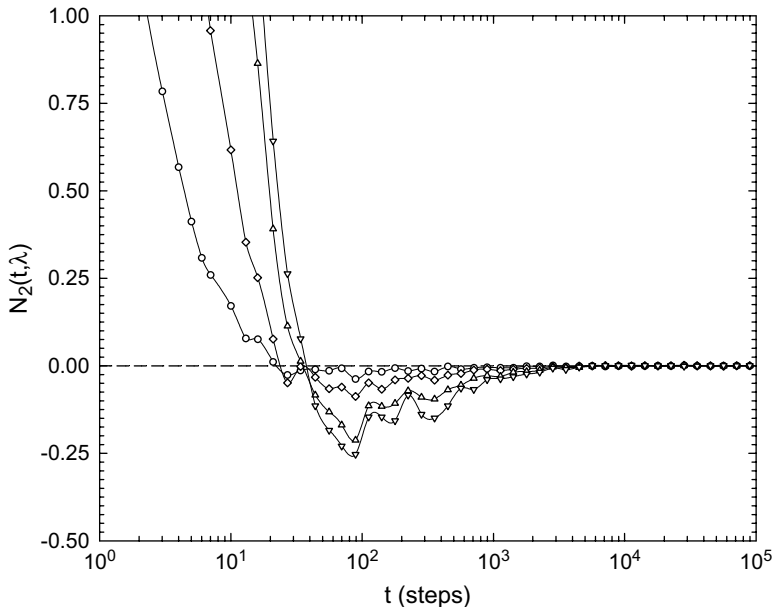


Fig. 18.2 Second normal stress $N_2(t, \lambda)$ obtained from simulations on the five-bead Fraenkel chain following the application of a step shear strain (\circ at $\lambda = 0.5$; \diamond at $\lambda = 1$; Δ at $\lambda = 2$; and ∇ at $\lambda = 4$).

the average tensile force along the segment start to increase greatly in a nonlinear way at $\lambda \approx 0.3$. The nonlinearly enhanced segmental tension is responsible for the strain hardening of the fast mode as can clearly be seen in Fig. 18.1. Besides this obvious result, it leads to the emergence of the second normal-stress difference (Fig. 18.2). The second normal-stress difference is of significant magnitude in the fast-mode region; as the time enters the slow-mode region, it declines towards the zero line and beyond; and finally relaxes as a negative diminishing tail. These effects of the nonlinearly enhanced segmental tension can be understood by means of the following analysis:

The use of the Langevin equation has implied that our studied system is ergodic.^{6,7} Thus, the concept or language of ensemble averaging may be used to discuss the results obtained by averaging the behavior of a single chain over time in the equilibrium state or over the repeating cycles following the step deformation. As obtained from the simulations under equilibrium conditions, the mean squared bond length $\langle \mathbf{b}^2 \rangle_0$ is only 1.3% larger than $b_0^2 = 1$; and the ensemble-averaged components of $\langle \mathbf{b}^2 \rangle_0$ are identical:

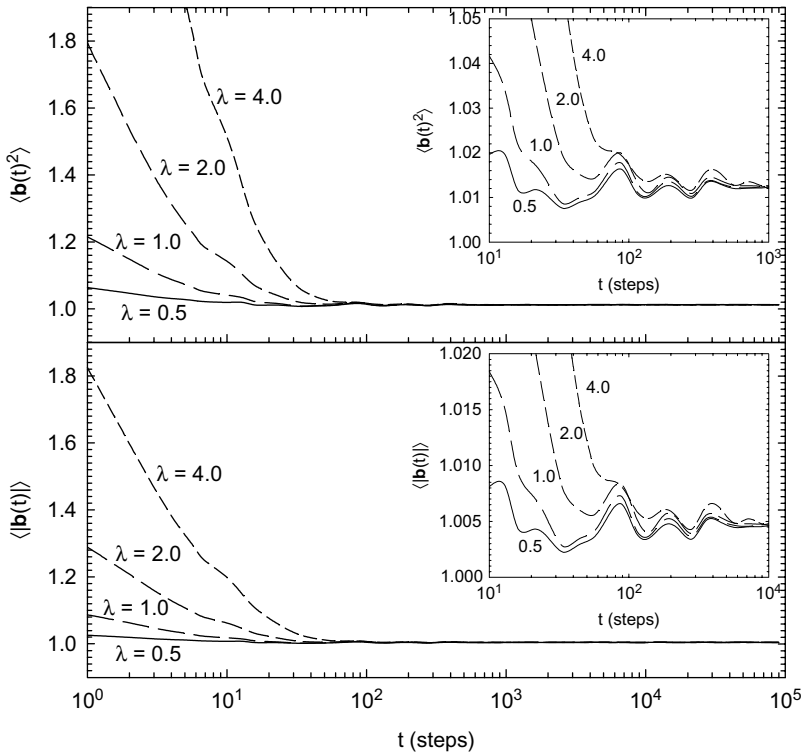


Fig. 18.3 $\langle \mathbf{b}(t)^2 \rangle$ (top) and $\langle |\mathbf{b}(t)| \rangle$ (bottom) as a function of time following the application of a step shear strain ($\lambda = 0.5, 1, 2$ and 4) obtained from simulations on the five-bead Fraenkel chain. The insets show the oscillations in $\langle \mathbf{b}(t)^2 \rangle$ and $\langle |\mathbf{b}(t)| \rangle$ visible in the time region of 10^2 – 10^3 before reaching their stable equilibrium values.

$\langle b_x^2 \rangle_0 = \langle b_y^2 \rangle_0 = \langle b_z^2 \rangle_0 = 0.3377$ as expected. However, in the ensemble, different segments have different b_x^2 , b_y^2 and b_z^2 values. Among the segments with the same b_x^2 , those with larger b_y^2 have to have a smaller b_z^2 on average. Following the step shear deformation \mathbf{E} as defined by Eq. (16.9), those segments with a larger b_y^2 and a smaller b_z^2 will be stretched more — leading to greater *nonlinear* enhancements of their tensile forces as characterized by the parameter $\delta(t)$ — than those with a smaller b_y^2 and a larger b_z^2 . Since the contribution of a segment to the normal stress in the y direction is proportional to $\delta(t)b_y(t)^2$ at time t , the average of the initial value $\delta(0_+)b_y(0_+)^2$ is much more weighted by those segments with larger b_y^2 ; the opposite can be said about the normal stress in the z direction. As a result, a positive second normal-stress difference ($N_2(t) > 0$) occurs in the short-time or

fast-mode region, as shown in Fig. 18.2. Such an effect will not occur in the Rouse-segment case, where the tensile force increases with bond length linearly (Chapters 6 and 7).

As explained above, the segmental tensile force created by the step deformation will shrink the segmental length back to its equilibrium value. Those segments with a larger initial y component, as having larger tensile forces, will be more affected by the recoiling effect. The average values $\langle b_x(0_+)^2 \rangle$, $\langle b_y(0_+)^2 \rangle$, and $\langle b_z(0_+)^2 \rangle$ in accordance with the affine deformation are expected to be given, respectively, by $\langle b_x^2(t = 0_+) \rangle = \langle b_x^2 \rangle_0 + \lambda^2 \langle b_y^2 \rangle_0 = 0.3377(1 + \lambda^2)$; $\langle b_y^2(t = 0_+) \rangle = \langle b_y^2 \rangle_0 = 0.3377$ and $\langle b_z^2(t = 0_+) \rangle = \langle b_z^2 \rangle_0 = 0.3377$. These values obtained from the simulations are in close agreement with the expected values at different strains. As the chain configuration evolves according to the Langevin equation, the recoiling effect causes all the $\langle b_x(t)^2 \rangle$, $\langle b_y(t)^2 \rangle$ and $\langle b_z(t)^2 \rangle$ values to decline, as shown in Fig. 18.4. Due to the nonlinearly enhanced initial tensile force associated with segments with larger b_y^2 , $\langle b_y(t)^2 \rangle$ decreases faster than $\langle b_z(t)^2 \rangle$ as $\langle \mathbf{b}(t)^2 \rangle$ declines reaching its equilibrium value at a time near the end of the fast mode, as shown in Fig. 18.3. As $\langle \mathbf{b}(t)^2 \rangle$ reaches or nears its equilibrium value, $\langle b_y(t)^2 \rangle$ and $\langle b_z(t)^2 \rangle$ reach their respective minimum points (at around 20–40 time steps), signifying the ending of recoiling. Due to its fast declining rate from the very beginning, $\langle b_y(t)^2 \rangle$ is smaller than $\langle b_z(t)^2 \rangle$ at the end of the recoiling process. Thus, at about this point the second normal-stress difference $N_2(t, \lambda)$ crosses the zero line and becomes negative. In the time-scale region of the early part of the slow mode, even though there is a significant degree of segment-orientation anisotropy, the segmental tensile force is oscillating within a very small range (as reflected by $\langle \mathbf{b}(t)^2 \rangle$ or $\langle |\mathbf{b}(t)| \rangle$; see the insets of Fig. 18.3) around a value virtually identical to the equilibrium value. The small overshooting (only observed at $\lambda = 0.5$ and 1) and damped oscillations should be the after effect of the recoiling of the stretched segment. As a result, as shown in Fig. 18.2, the second normal-stress differences in the region are of small magnitude and, being most sensitive to the small changes in the segmental tensile force, exhibit some waviness. One can observe most clearly in the region of 10^2 – 10^3 time steps that when $\langle \mathbf{b}(t)^2 \rangle$ or $\langle |\mathbf{b}(t)| \rangle$ is at its oscillation crests, $|N_2(t, \lambda)|$ is also at the crests of its wavy form (see Fig. 18.2). The mechanism interrelating chain dynamics and viscoelasticity as revealed by analyzing the results shown in Figs. 18.1–18.4 becomes more clearly visible as the applied strain λ increases.

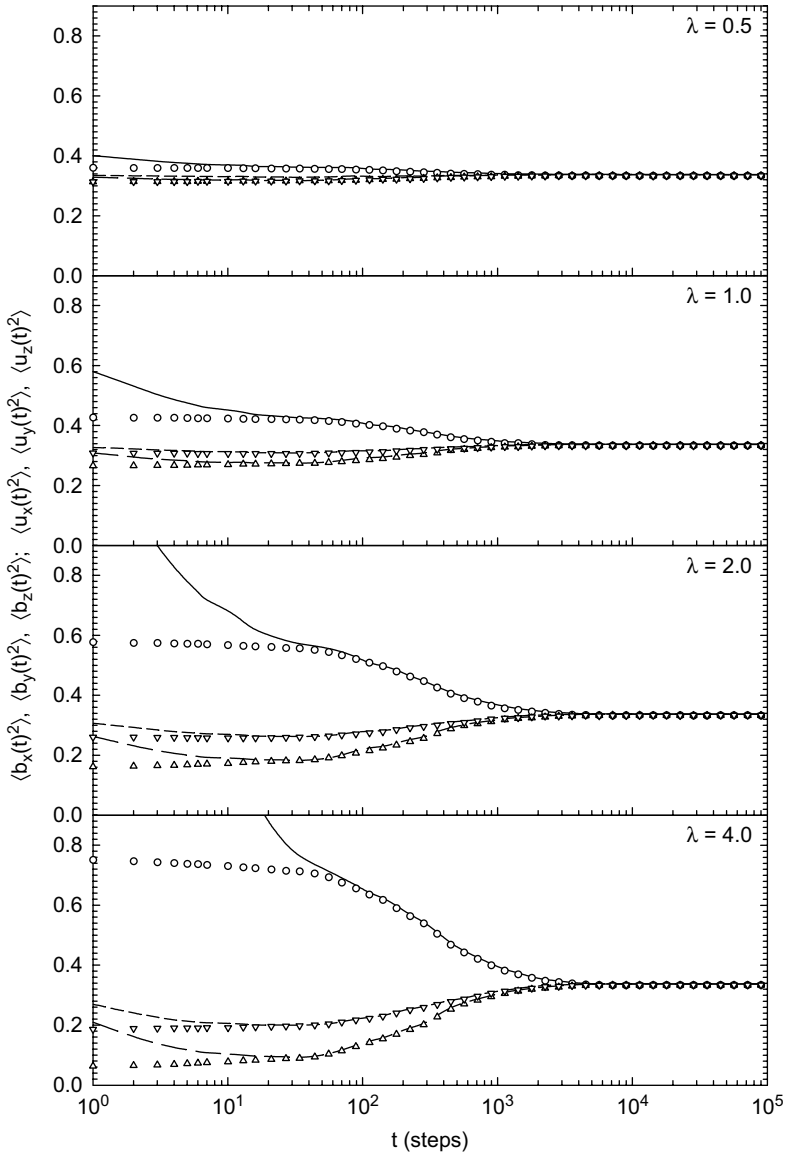


Fig. 18.4 $\langle b_x(t)^2 \rangle$ (solid line); $\langle b_y(t)^2 \rangle$ (long-dash line); $\langle b_z(t)^2 \rangle$ (short-dash line) and $\langle u_x(t)^2 \rangle$ (o); $\langle u_y(t)^2 \rangle$ (Δ); and $\langle u_z(t)^2 \rangle$ (∇) as a function of time following the application of a step shear strain ($\lambda = 0.5, 1, 2$ and 4) obtained from simulations on the five-bead Fraenkel chain.

18.2 The Lodge–Meissner Relation for the Fraenkel Chain

The relation $G_S(t, \lambda) = G_{\Psi 1}(t, \lambda)$ was first found by Lodge and Meissner using a phenomenological argument.⁸ However, the Lodge–Meissner relation observed in the simulations of the Fraenkel-chain model as shown in Fig. 18.1 can be proved analytically. This is done by considering the configurations of all the chains in a finite volume right after the application of a step deformation and their subsequent evolution.

Consider a volume V_0 containing n Fraenkel chains, each with N beads. Right after the application of a step shear deformation \mathbf{E} to such a system in equilibrium, the shear stress, $-\sigma_{xy}(0_+)$, is given by (setting $kT = 1$)

$$\begin{aligned} -\sigma_{xy}(0_+) &= \frac{n(N-1)}{V_0} \langle T_x(0_+) b_y(0_+) \rangle \\ &= \frac{H_F}{V_0 b_0^3} \sum_k^n \sum_s^{N-1} \delta_s^k(\lambda) (b_{s,x}^{o,k} + \lambda b_{s,y}^{o,k}) (b_{s,y}^{o,k}) \end{aligned} \quad (18.2)$$

where T_x denotes the x component of the tensile force \mathbf{F}_F along a *representative* Fraenkel segment in the ensemble. In the second part of Eq. (18.2), $b_{s,\alpha}^{o,k}$ ($\alpha = x, y$) denotes the α component of the s th segment on the k th chain of the system in an equilibrium state right *before* the application of the step deformation \mathbf{E} . Because of the presence of $\delta_s^k(\lambda)$, which depends on the applied strain and the orientation of the segment, the sum of the terms containing the products of $b_{s,x}^{o,k}$ and $b_{s,y}^{o,k}$ over all the segments in the ensemble is not zero. In the Rouse model, as $\delta_s^k(\lambda)$ is a constant, the sum equals zero. Because $\langle \mathbf{b}^2 \rangle = 1.013b_0^2$ in equilibrium, we may for convenience and easy understanding regard each segment as having unit length before the initial step deformation is applied.^a Then the stress component as given by Eq. (18.2) but normalized to that for a single segment (denoted by $-S_{xy}(0_+)$) can be expressed by

$$-S_{xy}(0_+) = H_F \langle \delta(\lambda) (u_x^o u_y^o + \lambda u_y^o u_y^o) \rangle_{\mathbf{u}^o} \quad (18.3)$$

^aNote: This is not a required assumption. In the ensemble, segments with a certain bond length are oriented in all directions with equal probability; this is true with any bond length that can occur in an equilibrium state. Each “group” of segments which have the same bond length can be normalized in the same way and averaged over all orientations as described in the text.

where

$$\delta(\lambda) = 1 - \frac{1}{\sqrt{(u_x^o + \lambda u_y^o)^2 + (u_y^o)^2 + (u_z^o)^2}}. \quad (18.4)$$

In Eqs. (18.3) and (18.4), u_x^o , u_y^o and u_z^o denote the x , y and z components of a unit vector \mathbf{u}^o representing the orientation of a segment in the equilibrium system right before the step shear deformation is applied; and $\langle f \rangle_{\mathbf{u}^o}$ denotes averaging f over all orientations of \mathbf{u}^o .

Similarly the first normal-stress difference $-(\sigma_{xx}(0_+) - \sigma_{yy}(0_+))$ can be expressed by

$$\begin{aligned} & -(\sigma_{xx}(0_+) - \sigma_{yy}(0_+)) \\ &= \frac{n(N-1)}{V_0} (\langle T_x(0_+) b_x(0_+) \rangle - \langle T_y(0_+) b_y(0_+) \rangle) \\ &= \frac{H_F}{V_0 b_0^3} \sum_k^n \sum_s^{N-1} [\delta_s^k(\lambda) (b_{s,x}^{o,k} + \lambda b_{s,y}^{o,k}) (b_{s,x}^{o,k} + \lambda b_{s,y}^{o,k}) - \delta_s^k(\lambda) (b_{s,y}^{o,k})^2]. \end{aligned} \quad (18.5)$$

In the same way as Eq. (18.3) is obtained from Eq. (18.2), the first normal-stress difference given by Eq. (18.5) but normalized to that for a single segment can be expressed by

$$\begin{aligned} N_1(0_+) &= -(S_{xx}(0_+) - S_{yy}(0_+)) \\ &= H_F \langle \delta(\lambda) (u_x^o + \lambda u_y^o) (u_x^o + \lambda u_y^o) - \delta(\lambda) (u_y^o)^2 \rangle_{\mathbf{u}^o}. \end{aligned} \quad (18.6)$$

As shown in Appendix 18.A, Eq. (18.6) can be rewritten as

$$N_1(0_+) = H_F \lambda \langle \delta(\lambda) (u_x^o u_y^o + \lambda u_y^o u_y^o) \rangle_{\mathbf{u}^o} = -\lambda S_{xy}(0_+). \quad (18.7)$$

As there exists a one-to-one correspondence between the segmental (molecular) representation and the orientation-based representation — i.e. between Eqs. (18.2) and (18.3) or between Eqs. (18.5) and (18.6) — the contribution of $\sum_k^n \sum_s^{N-1} \delta_s^k(\lambda) [(b_{s,x}^{o,k})^2 - (b_{s,y}^{o,k})^2 + \lambda b_{s,x}^{o,k} b_{s,y}^{o,k}]$ has to be zero as it corresponds to Eq. (18.A.1). In other words, as corresponding to Eq. (18.7), Eq. (18.5) may be rewritten as

$$-(\sigma_{xx}(0_+) - \sigma_{yy}(0_+)) = \frac{H_F}{V_0 b_0^3} \lambda \sum_k^n \sum_s^{N-1} \delta_s^k(\lambda) (b_{s,x}^{o,k} + \lambda b_{s,y}^{o,k}) (b_{s,y}^{o,k}). \quad (18.8)$$

Comparison of Eqs. (18.2) and (18.8) indicates that both the shear stress and the first normal-stress difference arise from the same molecular source(s) $\sum_k^n \sum_s^{N-1} \delta_s^k(\lambda)(b_{s,x}^{o,k} + \lambda b_{s,y}^{o,k})(b_{s,y}^{o,k})$; therefore, the evolutions of the corresponding configurations responsible for their relaxations are the same. As $N_1(0_+) = -\lambda S_{xy}(0_+)$ (Eq. (18.7)), the Lodge–Meissner relation holds. It is easier to apply the above analysis to the Rouse model, in which $N_1(0_+) = \lambda^2 G_S(0_+)$ and $-S_{xy}(0_+) = \lambda G_S(0_+)$. As opposed to $G_S(t)$ and $G_{\Psi_1}(t)$ being independent of strain as given by Eqs. (16.14) and (16.15) for the Rouse chain model, $G_S(t, \lambda)$ and $G_{\Psi_1}(t, \lambda)$ as defined by

$$G_S(t, \lambda) = -\frac{S_{xy}(t, \lambda)}{\lambda}, \quad (18.9)$$

and

$$G_{\Psi_1}(t, \lambda) = \frac{N_1(t)}{\lambda^2} \quad (18.10)$$

have the same strain dependence as shown in Fig. 18.1. The initial values of $G_S(t = 0_+, \lambda)$ (or $G_{\Psi_1}(t = 0_+, \lambda)$) at different λ may be calculated numerically from Eq. (18.3) (or Eq. (18.7)) by performing the averaging over all orientations for comparison with the values obtained from the simulations as shown in Fig. 18.5. As shown in the same figure, the agreement can be further improved when the calculated curve is multiplied by the correction factor $\langle \mathbf{b}^2 \rangle_0 / b_0^2 = 1.013$. The agreements between simulations and numerical calculations shown in Fig. 18.5 and between the simulation results of $G_S(t, \lambda)$ and $G_{\Psi_1}(t, \lambda)$ as shown in Fig. 18.1 confirm the above theoretical analysis.

Only after the performed averaging is so complete that $\sum_k^n \sum_s^{N-1} \delta_s^k(\lambda) [(b_{s,x}^{o,k})^2 - (b_{s,y}^{o,k})^2 + \lambda b_{s,x}^{o,k} b_{s,y}^{o,k}] \rightarrow 0$, Eq. (18.5) becomes identical to Eq. (18.8). Before this condition is fully realized, $G_{\Psi_1}(t, \lambda)$ should show a higher noise level than $G_S(t, \lambda)$ as indeed observed in the simulations. As the ideal is never fully realized in the practice, one may regard the Monte Carlo simulations as showing that the Lodge–Meissner relation holds only within some fluctuating noise.

The second normal-stress difference as a function of time obtained from the simulations on the five-bead Fraenkel chain is nonzero as shown in Fig. 18.2. By averaging over all orientations, the initial value of the second normal-stress difference calculated from

$$N_2(0_+) = -(S_{yy}(0_+) - S_{zz}(0_+)) = H_F \langle \delta(\lambda) ((u_y^o)^2 - (u_z^o)^2) \rangle_{\mathbf{u}^o}, \quad (18.11)$$

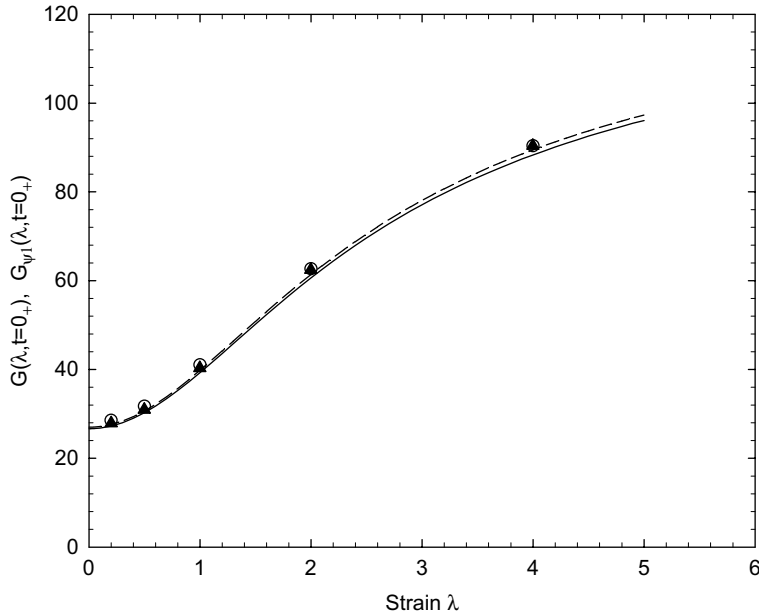


Fig. 18.5 Comparison of the initial values $G_S(t = 0_+, \lambda)$ (o) and $G_{\Psi_1}(t = 0_+, \lambda)$ (▲) obtained from simulations on the five-bead Fraenkel chain with the λ -dependent curve (solid line) calculated by averaging Eq. (18.3) or (18.7) over all orientations; the line (dashed) indicating the λ -dependent curve corrected for the ratio $\langle \mathbf{b}^2 \rangle_0 / b_0^2 = 1.013$.

is nonzero. In Fig. 18.6, the $N_1(0_+)$ and $N_2(0_+)$ values obtained from the simulations at different strains are compared, and are shown to be in close agreement with the values calculated from Eqs. (18.7) and (18.11), respectively.

18.3 Stress and Segmental Orientation

As shown in Chapter 17, the slow mode in the Fraenkel chain's linear relaxation modulus reflects the randomization of orientation of segments, whose average length is virtually the same as that in an equilibrium state. In other words, the slow mode is an entropy-driven dynamic process. At strains in the nonlinear region (from $\lambda = 0.5$ to 4), the strong correlation between the stress and the segmental orientation in the slow-mode region is maintained as well. Such strong correlation can be observed in Figs. 18.7, 18.8, and 18.9, in which $-S_{xy}(t)$, $\langle b_x(t)b_y(t) \rangle$ and $\langle u_x(t)u_y(t) \rangle$; $N_1(t)$, $\langle b_x(t)^2 \rangle - \langle b_y(t)^2 \rangle$

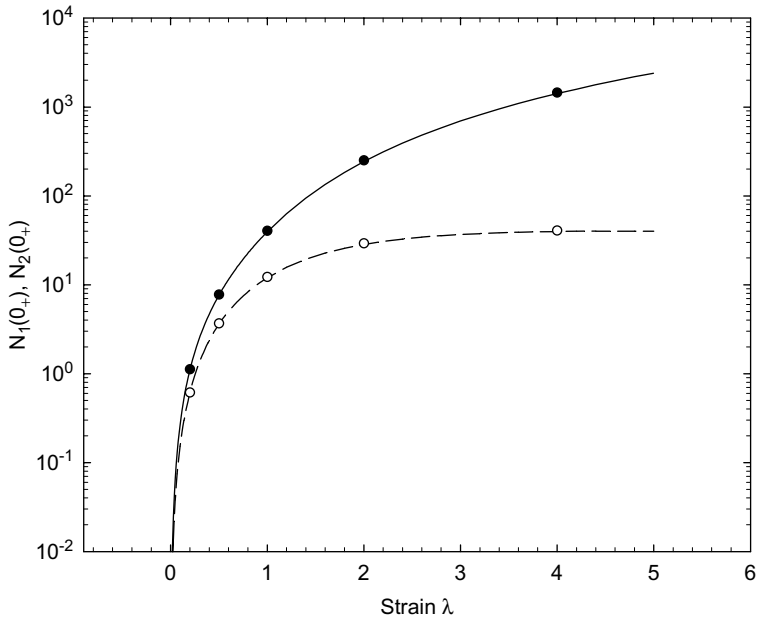


Fig. 18.6 Comparison of the initial first and second normal stress differences $N_1(0_+)$ (\bullet) and $N_2(0_+)$ (\circ) obtained from simulations on the five-bead Fraenkel chain at different strains with the λ -dependent curves of $N_1(0_+)$ (solid line) and $N_2(0_+)$ (dashed line) numerically calculated by averaging Eqs. (18.7) and (18.11), respectively, over all orientations.

and $\langle u_x(t)^2 \rangle - \langle u_y(t)^2 \rangle$; and $|N_2(t)|$, $\langle b_y(t)^2 \rangle - \langle b_z(t)^2 \rangle$ and $\langle u_y(t)^2 \rangle - \langle u_z(t)^2 \rangle$ are, respectively, compared. The most important feature of these results is that virtually over the whole slow-mode range, all the stress components are proportional to the corresponding orientation components by about the same factor 4, which can be concisely denoted by

$$-\mathbf{S}(t, \lambda) = 4\langle \mathbf{b}(t, \lambda)\mathbf{b}(t, \lambda) \rangle \quad (18.12)$$

or

$$-\mathbf{S}(t, \lambda) = 4\langle \mathbf{u}(t, \lambda)\mathbf{u}(t, \lambda) \rangle \quad (18.13)$$

with the difference between $\langle \mathbf{b}(t)\mathbf{b}(t) \rangle$ and $\langle \mathbf{u}(t)\mathbf{u}(t) \rangle$ being negligibly small. The Rouse theory predicts

$$-\mathbf{S}(t, \lambda) = 3\langle \mathbf{b}(t, \lambda)\mathbf{b}(t, \lambda) \rangle. \quad (18.14)$$

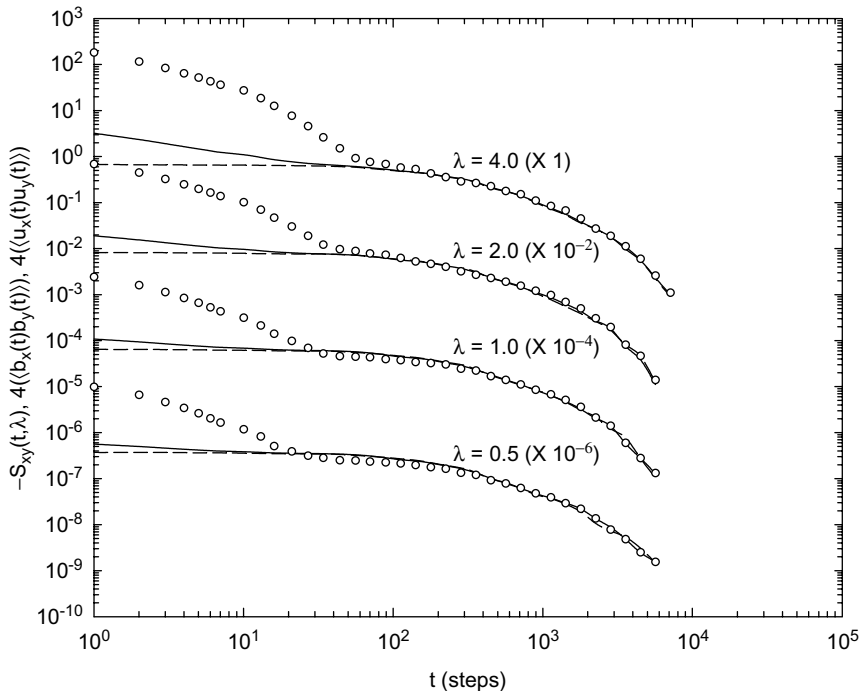


Fig. 18.7 Comparison of the time dependences of $-S_{xy}(t, \lambda)$ (\circ); $4 \times \langle b_x(t)b_y(t) \rangle$ (solid line); and $4 \times \langle u_x(t)u_y(t) \rangle$ (dashed line) obtained from simulations on the five-bead Fraenkel chain at $\lambda = 0.5, 1, 2$ and 4 . To avoid overlapping between shown curves, the results at different λ values have been shifted along the vertical axis by the indicated factors.

Note that $S_{xz}(t) = S_{yz}(t) = 0$ in both Eqs. (18.12) (or (18.13)) and (18.14); and $S_{yy}(t) \neq S_{zz}(t)$ in Eq. (18.12) (or (18.13)), while $S_{yy}(t) = S_{zz}(t)$ in Eq. (18.14). The factor 4 in Eq. (18.12) being so close to the value 3 predicted based on the entropic force constant of the Rouse segment (Eq. (18.14)) strongly indicates the entropic nature of the slow mode. The revealed entropic nature of the slow mode is very significant considering that the Fraenkel segment is much stiffer than the Rouse segment and that the segment has (initially) been greatly stretched by an applied strain well into the nonlinear region. Clearly, the entropic slow mode is made possible by the fast relaxation of segmental tension allowing the average segmental length to reach its equilibrium value while the segment-orientation anisotropy is still strong.

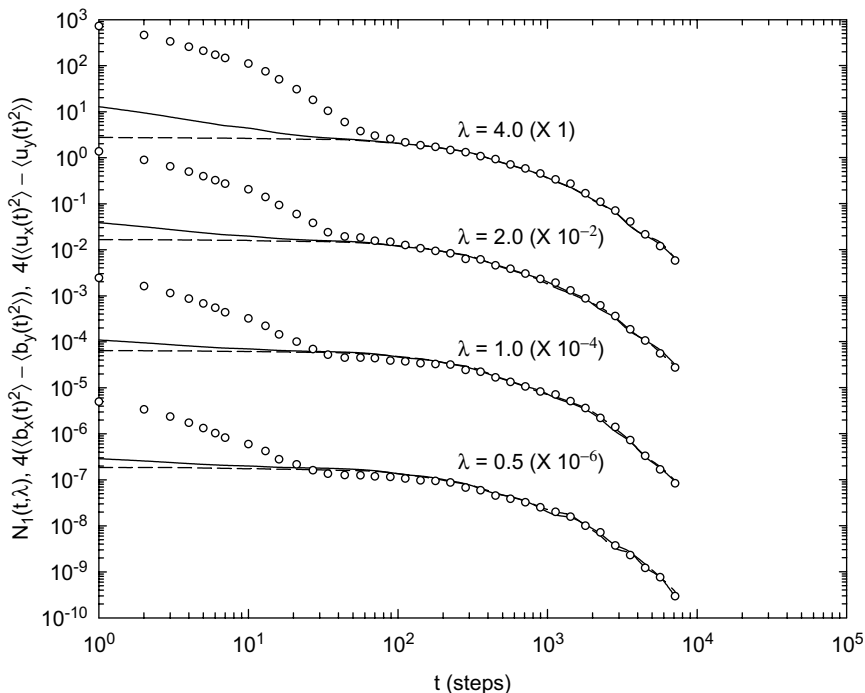


Fig. 18.8 Comparison of the time dependences of $N_1(t, \lambda)$ (○); $4 \times (\langle b_x(t)^2 \rangle - \langle b_y(t)^2 \rangle)$ (solid line); and $4 \times (\langle u_x(t)^2 \rangle - \langle u_y(t)^2 \rangle)$ (dashed line) obtained from simulations on the five-bead Fraenkel chain at $\lambda = 0.5, 1, 2$ and 4 . To avoid overlapping between shown curves, the results at different λ values have been shifted along the vertical axis by the indicated factors.

In the slow mode region, as $\langle \mathbf{b}(t)^2 \rangle$ has a value virtually identical to the equilibrium value, we may assume that all the Fraenkel segments in a chain have the same length — equal to the equilibrium value, which is not a bad assumption as $\mathbf{b}(t) \cdot \mathbf{b}(t)$ in an equilibrium state fluctuates within 10% above and below its mean value. With the unit vector \mathbf{u} representing the direction of a segment, we may denote the polarizability of the segment in the direction parallel to \mathbf{u} by α_{\parallel} and in the perpendicular direction by α_{\perp} . Then the anisotropic part of the polarizability tensor of each Fraenkel segment may be expressed as⁹

$$\alpha_{\alpha\beta} = (\alpha_{\parallel} - \alpha_{\perp}) \left(u_{\alpha} u_{\beta} - \frac{1}{3} \delta_{\alpha\beta} \right). \quad (18.15)$$

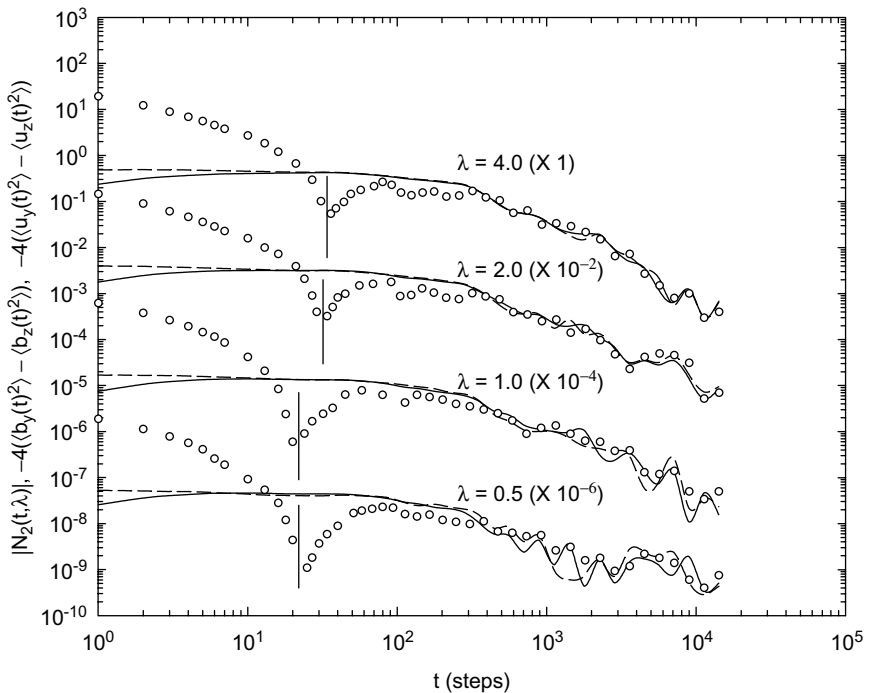


Fig. 18.9 Comparison of the time dependences of $|N_2(t, \lambda)|$ (\circ); $-4 \times (\langle b_y(t)^2 \rangle - \langle b_z(t)^2 \rangle)$ (solid line); and $-4 \times (\langle u_y(t)^2 \rangle - \langle u_z(t)^2 \rangle)$ (dashed line) obtained from simulations on the five-bead Fraenkel chain at $\lambda = 0.5, 1, 2$ and 4 ; the vertical lines indicate the points where $N_2(t, \lambda)$ changes sign. To avoid overlapping between shown curves, the results at different λ values have been shifted along the vertical axis by the indicated factors.

With the polarizability anisotropy given by Eq. (18.15), the relation as given by Eq. (18.13) means that the stress-optical rule holds in the entropic region. The widely observed stress-optical rule over the entropic region has always been explained by assuming that the distribution of the distance between any two segments in a chain is Gaussian.^{6,10,11} The Gaussian statistics as applied to the study of chain conformation is also used as the source from which the entropic force constant of the Rouse segment is derived. Here, we show that the entropic Rouse process occurring in the relaxation modulus and the stress-optical rule holding over its relaxation time scales can both be explained by the Fraenkel chain model without invoking the Gaussian statistics.

In the entropic region where the stress-optical rule is valid, the orientation angle χ' of the stress ellipsoid is identical to the extinction angle χ of the birefringence; and the stress relaxation corresponds to the decay of the birefringence Δn with time. In the simulated stress relaxation, because the Lodge–Meissner relation holds over the whole time range, the orientation angle χ' is predicted to remain the same in both the fast-mode and slow-mode regions (see Appendix 18.B). While $\chi = \chi'$ over the slow-mode region, it is not clear whether the same is true over the fast-mode region as the knowledge about how the polarizability changes with the elongation of the segment is required. However, it is expected that the stress-optical coefficient will be quite different if another stress-optical rule holds over the fast-mode region. Inoue *et al.*^{12–14} have analyzed the results of dynamic (linear) viscoelasticity and birefringence measurements on different polymers in terms of a sum of two stress-optical rules (a modified stress-optical rule): one for the high-frequency region (glassy component as denoted by Inoue *et al.*) and the other for the low-frequency region (rubbery component as denoted by Inoue *et al.*, which occurs in the entropic region and is the kind ordinarily encountered). The two stress-optical coefficients obtained are in general of very different magnitude and some with opposite signs;¹⁵ for instance, $C_R = -5 \times 10^{-9} \text{ Pa}^{-1}$ vs. $C_G = 3 \times 10^{-11} \text{ Pa}^{-1}$ for polystyrene melts.

18.4 Similarities in Nonlinear Relaxation Modulus between Entangled Polymer and Entanglement-Free Fraenkel-Chain Systems

(a) Overall line shapes of $G_S(t, \lambda)$

One may recall the two consecutive processes: the chain-tension relaxation process^{16–18} (denoted by $\mu_B^*(t, \mathbf{E})$) and the *terminal* mode (denoted by $\mu_C(t)$) occurring in the nonlinear relaxation modulus $G(t, \lambda)$ of an entangled system as studied in Chapter 12. There are some interesting similarities between the sequence of these two processes and that of the two relaxation modes in the $G_S(t, \lambda)$ of an entanglement-free Fraenkel chain studied in this chapter. To draw an analogy between the two kinds of systems, each Fraenkel segment may be regarded as corresponding to an entanglement strand and each bead as corresponding to a slip-link (of the Doi–Edwards model;¹⁹ see Chapter 8). As the discussion is on an analogy,

important differences between the counterparts need to be pointed out: Firstly, stronger-than-average chain tension on an entanglement strand will draw segments from neighboring entanglement strands slipping through the entanglement links; while uneven tension in the Fraenkel chain is basically localized in each segment. Secondly, the tensile force along the Fraenkel segment is quite large — proportional to H_F/b_0 (see Eq. (18.1)) — and is much greater than $3kT/b_0$; while the tensile force on an entanglement strand is typically of the order $\sim 3kT/a$ with a ($> b_0$) being the entanglement distance (Chapters 8, 9 and 13). Thus, the two different descriptions or pictures are suitably applied to different regions of a measured relaxation modulus. The segment-tension relaxation of the Fraenkel chain occurring in the short-time region of $G(t, \lambda)$ has very high modulus values as indicated by the comparison between simulation and experiment shown in Fig. 17.7. As shown in Figs. 14.17 and 14.18, in the short-time region, the $G(t, \lambda \rightarrow 0)$ of polystyrene has modulus values ranging from $\sim 4 \times 10^7$ to $\sim 10^{10}$ dynes/cm², which are much larger than the plateau modulus $G_N = 2 \times 10^6$ dynes/cm² (Chapter 10). In contrast, the chain-tension relaxation $\mu_B^*(t, \mathbf{E})$ occurs at modulus levels similar in order of magnitude to that of G_N as can be observed in Fig. 12.3. In spite of these differences between the two cases, the similarity in the $G(t, \lambda)$ line shape showing a two-step relaxation can be clearly observed by comparing Figs. (12.3)–(12.7) with Fig. (18.1). Furthermore, of great interest and importance is the effect of the same nature that exists in both kinds of long-time processes (the *terminal mode* in the entangled polymer case and the *slow mode* in the entanglement-free Fraenkel-chain case), each occurring following a different kind of tension-relaxation process (the chain-tension relaxation vs. the segment-tension relaxation). A discussion of the effect may shed light on the basic (entropic) nature of a physical effect (orientation) occurring in the nonlinear viscoelasticity of a polymer system, entangled or not, over a wide time-scale range. Following either the segment-tension or chain-tension relaxation process, it is the orientation randomization that is responsible for the relaxation of the remaining stress. In the entanglement-free Fraenkel-chain case, the randomizations of segmental orientation are caused directly by the Brownian motion of the beads in the chain. In comparison, the orientation associated with each of the entanglement strands (or primitive steps) in an entangled system is randomized by the reptation mechanism with assistance from the chain contour-length fluctuation process (Chapters 9 and 12).^{17,18,20,21} Either of the two different kinds of orientation

randomizations is an entropy-driven process: In the Fraenkel-chain case, the process is well described by the Rouse model as can be concluded by comparing the results shown in Figs. 17.2 and 17.5 and those shown in Fig. 18.10. In the entangled-polymer case, the process is well described by the $\mu_C(t)$ process contained in the extended reptation model (Figs. 12.4–12.8) with the strain dependence of the modulus quantitatively described by the damping function of the Doi–Edwards theory (Fig. 9.2).^{18,22–26} As it turns out in the Fraenkel-chain case, the strain dependence of $G_S(t, \lambda)$ over the entropic region also agrees with the Doi–Edwards damping function quite well for a different physical reason as analyzed in the following:

(b) Damping factor over the entropic region of $G_S(t, \lambda)$

As shown in Fig. 18.10, the Fraenkel-chain $G_S(t, \lambda)$ curves at different λ values can be superposed on one another over the entropic region closely by allowing a vertical shift. Thus from these simulation results, one can

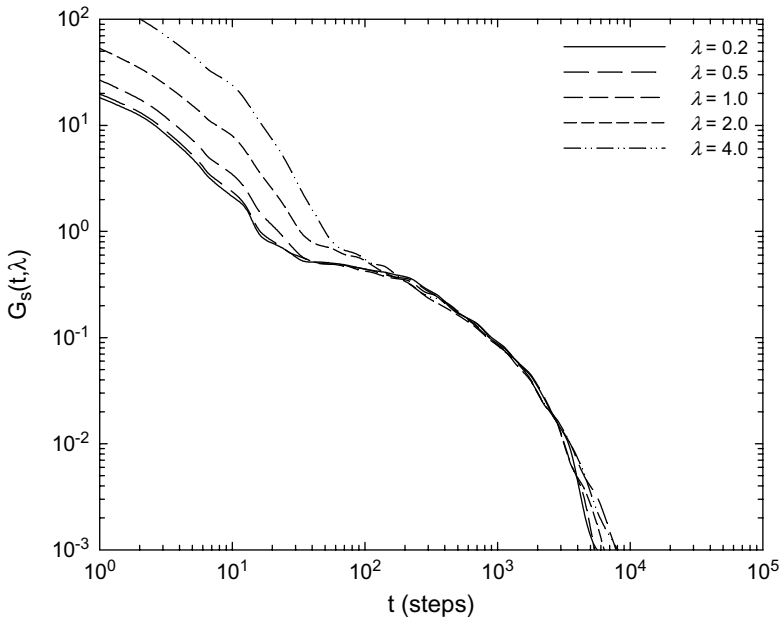


Fig. 18.10 Superposition of the $G_S(t, \lambda)$ curves at different strains obtained from simulations on the five-bead Fraenkel chain as shown in Fig. 18.1 by an upward vertical shift (multiplied by 1 at $\lambda = 0.2$ and 0.5 ; 1.1 at $\lambda = 1$; 1.5 at $\lambda = 2$; and 3.5 at $\lambda = 4$).

unequivocally determine the damping factors $h(\lambda)$ defined by

$$h(\lambda) = \left[\frac{G_S(t, \lambda)}{G_S(t, \lambda \rightarrow 0)} \right] \quad (18.16)$$

with t spanning only the slow-mode region.

As indicated by Eq. (18.13), the damping factor is closely related to the strain dependence of the orientation tensor $\langle \mathbf{u}(t, \lambda) \mathbf{u}(t, \lambda) \rangle$ over the entropic region. As shown in Figs. 18.7–18.9, $\langle \mathbf{u}(t, \lambda) \mathbf{u}(t, \lambda) \rangle$ in the very early part of the entropic region, remains basically the same as it is right after the application of the step strain. In other words, the randomization of segmental orientation has hardly taken place during the fast-mode relaxation — namely, during the recoiling of segments back to the equilibrium length. Thus the obtained damping factors $h(\lambda)$ can be approximated by the function $h_o(\lambda)$ calculated from the initial orientation caused by the step strain via affine deformation:

$$h_o(\lambda) = \frac{g(\lambda)}{g(\lambda \rightarrow 0)} \quad (18.17)$$

with

$$g(\lambda) = \left\langle \frac{(u_x^o + \lambda u_y^o) u_y^o}{\lambda ((u_x^o + \lambda u_y^o)^2 + (u_y^o)^2 + (u_z^o)^2)} \right\rangle_{\mathbf{u}^o}. \quad (18.18)$$

Eq. (18.17) is simply the definition of the Doi–Edwards damping function with the independent-alignment approximation (Chapters 8 and 12). The damping functions of Doi and Edwards with and without the independent-alignment approximation both explain well the experimental results of a well-entangled nearly monodisperse polymer system (Fig. 9.2). Note that here the unit vector \mathbf{u}^o represents the orientation of a Fraenkel segment as opposed to the orientation associated with an entanglement strand or primitive step in the Doi–Edwards theory.

In Fig. 18.11, we compare the $h_o(\lambda)$ curve calculated numerically from Eq. (18.17) and the $h(\lambda)$ values determined by superposing the $G(t, \lambda)$ curves over the entropic region (Fig. 18.10). As the difference between $G_S(t, \lambda = 0.2)$ and $G_S(t, \lambda = 0.5)$ is very small and $h_o(\lambda = 0.2)$ is only 1% smaller than $h_o(\lambda \rightarrow 0)$, $G_S(t, \lambda = 0.2)$ has been used to substitute for $G_S(t, \lambda \rightarrow 0)$ which is designated in Eq. (18.16) for determining $h(\lambda)$ at different values of λ . As shown in the figure, $h_o(\lambda)$ basically describes the strain dependence of $h(\lambda)$.

It is interesting and important to note that the relaxation modulus over the entropic region in the entanglement-free Fraenkel-chain case and that in the entangled system have very different relaxation functional forms, while their dependences on orientation are similar — both can be quite well described by the damping function given by Eq. (18.17). The relaxation strength in the former case receives equal contributions from all normal modes (Eq. (7.58)) as opposed to being dominated by the lowest normal mode (Eq. (9.11)) in the latter case.

In Fig. 18.11, $h_o(\lambda)$ is also compared with the damping factor associated directly with the unit vector \mathbf{u} over the entropic region, $h_u(\lambda)$, defined by

$$h_u(\lambda) = \frac{\langle u_x(t, \lambda)u_y(t, \lambda) \rangle / \lambda}{[\langle u_x(t, \lambda)u_y(t, \lambda) \rangle / \lambda]_{\lambda \rightarrow 0}}. \quad (18.19)$$

More directly representing the segmental orientation, the $h_u(\lambda)$ values appear to have a closer agreement with $h_o(\lambda)$ than $h(\lambda)$. The small differences between $h_u(\lambda)$ and $h(\lambda)$ — less than 10% — merely reflect the

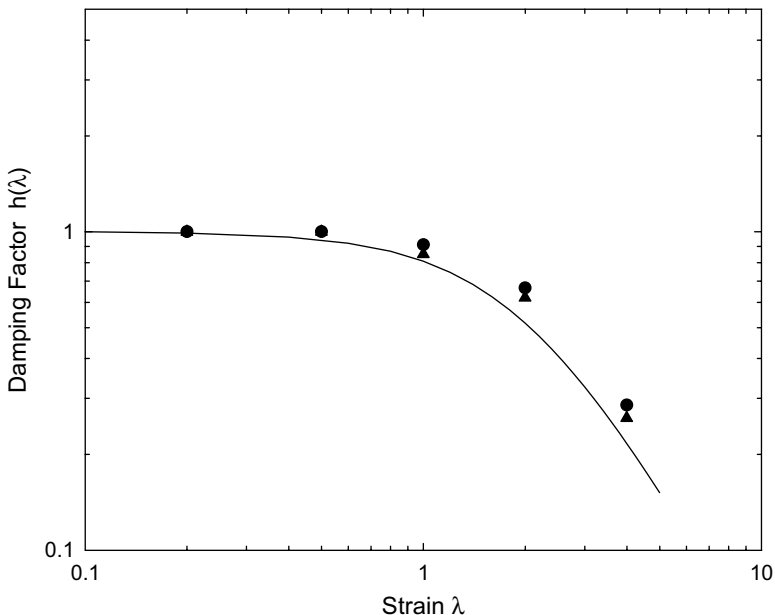


Fig. 18.11 Comparison of the damping factors $h(\lambda)$ (●) determined using Eq. (18.16) from simulations on the five-bead Fraenkel chain at different λ with the $h_o(\lambda)$ curve calculated numerically from Eqs. (18.17) and (18.18); also shown are the values of $h_u(\lambda)$ (▲) (Eq. (18.19)) obtained from the simulations.

small deviations of the proportional constant in Eq. (18.13) from a certain fixed value — such as 4 as used in Eq. (18.13) — at different strains. These small differences, which may arise from fluctuations in simulations or minor unaccounted-for effects, do not affect the basic physics that the slow mode is closely associated with the segmental orientation.

(c) Comparison of the first and second normal-stress differences

Experimentally the second normal-stress difference $N_2(t, \lambda)$ of a polymer is, in general, much smaller than the first normal-stress difference $N_1(t, \lambda)$; so is indicated by the comparison of the two obtained from the simulations as shown in Fig. 18.12. As pointed out above, as opposed to

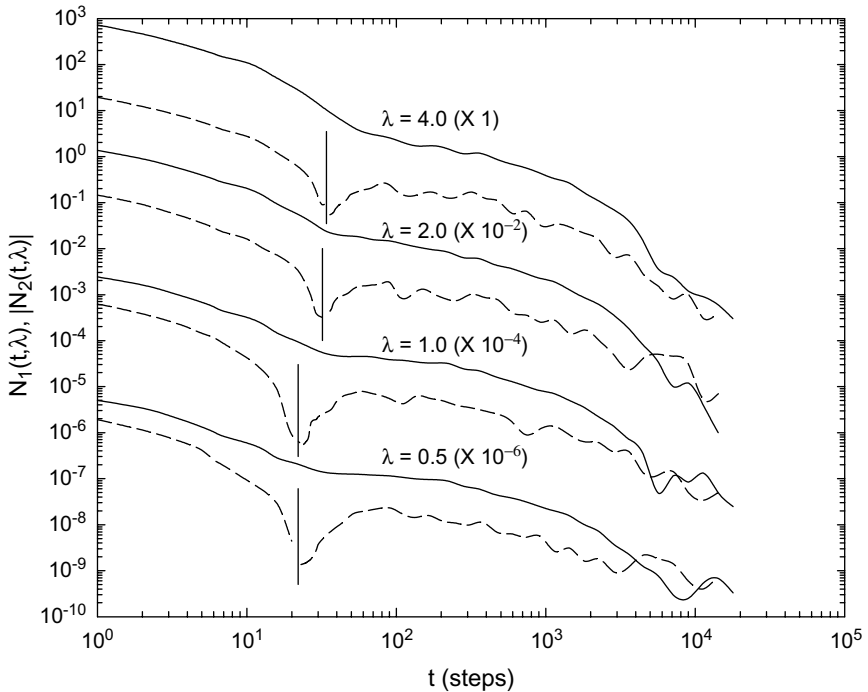


Fig. 18.12 Comparison of the $N_1(t, \lambda)$ (solid line) and $|N_2(t, \lambda)|$ (dashed line) results obtained from simulations on the five-bead Fraenkel chain at different strains ($\lambda = 0.5, 1, 2$ and 4); the vertical lines indicate the points where $N_2(t, \lambda)$ changes sign. To avoid overlapping between shown curves, the results at different λ values have been shifted along the vertical axis by the indicated factors.

$N_1(t, \lambda)$ being positive over the whole time range, $N_2(t, \lambda)$ is negative in the entropic region. Based on the understanding gained from the analysis given in Sec. 18.3, one may use birefringence measurements to determine the hard-to-obtain first and second normal-stress differences over the entropic region where the stress-optical rule is expected to be applicable. Interestingly, precisely in this way Osaki *et al.*²⁷ have carried out an experimental study on the stress relaxation of an entangled system. Making use of the stress-optical rule proven applicable in the rubbery (entropic) region, Osaki *et al.* studied the first and second normal-stress differences of an entangled nearly monodisperse polystyrene solution ($M_w = 6.7 \times 10^5$; 32.6% in Aroclor 1248) as a function of time over the terminal-mode region following a step shear deformation. The comparisons of their obtained first and second normal-stress differences over the terminal region are similar to the simulation results shown in Fig. 18.12 in several aspects. This may not be surprising as either the terminal mode of an entangled polymer system or the slow mode of an entanglement-free Fraenkel-chain system reflects the randomization of orientation — of the entanglement strands (or primitive steps) in the former case or of the segments in the latter case — as discussed above with respect to the damping factor. Despite the above-mentioned great difference in the relaxation functional form between the two different systems, their first and second normal-stress differences are of opposite sign in the same way and their $-N_2(t, \lambda)/N_1(t, \lambda)$ ratios have nearly the same values and λ dependence. Just as the damping function can be calculated from Eq. (18.17), the ratio $-N_2(t, \lambda)/N_1(t, \lambda)$ can be calculated as a function of λ from the Doi–Edwards expression with independent-alignment approximation (Eq. (12.17)). The calculated curve is compared with the simulation results and Osaki's experimental values in Fig. 18.13. Results of a well entangled nearly monodisperse polyisoprene melt consistent with those obtained by Osaki *et al.* have also been obtained by Olson *et al.* by means of birefringence measurements.²⁸ The simulation values of $-N_2(t, \lambda)/N_1(t, \lambda)$ being about 30% below the calculated curve should be mainly due to the mutual cancellation of the two effects — the positive effect ebbing while the negative effect rising — behind the $N_2(t, \lambda)$ changing sign upon entering the slow-mode region as discussed in Sec. 18.1. Such a mutual cancellation effect is indicated by the differences between $|N_2(t, \lambda)|$ and the corresponding orientation tensor component given in Eq. (18.13) (multiplied by 4) in the time region right before and after the point where $N_2(t, \lambda)$ changes sign as shown in Fig. 18.9.

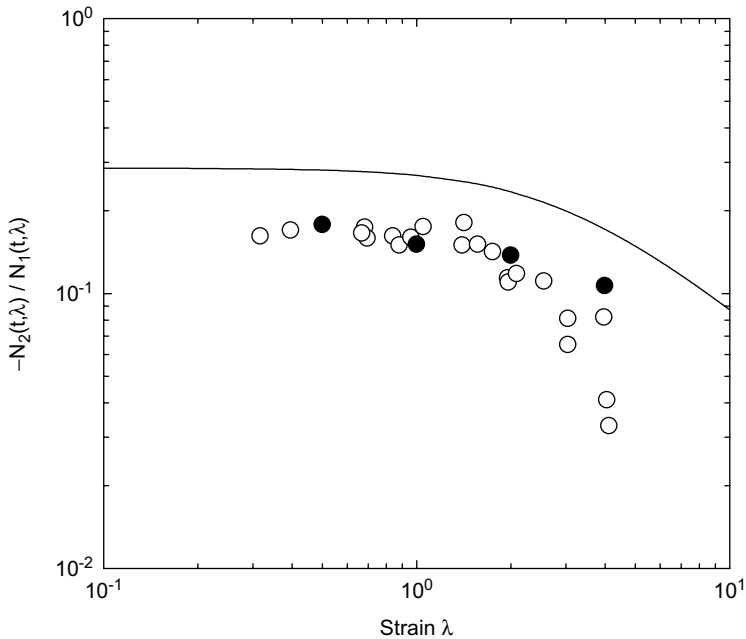


Fig. 18.13 Comparison of the simulation values (\bullet) of $-N_2(t, \lambda)/N_1(t, \lambda)$ in the slow-mode region obtained from the present study and the experimental values (\circ) in the terminal region of the entangled system studied by Osaki *et al.* with the curve (solid line) numerically calculated from the Doi–Edwards expression (Eq. (12.17)) with the independent-alignment approximation.

(d) *The observation of the Lodge–Meissner relation*

Based on the Lodge–Meissner relation being applicable over the whole time range and the stress-optical rule in the slow-mode region, the relation $(2 \cot 2\chi)/\lambda = 1$ (Appendix 18.B) is predicted to hold over the slow-mode region in the entanglement-free Fraenkel-chain case. The same relation has also been clearly observed by Osaki *et al.* over the terminal-mode region. In other words, in their studied entangled system, both the stress-optical rule and the Lodge–Meissner relation hold over the entropic (terminal-mode) region.

Simulations of the entanglement-free Fraenkel-chain model and experiments of an entangled system studied by Osaki *et al.* have been compared with respect to the damping factor, the ratio $-N_2(t, \lambda)/N_1(t, \lambda)$ and the Lodge–Meissner relation over the entropic region. As revealed, the sameness or close similarity in magnitudes and behaviors between the two

sets of results represents the great similarities between the slow mode of the entanglement-free Fraenkel-chain model and the terminal mode of the entangled polymer system. These shared properties and behaviors also suggest that the revealed close correlation of the slow mode or the terminal mode as well as its entropic nature with orientation anisotropy — as of the Fraenkel segments or the primitive steps in the Doi–Edwards model — is generally valid in polymer viscoelasticity.

18.5 A Final Note

In Chapter 17, it is shown that the Rouse and Fraenkel chains with the same number of beads, N , describe virtually equally successfully the slow entropic mode of the relaxation modulus of an entanglement-free system. In Chapter 18, it is shown that the entropic nature of the slow mode as well as the ordinarily observed (rubbery) stress-optical rule is due to the segmental orientation anisotropy. In sharp contrast with the picture revealed in these studies, the Gaussian chain model has been assumed in the molecular theories studied in this book (Chapters 2, 3, 6–9 and 12) and traditionally used to explain the stress-optical rule.^{6,10,11} However, the two models or pictures need not be regarded as mutually exclusive: as the polymer is sufficiently long, the chain statistics becomes Gaussian due to the central limit theorem, which is confirmed by the polymer conformation studies. In the first twelve chapters, the studies, both theoretical and experimental, mainly focus on the viscoelastic behaviors corresponding to length scales above and slightly below the entanglement distance. As these length scales are sufficiently large for the Gaussian chain statistics to be valid or at least nearly valid^{29–31} allowing us to develop molecular theories and obtain their analytical solutions, which would otherwise be unfeasible if not impossible. In this practical sense, the newly revealed effects or mechanisms can be viewed as extending the range of rubbery elasticity and applicability of the Rouse theory and the stress-optical rule to polymer chains too short to be regarded as Gaussian chains.

Appendix 18.A — Proof of The Lodge–Meissner Relation as Applied to the Fraenkel-Chain Model

If one proves

$$\langle \delta(\lambda) \left((u_x^o)^2 - (u_y^o)^2 + \lambda u_x^o u_y^o \right) \rangle_{\mathbf{u}^o} = 0, \quad (18.A.1)$$

then Eq. (18.6) becomes Eq. (18.7). In the expression obtained by substituting Eq. (17.4) into Eq. (18.A.1), the first term is zero as $\langle (u_x^o)^2 - (u_y^o)^2 + \lambda u_x^o u_y^o \rangle_{\mathbf{u}^o} = 0$ for the reason of symmetry; thus, Eq. (18.A.1) is true if

$$A(\lambda) = \left\langle \frac{(u_x^o)^2 - (u_y^o)^2 + \lambda u_x^o u_y^o}{\sqrt{(u_x^o + \lambda u_y^o)^2 + (u_y^o)^2 + (u_z^o)^2}} \right\rangle_{\mathbf{u}^o} \quad (18.A.2)$$

is zero for all values of λ . Both the numerator and denominator of Eq. (18.A.2) contain even and odd terms with respect to the transformation $u_x^o \rightarrow -u_x^o$ or $u_y^o \rightarrow -u_y^o$. The averaging over all orientations of \mathbf{u}^o is invariant to a rotation of the coordinate system. The way to show $A(\lambda) = 0$ is to perform an orthogonal transformation on Eq. (18.A.2) making its denominator contain only even terms. This is done by first finding the principal axes of the quadratic form inside the square root sign, which is simply $\mathbf{u}^o \cdot \mathbf{C} \cdot \mathbf{u}^o$ with \mathbf{C} being the Cauchy tensor. With \mathbf{C} represented by a matrix C :

$$C = \begin{pmatrix} 1 & \lambda & 0 \\ \lambda & 1 + \lambda^2 & 0 \\ 0 & 0 & 1 \end{pmatrix} \quad (18.A.3)$$

and the unit vector \mathbf{u}^o represented by a column U :

$$U = \begin{pmatrix} u_x^o \\ u_y^o \\ u_z^o \end{pmatrix}, \quad (18.A.4)$$

one may write

$$\mathbf{u}^o \cdot \mathbf{C} \cdot \mathbf{u}^o = U^T C U. \quad (18.A.5)$$

Expressing the unit vector \mathbf{u}^o with respect to the principal axes as

$$U' = \begin{pmatrix} u'_x \\ u'_y \\ u'_z \end{pmatrix}, \quad (18.A.6)$$

the orthogonal transformation is given by

$$U = S U' \quad (18.A.7)$$

with

$$S = \begin{pmatrix} \cos \alpha & -\sin \alpha & 0 \\ \sin \alpha & \cos \alpha & 0 \\ 0 & 0 & 1 \end{pmatrix} \quad (18.A.8)$$

where $\cos \alpha = \sqrt{2/(\mu + \lambda\mu^{1/2})}$ and $\sin \alpha = (\lambda + \mu^{1/2})/\sqrt{2(\mu + \lambda\mu^{1/2})}$ with $\mu = \lambda^2 + 4$. In terms of u'_x , u'_y and u'_z , Eq. (18.A.2) is expressed by

$$A(\lambda) = \left\langle \frac{-\sqrt{\mu}u'_x u'_y}{\sqrt{q_1(u'_x)^2 + q_2(u'_y)^2 + q_3(u'_z)^2}} \right\rangle_{\mathbf{u}'} \quad (18.A.9)$$

where q_1 , q_2 and q_3 are the three eigenvalues of C :

$$q_1 = \frac{\mu - 2 + \lambda\sqrt{\mu}}{2} \quad (18.A.10)$$

$$q_2 = \frac{\mu - 2 - \lambda\sqrt{\mu}}{2} \quad (18.A.11)$$

$$q_3 = 1. \quad (18.A.12)$$

While the denominator of Eq. (18.A.9) contains only even terms, the numerator contains just an odd term. Thus, $A(\lambda) = 0$ for all λ leading to the conclusion that the Lodge–Meissner relation $G_S(t, \lambda) = G_{\Psi_1}(t, \lambda)$ holds.

Appendix 18.B — The Stress-Optical Rule in the Case of Simple Shear

In the case of simple shear, the stress tensor of a polymer system is in general expressed as

$$\boldsymbol{\tau} = \begin{pmatrix} \tau_{xx} & \tau_{xy} & 0 \\ \tau_{yx} & \tau_{yy} & 0 \\ 0 & 0 & \tau_{zz} \end{pmatrix}. \quad (18.B.1)$$

The shear stress τ_{xy} and the normal stress differences: $N_{1\text{st}} = -(\tau_{xx} - \tau_{yy})$ and $N_{2\text{nd}} = -(\tau_{yy} - \tau_{zz})$ can be obtained by measuring the birefringence of the studied system. The measured optical properties are converted into τ_{xy} , $N_{1\text{st}}$ and $N_{2\text{nd}}$ through the stress-optical rule. One measures two birefringence quantities Δn_{xy} and Δn_{xz} corresponding to two mutually perpendicular cross sections (refractive index ellipses) of the refractive index ellipsoid, and the extinction angle χ , which defines the orientation of the

ellipse corresponding to Δn_{xy} . The stress-optical rule states that the birefringence Δn_{xy} is linearly proportional to the difference between the two principal stresses in the xy plane and the orientation of the optical axis χ coincides with that of the principal stress axis χ' . Clearly, the z direction is one of the principal axes of the stress tensor given by Eq. (18.B.1). The two principal axes in the xy plane can be found by the transformation (a rotation around the z axis) that diagonalizes the 2×2 matrix:

$$T = \begin{pmatrix} \tau_{xx} & \tau_{xy} \\ \tau_{yx} & \tau_{yy} \end{pmatrix}. \tag{18.B.2}$$

The two eigenvalues (principal stresses) of T are found to be

$$p_1 = \frac{\tau_{xx} + \tau_{yy} + \sqrt{\alpha}}{2} \tag{18.B.3}$$

$$p_2 = \frac{\tau_{xx} + \tau_{yy} - \sqrt{\alpha}}{2} \tag{18.B.4}$$

where $\alpha = m^2 + 4\tau_{xy}^2$ with $m = \tau_{xx} - \tau_{yy}$. And the transformation is represented by the matrix:

$$S = \begin{pmatrix} \cos \chi' & -\sin \chi' \\ \sin \chi' & \cos \chi' \end{pmatrix} \tag{18.B.5}$$

where $\cos \chi' = \tau_{xy} / \sqrt{(\alpha - m\alpha^{1/2})/2}$ and $\sin \chi' = (\alpha^{1/2} - m) / \sqrt{2(\alpha - m\alpha^{1/2})}$; and χ' denotes the orientation angle of the stress ellipse. The difference between the two principal stresses in the xy plane is given by

$$\Delta p = p_1 - p_2 = \sqrt{\alpha}. \tag{18.B.6}$$

Using Eq. (18.B.6), one obtains

$$\sin 2\chi' = 2 \sin \chi' \cos \chi' = \frac{2\tau_{xy}}{\sqrt{\alpha}} = \frac{2\tau_{xy}}{\Delta p}, \tag{18.B.7}$$

$$\cos 2\chi' = \cos^2 \chi' - \sin^2 \chi' = \frac{m}{\sqrt{\alpha}} = \frac{\tau_{xx} - \tau_{yy}}{\Delta p} \tag{18.B.8}$$

and thus,

$$\tan 2\chi' = \frac{\sin 2\chi'}{\cos 2\chi'} = \frac{2\tau_{xy}}{\tau_{xx} - \tau_{yy}} \tag{18.B.9}$$

When the stress-optical rule holds,

$$\Delta n_{xy} = C\Delta p \tag{18.B.10}$$

$$\chi = \chi' \tag{18.B.11}$$

where C is the stress-optical coefficient, which should be predetermined. Using Eqs. (18.B.10) and (18.B.11), one obtains from Eqs. (18.B.7) and (18.B.8), respectively:

$$\tau_{xy} = \frac{\Delta p}{2} \sin 2\chi' = \frac{\Delta n_{xy}}{2C} \sin 2\chi \quad (18.B.12)$$

$$-N_{1st} = \tau_{xx} - \tau_{yy} = \Delta p \cos 2\chi' = \frac{\Delta n_{xy}}{C} \cos 2\chi. \quad (18.B.13)$$

As τ_{xy} is relatively easy to measure, Eq. (18.B.12) is often used to check the validity of the stress-optical rule and determine the value of C .

When the Lodge–Meissner rule is applicable,

$$-N_{1st} = \tau_{xx} - \tau_{yy} = \lambda \tau_{xy}. \quad (18.B.14)$$

Using Eqs. (18.B.14) and (18.B.11), Eq. (18.B.9) is rewritten as

$$2 \cot 2\chi / \lambda = 1 \quad (18.B.15)$$

According to Eq. (18.B.15), the extinction angle of the birefringence, χ , is solely determined by the step strain applied initially and remains the same (independent of time) as long as the Lodge–Meissner rule holds.

Both Δn_{xy} and χ are measured with a light beam directed perpendicular to the xy plane. Using the third relation of the stress-optical rule,

$$\Delta n_{xz} = -C(N_{1st} + N_{2nd}), \quad (18.B.16)$$

the second normal stress difference can be calculated from the difference between the principal values of the refractive index ellipse Δn_{xz} on the shear plane (the xz plane) — measured with a light beam directed perpendicular to the shear plane.

References

1. Lin, Y.-H., and Das, A. K., *J. Chem. Phys.* **126**, 074902 (2007).
2. Lin, Y.-H., *Macromolecules* **19**, 168 (1986).
3. Lin, Y.-H., and Juang, J.-H., *Macromolecules* **32**, 181 (1999).
4. Lin, Y.-H., *J. Phys.: Condens. Matter* **19**, 466101 (2007).
5. Lin, Y.-H., and Das, A. K., *J. Chem. Phys.* **126**, 074903 (2007).
6. Doi, M., and Edwards, S. F., *The Theory of Polymer Dynamics*, Oxford Univ. Press (1986).
7. McQuarrie, D. A., *Statistical Mechanics*, Harper & Row, New York (1976).
8. Lodge, A. S., and Meissner, J., *Rheol. Acta* **11**, 351 (1972).

9. Berne, B. J., and Pecora, R., *Dynamic Light Scattering*, John Wiley, New York (1976).
10. Kuhn, W., *Kolloid Z.* **68**, 2 (1934); Kuhn, W., and Grun, F., *Kolloid Z.* **101**, 248 (1942); Kuhn, W., *J. Polym. Sci.* **1**, 360 (1946).
11. Janeschitz-Kriegl, H., *Adv. Polym. Sci.* **6**, 170 (1969).
12. Inoue, T., Okamoto, H., and Osaki, K., *Macromolecules* **24**, 5670 (1991).
13. Inoue, T., Hayashihara, H., Okamoto, H., and Osaki, K., *J. Polym. Sci., Polym. Phys. Ed.* **30**, 409 (1992).
14. Inoue, T., and Osaki, K., *Macromolecules* **29**, 1595 (1996).
15. Osaki, K., Inoue, T., Hwang, E.-J., Okamoto, H., and Takiguchi, O., *J. Non-Cryst. Solids* **172-174**, 838 (1994).
16. Doi, M., *J. Polym. Sci., Polym. Phys. Ed.* **18**, 1005 (1980).
17. Lin, Y.-H., *J. Rheol.* **29**, 605 (1985).
18. Lin, Y.-H., *J. Non-Newtonian Fluid Mech.* **23**, 163 (1987).
19. Doi, M., and Edwards, S. F., *J. Chem. Soc., Faraday Trans. 2* **74**, 1789 (1978); **74**, 1802 (1978).
20. Lin, Y.-H., *Macromolecules* **17**, 2846 (1984).
21. Lin, Y.-H., *Macromolecules* **19**, 159 (1986); **20**, 885 (1987).
22. Osaki, K., and Kurata, M., *Macromolecules* **13**, 671 (1980).
23. Osaki, K., Nishizawa, K., and Kurata, M., *Macromolecules* **15**, 1068 (1982).
24. Vrentas, C. M., and Graessley, W. W., *J. Rheol.* **26**, 359 (1982).
25. Lin, Y.-H., *J. Rheol.* **28**, 1 (1984).
26. Pearson, D. S., *Rubber Chem. Tech.* **60**, 439 (1987).
27. Osaki, K., Kimura, S., and Kurata, M., *J. Polym. Sci.: Polym. Phys. Ed.* **19**, 517 (1981).
28. Olson, D. J., Brown, E. F., and Burghardt, W. R., *J. Polym. Sci.: Part B: Polym. Phys.* **36**, 2671 (1998).
29. Wignall, G. D., Schelten, J., and Ballard, D. G. H., *J. Appl. Cryst.* **7**, 190 (1974).
30. Ballard, D. G. H., Rayner, M. G., and Schelten, J., *Polymer* **17**, 349 (1976).
31. Norisuye, T., and Fujita, H., *Polym. J.* (Tokyo) **14**, 143 (1982).

This page intentionally left blank

Index

- affine deformation, 20, 142, 245, 344, 386, 399
- α relaxation, *see* structural relaxation
- binary blends, 234–240
- binomial random walk, 46–49
 - relation to diffusion constant, 48
- birefringence, 267, 280, 396, 402, 406–408
- blend solutions
 - entangled, 215–225, 234–236, 240, 263
 - entanglement-free, 226–228
 - onset of entanglement, 226–233
- blending law, 183
 - basic form for a binary blend, 238, 239
 - linear-additivity rule for a nearly monodisperse system, 183, 184, 186, 240
- Boltzmann’s superposition principle, 57, 58
 - equivalence to generalized Maxwell equation, 57, 58
- breakdown of Stokes–Einstein relation (BSE), 331
 - basic mechanism shared with thermorheological complexity, 331, 332, 336–338
- Brownian motion, 28–33, 40, 43, 44, 49, 98, 122, 138, 156, 158, 177, 329, 397
 - see* binomial random walk, diffusion equation, ERT, Langevin equation, Monte Carlo simulations of stress relaxation, reptational motion of the primitive chain, Rouse theory, Smoluchowski equation
- BSE, *see* breakdown of Stokes–Einstein relation
- Cauchy tensor, 87, 89, 90, 113, 405
 - simple shear, 90
 - solid-body rotation, 90
 - uniaxial extension, 89
- central limit theorem, 5–7
 - applications, 11, 46, 48, 258, 329, 332, 337, 404
- chain dynamics
 - summary views at different length scales, 26, 27
 - see* chain-tension relaxation, diffusion constant, Doi–Edwards theory, ERT, glassy relaxation, Monte Carlo simulations of stress relaxation, Rouse theory, time-correlation function
- chain tension, *see* equilibrium tensile force
- chain tension in a Gaussian chain between two fixed points, 150
- chain-tension relaxation
 - comparison of theory and experiment, 252, 254, 255
 - Doi’s model, 243–248
 - incorporated with ERT, 248, 249

- characteristic function, 4–6, 10, 47
- characteristic ratio, *see* ratio of mean square end-to-end distance to molecular weight
- codeformational (convected) time
 - derivative, 103, 113
- complex modulus, 65
- complex viscosity, 63
- configurational distribution functions
 - elastic dumbbell in homogeneous flow, 101
 - freely jointed chain, 8, 10
 - Gaussian chain, 12
 - Rouse chain in homogeneous flow, 122
- connector force, 100, 106, 345, 350, 382
- constitutive equations
 - convected Maxwell model, 113
 - Doi–Edwards theory, 135
 - elastic dumbbell model, 104–109
 - neo-Hookean material, 90
 - Newtonian fluid, 93
 - objectivity or admissibility of, 115, 116, 118
 - Rouse model, 127, 128, 347, 348
- contour length, *see* primitive chain
- contour length fluctuation, *see* primitive chain
- contravariant component, 115
- convected base vector, 114, 115
- convected coordinate, 109, 114
- convected Maxwell model, 113
 - generalized, 113
- convected time derivative, *see* codeformational time derivative
- creep compliance, 71–73
 - calculation from $G(t)$, 72, 73, *see* also Hopkins–Hamming Method
 - full-range line-shape analysis of polystyrene melt(s)
 - entangled (with ERT as the reference frame), 271–286
 - entanglement-free (with Rouse theory as the reference frame), 272, 273, 286–294
 - fictional factors K'
 - extracted, 279, 291, 308
 - glassy-modulus values
 - extracted, 274
 - stretching parameters of the glassy-relaxation process extracted, 274
 - structural-growth
 - parameters extracted, 279, 282, 291, 307
 - structural-relaxation times
 - extracted, 279, 291, 306
 - smearing effect, 284–286
- creep measurement, 68, 71
- critical molecular weight M_c , 61, 62
 - see* entanglement molecular weight
- critical molecular weight M'_c , 69, 70
 - see* entanglement molecular weight
- curvilinear diffusion constant, *see* primitive chain
- damping factor (or function) of
 - entangled system, 153, 250
 - based on independent alignment approximation, 155, 250
 - comparison of theory and experiment, 154, 155, 250–254
 - Doi–Edwards model, 144, 145, 155
 - effect on flow curve, 255
 - universality of, 154, 155
- damping factor of entanglement-free Fraenkel chain system, 398–400
 - comparison with independent alignment approximation, 400
 - relation with segmental orientation, 400
- deformation gradient tensor, 84, 113, 142, 171, 243–245, 388
 - simple shear, 86, 145, 344
 - solid-body rotation, 86
 - uniaxial extension, 84–86

- diffusion constant, 29, 48, 342
 comparison with viscoelastic results in terms of ERT, 205–210
 Doi–Edwards theory, 138–140
 reciprocal relation to the frictional factor, 329, 330
 Rouse model, 35, 45
 translational diffusion
 enhancement factor, 331–333, 336–338
see binary random walk, curvilinear diffusion constant, Einstein relation
- diffusion equation, 28–30, 48, 49
- Dirac delta function, 3, 13–15
- displacement function, 110, 111, 113
- Doi’s equation of steady-state compliance, 166
- Doi’s equations of viscosity, 166
- Doi’s equation of chain-tension relaxation, 247, 248
- Doi–Edwards theory, 133–150
 diffusion constant, 140, 205
 (pure) reptation time, 148, 149
 stress tensor, 141
 viscoelastic-quantity equation, 149, 150
see curvilinear diffusion constant, damping factor, ERT, primitive chain, slip-link picture
- dyadic product, 96
- dynamic (or motional) anisotropy
 as related to T_g correction, 194, 201, 298–301, 308–311
 $K'/K > 1$ for $M > M_e$ and $K'/K \rightarrow 1$ as $M \rightarrow M_e$, 194, 298–301
 (normalized-)molecular-weight dependence of K'/K in polystyrene, 193, 219
 relevance of the ratio $R_K = K'/K$, 272, 278, 281, 298–303, 310, 317, 318, 328, 329
see frictional factor, K'
- dynamic-mechanical spectroscopy, 61
- Einstein relation, 29, 138
- elastic dumbbell model, 98–113
 constitutive equation, 109
- end-to-end vector
 of freely jointed chain, 7–9
see mean square end-to-end distance, time correlation function
- energetic region (in $G(t)$), 163, 211–213, 258, 267, 269
 figures showing partition into energetic and entropic regions, 283, 285, 314, 315
 of Fraenkel chains, *see* Monte Carlo simulations of stress relaxation
see glassy relaxation
- entanglement
 onset concentration, 226, 230
 onset molecular weight, 231–233
 onset of, 202, 203, 226–233
see Doi–Edwards theory ERT, slip-link picture
- entanglement distance, a , 137, 138, 169, 179, 216, 257–264, 404, *see* tube diameter
 as an internal yardstick, 313
 number of entanglement strands per a^3 , n_t , 257–266
 basis and support for n_t being a universal constant, 259–262
 values of various flexible linear polymers, 260–262
- entanglement molecular weight M_e , 24, 134, 137, 216, 259, 278
 as used to normalize molecular weight in ERT, 160–166
 concentration dependence, 216–225, 240, 263
 determination from plateau modulus, 24, 134, 192, 216, 259, 263

- effective value in binary blend, 185, 234, 237, 238
- equivalence to onset molecular weight of entanglement, 230–233
- relation to critical molecular weight M_c
 - experiment and ERT, 198–202, 208, 209
- relation to critical molecular weight M'_c
 - experiment and ERT, 203, 204
- values of various flexible linear polymers, 260–262
- entanglement strand, 136–138, 141–148
 - orientation, 144–148, 243–247, 397, 399, 402
 - Rouse motions of, *see* Rouse–Mooney model
 - tensile force, 141, 142, 397
 - see* entanglement distance, primitive step
- entropic force constant, 100, 103
- entropic region (in $G(t)$), 72, 73, 130, 159, 163, 211–213, 258, 267, 269–273, 280
 - figures showing partition into energetic and entropic regions, 283, 285, 314, 315
 - region of the entropy-driven mode in Fraenkel chains, *see* Monte Carlo simulations of stress relaxation
- equilibrium tensile force, *see* primitive chain
- ERT, *see* extended reptation theory
- extended reptation theory (ERT), 153–180, 201–211, 217, 218
 - consistency with Rouse theory, 218–225, 233, 272, 309, 318, 320
 - equivalence between K and K'' , *see* frictional factor K''
 - universality in, 164–166
 - validity of the theory, 209
 - viscoelastic-quantity equation, 158, 160, 161, 163, 164, 166, 175
 - see* creep compliance, relaxation modulus, structural factors of relaxation times, viscoelastic spectrum
- Fick's law, 28, 29
- fictitious tensile force, *see* equilibrium tensile force
- Finger tensor, 88–90, 92, 113, 114, 151
 - simple shear, 90
 - solid-body rotation, 90
 - uniaxial extension, 89
- flow curve, 255
- fluctuation–dissipation theorem
 - for relaxation modulus, 346, 353–357
 - general proof, 350–353
 - perfect validity in the Rouse chain model, 349
 - quasi-version in the Fraenkel chain model, 370
- fluid velocity field, 100
- forward recoil spectroscopy, 26, 205
- Fraenkel chain, 359
- Fraenkel segment, *see* segments in Fraenkel chains
- free-volume correction, *see* T_g correction
- freely jointed chain, 7–11, 17, 18, 137, 258, 259, 264, 266–268, 375, 376
- friction constant, 29, 99, 194, 201, 216, 224
- frictional factor, K
 - as normalization reference for the average glassy-relaxation time, 272
 - see* structural-growth parameter, thermorheological complexity

- definition, 38
- general temperature dependence, 40
- in relaxation-time functional forms, 38, 39, 128, 149, 158, 160, 164, 175
- in viscosity functional forms, 130, 150, 166
- molecular weight independence of K in entangled polystyrene melts (as analyzed in terms of ERT), 193, 209, 210
- K in the close neighborhood of T_g , 319
- frictional factor, K'
 - as normalization reference for the average glassy-relaxation time, 300
 - see* structural-growth parameter, thermorheological complexity
 - definition, 193, 218
 - universal dependence on $\Delta T = T - T_g$ in polystyrene, 308
 - see* dynamic anisotropy
- frictional factor, K''
 - definition, 218
 - equivalence between K and K'' , 219, 224, 272, 300, 318
- Gaussian chain, 8, 11–13, 27, 28, 404
 - entangled, 137, 138, 141, 156, 158, 243
 - entanglement-free, 33, 119
- generalized Maxwell equation, 56, 57
- Giesekus stress tensor, 108
- glass transition temperature, T_g (of polystyrene)
 - calorimetrically determined, 274, 299, 303
 - molecular-weight dependence, 299
 - defined by the structural-relaxation time $\tau_S = 1000$ sec, 274, 303–305
- glassy compliance, 281
- glassy modulus, 281
- glassy relaxation, 72, 163, 200, 211–213, 258, 269–322, 329–335, 359, 376, 381
 - average time, 272, 303, *see* structural-relaxation time
 - see* structural relaxation, internal viscosity
- homogeneous flow, 100, 103, 122
- Hookean solid, 53–55
- Hopkins–Hamming Method, 75, 76
- hypothetical tensile force, *see* equilibrium tensile force
- ideal gas as analogous to ideal rubber, 18, 24
- incompressible fluid, 93, 100
- independent alignment
 - approximation, 155, 244, 247, 249, 250, 399, 402, 403
- internal viscosity, 200, 290, 293, 321, 322
- Kohlrausch, Williams and Watts (KWW) function, 270–272
- Kramers matrix, 130
 - trace of, 131
- Kuhn segment, 9, 15, 258, 259, 263, 264, 266–268, 358, 359, 375, 376
 - see* freely jointed chain, persistence length, Rouse–Kuhn paradox
- Langevin equation
 - general form, 32, 33
 - of entanglement strand, 171–175
 - of particle in a harmonic potential, 42, 43
 - of primitive chain, 168, 169
 - of Rouse chain, 34–37, 43–45

- see* Monte Carlo simulations of stress relaxation
- Lodge–Meissner relation
 - experimental observation, 403
 - for Fraenkel-chain model, 382, 383
 - proof, 388–390, 404–406
 - for Rouse-chain model, 347–349
- loss modulus, 65, 67, *see* viscoelastic spectrum
- loss tangent, 65
- marker displacement technique, 205
- material time derivative, 117
- Maxwell equation, 52–55
- Maxwellian distribution, 106, 107
- mean square end-to-end distance, 9, 100, 112, 137, 177, 205, 259, 267
 - of entanglement strand, 259
 - see* ratio of mean square end-to-end distance to molecular weight
- memory function, 57, 351
- microstructure of polymer, 1, 2, 27, 163, 260–262, 269, 372, 375
- mobility matrix, 31, 34
- mobility tensor, 34
- modulus plateau, 59, 133, 134, 186, 187, 192, 224, 265
 - see* plateau modulus
- molecular weight of a chain strand
 - between two cross-links, 22
- moments of a stochastic variable, 3, 4
- Monte Carlo simulations of stress relaxation
 - Basic simulation scheme, 341–345
 - Fraenkel chain model, 358–379, 381–404
 - basis for the (rubbery) stress-optical rule, 394–396
 - comparison with experimental relaxation modulus, 372–375
 - comparison with Rouse theory, 360–362, 378, 379, 392
 - energy-driven mode, 361, 364, 368, 374, 375, 381, 382
 - entropy-driven mode, 361, 363, 368, 374, 375, 381, 391, 398
 - first normal stress difference, 383, 390–394, 401
 - quasi-version of fluctuation–dissipation theorem, 369, 370
 - ratio of the first and second normal stress differences, 401–403
 - resolution of Rouse–Kuhn paradox, 375, 376
 - second normal stress difference, 384, 392, 393, 395, 401, 403
 - similarity to entangled systems in nonlinear viscoelastic behavior, 396–404
 - simulations following the application of a step shear strain,
 - effects of nonlinearly enhanced tensile force, 382–387
 - initial values, 390–392
 - relation to segmental orientation, 391–395
 - simulations in equilibrium state, 360–368
 - correspondence between fluctuations and randomization of segmental orientation, 368–372
 - strain dependence, 383, 387, 391–395, 398–403

- see* damping factor,
 - segment in Fraenkel chain, independent alignment
 - approximation,
 - Lodge–Meissner relation
- Rouse chain model, 341–349
 - simulations following the application of a step shear strain, 344–349
 - simulations in equilibrium state, 346–349
 - comparison with theory, 347–349
 - validity of
 - fluctuation–dissipation theorem, 348, 349
- Virial theorem as tested in
 - Fraenkel dumbbell case, 376, 377
- neo-Hookean material, 90–92
- Newtonian fluid, 52, 54, 55, 92–94
- normal-stress difference, 82, 91, 92, 111, 112, *see* Monte Carlo simulation of stress relaxation
- normalized molecular weight
 - ratio K'/K as a function of, 219
 - relaxation strengths as a function of, 161
 - relaxation-time ratios as a function of, 161, 164, 178, 180, 253
 - viscoelastic quantities as a function of, 166
 - viscoelastic response-function
 - line shape as a function of, 160, 161, 163–165, 218, 219,
 - see* universality in polymer viscoelasticity
- number of entanglement strands per cubed entanglement distance, n_t , 257–266
 - concentration dependence of n_t , 263
 - persistence length, 15, 266, 267
 - plateau modulus, 134, 149, 182–184, 257, 259–265
 - concentration dependence of, 218, 223–225, 239
 - determination methods, 192
 - values of various flexible linear polymers, 260–262
 - plateau region, 154, 156, 161, 184–188, *see* modulus plateau
 - primitive chain, 135–138
 - contour length, 141, 143, 144, 147, 160
 - contour length fluctuation
 - dynamics, 156–161, 168–171
 - effect on reptation, 159–161, 248
 - effect on steady-state compliance, 166
 - effect on viscosity, 166
 - fluctuation amplitude, 157–161
 - curvilinear diffusion constant, 138–140
 - Langevin equation, 170
 - relation to translational diffusion constant, 140
 - relation to terminal relaxation time, 148, 159
 - relations to relaxation times at different length scales, 178
 - equilibrium tensile force, 136, 137, 141–143, 169, 247
 - reptational motion
 - with fixed contour length, 138–140, 143, 148,
 - with fluctuating contour length, 158, 159
 - segmental equilibrium time on, 142–144, 146, 148, 153, 156, 157, 160–162, 242, 244, 246, 247, 250
 - distinction between linear and nonlinear regions, 242

- primitive path, 136, 137, 147, 163, 168–170, 194, 242, 244, 299, 300, 320
 - see* primitive chain
- primitive step, 137, 139, *see* entanglement strand
 - length, *see* entanglement distance
 - orientation, 144, 147, 148, 397, 399, 402, 404
- probability distribution functions, 2–5
 - displacement of a random walk, 48
 - end-to-end vector of freely jointed chain, 10, 11, 18
 - freely jointed-chain segment, 7
 - vector between two beads in Gaussian chain, 13
- pure reptational time, 148, 149, 157–160, 179, 206
- random walk, *see* binomial random walk
- rate-of-strain, 52, 58
- rate-of-strain tensor, 92–94, 104, 107–109, 117, 118, 128
- ratio of mean square end-to-end distance to molecular weight, K_∞ , 205, 216, 257, 259, 263, 313
 - values of various flexible linear polymers, 260–262
- relative strain tensor, 109, 114, 128
- relaxation modulus in linear region, 58–60
 - comparison with relaxation modulus in nonlinear region, 154, 250, 255
 - Doi–Edwards theory, 149
 - elastic dumbbell model, 110
 - equation for binary blend, 238–240
 - equation for blend solution (linear combination of ERT and Rouse theory), 217, 218
 - experimental results, 60
 - extended reptation theory (ERT), 156–165, 217, 218
 - $\mu_A(t)$ process, 163, 175
 - $\mu_B(t)$ process, 158–161, 170, 171
 - $\mu_C(t)$ process, 159–161
 - $\mu_X(t)$ process, 162, 164, 177–180
 - line-shape analysis of polystyrene binary blends, 234–238
 - line-shape analysis of polystyrene blend solutions, entangled (in terms of the linear combination of ERT and Rouse theory), 218–225
 - entanglement-free (in terms of Rouse theory), 226–228
 - line-shape analysis of polystyrene melts, entangled (in terms of ERT), 186–197
 - Rouse theory, 129
 - see* Monte Carlo simulations of stress relaxation
- relaxation modulus in nonlinear region,
 - comparison of theory and experiment, 251–255
 - comparison with relaxation modulus in linear region, 154, 250, 255
 - theory (combination of ERT and Doi's equation of chain-tension relaxation), 243–249
 - see* chain-tension relaxation, damping function, Monte Carlo simulations of stress relaxation
- relaxation strength
 - of $\mu_B(t)$ process, 161
 - of $\mu_B^*(t, \mathbf{E})$ process, 248
 - of $\mu_C(t)$ process, 161

- of $\mu_X(t)$ process, 162
- relaxation time
 - see* frictional factor, structural factors of relaxation times
- relaxation-time distribution, 70, 212, 322–324
- rheological equation of state, *see* constitutive equation
- rod-climbing phenomenon, 92
- Rouse–Kuhn paradox, 267, 268, 358, 359
 - resolution of, *see* Monte Carlo simulations of stress relaxation
- Rouse matrix, 36, 121, 122, 130, 131
 - eigenvalues and eigenvectors, 40–42
 - inverse of, *see* Kramers matrix
 - trace of, 131
- Rouse–Mooney matrix, 172
 - eigenvalues and eigenvectors of, 176, 177
- Rouse–Mooney model
 - continuous model, 175
 - discrete model, of finite number of beads, 171–175
 - in ERT, 163
- Rouse segment,
 - connector potential, 34, 100
 - connector force, 100
 - mass, 38, 273
 - relation to the upper bound of rubbery (entropic) modulus, 164, 266, 267, 280
 - value for polystyrene, 192, 267, 280
 - motional time, 317
- Rouse-segment-based molecular theories, 28, 163, 213, 267, 269, 358, 359
- Rouse theory
 - consistency with ERT, 218–225, 233, 272, 300, 309, 318, 320
 - constitutive equation, 128
 - continuous model, 43–46
 - diffusion constant, 35, 45
 - discrete model, of finite number of beads, 33–38, 119–130
 - time-correlation function of the end-to-end vector, 38, 46, 344, 345
 - comparison of theory and experiment, 226–228, 231, 286–298
 - comparison of theory and simulations, 343–349
 - viscoelastic-quantity equations, 128–130
 - see* creep compliance, relaxation modulus, structural factors of relaxation times, viscoelastic spectrum
- rubber elasticity
 - analogy to ideal gas, 18, 24
 - entropy change, 17–23
 - equivalent expressions for, 151
 - modulus, 22
 - molecular theory, 18–22
- Schulz distribution, 186, 187
- segments in Fraenkel chains
 - connector potential, 359
 - connector force, 382
 - orientation anisotropy, 371, 381, 391–396, 399–401, 404
 - associated entropic nature (of the slow mode), 372, 375, 381, 391–396, 404
 - orientation fluctuation, 372, 375, 381
 - orientation randomization, 372, 381, 391–397, 399
 - tension fluctuation, 366, 371, 381
 - tension relaxation, 371, 381, 397
 - see* Monte Carlo simulations of stress relaxation
- self-diffusion constant, 205, *see* diffusion constant
- shear (deformation) rate, 52, 93
- shear strain, 53, 86
- shear viscosity, 93, *see* viscosity

- simple shear, 85, 86, 90, 93, 145, 246, 406
- slip-link picture, 134–146, 177–180
 - extended, 179–180
- slip-stick melt fracture (as related to chain dynamics) 253–256
- Smoluchowski equation
 - elastic dumbbell model in
 - homogeneous flow, 98–102
 - general form, 28–34
 - Rouse model in homogeneous flow, 122–126
- solid-body rotation, 86, 87, 90
- steady-state compliance, 65–71
 - comparison of experiment and ERT, 203, 204
 - comparison of Doi–Edwards theory, ERT and Rouse theory, 203
- Doi's equation, 166
- Doi–Edwards theory, 150
- experimental results, 70, 203
- ERT, 165, 166, 203, 204
- of an entanglement-free polystyrene sample
 - experimental and calculated values, 291
 - structural growth
 - parameter extracted from, 287, 288
 - temperature dependence (measured and calculated), 294
- Rouse theory, 129, 130
- steady-state shear flow, 60, 111, 129
- step strain or step deformation,
 - 57–59, 110, 142–146, 153, 171, 242–245, 344–346, 353–356, 368–372, 381–404
- stochastic variable, 2–6
- Stoke's law, 99, 338
- storage modulus, 65, 66, *see* viscoelastic spectrum
- stress-optical rule, 167, 267, 402, 403, 406–408
 - basis for, *see* Monte Carlo simulations of stress relaxation
- stress relaxation, *see* relaxation
 - modulus in linear region, relaxation
 - modulus in nonlinear region, Monte Carlo simulations of stress relaxation
- stress tensor, 79–82
 - bead-spring model, 127
 - contravariant component, 115
 - contravariant convected derivative, 117
 - Doi–Edwards model, 141–144
 - Doi's model, 243–248
 - elastic dumbbell model, 104–107
 - Giesekus expression, 108
 - Kramers expression, 107
 - molecular expression, 105, 106, 350
 - neo-Hookean material, 90
 - rubber network, 146, 151
 - symmetry of, 82
 - see* constitutive equation
- stretched exponential function, *see* Kohlrausch, Williams and Watts (KWW) function
- stretching parameter β , 271, 274, 301, 302, 334
- structural factors of relaxation times
 - Rouse modes, 38, 39, 128
 - pure reptation, 149
 - ERT processes
 - τ_A^p (Rouse–Mooney modes), 175
 - τ_B , 158
 - τ_C , 160
 - τ_X , 164, 178–180
 - chain tension relaxation, τ_B^* , 248
- structural-growth parameter s ,
 - 278–294, 298, 300, 301, 304, 328, 329
 - definition, 272, 304
- structural-growth parameter s' ,
 - 304–311, 316–318, 328–336
 - definition, 300, 301, 304

- universal dependence on
 - $\Delta T = T - T_g$ in polystyrene, 307
- values at different temperatures, 279, 291
- structural relaxation
 - length scale, 312–316, 335
 - universality in polystyrene, 305–310
 - deviations from universality at low molecular weights, 310, 311
 - see* glassy relaxation
- structural-relaxation time τ_S , 279, 291, 303–326, 328–338
 - definition, 303, 304
 - universal dependence on
 - $\Delta T = T - T_g$ in polystyrene, 305, 306
- tensile viscosity, 94
- tensor, 81
 - operations, 94
 - see* Cauchy tensor, deformation, gradient tensor, Finger tensor, stress tensor
- terminal process or region, 153–155, 163, 182, 183, 185, 187, 192, 206, 224, 234–237, 248–253, 259, 280, 286, 290, 326, 396, 397, 402–404
- T_g correction, 199–202, 208, 233, 300, 305–322, 328, 329, 332, 333
- thermo-elastic inversion effect, 17
- thermorheological complexity (TRC), 215, 269–322
 - basic mechanism, 328–338
 - shared with the breakdown of Stokes–Einstein relation (BSE), 331, 332, 336–338
 - characterization in terms of the structural-growth parameter, 282–284
 - comparison of the TRC and BSE results, 332, 333
 - temporal unevenness, 283–286
- thermorheological simplicity, *see* time–temperature superposition principle
- θ solutions, 39, 260
- time-correlation function
 - form for relaxation modulus, 350–357
 - of particle in a harmonic potential, 43
 - of end-to-end vector of a Rouse chain, 38, 39, 46
 - Monte Carlo simulation, 343–345
 - of primitive-chain contour-length fluctuation, 158, 168–171
- time (or frequency)–temperature superposition principle, 159, 215, 269, 270
 - failure of, *see* thermorheological complexity
- topological interactions, *see* entanglement
- tracer diffusion constant, 205, 206
- transition region (I) (from glasslike to rubberlike consistency), 167, 168
- transition region (II), 153, 154, 163, 167, 168
- translational diffusion, *see* diffusion
- TRC, *see* thermorheological complexity
- Trouton’s rule, 94
- tube diameter, 136, 137, 183–186, 194, 216
 - see* entanglement distance, entanglement molecular weight, tube dilation
- tube model, *see* primitive chain
- tube stress, 156–160, 185, 249
- tube-dilation, 184–186, 217, 234–239
- tube-renewal process, 239
- uniaxial extension, 19, 84–86, 89, 91, 93
- unit dyad, 81
- universal constant, n_t , 259–262
- universality in glass transition-related dynamics, 305–310

- deviations from (at low molecular weights), 310, 311
- universality in polymer viscoelasticity, 27, 62, 154, 155, 251, 259–262
 - in terms of ERT, 160–167, 182, 183, 186–211, 217–225
- velocity distribution function, 106
- velocity field, 100
- velocity gradient tensor, 100, 355
- virial theorem, 366–368, 375–377
- viscoelastic response functions, 58, 65, 71, 74, 269, 351
 - see* relaxation modulus,
 - viscoelastic spectrum, creep compliance
- viscoelastic spectrum, 65–67, 74
 - full-range line-shape analysis of entanglement-free polystyrene melts (with Rouse theory as the reference frame), 294–298
 - structural-growth parameters extracted, 307
 - structural-relaxation times extracted, 306
 - frictional factors $K' = K$ extracted, 308
- line-shape analysis of polystyrene blend solutions
 - entangled (in terms of the linear combination of ERT and Rouse theory), 220–225
 - entanglement-free (in terms of Rouse theory), 226–228
 - for probing onset of entanglement, 228–231
- line-shape analysis of polystyrene melts
 - entangled (in terms of ERT), 186–197
 - entanglement-free (in terms of Rouse theory), 231
 - for probing onset of entanglement, 231, 232
- viscosity
 - comparison of Doi–Edwards theory, ERT, and Rouse theory, 199–203
 - comparison of experiment and ERT, 198–203, 207, 209, 210
 - comparison of viscosity and diffusion data in terms of ERT, 205–210
 - Doi–Edwards theory, 150
 - Doi’s equations, 166
 - elastic dumbbell model, 111
 - ERT, 165, 166
 - experimental results, 62
 - of an entanglement-free polystyrene melt
 - enhancement due to glassy relaxation, 290–293
 - experimental and calculated values, 291
 - Rouse theory, 129, 130
 - 3.4 power law, 62
 - 3.4 power law as explained by ERT, 199, 202
- Vogel–Tammann–Fulcher (VTF) equation, 40
 - data fitted to the VTF equation, 293, 304–308, 317, 319, 320
 - data fitted to a modified VTF equation, 282, 305–307, 333
- Williams–Landel–Ferry (WLF) equation, 40, 293
- worm-like chain, 15
- Young’s modulus, 91, 92, 94, 266
- zero-shear viscosity, *see* viscosity